INTELLIGENT MATERIAL SYSTEMS LAB

UNIVERSITÄT DES SAARLANDES

Shape Memory Alloy Modeling and Simulation Tool for Elastocaloric Systems

Dissertation

zur Erlangung des Grades des
Doktors der Ingenieurwissenschaften (Dr.-Ing.)
der Naturwissenschaftlich-Technischen Fakultät der
Universität des Saarlandes

von
M.Sc. Felix Ulrich Welsch

Saarbrücken
2025

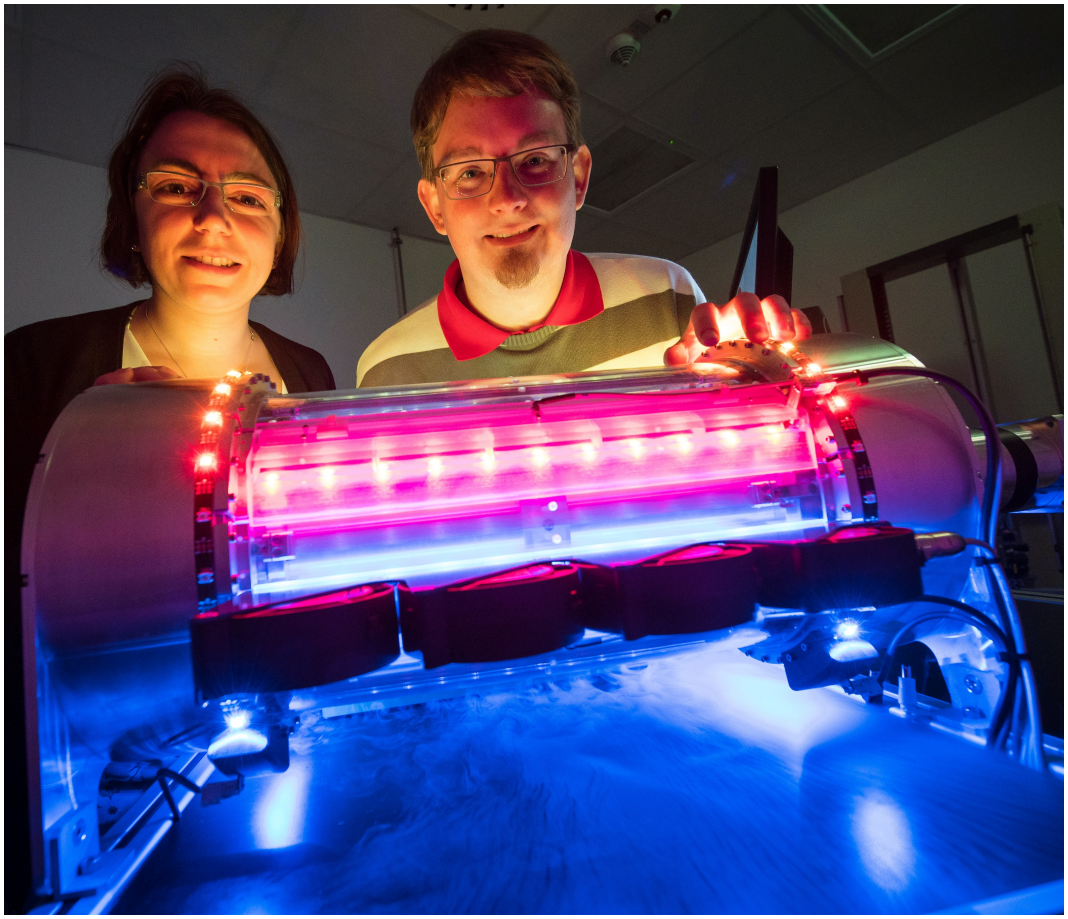

Tag des Kolloquiums:	10.09.2025
Dekan:	Prof. Dr.-Ing. Dirk Bähre
Berichterstatter:	Prof. Dr.-Ing. Stefan Seelecke Prof. Dr.-Ing. Stefan Diebels
Akad. Mitglied:	Dr.-Ing. Oliver Maurer
Vorsitz:	Prof. Dr.-Ing. Matthias Nienhaus

Contents

Abstract

Solid-state cooling is an environmentally friendly, no global warming potential alternative to vapor compression-based systems. Elastocaloric (EC) cooling based on Nickel–Titanium (NiTi) shape memory alloys (SMAs) exhibits excellent heating and cooling capabilities. Because of the high specific latent heat activated by mechanical loading and unloading, large temperature changes can be generated in the material. The small required mechanical work input enables a high coefficient of performance (COP).
Recently, a fully functional and illustrative continuous operating EC air heating and cooling system based on SMA was developed and realized. The heat pump (HP) device operates with a novel rotary drive concept using numerous tensile-loaded wire bundles. To assist the design process of an optimized device with given performance and efficiency requirements, a fully coupled thermo-mechanical system-level simulation tool is required. The simulation tool of the multi-element EC HP system is based on a physics motivated SMA model and implemented in MATLAB. This compact simulation tool is qualified for massively parallel computation on modern multi-core computers, which allows fast and comprehensive parameter scans.
The current work gives, at first, an overview of ferroic-based HP concepts, the basic principles of SMAs, through EC specifics such as thermodynamic cycle, material characterization, and optimization, as well as SMA modeling. These basics are followed by the presentation of the currently realized EC systems and existing physics-based SMA models, resulting in the introduction of the Müller-Achenbach-Seelecke (MAS) model as the thermo-mechanical foundation for the aimed simulation tool. To understand the phase transformation (PT) behavior, a physics-based localized model is developed based on the MAS, validated, and simulations are performed, imitating experiments of a thin-film.
A material test bench is developed and realized for the application-related material model calibration. Besides the conventional mechanical material parameters, this test bench enables the investigation of the local strain and temperature distribution along the specimen. As a result, it allows for the complete characterization of the needed thermo-mechanical material parameters in a single test bench under load conditions similar to those of the real EC HP system.
Based on the material parameter set, the EC system model is implemented and validated according to the kinematics and fluidics of the realized EC HP system. To support the systematic study of distinct parameters, the system model is embedded in a developed control and data visualization tool. This tool enables massive parallel computation of numerous parameter sets and manages the comprehensive representation of the simulation

results. First parameter studies are executed with the realized EC HP simulation tool presenting the result interpretation and trend detection.
To get an impression of the EC HP system behavior, different load profiles, system dimensions, rotation frequencies, flow rates, strains, and system losses are simulated, compared, and interpreted. Concluding the HP topic, parameter studies are executed presenting possible system improvements. On the one hand, internal heat recovery concepts are introduced and simulated, which significantly improves the system performance for higher input temperature spans. On the other hand, water is used as heat exchange (HE) and heat transport (HT) medium, which enhances the heat exchange coefficient and specific heat capacity, enabling significantly higher system performance with unchanged design space. To demonstrate the complete capability range of the EC system simulation tool, a parameter study is performed using the system as a low-temperature heat engine.
The presented work is performed within the Priority Programme SPP 1599 “Caloric effects in ferroic materials: New concepts for cooling” of the German Research Foundation [67].

Keywords

Modeling, system model, simulation tool, ferroic cooling, elastocaloric effect, refrigeration, cooling process, heating and cooling, heat exchange, heat transport, heat pump system, thermodynamic cycle, thermo-mechanical coupling, phase transformation, superelasticity, shape memory alloy, Nickel–Titanium

Introduction

This chapter consists of the motivation in which the questions should be answered: Why do we need elastocalorics (ECs)? What are the key aspects of the EC technology? Finally, the objectives and outline of this work are described.

Motivation

The current climate change and the worldwide gain in prosperity combined with the growing world population will lead to an increasing energy demand in the area of air conditioning and cooling in the coming decades [140]. According to the Paris Agreement, global warming should remain significantly below 2 °C increase compared to pre-industrial levels, ideally limited to 1.5 °C [129]. For the raised demand in cooling energy [258, 132, 151], one of the challenges is to reduce the climatic impact of refrigerants and enhance the efficiency of the cooling systems. Following the Paris Agreement to reduce the greenhouse effect and protect the ozone layer, the European Parliament established the regulation of fluorinated refrigerants [138]. Therefore, the investigation in environmentally friendly cooling increases [198, 166], but the newest techniques come with other disadvantages like flammable refrigerants or high-pressure systems [86, 31]. Especially in the context of the current energy and climate discussion, it is trend-setting that the European Commission [111] and the Department of Energy of the United States [139] recently declared EC as the most promising alternative to conventional vapor-compression.
EC is a novel disruptive technology for building highly efficient and environment-friendly heating and cooling systems. It offers enormous energy saving potential [195, 167] with a material *COP* of up to 23 [165, 104, 93] compared to existing HP systems with a system *COP* of 6 [28] based on the well-known and optimized vapor-compression. In addition, EC does not contribute to the greenhouse effect or deplete the ozone layer because of its solid-state refrigerant. Therefore, EC complies with the global climate challenges. The mainly used EC materials belong to the family of SMAs, which are established in different engineering domains [143, 119], like aerospace [212], automotive [201, 209], and medical technologies [223, 16].
As SMAs are typically used for actuation [155] or passive superelastic (SE) applications [161], they have recently attracted considerable attention as an environment-friendly refrigerant [118, 68]. Besides the magnetocaloric and electrocaloric effect, the EC effect represents a mechanism or phenomenon in ferroic materials that can be used for solid-state cooling processes [167]. Thus, EC material are a potential replacement for volatile liquid or gaseous

refrigerants [130]. Compared to other caloric materials [60], SMA materials may provide large single stage temperature changes of up to 40 K [165, 144] based on mechanical loading and unloading without the need for strong magnetic or electric fields. The cooling capability of the mostly investigated SE SMA [131] is based on the specific latent heat accompanying the austenite (A)-martensite (M) phase transformation (PT) in the crystal lattice structure (CLS). During loading and unloading, the material transforms exothermically from A to M and endothermically in the reverse direction, thus allowing the realization of a thermodynamic cycle for heating and cooling purposes. In particular, NiTi based EC materials exhibit very large specific latent heat of up to 30 J/g [115] during the diffusionless first-order PT which requires only a small mechanical work input leading to the prementioned material *COP* of up to 23 [165, 104, 93].
The key aspects of cooling technologies are the combined efficiency of the cooling medium [216, 164, 98, 77], process control [162], and system design [74, 65] with an efficient heat exchange (HE) [88, 64, 11]. To develop an efficient EC HP with high performance, the system's key aspects have to be tuned to each other.

Outline

Recently, a fully functional and illustrative continuous operating EC air heating and cooling system based on multiple SMA elements was developed and realized [74]. This HP device operates in a rotary mode with tensile loaded wire bundles [10, 11], using a novel loading and unloading concept [100]. Due to the design, the heating and cooling power, along with efficiency, can be adjusted by suitable material scaling and operating parameters like rotation speed and air flow rate [50]. A multi-physics design tool is needed to assist the design and development of an optimized EC HP system with given performance and efficiency requirements.
This work presents in five chapters the development, implementation, and validation of a fully coupled thermo-mechanical system-level simulation tool [74].
At first, in the chapter 1, an overview from the basic principles of SMAs, through EC specifics such as thermodynamic cycle, material characterization, and optimization, to the SMA modeling is given.
The following chapter 2 presents different mechanisms of realized EC systems with the corresponding models. Next, the Müller-Achenbach-Seelecke (MAS) is introduced as a foundation for the aimed physics-based, thermo-mechanical coupled simulation tool.
After the introductory chapters, which provide the essential knowledge for this work, in chapter 3 the localized version of the MAS model is presented [80]. The developed 1D model is implemented in the finite element (FE) software package COMSOL and enables the prediction of heterogenic nucleation behavior in materials with nearly perfect CLS.

This part of the work presents experimental results on thin-films, the adapted modeling approach, and the implementation of the model. The parameter identification is based on a single experiment. Following, the predicted simulation results are compared with further experiments.
The work on the localized nucleation model calls for an extended test bench. Therefore, in chapter 4, a newly developed and realized material test bench is presented [74, 11]. This test bench is developed for application-related scientific investigation of macroscopic material samples like SMA wires. Besides the conventional mechanical material parameters, it enables the investigation of the local strain and temperature distribution along the specimen. As a result, it allows the complete characterization of the needed thermo-mechanical material parameters in a single test under similar conditions as in an EC HP system. This part presents first the experimental setup with the data acquisition methods, specimen preparation, and test procedure. Finally, experimental results are presented and discussed.
The last part, chapter 5, presents the development, implementation, validation, and parameter studies of the physics-based system modeling tool for EC HPs [74, 62, 40]. This tool is implemented in the numerical computing environment MATLAB and incorporates the MAS model. First, the modeling approaches for the kinematics, SMAs, and fluidics are presented. Multiple partial differential equations (PDEs) are implemented with the finite difference (FD) method to describe the physical behavior of the system. The simulation tool includes a control and data visualization tool to support systematic studies of distinct parameters. To manage comprehensive parameter scans, the simulation tool allows for massively parallel computation of numerous parameter sets and their comparison. Subsequently, the validation and parameter determination for the kinematics, fluidics, and SMA material is presented. Next, parameter studies are conducted, visualized, and discussed, showing trends and dependencies on the system parameters. For example, different cam track geometries, system dimensions, rotation frequencies, air flow rates, and applied strain are compared. In addition, further studies considering thermal, mechanical, and fluidic losses are discussed. Completing the parameter studies of EC HPs, future system improvements, like internal heat recovery, optimized EC materials, and different heat exchange (HE) and heat transport (HT) media are presented.
As additional work, to present the complete capability range of the realized simulation tool, the operating principle of the EC machine is reversed so that the system works as a heat engine. Following, parameter studies of an SMA based heat engine are computed and discussed.
Finally, the results of the work are concluded, and an outlook on future applications of the system simulation tool is given.

1 Fundamentals

This chapter introduces the novel techniques of EC HP systems. In order to comprehend the EC HP systems that were discussed, it is necessary to have an understanding of the underlying material behavior. Therefore, the fundamentals of the SMA material and the underlying effects of the shape memory effect and superelastic effect are introduced. Next, the EC is introduced with the thermo-mechanical cycle, efficiency determination, cycle optimization, and material research will be presented. Finally, different aspects and approaches for modeling theSMA behavior will be introduced.

1.1 Thermal shape memory alloy

Generally, the mechanical behavior of conventional materials under deformation is characterized by reversible deformation or elasticity, thermal expansion, plastic deformation, and fracture. In contrast to this, a shape memory (SM) material is able to restore its original shape after mechanical deformation like bending or elongation by applying a non-mechanical field like joule heating. Such an *intelligent* material can undergo a diffusionless, crystallographic, and nearly reversible transformation between at least two phases within a specific temperature interval.
Based on the first reported observation of the SM behavior on metals in 1932 by Swedish physicist Arne Ölander [119], these *smart* materials support the development of intelligent systems [205, 136, 59], like light-weight multifunctional structures, adaptive devices, and sensor systems. Nowadays, the range of smart materials has expanded to include electroactive polymers and composites, [240, 183] in addition to SMA. SMAs are also known as active materials. Also, other materials like piezoelectric, piezomagnetic, electrostrictive, and magnetostrictive materials can generate a mechanical output by applying a non-mechanical field [205].
Regarding the activation method, the SM materials can generally be divided into two groups: magnetic-based [119], which returns to their original phase after deformation while applying an external magnetic field, and thermal-based [34], where a thermal input is needed to restore the previously occurred deflection.
The first report on thermal SMAs dates back to 1951 [277]. With this discovery, the investigation of NiTi-based SMAs [276, 254], which are mainly used today, began. The SMA base on NiTi exhibits an excellent combination of mechanical and thermal properties [186]. In addition, they are biocompatible due to their chemically inert surface [260].

Another group of SMAs based on copper or iron are also available [36]. However, due to their brittleness and aging behavior [143, 95], they are currently not favored in engineering applications. In addition, the copper-based SMAs are more cost-effective than NiTi-based ones.

Nowadays, NiTi-based material products are also available in industrial quantities [29, 27, 39]. Therefore, this scientific work will mainly focus on NiTi-based thermal SMAs.

The underlying mechanism of the SM ability is a reversible PT of the CLS, which can be induced by temperature called *SM effect* or by stress, called *superelastic (SE) effect* [186]. These behaviors are achieved in NiTi by a Ti percentage of approximately 50 % in the alloy [234]. The detailed composition of Ni, Ti, and additional alloying elements defines the temperature-dependent PT behavior [189, 181, 115], and, with this, the regimes of the two coexisting phenomena: SM effect and SE effect.

1.1.1 Shape memory effect

The SM effect describes the ability of a material to *remember* its initial shape and return to it after external or Joule heating. This is still possible even after a mechanical deformation of up to 10 % [119], which is way beyond the normal yield strain of metals, typically ranging from 0.2 to 0.5 % [186].

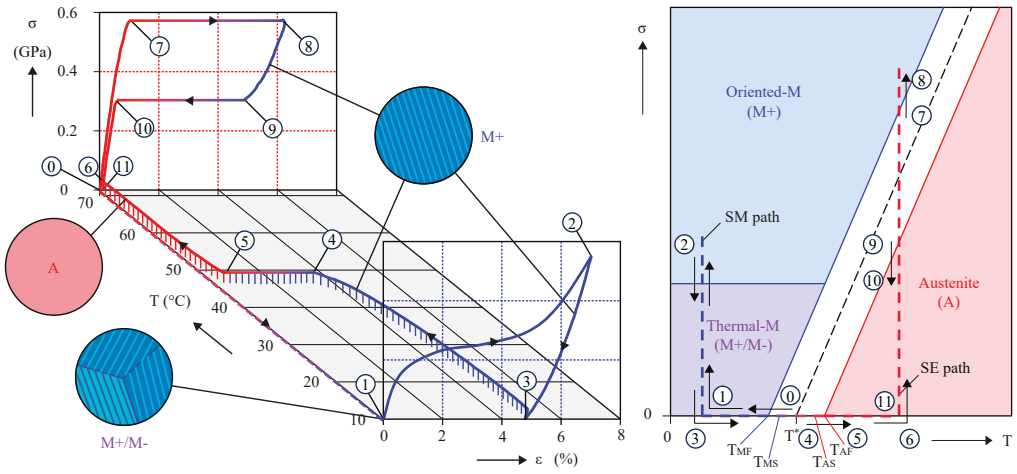

Figure 1.1: Uniaxial thermo-mechanical response of the a) NiTi-based SMA wire: SM, and SE effect, and b) corresponding idealized (quasi)-phase diagram. Adapted from Shaw et al. [186], using with permissions.

The thermo-mechanical behavior of SMAs can be visualized on a stress (σ) - strain (ε) - temperature (T) diagram presented in Figure 1.1 (a) [186].

At a material temperature above austenite finish temperature (T_{AF}), the CLS of the unloaded material is based on a generally face-centered cubic lattice. This material

configuration is called the high-temperature phase or austenite (A). An unloaded specimen shows its original shape if the material is orientated in the A phase. In Figure 1.1, the A is highlighted in red within the graphs.
While reducing the temperature of the material under the martensite start temperature (T_{MS}), the material transforms, while remaining a constant volume, to the low-temperature phase, until reaching the martensite finish temperature (T_{MF}). This configuration of the CLS is called martensite (M). This microscopic CLS is based on a generally body-centered tetragonal lattice. In Figure 1.1, the M is highlighted in blue within the graphs.
M offers two main orientations of the CLS: At compression loading of the material, M- is preferred. Whereas M+ is the predominant CLS when the material is tension-loaded. Both pure configurations are known as de-twinned M [205]. During the unloaded forward transformation (FT) from A to M, the material arranges in the microscopic structure a combination of M+ and M-, called twinned M, which shows on a specimen macroscopic nearly the same shape as A [205].
Tensile loading of the twinned M, under the austenite start temperature (T_{AS}), leads in microscale to a PT to M+ and macroscopically to a *remaining*, *quasi-plastic* elongation of the specimen. The maximal reachable elongation of the material is in the range of 8 % to 10 % strain [186, 119] and depends on the material composition [234]. However, the mechanisms of M deformation differ due to frictional effects during subsequent detwinning. As a result, the stress level of the transformation plateau is significantly higher, and the maximal reversible deformation is lower under compressive loading compared to tensile loading [235, 148].
The achieved deformation (reduction or elongation) of the specimen can be restored by increasing the material temperature above T_{AS}. After reaching the T_{AF}, the material is fully transformed to A, and the macroscopic shape of the specimen reaches its initial one. The microscopic phase composition between T_{AS} and T_{AF}, and T_{MS} and T_{MF}, is characterized by temperature and stress dependent number of the CLS cells in the A and M phase. The level of the PT temperature, is normaly definded by the T_{AF} at an unloaded state and is in the range of $-50\,^{\circ}\mathrm{C}$ to $480\,^{\circ}\mathrm{C}$ [112, 82].
The SM effect can be visualized via a thermo-mechanical cycle, as presented in Figure 1.1 (a). Initially, the material is in the A phase.

- points 0-1: If the material temperature of the unloaded material decreases under the T_{MS}, the material transforms to twinned M. The PT is finished if T_{MF} is reached.

- points 1-2: During loading at constant material temperature, the material transforms to detwinned M.

- points 2-3: During unloading at constant material temperature, the material remains in detwinned M.

- points 3-4: During the temperature increase from the T_{MF} to the T_{AS} the material orientation stays in M.

- points 4-5: During the temperature increase from the T_{AS} to the T_{AF} the material transforms to A.

Figure 1.1 (b) presents the dependency of the stress (σ) and the temperature (T) during the thermo-mechanical cycle. In this diagram, the corresponding transformation state of the CLS during the described cycle is visualized again. The PT temperatures increase with increasing stress and depend on the material compositions and the energy equilibrium of the PT in the material [259, 213]. Therefore, the barrier, colored in white, between M and A is inclined. The inclination angle, and with this, the stress rate are described more in detail in section 2.2.
The cycle described before is also known as the *One-Way* effect [205, 119]. Training of the SMA, which means multiple repetitions of this thermo-mechanical cycle at a specific loading profile, leads by some material compositions to an additional macroscopic shape change and a microscopic PT behavior, called the *Two-Way* effect [205, 186, 119]. After training, the material shows macroscopic residual deformation compared to its initial shape. Microscopically, some CLS cells of the material are captured in M+ or M- depending on the training load due to lattice defects [205, 119]. This generated behavior enables a reversible shape change triggered by thermal cycling without an external load.
Both effects, *One-Way* and *Two-Way* SM effect are typically used at an ambient temperature lower than T_{AS}, leading to the temperature order of T_{MF}, lower than T_{MS}, lower than T_{AS}, and lower than T_{AF}. If the material is used at a temperature for FT to A which is higher than T_{AS} and lower than the T_{AF} or the T_{MS} is higher than T_{AS} due to the material composition, an incomplete return of the shape change at backward transformation (BT) is reached and internal hysteresis loops are generated. The hysteresis width between the T_{AF} and T_{MS} is in range of 10–50 K, and the temperature difference between start and end of the PT is in the range of 5–20 K [119]. The exact values depend on the material composition.
Regarding the underlying effect of the PT between A and M, the external temperature change of the material forces the microstructure to transform into a CLS, which is stable at the current internal energy [257, 169]. This behavior enables the temperature-introduced macroscopic shape change from M to A. The macroscopic shape change, in combination with the high energy density of the SMA material, allows for use as lightweight and adaptable actuators [212, 186, 143, 59, 26]. Avoiding the two-way SM effect on an actuation system,

the SMA is generally pre-loaded above the quasi-plastic deformation of M and lower than the restoring force of A.
In addition, after appropriately thermo-mechanically pretreated NiTi-base SMAs, a rhombohedral CLS can occur during the back transformation from A to M. The so-called R-phase [85] presents a sub-orientated rule in the current state of scientific investigation. Therefore, it will not be discussed in more detail below.

1.1.2 Superelastic effect

The SE effect describes the ability of the material to "remember" its initial shape and return to it after removing the external force, even if the mechanical deformation is with up to 10 % [119] largely higher than the conventionally known yield strain of metal-based materials [266, 186], and in the same range as the SM effect.
Similar to the SM effect, the SE effect can also be visualized via a thermo-mechanical cycle, as presented on a stress (σ) - strain (ε) - temperature (T) diagram presented in Figure 1.1 (a) [186]:

- points 5-6: If the material temperature of the unloaded material increases above the T_{AS}, the material transforms to A, its original shape. The material is fully transformed if T_{AF} is reached.
- points 6-7: During loading at isothermal conditions and at stress value lower than the transformation stress of the FT, the stress-strain behavior follows the elastic path pre-described by the Young's modulus of A.
- points 7-8: If the induced stress value is higher than the transformation stress of the FT, the material transforms from A to M. This leads to a macroscopic shape change. Further loading after reaching the full PT, the stress-strain behavior follows the Young's modulus of M elastically.
- points 8-9: During unloading, the stress-strain behavior follows the Young's modulus pre-described of M elastically until reaching the BT stress.
- points 9-10: If the induced stress value is lower than the BT stress, the material transforms from M to A. This leads to a macroscopic shape change back to the initial shape.
- points 10-11: Further load reduction, after reaching the full PT to A, the stress-strain behavior follows the Young's modulus of A elastically.

The mechanical hysteresis height between FT and BT is in the order of 70–100 MPa [93] and depends on the material compositions. This stress-induced M only exhibits one of the main orientations M- or M+ depending on the loading force [205].

The SE effect is typically used at an temperature higher than T_{AF} [205]. That behavior enables a very huge macroscopic repeatable shape change in metal-based materials. Therefore, it offers the ability to use SMA in biomedical applications and structural damping mechanisms [212, 186, 143, 59, 26].
In the SE behavior described before, the material's HE and the ambient temperature are selected to reach isothermal conditions in the material during loading and unloading. In the case that the SE cycle is executed at non-isothermal conditions, the suited HE and HT can be realized due to the thermo-mechanical coupling of the A and M with the internal energy [257, 169]: Starting at a material temperature above T_{AF}, the unloaded material is in A phase, its original shape. During loading, the material transforms from A to M, which leads to a macroscopic shape change and a release of the specific latent heat due to an internal change of the CLS. This release of thermal energy increases the material temperature. During unloading, the material transforms back to A and absorbs specific latent heat from the material, decreasing the material temperature. This behavior is also known as the EC effect [202, 195] and is described in more detail in the following section 1.2.
In recent years, this effect has become known as solid-based HT for EC cooling [67, 74, 65]. The reverse caloric effect can be used in energy-harvesting applications like heat engines [241, 51].

1.2 Elastocaloric

In conventional HP systems, volatile refrigerants are used in a vapor-compression process. The PT of the refrigerant occurs during evaporation and condensation isothermally [146]. The refrigerants temperature change is linked to the adiabatic compression and expansion. In contrast to conventional HPs, elastocaloric heat pump (EC HP) systems use solid-state materials as refrigerant. In an EC cycle, during the stress-induced PT, the corresponding release or absorption of the material's latent heat is directly responsible for temperature changes in the caloric material [167, 144].
Solid-state caloric materials enable the ability to transport thermal energy from a low temperature level to a higher one [237, 109, 118, 67], and act as refrigerant. However, the main advantage of solid-state refrigerant is the state of aggregation, which does not contribute to the greenhouse effect or depletion of the ozone layer in the case of system leakage. Therefore, solid-state refrigerants are commonly known as environment-friendly. The externally induced field change of a physical field leads to a PT of the material and, with this, to the change of the lattice energy. The caloric effect has been studied in the last decades by applying different physical fields. The namesake of each effect is the *field* required to induce the effect in a specific material: These include the electrocaloric [177, 23],

magnetocaloric [33], elastocaloric [74], and barocaloric effects [38]. Each group has different advantages, characteristics, and challenges regarding heating and cooling efficiency, as well as system effort. Also, multicaloric materials [70] are investigated, using different caloric effects to combine their advantages. In literature, different comparisons of the caloric effects are presented regarding both, application and design [147, 118, 114, 121, 104, 74, 42, 47, 44, 18]. Concerning caloric HP systems, there are some parallels between the electrocaloric, magnetocaloric, and elastocaloric also in the modeling approaches [131, 72].
The EC effect is based on the loading and unloading of a SE material. In the case of EC, the material has to be deformed by a mechanical work input. Despite the assumed disadvantage of the needed conversion from electrical to mechanical energy, EC is mentioned as the most promising heating and cooling alternative to the conventional vapor-compressed technology [139, 111]. Therefore, the primary research of EC systems can be performed with commercially available SE NiTi material used in medical applications, which provides a constant quality for large quantities. Additionally, the recently developed special EC materials can withstand millions of load cycles, supporting the idea of using EC in heating and cooling applications for the future [113, 102].
The history of EC goes back to 1806, when the rapid elongation of natural rubber revealed an unexpected temperature increase, and the first observation of the EC effect is reported by Holme [280]. A few years later, the EC effect is reported in wood and metal [279]. The investigations of the EC effect in SMAs [271, 269] in the eighties and nineties in NiTi [265] lay the foundations for the start of the intensive scientific investigation around the millennium [244, 231, 202, 167].
The stress induced PT of the CLS leads to a release of specific latent heat during the forward transformation (FT) from A to M and absorption during the backward transformation (BT) according to the law of Clausius-Clapeyron [227]. The temperature change depends on the material composition with a maximal temperature difference of up to 40 K [219, 165, 144]. During the last decade, specific materials for EC applications are developed [93] with large specific latent heat of up to 30 J/g [115] and small work input [165, 115, 104]. This leads to material *COP* of up to 23 [104, 93].
The existing systems, known from the literature, can be divided regarding the used loading type like compression [124], tension [123, 127], bending [78], and torsion [61] of the EC element. Additionally, a multistage test stand was published by Snodgrass et al. [58], in which EC elements are thermally arranged in series to exceed the temperature difference of a single element. Recently, the first continuous operating EC technology demonstrator based on multiple NiTi wire bundles was presented by Kirsch et al. [74].
The following part briefly discusses the primary and improved EC cycles. Next, the characterization of EC materials and their optimization potential will be presented. These topics are also published by Kirsch et al. [74].

1.2.1 Thermodynamic cycle

A thermodynamic cycle typically involves a series of connected thermodynamic processes. These processes include transferring heat and work into or out of the system while changing pressure, temperature, and other state variables within the system. Ultimately, the cycle returns the system to its initial state. In a cycle, the different states are connected by a series of processes, and the system passes from one state to another by paths. The series of paths that guide the system from one to another equilibrium state is called *process*.
Figure 1.2 shows a typical adiabatic EC heating and cooling cycle based on the SE effect discussed in subsection 1.1.2. The four sections of the cycle are each illustrated in a temperature (T) - strain (ε) diagram.

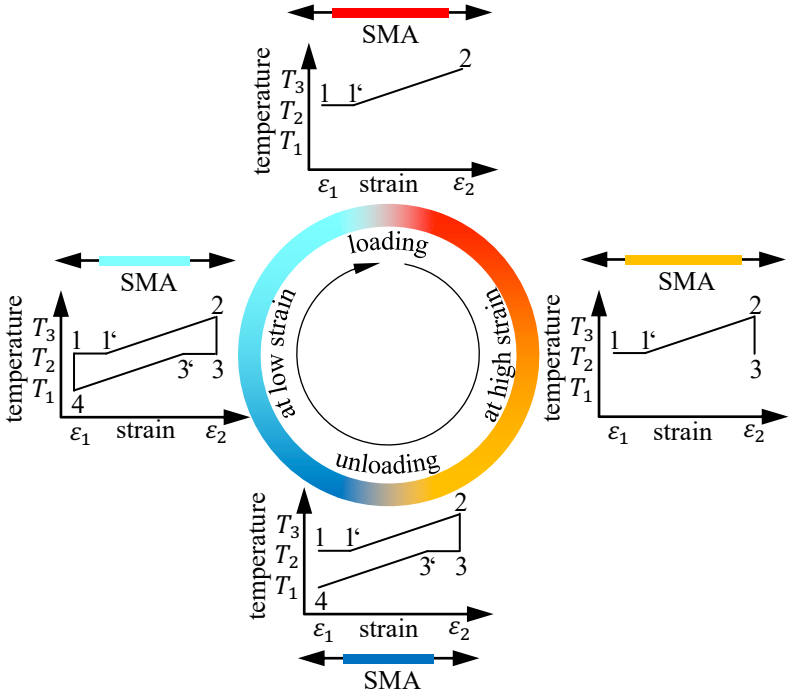

Figure 1.2: Adiabatic EC cycle: Adiabatic loading and unloading of a SE SMA with holding state. Illustration of the temperature (T) - strain (ε) behavior in a four-stage cycle.

In the first section, mechanical loading is applied to the SMA element between point 1 and point 2 with increasing strain (ε) from ε_1 to ε_2. At point 1' the PT starts from A to M. Due to the release of the specific latent heat, the temperature (T) in the SMA increases from T_2 to T_3. If the loading is performed sufficiently fast or the HE is suppressed due to the ambient conditions, the PT occurs under nearly adiabatic conditions. This means the amount of released specific latent heat is fully used to heat the material, and T_3 reaches its maximum.
During the holding state in the second stage, between point 2 and point 3, the strain, which is applied to the SMA element at the loading in the first stage, is kept constant. At this

time, the HE with the environment occurs, cooling the SMA element from T_3 to T_2, back to the start temperature of the loading state.
Unloading occurs between point 3 and point 4, under nearly adiabatic conditions, with decreasing strain from ε_2 to ε_1 in the third stage. The BT starts at point 3', and the specific latent heat absorption leads to a temperature decrease of the material. The material temperature drops from T_2 to T_1 significantly below the ambient temperature.
In the fourth path, the HE occurs at constant strain, comparable to the second stage. Therefore, the material temperature increases from T_1 to T_2, back to the initial one.
This process control with nearly adiabatic loading and unloading conditions is known as the Brayton cycle [150].
The thermodynamical definition of the EC cycle and, with this, the relevant material-specific thermo-mechanical dependencies can be explained by using the temperature (T) - strain (ε) diagram as discussed in Figure 1.2. Further thermal and mechanical diagrams like a stress (σ) - strain (ε) diagram and a temperature (T) - entropy (S) diagram, as presented in Figure 1.3, can be used to determine key values of the cycle like mechanical work, thermal energy, and COP. The diagrams' point numbers 1-4 correspond to the four-stage cycle described in Figure 1.2.

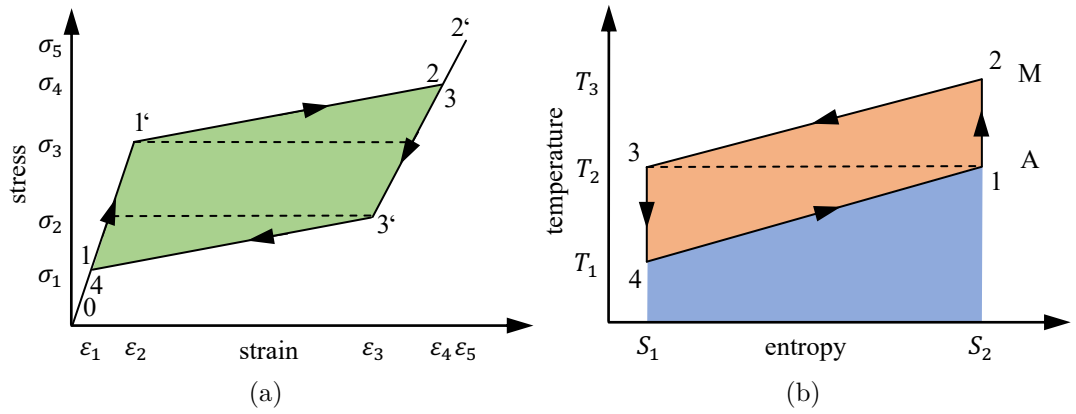

Figure 1.3: Adiabatic EC cooling cycle: Adiabatic loading and unloading of a SE SMA with holding state. Illustration of the a) stress (σ) - strain (ε) diagram, and b) temperature (T) - entropy (S) diagram.

Mechanical work input

Figure 1.3 (a) presents the idealized mechanical correlation between the applied strain (ε) and the resulting stress (σ) change of a SE SMA. The stress (σ) - strain (ε) diagram shows the typical elastic behavior at A between points 0-1-1' while increasing strain from 0 to ε_1 to ε_2 with elastically increasing stress from 0 to σ_1 to σ_3. At point 1' the PT starts. During the FT, between points 1'-2, strain increases from ε_2 to ε_4 and the stress continues to increase with a changed slope due to the rising temperature of the SMA from σ_3 to σ_4.

This is related to the release of the specific latent heat and the suppressed HE between the SMA and the ambient.
In contrast to the isothermal case, in which the HE is assumed as perfect, here suggested as dashed lines, the slope of the stress-strain curve increases with increasing material temperature, due to the temperature dependency of the transformation stress, following the law of Clausius-Clapeyron [263] and will be explained in detail in section 2.2. The law of Clausius-Clapeyron describes the temperature-dependent transformation stress which is related to the released specific latent heat and the applied strain [259, 227, 215]. The material-specific slope value is given for SE SMA in the literature with a range of 5–8 MPa/K [268, 110]. Due to the positive temperature coefficient of the transformation stress, the plateau of the stress (σ)-strain (ε) behavior is inclined during loading and declined during unloading under adiabatic conditions.
At point 2, the PT is finished, and the material is fully transformed to M. Further loading leads to an elastic behavior at M between points 2-2'with increasing strain from ε_4 to ε_5 and corresponding stress from σ_4 to σ_5. Due to the fully transformed material, there is no decrease in stress, induced by the decreasing temperature during the holding state.
After the holding stage for HE, the SMA is unloaded on path 2'-3-3'-4. Between points 2'-3-3'the stress-strain curve follows the elastic path of M from ε_5 to ε_4 to ε_3 with the corresponding stress decrease from σ_5 to σ_4 to σ_2. The BT occures, between points 3'-4, with the decreasing strain from ε_3 to ε_1 and the corresponding stress realease from σ_2 to σ_1. In this state, the temperature decrease due to the suppressed HE, leading to a decreasing transformation stress and resulting in the change of stress-strain curve slope. The isothermal hysteresis path for the BT is also presented as a dashed line.
The stress - strain diagram visualizes dissipatedthe mechanical work (W) for the performed cycle as green area. The specific mechanical work (w) is used in the following to make the value independent from the quantity and certain scalings of the individual system, like the quantity of the used material. This makes this formula more straightforward to handle in calculations, and only the density (ρ) of the SMA is needed.
The area between the loading path and the x-axis represents the applied specific mechanical work (w_{ap}). It can be calculated with Equation 1.1 using the density (ρ), stress (σ), and strain (ε). The limits of the integral do not represent the values of strain, but rather the number of the thermodynamic processes.

$$w_{\mathrm{ap}} = \frac{1}{\rho} \int_{12} \sigma \cdot d\,\varepsilon \tag{1.1}$$

In contrast, the area between the unloading path and the x-axis represents the recovered specific mechanical work (w_{rc}). It can be calculated with Equation 1.2.

$$w_{\mathrm{rc}} = \frac{1}{\rho} \int_{34} \sigma \cdot d\,\varepsilon \tag{1.2}$$

Due to the hysteretic material behavior, both curves include an area that represents the unrecoverable mechanical work, which is captured by the four paths of the cycle and colored in green in Figure 1.3 (a). The mechanical work that can not be recovered under the assumption of mechanical work recovery while unloading is called dissipated specific mechanical work (w_{dis}). This work is equivalent to the circular integral over the four process steps and can be calculated with Equation 1.3.

$$w_{\mathrm{dis}} = \frac{1}{\rho} \oint_{1234} \sigma \cdot d\,\varepsilon \tag{1.3}$$

Thermal energy input

Figure 1.3 (b) presents the idealized thermal correlation between the applied entropy (S) and the resulting temperature (T) change of a SE SMA. The temperature (T) - entropy (S) diagram shows between point 1-2 a rise of the temperature from T_2 to T_3 with a constant entropy of S_2 at the loading state under ideal adiabatic conditions. The assumption of suppressed HE during PT leads to reversible entropy changes, resulting in an isentropic process.

At the holding stage after loading, between points 2-3, the SE SMA releases the thermal energy to the ambient. Therefore, the material temperature decreases from T_3 to T_2 with decreasing entropy from S_2 to S_1. This behavior is based on the second law of thermodynamics [84] following an approximated linear path due to the released thermal energy back to the ambient.

At the unloading stage between the point 3-4 a decline of the temperature from T_3 to T_4 with a constant entropy of S_1 under ideal adiabatic conditions is shown. During the holding stage after unloading, between points 4-1, the material temperature increases from T_1 to T_2 with increasing entropy from S_1 to S_2, following an approximate linear path, due to the absorbed thermal energy from the ambient.

Typically, the temperature-related entropy change at the pure A or M phase follows an exponential function. Only in the case of small temperature changes during the PT of SE SMA can the curve be fitted with a linear function [263, 106].

With the temperature (T) - entropy (S) diagram the absorbed or released specific thermal energy (q) and dissipated specific mechanical work (w_{dis}) can be visualized and calculated using Equation 1.4 between points x-y [84]. The limits of the integral do not represent the values of strain, but rather the number of the thermodynamic process. To make the values

independent from the quantity and certain scalings of the individual system, the specific entropy (s) can be calculated by dividing the entropy (S) through the SMA mass (m).

$$q + w_{\mathrm{dis}} = \int_{xy} T \cdot d\,s \tag{1.4}$$

The area below the M curve, between points 2-3, the holding path after loading, and the x-axis, visualized in Figure 1.3 (b) as a combination of the area colored in red and the blue one, represents the released specific thermal energy (q_{re}). In the holding process after loading, the dissipated specific mechanical work ($w_{\mathrm{dis}23}$=0) is equal to zero due to the constand strain, as visible in Figure 1.3 (a). Therefore, the released specific thermal energy (q_{re}) can be calculated with Equation 1.5, using the temperature (T) and specific entropy (s).

$$q_{\mathrm{re}} = \int_{23} T \cdot d\,s \tag{1.5}$$

The area below the A curve, between points 4-1, the holding path after unloading, and the x-axis, represents the absorbed specific thermal energy (q_{ab}), colored in blue in Figure 1.3 (b). It can be calculated with Equation 1.6, assuming the dissipated specific mechanical work of the holding process after unloading equal to zero ($w_{\mathrm{dis}41}$=0), using the temperature (T) and specific entropy (s).

$$q_{\mathrm{ab}} = \int_{41} T \cdot d\,s \tag{1.6}$$

Due to the entropy change caused by the HE and the related temperature change, following the Carnot cycle as an idealized thermodynamic cycle, the released specific thermal energy (q_{re}) is higher than the absorbed specific thermal energy (q_{ab}). This net thermal energy is captured by the four paths of the cycle and is visualized by the area colored in red in Figure 1.3 (b) and represents the unrecoverable thermal energy done by the system. Therefore the value is comparable to the dissipated specific mechanical work (Equation 1.3) visualized by the area colored in green in Figure 1.3 (a). The red area is equivalent to the integral over the four process steps. It can be calculated with Equation 1.7 using temperature (T), and specific entropy (s), while assuming adiabatic conditions during the PT and with w_{dis}= 0 during HE.

$$q = \oint_{1234} T \cdot d\,s \tag{1.7}$$

Note that the internal friction in the CLS during the PT of a real material induces irreversibility, leading to a non isentropic process during loading and unloading. In most

applications, the irreversible specific entropy change during PT can be neglected [110, 106, 125].

Coefficient of performance

To evaluate the EC cycles regarding their efficiency, the COP can be used [106]. Regarding cooling applications, the COP_{cool} is defined as the ratio of the absorbed specific thermal energy (q_{ab}) and the dissipated specific mechanical work (w_{dis}) shown in Equation 1.8.

$$COP_{\mathrm{cool}} = \frac{q_{\mathrm{ab}}}{w_{\mathrm{dis}}} \tag{1.8}$$

Whereas, at the heating applications, the COP_{heat} is defined as the quotient of the released specific thermal energy (q_{re}) and the dissipated specific mechanical work (w_{dis}) as shown in Equation 1.9.

$$COP_{\mathrm{heat}} = \frac{q_{\mathrm{re}}}{w_{\mathrm{dis}}} \tag{1.9}$$

Under ideal process conditions with fully transformed SE SMA material and completed HE, the absorbed thermal energy can be replaced with the specific latent heat (H), this ideal coefficient of performance (COP_{ideal}) can be calculated using Equation 1.10.

$$COP_{\mathrm{ideal}} = \frac{H}{w_{\mathrm{dis}}} \tag{1.10}$$

Note that the Equation 1.10 is calculated with the assumption of an isentropic loading and unloading of the SMA.

1.2.2 Cycle optimization

Regarding the implementation of an EC system, optimizing the EC process control is crucial as it significantly impacts the heating or cooling performance and COP. The efficiency of the EC cycle strongly depends on the thermodynamic boundary conditions. The temperature dependency of the thermo-mechanical coupled material behavior [263, 259, 215, 162] leads to a strain rate dependence of cycled SE SMA at unchanged HE conditions [252, 227, 162]. The dissipated mechanical work increases with increasing strain rate [252], leading to a disadvantage regarding fast operating heating and cooling devices. The following will discuss different process parameters to overcome the challenge of the high work input at pure adiabatic loading, shown in Figure 1.3. The thermodynamic process control offers numerous possibilities between a pure adiabatic and a pure isothermal loading and unloading processes with different COPs, heating and cooling power, as well as temperature difference [106].

In the last decade, a systematic variation of the control parameters has been performed to develop an efficient EC cooling process [89]. Different thermodynamic cycles with various mechanical and thermal boundary conditions were investigated. The used scientific test setup, shown in Figure 1.4, enables an independent investigation of the influence of each control parameter on the process variables [127, 108].

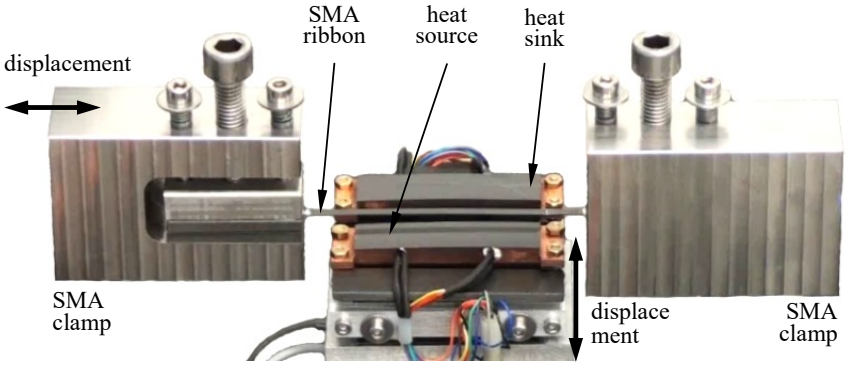

Figure 1.4: Scientific testing platform for investigation of EC process parameter, using conductive HE.

In this test setup, the SMA element is elongated by a linear drive and connected with a defined contact force to a movable heat sink or heat source for a defined time period. The in-plane arrangement of the heat sink and heat source, combined with the conductive-based HE using the ribbon-shaped NiTi samples, results in a frequently interrupted and discontinuous HE.

This in-plane arrangement allows simultaneous temperature field measurements with an IR camera system for thermal energy determination combined with force and displacement measurements to calculate the mechanical work input. The temperature of the heat sink and heat source were also measured with PT100 sensors integrated into the heat sink and heat source.

As discussed before, the loading or unloading of an SMA element with a suppressed HE leads to an adiabatic PT. Assuming a complete PT, the entire amount of specific latent heat contributes to the temperature change in the material. If loading or unloading occurs while the SMA is in contact with the heat sink or source, the PT occurs under near isothermal conditions. Due to the thermo-mechanical coupling, this leads to a change of the applied mechanical work, among other things. A combination of these two limiting cases is also possible. This leads to an optimization for the desired temperature difference, heating and cooling power, as well as efficiency.

In Figure 1.5, an adiabatic/isothermal hybrid EC cycle is illustrated using the temperature (T) - strain (ε) diagram (a), the stress (σ) - strain (ε) diagram (b), and the temperature (T) - entropy (S) diagram (c). The diagrams' point numbers 1-4 correspond to the four-stage cycle described in Figure 1.2 and Figure 1.3. The dashed lines show the alterna-

tive path in the case of isothermal HE, and the dotted lines show the one for adiabatic HE, known from Figure 1.3.
The SMA is loaded between points 1-1'-1"-2-2'. In the first part of the loading between points 1-1'-1", the HE is suppressed. Therefore, the thermo-mechanical behavior of the SMA follows the known path from the adiabatic cycle (Figure 1.3).

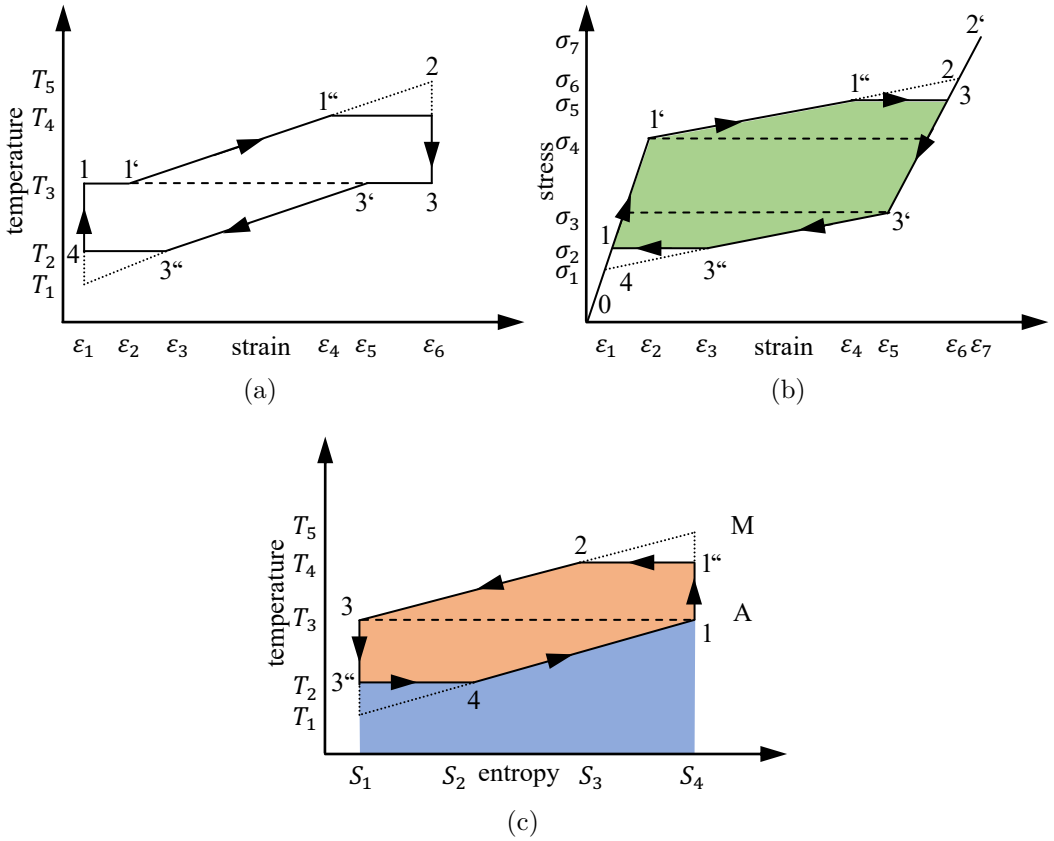

Figure 1.5: Adiabatic/isothermal hybrid EC cycle: Illustration of the a) temperature (T) - strain (ε) diagram, b) stress (σ) - strain (ε) diagram, and c) temperature (T) - entropy (S) diagram.

At point 1", the SMA is connected to the heat sink, and the conductive HE starts. The further loading between points 1"-2-2' is performed isothermally. Isothermal PT from ε_4 to ε_5 leads in comparison to the pure adiabatic loading at the temperature - strain diagram (Figure 1.5 (a)) to a decreased temperature slope with further increasing strain. Therefore, the temperature reaches with T_4 a reduced maximum in comparison to T_5 under pure adiabatic PT.
The decreased temperature slope leads in the stress - strain diagram (Figure 1.5 (b)), to a reduced stress slope with further increasing strain, due to temperature dependent transformation stress. Therefore, the stress reaches with σ_5 a reduced maximum in comparison to σ_6 at pure adiabatic PT.

The fully transformed material and the same amount of thermal energy leads in the temperature - entropy diagram (Figure 1.5 (c)) to the same entropy value S_4. The HE during the loading stage changes the thermodynamic condition at point 1" from isentrope to non-isentrope. Therefore, compared to the pure adiabatic cycle, the entropy changes as expected from S_4 to S_3 due to the release of thermal energy during the PT.
At the elastic loading on the M branch, the contact with the heat sink does not affect the behavior. During the holding stage between points 2'-3, the HE with the heat sink continues until the thermal equilibrium is reached. In this stage, the thermodynamic boundary condition is not changed. Therefore, the material behavior and, with this, the curve between points 2'-3 is the same in all three diagrams of Figure 1.5.
The SMA is unloaded during the transition 3-3'-3"-4. In the first part of the unloading between points 3-3'-3", the HE is suppressed. Therefore, the thermo-mechanical behavior of the SMA follows the known paths during the pure adiabatic cycle (Figure 1.3).
Between point 3"-4, unloading from ε_3 to ε_1 is performed with HE due to the contact between the SMA and the heat source. During the isothermal PT, the temperature slope is reduced. Therefore the reached temperature minimum is with T_2 in the temperature - strain diagram higher than T_1, which is reached during pure adiabatic PT.
The decreased temperature slope leads in the stress - strain diagram to a decreasing stress slope. Therefore, the stress reaches with σ_2 a higher minimum in comparison to σ_1, which is reached at the pure adiabatic PT.
The fully transformed material and the same amount of thermal energy leads in the temperature - entropy diagram to the same entropy value S_1. The HE during the unloading stage changes the thermodynamic condition at point 3" from isentrope to non-isentrope. Therefore, compared to the pure adiabatic cycle, the entropy changes as expected from S_1 to S_2 due to the absorbed thermal energy during the PT.
During the holding stage between points 4-1, the HE with the heat source continues until the thermal equilibrium is reached. In this stage, the thermodynamic boundary condition is not changed and the behavior is the same in all three diagrams.
The reduced temperature in the SMA material at high strain leads to a reduced required mechanical work input. The increased temperature in the SMA material at low strain leads to an increased mechanical work recovery. Therefore, the reduced dissipated specific mechanical work at the hybrid cycle can improve the *COP*, assuming constant thermal energy for heating and cooling. The change in the thermodynamic boundary conditions during the PT leads to a complex combination of the dissipated specific mechanical work (w_{dis}) and absorbed or released specific thermal energy (q). Therefore, the released thermal energy and the absorbed thermal energy have to be calculated using Equation 1.4.
The discussed EC cycle enables an adjustment of the achieved heating and cooling temperatures of the material and thus affects the maximum and minimum temperature

of the heat sink and the heat source. This temperature variation enables an adjustment of the heating or cooling power to the desired values and offers an optimization of the corresponding efficiency.
These investigations show that each parameter set of the EC cycle leads to a different thermal power and efficiency. One of the significant findings is that a hybrid EC cycle with a combination of adiabatic and isothermal thermodynamic process control shows the best performance [89]. The EC hybrid cycle is also investigated in magnetic refrigeration [141]. The variation of the process parameters at the same HE conditions, like strain rate dependency and the resulting influence of peak temperature in the SE SMA is investigated by Schmidt et al. [107]. In addition to the EC process control [106, 47, 24], the strain rate [107], the maximum strain [107], the thermal boundary condition, and various material compositions [116] influence the temperature change, as well as the heating and cooling performance.
Based on the thermodynamic analysis of EC cycles, an efficient EC cooling process can be developed and implemented in an SMA-based HP system. Regarding the fundamental efficiency and power of the EC-based HP system, the SMA material itself has to be improved, as presented in the following part.

1.2.3 Material research

Regarding the application area of EC systems, literature reports various material compositions, as well as values of temperature difference, *COP*, and loading methods for characterization. Following, keystones of the EC material parameter, characterization methods, and optimization steps will be introduced.
The composition of material alloys is usually named by the *alphabetic formula*, in which the main components are named first, followed by any additional alloy elements, in the alphabetic order. Alternatively, the *standard formula* names the material alloy based on the percentage composition of its components. Ideally, the *standard formula* should be used, but in practice, materials are often named using a combination of both methods. This work aims to use the commonly known material names for unspecified materials like NiTi. When specific materials are mentioned, the *standard formula* is used unless a different name is specified in a reference; in this case, the reference name is used.

Typical Values

Conventional NiTi wires exhebits a temperature change of 17 K during adiabatic PT [165]. Whereas in TiNiCuCo thin films 12 K are reported [122]. The air cooling behavior of NiTiCo single wires [55], and bundle arrangement [35, 11] has been analyzed on parameter studies with different wire diameters, and air flow rates. The reported air temperature

changes are 1.5 K [55] for single wires, and 8 K [35] for bundles consisting of 30 wire segments arranged in two lines.
The fatigue life of TiNi and TiNiCu wires shows a material lifetime of up to 10^6 cycles [249] for small tensile loading strains below 2 %. Also, functional stability is discussed in the literature: TiNiCu thin films for small-scale applications exhibit very high cyclic stability of up to 10^7 cycles [164]. Whereas the functional lifetime of NiTi tubes under compressive loading reaches up to 7×10^7 cycles [41].
The performance of an EC HP system depends significantly on the properties of the used SMA material and the loading conditions [131, 104, 106, 94, 69, 8]. Typical *COP* values for EC HP systems using SMA are in the range of 5–20 [107, 69].
In addition, the material stabilization and training effect of the material is important for the development of a continuous operating system. As known from the literature, a nearly perfect CLS exhibits an almost constant heterogeneous PT behavior throughout its lifetime [122]. Whereas, the polycrystalline material shows an initial PT behavior under cyclic loading and unloading, which is visible as carving of the curve in the first cycles of the stress-strain behavior [239, 128, 74, 56]. This behavior diminishes cycle by cycle, especially under homogeneous tensile and compressive stresses across the cross-sectional area, leading eventually to an almost uniform PT after 50 loading cycles, depending on the material composition [128, 56]. This requires a good understanding of the material behavior and adequate characterization methods for the material and the system.

Characterization

Research in optimizing EC materials requires the characterization of material samples with different geometries like wires, ribbons, and tubes to identify the thermo-mechanical behavior under different loading and HE conditions. The local temperature changes in the material resulting from such processes are usually investigated with combined thermography and force-displacement tests. In the literature, various methods for characterizing EC materials are presented, including differential scanning calorimetry (DSC) [208, 181, 117], and mechanical testing including thermography for localized temperature investigation during PT [227, 215, 110, 79, 54]. The local PT behavior during such tests typically can also be observed by using an optical camera. The time series of images are evaluated for local strain investigation by digital image correlation (DIC) [259, 247, 219, 122, 74, 25].
Recently, a novel characterization method has been presented that enables the experimental analysis of relevant EC material parameters under varying conditions like wire geometry, material composition, and process parameters by using only one thermo-mechanical test bench [53, 54]. The specific latent heat of the SE SMA material is experimentally identified with a novel approach based on comparing dynamic temperature changes achieved by

PT with synchronized joule heating to suppress the materials self-cooling or mimic its self-heating.
This method is crucial for accurately predicting the specific latent heat under mechanical loading and unloading. There is a significant difference of over 50 % between the specific latent heat value obtained by thermal cycling using DSC and the amount accessible by mechanical cycling [145, 110]. This difference in specific latent heat, between temperature-, and stress-induced PT, can be based on a locally incomplete PT as discussed in [224, 232]. Furthermore, the influence of different fluid flow rates on the HE from SMA element to fluid and the coherent convective heat exchange coefficient and the approximate fluid temperature is investigated in literature [55, 35, 11]. This advanced characterization technique enables the investigation of real specimens and saves the time-consuming data combination from the different sample- and test setups. Therefore, it will significantly improve the simulation, development, realization, and optimization of EC HPs.
Regarding fatigue, the lifetime is usually characterized by a rotary bending test [230, 157], which describes the structural stability of the material. In the case of EC systems, also the functional stability has to be investigated, for example, by using a conventional mechanical test bench with IR thermography, as presented by Bechhold et al. [164].

Optimization

For the design of highly efficient EC applications, three criteria can be defined with the knowledge of the four-step thermodynamic cycle (Figure 1.5) to assess the potential of an EC material:

- The first criterion aims for a high adiabatic temperature change. Therefore, large specific latent heat is needed.
- The second one aims for a PT temperature slightly below the application temperature to reduce the necessary stress level and, with this, the mechanical effort of the system.
- The third one aims for low dissipated mechanical work to enlarge the *COP*.

In addition, the lifetime of a EC HP system is essential. Therefore, a high functional and structural stability of the material is needed: Functional fatigue refers to the cyclic degradation of recoverable strain and specific latent heat [225]. Structural fatigue describes the formation and growth of cracks under cyclic mechanical loading [225].
The composition [181] and microstructure [236, 176, 153] of the material influences the specific latent heat, the mechanical work, and the functional stability. A low mechanical work input based on a low hysteresis can be achieved by adding Cu, Pd, or Au, to binary NiTi [216, 194, 189, 200]. But the hysteresis area is directly related to the amount of specific latent heat [115] and the crystallographic compatibility between A and M phase [200].

Therefore, a change in hysteresis width also results in a change of the residual strain [153] and functional stability [189].
In addition, the EC material needs to have a relatively low T_{AF} to enable the complete BT at the low temperature level. The PT temperature of TiNi-based materials can be adjusted by changing the Ni/Ti ratio in binary NiTi [181, 221] or by adding further elements like V as ternary additions [250].
The fatigue behavior can be affected by the material properties [104, 159], the surface conditions [206, 171, 158], the inclusions [142, 126], the loading conditions like tension or compression loading [248, 243, 248, 165, 8], and the training [98, 37].
Despite the codependency requirements, it has been possible in recent decades to develop EC-optimized materials [69] and to make good progress with optimized fatigue properties [113, 96, 96, 71, 30].

1.3 Modeling

Generally, simulation models should provide qualitative and, in the best case, quantitative predictions of the system behavior to subsequently replace the time-consuming and expensive development of several prototypes of a new or optimized engineering device. The development process of a mechatronic system consists of numerous steps and iterations. Each subsystem is specified by its different requirements and challenges to complete the subordinated development steps. To reduce the workload at each process step, only the relevant conditions of the subsystem are typically calculated and simulated. Therefore, different modeling aspects have to be considered in practice, and multiple approaches can be applied.
The following part presents the typical model aspects and the different modeling approaches in the topic of SMA and especially EC.

1.3.1 Model aspects

In the early 1990s, numerous models were developed to enhance the understanding of nonlinear, hysteretic, thermo-mechanical coupled material behavior and to improve the development of SMA based systems. Several publications of SMA modeling can be found in the literature [135, 133, 43, 85, 193, 173, 120, 110, 63, 63, 21].
Every model or simulation tool has applicability in its field, and its use depends on the desired prediction accuracy of the material behavior and its computational effort. Figure 1.6 presents an overview of the most important aspects in modeling the SMA material behavior, especially when integrated into a system.

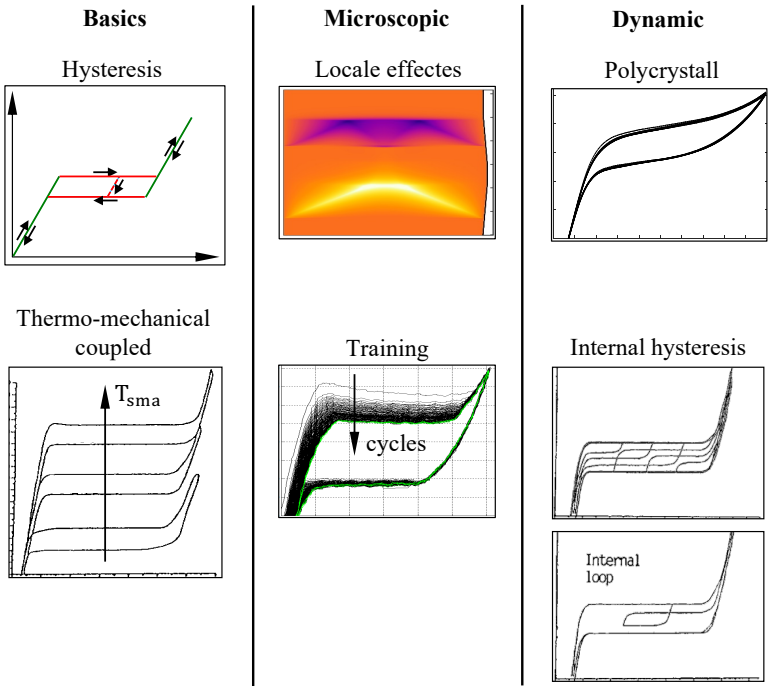

Figure 1.6: Model aspects

The left column addresses the basic thermo-mechanical behavior with the hysteresis in the stress-strain diagram, and the hysteresis shift due to the thermo-mechanical coupling and the temperature-dependent transformation stress. The underlying material model should ideally be able to predict the thermal and mechanical SMA behavior under various boundary conditions. Reducing the mathematical complexity and with this computational effort, some models deal with the assumption of a single crystalline CLS, which leads to a discrete PT approximation on the SMA also known as the *box model* [169].
The middle column focuses on the microscopic PT behavior of A and M with the local effects and the possible training effect. To make meaningful predictions in terms of EC thermal energy and mechanical work, it is essential to understand and reproduce the microscopic local PT behavior and temperature evolution combined with the local stress-strain behavior, as described in literature [247]. This includes, amongst other things, the formation of phase front (PF) and thermal conductivity. The efficiency of the HE strongly depends on the temperature distribution in the SMA due to the thermo-mechanical coupling. Thus, considering local effects is crucial for precisely calculating the absorbed or released thermal energy and the efficiency of the material and device.
The upper part of the middle column illustrates a heterogenic nucleation and propagation behavior of the PF during the PT of a SE SMA using IR thermography and center-line imaging. It is known from the literature, [247, 243, 192, 113, 80, 92, 65] that single-crystalline SMA specimens and SMA thin films with a nearly perfect CLS exhibit nearly persistent inhomogeneous PT behavior at lower strain rates from the beginning of cyclic

loading to failure under the same thermal and mechanical conditions along the sample. Single-crystal SMAs are only negligibly affected by the training effect due to the reduced number of lattice imperfections. Therefore, they show good repeatability over cycles serving outstanding observation capabilities [113]. In the case of higher strain rates or hybrid thermodynamic conditions along the sample, the number of PF along the SMA elements increases. However, the heterogenic PT behavior still dominates in SMA elements with nearly perfect CLS throughout the lifetime of the SMA element. Detailed discussion on the local PT behavior can be found in chapter 3. The lower part of the middle column illustrates the PT behavior of a commercial polycrystalline SE SMA wire. The initial behavior of cyclic loading and unloading, characterized by peaks in the first cycles of the stress-strain relationship, diminishes with each successive cycle. Therefore, the propagating PFs during the PT represents only an initial behavior under homogeneous tensile and compression stress along the cross-sectional area. In the first 100 loading cycles, a homogenization of the PT can be observed, resulting in nearly consistent thermo-mechanical material behavior under the same thermal and mechanical conditions along the sample [239, 128, 56]. This initial behavior is also known as the *training effect* or the *material stabilization*, caused by the imperfect CLS of the SMA element and the presence of hiking and jamming imperfections and impurities, leading to a local stress concentration and preferred nucleation [255]. The details of the training effect depend on the material composition, and they result in PT behavior with numerous PF almost independent of the strain rate. Further details on the training effect can be found in the literature [128, 56]. In simulation models for macroscopic SMA applications with consistent cyclic tension and compression loading, especially for wires-like geometries, the experimentally observed localized PT can usually be neglected, as presented in chapter 4. Therefore, the majority of simulation models describe the stress-strain-temperature behavior of the material in a homogenous state.

However, in bending problems, the deformation case already induces a localized PT due to the inhomogeneous stress distribution in the cross-sectional area [152]. In applications with inhomogeneous stress states along the cross-sectional area or inhomogeneous temperature distribution along the sample, a heterogenic nucleation behavior with local PF can be induced due to the thermo-mechanical dependency of the transformation stress over the lifetime of the system.

The right column presents the dynamic behavior with a rounding effect due to the material's polycrystalline structure, averaging over all crystals, and internal hysteresis loops under changing loading conditions. The upper part of the right column shows a stress-strain diagram with a smooth curve during the PT [57]. This behavior of the SMA depends on innumerable grains of the CLS called *polycrystalline*. The dynamic part is only considered if the assumption of the *box-shaped* stress-strain behavior does not provide the needed

accuracy. This is the case in actuation systems where the cyclic actuation leads to internal hysteresis, and the SMA based system can only be controlled when the model includes this dynamics [57].
A computational model can significantly reduce the experimental effort for material characterization and system behavior prediction. However, the effort of implementation and the calculation time scale with the number of considered aspects and the possible simplifications from 3D to 2D or 1D due to the system boundary conditions.

1.3.2 Model aproaches

Commonly known models can be classified into two main approaches: *phenomenological* and *physics-based*. Depending on the complexity of the operation area, the computational effort, and the accuracy of the prediction, one or the other or a hybrid model consisting of both classes is used [243, 97, 66].

Phenomenological-based

A phenomenological model attempts to reproduce one or more key aspects using mathematical functions without considering or incorporating the system's underlying physical properties. These models are generally used to represent a single aspect of SMA behavior, such as plasticity or thermo-mechanical coupled behavior [243, 97, 66, 193, 85]. The mathematical framework of the model is calibrated using a specific experimental parameter set of the target system. Therefore, it can use mathematical functions [256, 238], state machines [264, 43], and look-up tables [134], to predict the system behavior of similar parameter sets under defined ambient conditions and constraints, with varying accuracy [45]. These models are typically used to describe simple macroscopic system designs [136]. However, this approach facilitates integrated system control [217], and fatigue prediction [90] with low computational effort.

Physics-based

The physics-based model aims to replicate the characteristics of SMA material, such as the SM effect and the SE effect, by utilizing the underlying physical properties of the system. These models consider one or more key aspects of the micro-, meso-, and macroscopic thermo-mechanical behavior, using continuum mechanical and thermodynamical laws combined with statistical approaches [256, 251, 242, 238, 226, 220, 204, 199, 187, 174, 169, 92, 91, 57]. Most of the parameters defined in this model approach have physical analogies. Microscopic-based models provide a more detailed view and accurately resolve the PT behavior, enhancing the understanding of the thermo-mechanical behavior in the CLS of the SMA-based system. For example, Wendler et al. [92] introduces an interface energy

that enables the adjustment of the strain band evolution on the micro-scale. In the local implementation of Welsch et al. [80], the physics-based model is combined into a hybrid model, incorporating phenomenologically motivated parameters that cover the micro-scale PT effects. However, for the system-level modeling of the SMA-based application, which refers to the macroscopic domain, the detailed view of the CLS is less suitable [243, 97, 66]. The physics-based description rebuilds the fundamental relationships of thermo-mechanical coupled SMA. This model approach inherently captures the nonlinear and hysteretic stress-strain-temperature relationship, enabling the prediction of system behavior under arbitrary physical constraints beyond the fitted experimental parameter set. Because of this structural base, it becomes possible to predict both the microscopic and macroscopic behavior using a similar approach. Physics-based models are commonly used to develop complex systems based on SMAs, allowing for prediction of system performance under different ambient conditions [215, 169, 62].

2 State of the Art

In this part, various existing EC HP systems will be presented based on the fundamentals of SMA, the material science, and model aspects of EC. Additionally, the physics-based MAS model will be introduced, which will serve as the basis for the following simulation work.

2.1 Elastocaloric heat pump system

In the 1980s, the first caloric devices based on SMA were heat engines [270]. These systems use the same operation principle as HP, but the thermodynamic cycle is inverted. In recent decades, the interest in EC technologies based on caloric effects in ferroic materials has grown. The literature contains numerous overviews and comparisons of the developed EC systems [147, 118, 104, 74, 42, 47, 18, 5]. The systems can be classified according to the type of load (tension, compression, bending, and torsion), the HE mechanism (conductive and convective), the operation principle (simple HE, heat recovery, active regeneration), as well as the number of material units in a system and how they are arranged (single-stage or multi-stage, cascade or parallel).
Subsequently, this section will summarize the EC devices for different loading types and application scales and discuss the thermo-mechanical performance and the simulation models.

2.1.1 Tensile loaded

In this part, various devices utilizing tensile loaded SMA elements are introduced and named after their first publication author.

Takeuchi

The first EC heating and cooling demonstrator was showcased at the ARPA-E Energy Innovation Summit Technology Showcase 2012 [172] by the researcher group of Professor Takeuchi. This device consists of multiple NiTi single wires mounted around the circumference of two non-parallel, synchronously rotating, annular rings between two concentrically mounted tubes. As the rings rotate, the wires are tensionally loaded and unloaded due to the inclination angle of the upper annular ring. Consequentially, stationary cold and hot semicircles are formed between the tubes. Two independent air flows, guided across each wire group, produce a continuous air heat flux for heating and cooling. However, the

achievable temperature difference between the inlet and outlet of the hot and cold duct is not reported, and there is no numerical simulation of the demonstrator reported in the literature.

Schmidt

Schmidt et al. [149] presents an EC test bench for single SMA elements. This test bench allows for the characterization of specimens with different geometries under different thermodynamic boundary conditions [107]. The SMA element undergoes the EC cycle while alternately increasing the temperature difference of the heat sink and heat source based on conductive HE. The test stand also enables the variation of EC process parameter to optimize the temperature difference, heating and cooling power, and *COP*. Schmidt et al. [106] reported a maximum temperature difference of 21 K between the heat sink and heat source, and a maximum *COP* of 8.3 at no thermal load, for NiTiCuV. Ullrich et al. [152] presented a physics-based 2D simulation approach based on the MAS model.

Tušek

A discontinuously working active EC regenerator based on convective HE with guided liquid between axially tensile loaded SMA plates stacked in several planes was presented by Tušek et al. [109]. In this mechanical setup, a piston moves the HT medium, and control valves manage the separation of the thermal energy. The thermal energy is gradually extracted by a hot and cold heat exchanger, resulting in a maximum temperature difference of 19.9 K [83] between the two at no thermal load. Tušek et al. [131] uses a 1D coupled energy equations of the HE fluid and solid matrix for cyclical steady state operation to predict the temperature difference, thermal power, and *COP*. This model is also utilized in their magnetocaloric simulations [178, 163]. The input work accounts for the mechanical work required to load the material adiabatically and the work needed to pump the fluid. It is assumed that the work released during unloading can be fully recovered, and the input work is only associated with the enclosed area of the performed cycle in the stress - strain diagram.

Ossmer

Ossmer et al. [103] developed and realized an SMA thin-film-based cooling demonstrator on the microscale. In this framework, the SMA film is loaded out-of-plane, and the conductive HE, by alternating contact with the heat sink or heat source, generates a discontinuous heat flux. The single stage demonstrator achieves a temperature difference of 14 K at no thermal load [81]. Whereas, the cascaded device achieves a temperature difference of 27.3 K at no thermal load [6]. The EC behavior of the thin films was simulated using the

local PT properties with two different approaches: Wendler et al. [92] have implemented the MAS model [233] approach in COMSOL, utilizing the unsimplified calculation of the transition probabilities. The interface energy of the local PT behavior is implemented purely physics-based for three dimensions. Welsch et al. [80] implemented the extended MAS-model [226] in COMSOL, incorporating the barrier-evaluated transition probabilities. The implementation of local PT behavior in one dimension is implemented using non-local extensions and a strain-softening part, resulting in a hybrid model that combines physics-based and phenomenological-motivated approaches.

Kirsch

A further application for tensile loaded EC material in a continuous operating EC HP system based on a multitude of tensile loaded SMA elements is presented by Kirsch et al. [74]. In this setup, SMA wire bundles are arranged along the circumference between two co-rotating disks, allowing a synchronous guiding of the SMAs during rotation. The adjustable loading profile, defined by a rotary cam track, determines the tensile strain for each SMA element traveling along the circumference, enabling an optimized thermodynamical process [100]. Forced convective HE, realized between an inner and outer cylinder, achieved a temperature difference of 8 K in initial experiments with the ambient airflow as the thermal load [50]. A fully coupled thermo-mechanical system simulation, implemented in MATLAB, covers the thermal and mechanical aspects of the system [40]. The EC effect of the SMA material, along with the specific latent heat dependent temperature evolution, is considered and implemented using an 1D model for the SMAs with *box-shaped* PT kinetics, based on the lumped extended MAS-model [226]. Recently, this system and model approach was adapted by Cirillo et al. [4].

2.1.2 Compression loaded

This part introduces different devices with compression-loaded SMA elements, each named after their respective first publication author.

Qian

Qian et al. [105] develop an EC HP system based on compression-loaded SMA tube packets surrounded by a fluid. The convective HE produces a discontinuous heat flux between the liquid and the SMA using control valves. With a heat recovery approach, the device achieves a temperature difference of up to 27.8 K at no thermal load [124]. This system approach is implemented and simulated in Simulink [87, 76]. In this model, a 1D approach is used to consider the specific latent heat dependent temperature evolution, incorporating PT kinetics for polycrystalline SMA material. This model approach is based on the

MAS model [233]. The system simulation is based on the unsimplified calculation of the transition probabilities, using the error function. Therefore, a high computation time of the model is assumed. It also considers a phase-dependent transformation stress. The fluidics uses central difference, and the convective HE terms were discretized with the second-order upwind scheme, and the forward Euler method was applied to solve time evolution.

Ahcin

Ahcin et al. [12] recently improved the concept of compression loading and demonstrated its validation using multiple SMA tubes. The surrounding HE fluid produces a discontinuous heat flux using control valves. With the regenerative concept, a temperature difference of up to 31.3 K [12] is achieved at no thermal load and 5.2 K at 25.9 W heating power [12]. The HE of this setup is numerically modeled in MATLAB [19, 13]. A lumped HE model is used to represent the temperature evolution over time between the SMA material and the HE fluid while accounting for the losses to the housing. The temperature change in the SMA tubes is implemented by applying thermal energy. The model approach does not consider the PT behavior of the SMA material and the specific latent heat dependent temperature evolution.

Bachmann

Bachmann et al. [20] presented a continuous operating EC HP system based on a multitude of compression loaded SMA elements. The SMA tube bundles are arranged along the circumference and loaded by a concentrically rotating excenter. The HE medium flows passively along five elements and achieves a temperature difference of 6 K [20] with no thermal load. The HE of this setup is numerically modeled in MATLAB [14]. The system simulation approach is based on lumped HE characteristics without considering the underlying thermo-mechanical EC effect.

Zhou

Zhou et al. [7, 2] presented a discontinuous multi-material cascaded EC regenerator based on compression loaded SMA tubes. In this arrangement, single tubes, out of three different SMA materials, are inline arranged and surrounded by the HE fluid. The HE medium, guided by control valves, achieves a temperature difference of 75 K with no thermal load. However, no numerical simulation of the demonstrator has been reported in the literature.

2.2 Müller-Achenbach-Seelecke model

During the PT of an SMA, changes in internal energy occur due to energy exchange with the environment, resulting in either increase or decrease of the SMA's temperature until reaching a thermodynamic equilibrium. Therefore, it is essential to consider the energy balance of the SMA using a physics-based modeling approach. Additionally, the SMA material exhibits strong hysteretic mechanical and thermal behavior [259, 247, 243, 192]. Several models, known from the literature, based on free energy principles have been proposed for the simulation of SMAs [233, 205]. These models, catching the essential characteristics of the material response, are also known as constitutive models [267, 261, 256, 251, 242, 238, 226, 220, 204, 199, 187, 174, 169, 91, 57]. Mainly, the models provide a physically motivated description of the thermo-mechanically coupled behavior of SMA material, while others only assume an isothermal case. Several approaches in the literature describe the simulative replication of the EC cycle [110, 76].

One of the most commonly used physics-based SMA material models in recent decades is the Müller-Achenbach-Seelecke (MAS) model [233, 204]. This model considers a mesoscopic material layer, averaging over the microscopic lattice cells. Due to its mathematical approach based on the Gibbs free enthalpy with its dependency on stress, strain, and temperature, this model exhibits an inherent thermo-mechanical coupling. The irreversibilities are inherent in the model due to the multiwell free energy system of the Helmholz free energy. Therefore, the MAS model approach is able to predict the thermal dependence of the transformation stress by taking into account the underlying mechanism of the PT and recreates the mechanical work input, as well as the exchanged thermal energy output. This allows the calculation of the *COP*, a significant reference value for caloric processes. The MAS model has been used for 1D thermo-mechanically coupled simulation in finite element software of actuator wires [226, 168, 57], tensile loaded superelastic wires and beams [196, 199, 187, 152], as well as single crystalline thin-films [80] and compressive loaded polycrystalline tubes [76]. Shaw and coworkers proposed another approach for the simulation of actuator wires [227, 243, 247, 215]. Welsch et al. [80], present a variant of the MAS model modified with local extensions that covers the micro-scale PT effects. Qian et al. [76], present a variant of the MAS model modified with a transformation stress depended on PF which covers the polycrystalline effect of the material. In some of those implementations, the polycrystallinity [57], thermal boundary condition effects [168], and the macroscopic field effects [128], were pointed out in detail.

Using the MAS model, also multidimensional simulations have been performed in the last decade [203, 210, 92, 76]. Wendler et al. [92] present a variant of the MAS model modified for plane stress conditions, appropriate for polycrystalline thin-films with conductive and convective HE.

Also, the dynamic system behavior prediction can be simulated based on the MAS model [242]. In this application, the transformation probabilities of the PF based on the Boltzmann equation are calculated in slightly different variations. However, each form is still based on the same parent equation, leading to different computational efforts.
Due to the generality of thermal activation and mesoscopic free energy framework, the MAS model enables the adaption to represent other ferroic materials, like ferroelectric and magnetic implementations [211].
The following part replays the fundamental mathematical structure of the MAS [233] model as known from literature [80, 74]. It presents the set of thermo-mechanically coupled multi-field equations, including the Helmholz free energy, Gibbs free enthalpy, kinetics law, stress-strain equations, and energy balance.
This work presents only the needed formulas and information to implement a physics-based SMA model. The detailed information on the model is given in literature [242, 233, 21, 188, 168, 80].

2.2.1 Internal energy

In the context of the SM effect and SE effect, the HE between the SMA and the environment affects the thermodynamic equilibrium of the SMA material. Due to the thermo-mechanical coupling, the relationship between the mechanical stress and strain is affected. In addition to mechanical stress, the temperature of the material directly influences the PT behavior of the SMA [259]. The specific parameters related to mass or volume are used to make the equation independent of the system's scale.
Equation 2.1 presents the first law of the thermodynamic with specific parameters [190].

$$\underbrace{\frac{du_{\mathrm{sma}}}{dt}}_{\mathrm{a}} = \underbrace{\frac{dq}{dt}}_{\mathrm{b}} + \underbrace{\frac{dw}{dt}}_{\mathrm{c}} = \underbrace{\dot{q}}_{\mathrm{d}} + \underbrace{\sigma \cdot \dot{\varepsilon}}_{\mathrm{e}} \tag{2.1}$$

The change in specific internal energy of the SMA (u_{sma}) (2.1) (a) of a closed system is equal to the sum of the change in specific thermal energy (q) (2.1) (b) and the change in specific mechanical work (w) (2.1) (c). The change in specific thermal energy (q) (2.1) (b) indicates the absorption of specific thermal energy by the system with a positive sign and the release from the system with a negative sign. This term is know as specific thermal power ($\dot{q}$) and can be simplified to (2.1) (d). The change in specific mechanical work (w) (2.1) (c) indicates the work done on the system with a positive sign. The mechanical work depends on the stress (σ)-strain (ε) conditions as introduced in section 1.2. The transformation to time-dependent parameters leads to the simplification of (2.1) (e) with strain rate ($\dot{\varepsilon}$) as a parameter [233].

2.2.2 Stress-strain relation

For the better unterstanding of the relationship between stress and strain introduced in (2.1) (e), geometry-dependent parameters force (F), area (A), and length (l) are defined on an unloaded/undeformed SMA in Figure 2.1 (a) and on a loaded/deformed SMA in Figure 2.1 (b). The internal stress within a single-crystalline SMA element can be

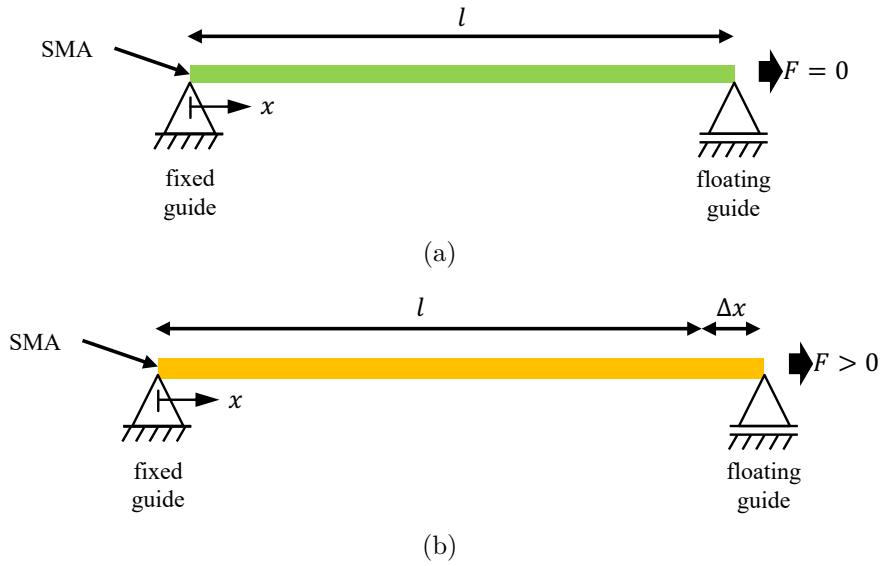

Figure 2.1: Relationship between force (F), length (l), stress (σ) and strain (ε): Unloaded/undeformed SMA (a) and a loaded/deformed SMA (b)

calculated using the stationary 1D momentum balance, introduced in Equation 2.2. This can be calculated with the applied force (F) and the cross-sectional area (A) of the SMA.

$$\frac{\partial F}{\partial x} = \frac{\partial (\sigma \cdot A)}{\partial x} = 0 \tag{2.2}$$

This is also known in the simplified representation as Equation 2.3, assuming a constant cross-sectional area (A) along the sample and no distributed load along the SMA.

$$\sigma = \frac{F}{A} \tag{2.3}$$

The strain (ε) of the SMA can be calculated using Equation 2.4, with the original length (l) and the applied displacement (Δx).

$$\varepsilon = \frac{l + \Delta x}{l} \tag{2.4}$$

The conventional materials, without stress, strain or temperature-induced PT, typically show a direct relationship between the stress and strain values, which can be described piecewise with a linear, quadratic or cubic mathematic function. The *box-shaped*, hysteretic

stress (σ) - strain (ε) diagram of the SMA is presented in Figure 2.2. In this schematic, the commonly known material parameters like Young's modulus for A (E_A), M (E_M), and transformation strain (ε_t) are highlighted. This representation of the stress-strain relation

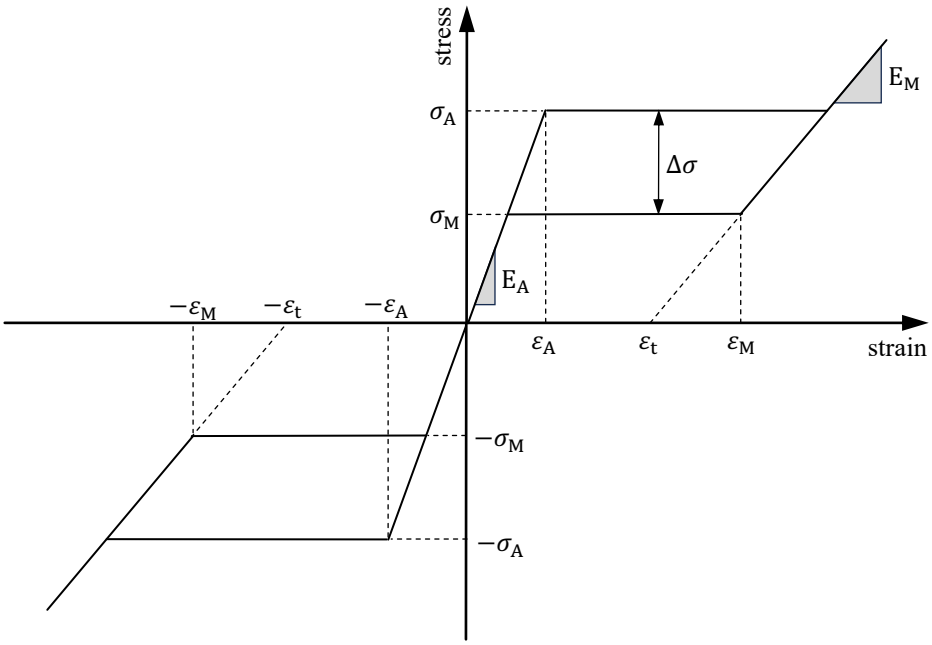

Figure 2.2: *Box-shaped*, hysteretic stress (σ) - strain (ε) diagram of the SMA element.

assumes symmetric material conditions of tensile and compressive loaded SMA material. It should be noted, that in reality the SMA material exhibits a tension-compression asymmetry [248, 243, 248, 165, 8].
Due to the aim of using thin SMA elements with fast HE capabilities, the following discussion of the modeling and implementation focuses on SMA material under tensile load. As a result, this work will provide a detailed description of the tensile-loaded path, using only a typical value of Young's modulus for M (E_M) and transformation strain (ε_t), without limiting its applicability.

Transformation stress from A to M

Further parameters are essential for describing the material behavior in a model and can be derived from Figure 2.2. The transformation stress from A to M (σ_A) describes the height of the upper plateau of the hysteresis. This value can be calculated using Equation 2.5, with the σ_A at the reference temperature (T_ref) (a), and the change in the transformation

stress from A to M (σ_{A}) (b) with varying SMA temperature (T), in accordance with the law of Clausius-Clapeyron [259, 227, 215].

$$\sigma_{\mathrm{A}}(T) = \underbrace{\sigma_{\mathrm{A}}(T_{\mathrm{ref}})}_{\mathrm{a}} + \underbrace{\frac{\partial \sigma_{\mathrm{A}}(T)}{\partial T} \cdot (T - T_{\mathrm{ref}})}_{\mathrm{b}} \tag{2.5}$$

To ensure that the stress-strain relationship is physically feasible, the value σ_{A} must be restricted at the lower limit to at least half of the hysteresis height ($\Delta\sigma$). The corresponding strain value at the point of σ_{A} is known as corresponding strain from A to M (ε_{A}). This point can be calculated using Equation 2.6, which utilizes the value of transformation stress from A to M (σ_{A}) and Young's modulus of A (E_{A}).

$$\varepsilon_{\mathrm{A}} = \frac{\sigma_{\mathrm{A}}}{E_{\mathrm{A}}} \tag{2.6}$$

Transformation stress from M to A

The transformation stress from M to A (σ_{M}) describes the height of the lower hysteresis plateau. This value can be calculated using Equation 2.7 (a)-(b) as the equivalent to Equation 2.5.

$$\sigma_{\mathrm{M}}(T) = \underbrace{\sigma_{\mathrm{M}}(T_{\mathrm{ref}})}_{\mathrm{a}} + \underbrace{\frac{\partial \sigma_{\mathrm{M}}(T)}{\partial T} \cdot (T - T_{\mathrm{ref}})}_{\mathrm{b}} = \underbrace{\sigma_{\mathrm{A}}(T) - \Delta\sigma(T_{\mathrm{ref}})}_{\mathrm{c}} \tag{2.7}$$

Using the hysteresis height at the reference temperature ($\Delta\sigma(T_{\mathrm{ref}})$) and assuming similar temperature dependency of FT and BT, the calculation of the lower hyateresis plateau can be simplified to Equation 2.7 (c). The value of the transformation stress from M to A has also been limited downward to the negative half of hysteresis height ($-0.5 \cdot \Delta\sigma$). The value corresponding strain from M to A (ε_{M}), corresponding to the point of transformation stress from M to A, is calculated using Equation 2.8, with transformation stress from M to A (σ_{M}), Young's modulus of M (E_{M}), and transformation strain (ε_{t}).

$$\varepsilon_{\mathrm{M}} = \frac{\sigma_{\mathrm{M}}}{E_{\mathrm{M}}} + \varepsilon_{\mathrm{t}} \tag{2.8}$$

The formulars (2.5), (2.6), (2.7), and (2.8) are provided for the case of tensile-loaded SMA material. In the case of compressive load, the signs of the equation terms and the specific values need to be adjusted.
Note that the transformation strain (ε_{t}) is the additional strain value which is gained or lost during PT at zero stress. However, the corresponding strain from A to M (ε_{A}), and corresponding strain from M to A (ε_{M}) are calculated using (2.5) and (2.7) and represent the strain value at the calculated value of the transformation stress.

2.2.3 Phase transformation kinetics

The PT between A and M phases and vice versa occurs when the stress level is higher or lower than the temperature-dependent transformation stress, defined in Equation 2.5 and Equation 2.7. The momentum balance in Equation 2.2 is affected by the microscopic phase conditions, as shown in Figure 2.3, for a thin SMA element. The number of the CLS cells of each phase (M-, A, M+) weighted by the number of all cells in the SMA element is called phase fraction of M- (ξ_-), A (ξ_A), and M+ (ξ_-). In this schematic, the

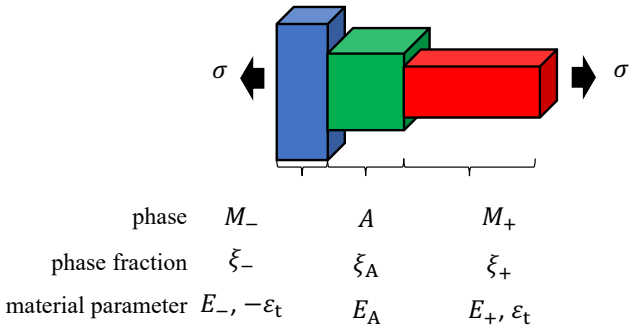

Figure 2.3: Relationship between stress (σ), phase (M-, A, M+), phase fraction (ξ), and material parameters of a thin SMA element.

fictive SMA element consists of three different PT states: The section on the left side, highlighted in blue, is transformed into compression martensite (M-) with the associated phase fraction of the M- (ξ_-) and the material parameters Young's modulus of M- (E_-), and the negative transformation strain (-ε_t). The middle section, highlighted in green, is transformed into austenite (A) with the associated phase fraction of the A (ξ_A) and the material parameters Young's modulus of A (E_A). The section on the right side, highlighted in red, is transformed into tensile martensite (M+) with the associated phase fraction of the M+ (ξ_+) and the material parameters Young's modulus of M+ (E_+), and positive transformation strain ($+\varepsilon_\mathrm{t}$).
Typically, the SMA bulk material consists of multiple layers. The macroscopic strain of the SMA element is calculated by the weighted average of each layer. The distribution of the phase fractions in each layer and between the layers is independent and also independent of the geometric shape of the material [243].

Constitutive relation

The constitutive relation represented by Equation 2.9 depicts the relation between the macroscopic stress (σ) and strain (ε). This relation is dependent on the phase fractions of

M- (ξ_-) and M+ (ξ_+), along with the material parameters such as the Young's modulus of M (E_M), A (E_A) and the transformation strain (ε_t).

$$\sigma = \frac{\varepsilon - \varepsilon_\mathrm{t} \cdot (\xi_+ - \xi_-)}{\frac{\xi_+ + \xi_-}{E_\mathrm{M}} + \frac{\xi_\mathrm{A}}{E_\mathrm{A}}} \tag{2.9}$$

The phase fraction of the A (ξ_A) can be determined by using the continuity law in Equation 2.10, which states that each part of the material must be in one of the three possible PT states: A (ξ_A), M+ (ξ_+), and M- (ξ_-). This provides the current material composition of the SMA element.

$$\xi_\mathrm{A} + \xi_+ + \xi_- = 1 \tag{2.10}$$

Transition probability

The change in phase fraction of each cell in the SMA element due to the thermo-mechanical induced PT can be calculated using transition probability based on Boltzmann statistics [242, 233]. This indicates the probability of finding a physical system in a particular state when it is in its thermodynamic equilibrium, depending on the source phase fraction ($_\alpha$) and target phase fraction ($_\beta$). The rates of transformation between the three global phase fractions can be described by differential equations derived from the algebraic relation in Equation 2.10 and statistical thermodynamics. The change in phase fraction consists of two parts: The cells of the SMA element leaving the specified phase fraction from M+ or M- to A. Alternatively, the cells change their phase and join to the specified phase fraction from A to M+ or M-. In the model, the transitions between M+ and M- always occur via A. Therefore, it is only being calculated for M+ and M-.
In Equation 2.11, the change of the M+ phase fraction (ξ_+) is defined. The leaving part (a) is calculeted by multiplying the source phase fraction (ξ_+) with the corresponding transition probability from M+ to A ($\delta_{+\mathrm{A}}$). The joining part (b) is calculeted by multiplying the source phase fraction (ξ_A) with the corresponding transition probability from A to M+ ($\delta_{\mathrm{A}+}$).

$$\frac{\partial \xi_+}{\partial t} = \underbrace{-\xi_+ \cdot \delta_{+\mathrm{A}}}_{\mathrm{a}} \underbrace{+\xi_\mathrm{A} \cdot \delta_{\mathrm{A}+}}_{\mathrm{b}} \tag{2.11}$$

The equivalent calculation for the M- phase fraction (ξ_-) is presented in Equation 2.12.

$$\frac{\partial \xi_-}{\partial t} = \underbrace{-\xi_- \cdot \delta_{-\mathrm{A}}}_{\mathrm{a}} \underbrace{+\xi_\mathrm{A} \cdot \delta_{\mathrm{A}-}}_{\mathrm{b}} \tag{2.12}$$

The transition probability for each CLS cell from one phase to another phase can be calculated using Equation 2.13.

$$\delta_{\alpha\beta} = \underbrace{\frac{1}{\tau_\xi}}_{\text{a}} \cdot \exp\left(-\frac{\overbrace{\Delta G_{\alpha\beta}\left(\sigma,T\right)\cdot V_{\text{char}}}^{\text{b}}}{\underbrace{\text{k}_\text{B}\cdot T}_{\text{c}}}\right) \tag{2.13}$$

Part (a) of Equation 2.13 defines a rate at which the system attempts to change its current phase fraction, while assuming that the PT occurs much faster compared to the applied strain rate of the SMA. The time constant of the phase fraction (τ_ξ) is a material-specific scaling constant. When using the MAS model for nummerical calculations, the time constant is typically assumed to τ_ξ=0.001 s [168].
Part (b) of Equation 2.13 defines the energy at the considered phase based on the current stress (σ) and the SMA temperature (T_{sma}). This energy is calculated using the Gibbs free energy difference ($\Delta G_{\alpha\beta}$) between the source phase fraction ($_\alpha$) and target phase fraction ($_\beta$). The multiplication with the characteristic material volume element (V_{char}) makes it dimensionless. For nummerical calculation with the MAS model it is typically assumed that V_{char}=5×10^{-20} m^3 [169]. Part (c) of Equation 2.13 relates the energy to the Boltzmann constant (k_B) as scaling constant as well as to the absolute temperature of the SMA (T_{sma}).
The laws of thermodynamics dictate that the transition probability must be calculated using an error function and integration over each energy barrier at each time step of the numerical simulation. However, for the *box-shaped* stress–strain material behavior, only a discrete transformation behavior is required. This means that knowing the exact shape of the transition probabilities is not necessary for this application. As a result, the simplified calculation of barriers reduces the model's numerical computation effort without compromising accuracy [226].

Free Energy relation

The material strain (ε) allows for the identification of the current PT state as the order parameter of the system. Compared to a commonly known system, density is the order parameter from water to water vapor in the PT. To calculate the Gibbs free energy difference, a free energy landscape that is dependent on stress and temperature can be utilized, following the MAS model [242, 233]. This approach allows for the calculation of the phase fraction and the internal transitions between M-, A, and M+.

The Gibbs free enthalpy, calculated using Equation 2.14, naturally incorporates the thermo-mechanical coupling into the SMA model due to its stress and temperature dependency.

$$G = \underbrace{HFE}_{\text{a}} \underbrace{+\sigma \cdot \varepsilon}_{\text{b}} \tag{2.14}$$

The Gibbs free enthalpy consists of the Helmholz free energy (HFE) (2.14) (a) and a linear strain (ε)-dependent deformation term (2.14) (a) with stress (σ) as slope. Therefore, the following will first introduce the Helmholz free energy, which equates to the Gibbs free enthalpy at zero stress. The energy landscape of the Helmholz free energy needs to be dependent on the strain. It should have three minimum points representing the three possible PT states, along with two maxima as a separation between them. A multi-parabola approach, consisting of five parabolas, enables an approximation of the Helmholz free energy (HFE) and is presented in Figure 2.4 [233]. The parabolas create pits and

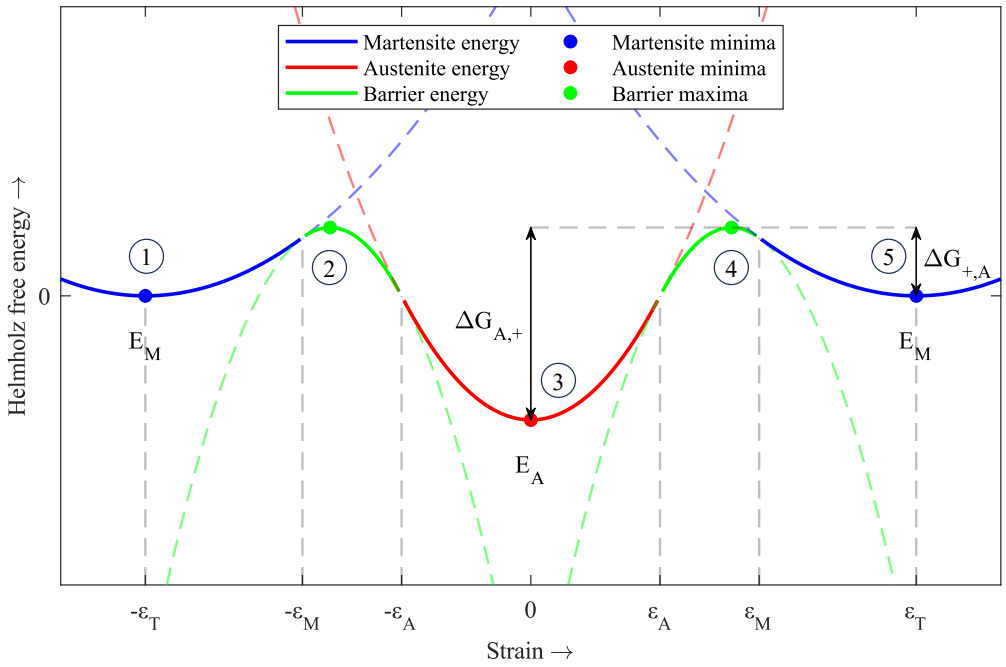

Figure 2.4: Schematic representation of the Multi-parabola approach [233] for the Helmholz free energy (HFE). Extrema are marked as dots.

barriers due to their curvature: Each mesoscopic cell cluster in the SMA behaves like a gravity-influenced sphere, constantly rolling into the possible lowest accessible pit of the landscape. The pits are framed by the barriers formed by the neighboring parabolas. The numbers 1, 3, and 5 are convex and generate a pit comparable to a thermodynamic local minimum and the stable state for each phase. On the other hand, the numbers 2, and 4 are concave, representing the barrier between the pits, which correlates with a local maximum. Assuming the symmetric behavior of M- and M+, the landscape is symmetrically aligned with the y-axis and the minimum point of the A horizontally fixed to zero strain. At

the x-axis, the interesting strain values are highlighted: The local minimum of the M- corresponds to the negative transformation strain $(-\varepsilon_\mathrm{t})$. Whereas, the local minimum of the M+ corresponds to the positive transformation strain (ε_t).
The intersection point between parabola number 1 to 2 corresponds to the negative corresponding strain from M to A $(-\varepsilon_\mathrm{M})$ value. At this point, the M- loses its stability. The intersection point between parabola number 5 to 4 corresponds to the positive corresponding strain from M to A (ε_M) value. At this point, the M+ loses its stability. Furthermore, the intersection points between parabola number 3 to 2 correspond to the negative corresponding strain from A to M $(-\varepsilon_\mathrm{A})$ value and number 3 to 4 to the positive corresponding strain from A to M (ε_A). At this point, the A loses its stability. Those intersection points represent the border between the phases and the inflection point of the combined continuously differentiable function.
The Helmholz free energy depends on the strain (ε) and temperature (T) and can be calculated using Equation 2.15.

$$HFE\left(\varepsilon, T\right) = \underbrace{u_\mathrm{sma}}_{\mathrm{a}} - \underbrace{T \cdot s}_{\mathrm{b}} \tag{2.15}$$

It consists of the specific internal energy of the SMA (u_sma) (2.15) (a) and a linear specific entropy (s)-dependent deformation term (2.15) (b) with the temperature (T) as slope. Therefore, the energy landscape, displayed in Figure 2.4, is a snap-shot at a certain temperature (T).
The energy landscape of the Helmholz free energy for different temperatures is presented in Figure 2.5. With increasing temperature, the parabola number 3 curves downwards, and the A becomes more attractive. Whereas, with decreasing temperature, the parabola number 3 shifts upward, and A leaves the reachable landscape. Thus the material transforms to M- or M+ depending on the current stress level. Therefore, the temperature-dependent vertical position of parabola number 3 inherently determines the material behavior as either the SE or the SM effect.
The free energy cannot be measured directly, only its derivative. Therefore, the free energy can only be determined up to a constant offset. The initial point at zero strain ($HFE_0 = HFE(\varepsilon = 0)$) is set to Equation 2.16. Additionally, the Helmholz free energy values of the minima for M- and M+ are set to zero.

$$HFE_0 = \frac{1}{2} \cdot \left[E_\mathrm{M}\left(\varepsilon_\mathrm{t} - \varepsilon_\mathrm{A}\right) \cdot \left(\varepsilon_\mathrm{t} - \varepsilon_\mathrm{M}\right) - E_\mathrm{A} \cdot \varepsilon_\mathrm{A} \cdot \varepsilon_\mathrm{M}\right] \tag{2.16}$$

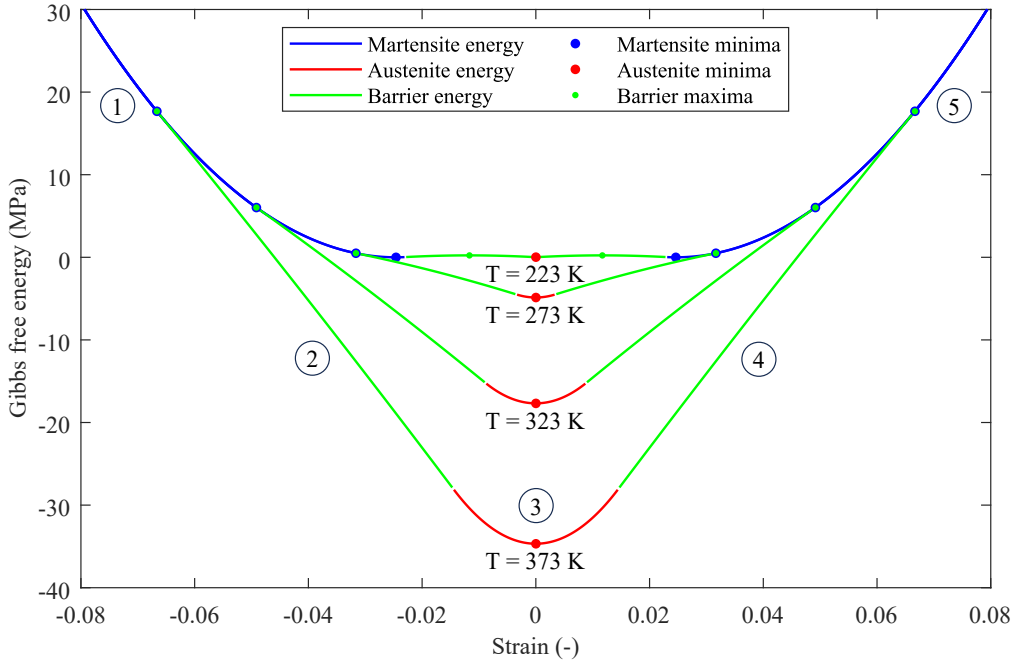

Figure 2.5: Energy landscape of the Gibbs free enthalpy for different temperatures at zero stress. Extrema are marked with dots.

The turning points of the Helmholz free energy can be identified using Equation 2.17, with Equation 2.1, Equation 2.15 and the Legendre transformation and the total differential of itself.

$$d\,HFE = \left.\frac{\partial\,HFE}{\partial\,\varepsilon}\right|_T \cdot d\,\varepsilon + \left.\frac{\partial\,HFE}{\partial\,T}\right|_\varepsilon \cdot d\,T = \sigma \cdot d\,\varepsilon - s \cdot T \tag{2.17}$$

Following Equation 2.17, the first derivative after strain is the stress, and the second one is the Young's modulus.
The Helmholz free energy for each parabola with the number i can be calculated using Equation 2.18, extracted with multi-parabola approach (Figure 2.4) and Equation 2.15.

$$HFE_i = \underbrace{pc1_i \cdot \varepsilon^2 + pc2_i \cdot \varepsilon + pc3_i}_{\mathrm{c}} \tag{2.18}$$

The individual parabola parameters ($pc1$, $pc2$, and $pc3$) can be calculated using Table 2.1. These are generated using general parabola equations and assuming continuous differences between the intersection points and the reasonable corresponding scope of application for each parabola i.
Up to this point, integrating the material-specific parameters into the model is possible, but for the kinetics description of the PT processes, the Gibbs free enthalpy is necessary. The

i	**Scope**	**pc1**	**pc2**	**pc3**
1	$-\infty < \varepsilon \leq -\varepsilon_\mathrm{M}$	$\frac{E_\mathrm{M}}{2}$	$E_\mathrm{M} \cdot \varepsilon_\mathrm{t}$	$\frac{E_\mathrm{M}}{2} \cdot {\varepsilon_\mathrm{t}}^2$
2	$-\varepsilon_\mathrm{M} < \varepsilon \leq -\varepsilon_\mathrm{A}$	$\frac{E_\mathrm{M}\cdot\varepsilon_\mathrm{tM}+E_\mathrm{A}\cdot\varepsilon_\mathrm{A}}{2\cdot\varepsilon_\mathrm{AM}}$	$\varepsilon_\mathrm{A} \cdot \frac{E_\mathrm{M}\cdot\varepsilon_\mathrm{tM}+E_\mathrm{A}\cdot\varepsilon_\mathrm{M}}{\varepsilon_\mathrm{AM}}$	$\frac{2\cdot G_0\cdot\varepsilon_\mathrm{AM}+{\varepsilon_\mathrm{A}}^2\cdot(E_\mathrm{M}\cdot\varepsilon_\mathrm{tM}+E_\mathrm{A}\cdot\varepsilon_\mathrm{M})}{2\cdot\varepsilon_\mathrm{AM}}$
3	$-\varepsilon_\mathrm{A} < \varepsilon \leq \varepsilon_\mathrm{A}$	$\frac{E_\mathrm{A}}{2}$	0	G_0
4	$\varepsilon_\mathrm{A} < \varepsilon \leq \varepsilon_\mathrm{M}$	$\frac{E_\mathrm{M}\cdot\varepsilon_\mathrm{tM}+E_\mathrm{A}\cdot\varepsilon_\mathrm{A}}{2\cdot\varepsilon_\mathrm{AM}}$	$-\varepsilon_\mathrm{A} \cdot \frac{E_\mathrm{M}\cdot\varepsilon_\mathrm{tM}+E_\mathrm{A}\cdot\varepsilon_\mathrm{M}}{\varepsilon_\mathrm{AM}}$	$\frac{2\cdot G_0\cdot\varepsilon_\mathrm{AM}+{\varepsilon_\mathrm{A}}^2\cdot(E_\mathrm{M}\cdot\varepsilon_\mathrm{tM}+E_\mathrm{A}\cdot\varepsilon_\mathrm{M})}{2\cdot\varepsilon_\mathrm{AM}}$
5	$\varepsilon_\mathrm{M} < \varepsilon < \infty$	$\frac{E_\mathrm{M}}{2}$	$-E_\mathrm{M} \cdot \varepsilon_\mathrm{t}$	$\frac{E_\mathrm{M}}{2} \cdot {\varepsilon_\mathrm{t}}^2$
with $\varepsilon_\mathrm{tM} = \varepsilon_\mathrm{t} - \varepsilon_\mathrm{M}$ and $\varepsilon_\mathrm{AM} = \varepsilon_\mathrm{A} - \varepsilon_\mathrm{M}$				

Table 2.1: Parameters of the multi parabola landscape, adapted to the SMA material

energy landscape of the Gibbs free enthalpy for different stress (σ) values can be calculated using Equation 2.19, which is a combination of Equation 2.14 and Equation 2.18.

$$G_i = HFE_i + \sigma \cdot \varepsilon = pc1_i \cdot \varepsilon^2 + pc2_i \cdot \varepsilon + pc3_i - \sigma \cdot \varepsilon \tag{2.19}$$

The integration of the stress in the energy landscape results in s stress-dependent tilting, as presented in Figure 2.6 for an applied tensile stress ($\sigma \geqq 0$). In the case of a compression-based stress ($\sigma \leqq 0$), the graphs will be mirrored at the y-axis.
Looking back to the transition probability ($\delta_{\alpha\beta}$) introduced in Equation 2.13, the Gibbs free energy difference ($\Delta G_{\alpha\beta}$) between the source phase fraction ($_\alpha$) and target phase fraction ($_\beta$), can be calculated using all four equations from (2.20) to (2.23) depending on source and target.

$$\Delta G_{-\mathrm{A}} = G_2\left(\varepsilon_{\mathrm{ex},2}\right) - G_1\left(\varepsilon_{\mathrm{ex},1}\right) \tag{2.20}$$

$$\Delta G_{\mathrm{A}-} = G_2\left(\varepsilon_{\mathrm{ex},2}\right) - G_3\left(\varepsilon_{\mathrm{ex},3}\right) \tag{2.21}$$

$$\Delta G_{\mathrm{A}+} = G_4\left(\varepsilon_{\mathrm{ex},4}\right) - G_3\left(\varepsilon_{\mathrm{ex},3}\right) \tag{2.22}$$

$$\Delta G_{+\mathrm{A}} = G_4\left(\varepsilon_{\mathrm{ex},4}\right) - G_5\left(\varepsilon_{\mathrm{ex},5}\right) \tag{2.23}$$

The strain value at the extremum ($\varepsilon_{\mathrm{ex},i}$), marked as dots in Figure 2.5 and Figure 2.6, can be calculated using Equation 2.24 for each parabula.

$$\varepsilon_{\mathrm{ex},i} = \frac{\sigma - pc2_i}{2 \cdot pc1_i} \tag{2.24}$$

The multi-parabola approach inherently determines material behavior as either SE or SM effect. This approach also implies a part of the thermo-mechanical coupling due to

the strain-, temperature-, and PF dependent stress determination. With the mesoscopic free-energy function, the model can predict the macroscopic, hysteretic material behavior of SMAs. However, to account for the temperature change related to the released or absorbed specific latent heat, the energy balance of the SMA must be considered.

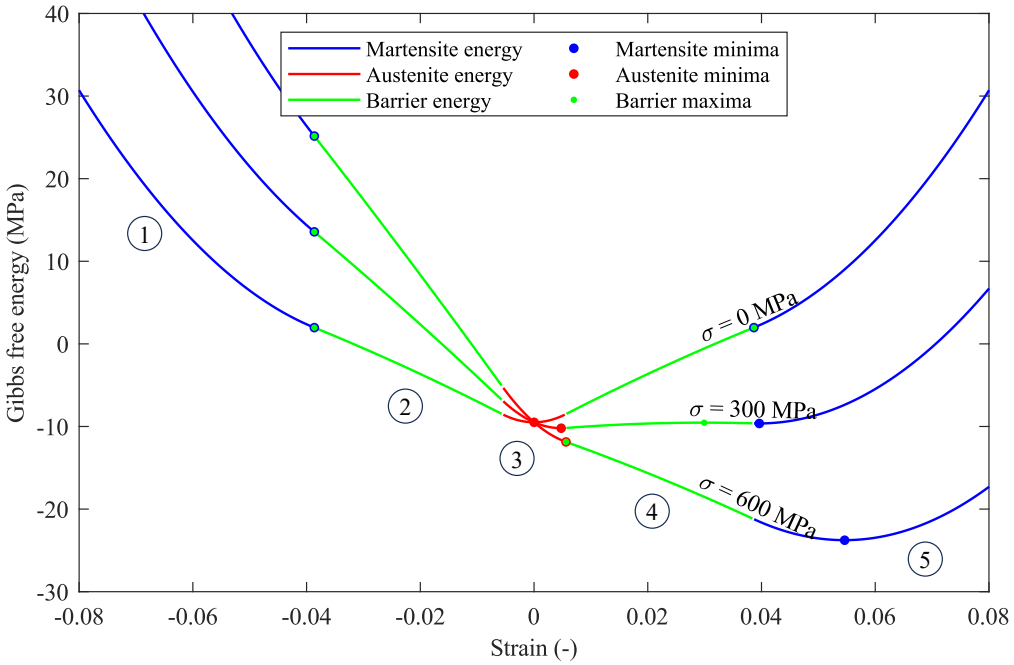

Figure 2.6: Energy landscape of the Gibbs free enthalpy for different stress (σ) values and constant temperature. Extrema are marked with dots.

2.2.4 Energy balance

The energy balance of the SMA material can be calculated using Equation 2.25 [168], following the first law of the thermodynamics, which is introduced in Equation 2.1. The change of the specific internal energy of the SMA (u_{sma}), can be calculated using (2.25) (a) with the material-specific value of density (ρ), and specific heat capacity (c), as well as the temperature (T). This specific internal energy (u_{sma}) can also be modified by accounting for the thermal power into the SMA. The release or absorption of the specific latent heat (H) is dictated by the energy landscape, influenced by the current strain, stress, and temperature, leading to changes in the phase fraction (ξ) of M+ and M- as considered in term (b). HE with the environment is an additional term that influences the specific internal energy. This is calculated using (c), with the heat exchange coefficient (h), the surface area of the SMA ($A_{\mathrm{sma,surf}}$), the volume of the SMA (V_{sma}), and the temperature difference between SMA and ambient. The last part is the Joule heating (d), with which

the specific internal energy of the SMA (u_{sma}) can also be changed, for example, to induce the SM effect.

$$\frac{du_{\mathrm{sma}}}{dt} = \underbrace{\frac{\partial}{\partial t} \cdot \rho_{\mathrm{sma}} \cdot c_{\mathrm{sma}} \cdot T_{\mathrm{sma}}}_{\mathrm{a}} = \\ \underbrace{+ \rho_{\mathrm{sma}} \cdot H \cdot \left(\frac{\partial \xi_{+}}{\partial t} + \frac{\partial \xi_{-}}{\partial t} \right)}_{\mathrm{b}} \underbrace{- h \cdot \frac{A_{\mathrm{sma,surf}}}{V_{\mathrm{sma}}} \cdot (T_{\mathrm{sma}} - T_{\mathrm{amb}})}_{\mathrm{c}} + \underbrace{j\,(t)}_{\mathrm{d}} \tag{2.25}$$

The energy balance involves the full integration of the thermo-mechanical behavior into the system, which includes the internal heating and cooling of the SMA related to specific latent heat. The energy landscape changes due to a mechanical input, which affects the phase fraction. The change in phase fraction leads to the release or absorption of the specific latent heat, resulting in a change in temperature and consequently altering the energy landscape. This interdependence of thermal and mechanical inputs shows that only a thermo-mechanically coupled model can qualitatively and quantitatively predict the complex behavior of an SMA-based system with sufficient accuracy.

3 Local phase transformation model

The preceding chapters have highlighted that understanding the thermo-mechanical material behavior, particularly local effects such as the formation and propagation of PFs during the PT, is crucial for qualitatively and quantitatively accurate SMA modeling. Therefore, this chapter presents numerical simulations of the thermo-mechanically coupled behavior of Titanium-Nickel-Copper-Cobalt (TiNiCuCo) thin-film samples and compares them to experimental measurements [80].
As known from subsection 1.3.1, when dealing with inhomogeneous stress states along the cross-sectional area or SMA elements with a nearly perfect CLS, a heterogenous nucleation behavior can be expected over the lifetime of the system. The calculation of the absorbed or released thermal energy by averaging along the entire surface of the SMA without considering the position of the thermal energy spot, as described in literature [247], leads to significant deviations, especially in microscale applications. In the case of strain rate variation, the number of PF differs. Hence, proper guidance of the HE fluid in convection-based systems or appropriate contact between the heat sink and heat source in conduction-based HE needs to be adjusted. Additionally, controlling the thermal energy output allows the development of an efficient system.
This part of the work focuses on developing a model including the local nucleation behavior, as well as the thermo-mechanical material behavior of SMAs. The primary goal is to accurately replicate the localized PT behavior of an SMA element during an EC heating and cooling cycle. To achieve this, the MAS model, as described in section 2.2, is implemented into the commercially available finite element (FE) software COMSOL Multiphysics. To incorporate localized PT effects, lateral contraction and a transformation softening behavior are implemented into the basic model. Furthermore, a non-local extension is added to the model that takes into account the scaled contribution of the second spatial derivative of the M field to the kinetics equations of PT, which considers the interfacial energy.
First, the experimental setup will be introduced, followed by the modeling approach, model implementation, calibration, and validation. Finally, the results will be presented and discussed.

3.1 Experimental system

In this section, the experimental data of the TiNiCuCo-based films are presented [145]. The experimental data of SE SMA thin films were generated and provided by the research

group in Karlsruhe that investigated EC cooling on the micro-scale during the German Research Foundation Priority Programme SPP1599 [122, 145].
The Ti overhead exhibits almost no fatigue behavior even after millions of load cycles [113]. Therefore, this material is investigated for its heating and cooling properties [102]. Because of the microscopic scale of the SMA element, the global thermo-mechanically coupled behavior is investigated, and the local effects of the PT were observed in the experimental measurements.
The experiments presented in the following were conducted using a sputter-deposited Ti 55.2 Ni 29.3 Cu 12.7 Co 2.8 single target thin-film of the dimensions: length (l=15 mm), width (lw=1.75 mm), and depth (ld=18 µm).
First, the mechanical setup is introduced, and then the experimental results are presented and discussed.

3.1.1 Mechanical setup

Figure 3.1 presents the experimental setup of the uniaxial tensile test procedure. The mechanical setup consists of a commercially available universal tensile testing machine from the company *Zwick*. The SMA thin-film sample is attached to alumina plates on both ends using a two-component adhesive to ensure uniform stress at the clamping. These prepared ends are then placed in the standardized sample holder.
During the experiment, the lower end of the sample remains stationary while a ball screw drive moves the upper end. Force is measured by a force sensor with a resolution of 0.25 N. The distribution of the sample's temperature is monitored using an IR camera, the *A655sc* from the company *FLIR*, with a spatial and temporal resolution of 25 µm and 10 ms. The macro lens with factory calibration allows a temperature range of −40 °C to 150 °C. The sample is then coated with a graphite lacquer to achieve a defined emissivity compared to the surface of the metallic specimen [229, 186].

Data acquisition

The main program triggers synchronous data acquisition between force and displacement. The trigger signal is also sent via a TTL signal to the camera system for image acquisition. The synchronized time-resolved position and force measurements are stored in a csv-file. This file format allows for the evaluation of the time series data points using various software such as Excel or MATLAB. The time series of images is stored on the PC and then post-processed during the data evaluation, as described later in detail.

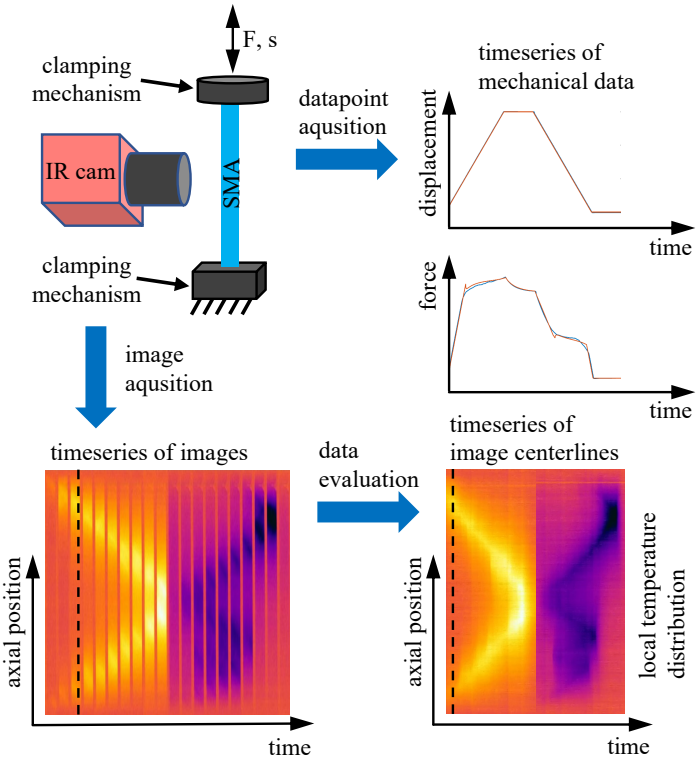

Figure 3.1: Experimental setup for uniaxial tensile tests with IR thermography.

Test procedure

Figure 3.2 illustrates the load path used in the experiments. Before starting the test cycle, a small force of 1 N is applied to the sample to prevent buckling. This pre-loading force represents a stress of 32 MPa and a strain of 8.0×10^{-4}, considering the size of the sample. The displacement at this point is approximately 0.01 mm. The test sequence consists of four displacement-controlled steps:

- First, the SMA element is loaded up to a strain of 0.02 with the defined strain rate.
- In the second state, the strain remains constant for a duration of 10 s. The holding period duration is chosen so that the sample returns back to ambient temperature.
- In the third state, the thin-film is unloaded with a defined strain rate until the force reaches downwards a minimum of 1 N to avoid buckling.
- In the last state, the force remains constant for a duration of 10 s.

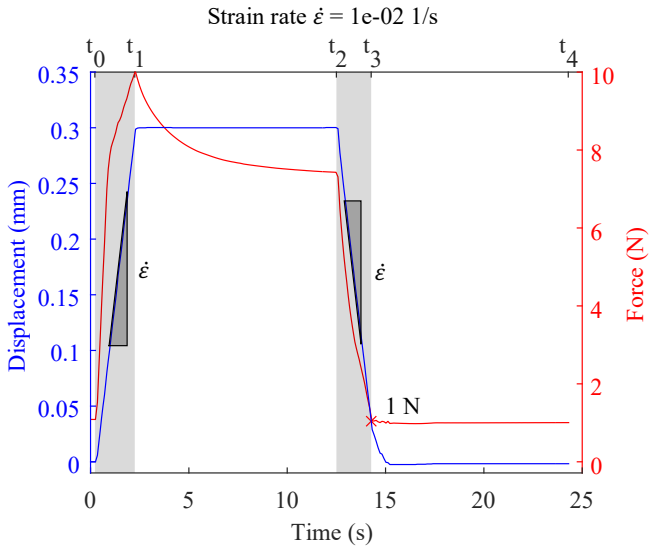

Figure 3.2: Example load path for a strain rate of $\dot{\varepsilon} = 1 \times 10^{-2}\,1/\mathrm{s}$.

3.1.2 Experimental results

The experimental results for thermo-mechanical testing are shown in Figure 3.3 for three different strain rates [145]. The used sputter-deposited thin-film of the EC-enhanced alloy TiNiCuCo, exhibits due to is nearly perfect CLS quasi single-crystal thermal and mechanical behavior. The first and second rows show the evolution of displacement and

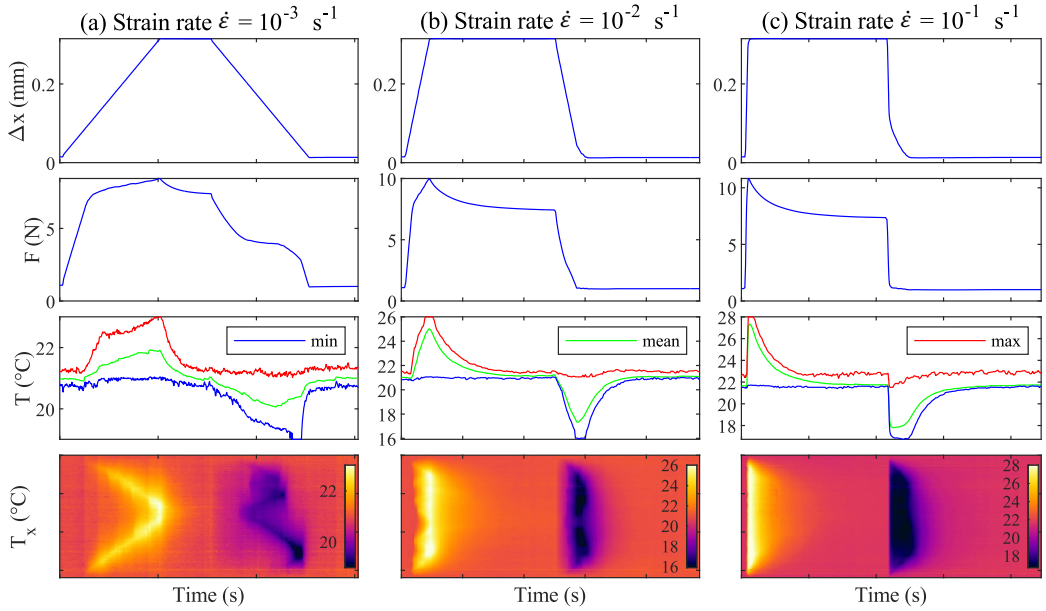

Figure 3.3: Experimental data of the tensile loaded sputter-deposited Ti55.2-Ni29.3Cu12.7Co2.8 thin-film for different strain rates.

force over time. The diagrams in the third row display the minimum, mean, and maximum temperature at the centerline of the sample. These temperature values can be used for description when the variations of the material behavior over the width and thickness of

the sample can be neglected. In the case of thin-film, the thickness is negligible in any case. The slight variation of temperature profiles in the lateral direction due to the inclination angle of strain bands is also neglected because essential measures like the number of strain bands and their propagation velocity are independent of the lateral position [145]. In this row, it is evident that all temperature values almost return to their initial temperature after the loading and holding state, as well as after the unloading and holding state. This is crucial for maximizing or minimizing the temperature difference obtained during the EC cycle, which is a crucial parameter for heating and cooling devices [106]. The presentation of the local temperature distribution over time is shown as a waterfall diagram in the fourth row. The spatio-temporal waterfall diagram is created by tracing the specimen's centerline in each image of the time series and plotting them next to each other. This illustrates the evolution of the temperature vs. position and time in a 2D diagram. The spatio-temporal waterfall diagram of the local temperature distribution enables better visualization and easier comparison. This diagram can be used under the assumption of homogeneous material conditions of the sample.

In the first column, the results of the lowest strain rate ($\dot{\varepsilon} = 10^{-3}\,1/\mathrm{s}$) are presented: While loading, the SMA begins transforming at both ends almost simultaneously. This is indicated by the temperature change of the material due to the release of the specific latent heat. These two PFs travel along the thin-film and merge, producing the maximum temperature at the meeting point. During the holding phase, the sample returns to ambient temperature due to the convective HE with the environment. At unloading, the material begins to transform in the middle, with distinct PFs traveling towards the ends while cooling the material due to the absorption of the specific latent heat. The merging of the PF results in the lowest temperature at the meeting point. During the holding phase, the sample returns to the ambient temperature due to convective HE with the environment. The unsymmetric PT behavior can be caused by slight variations in the surface temperature of the sample.

The different start behavior of the PT during loading and unloading in the IR images indicates an incomplete PT of the material. The PT starts at both sample ends during loading. During unloading, however, the PT starts near the center, where the temperature peaks joined previously during the loading state. This indicates that the apparent meeting of the PFs did not result in a full PT state. Instead, an un- or less transformed region remains, where nucleation is preferred during unloading.

A drop in the force curve is observed during the holding period after loading. This also indicates that the PT was not completed during loading because a decreasing temperature due to HE also reduces the transformation stress, allowing further material to transform. This ongoing PT process leads to further local expansion of the material, resulting in the

force relaxation. If the PT is already complete during loading, no reduction in force can be observed during the holding phase.
With the increasing and decreasing strain, the PFs travels along the SMA element and induces a local change in the materials's temperature. Higher strain rates, which are presented in columns two and three, lead to the occurrence of a higher number of traveling temperature peaks, which indicates propagating PFs. New PFs emerge when existing ones cannot travel fast enough to transform sufficient material to account for the global applied length change, in combination with the local temperature depended transformation stress as introduced in Equation 2.5. This leads to a search for the next possible and suited nucleation point along the SMA element [259]. In case of loading, the local self-heating of the material at the PFs during PT hinders their propagation because a higher local stress would be required to reach transformation stress. Conversely, during unloading, the local self-cooling effect hinders their propagation. Depending on the distribution of temperature along the sample, the formation or nucleation of new PFs appears to be more energetically favorable than maintaining or increasing the propagation velocity of existing PFs. At higher strain rates, the convective and conductive HE away from or to the PFs does not keep pace with transformation-induced temperature change caused by the specific latent heat, which is followed by the change of the local transformation stress. This leads to more PF with increasing strain rate.

3.2 Model Approach

This section presents the modeling approach based on the experimental system and results. The simulation model comprises various elements that need to be discussed in this approach. This will include the selected model type, constraints for model dimensions, segmentation, and discretization method, boundary conditions between the simulated system and the environment, as well as model enhancements.
The used sputter-deposited thin-film of the EC-enhanced alloy TiNiCuCo, exhibits due to is nearly perfect CLS quasi single-crystal a mechanical behavior with negligible fatigue [113]. Therefore, it is necessary to consider the basic hysteretic material behavior with thermo-mechanical coupling and local effects, as introduced in Figure 1.6. Training and dynamic effects can be excluded.
For the simulation of the hysteretic SMA material during tensile loading, the physics-based MAS model is used as the foundation. This includes also the thermo-mechanical coupling, as introduced before (section 2.2). The arbitrary MAS model normally considers global, time-dependent phase fraction ($\xi(t)$). Therefore, the model will be extended in the following part.

3.2.1 Dimension

The SMA element is actually a 3D body. When creating models, it is best to opt for a simple replication of the simulation's focal element, boundary conditions, and operating cycle. This simplification reduces the model's complexity and minimizes computational effort. However, reducing the model's dimensions and simplifying the boundary conditions during the operational cycle can lead to discrepancies between the simulated behavior and the actual behavior of the focal element within the system.
In the case of the thin-film-based SMA element, which exhibits a uniform load and temperature profile throughout the EC cycle along its depth, the small aspect ratio between the depth and width of the sample (ld=18 µm and lw=1.75 mm respectively), as well as between the depth and length of the sample (ld=18 µm and l=15 mm respectively), allows for neglecting the dimension of the thickness in the model.
A loading or unloading along the length of the SMA, with a uniform load and temperature profile throughout the cycle along its width, leads to the formation of sharp local strain bands along the lateral direction, as presented in Figure 3.1 time series of images [145]. These *Lüder*-like strain bands show an angle that depends on the loading direction, measuring 53° for the PT from A to M, and 59° for the PT from M to A [255, 247]. However, the bands have a consistent length across the width of the sample [255, 247, 222]. Therefore, the temperature and PT profile in the lateral direction due to the inclination angle of strain bands slightly differ in position along length of the sample. But the number of discretized parts at a specific temperature and PT state along the sample's length do not significantly differ, allowing for neglecting the dimension of the width in the model.
The essential values, such as the number of strain bands and their propagation velocity, can be independent of the lateral position measured and also simulated by one line along the length of the SMA element. Finally, the simulation model only needs to be developed and implemented as a one-dimensional problem while assuming homogeneous material conditions of the sample and compared with the one-dimensional temperature data from measurements collected along the centerline on the film's surface, as introduced in section 3.1.

3.2.2 Segmentation

In the local regime, the centerline of the thin-film can be considered as numerous discrete cell elements [243], as shown in Figure 3.4. Each element of the SMA has its own PT state and is subordinated to a phase fraction (ξ) depending on the global stress (σ). To

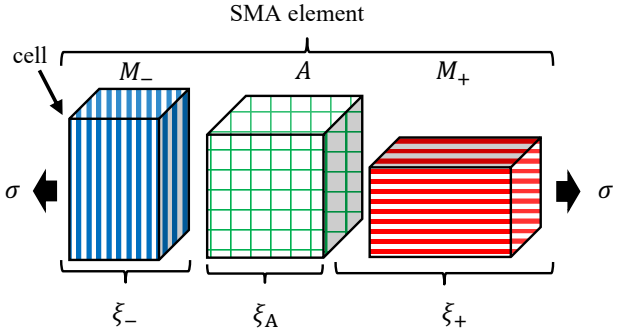

Figure 3.4: The SMA element is assumed as numerous discrete cell elements.

determine the material states of each element, the local strain and can be determined from the displacement field (Δx) using Equation 3.1.

$$\varepsilon = \frac{\partial \Delta x}{\partial x} \tag{3.1}$$

The change in length of the local cell within the SMA element is mainly caused by the strain related to the PT (ε_t) and the elastic strain ($\varepsilon_\mathrm{elast}$). The transformation state of each cell, represented by the phase fraction of the M+ (ξ_+), enables the calculation of the phase fraction strain ($\varepsilon_{\mathrm{t},\xi}$) for each cell, using Equation 3.2.

$$\varepsilon_{\mathrm{t},\xi} = \xi_+ \cdot \varepsilon_\mathrm{t} \tag{3.2}$$

Assuming negligible thermal expansions, the portion of the elastic strain ($\varepsilon_\mathrm{elast}$) can be calculated using Equation 3.3.

$$\varepsilon_{\mathrm{elast},\xi} = \varepsilon - \varepsilon_{\mathrm{t},\xi} \tag{3.3}$$

The transformation strain induces an isochoric lateral contraction (ν_t=0.5) [243], resulting in an non-constant cross-section area for each cell. This area can be calculated using Equation 3.4, with the commonly known value of Poisson's ratio for elastic deformations in metals (ν_elast=0.33), as well as the element's width (lw), and depth (ld).

$$A = lw \cdot ld \cdot \left(1 - \nu_\mathrm{elast} \cdot \varepsilon_\mathrm{elast} - \nu_\mathrm{t} \cdot \varepsilon_\mathrm{t}\right)^2 \tag{3.4}$$

This reduces the cross-section as the strain increases, which leads to locally increased stress.

The mechanical behavior of the SMA element on the global scale is governed by the stationary momentum balance in the loading direction, known from Equation 2.2. Summing up over the entire SMA element with N numbers of cells, the product of stress (σ_i) and area (A_i) must be the same for each cell.

3.2.3 Boundary conditions

The boundary conditions are defined based on the experimental setup presented in section 3.1. The clamps at both ends of the SMA element are assumed to have similar thermal and mechanical impact. Therefore, equal boundary conditions for temperature, displacement, and force are considered at both ends. Using this symmetry, the simulation model only needs to implement half of the SMA element length. This results in symmetric propagation of the phase front along the sample.
To establish the mechanical boundary conditions of the one-dimensional geometry, one end, which corresponds with the half length to the center of the sample, of the SMA is fixed. Therefore, the position (x) and time (t) depending displacement (Δx) at this end is set to zero for the entire test period, as presented in Equation 3.5.

$$\Delta x\,(x = 0, t) = 0 \tag{3.5}$$

On the other end, the position (x) and time (t) depending displacement (Δx) is set to the displacement which is pre-defined by the performed cycle $(\tilde{\Delta} x)$, as presented in Equation 3.6.

$$\Delta x\,(x = l/2, t) = \frac{\tilde{\Delta} x}{2} \tag{3.6}$$

This displacement is specified to the half of the displacement value generated by the experimental test setup, presented in the first row of Figure 3.3.
At the holding phase after unloading, the boundary condition, introduced in Equation 3.6, is replaced by a boundary condition that defines a constant force of 1 N to avoid buckling of the thin-film, as presented in Equation 3.7. This condition is limited to the time interval of $t = [t_3, t_4]$, introduced in Figure 3.2, during unloading after reaching the minimum force and the subsequent holding phase.

$$F\,(x = l/2, t = [t_3, t_4]) = 1\,\mathrm{N} \tag{3.7}$$

The testing machine's form- and friction-locked clamping mechanism acts as a heat sink for each sample end due to the thin-film's low specific heat capacity compared to the significantly higher mass of the substrate. Therefore, the temperature at this position $(x = l/2)$ remains at ambient temperature, as presented in Equation 3.8.

$$T\,(x = l/2, t) = T_{\mathrm{amb}} \tag{3.8}$$

Concerning the symmetry assumption with respect to the midpoint of the sample, the temperature gradient must be assumed to be zero, according to Equation 3.9.

$$\frac{\partial T}{\partial x}\left(x = 0, t\right) = 0 \tag{3.9}$$

The traveling of the PFs must be mathematically restricted to the sample area. Therefore, homogeneous Neumann boundary conditions must be assumed for the phase fraction (ξ) on the sample ends, following Equation 3.10.

$$\frac{\partial \xi_+}{\partial x}\left(x = 0, t\right) = \frac{\partial \xi_+}{\partial x}\left(x = l/2, t\right) = 0 \tag{3.10}$$

3.2.4 Model improvements

In order to consider localized PT effects, as observed in the experiments discussed in section 3.1, the MAS model introduced in section 2.2 needs to be extended. Therefore, the temperature (T), and the displacement (Δx), as well as the phase fraction (ξ) field need to be considered as position- and time-dependent (x,t) local quantities.
The EC behavior of the thin-films was simulated with the local PT properties by Wendler et al. [92]. In this contribution, the MAS model [233] approach is also implemented in COMSOL, utilizing an interface energy for the local PT behavior in each layer and an unsimplified calculation of the transition probabilities based on error functions. This purely physics-based approach is implemented for three dimensions.
In literature, a few approaches were discussed to model localized behavior in finite element software [247, 243, 192, 168, 145, 92]. In order to consider localized PT and continuous transitions between A and M regions, a non-local extension can be utilized [215, 175, 170, 137, 184]. The localization effect in the material can be generated by a local softening behavior during the PT [243]. In general, field effects can be accounted for by implementing the fundamental material law into a more extensive field solution [168] or by including additional gradient-based free energy terms. Various approaches for the non-local extension exist and vary from strain gradient methods [215] over phase gradient energy [170, 137, 184] to Green's functions [175].

Transformation stress

The segmentation of the SMA element into multiple cells, as presented in Figure 3.4, requires adapting the ordinary MAS formulas, known from section 2.2, to enable local prediction of the thermo-mechanical SMA behavior. Focussing on the local PT of only one discrete cell of the SMA: If this cell begins to transform, its T changes due to the release or absorption of the specific latent heat, followed by the change of the transformation stress (Equation 2.5). When the transformation stress changes, the PT requirement for this

specific cell also changes, causing the ongoing PT to stop and resulting in an incomplete transformation state. At this point, a neighboring cell initiates the PT. It halts at the same time, similarly to the preceding cell, resulting in a gradual homogenization of the PT within the SMA element. This described behavior does not align with the transformation behavior observed in the experiments (Figure 3.3). The observed local PT behavior indicates once a cell initiates the PT process, it continues despite its temperature increase until the cell's PT is completed. The internal stress in the material at the PF prefers full PT, which is caused physically by lattice mismatch of A and M and the introduced stress between the lattice edges.

The full PT for each cell can be captured by a phase fraction dependent transformation stress by inclining the plateau stress depending on the PT and the current phase fraction [243, 227]. Similar approaches from the literature include adapting the coherency energy contribution [245], and interaction energy [215], also resulting in a softening material effect during FT and a hardening material effect during BT under isothermal conditions. This approach is visible as a force drop in the stress - strain diagram during the PT [247, 215, 192].

The local term (c) extends the transformation stress from A to M (σ_{A}) which consists of term (a) and (b), resulting in the Equation 3.11. This enables full FT from the A to M due to the degradation in transformation stress of the currently transforming cell using a material-dependent parameter *phase fraction dependence of* σ_{A} (β_{A}) and the phase fraction (ξ).

$$\sigma_{\mathrm{A}}\left(T,\xi\right)=\underbrace{\sigma_{\mathrm{A}}\left(T_{\mathrm{ref}}\right)}_{\mathrm{a}}+\underbrace{\frac{\partial\sigma_{\mathrm{A}}\left(T,\xi\right)}{\partial T}\cdot\left(T-T_{\mathrm{ref}}\right)}_{\mathrm{b}}-\underbrace{\beta_{\mathrm{A}}\cdot\left(\xi_{+}+\xi_{-}\right)}_{\mathrm{c}} \tag{3.11}$$

Also the transformation stress from M to A (σ_{M}) is extended by the local term (c), resulting in the Equation 3.12. Increased transformation stress of the currently transforming cell leads full BT from M to A during unloading, using a material-dependent parameter *phase fraction dependence of* σ_{M} (β_{M}) and the phase fraction (ξ).

$$\sigma_{\mathrm{M}}\left(T,\xi\right)=\underbrace{\sigma_{\mathrm{M}}\left(T_{\mathrm{ref}}\right)}_{\mathrm{a}}+\underbrace{\frac{\partial\sigma_{\mathrm{M}}\left(T,\xi\right)}{\partial T}\cdot\left(T-T_{\mathrm{ref}}\right)}_{\mathrm{b}}+\underbrace{\beta_{\mathrm{M}}\cdot\left(1-\left(\xi_{+}+\xi_{-}\right)\right)}_{\mathrm{c}} \tag{3.12}$$

This strain-softening part for the PT changes the classification of the MAS model from a purely physics-based model to a hybrid model between physics-based and phenomenologically motivated.

Phase fraction

The transitions between phases are defined by transition probability motivated in statistical thermodynamics. The kinetics equations of the phase fractions for the consideration of a global PT behavior, known from Equation 2.11 and Equation 2.12, only depend with term (a), (c), and (d) on the time (t), and the transition probability (δ), as replayed Equation 3.13.

$$\underbrace{\frac{\partial \xi_+}{\partial t}}_{\text{a}} - \underbrace{\eta \cdot \frac{\partial^2 \xi_+}{\partial x^2}}_{\text{b}} = -\underbrace{\xi_+ \cdot \delta_{+\text{A}}}_{\text{c}} + \underbrace{\xi_\text{A} \cdot \delta_{\text{A}+}}_{\text{d}} \tag{3.13}$$

$$\underbrace{\frac{\partial \xi_-}{\partial t}}_{\text{a}} - \underbrace{\eta \cdot \frac{\partial^2 \xi_-}{\partial x^2}}_{\text{b}} = -\underbrace{\xi_- \cdot \delta_{-\text{A}}}_{\text{c}} + \underbrace{\xi_\text{A} \cdot \delta_{\text{A}-}}_{\text{d}} \tag{3.14}$$

The original formulas tend to produce a discontinuous PT behavior because of the discretization of the SMA element into independent cells and the resulting variation in temperature (T) and phase fraction (ξ) among cells. One cell transforms, and the neighboring one does not because of the slightly different boundary conditions. This scenario is different from the local behavior of the PT observed in the experiments (Figure 3.3), where also at higher strain rates clusters of cells transform in the same time period. In material science, a transition zone between a cluster of A and M is reported on a partially transformed NiTi wire [188]. Continuity between the phase fractions is enforced by adapting the calculation using the diffusion term (b) in Equation 3.13. The second spatial derivative of the phase fraction (ξ) enables a continuous spatial transition between phases. The size of the transition zone can be adjusted using the material-dependent parameter *phase fraction diffusion coefficient* (η). Neighboring areas ahead of the phase fronts are slightly pre-transformed, making them preferred for further transformation. Other similar approaches in the literature introduce interface energy [262, 253, 156, 218]. The calculation for the phase fraction is independent of the loading type, therefore phase fraction of M- can be calculated using Equation 3.14.

This non-local extension in the calculation of the phase fractions changes the MAS model from a purely physics-based model to a hybrid model between physics-based and phenomenologically motivated. This modification enables a simplified barrier calculation of the transition probabilities, incorporating a material-dependent parameter, compared to the approach of Wendler et al. [92].

Energy balance

The local PT behavior can introduce a significant difference in temperature between two neighboring cells, which leads to a HT from one to the other. This PT independent conductive HE changes the specific internal energy of a cell in the SMA (u_{sma}), known from Equation 2.25, only dependant on term (a), (c), (d) and (e). In Equation 3.15, constant SMA material parameters for density (ρ_{sma}), and specific heat capacity (c_{sma}) are assumed, with no Joule heating, without loss of generality.
The HT within the material between cells can be described by a diffusion term (b) using Equation 3.15 and following the law of Fourier for heat conduction. The second spatial derivative of the temperature (T), enables the transfer of thermal energy (HT) between cells. The HT can be adjusted using a material-specific parameter known as *thermal conductivity* (κ).

$$\underbrace{\rho_{\mathrm{sma}} \cdot c_{\mathrm{sma}} \cdot \frac{\partial T_{\mathrm{sma}}}{\partial t}}_{\mathrm{a}} = \\ + \underbrace{\kappa_{\mathrm{sma}} \frac{\partial^2 T_{\mathrm{sma}}}{\partial x^2}}_{\mathrm{b}} - \underbrace{h \cdot \frac{A_{\mathrm{sma,surf}}}{V_{\mathrm{sma}}} \cdot (T_{\mathrm{sma}} - T_{\mathrm{amb}})}_{\mathrm{c}} + \underbrace{\rho_{\mathrm{sma}} \cdot H_{+} \cdot \frac{\partial \xi_{+}}{\partial t}}_{\mathrm{d}} + \underbrace{\rho_{\mathrm{sma}} \cdot H_{-} \cdot \frac{\partial \xi_{-}}{\partial t}}_{\mathrm{e}} \tag{3.15}$$

The thermal conductivity is typically determined for the different phase fractions, not for the composition of more than one. Therefore, in order to consider the ongoing transformation process, an effective thermal conductivity (κ_{sma}) needs to be calculated for each cell, using Equation 3.16.

$$\kappa_{\mathrm{sma}} = \kappa_{\mathrm{M}} \cdot (\xi_{+} + \xi_{-}) + \kappa_{\mathrm{A}} \cdot \xi_{\mathrm{A}} \tag{3.16}$$

The material parameters for thermal conductivity of M (κ_{M}), and A (κ_{A}) are combined based on the current mixture of the phase fractions in the cell. The adaption makes the energy balance transformation direction-dependent and rate-dependent. This allows for the calculation of time-dependent temperature change, which can be calculated at each position in the SMA.
The numerical calculation of the thermo-mechanical SMA material behavior based on the MAS model requests for iterative calculations. Each individual cell, introduced in Figure 3.4, follows a calculation procedure. The model improvements discussed above, enabling the prediction of local effects, account for localized PT with a non-local extension and strain-softening component. This hybrid model combines physics-based and phenomenological motivated approaches, enabling reproduction of traveling temperature peaks caused by PT at multiple PFs using material-dependent parameters. The equations written assume

homogeneous material properties of density (ρ_{sma}), specific heat capacity (c_{sma}), and thermal conductivity (κ_{sma}). Note that the calculation order of the presented formulas must be adapted to the used numerical simulation program.

3.3 Implementation

The thermo-mechanical coupled SMA model is implemented into the commercially available FE software COMSOL Multiphysics. This software allows simulating custom PDE systems on a one-dimensional geometry. The system of PDEs, which includes the momentum balance, introduced in Equation 2.2, calculation of the phase fraction, introduced in Equation 3.13, and the energy balance, introduced in Equation 3.15, is implemented into the software for solving the position and time depending displacement ($\Delta x(x,t)$), as well as phase fraction ($\xi_+(x,t)$) and temperature ($T(x,t)$) fields.
For the modeling of the localized PT behavior with the extend MAS model of the thin-film, only tensile stress is needed. The compression martensite variant is excluded by the test procedure, discussed in section 3.1. The phase fraction of the compression martensite (ξ_-) remains at zero and is therefore omitted.
The mechanical boundary conditions, defined in subsection 3.2.3, are applied in a sequence corresponding to the performed loading cycle of the experiments, presented in section 3.1. The pre-load applied to the SMA during the experiments results in purely elastic deformation of the material. Therefore, the simulation can start the load cycle from zero force, which differs from the experiments but does not influence the PT behavior. For a direct comparison between the experiment and simulation results, the simulation's time axis will be adjusted. The HE between the SMA element and the environment is always active throughout the entire cycle, resulting in the same condition as those in the experiment.
For the different strain rates, the varying duration of the cycle stages (loading, unloading, and HE), as provided by the experiments, are listed in Table 3.1, along with the total cycle time. The cycle's loading path follows an increasing displacement preset with the selected strain rate until the maximum displacement (Δx_{max}=0.3 mm) is reached. The

Strain rate	**Loading/unloading time**	**HE time**	**Cycle time**
10^{-4} 1/s	200 s	10 s	420 s
10^{-3} 1/s	20 s	10 s	60 s
10^{-2} 1/s	2 s	10 s	24 s
10^{-1} 1/s	0.2 s	10 s	20.4 s

Table 3.1: List of total cycle time and internal steps of the load cycle at different strain rates.

maximum displacement ($\Delta x_{\max}$=0.3 mm) corresponds with the sample length (l=15 mm) to a maximum strain ($\varepsilon_{\max}$=0.02).
During the HE time after loading at the high temperature level, the displacement is held constant. The unloading path of the cycle and the process of displacement control must terminate by the solver once the minimum force ($F_{\min}$=1 N) is reached. An event detection provided by the FE software determines the precise moment. It interrupts the simulation and changes the mechanical boundary condition from being displacement controlled (Equation 3.6) to force controlled (Equation 3.7). Suppose the BT from M to A is not already completed during unloading. In that case, changing to force-control allows further axial contraction of the sample during the HE time, at the low temperature level. This is induced by the continued PT due to the temperature increase of the SMA material. The following evaluates the specific parameters for the model, material, and environmental conditions based on the thermo-mechanical behavior observed in the experiments.

3.4 Calibration

This section evaluates the parameters for the model and material, as well as the environmental conditions needed to adapt the simulation to the executed experiments. First, the basic material parameters typically found on the datasheet of the used SMA material were introduced. Next, mechanical and thermal parameters were determined, considering the specific sample, the performed loading procedure, and the constraints to the ambient. Finally, the model-specific parameters for the MAS model were derived and summarized, along with all other parameters, in a table for a better overview.

3.4.1 Basic parameter

The commonly known density value for pure NiTi is 6450 kg/m^3. Due to the alloy additives of Cu and Co, the material exhibits a higher specific weight. Thus, the density (ρ) of the sample is assumed to be 6500 kg/m^3 [145].
The specific heat capacity of the sample material can be measured by a DSC measurement using a synthetic Sapphire standard, resulting in a specific heat capacity (c) of 420 J/(kg $\cdot$ K) for A and M [122]. The DSC can also be used to characterize the basic thermal material parameters of the SMA material associated with the FT and BT [208, 181, 117].
Figure 3.5 shows the neededspecific thermal power for changing temperature. This DSC measurement is performed on a *NETZSCH Phoenix* device with a temperature rate ($\dot{T}$) of 10 K/min. Due to the heterogeneity of the sample material, the paths in of the thermal power in Figure 3.5 show double peaks during the PT [115].

The specific latent heat (H) for heating and cooling can be calculated from the related DSC curve using Equation 3.17 [182, 52].

$$H = \frac{1}{\dot{T}} \cdot \int_{T_s}^{T_f} \dot{q}\, dT \tag{3.17}$$

Therefore, the specific thermal power ($\dot{q}$) is integrated, between the start (T_s) and finish (T_f) temperature of the A or M, divided by the temperature rate, which corresponds to the area under the transformation path. The specific latent heat (H) of the used material is determined to 13.7 J/g [122].

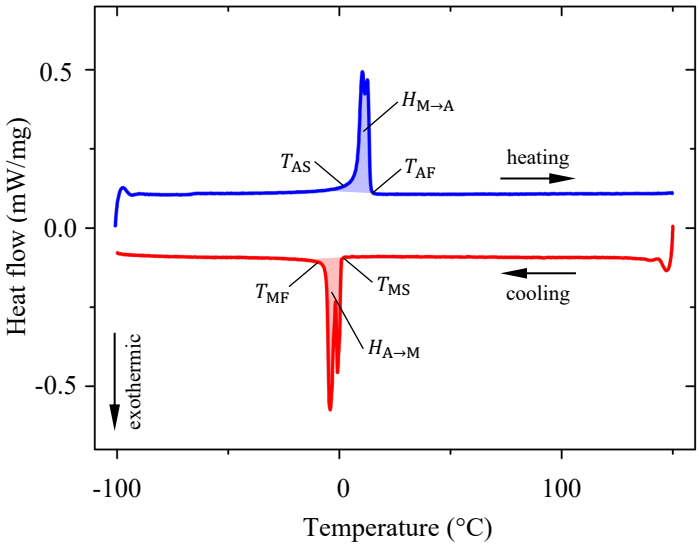

Figure 3.5: DSC measurement of the Ti 55.2 Ni 29.3 Cu 12.7 Co 2.8 sample

But, the related specific latent heat, by applying a tensile load, is often smaller than the value obtained from the DSC measurement [122]. This difference in specific latent heat, between temperature-, and stress-induced PT, can be based on a locally incomplete PT as discussed in [224, 232]. Therefore, in literature for larger sample geometries like wires, an additional method of characterization is introduced [54], which is based on compensating the thermal energy during PT of the SMA.
This new method is not currently applied to the sample being used. Therefore, for the current simulation approach of the thin-film, the value of the specific latent heat will be adjusted, as explained later.

3.4.2 Mechanical and thermal parameter

The following, the mechanical and thermal parameters, will be evaluated.

Young's modulus

Figure 3.6 shows the relationship between force and displacement, representing the material behavior of all conducted experiments, as presented in section 3.1. In this diagram, the zero displacement position of each experiment is adjusted to account for the slightly different initial state caused by the pre-load of the thin film. As mentioned in the legend of Figure 3.6, the ambient temperature near the sample varies slightly among the presented experiments. Therefore, the stress - strain behavior of the experiments with the same strain rate differs. This is visible in the transformation plateau of the experiments with a strain rate of $10^{-4}\,1/\mathrm{s}$, highlighted in red and blue. Due to limitations in the sampling rate of the tensile test machine, the data from the experiment with the highest strain rate of $10^{-1}\,1/\mathrm{s}$ exhibits deviations at the elastic A branch during loading and a curved representation of PT start.
The Young's modulus of A (E_A) is derived to 35.2 GPa by using the slope of a straight line fitted to the linear elastic A branch and taking the specimen geometry into account. For the identification of the Young's modulus of M (E_M) and the transformation strain (ε_t) a completely transformed material is necessary. The force reduction observed during the holding phase in the force - time diagram of Figure 3.3 is also visible in this representation. It confirms with the vertical force drop the assumption of the incomplete transformation. To satisfy a complete PT, a quasi-isothermal tensile test with a strain rate of $10^{-4}\,1/\mathrm{s}$ is conducted until the linear elastic M branch is reached. This experiment is depicted by the red line in Figure 3.6. The Young's modulus of M is determined as 14.8 GPa by using the slope of a straight line fitted to the linear elastic M branch and taking the specimen geometry into account. The transformation strain (ε_t) is read as 0.006 12 by using the strain value at the crossing point between the fit and the strain axis.

Transformation stress

The increasing transformation stress during PT due to the thermo-mechanically coupled material behavior is indicated by the inclination of the plateau curve and the hysteresis area with increasing strain rates. The transformation stress directly depends on the temperature of the material portion undergoing PT, thus the PF. Other zones of the specimen that are not transforming yet or are already fully transformed and do not influence the current force. Figure 3.7 illustrates the relationship between the force and temperature of the PF for different strain rates. The PFs are tracked by identifying local maxima in temperature during loading and minima during unloading on the spatially resolved temperature data obtained from the IR images. During the loading process, marked with red dots, the force increases as the temperature of the PF rises from ambient to a maximum dependent on the strain rate. The temperature dependency of the transformation stress from A to M ($\frac{\partial \sigma_\mathrm{A}}{\partial T}$),

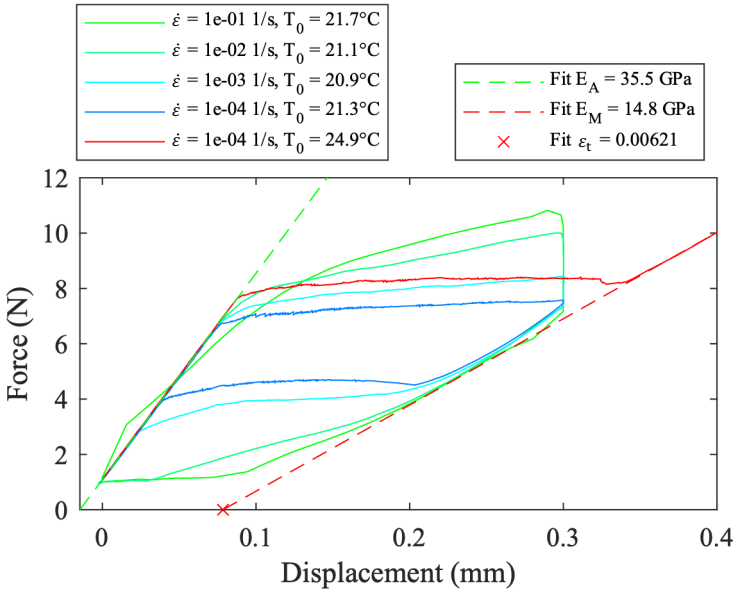

Figure 3.6: Force - displacement diagram of the TiNiCuCo thin-film experiments for different strain rates ($\dot{\varepsilon}$), and fitted parameters like Young's moduli of A (E_A), and M (E_M), as well as transformation strain (ε_t)

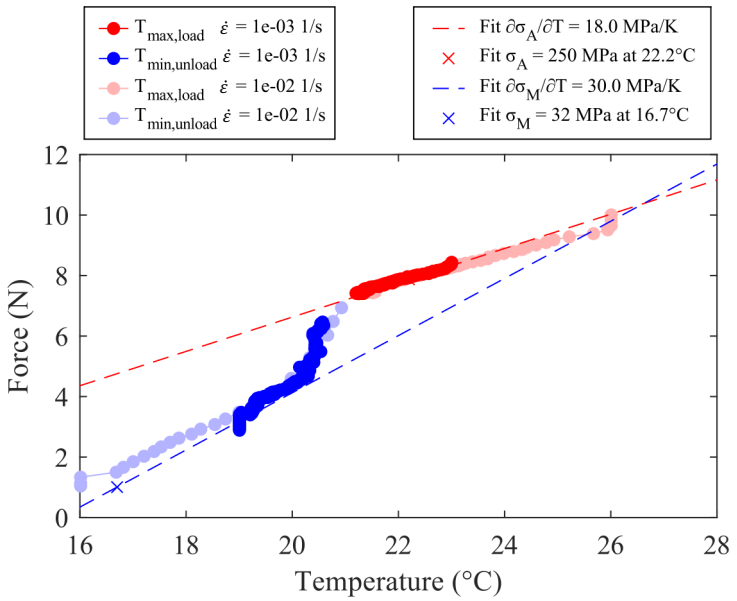

Figure 3.7: Force - temperature diagram at the PF of the TiNiCuCo thin-film experiments for different strain rates in order to derive the temperature dependence of the transformation stress and stress at reference temperature.

as introduced in Equation 3.11 (b), can be derived to be 18 MPa/K. This determination is based on the slope of a straight line fitted to the data points and considering the specimen's size. At unloading, marked with blue dots, the force decreases with decreasing temperature of the PF, starting again at ambient and then dropping to a strain rate dependent minimum. The imperfections in the CLS result in an amplification of the stress in some cells and their transformation, even when the mean stress of the neighboring cells is lower. This premature PT of some cells is also visible as a bent M branch during the BT in the force - displacement diagram of Figure 3.6 and leads to the initial kink in data points in the Figure 3.7. After the initial kink and bend, the evaluated data points follow a linear curve. The temperature dependency of the transformation stress from M to A ($\frac{\partial \sigma_M}{\partial T}$), as introduced in Equation 3.12 (b), can be derived to be 30 MPa/K. This determination is based on fitting a straight line to the aligned data points while considering the specimen's geometry.
For binary NiTi, the temperature dependency of the transformation stress for FT and BT is assumed with a typical value of around 7 MPa/K, as determined by isothermal tensile tests at different temperature [106]. In comparison, the quaternary TiNiCuCo show significantly unequal values for FT and BT, which are two to four times higher. Still, the selected material composition significantly changes the hysteresis behavior and, with this, also the T dependency of the transformation stress, as introduced in subsection 1.2.3.
Figure 3.7 also enables the determination of the transformation stress from A to M at the reference temperature ($\sigma_A(T_{ref})$) to be 250 MPa, as introduced in Equation 3.11 (a), with its corresponding reference temperature (T_{ref,σ_A}) of 22.2 K. The transformation stress from M to A at the reference temperature ($\sigma_M(T_{ref})$) can be determined to be 32 MPa with its corresponding reference temperature (T_{ref,σ_M}) of 16.7 K, as introduced in Equation 3.12 (a). The linear relationship between transformation stress and temperature for A and M is defined by these four values.

Heat exchange coefficient

The thermal connection between the sample and the environment influences the sample's thermal behavior during the loading, holding, and unloading periods. The HE and the temperature profile of the sample are mainly based on the convective heat exchange coefficient, and the ambient temperature of the surrounding air. If the sample had sufficient time to equalize any temperature differences before the experiment starts, the ambient temperature (T_{amb}) can be derived directly from the average sample temperatures at the beginning of the experiment to be 21 °C. The heat exchange coefficient (h) can be determined from the temperature decline of the samples center region during the holding phases.

The thermal and mechanical influence of the clamping can be neglected due to the long sample length and the short influence area of the clamping as visible in Figure 3.3. In the center region of the sample, the distance to the camping is sufficiently large, and the propagating and merging PFs create an almost homogeneous temperature field.
For the calculation of the heat exchange coefficient (h), the energy balance known from Equation 3.15 can be simplified by neglecting the diffusion term (b) due to a homogeneous temperature distribution along the specimen. Also, the production and reduction terms (d, and e) leave since no PT occurs. This assumption leads to Equation 3.18.

$$\rho_{\mathrm{sma}} \cdot c_{\mathrm{sma}} \cdot \frac{\partial T}{\partial t} = -h \cdot \frac{A_{\mathrm{sma,surf}}}{V_{\mathrm{sma}}} \cdot (T - T_{\mathrm{amb}}) \tag{3.18}$$

Under the assumption of a uniform distribution of temperature, negligible influence of the clamping, and no generation or absorption of specific latent heat, the temperature evolution in the sample is governed by an exponential decay dependent on the heat exchange coefficient (h). To facilitate the comparison between experiments with different strain rates due to the differing sample temperatures after loading and unloading, as well as start temperatures (T_{s}), a normalized temperature is introduced. This normalized temperature ($\tilde{T}$) can be calculated using Equation 3.19, with the geometry parameters of the sample, volume (V) and surface area (A), as well as the material parameters of the SMA, density (ρ) and specific heat capacity (c).

$$\tilde{T}(t) = \frac{T(t) - T_{\mathrm{amb}}}{T_{\mathrm{s}} - T_{\mathrm{amb}}} \approx \exp\left(-\frac{h \cdot A_{\mathrm{surf}}}{\rho_{\mathrm{sma}} \cdot c_{\mathrm{sma}} \cdot V_{\mathrm{sma}}} \cdot t\right) \tag{3.19}$$

Figure 3.8 shows the decay of the normalized temperature ($\tilde{T}$) over the time (t) during the holding period after loading or unloading at different strain rates, evaluated from the spatially resolved temperature data of the sample's center region. Assuming the same ambient condition for all different strain rates, the pathway should be the same. For lower strain rates ($\dot{\varepsilon} = 10^{-4}\,1/\mathrm{s}$ and $\dot{\varepsilon} = 10^{-3}\,1/\mathrm{s}$), the difference between the ambient temperature and the maximum temperature of the sample after loading, as well as the ambient temperature and the minimum temperature of the sample after unloading, is too small to produce a consistent trend. This is due to the nearly isothermal cycle conditions. Therefore, only the faster strain rates ($\dot{\varepsilon} = 10^{-2}\,1/\mathrm{s}$ and $\dot{\varepsilon} = 10^{-1}\,1/\mathrm{s}$) are presented in the diagram and considered for the calculation.
In experiments with higher strain rates, the sample is not fully transformed after the loading or unloading. This post-transformation is visible as a vertical fall or rise on the force - displacement diagram, shown in Figure 3.6. The release or absorption of specific latent heat due to the stress relaxation during the holding period changes the specific

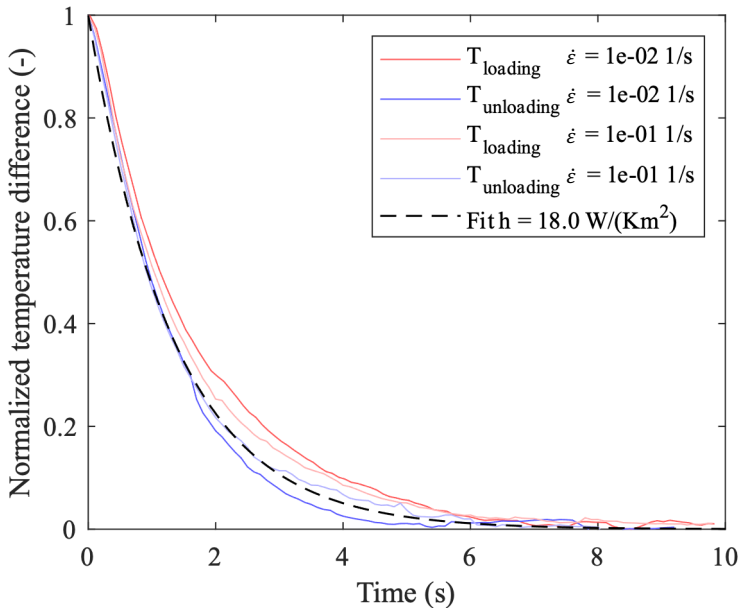

Figure 3.8: The normalized temperature $(\tilde{T})$ decay over the time (t) of the holding period after loading or unloading at different strain rates for the identification of the convective heat exchange coefficient (h).

internal energy of the SMA (u_{sma}) and influences the normalized temperature decay. When the relaxation induced PT completes, the temperature balancing between the sample and the ambient is faster. Therefore, a kink in each curve is visible. The change to a higher slope on each path identifies the end and magnitude of the relaxation process. Since the curves show no prominent slope change, the influence of relaxation is assumed to be negligible.

The heat exchange coefficient (h) is estimated to $18\,\mathrm{W/(m^2{\cdot}K)}$ using an exponential fit on the data points, as presented by the dashed line in Figure 3.8.

3.4.3 Solver settings

Each simulation model's specific physical dependency and complexity require different solving methods to improve the solution's accuracy and computation speed. Therefore, COMSOL provides a set of solvers, each embodying a particular approach to solve a model based on the system dynamics, solution stability, and solver robustness [214, 32]. The presented simulation setup requires an implicit time-dependent solving method due to the partial differential equations of the SMA model and its kinetic. The settings are chosen to have no consistent initialization due to the user-defined initial values for each dependent variable. The calculation tolerances are manually set to 10^{-3} for both relative and absolute values. The discretization method is chosen as *Backward Differentiation Formula* (BDF) with a maximum order of 3, which is used due to its robust and stable performance. The rapid fluctuation of the transition probability in contrast to the strain

or temperature change in the SMA, categorizes the presented simulation model as a stiff problem. To enhance the accuracy of the solution for the stiff model, the solver's steps are set to *intermediate*, starting with an initial time step of 10^{-5} s. This configuration ensures that the solver performs an intermediate calculation between each predefined time step. To support the solution, a direct solver called *MUMPS* is used, which enhances robustness and generality. Although this method requires more computational performance and time, it allows for stable calculations with varying input parameters. Finally, the solving procedure must be performed in a *fully coupled* manner using an *automatic nonlinear* method due to the thermo-mechanical coupling of the SMA model and the corresponding dependencies of the partial differential equations (PDEs) of the system. The initial damping is set to 10^{-2}, and the minimum damping during the solving process is set to 10^{-6}. The maximum number of iterations is increased to 50, and the tolerance factor is chosen as 10^{-3} to assist in solving the stiff problem.

3.4.4 Parameter overview

All the model, sample, and material parameters that have been discussed and derived are summarized in Table 3.2. This table also includes the empirically determined or adapted parameters, highlighted in red for clarity and completeness, in anticipation of the model's validation. The final column specifies the origin or dependency of the parameter's value.

Name	Symbol	Value	Source
Length	l	15 mm	sample
Width	lw	1.75 mm	sample
Sample depth	ld	18 µm	sample
SMA density	ρ	6500 kg/m^3	sample
Specific heat capacity	c	420 J/(kg · K)	sample
Specific latent heat	H_{DSC}	13.7 J/g	sample
Specific latent heat	H_{sim}	5 J/g	adoption
Young's modulus of A	E_{A}	35.2 GPa	experiment
Young's modulus of M	E_{M}	14.8 GPa	experiment
Transformation strain	ε_{t}	0.006 12	experiment
Transformation stress of A to M	$\sigma_{\mathrm{A}}(T_{\mathrm{ref},\sigma_{\mathrm{A}}})$	250 MPa	experiment
Reference temperature of σ_{A}	$T_{\mathrm{ref},\sigma_{\mathrm{A}}}$	22.2 °C	experiment
Temperature dependence of σ_{A}	$\frac{\partial \sigma_{\mathrm{A}}}{\partial T}$	18 MPa/K	experiment
Transformation stress of M to A	$\sigma_{\mathrm{M}}(T_{\mathrm{ref},\sigma_{\mathrm{M}}})$	32 MPa	experiment
Reference temperature of σ_{M}	$T_{\mathrm{ref},\sigma_{\mathrm{M}}}$	16.7 °C	experiment
Temperature dependence of σ_{M}	$\frac{\partial \sigma_{\mathrm{M}}}{\partial T}$	30 MPa/K	experiment
Poisson's ratio of elastic strain	ν_{elast}	0.33	MAS model
Poisson's ratio of transformation	ν_{t}	0.5	MAS model
Characteristic volume	V_{char}	5×10^{-20} m^3	MAS model
Time constant of phase fraction	τ_{ξ}	0.001 s	MAS model
Ambient temperature	T_{amb}	21 °C	experiment
Heat exchange coefficient	h	18 W/(m^2·K)	experiment
Thermal conductivity for A	κ_{A}	9 W/(m · K)	adoption
Thermal conductivity for M	κ_{M}	4.5 W/(m · K)	adoption
Phase fraction dependence of σ_{A}	β_{A}	24 MPa	adoption
Phase fraction dependence of σ_{M}	β_{M}	24 MPa	adoption
Phase fraction diffusion coefficient	η	12×10^{-8} m^2/s	adoption

Table 3.2: List of utilized parameters for simulating the localized PT behavior of the Ti 55.2 Ni 29.3 Cu 12.7 Co 2.8 sample.

3.5 Validation

This section presents the performed simulation for three different strain rates ($\dot{\varepsilon} = 10^{-3}\,1/\mathrm{s}$, $\dot{\varepsilon} = 10^{-2}\,1/\mathrm{s}$, and $\dot{\varepsilon} = 10^{-1}\,1/\mathrm{s}$) using the implemented model and the parameters from Table 3.2. It aims to validate and calibrate the simulation model by adapting the material and model parameters.
The experimental and simulation results are compared in Figure 3.9. Regarding the comparability of all essential data for the different strain rates, the diagram is organized in a matrix-like format:

1. Row presents the total displacement over time ($\Delta x(t)$).
2. Row presents the force over time ($F(t)$).
3. Row presents the minimum temperature ($T_{\min}(t)$) in blue, maximum temperature ($T_{\max}(t)$) in red, and mean temperature ($T_{\mathrm{mean}}(t)$) in green of the whole sample over time.
4. Row presents spatio-temporal thermograms of the experimental results.
5. Row presents spatio-temporal thermograms of the simulation results.
6. Row presents spatio-temporal strain evolution of the simulation.
7. Row presents global M+ phase fraction over time ($\xi_+(t)$) of the simulation.
8. Row presents the specific mechanical work over time ($w(t)$).
9. Row presents the specific thermal energy over time ($q(t)$).

The resulting field values are presented along the rows over time, while the strain rate varies along the columns. Solid lines represent the experimental data in the line diagrams, while dashed lines represent the simulation data.
The adaptation process and its criteria are described below, and the presented results will be discussed in detail subsequently.

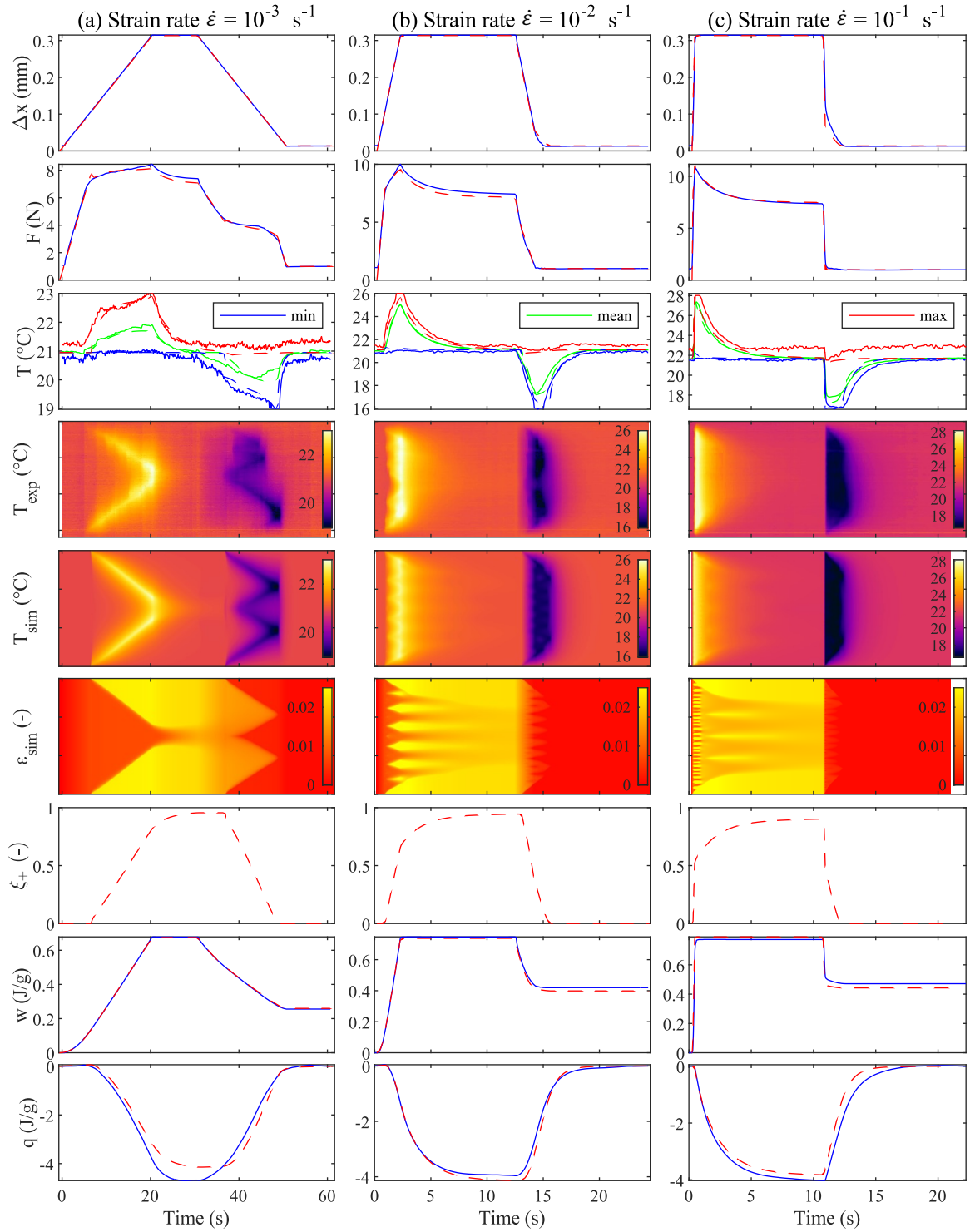

Figure 3.9: Comparison of experimental data (solid line) and simulation (dashed line) for displacement, axial force, minimal/average/maximal temperature of the whole sample, spatio-temporal temperature evolution, spatio-temporal strain evolution, global M+ phase fraction, specific mechanical work and specific thermal energy.

3.5.1 Specific latent heat and temperature

The specific latent heat (H) determines the level of temperature change in the material during the PT in the adiabatic limit. At the adiabatic limit, which is reached by the highest strain rate ($\dot{\varepsilon}$) of 10^{-1} 1/s, the temperature evolution in the sample only depends on the percentage of transforming material, specific latent heat, and specific heat capacity. Due to the short loading time (t) of 0.2 s, the HE between the ambient and the sample, and thus the precise value of the heat exchange coefficient is negligible, despite the large surface to volume ratio of the SMA sample. The specific heat capacity is reliably determined through DSC measurement. The amount of transforming material is defined by the applied strain and the temperature during the loading or unloading process. The specific latent heat is the only remaining quantity that is independent of all others.
Starting from a specific latent heat (H) of 13.7 J/g measured by DSC, this value is adjusted manually through an iterative process to adapt the peak temperature values obtained in simulations to the peak temperature values observed in experiments at high strain rates in the adiabatic limit. A good agreement is observed in the temperature evolution of the maximum and minimum temperature during the loading and unloading process at the highest strain rate for a specific latent heat (H) of 5 J/g, as shown by the red and blue curves in row three, column three of Figure 3.9. Using this specific latent heat value for the simulation of the two other strain rates ($\dot{\varepsilon} = 10^{-3}$ 1/s, and $\dot{\varepsilon} = 10^{-2}$ 1/s), the first and second column of the third row demonstrate a good agreement between simulation and experimental data for the maximum and minimum temperature during the loading and unloading process. During loading and unloading, the curves also show that convective HE becomes more influential as the strain rate decreases. This is supported by the smaller temperature difference between the ambient temperature and the maximum temperature after loading, as well as the minimum temperature after unloading. Finally, the mean temperature, shown in green, indicates a good agreement between the simulation and experimental data for the specified specific latent heat value of 5 J/g over the whole PT process of the sample, across all strain rates.
During loading, the maximum temperature is determined by the total amount of specific latent heat. During unloading and holding, only a reduced amount of specific latent heat generates the temperature difference due to the blocked BT after reaching the material specific austenite finish temperature. Therefore, the temperature difference between the ambient temperature and the maximum temperature is highter than between the ambient temperature and the minimum temperature.

3.5.2 Phase fraction dependence of the transformation stress

The material-dependent phase fraction dependence of $\sigma_{\mathrm{A}}(\beta_{\mathrm{A}})$ controles the material softening effect while loading. This effect is introduced with the local extension of transformation stress from A to M (σ_{A}) in Equation 3.11 (c). The corresponding material-dependent phase fraction dependence of $\sigma_{\mathrm{M}}(\beta_{\mathrm{M}})$ controls the material hardening effect while unloading. This effect is introduced with the local extension of transformation stress from M to A (σ_{M}) in Equation 3.12 (c). These two parameters are the counterparts to the temperature dependend transformation stress from A to M $(\frac{\partial \sigma_{\mathrm{A}}}{\partial T})$ and transformation stress from M to A $(\frac{\partial \sigma_{\mathrm{M}}}{\partial T})$.
In the case of the FT, the transformation stress from A to M increases due to the released specific latent heat and the resulting temperature rise, but this increase has to be reduced using Equation 3.11 (c) with β_{A}. In the case of the BT, the transformation stress from M to A decreases due to the absorbed specific latent heat and the resulting temperature drop, but this decrease has to be reduced using Equation 3.12 (c) with β_{M}. A rough estimation of the parameters can be obtained from the experimental test. In a test series with increasing strain rates, when a homogeneous PT of the whole sample is observed for the first time, the parameter corresponds to the value of the peak temperature difference multiplied by $\frac{\partial \sigma_{\mathrm{A}}}{\partial T}$ or $\frac{\partial \sigma_{\mathrm{M}}}{\partial T}$.
The fine-tuning is made with two further simulations, one with a smaller strain rate and one with a larger one: In case of too small values, for β_{A} or β_{M}, the cell does not finish transforming at a certain strain rate, and a neighboring cell starts transforming due to its lower transformation stress, this leads to an unphysical homogeneous PT behavior of the whole sample in the simulation. This implies that in simulations with lower strain rate, fewer individual traveling PFs are formed up to the point of homogeneous PT compared to the experiment data. Suppose the selected values for β_{A} or β_{M} are too large. In that case, a material portion finishes transforming at a certain strain rate; after this, another cell starts transforming, leading to individual traveling PFs. This means no homogeneous transformation is shown for the simulation with a higher strain rate, and more individual traveling PFs are formed compared to the experiment data.
This procedure leads to determining the values for phase fraction dependence of σ_{A} and σ_{M} to 24 MPa, which shows a good agreement of the PF numbers for all strain rates between experiment and simulation in row four and five of Figure 3.9.

3.5.3 Thermal conductivity and phase fraction diffusion coefficient

The material-dependent parameters thermal conductivity (κ) and phase fraction diffusion coefficient (η) define the expansion of the temperature peaks at the spatio-temporal temperature evolution in the material.
The thermal conductivity (κ) is the diffusion coefficient of the temperature field. It controls the size of the pre-heated zone in front of the PF, and thus the area of the temperature change, as introduced in Equation 3.15 (b), and Equation 3.16.
At the lowest strain rate ($\dot{\varepsilon} = 10^{-3}\,1/\mathrm{s}$) only two traveling temperature fronts are observed in column one, row four of Figure 3.9. The expansion of the temperature peak along the specimen is defined by the thermal conductivity, phase fraction diffusion coefficient, the HE with the ambient and the available time. The size of the transformation area and with this, the phase fraction diffusion coefficient is not directly measurable in this setup. Still, it is assumed to be in the order of the sample depth (ld=18 µm) resulting in few individual pixels in the IR image. Consequentially, the expansion of the temperature peak mainly depends on the thermal conductivity. But not only must the temperature value of the PF fit, the formation process of the PF must also be qualitatively suitable.
At the medium strain rate ($\dot{\varepsilon} = 10^{-2}\,1/\mathrm{s}$), in the loading path, more than two PFs are observed in the experiment as presented in row four, column two of Figure 3.9. This distance between the propagating PFs is influenced by the magnitude of the temperature peaks, as the pre-heated material at the leading edge of the PF prevents transformation due to the now increased transformation stress from A to M.
Usually, the thermal conductivity of materials can be determined by measuring the local temperature decay with a high resolution IR camera after heating a small size of the sample which is placed in an environment without HE to the ambient. However, the material parameter set of the investigated sample does not provide direct measurement values for thermal conductivity for A or M. In literature, different values are mentioned for standard NiTi, whereby the values for M are only half those for A [59, 246]. Thus, the thermal conductivity for A (κ_A) and thermal conductivity for M (κ_M) need to be adapted empirically through an iterative process.
The area of the temperature change is further increased due to the phase fraction diffusion coefficient. The loading or unloading of the SMA material induces a PT of one cell. This, the change in phase fraction leads to pre-transformation of the neighboring cells, which enables a continuous transition between two phase fractions. The phase fraction diffusion coefficient (η) can be seen as phase fraction conductivity. It controls the size of the pre-transformation, or in other words, the number of cells and thus the area of the transforming region introduced in Equation 3.13 (b) and Equation 3.14 (b). The PT leads

due to the specific latent heat to a temperature change in this area. Therefore, the phase fraction diffusion coefficient value influences the sample's temperature evolution.
The size of the transforming area and with this, phase fraction diffusion coefficient can be generally determined by evaluating the locally resolved strain data of the sample. In the currently focused experimental setup, this measurement is not available. Therefore, the parameter phase fraction diffusion coefficient (η) needs to be determined empirically through an iterative process.
Starting from the thermal conductivity for A (κ_A) of $18\,\mathrm{W/(m \cdot K)}$ and thermal conductivity for M (κ_M) of $9\,\mathrm{W/(m \cdot K)}$, these values were iteratively reduced while maintaining their ratio until the simulated temperature distribution of the propagating PFs at the lowest strain rate fits to the experimental results. As part of this process, the value of phase fraction diffusion coefficient (η) is also changed, starting from $18 \times 10^{-6}\,\mathrm{m^2/s}$.
The fourth and fifth row of Figure 3.9 shows an adequate match between the spatio-temporal temperature evolution of experiment and the simulation, regarding size, number, and distance of the PFs during loading and unloading for all strain rates. These results were obtained with a thermal conductivity for A (κ_A) of $9\,\mathrm{W/(m \cdot K)}$, a thermal conductivity for M (κ_M) of $4.5\,\mathrm{W/(m \cdot K)}$, and a phase fraction diffusion coefficient (η) of $12 \times 10^{-8}\,\mathrm{m^2/s}$.

3.5.4 Displacement and force

Based on the fine-tuned material-specific model parameters, the evolution of mechanical values such as displacement (Δx) and force (F) should show a good agreement between simulation and experiment for the determined parameter set of Table 3.2.
The first row of Figure 3.9 shows displacement over time and the second row shows force over time. The comparison between the simulation (dashed line) and experimental (solid line) results shows a perfect agreement for the displacement path and a good match for the force curve at the lowest strain rate ($\dot{\varepsilon} = 10^{-3}\,1/\mathrm{s}$).
When observing the middle strain rate ($\dot{\varepsilon} = 10^{-2}\,1/\mathrm{s}$), shown in the second column, there is a slight deviation in the displacement path at the transition point between the unloading and holding phases. The minor difference during the experiment can be attributed to the response time needed by the test bench's control system when the minimum pre-load is reached. This difference is not evident in the force graph.
Observation of the fast strain rate ($\dot{\varepsilon} = 10^{-1}\,1/\mathrm{s}$), shown in the third column, exhibits a minimal delay in the experimental data of the displacement at the switchover point. This delay can be explained by the insufficiently high sample rate of the test stand.
The change in slope of the force during the holding phase after loading is caused by the decreasing transformation stress with decreasing material temperature. Whereas the change in slope of the force during the holding phase after unloading is caused by the blocked BT after reaching the material-specific austenite finish temperature.

In general, the force prediction of the simulation agrees very well with the qualitative experimental data. The minor quantitative deviations are due to variations in the used and determined material parameters related to the actual sample material.

3.5.5 Local temperature and strain

The experiment's spatio-temporal temperature in row four of the Figure 3.9 is observed by the IR camera to analyze the local PT behavior. The model's spatio-temporal temperature is presented in row five. However, this method leads to a blurry illustration of the PF due to the HT along the SMA element. Therefore, the local PT behavior could be observed with an optical camera enabling the local strain measurement using digital image correlation (DIC) [259, 247, 219, 122, 74], as introduced in subsection 1.2.3. This methode enables the identification of the material-specific phase fraction diffusion coefficient (η) introduced in Equation 3.13 and Equation 3.14. The comparison between the spatio-temporal strain and temperature improves the determination of the material-specific thermal conductivity of the SMA (κ_{sma}) introduced in Equation 3.16.
The local strain observation was not implemented in the experiments under discussion. As a result, the spatio-temporal strain is only presented for the simulation results in the sixth row of Figure 3.9. Therefore, the determination of material-specific parameters using the spatio-temporal strain measurement will be discussed in detail in the chapter 4.
The comparison of the temperature evolution between experiment and simulation for the lowest strain rate ($\dot{\varepsilon} = 10^{-3}\,1/\mathrm{s}$), presented in row four and five of column one, shows that the model is able to capture the inhomogeneous starts of the PT at the clamping due to the preferred local low material temperature, which produces two PFs traveling towards the sample center. A closer look at the force (F) presented in row two at column one exhibits a parted decay with two different slopes during the holding phase after loading. The relaxation in the first part with the smaller slope is caused by the post-transformation. The HE with the ambient and HT along the material enables a further PT of the material from A to M, leading to local strain changes. This change in strain occurs only in regions with previously incomplete transformed material introduced by a change of the transformation stress when the sample cools down after loading or heated up after unloading. The simulated local strain ($\varepsilon_{\mathrm{sim}}$), row six at column one, shows that the PT from A to M is not completed after loading and confirmes the assumption induced by the force path, even though the temperature peaks join at the end of the loading phase. As the strain in the transforming region increases, the strain in the fully transformed regions decreases elastically, and a new force equilibrium is reached at a lower level at the end of the holding time.
The post-transformation behavior is also proved by the evolution of the phase fraction (ξ_+) over time, presented in row seven of Figure 3.9. The total amount of M+ keeps rising

during the holding phase. During unloading, the BT starts in the region where the PT was still not completed. The simulation reproduces the experimentally observed PFs, where more nucleation points are generated than during loading.
Even at higher strain rate ($\dot{\varepsilon} = 10^{-2}$ 1/s, and $\dot{\varepsilon} = 10^{-1}$ 1/s), the local strain and temperature predictions of the simulation fit to the local temperature diagrams of the experiments. With increasing strain rate, from column one to three, there is an increasing number of simultaneous nucleation points for the local temperature and strain, showing an excellent agreement between rows four, five, and six. As the strain rate increases, the phase fraction of M+ in row seven shows a higher increase during the holding phase, which is also caused by the post-transformation. The rapid temperature change in the sample increases the transformation stress during loading and decreases it during unloading with increasing strain rate. Therefore, more material must continue the PT during the holding phases with increasing strain rate.

3.5.6 Mechanical work

The calculated mechanical work (W) for the different strain rates is depicted in the eighth row of Figure 3.9 for experiment (solid line) and simulation (dashed line). It can be calculated using Equation 1.1, Equation 1.2, and Equation 1.3. The mechanical work increases starting from zero during the loading phase and decreases during unloading. The remaining value ≥ 0 at the end of the cycle corresponds to the dissipated mechanical work (W_{dis}), following subsection 1.2.1. Due to the increasing temperature change with higher strain rates, the hysteresis area increases, and with this, the dissipated mechanical work, following subsection 1.2.2. The model also adequately reproduces the path of the mechanical work, neglecting the slight difference due to the delayed switching behavior of the experimental test bench at the unloading to the constant force, discussed above.

3.5.7 Thermal energy

The calculated specific thermal energy (q) for different strain rates is depicted in the ninth row of Figure 3.9 for experiment (solid line) and simulation (dashed line). It is calculated using Equation 1.6 and Equation 1.5. During the loading phase and the holding phase, the thermal energy caused by the released specific latent heat is exchanged (HE) to the ambient while the sample reaches the ambient temperature again. The good agreement between the experimental and the simulation data confirmes the chosen value for the specific latent heat (H=5 J/g), as the sample transforms almost completely by the joining temperature fronts. The sample has sufficient time to exchange all specific latent heats, and the thermal energy is nearly independent of the strain rate. This is because the amount of transformed material remains consistent in all experiments due to the identical

applied strain, and ambient temperature is reached again at the end of the holding phase after loading or unloading.
The comparison between experiment and simulation over all strain rates shows that the beginning and end points fit very well. The course at the beginning of the cycle also fits, up to the first switching point between displacement and force control at higher strain rates ($\dot{\varepsilon} = 10^{-2}\,1/\mathrm{s}$, and $\dot{\varepsilon} = 10^{-1}\,1/\mathrm{s}$). At these, the mean deviation of both data sets is negligible and caused by the delayed switching behavior of the test bench's control system. Upon closer examination of the spatio-temporal temperature evolution of the experiment in row four, it is evident that there is a slightly uneven PT behavior along the sample. This can be caused by minor imperfections of the CLS in the sample, leading to slight deviations in the release of specific latent heat compared to the simulation depicted in row five. This slight time shifted heating and cooling behavior results in a quantitatively different progression of thermal energy during the cycle.
At the smallest strain rate ($\dot{\varepsilon} = 10^{-3}\,1/\mathrm{s}$), the temperature evolution during the experiment in row four shows a slightly asymmetric meeting point of the two PF during the loading. This fusion leads to a difference in thermal energy during the loading and holding phase due to the slight differences in time and position of the maximum temperature. During unloading, the previous asymmetric PFs also causes a shift in both time and position of the minimum temperature, resulting in the variation between the experimentally and simulative thermal energy.

3.5.8 Thermo-mechanical coupling

Figure 3.10 presents the force - displacement diagram for the three different strain rates ($\dot{\varepsilon} = 10^{-3}\,1/\mathrm{s}$, $\dot{\varepsilon} = 10^{-2}\,1/\mathrm{s}$, and $\dot{\varepsilon} = 10^{-1}\,1/\mathrm{s}$) of experiment (solid lines) and simulation (dashed lines). The simulation accurately predicts the thermo-mechanically coupled material behavior of the SMA observed in experiments for the lowest and middle strain rate. The higher slope during loading with increasing strain rate and the higher stress at the end of the loading phase corresponds to the temperature-dependent transformation stress. At the end of the loading, the force drops due to the post-transformation from A to M is evident. The relaxation of the force to nearly the same value for all different strain rates shows that the duration of the holding phase is sufficiently long for this sample geometry and ambient conditions. During unloading, the PT from M to A is completed at the lowest strain rate before the control is changed from displacement to force, and the force is held constant. The horizontal path during the BT at higher strain rates indicates the incomplete PT state up to the control switching.
The simulation results of the highest strain rate fulfill the expectation in terms of increasing and decreasing stress slopes during loading and unloading. The experimental data set provides only a few data points for the comparison due to the test bench's insufficient

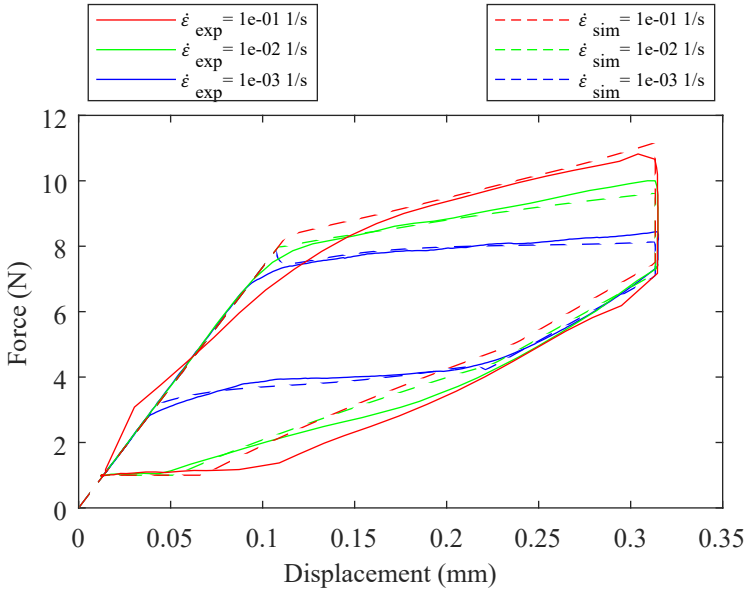

Figure 3.10: Force - displacement diagram for different strain rate: Comparison of experimental (solid lines) and simulation (dashed lines) results

sample rate. These data points fit the simulation results well during the loading and subsequent holding phases. During the unloading and holding phase, the values of the experiment are too small due to the delayed switching of the test bench to force control and the following readjustment.
The agreement between the experiment and simulation in the force - displacement diagram for all different strain rates shows the good accuracy of the evaluated thermal and mechanical parameters, closing the validation of the model.

3.6 Results and discussion

The experimental setup presented above can be specified as HP system with heat sink and heat source at ambient temperature. The performance of such a HP system in terms of heating and cooling can be assessed by comparing peak temperatures, thermal energy, and calculating the *COP* for each experiment, as outlined in section 1.2. The calculations presented below are implemented in the FE program to evaluate the predictive power of the presented SMA model for heating and cooling performance. This is achieved by comparing the simulation results with the experimental data.

3.6.1 Mechanical work

The mechanical work (W) stored in the sample can be expressed as the time (t) integral of the power (P) input at the clamping based on stress (σ), cross-sectional area of the sample (A), strain rate ($\dot{\varepsilon}$), and sample length (l), calculated with Equation 3.20.

$$W = \int_{t_s}^{t} P(t')\, dt' = \int_{t_s}^{t} F(t') \cdot v(t')\, dt' = \int_{t_s}^{t} \sigma(t') \cdot A(t') \cdot \dot{\varepsilon}(t') \cdot l\, dt' \tag{3.20}$$

Due to the hysteresis in the stress-strain behavior of the material, only a portion of the mechanical work introduced during loading is recovered during unloading, as described in subsection 1.2.1. This irrecoverable mechanical work, known as dissipated mechanical work (W_{dis}), can be expressed as the difference in mechanical work between start ($t_{\mathrm{s,AM}}$) of loading and finish (t_{f}) of a cycle, and can be calculated with Equation 3.21.

$$W_{\mathrm{dis}} = W(t_{\mathrm{f}}) - W(t_{\mathrm{s,AM}}) \tag{3.21}$$

3.6.2 Thermal energy

The thermal energy (Q) exchanged with the environment can be calculated using Equation 3.22 with the time (t) integral of the thermal power ($\dot{Q}$) through the surface area (A_{surf}) of the specimen, as described in subsection 1.2.1.

$$Q = \int_{t_s}^{t} \dot{Q}(t')\, dt' = \int_{t_s}^{t} \left(- \oiint h \cdot (T(x,t') - T_{\mathrm{amb}})\, dA_{\mathrm{surf}} \right) dt' \tag{3.22}$$

The thermal power is determined for each position (x) of the surface area (A_{surf}) using the local temperature difference between the sample ($T(x,t)$) and the ambient (T_{amb}), multiplied by the heat exchange coefficient (h). Due to the short duration of the experiment, the ambient temperature corresponds to start temperature of the sample.
The surface area (A_{surf}) of the specimen is defined by Equation 3.23 with the dimensions length (l=15 mm), width (lw=1.75 mm), and depth (ld=18 µm).

$$A_{\mathrm{surf}} = 2 \cdot (lw + ld) \cdot l \tag{3.23}$$

The absorbed thermal energy (Q_{ab}) during unloading and holding phase is the difference in thermal energy between start ($t_{\mathrm{s,MA}}$) of unloading and finish (t_{f}) of a cycle. It can be calculated using Equation 3.24.

$$Q_{\mathrm{ab}} = Q(t_{\mathrm{f}}) - Q(t_{\mathrm{s,MA}}) \tag{3.24}$$

3.6.3 Coefficient of performance

The cooling efficiency of the performed experiments can be expressed as the COP_{cool}, which is introduced in Equation 1.8. It can be calculated using Equation 3.25 with the absorbed thermal energy (Q_{ab}) and the dissipated mechanical work (W_{dis}) of the experiment and simulation

$$COP_{\text{cool}} = \frac{Q_{\text{ab}}}{W_{\text{dis}}} \tag{3.25}$$

3.6.4 Results

Figure 3.11 illustrates the comparison of the dissipated mechanical work (W_{dis}) and the absorbed thermal energy (Q_{ab}) at different strain rates, represented by the experimental (solid line) and simulation results (dashed line) in the upper part. Additionally, it shows the calculated COP for cooling in the lower part. The green curve in the upper part

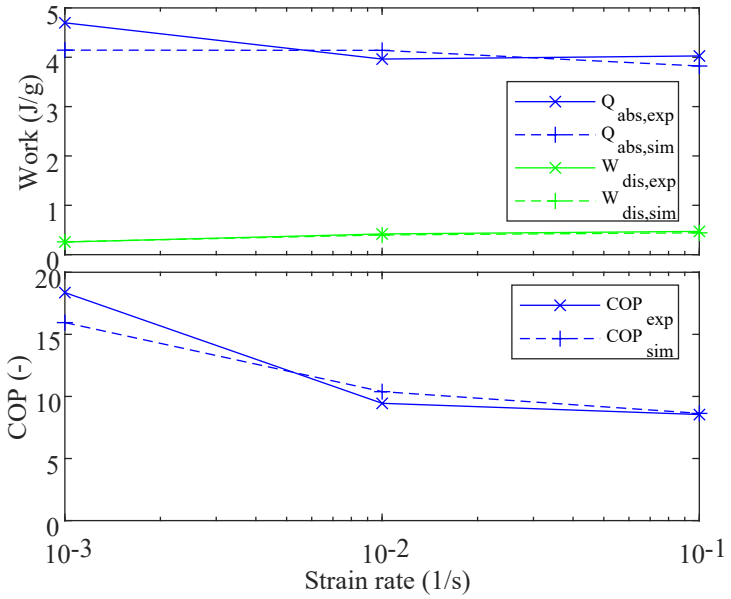

Figure 3.11: Comparison of the mechanical work (W), and absorbed (Q_{ab}) of the experimental results (solid line) and simulation data (dashed line) in the upper part and the calculated COP.

represents the dissipated mechanical work (W_{dis}), which increases with increasing strain rates due to the growing hysteresis area of the SMA, as shown in Figure 3.10. The simulation model accurately reproduces the qualitative trend and quantitative value for all strain rates. The blue curve in the upper part presents the absorbed thermal energy (Q_{ab}). This value remains nearly constant with increasing strain rates due to the same amount of transformed material for these experiments and sufficient time for HE, as shown in Figure 3.9. The simulation model reproduces the qualitative trend very well for all strain rates. Additionally, it accurately captures quantitative value for the middle and the highest

strain rates. The quantitative value at the absorbed thermal energy at the lowest strain rate slightly differs due to the asymmetric local PT behavior as discussed in section 3.5. The lower part of Figure 3.11 compares the calculated *COP*s for different strain rates, using Equation 3.25. The range of 8–19 of the *COP* corresponds to the typical values for EC HP systems using SMA as discussed in subsection 1.2.3. Both the experimental data and the simulation results show that the *COP* decreases as the strain rate increases due to the increase in dissipated mechanical work at approximately constant thermal energy. The simulation model reproduces the qualitative trend very well for all strain rates. Additionally, it accurately captures quantitative value for the middle and the highest strain rates. The quantitative value at the lowest strain rate slightly differs due to the divergence of the absorbed thermal energy as discussed before.

3.6.5 Discussion

The presented simulation results reproduce the experimental results of SE SMA thin films [122, 145] from the Karlsruhe research group, which investigate EC cooling on the micro-scale the Priority Programme SPP1599 funded by the German Research Foundation. The inhomogeneous PT behavior causes hot and cold areas along the SMA sample during loading and unloading, depending on the strain rate. This localized temperature evolution, caused by the released and absorbed of H, directly influences the HE with the ambient. Numerical simulation methods are used to replicate the experimental results for varying strain rates, aiming to better understand these local material effects.
Based on the MAS model, introduced in section 2.2, the model is adapted to reproduce the local PT behavior, as introduced in subsection 3.2.4 and implemented in COMSOL. In this approach, different Poisson's ratio values for elastic and transformation strain are included to induce 3D effects such as lateral contraction in a 1D model. The material's tendency to undergo a complete transformation is also induced by the phase fraction-dependent transformation stress. Furthermore, the continuous transformation between neighboring material cells is ensured by a gradient term, added in the kinetics equation of the phase fraction.
After performing a parameter identification of the mechanical and thermal behavior on the experimental results, the model is capable of accurately reproducing the material behavior both qualitatively and quantitatively with a single set of parameters for strain rates spanning three orders of magnitude. The local thermo-mechanical properties, including thermal dependence of transformation stress, strain rate dependence of the PF localization, incomplete PT during loading and unloading, as well as continued PT during holding phases, are replicated very well despite the simplification based on a one-dimensional single-crystal approach. In addition, the model effectively captures the influence of the strain rate dependent number of PFs, considering position and time, influencing the

local HE with the ambient. Regarding the design of an EC HP, the model captures the effect of blocked BT after reaching the material specific austenite finish temperature, and therefore predicts accurately the reduced temperature change during unloading [252, 162]. Furthermore, the model reproduces the input mechanical work as well as the exchanged thermal energy output, allowing for the calculation of the *COP*.
Due to the accurate prediction of the mechanical and thermal SMA material behavior, the calibrated model can used to investigate caloric properties of the SE SMA material under different ambient and loading conditions. Therefore, the presented model is able to support and facilitate the development process of EC HP systems.

4 Thermo-mechanical material characterization

The calibration of the physics-based SMA model requires the investigation of the material parameters under various mechanical and thermal boundary conditions, as introduced in subsection 1.2.3. In the literature, several scientific test platforms are presented with different characterization methods, each with its own advantages compared to the others [259, 247, 227, 215, 191, 192, 179, 180, 160, 74].
As introduced in section 3.4, in addition to the basic material parameter, further parameters need to be extracted through material characterization to enable the material-specific prediction of the PT, HE, and HT behaviors following subsection 3.2.4.
The measurement of material parameters such as stress-induced specific latent heat (H), thermal conductivity (κ), phase fraction diffusion coefficient (η), and the precise transformation strain (ε_t), requires the investigation of the local strain distribution in combination with the local temperature and mechanical parameters like force and displacement.
The time series of thermography images only display the spatio-temporal temperature evolution in the sample and do not accurately reflect the strain distribution, as seen in Figure 3.9. This is due to the blurring effect of the HT along the sample arising from the thermal conductivity of the material. By combining the local temperature distribution obtained using an IR camera with the local strain distribution, captured by an optical camera system and processed by DIC, as introduced in the literature [259, 247, 219, 122, 74, 46, 25, 17] it is possible to evaluate the missing material parameters.
This chapter presents the methodology for the evaluation, using SMA wires as sample geometries without restricting the generality. It is based on Kirsch et al. [74].
The first part will cover the experimental setup, including test procedure, data acquisition, and specimen preparation. Following that, the results will be presented based on experiments conducted using a 0.87 mm diameter SE SMA wire made of NiTiCo, supplied by the company *Fort Wayne Metals* under the product name *NiTi#3* and with the surface treatment *etched-polished* [29]. Finally, the method of identifying material parameters will be presented and discussed.

4.1 Experimental setup

The testing platform used is based on the *TIRA test 2710*, a universal material testing machine from the company *TIRA*. It can be utilized for conducting tensile, compression,

and bending tests. The mechanism comprises two pillar guides with ball screws and free-of-play adjusted single nuts. The test room has dimensions of 1.2 m height and 0.45 m width, with a maximum stroke of 1 m without clamps. The DC drive with the gearbox is capable of applying a maximum testing force of 5 kN with a maximum movement speed of 1 m/min. The encoder used in the drive has a displacement resolution of 0.45 µm. The force sensor is easily interchangeable, allowing for the use of different sensors with suitable force ranges for each specimen geometry. The force sensor can be directly attached to the specimen. Moreover, the testing platform is equipped with adjustable limit switches.
During the second funding period of the German Research Foundation Priority Programme SPP 1599, this testing platform is adapted for investigating the thermo-mechanical coupled material behavior of SMAs, as shown in Figure 4.1 [74]. The test bench is mounted on a

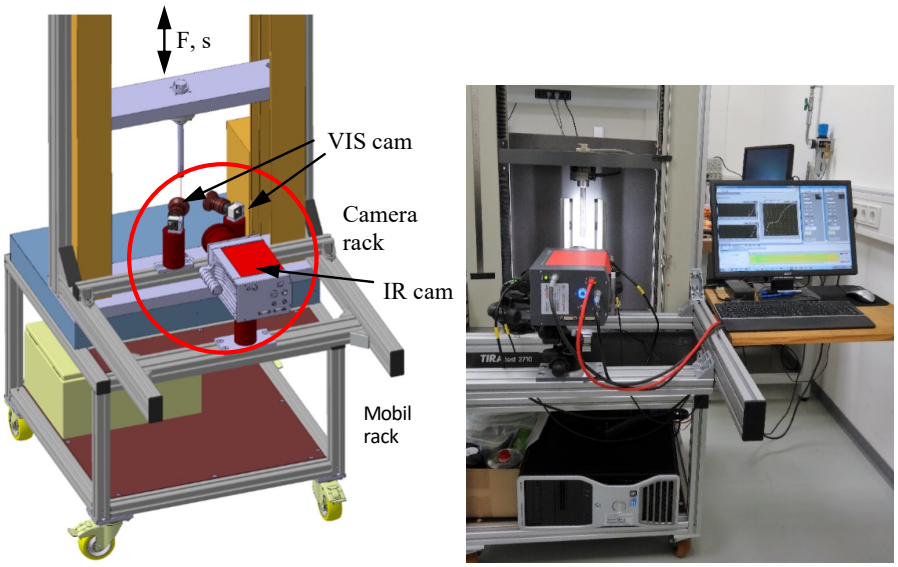

(a) (b)

Figure 4.1: Experimental setup for combined thermography and digital image correlation: a) Schematic view and b) realization.

mobile rack, allowing tests in a climatic chamber at varying temperatures and humidities to explore a wide range of material parameters, including different transformation temperatures. In addition, to enable test procedures with electrical current flow through the specimen, the mounting positions in the clamps are isolated electrically with a glass fiber-reinforced epoxy sheet. Furthermore, the platform for force-displacement testing is expanded with an adjustable camera setup, including an IR camera for thermography and two optical cameras for DIC, enabling combined investigations of spatio-temporal temperature and strain evolution. The cameras are attached to a mounting device with a tripod head and guiding systems, which allows the image section to be adjusted to the size of the specimen.

4.1.1 Infrared temperature field measurement

The local temperature distribution across the entire sample surface can be continuously monitored during the test to analyze its spatial and temporal temperature evolution. Therefore, a high-speed middle-wave length infrared camera *ImageIR9360* from the company *InfraTec* is used. The cooled 1280×1024 pixel sensor with a pitch of 15 µm supports a frame rate of up to 106 Hz in the full frame, and up to 3.2 kHz of free configurable sub-images. The camera uses the InSb focal-plane array sensor to capture images in the spectral range of 2–5.7 µm. The temperature change on the specimen's surface is measurable with a resolution of 0.025 K and a measurement accuracy of ±1 K. The operating temperature ranges from −20 °C to 40 °C with a maximum humidity of up to 95 % without condensation, while the measurable temperature range is from −40 °C to 1500 °C. The images are captured, saved, and evaluated using a control and acquisition software called *IRBIS* from the company *InfraTec*. This program provides an user interface for the experiment configuration, such as windowing, frame rate, trigger mode, sequence programming, and post-processing.

4.1.2 Optical strain field measurement

The distribution of the local displacement across the entire sample surface can be continuously monitored during the test to analyze its spatial and temporal strain evolution. Therefore, two visible range CMOS cameras *UI-3360CP-M-GL* from the company *iDS* are used. The uncooled 2048 x 1088 pixels sensor with a pitch of 5.5 µm supports a frame rate of up to 140.9 Hz in full frame. The operating temperature ranges from 0 °C to 40 °C with a maximum humidity of up to 80 % without condensation. The images are captured and saved using a custom-build virtual instrument programmed in *National Instuments LabVIEW*. Additionally, it is possible to load a parameter settings file to the camera. The stereo camera system can observe and save variations in three dimensions and can cover different areas due to the versatility of the camera rack. The spatio-temporal strain evolution can be extracted during postprocessing with DIC using the software *Vic2D* from the company *Correlated Solutions*.

4.1.3 Control system

The enhancement of the test bench necessitates a corresponding adaptation of the control system. A control system with an adaptable testing procedure and synchronous data acquisition is necessary to facilitate experimental scenarios with various thermo-mechanical boundary conditions. The adaptation of a new experiment scenario and the testing procedure must be time-saving and reproducible. Also, system control and data acquisition must be reliable. A schematic view of the test procedure with its data acquisition methods

is shown in Figure 4.2. A real-time system is required, and a programmable control unit like *cRIO* is necessary due to compatibility with existing testing platforms and modifiability. The testing platform should have a simple handling to avoid application errors. Hence, a virtual instrument (VI) programmed in LV with an organized user interface is utilized. To enable stand-alone test execution on the real-time system, a *Remote Panel* is provided, allowing test control with any PC. This feature is particularly valuable for long-term tests.

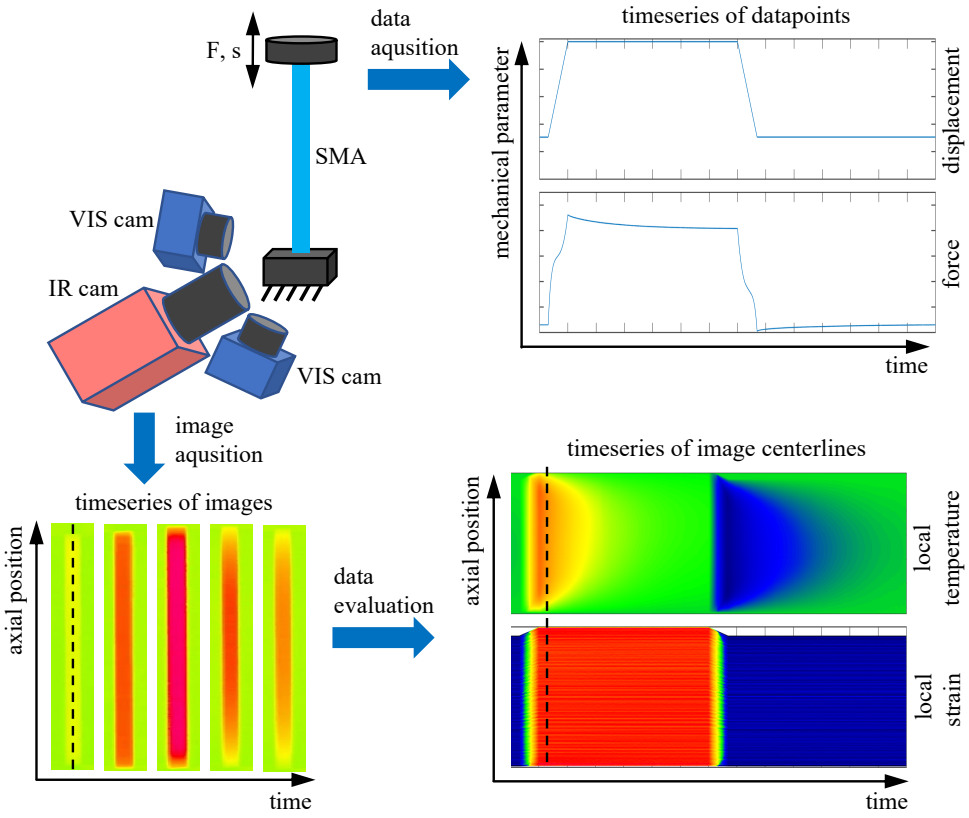

Figure 4.2: Schematic representation of the experimental setup for combined thermography and digital image correlation of SMA elements. The time series of images is postprocessed to generate spatio-temporal plots.

4.1.4 Data acquisition

The main program initiates synchronous data acquisition for force, displacement, and images using a TTL signal to trigger both camera systems. The time-resolved position and force measurements are saved in a csv- or hdf file. This format allows for evaluating the time series of data points with various software, such as Excel or MATLAB. The time series of images from both camera systems are stored on the PC and then processed to generate waterfall diagrams showing the spatio-temporal evolution of temperature and strain. The waterfall diagram is created for both camera systems in the same way. This is

done by selecting the specimen's centerline from each image in the time series and plotting it successively against each other. This helps illustrate the evolution of the transformation behavior versus position and time in a 2D diagram.

4.1.5 Test procedure

Figure 4.3 presents the front panel of the control VI. The experiment can be assembled successively as required using multiple sequences. The stack of subsequences can run with the desired number of cycles. On each subsequence, the absolute position, force limit, velocity, and sampling time for each camera can be adjusted. Additionally, the user can specify the position and force values for the initial setup or reset them to zero for starting a new test series, which is crucial for performing multiple tests consecutively. The user can choose which values to display in the two diagrams during the test. For example, the user can select to view time vs. position or position vs. force. In addition to the trigger outputs, eight digital outputs can be individually configured in each subsequence, allowing for control of accessory devices such as switching a current source to electrically heat the specimen or activating a fan to convective cool. Each register card can be individually

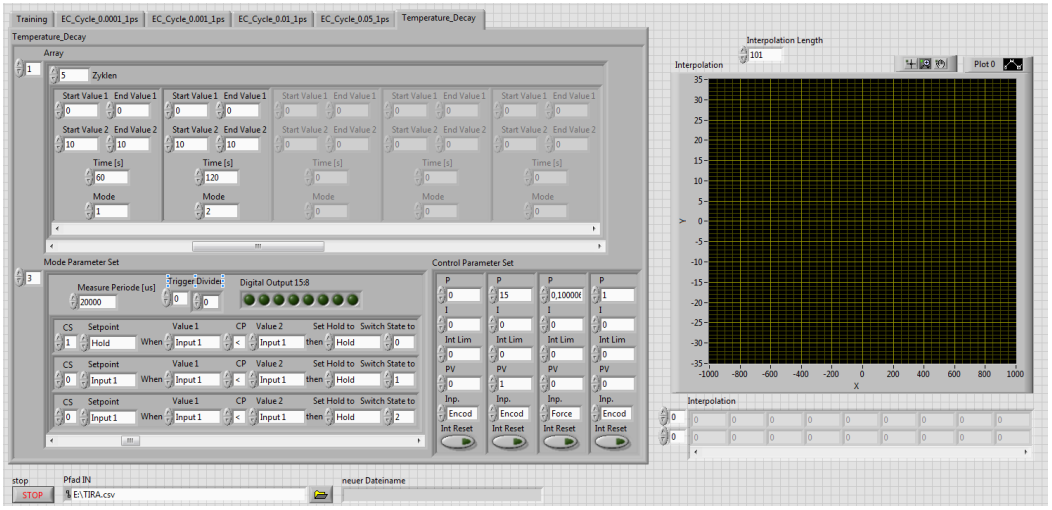

Figure 4.3: Front panel of custom VI for multifunctional test procedures with synchronous data acquisition.

configured to save templates of experiments or frequently used test sequences. The register card contains arrays of subsequences that can be cycled. The output file contains eleven columns: Number in time series, day, month, year, hour, minute, second, relative time since starting the test, current position, current velocity, and current force. If the current sampling time has passed, a trigger signal will be sent to the cameras, and a new set of values will be measured and saved in the next row of the file. The test sequence configuration and all adjusted parameters and subsequences are automatically saved in

the output folder. This allows for reconstructing the experiment process and re-importing it if the procedure is not saved as a register card.

4.1.6 Specimen preparation

The analysis of the spatio-temporal strain measurement using DIC requires preparing the specimen with a random speckle pattern on the observed surface and providing suitable illumination to capture the local shift and deformation in the speckle pattern on the sample. The size of the speckle pattern has to be in the same magnitude as the desired displacement resolution.

Figure 4.4 presents a detailed view of the camera setup and the prepared specimen: In this setup, thermo-mechanical properties of an SMA wire with a diameter of 0.87 mm, and a free length of 90 mm should be investigated. Figure 4.4 (a) provides an overview of the test setup with the camera rack and the specimen illuminated by the lights. Due to the high aspect ratio, the VIS cam system is equipped with two different lenses, as shown in the close-up in Figure 4.4 (b): The VIS camera on the right-hand side is equipped with a lens for capturing the complete specimen, while the one on the left-hand side has a macro lens for providing a detailed view at the middle height of the specimen. This is useful for resolving the PF with high resolution. To minimize mismatches in the local view around the wire, the angle between each camera is chosen to be as small as possible. The specimen in Figure 4.4 (c) is shown with a polymer housing that has a dull surface to minimize airflow, light reflections, and IR reflections from the ambient. Figure 4.4 (d) povides a detailed view of the specimen. The unprepared metallic surfaces of the sample

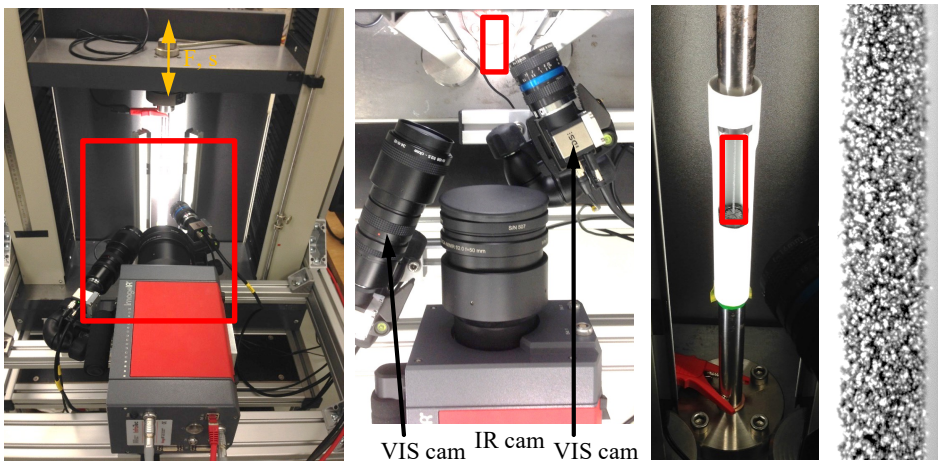

(a) (b) (c) (d)

Figure 4.4: Experimental setup for combined thermography and 3D digital image correlation: a) Testsetup with camera rack, b) camera arragement, c) clamped specimen with housing and d) speckled SMA wire.

exhibit a low emissivity of less than 0.1 [154], resulting in a poor signal-to-noise ratio for small temperature changes that typically occur during isothermal loading of a SE SMA. Therefore, the specimen is coated with a black, matt camera spray to enable precise temperature measurements and enhance emissivity. The used paint with the number *105202* is manufactured by *TETENAL*. They assure a light absorption coefficient of 0.95 and an emissivity independent of the substrate. In the case of combined IR and DIC measurements, white-colored speckles are added to the black-coated wire. Due to the small size of the white speckles, their interaction with the thermography is not measurable. Meanwhile, the color thickness should be as thin as possible to minimize the time delay between the PT and the detected temperature change of the specimen. This allows for an accurate correlation between thermographic and strain distribution.

4.2 Experimental results

To investigate the thermo-mechanical properties and the PT behavior of a SE SMA, the cycle of the experiment consists of four steps:

1. Loading to a maximum strain of 5.5 % at a defined strain rate.
2. Holding at constant strain for 60 s, allowing the sample temperature to return to ambient temperature due to HE.
3. Unloading to a minimal force (5 N) to avoid buckling at a defined strain rate.
4. Holding at constant force for 60 s, allowing the sample temperature to return to ambient temperature due to HE.

Figure 4.5 provides the results of the thermo-mechanical testing with a defined strain rate ($\dot{\varepsilon} = 10^{-2}\,1/\mathrm{s}$) and a maximum strain of 5.5 % for numerous cycles. These results were obtained using a SE NiTiCo wire manufactured by *Fort Wayne Metals* under the product name *NiTi#3*. The wire had a surface treatment of *etched-polished* and a diameter (d) of 0.87 mm [74]. The first row presents the applied displacement over time. In this experiment, a constant maximum strain (ε) of 5.5 % is applied leading with the wire length ($l = 90\,\mathrm{mm}$) to a maximum displacement (Δx) of 5 mm. The second row presents the resulting force over time. In this experiment, the reversal point between two cycles is defined by the minimal tolerable force (5 N) to avoid buckling during unloading and the following holding phase. Due to the remaining strain in the wire with increasing cycle number, the minimal displacement increases, and the maximum force decreases. The third and fourth rows display the spatio-temporal evolution of temperature and strain as a waterfall diagram over the duration of the experiment. The spatio-temporal diagram is created by tracing the specimen's centerline in each image of the time series. The centerline data are then

plotted against each other to enable better visualization and easier comparison. This illustrates the evolution of the temperature vs. position and time in a 2D diagram in the third row and strain vs. position and time diagram in the fourth row. This diagram can be used under the assumption of homogeneous material conditions in the sample.

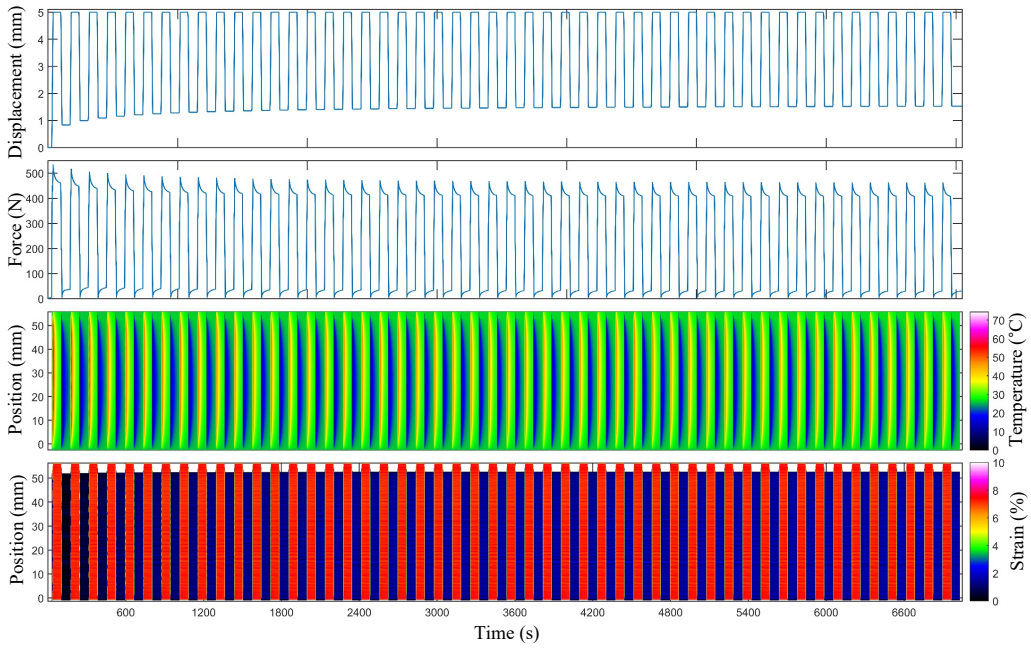

Figure 4.5: Experimental data of the tensile loaded NiTiCo SE SMA wire with a defined strain rate ($\dot{\varepsilon} = 10^{-2}\,1/\mathrm{s}$).

4.2.1 Loading

For a detailed analysis of the local PT behavior, a closer look is provided in Figure 4.6 of the first cycle for loading and the following holding phase. The first and second rows present the displacement and force over time. The local temperature is presented in the third row, and the strain evolution is in the fourth row. While loading, the SMA begins transforming at both ends almost simultaneously, as indicated by the nucleation of PF in the third row. This is also indicated by the temperature change of the material due to the release of the specific latent heat. These two PFs travel along the sample.

New PFs emerge when existing ones cannot travel fast enough to transform sufficient material to account for the global applied length change, in combination with the local temperature depended transformation stress as introduced in Equation 2.5. This leads to search for the next possible and suited nucleation point along the SMA element [259]. In case of loading, the local self-heating of the material at the PFs during PT hinders their propagation because a higher local stress would be required to reach transformation stress. Depending on the distribution of temperature along the sample, the formation or

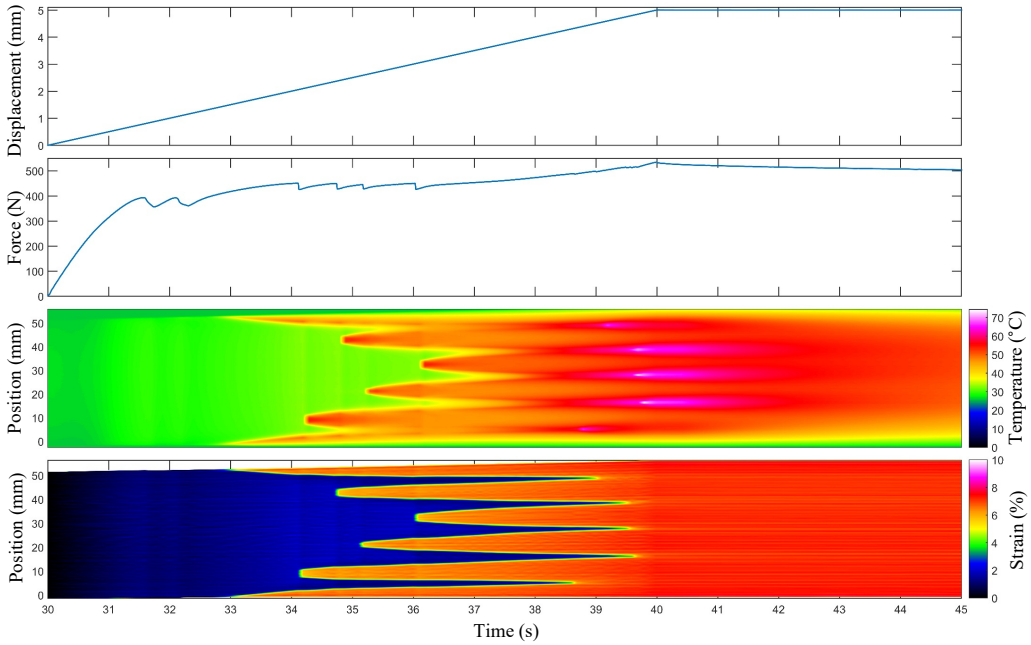

Figure 4.6: Detailed view of the experimental data from the first cycle of the loading phase with the following holding phase.

nucleation of new PFs appears to be more energetically favorable than maintaining or increasing the propagation velocity of existing PFs.
Hence, new PFs are formed repeatedly. While traveling along the sample, the PFs merge and produce maximum temperature at the meeting point. Each nucleation of PF is accompanied by a force drop, as visible in row two, due to the length change of the CLS caused by PT.
During the holding phase, the sample returns to ambient temperature due to the convective HE with the environment. A drop in the force curve is observed during the holding period after loading. This indicates that the PT was not completed during loading because a decreasing temperature due to HE also reduces the transformation stress, allowing further material to transform. This ongoing PT process leads to further local expansion of the material, resulting in the force relaxation. If the PT is already fully complete during loading, no reduction in force can be observed during the holding phase.

4.2.2 Unloading

For a detailed analysis of the local PT behavior, a closer look is provided in Figure 4.7 of the first cycle for unloading and the following holding phase. At unloading, the material begins to transform at the ends, with distinct PFs traveling towards the middle while cooling the material due to the absorption of the specific latent heat. The same start behavior of the PT during loading and unloading indicates a complete PT of the material after loading and the following holding phase. During unloading, the local self-cooling

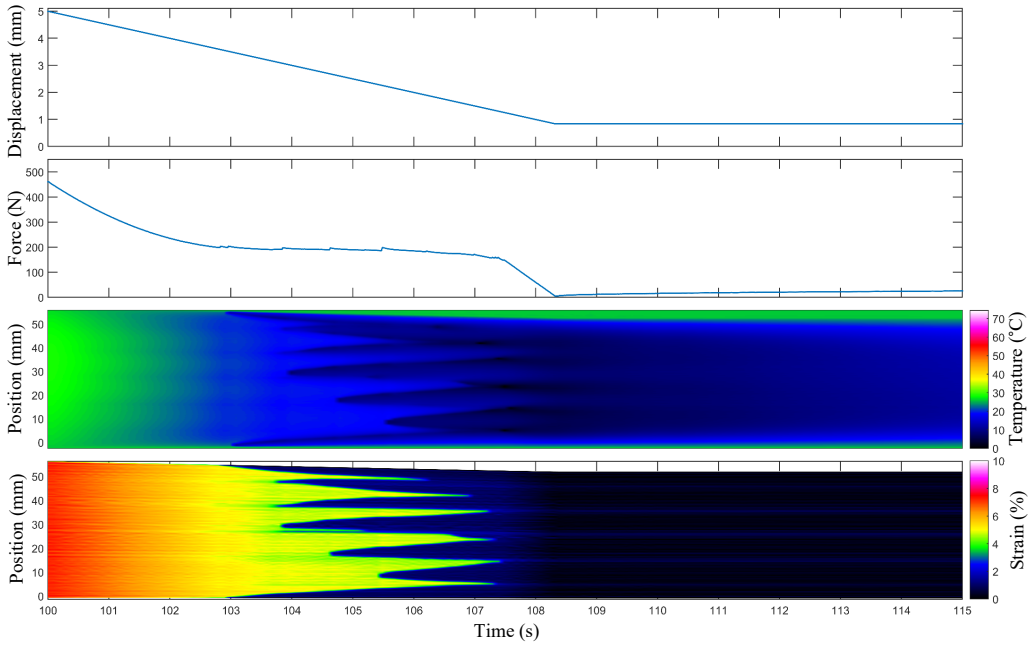

Figure 4.7: Detailed view of the experimental data from the first cycle of the unloading phase with the following holding phase.

effect hinders the propagation of the PF. Therefore, due to the current stress-strain state, new PFs are formed repeatedly, as discussed during loading. The merging of PFs results in the lowest temperature at the meeting point. During the holding phase, the sample returns to the ambient temperature due to convective HE with the environment. The unloading and subsequent holding phase also lead to force carving, which can be correlated with the formation of PFs induced by temperature change.

Figure 4.6 and Figure 4.7 show the typical evolutions of PFs for the first cycle of an untrained polycrystalline SMA material, as introduced in subsection 1.3.1. This behavior is comparable with the PT behavior of a nearly perfect CLS under a loading cycle with a moderate strain rate, as presented in the second column of Figure 3.9.

4.2.3 Stabilization

Whereas, after 50 cycles, presented in Figure 4.8, the IR and also the DIC shows a homogenous PT behavior with no single nucleation fronts, known as trained SMA material behavior. The imperfect CLS of the polycrystalline SMA leads to local stress concentrations and preferred PF nucleation due to the presence of hiking and jamming imperfections and impurities [255, 179]. This behavior is comparable with the PT behavior of a nearly perfect CLS under a loading cycle with a fast strain rate, as presented in the third column of Figure 3.9.

The drop in the F curve is still observed during the holding period after loading, indicating that the PT was not completed during loading.

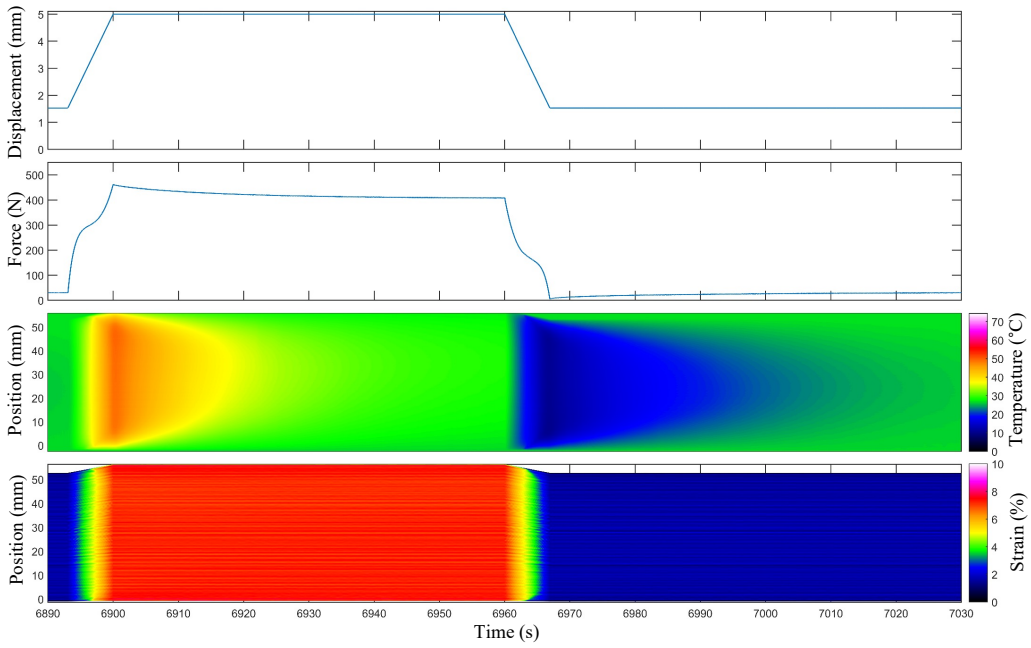

Figure 4.8: Detailed view of the experimental data from the 50th cycle.

4.3 Parameter identification

Figure 4.9 shows the relationship between force and displacement, representing the material behavior for different strain rates ($\dot{\varepsilon} = 10^{-2}\,1/\mathrm{s}$, $\dot{\varepsilon} = 10^{-3}\,1/\mathrm{s}$, and $\dot{\varepsilon} = 10^{-4}\,1/\mathrm{s}$). In these experiments, a constant maximum strain (ε) of 10 % is applied leading with the wire length ($l = 50\,\mathrm{mm}$) to a maximum displacement (Δx) of 5 mm. The minimal force required to prevent buckling is set to 5 N. In this diagram, the gray color represents an experiment with 50 loading cycles of an unused NiTiCo SMA wire (*NiTi#3*, [29]) with a wire diameter (d_{sma}) of 0.8 mm using a strain rate ($\dot{\varepsilon}$) of $10^{-2}\,1/\mathrm{s}$ as introduce in Figure 4.5. The last five cycles, highlighted in red, show a slight deviation in the curve, indicating that the sample reaches its trained behavior after 50 cycles, as discussed in subsection 1.2.3 and subsection 1.3.1.

The detailed process for evaluating all necessary material parameters will be presented below. The specific values will be summarized for clarity in Table 5.5.

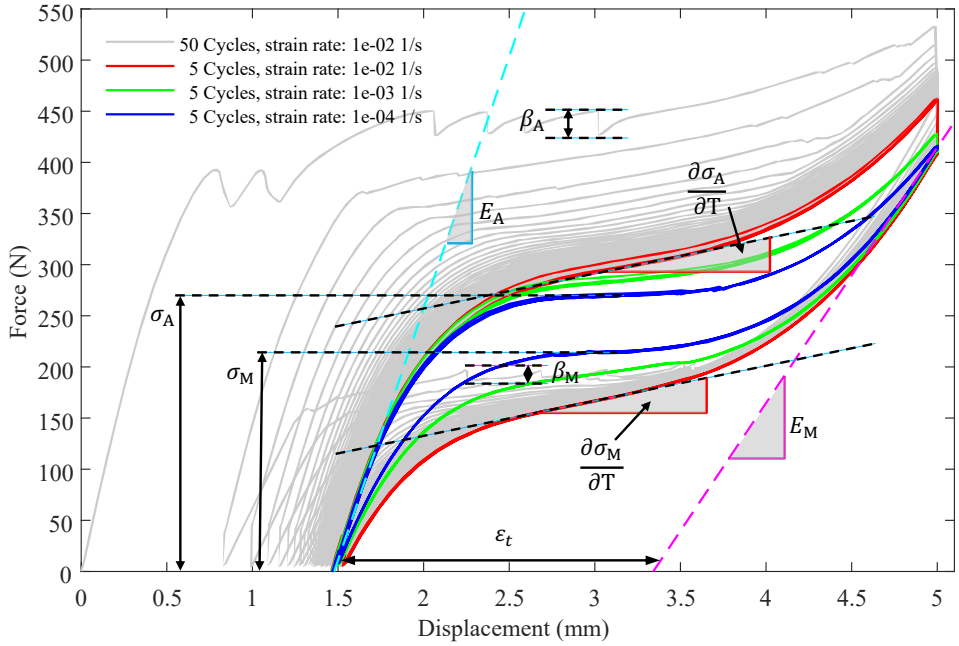

Figure 4.9: Force - displacement diagram of the NiTiCo wire experiments for multiple cycles, different strain rates ($\dot{\varepsilon}$), and fitted parameters.

4.3.1 Young's modulus

The Young's modulus of A (E_A) can be derived by using the slope of a straight line fitted to the linear elastic A branch of Figure 4.9 and taking the specimen geometry into account. For the identification of the Young's modulus of M (E_M) and the transformation strain (ε_t) a completely transformed material is necessary. The force reduction observed during the holding phase in the force - time diagram of Figure 4.8 is also visible in this representation. It confirms with the vertical force drop the assumption of the incomplete transformation. To satisfy a complete PT, a quasi-isothermal tensile test with a strain rate ($\dot{\varepsilon}$) of 10^{-4} 1/s is conducted until the linear elastic M branch is reached. This experiment is depicted by the blue line in Figure 4.9. The Young's modulus of M (E_M) can be determined by using the slope of a straight line fitted to the linear elastic M branch and taking the specimen geometry into account. The transformation strain (ε_t) can be determined by using the strain value at the crossing point between the fit and the strain axis.

4.3.2 Transformation stress

The increasing transformation stress during PT as a result of the thermo-mechanically coupled material behavior is indicated by the inclination of the plateau curve and the hysteresis area as the strain rate increases. The transformation stress directly depends on the temperature of the actively transforming zones, the PF. Other zones of the specimen that are not transforming yet or already fully transformed do not influence the current

force. Figure 4.10 illustrates the relationship between the stress and temperature of the PF for different strain rates. The PFs are identified by finding the local maximum in temperature during loading and the local minimum during unloading in the spatially resolved temperature data obtained from the IR thermography. The loading process is

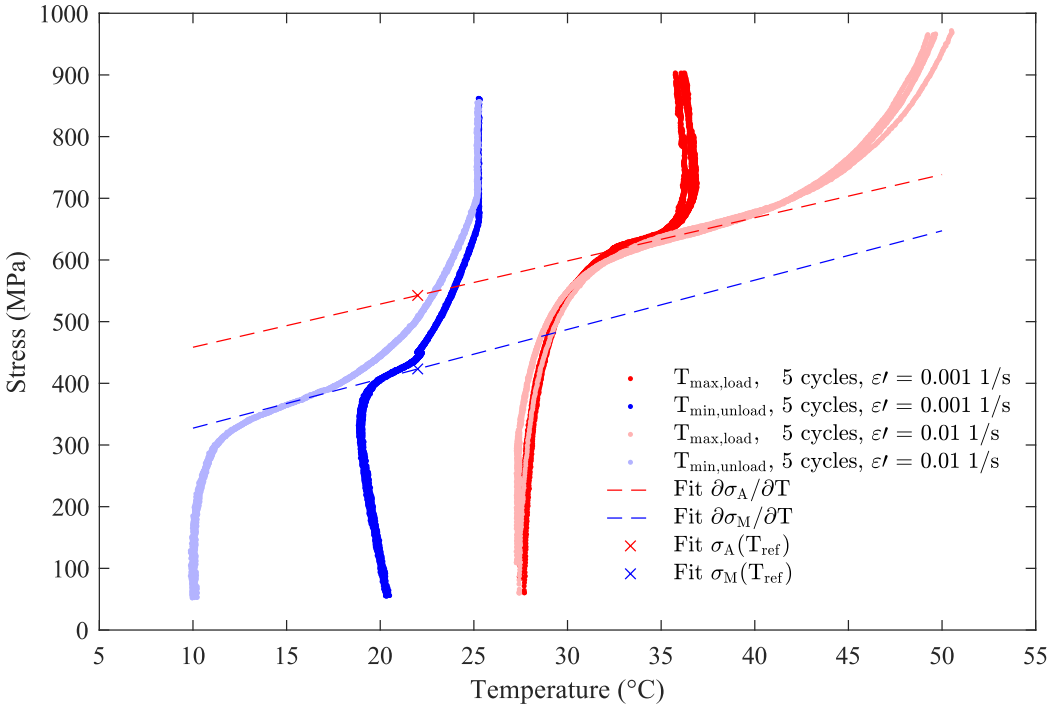

Figure 4.10: Stress - temperature diagram at the PF of the NiTiCo wire experiments for different strain rates in order to derive the temperature dependence of the transformation stress and stress at reference temperature.

marked with red dots. In the first part of the *S*-shaped curve, the stress increases without influencing the temperature. The following section builds the transition between the nearly vertical and the nearly linear parts; the temperature only slightly increases in this curved section. At next, the stress increases as the temperature of the PF rises from ambient to a maximum dependent on the strain rate. In this section, a nearly linear dependency between temperature and stress can be assumed with a strain rate independent slope. The temperature dependency of the transformation stress from A to M ($\frac{\partial \sigma_A}{\partial T}$), as introduced in Equation 3.11 (b), can be derived by using the slope of a straight line fitted to the data points. The following section builds the transition between the nearly linear part and the nearly vertical part; in this curved section, the temperature only slightly increases. In the last part of the *S*-shaped curve, the stress increases without influencing the temperature in the case of a small strain rate ($\dot{\varepsilon} = 10^{-3}\,1/\mathrm{s}$). With increasing strain rate ($\dot{\varepsilon} = 10^{-2}\,1/\mathrm{s}$), the material shows a post-transformation behavior. In this case, the last part of the *S*-shaped curve shows no perfect vertical part due to the slightly increasing temperature.

The unloading curve, marked with blue dots, follows a starting and ending behavior like the loading curve. In the middle part, the stress decreases with decreasing temperature of the PF, starting again at ambient and then dropping to a strain rate dependent minimum. The temperature dependency of the transformation stress from M to A ($\frac{\partial \sigma_M}{\partial T}$), as introduced in Equation 3.12 (b), can be derived by fitting a straight line to the aligned data points. The behavior of the last part at larger strain rate is also influenced by the post-transformation of the material.
The imperfections in the polycrystalline CLS result in an amplification of the stress in some cells and their transformation, even when the mean stress of the neighboring cells is lower. This premature PT of some cells is also visible as a bent in the A and M branch during the PT in the force - displacement diagram of Figure 4.9 and leads to the transitions between the linear parts of Figure 4.10.
For binary NiTi, temperature dependency of the transformation stress for FT and BT is assumed with a typical value of around 7 MPa/K, as determined by isothermal tensile tests at different temperatures [106]. In comparison, the NiTiCo show significantly unequal values for FT and BT, but in the same range of the binary material.
The determination of the transformation stress from A to M at the reference temperature ($\sigma_A(T_{ref})$) with its corresponding reference temperature (T_{ref,σ_A}) is also possible with this diagram, as introduced in Equation 3.11 (a). The transformation stress from M to A at the reference temperature ($\sigma_M(T_{ref})$) can be determined with its corresponding reference temperature (T_{ref,σ_M}), as introduced in Equation 3.12 (a). The linear relationship between transformation stress and temperature for A and M is defined by these four values.
Additionally, the degradation of σ_A during FT or the increase of σ_M during BT which allows for full PT with the material-depend parameters phase fraction dependence of σ_A (β_A) and phase fraction dependence of σ_M (β_M) is included with term (c) of the corresponding equations. In section 3.5, these values are adjusted based on the number of PF. However, these values can also be determined by assessing the PF-dependent change in force, as depicted in Figure 4.9 during the first cycle. The values for phase fraction dependence of σ_A and phase fraction dependence of σ_M correspond to the height of the peak during the nucleation of a PF in the isothermal case.

4.3.3 Heat exchange coefficient

The thermal connection between the sample and its environment influences the sample's thermal behavior during the loading, holding, and unloading periods. Natural convection leads to a heat exchange coefficient of 2.5–25 $W/(m^2 \cdot K)$, while forced convection can increase the value to 500 $W/(m^2 \cdot K)$ [64, 22]. Generally, the heat exchange coefficient changes with varying flow conditions such as sample surface properties, velocity, and flow

type (laminar or turbulent). Due to the wide span of values given in the literature, the determination of the application-specific heat exchange coefficient is essential.
The HE and temperature profile of the sample are mainly based on the convective heat exchange coefficient, influenced by the surrounding heat transport fluid and its temperature. If the sample had sufficient time to equalize any temperature differences before the experiment starts, the ambient temperature (T_{amb}) can be derived directly from the average sample temperatures at the beginning of the experiment. The heat exchange coefficient (h) can be determined from the temperature decline of the sample during holding phases as introduced in section 3.4.
Alternatively, heat exchange coefficient can be measured with an additional test procedure using Joule heating of the specimen, as presented in Figure 4.11. During this test, the heat exchange coefficient is determined using the temperature decay during the HE process of the sample from a higher temperature level back to the ambient. The SMA wire is clamped like before, and the clamping mechanism is connected to a power supply. The performed test cycle consists of two steps:

- First, the sample is Joule heated with a constant current of 2.5 A for 60 s.
- Next, the current is switched off, and the HE with the environment results in a decrease in the temperature of the sample due to natural convection with the surrounding air, reaching the ambient temperature within 120 s.

The testing machine applies a constant tensile force of 5 N to avoid buckling and enable a continuous observation for evaluation. With a current of 2.5 A, the wire is approximately heated up to 100 °C.
The thermal and mechanical influence of the clamping can be neglected due to the long sample length and the short influence area of the clamping as visible in Figure 4.8. In the center region of the sample, the distance to the camping is sufficiently large, and the Joule heating creates an almost homogeneous temperature field. The temperature decay is evaluated at the center point of SMA without forced airflow, using thermography and the postprocessing described before. Due to these assumptions, the simplified energy balance known from Equation 3.18 can be used.
Under the assumption of a uniform distribution of temperature, negligible influence of the clamping, and no generation or absorption of specific latent heat, the temperature evolution in the sample is only governed by the exponential decay dependent on the heat exchange coefficient (h). To facilitate comparison between experiments with different strain rates due to differing sample temperatures, a normalized temperature is used. This normalized temperature ($\tilde{T}$) is calculated using Equation 3.19, with the geometry parameters of the sample, volume (V) and surface area (A), as well as the material parameters of the SMA, density (ρ) and specific heat capacity (c).

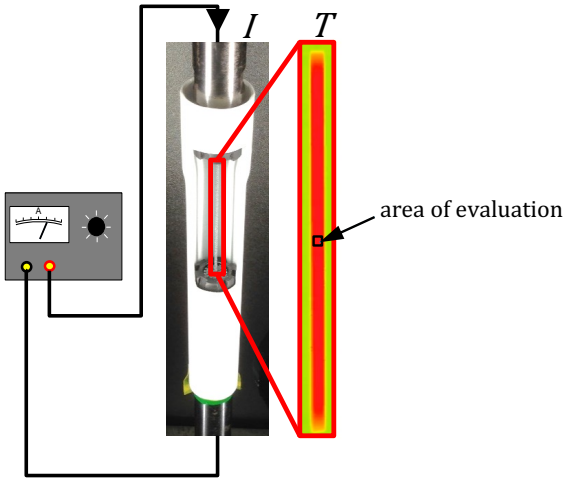

Figure 4.11: Detailed view of the experimental setup for a heated SMA wire and the corresponding convective cooling behavior.

Figure 4.12 shows the decay of the normalized temperature over the time (t) at different experiment cycles, evaluated from the spatially resolved temperature data of the sample's center region.

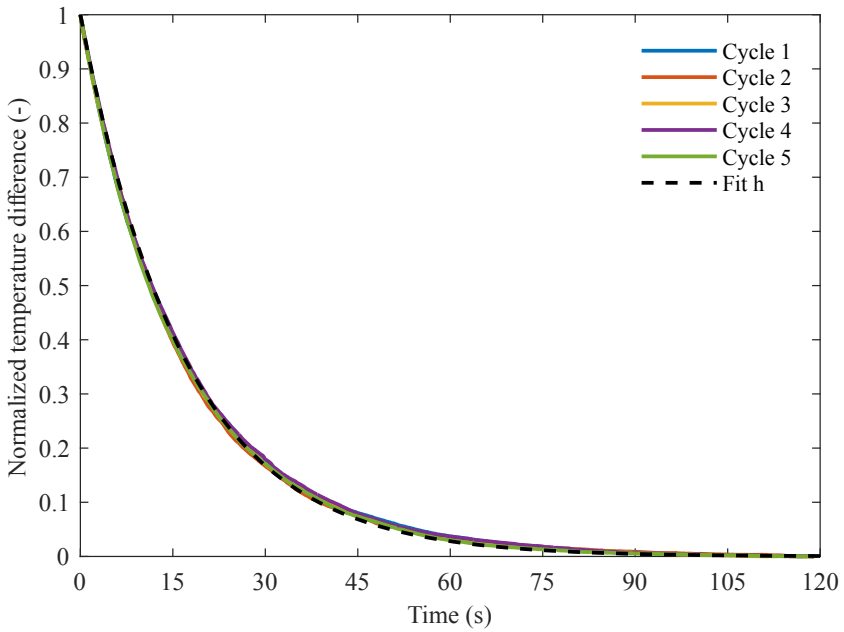

Figure 4.12: The normalized temperature decay over the time at different experiment cycles for the identification of the convective heat exchange coefficient (h).

The homogeneous HE without any changes to the thermal boundary conditions leads to a monotonic curve. Assuming the same ambient condition for all different experiment cycles, the pathway should be the same. The measurements for the five completed cycles and the exponential fit match perfectly.
The determined value of the heat exchange coefficient (h) of 32.3 $\mathrm{W/(m^2{\cdot}K)}$ slightly exceeds the suggested value for not forced convection due to the vertical arrangement of the test

stand. Further investigations are executed based on forced convection and a horizontal arrangement [75, 55].

4.3.4 Phase transformation parameter

The detailed comparison between the spatio-temporal strain and temperature evolution, shown in Figure 4.13, enables the determination of the missing material parameters thermal conductivity (κ) and phase fraction diffusion coefficient (η). In the upper part, the time correlated local distributions of temperature (T) and strain (ε) are presented using the color legend of Figure 4.8. The diagram below displays the local strain, indicated in blue, and the local temperature, indicated in red, at the same time along the one-pixel line in the middle of the sample.
The amplitude of the local strain allows concluding the magnitude of the transformation strain (ε_t). Whereas the amplitude of the local temperature allows the conclusion of the magnitude of the stress-induced specific latent heat (H). The thermal conductivity (κ), known as temperature diffusion coefficient and introduced in Equation 3.15 (b), controls the size of the pre-heating zone in front of the PF. The comparison of the local strain and temperature after heating or cooling due to the PT of the single PF under nearly adiabatic conditions enables the phase-specific determination of the thermal conductivity (κ).
The shape of the local strain increase and decrease enables concluding the phase fraction diffusion coefficient (η). It supports the precise prediction of the phase fraction, following Equation 3.13 and Equation 3.14.

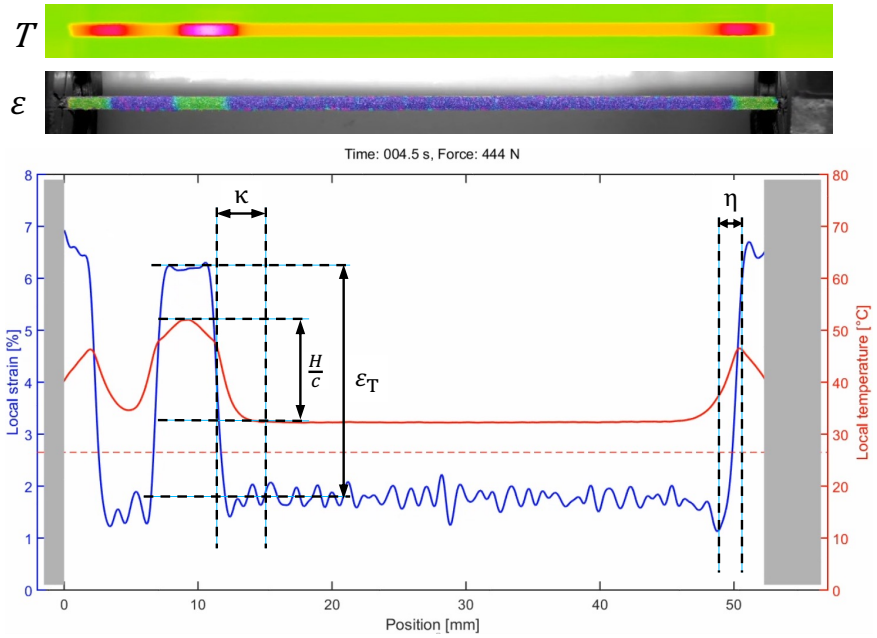

Figure 4.13: Detailed comparison between the spatio-temporal strain and temperature evolution of the first cycle.

4.4 Discussion

The presented thermo-mechanical test setup enables the evaluation of all thermal and mechanical parameters needed to calibrate the local SMA model. The combination of the spatio-temporal strain and temperature measurement enables a method for the evaluation of the stress-induced specific latent heat in addition to the methods introduced in subsection 1.2.3.

The knowledge of material behavior under various boundary conditions is essential to realize efficient EC processes and develop an optimized EC HP system. The experimental investigation of the interaction and cross-coupling of the boundary conditions by scanning a parameter space with a realized system is very time-consuming and requires much effort. Hence, it is crucial to simplify and improve the reliability of material characterization. Furthermore, a calibrated model can predict the material behavior under diverse boundary conditions and extend the limits of experimental investigation.

In addition to the material parameters, the experimental investigation shows the expected homogenization of the material after a small cycle number of 50 in comparison to the expected fatigue cycle number of 10^6, introduced in subsection 1.2.3. The inhomogeneous transformation behavior is observed in many SE samples but usually disappears in a polycrystalline material behavior over many loading cycles due to the training effect, introduced in subsection 1.2.3 and subsection 1.3.1. Whereas the single-crystal SMAs are only negligibly affected by the training effect due to the reduced number of lattice pinning sites, as introduced in subsection 1.3.1.

Regarding the realization of a macroscopic continuous operation EC HP system, the aim of using single-crystal SMA material is inconvertible since all commercially available materials are based on polycrystalline structures. A precise simulation tool that predicts the behavior of a single element and, subsequently, the entire HP system can significantly reduce the experimental effort. Nevertheless, the simulation time of the system simulation model should be as short as possible to minimize calculation costs. The cycling of the polycrystalline SMA material stabilizes a uniform PT, establishes a consistent temperature profile along the SMA element, and generates a global material performance. Therefore, a simplified lumped model for high computational efficiency is adequate for the system simulation approach introduced in the following chapter.

5 System simulation tool

The realization of an efficient EC process and the development of an optimized EC HP system requires a fundamental understanding of the material behavior and predictive system simulation tools. The previous chapters number 2 and 3 have focused on the thermo-mechanical behavior of SMA materials. This includes an emphasis on local effects and the modeling of these effects based on a micro-scale thin-film SMA element. Additionally, chapter 4 introduces the experimental methods for evaluating the thermo-mechanical material-specific model parameters. Therefore, this chapter presents the numerical simulation of the thermo-mechanically coupled behavior of an EC HP system based on polycrystalline SMA elements [74].

The desired macroscopic EC HP system will utilize a significant amount of commercially available SMA material to achieve substantial thermal power for heating and cooling applications. Therefore, the SMA material will exhibit a polycrystalline material behavior. To reduce the mechanical complexity of the system, the material should pass through the EC cycle in a simple manner. To maximize the material's lifespan while reducing the complexity of the mechanical stress state in the material. Due to these limitations, the geometry of the SMA element will be wire-like, and the HE will be conducted convectively in a homogeneous manner along the material's elongation. The assumed polycrystalline behavior and homogeneous thermal profile along the sample led to a homogeneous PT in the material after training, as introduced in chapter 4. Therefore, a lumped representation of the SMA behavior is sufficient. This representation reflects the behavior of a global PT and associated deduced properties instead of the local PF nucleation.

This part of the work focuses on developing a thermo-mechanically coupled model based on global PT behavior of SMAs, which includes the complex mechanical and thermal structure of whole EC HP system. The primary goal is to accurately replicate the temperature changes under various system conditions, as well as predict the mechanical work input and thermal power output quantitatively and qualitatively. To achieve this, the MAS model, as described in section 2.2, is implemented with the system approximation into the commercially available *MATLAB* programming platform. This model encompasses the interaction of the multiple individual system components of the desired macroscopic EC HP system and their specific behavior. It also supports the economic development of an optimized EC HP system. To find the optimized parameter set for a highly efficient heating and cooling unit with a wide temperature range while using a minimal amount of SMA material, a thorough search through a large parameter space is necessary. Some parameters, including the rotation frequency, allow a simple adjustment during an experiment. In

contrast, others, like the loading function or the SMA arrangement, require a redesign and reconstruction of the EC HP system. To enable parameter studies in the simulation and reduce the cost and time of experiments, the system model implementation will be expanded to create a system simulation tool and will be optimized for computation time. This tool should make it easy to scan all system parameters within a specified range. Additionally, this simulation tool enables a clear and comparable presentation of the parameter studies results.
First, the experimental setup will be introduced, followed by the modeling approach, model implementation, calibration, and validation. Finally, the results will be presented and discussed.

5.1 Experimental system

In this section, the EC HP system [10], shown in Figure 5.1, will be introduced, as the basement for the aimed simulation tool. The development, realization, and experimental investigation are conducted as part of the German Research Foundation Priority SPP1599 [74, 73, 50, 10].

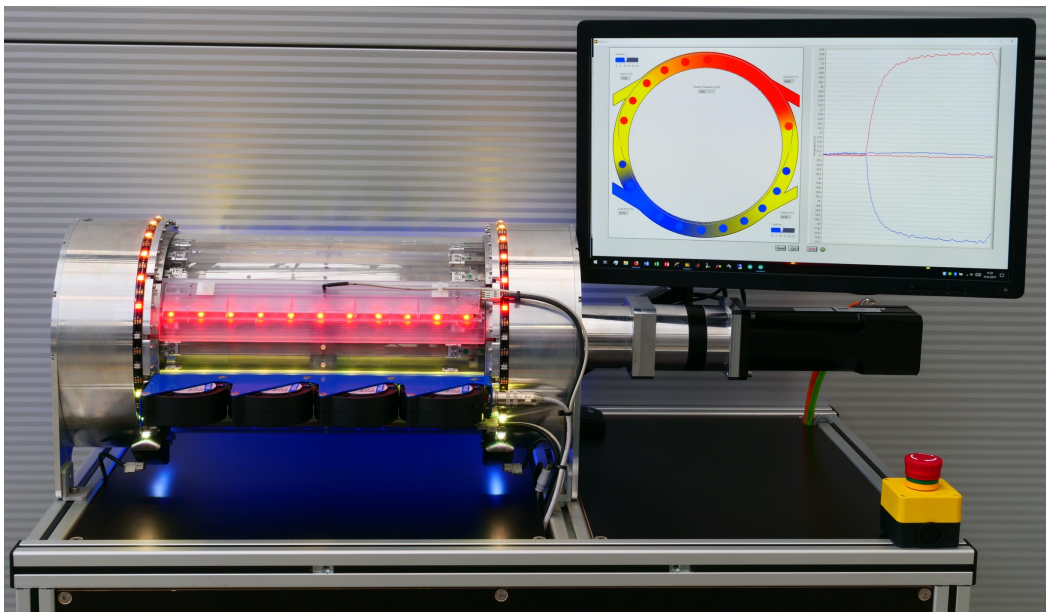

Figure 5.1: Photograph of the realized EC HP system. Adapted from Kirsch et al. [10].

5.1.1 Mechanical setup

Elastocalorically valuable materials are available in various geometries, each offering different properties for EC heating and cooling. Compared to other geometries, such as

tubes, plates, ribbons, and thin films, EC wires offer the best combination of availability in large quantities, manufacturing efficiency, and surface-to-volume ratio. However, they allow only tensile loading. The surface-to-volume ratio can be made considerably larger by reducing the wire diameter without buckling concerns, thus significantly improving HE and thermal power scalability.

The realized EC HP system comprises a fluid HE system and an integrated loading unit for elongating the numerous SMA elements. Figure 5.2 presents the schematic view with the

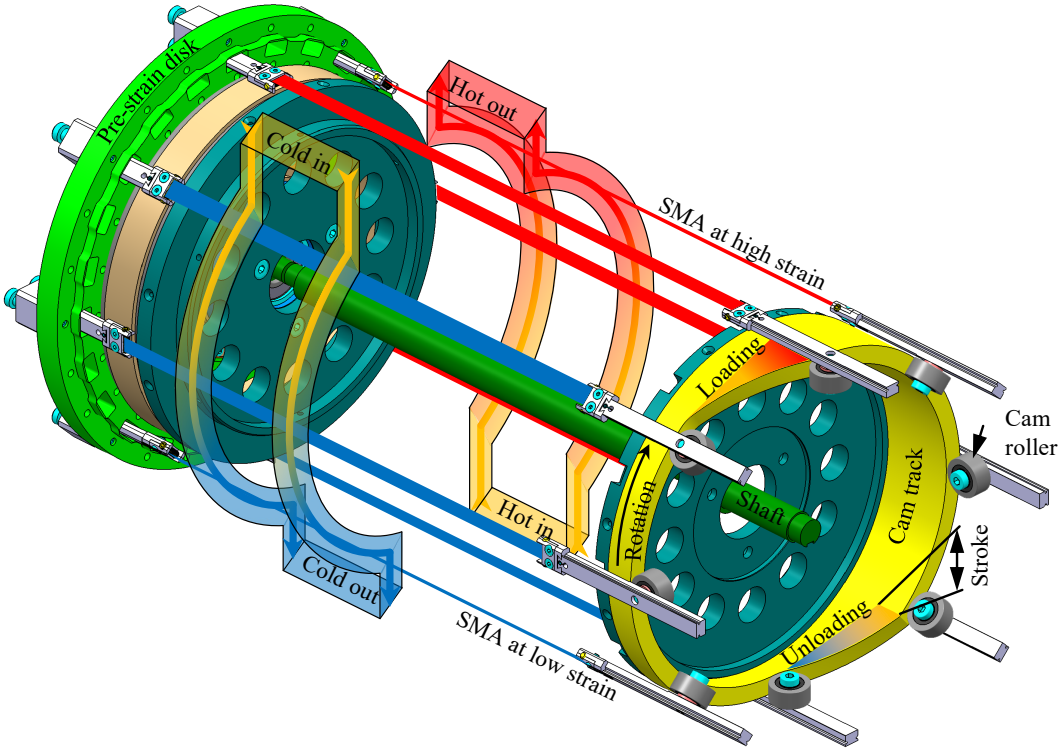

Figure 5.2: Schematic view of the EC HP system with load profile, SMA elements, and fluid ducts. Adapted from Kirsch et al.[10].

load profile, SMA elements, and indicated fluid ducts. The mechanical concept consists of two co-rotating discs, which have the potential to accommodate a large number of SMA elements within a compact assembly space. The SMA elements are evenly spaced around the circumference between the two rotating disks, ensuring synchronized guidance of the SMA element ends during rotation. The pre-strain disk prevents buckling of the SMA elements at low strain by applying an individual tensile low force for each SMA element produced by a spring. A transmission shaft coordinates the synchronous rotation of the two co-rotating disks. The axial guiding system on the loading disk individually manages the force transmission for each SMA element to a purely axial direction. In Figure 5.2, only the pre-strain disk is shown to provide a descriptive figure.

The first device is constructed with a cam diameter (d_{cam}) of 220 mm, SMA element number (N_{bun}) of 24, and a system length (l_{sma}) of 300 mm.

5.1.2 Adaptable loading

The cam track, presented in Figure 5.2, converts the rotary motion of the SMA elements into a linear stroke. The cam track guides the cam roller and generates a linear axial movement in an attached SMA element. Based on a rotary cam track, the adaptable load profile defines the tensile strain for the individual SMA element traveling along the circumference. The motion function of the cam roller can be adjusted by the cam profile to the desired thermodynamic cycle [100, 48], which enables performing an optimized EC hybrid cycle, as introduced in subsection 1.2.2, leading to an efficient EC device. The symmetric arrangement of the SMA elements with the cam rollers around the circumference leads to inherent work recovery. While one element is loaded, the opposite SMA is unloaded. The loading force of the SMA element depends on the applied strain. Additionally, this loading concept provides a pure axial loading to the SMA element. While moving on the loading/unloading part of the cam profile, the SMA element heats up/cools down and transits between the two temperature zones. During the holding phase at constant strain, the SMA element can exchange thermal energy with the surrounding HT medium.
The first realized cam track profile provides a symmetric loading and unloading area, each with a width of 40°, but can be easily replaced and adapted due to the versatile system design.

5.1.3 Heat transport

The cyclic loading and unloading of the SMA elements induce a temperature change along the circumference of the device. In combination with the accompanying holding part of the cam track, a hot and cold semicircle is formed by the SMA elements. The HE is based on convection using a fluid as the HT medium, simplifying the mechanical setup. To guide the HT medium across the ring of SMA elements, an inner and outer cylinder forms the fluid channel. This concept of loading and fluid channel, which is divided with inlets and outlets into fluid ducts, creates a stationary heat sink and source while using a rotary drive.
The SMA elements change their temperature while loading and unloading due to the specific latent heat. During the holding phases at constant strain, the SMA elements exchange the thermal energy with the surrounding fluid. The surrounding HT medium represents the heat sink around the SMA elements at high strain and the heat source around the SMAs at low strain. The temperature profile of the surrounding fluid is illustrated by color in Figure 5.2: The inlet of the hot and the cold duct is indicated in orange, the outlet of the cold duct is represented in blue, and the outlet of the hot duct is shown in red. During movement on the cam track's loading and unloading ramp, the SMA elements transition between the two temperature zones. The area between the inlet

and outlet of different temperature zones in the fluid channel is called a *transition zone* or *cross-flow area*. An efficient convective HE is achieved by a transversally guided fluid flow into the inlets of the fluid duct and transversally arranged outlets, as indicated by the cross-sectional view of the device in Figure 5.1. This flow-optimized design of the inlets and outlets reduces the overflow of HE fluid into the other half of the fluid channel. The HT medium can flow, as shown, in counterflow to the rotation direction of the SMA elements or, alternatively, in parallel flow due to the versatile realization of the fluid channel. The arrangement of inlets and outlets for the HT medium on each semicircle, along with a large number of individual SMA elements, enables the simultaneous continuous extraction of hot and cool thermal energy.

The initial EC HP system implementation is designed as a direct air heating and cooling unit, eliminating the need for additional heat exchangers. Even though air exhibits relatively poor HE characteristics compared to liquids, it offers simple handling and mechanical design with negligible sealing problems. The fluid flow is generated using four *RL65-21/14H* fans from the manufacturer *ebm-papst*, which are mounted at the inlet of each fluid duct. The speed of these fans can be adjusted continuously by changing the applied voltage.

In the initial setup, the inlets and outlets of the fluid ducts are symmetrically arranged around the loading and unloading of the cam track. This results in a fluid duct length of 140° on each side, with the midpoint for the hot duct at 90° and the cold duct at 270°.

5.1.4 Shape memory alloy element

Figure 5.3 presents the SMA element used in the EC HP device consisting of a novel multi-element clamping mechanism which provides a clamping potential of numerous SMA parts with different diameters while creating a minimized mechanical and assembly effort. Those bundles consist of numerous thin wires to improve the HE and, thus the device's efficiency.

The realized bundles consist of 30 wire segments (N_{wpb}) with a diameter (d_{sma}) of 200 µm, separated into two layers. A threaded spool realizes the separation of the wire segments. The resulting distances are chosen to be 0.7 mm (lw_{lay}) between the wires in each level and 3.34 mm (lh_{lay}) between both groups. After arranging the wire segments, they are secured in position using two fixing screws that apply equal mechanical load to each wire segment. This wire arrangement is thermo-mechanical validated using numerous bundles [10, 1]. The heating and cooling potential of this bundle arrangement is investigated for different airflow velocities by Michaelis et al. [35]. Additionally, the HE between NiTi-wire bundles with different wire arrangements and airflow is investigated [11].

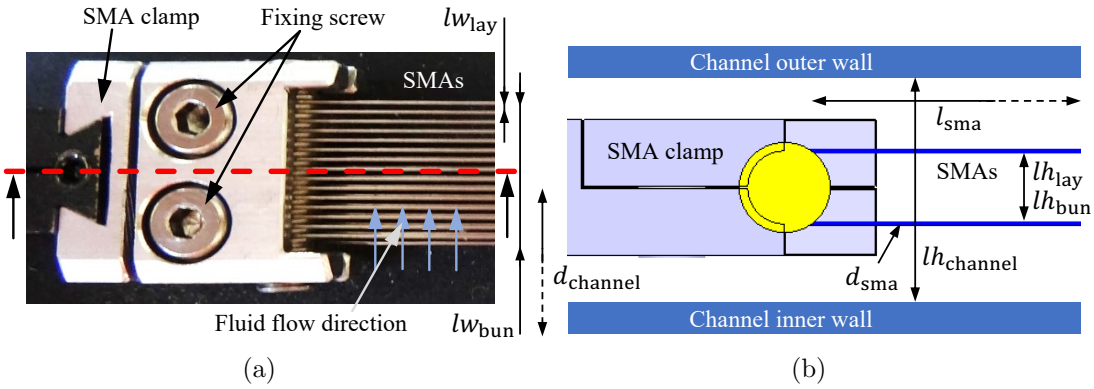

Figure 5.3: SMA element: a) Photograph of the realized bundle with the illustrated flow direction of the HE and HT fluid, and b) cross-sectional view with the illustrated fluid channel. Adapted from Kirsch et al.[10]

5.1.5 Summary

The discussed EC HP system provides a continuous thermal power of the hot and cold duct on the macroscale due to its mechanical setup, as introduced in section 2.1. In addition, the loading unit of the SMA elements enables the variation of the EC cycle, providing optimization potential for temperature range, thermal power, and *COP*, following subsection 1.2.2. The innovative approach in using SMA material as SMA elements, combined with these key points, results in a uniquely powerful EC HP system. The application scale, SMA element geometry, load case, HE type, and medium can be adapted easily.

The versatile design enables independent modification of the process parameters such as type and amount of SMA material, load profile, rotation frequency, fluid channel geometry, flow direction, inlet temperature, and flow rate. In the literature, first experimental results are presented for the continuous operating EC HP system variating rotation frequency and air flow rate[49, 50].

The presented concept offers a large number of individually adjustable design and operating parameters. To achieve an optimal EC HP system, a simulation tool that covers the complex relationships of the design is essential for the economic development and realization of the device. Due to the large number of possible parameter sweeps, a data visualization tool is also needed to enable the comparison of different trends and influencing factors. The following sections describe the development and realization of a highly efficient simulation tool using the results of the foregoing chapters.

5.2 Model approach

The modeling approach described in the following section is based on the experimental system presented before. The system simulation comprises various elements and starting points that need to be discussed in this approach. This involves specifying the model type, constraints for model dimensions, segmentation and discretization method, boundary conditions between the simulated system and the environment, as well as model enhancements for all system modules.

The fully coupled system-level model must represent all physical subunits of the EC device. Therefore, the system is divided into modules. Figure 5.4 presents the structure of the system-level modeling approach, with the input parameters on the left, the output key values on the right, and the model with its subunits of the system in the middle. The

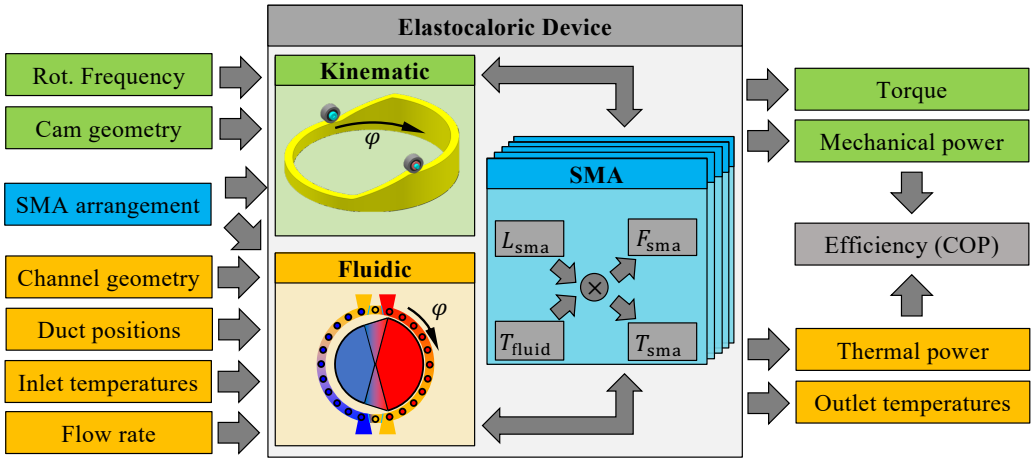

Figure 5.4: Structure of the *simulation tool* with input and output parameters. Adapted from [74].

loading and unloading processes are managed by the *Kinematic* module, and the fluid-based HT in the hot and cold ducts on both sides of the device are covered by the *Fluidic* module. Additionally, the *SMA* module covers each SMA element's behavior with respect to the HE with the HT medium. The coupling between the kinematic and the SMA unit generates the strain input for the SMA material. It transmits the SMA force and enables with the load profile a drive torque calculation. The interaction between the SMA material and the surrounding fluid consists of the HE based on their temperature differences. For the simulation of the hysteretic SMA material during tensile loading, the physics-based MAS model is used as the foundation. This includes also the thermo-mechanical coupling, as introduced before (section 2.2).

The three main components of the EC simulation tool will be linked together by the rotation angle (φ) as a clockwise positive state variable. It interacts with the *Kinematic* to provide the loading state, the *SMA* determines the temperature of each element, and the *Fluidics* determines the temperature of the fluid around the circumference. This interaction

results in the duct's outlet temperature, which affects the thermal power, torque, and mechanical work.
In the following, the *SMA* model with its dimensions will be discussed, followed by the *Kinematic* and the *Fluidic* approach.

5.2.1 Shape memory alloy model

The SMA element is actually a 3D body. When creating simulation models, it is best to opt for a simple replication of the simulation's focal element, boundary conditions, and operating cycle. This simplification reduces the model's complexity and minimizes computational effort. However, reducing the model's dimensions and simplifying the boundary conditions during the operational cycle can lead to discrepancies between the simulated behavior and the actual behavior of the focal element within the system.

Dimensions

In the case of an SMA wire with a polycrystalline CLS, where a uniform load and temperature profile throughout the EC cycle along its length will be applied, no local PT effects have to be considered due to the homogenization effect discussed in Figure 4.5. The single SMA wire segment within the SMA element has a diameter of 200 µm and a length of 300 mm, resulting in a very small aspect ratio between cross-sectional area and surface area. Hence, a discretization at the crosssection is not required for implementing the SMA geometry as the diameter-to-length ratio is insignificant. Additionally, the radial temperature gradient of the SMA can be neglected since the thermal conductivity of the SMA material is much greater than that of the surrounding fluid, and the heat exchange coefficient between the SMA and the fluid. This allows for a homogeneous temperature to be assumed in the cross-sectional area of the SMA [243]. It is applicable for each SMA wire segment in the SMA element due to the large distance of 700 µm between two wire segments. Additionally, the thermal and mechanical influence of the clamping can be neglected due to the long sample length and the short influence area of the clamping as visible in Figure 4.8. This allows for assuming a homogeneous temperature along the axial direction of the EC system.
This approach does not account for field fluctuations, such as the formation and propagation of PFs during the PT. It, therefore, supports a simplified model calculation without losing predictive power.
The used SMA geometry and size, as well as the thermo-mechanical setup, enable the approximation of the SMA element with a single temperature and phase fraction. The flexibility implementation allows for easy upgrading of the implementation to accommodate

more sets of values per element. The shape of the SMA element, such as the surface area and volume of the SMA material, remains unaffected.
As known from section 2.2, the modeling tool can have numerous aspects as presented in Figure 1.6. The desired system simulation tool will predict the system's behavior. Therefore, the experimentally observed localized PT will be neglected in the model.
Since the focus is on using the complete potential of the integrated SMA material, with full FT and BT, an exact replication of internal hysteresis loops is not necessary.
Regarding its use as a development assistant tool, computation time is one of the essential aspects. Therefore, the polycrystalline shape is neglected, and the material behavior is assumed to be box-shaped. Finally, the arbitrary MAS model, introduced in section 2.2, can be used, which considers a global, time-dependent phase fraction.

Mathematics

The SMA model provides the coupling between the mechanical deformation of the SMA applied by the kinematic unit and the thermal response affecting the fluidic unit. This thermo-mechanical coupling is replicated using the MAS model [233]. It includes the constitutive relation between stress (σ), strain (ε), and the current material composition as phase fraction (ξ) (Equation 2.9), as well as the energy balance of the SMA (Equation 2.25). The used SMA elements of the EC system are restricted to tensile force. Therefore, only M+ (ξ_+) and A (ξ_A) are considered as relevant phase fractions. This changes the constitutive relation from Equation 2.9 to Equation 5.1 by using Equation 2.10.

$$\sigma_j = \frac{\varepsilon_j - \varepsilon_\mathrm{t} \cdot \xi_{+,j}}{\frac{\xi_{+,j}}{E_\mathrm{M}} + \frac{1-\xi_{+,j}}{E_\mathrm{A}}} \tag{5.1}$$

The resulting constitutive equation depends in addition to the material parameters Young's modulus of M (E_M), Young's modulus of A (E_A), transformation strain (ε_t), and phase fraction (ξ). Since the phase fraction of M+ ($\xi_{+,j}$) is the system's state variable, it is specified by the index of SMA element ($_j$). The input strain value (ε_j) in Equation 5.1 is provided by the load profile and must be calculated for each of the 24 SMA elements in the EC system. The phase fraction of M+ is calculated using Equation 2.11. The simplification of only considering tensile loading removes the need to calculate a further PDE for each SMA element. This results in significant savings in computational effort.
The consideration of only the tensile-based M phase fraction changes the energy balance of the SMA element from Equation 2.25 to Equation 5.2.

$$\rho_\mathrm{sma} \cdot c_\mathrm{sma} \cdot \frac{\partial T_{\mathrm{sma},j}}{\partial t} = +\rho_\mathrm{sma} \cdot H \cdot \frac{\partial \xi_{+,j}}{\partial t} - h_{\mathrm{sma,fld}} \cdot \frac{A_\mathrm{sma,surf}}{V_\mathrm{sma}} \cdot (T_{\mathrm{sma},j} - T_\mathrm{fld}) \tag{5.2}$$

In this calculation, time-constant SMA material parameters of density (ρ_{sma}), and specific heat capacity (c_{sma}) is assumed, and no Joule heating is taken into account. Equation 5.2 describes the energy balance in the EC material by linking the temperature rate with the release or absorption of specific latent heat (H), due to PT, as well as with the HE betweeen the SMA and the surrounding fluid ($_{\mathrm{fld}}$). The HE, in addition to the temperature difference between the SMA (T_{sma}) and the surrounding fluid (T_{fld}), depends on the heat exchange coefficient ($h_{\mathrm{sma,fld}}$), and the ratio of SMA surface ($A_{\mathrm{sma,surf}}$) to volume (V_{sma}).

5.2.2 Kinematics

The current rotation angle of the SMA arrangement ($\varphi(t)$) in the EC HP depends on the duration of operation (t) and can be calculated using Equation 5.3.

$$\varphi(t) = \int_0^t \omega(t')\, dt' = 2 \cdot \pi \cdot \int_0^t f(t')\, dt' \tag{5.3}$$

With this dependency, the current position of each specific SMA element at a certain point in time ($\varphi_j(t)$) can be evaluated with the initial position of the SMA element in the SMA arrangement ($\varphi_{j,0}$) using Equation 5.4.

$$\varphi_j(t) = \varphi(t) + \varphi_{j,0} = \varphi(t) + \frac{360^\circ}{N_{\mathrm{bun}}} \cdot (j-1) \tag{5.4}$$

The cam track provides a prescribed displacement based on its load profile to achieve the desired loading of the SMA elements during the EC cycle. Furthermore, the mechanical power input is influenced by the load profile and the arrangement of the SMA elements.

Strain

The kinematic correlation between mechanics and SMA provides the strain input for each SMA element ($\varepsilon_j(\varphi_j)$), which is needed for Equation 5.1, based on the maximal stroke, angle of loading with start and end, and angle of unloading with start and end, as presented in Figure 5.5 (a). The loading process comprises four main stages:

- loading with a specific slope,
- holding at the maximum strain ($\varepsilon_{\max}$),
- unloading with a specific slope,
- and holding at minimum strain ($\varepsilon_{\min}$).

The cam rollers move in the direction of rotation of the SMA elements with the rotation frequency (ω). Between the specific points, the strain function ($\varepsilon(\varphi)$) can be interpolated

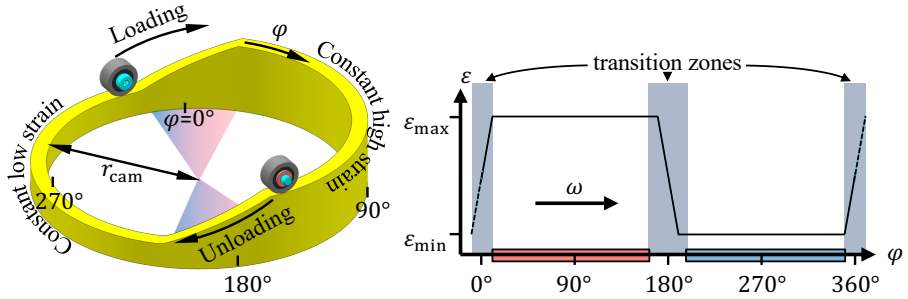

Figure 5.5: Kinematic correlation between mechanics and SMA elements: a) Schematic view of the cam track, b) strain (ε)-rotation angle (φ) diagram of the unrolled cam track.

as presented as an unrolled cam track in Figure 5.5 (b). The hot and cold fluid ducts are depicted in color, and the transition zones are indicated in gray. More sections can easily be added to the piecewise-defined function to mimic an adiabatic-isothermal hybrid process with different slopes during loading and unloading.

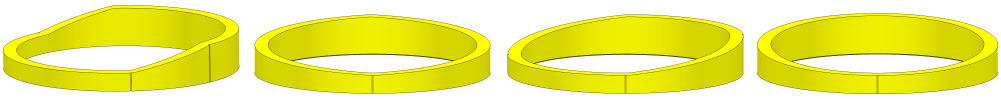

(a) Symmetric 40° (b) Symmetric 180° (c) Unsymmetric (d) Sinus

Figure 5.6: Cam track geometry: Exemplary presentation of cam discs with different loading/unloading types.

The load profile of the SMA controlling the EC cycle, applied by the cam track, is defined by characteristic points and modeled as a stationary, piecewise strain function ($\varepsilon_j{=}\varepsilon(\varphi_j)$) depending on the rotation angle (φ) of the SMA arrangement. The loading and unloading profiles can be defined as interpolated lool-up tables or mathematical functions. Due to this versatile approach, unsymmetric and arbitrary load profiles around the circumference are achievable, as well as sinusoidal functions, as shown in Figure 5.6.

Torque

Figure 5.7 explains the correlations for loading (a) and unloading (b) between the rotation angle (φ) and the cam track radius (r_{cam}) with the stroke, expressed by the strain (ε) and SMA length (l_{sma}). With this relation, the angle of inclination (α) can be calculated as a function of the rotation angle (φ) as presented in Equation 5.5.

$$\tan(\alpha) = \frac{l_{\text{sma}} \cdot d\varepsilon(\varphi)}{r_{\text{cam}} \cdot d\varphi} \tag{5.5}$$

The transmission ratio between the SMA force (F_{sma}) and the resulting tangential force (F_{tan}) on the cam track depends on the inclination angle ($\alpha(\varphi)$).
Using the resulting tangential force (F_{tan}) and the radius of the cam track (r_{cam}), the required torque (M_{sma}) for moving the SMA element along the load profile can calculated using Equation 5.6.

$$M_{\mathrm{sma}} = \sum_{j}^{N_{\mathrm{bun}}} M_{\mathrm{sma},j} = \sum_{j}^{N_{\mathrm{bun}}} F_{\mathrm{tan},j} \cdot r_{\mathrm{cam}} \tag{5.6}$$

The total required torque consists of the individual components generated by the resulting tangential force ($F_{\mathrm{tan},j}$) of each SMA element with the lever arm given by the cam track (r_{cam}). In addition to the SMA force ($F_{\mathrm{sma},j}$) motion of each cam roller on the cam track produces an individual friction force ($F_{\mathrm{fri},j}$), which has to be also covert by the tangential force ($F_{\mathrm{tan},j}$).

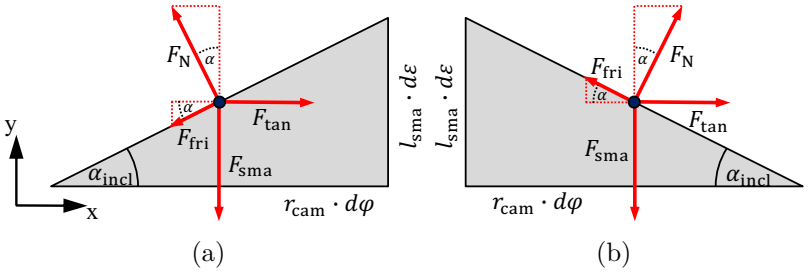

Figure 5.7: Kinematic correlations between mechanics and SMA elements: Schematic view of the forces while loading (a), and unloading (b).

The evaluation of the force equilibrium in horizontal direction (F_{x}) and vertical direction (F_{y}) for the inclined ramp while loading of the SMA is presented in Equation 5.10 and the declined ramp while unloading of the SMA is presented in Equation 5.14.

$$\sum F_{\mathrm{x}} = F_{\mathrm{tan}} - F_{\mathrm{N}} \cdot \sin(\alpha) - F_{\mathrm{fri}} \cdot \cos(\alpha) = 0 \tag{5.7}$$

$$\sum F_{\mathrm{y}} = -F_{\mathrm{sma}} + F_{\mathrm{N}} \cdot \cos(\alpha) - F_{\mathrm{fri}} \cdot \sin(\alpha) = 0 \tag{5.8}$$

$$F_{\mathrm{fri}} = \mu \cdot F_{\mathrm{N}} \tag{5.9}$$

$$F_{\mathrm{tan}} = F_{\mathrm{sma}} \cdot \frac{\sin(\alpha) + \mu \cdot \cos(\alpha)}{\cos(\alpha) - \mu \cdot \sin(\alpha)} \tag{5.10}$$

$$\sum F_{\mathrm{x}} = F_{\mathrm{tan}} + F_{\mathrm{N}} \cdot \sin(\alpha) - F_{\mathrm{fri}} \cdot \cos(\alpha) = 0 \tag{5.11}$$

$$\sum F_{\mathrm{y}} = -F_{\mathrm{sma}} + F_{\mathrm{N}} \cdot \cos(\alpha) + F_{\mathrm{fri}} \cdot \sin(\alpha) = 0 \tag{5.12}$$

$$F_{\mathrm{fri}} = \mu \cdot F_{\mathrm{N}} \tag{5.13}$$

$$F_{\mathrm{tan}} = -F_{\mathrm{sma}} \cdot \frac{\sin(\alpha) - \mu \cdot \cos(\alpha)}{\cos(\alpha) + \mu \cdot \sin(\alpha)} \tag{5.14}$$

During unloding, the angle of inclination (α) is < 0. The identity of the trigonometric functions, $\sin(-\alpha) = -\sin(\alpha)$ and $\cos(-\alpha) = \cos(\alpha)$, indicates that Equation 5.10 and Equation 5.14 are the same. Therefore, there is no need for a case distinction, which saves time during calculation.
In the case of the loading, the powertrain has to provide a higher force for each SMA bundle for a friction coefficient $\mu > 0$. At unloading, the powertrain has to provide a lower negative force for each SMA bundle for a friction coefficient $\mu > 0$. Thus, the total torque of the hole EC system increases with friction.

5.2.3 Fluidics

In Figure 5.8, the cross-sectional view of the channel presents the input temperature on the hot (T_{hi}) and cold (T_{ci}) duct, as well as the output temperature on the hot (T_{ho}) and cold (T_{co}) ducts. The evolution of the temperature in the channel is indicated by the familiar color order, based on the strain profile (ε) inside the circle and the rotation direction of the SMA elements with the rotation frequency (ω). The thermo-mechanical behavior of the fluid flow ducts is specified by the temperature (T) of the inlet and outlet and the flow rate $(\dot{V})$. The fluid flow velocity is calculated by using the channel geometry and flow rate. The primary flow direction of the fluid is assumed to be counter to the rotation direction of the SMA elements.
Figure 5.9 (a) illustrated the unrolling of the expected temperature distribution in the stationary state along the rotation angle (φ) during counterflow. The standard hot and cold channels are depicted in color, and the transition zones are indicated in gray. Figure 5.9 (b) presents the fluidics correlations between the fluid flow in the channel and the SMA elements, depending on the channel geometry, height (lh_{channel}) and radius (r_{channel}). Note that the radius of the channel (r_{channel}) describes the middle of the channel at which the SMA element exchanges its thermal energy, while the radius of the cam track (r_{cam}), describes where the cam rollers of the SMA elements insert their mechanical work. The length of the channel correlates for the HE with the length of the SMA (l_{sma}).

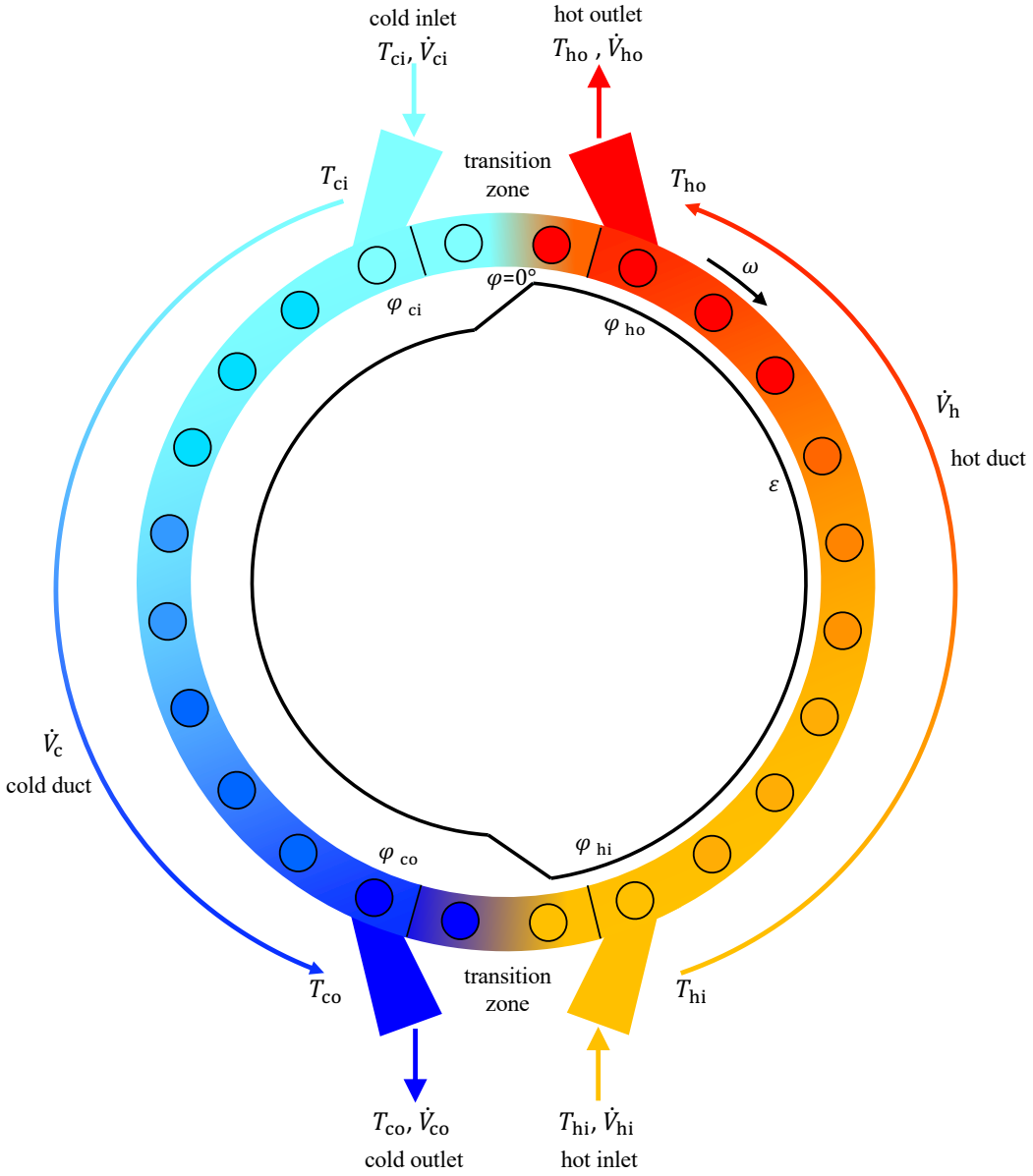

Figure 5.8: Cross-sectional view of fluid channel with inlet and outlet of hot and cold ducts, as well as the principal flow direction.

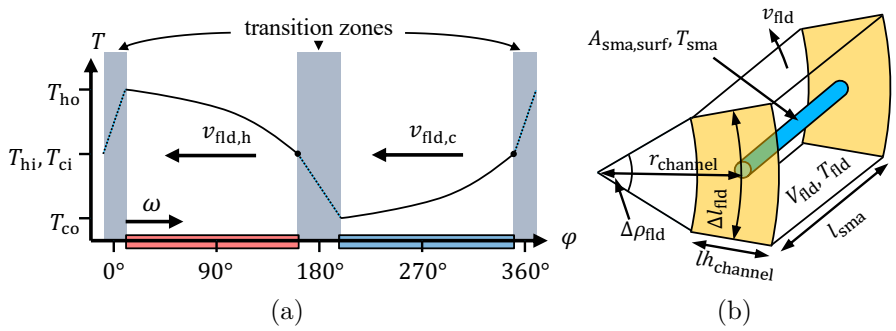

Figure 5.9: Fluidics correlations between fluid flow and SMA elements: a) Temperature (T) - rotation angle (φ) diagram of the unrolled channel and the SMAs, and b) draft of one fluid element.

Dimensions

For the calculation of the temperature distribution between the in- and outlets, the fluid channel is discretized along the circumference into numerous stationary volume elements with a specific length (Δl_{fld}). The temperature profile over the height (lh_{channel}) of the channel is homogenized due to the distance along the circumference between two neighboring SMA elements. Therefore, the initial version of the simulation tool approximates the fluid channel as a circumferential line, with the flexibility to easily upgrade the implementation to accommodate more concentric lines of fluid along the height of the channel. In the case of multiple concentric channels, the transferred thermal energy by HE between SMA and corresponding fluid element is divided. At the output, the temperature and the thermal energy are calculated using the weighted mean value of the multiple channel lines. Therefore, the resulting output values of the EC system are not affected by dividing the channel.

Thermal energy transport

The thermal energy transport along the fluid channel is numerically realized by using a conventionally advection-diffusion equation as presented in Equation 5.15.

$$\frac{\partial u}{\partial t} = \nabla \cdot (DFC \, \nabla \, u - \mathbf{v} \, u) + ST \tag{5.15}$$

This equation describes the transfer of energy or other physical quantities in a physical system based on diffusion, convection, or advection. The variable of interest, specific internal energy (u), changes its state over time due to the direkt HE with an energy source or sink (ST). This part can be a function based on the specific internal energy or other parameters. The central part of the partial differential equation is the divergence of the general diffusion coefficient (DFC) combined with the concentration gradient of the specific internal energy ($\nabla \, u$), and the velocity field ($\mathbf{v}$) of the specific internal energy.

Equation 5.16 presents the adaption of the thermal energy transport equation of the fluid to the desired application in the EC system.

$$\underbrace{\frac{\partial}{\partial t}\left(\rho_{\mathrm{fld}} \cdot c_{\mathrm{fld}} \cdot T_{\mathrm{fld},k}\right)}_{\mathrm{a}} = \underbrace{+\frac{\partial}{\partial x} \cdot \kappa_{\mathrm{fld}} \cdot \frac{\partial}{\partial x}\left(\rho_{\mathrm{fld}} \cdot c_{\mathrm{fld}} \cdot T_{\mathrm{fld},k}\right)}_{\mathrm{b}} \underbrace{-\frac{\partial}{\partial x} \cdot v_{\mathrm{fld}} \cdot \left(\rho_{\mathrm{fld}} \cdot c_{\mathrm{fld}} \cdot T_{\mathrm{fld},k}\right)}_{\mathrm{c}} + \underbrace{h_{\mathrm{sma,fld}} \cdot \frac{A_{\mathrm{sma,surf}}}{V_{\mathrm{fld}}} \cdot \left(T_{\mathrm{sma}} - T_{\mathrm{fld},k}\right)}_{\mathrm{d}} + \underbrace{\dot{Q}_{\mathrm{wall}}}_{\mathrm{e}} \tag{5.16}$$

The temporal derivative of the specific internal energy of a fluid element which is specified by the index of fluid element $(_k)$ (5.16) (a) depends on its density (ρ_{fld}), specific heat capacity (c_{fld}) and temperature $(T_{\mathrm{fld},k})$. The energy of the fluid element can be changed by the local changes in Fourier heat conduction (5.16) (b), which transfers thermal energy to neighboring elements based on the thermal conductivity of the fluid (κ_{fld}). In addition, the local change in energy is induced by the motion of the fluid. The advection-based part (5.16) (c) describes the mass transport out of the stationary fluid element based on the velocity of the fluid (v_{fld}). Further the energy changes due to the convective HE (5.16) (d) depending on the heat exchange coefficient $(h_{\mathrm{sma,fld}})$ between fluid and SMA, as well as the surface area of the SMA $(A_{\mathrm{sma,surf}})$, the volume of the fluid element (V_{fld}), and the temperature difference of both.
The time-dependent fluid temperature $(T_{\mathrm{fld},k})$ of each volume element can be calculated by solving this partial differential equation. In the following, the additional heat source or sink term in Equation 5.16 (e) will be introduced.

Wall losses

Regarding the application as a prediction tool for the EC system, the heat conduction losses in the channel wall must be considered. Therefore, the equation is extended by Equation 5.16 (e) to include the losses though different wall layers, as shown in Figure 5.10. The fluid duct, presented in the middle of Figure 5.10 (a), is on the left side, connected to the inner wall with the heat exchange coefficient $(h_{\mathrm{fld,wall}})$ and the inner ambient with the heat exchange coefficient $(h_{\mathrm{wall,amb}})$. Inside the wall, the thermal energy flows with the thermal conductivity of the wall (κ_{wall}) along the height of the wall (lh_{wall}). Due to the symmetric arrangement, the outer side is similar in terms of the wall and the ambient.
Figure 5.10 (b) presents the equivalent thermal resistance network of one side of the duct. With the total thermal resistance $(R_{\mathrm{th,tot}})$, as well as the temperature difference between

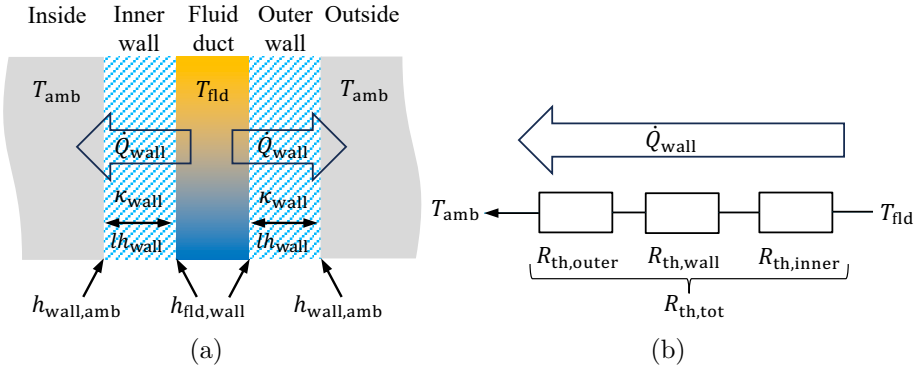

Figure 5.10: Thermal losses through duct walls: Schematic view of the layers around the duct (a), and equivalent network of the thermal resistance (R_{th}) (b).

the fluid (T_{fld}) and the ambient (T_{amb}), the thermal power through the wall ($\dot{Q}_{wall}$) can be calculated using Equation 5.17 with contact area between fluid and wall (A_{wall}). The wall losses have to be considered two times as a heat sink due to the symmetric arrangement.

$$\dot{Q}_{wall} = 2 \cdot \frac{(T_{fld} - T_{amb})}{R_{th,tot}} = 2 \cdot \frac{(T_{fld} - T_{amb})}{R_{th,inner} + R_{th,wall} + R_{th,outer}} = 2 \cdot \frac{A_{wall}}{\underbrace{\frac{1}{h_{fld,wall}}}_{a} + \underbrace{\frac{lh_{wall}}{\kappa_{wall}}}_{b} + \underbrace{\frac{1}{h_{wall,amb}}}_{c}} \cdot (T_{fld} - T_{amb}) \tag{5.17}$$

The thermal resistance of the inner interface between fluid and wall ($R_{th,inner}$) and between wall and ambient ($R_{th,outer}$) corresponds to the reciprocal of the related heat exchange coefficient for the fluid ($h_{fld,wall}$), and the wall ($h_{wall,amb}$), as introduced in (5.17) (a) and (5.17) (c). The thermal resistance of the wall can be calculated by dividing the thickness of the wall (lh_{wall}) by the thermal conductivity of the wall (κ_{wall}), as introduced in (5.17) (b). These equations result in the extension term (e) of the thermal energy transport equation of the fluid known from Equation 5.16.

Flow mixture and heat recovery

Figure 5.11 provides a detailed view of the channel's inlet and outlet areas, including the transition zones. The ring of SMA elements is surrounded by the inner and outer channel walls. At the inlets and outlets, the outer wall is opened to allow the fluid exchange. This structure is designed to guide the fluid tangentially into or out of the channel. At the inlets, the fluid flow can be forced by fans in the case of an air-based system or by pumps in the case of a liquid-based system. The forced fluid flow leads to an increased pressure at the inlet areas. At the outlets, the air-based system exhibits ambient air pressure. This pressure gradient encourages a cross-flow from the inlet through the transition zone to the

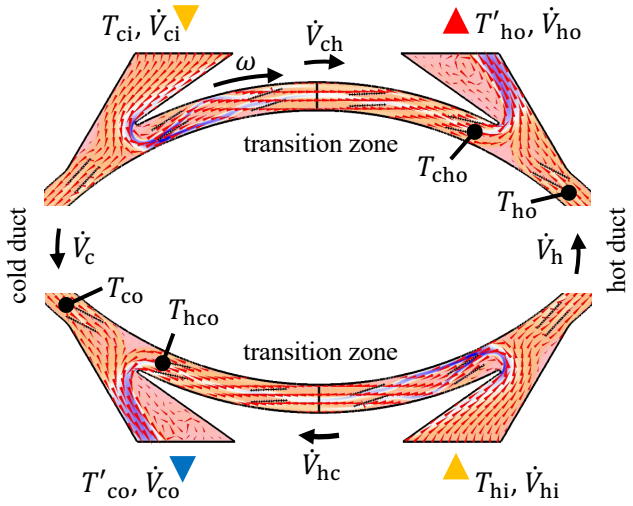

Figure 5.11: CFD simulation of fluid channel with inlet and outlet for a hot and cold duct with flow mixture in the transition zone.

nearby outlet. The cross-flow moves toward the outlet because of the pressure difference between the outlet and the main channel of the hot or cold side. The fluid flow in this direction, indicated in Figure 5.11 with the small red arrows, is increased in the case of a counter flow and reduced in the case of a co-flow between SMA elements and main flow in the hot and cold channel.

In the system simulation model, the flow mixture can be individually considered by a cross flow coefficient for the hot (cf_h) and cold (cf_c) side in the range of 0–1. The flow rate from the cold input ($\dot{V}_{ci}$) is split into the flow rate for the main cold channel ($\dot{V}_c$), which is defined by Equation 5.18, and the cross-flow from the cold input to the hot output ($\dot{V}_{ch}$), given by Equation 5.19.

$$\dot{V}_c = (1 - cf_c) \cdot \dot{V}_{ci} \tag{5.18}$$

$$\dot{V}_{ch} = cf_c \cdot \dot{V}_{ci} \tag{5.19}$$

The flow rate from the hot input ($\dot{V}_{hi}$) is split into the flow rate of the main hot channel ($\dot{V}_h$) and the cross-flow from the hot input to the cold output ($\dot{V}_{hc}$), which can be calculated using Equation 5.20 and Equation 5.21.

$$\dot{V}_h = (1 - cf_h) \cdot \dot{V}_{hi} \tag{5.20}$$

$$\dot{V}_{hc} = cf_h \cdot \dot{V}_{hi} \tag{5.21}$$

If the cross flow coefficient for the hot side (cf_h) or cold side (cf_c) is > 0, the simulation model will be expanded to include the corresponding transition zone as an additional channel. In this channel, the fluid flow generates HE with the SMA and affects the temperature profile of the entire EC system. The resulting flow rate at the hot outlet ($\dot{V}_\mathrm{ho}$), or cold outlet ($\dot{V}_\mathrm{co}$) is calculated using Equation 5.22 and Equation 5.23.

$$\dot{V}_\mathrm{ho} = \dot{V}_\mathrm{h} + \dot{V}_\mathrm{ch} \tag{5.22}$$

$$\dot{V}_\mathrm{co} = \dot{V}_\mathrm{c} + \dot{V}_\mathrm{hc} \tag{5.23}$$

The outlet temperatures of the hot (T'_ho) and cold side (T'_co) are calculated using Equation 5.24 and Equation 5.25, with the resulting temperatures at the end of the transition zone from cold to hot (T_cho) and from hot to cold (T_hco). This calculation is based on the calculation of the weighted arithmetic mean.

$$T'_\mathrm{ho} = \frac{T_\mathrm{ho} \cdot \dot{V}_\mathrm{h} + T_\mathrm{cho} \cdot \dot{V}_\mathrm{ch}}{\dot{V}_\mathrm{ho}} \tag{5.24}$$

$$T'_\mathrm{co} = \frac{T_\mathrm{co} \cdot \dot{V}_\mathrm{c} + T_\mathrm{hco} \cdot \dot{V}_\mathrm{hc}}{\dot{V}_\mathrm{co}} \tag{5.25}$$

With these formulas, the model can handle any number of fluid duct combinations. This can be used for investigating the cross-flow between the hot and cold fluid duct, as presented in Figure 5.11.
Furthermore, the concept of additional ducts enables the simulation of internal thermal energy recovery, as known from other EC systems introduced in section 2.1. This approach can help to increase the maximum meaningful temperature difference of the inlets while keeping the same EC material. By doing this, the remaining thermal energy in the SMA elements after the hot or cold duct can be used to pre-heat or pre-cool the SMA elements before the loading or unloading begins, as illustrated in Figure 5.12.

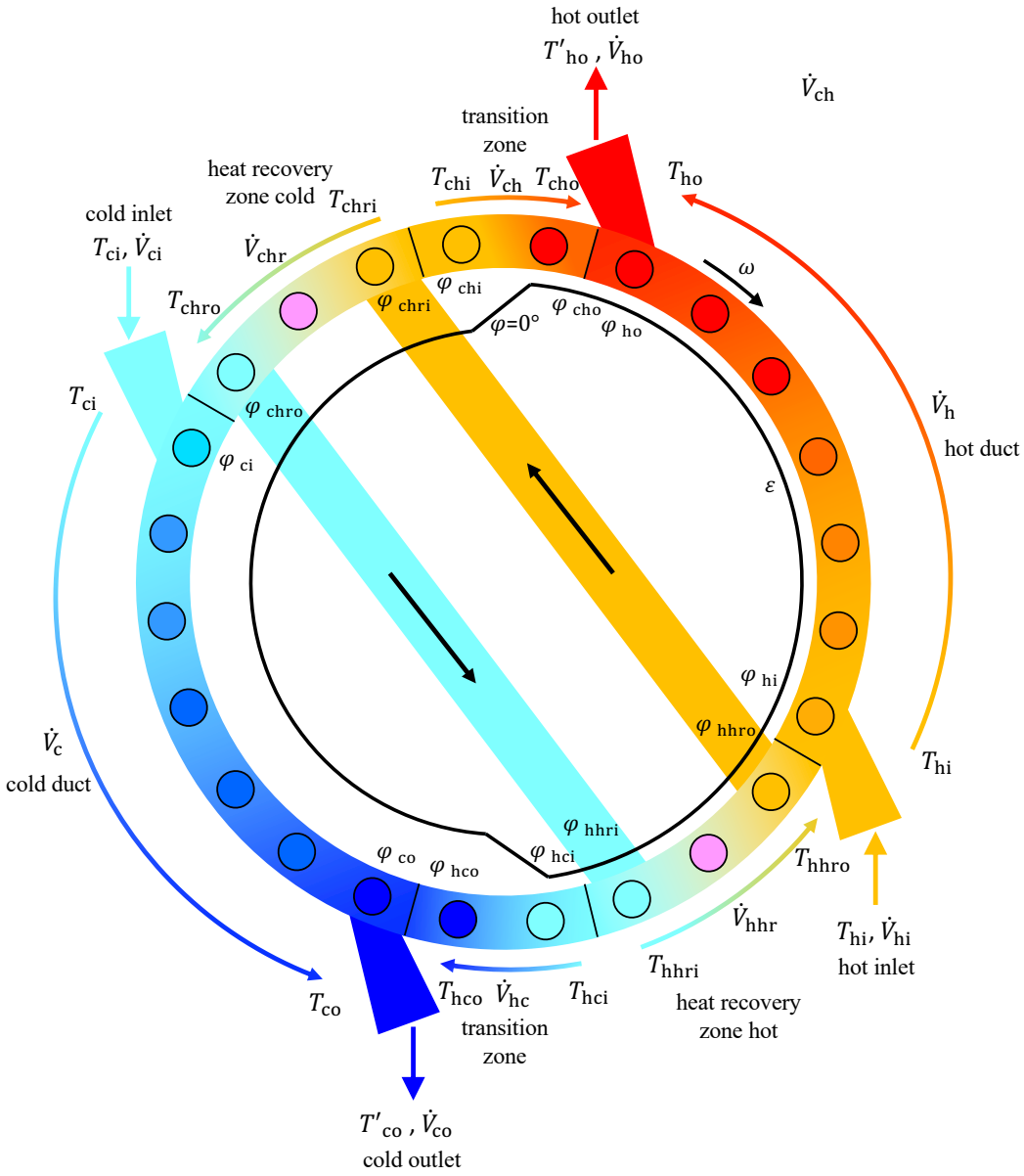

Figure 5.12: Cross-sectional view of fluid channel with cross-flow and internal heat recovery concept.

5.2.4 Heat exchange coefficient

The heat exchange coefficient between SMA and fluid ($h_{\mathrm{sma,fld}}$) changes significantly under different flow conditions, such as laminar or turbulent flow, surface properties of the SMA, and the velocity at which the fluid flow passes the SMA surface. To enable accurate prediction of the HE between SMA and fluid as introduced in Equation 5.2 and Equation 5.16, the value of the heat exchange coefficient has to be chosen according to the actual conditions in the EC system.

The heat exchange coefficient directly influences the minimal time needed for a sufficient HE between the wire and fluid during the holding phase of the process cycle. This time dictates the device's maximal meaningful rotation frequency. In literature, various values and empirical correlations are presented to overcome the uncertainty in this crucial influence factor; in the following, a suited concept for the determination of the heat exchange coefficient is evaluated.

Fluid flow simulation

The heat exchange coefficient between SMA and fluid can be determined using a CFD in *COMSOL*. The finite element (FE) software calculates the distribution of physical quantities such as pressure, flow velocity, and temperature in the fluid flow with the SMA arrangement. Figure 5.13 presents the implemented wire bundle in the channel with the colored flow velocity of the HT fluid. Only the significant part of the fluid channel

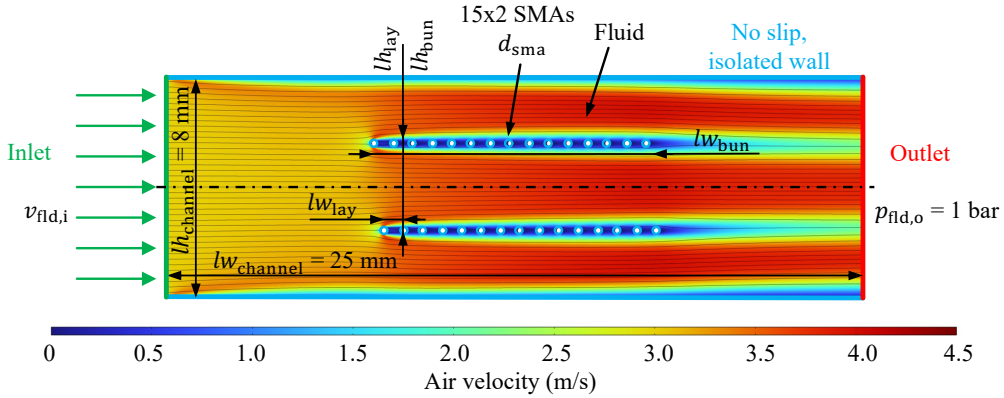

Figure 5.13: Schematic view of the wire bundle in the channel with the colored flow velocity of the HT fluid.

geometry is modeled in the simulation program. Due to the small aspect ratio between diameter and length of the SMA wire, as well as the height and length of the channel, the axial boundary effects along the EC system are negligible, resulting in a homogeneous distribution along the length of 300 mm. Therefore, the cross-section of the channel is designed in two dimensions with a width (lw_{channel}) of 25 mm, corresponding to the actual channel part associated with one bundle. The flow inlet is located on the left side, and the

outlet is on the right side. The top and bottom of the channel and the wire are defined as walls with a no-slip condition, accounting for the boundary layer effect.
For the determination of the fluid flow condition, the Reynolds number is calculated using Equation 5.26 [99].

$$Re = \frac{\rho_{\mathrm{fld}}}{\psi_{\mathrm{fld}}} \cdot v_{\mathrm{rel}} \cdot l_{\mathrm{char}} \tag{5.26}$$

It describes the ratio of inertial force to frictional force. Based on the so-called color thread experiment developed by O. Reynolds in 1883, the flow form can be determined related to the flow characteristics. These includes the density (ρ_{fld}) and dynamic viscosity (ψ_{fld}) of the fluid, as well as the flow-specific values like relative velocity (v_{rel}) and characteristic length (l_{char}) [99]. The fluid specific values are summarized in Table 5.4. The relative velocity (v_{rel}) is calculated using Equation 5.27 with the velocity of the SMA (v_{sma}) and the fluid (v_{fld}).

$$v_{\mathrm{rel}} = v_{\mathrm{sma}} - v_{\mathrm{fld}} = r_{\mathrm{channel}} \cdot \omega - v_{\mathrm{fld}} \tag{5.27}$$

The critical Reynolds number (Re_{crit}) is found at 2300. In practice, this means that a laminar flow is expected when Re is less than 2000. Whereas, for a Re between 2000 and 4000, the laminar flow is unstable. If the Re exceeds 4000, one can assume a turbulent flow. In this case, turbulent flow means that the fluid's movement is not predictable regarding its spatial-temporal structure, leading to irregular transverse movements with a strong flow mixture. Concerning thermodynamics, the turbulent flow favors the HE to the components located in the channel, such as the SMA wires and the channel walls.
The characteristic length (l_{char}) is defined as the streamed length which is given by Equation 5.28.

$$l_{\mathrm{char}} = \frac{\pi}{2} \cdot d_{\mathrm{sma}} \tag{5.28}$$

Due to the small SMA diameter (d_{sma}) of 200 µm the fluid flow in the channel is assumed as almost free of turbulence and thus defined as laminar flow. In this work, airflow velocities of up to 24 m/s are considered, leading to laminar flows only. The pressure on the outlet ($p_{\mathrm{fld,o}}$) is set to 1 bar covering ambient conditions.
In the flow profile, the laminar flow splits into three flow strands through the wire layers, creating a region of lower velocity behind the wires. Therefore, the local distribution of the flow velocity field falls below and exceeds the flow velocity specified in the channel entrance via the channel height, as indicated by the green and blue color.
An extremely fine, physics-controlled mesh is used for calculating the fluid dynamics and temperature fields. The simulation for the temperature prediction consists of two steps:

In the first step, the SMA wires are heated by 1 K, and the temperature evolution along the channel is investigated. In the second step, the wire heating is switched off at time of 0 s to investigate the SMA's temperature decay over time. The simulated time duration is 10 s with increments of 0.05 s.
The energy balance known from Equation 5.2 can be simplified to Equation 3.18 by neglecting the production and absorption term since no PT occurs.
Under the assumption of a uniform distribution of temperature, negligible influence of the clamping, and no generation or absorption of specific latent heat, the temperature evolution in the sample is governed by an exponential decay dependent on the heat exchange coefficient, as known from Equation 3.19. The calculation of the heat exchange coefficient ($h_{\mathrm{sma,fld}}$) is performed in the data evaluation using Equation 5.29 based on an exponential fit of SMA temperature (T_{sma}) over time (t) with the start temperature ($T_{\mathrm{sma,s}}$).

$$T_{\mathrm{sma}}(t) = (T_{\mathrm{sma,s}} - T_{\mathrm{fld}}) \cdot \exp\left(\frac{-4 \cdot h_{\mathrm{sma,fld}}}{\rho_{\mathrm{sma}} \cdot c_{\mathrm{sma}} \cdot d_{\mathrm{sma}}} \cdot t\right) + T_{\mathrm{fld}} \tag{5.29}$$

The resulting values for the heat exchange coefficient between SMA and air for different fluid velocities are presented in Figure 5.14.

Empirical approaches

In literature, various approaches are used to predict the heat exchange coefficient depending on geometry and flow conditions. Figure 5.14 compares different empirical approaches to calculate the heat exchange coefficient for changing relative velocities between SMA element and air.
The heat exchange coefficient of a single wire is experimentally investigated for different airflow velocities as introduced in chapter 4 and [75, 55]. These results are presented as a red line with dots in Figure 5.14. The value of the heat exchange coefficient increases degressive as the airflow velocity increases.
The *VDI Heat Atlas* [185] provides an overview of calculations for various flow geometries, for cross-flow around single tubes and tube arrangements, suitable for HE between SMA and fluid. The prediction for wire bundles, as described in section 5.1, and for single wires yields almost identical values for the geometry of the discussed bundle in Figure 5.13. This is primarily due to the wide spacing between the wires in the bundle arrangement, as well as between the wall and the bundle. In addition, the prediction for a single wire overestimates the value for the heat exchange coefficient in comparison with the values obtained experimentally for different relative velocities between SMA and the fluid.
Churchill et al. [273] provides a calculation for single cylinders in a fluid flow. This prediction for a single wire also overestimates the heat exchange coefficient in comparison

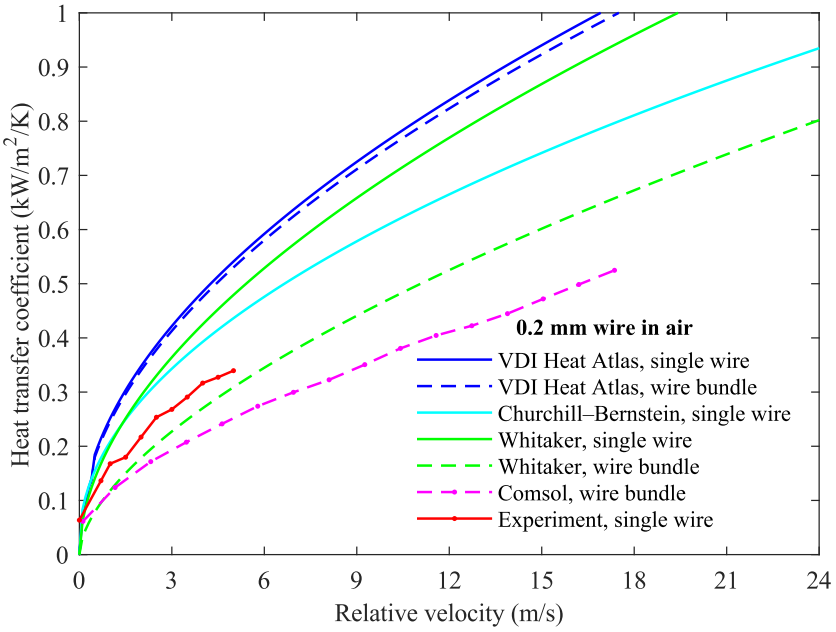

Figure 5.14: Comparison of different approaches for calculating the heat exchange coefficient between SMA and fluid, while using air as fluid.

with the experimental values given for different relative velocities between SMA and fluid, but less than the *VDI Heat Atlas*.

Whitaker et al. [275] provide a calculation method for single tubes and bundles of tubes. The prediction for the single tubes is settled between *VDI Heat Atlas* and *Churcill*. Further, the prediction for the bundle arrangement is lower than the experimental values of the single wire.

The heat exchange coefficient calculated with the approach from Whitaker et al. [275] for bundle arrangements fits to the results obtained by the COMSOL simulation.

In the following, the Whitaker [275] approach is used to calculate heat exchange coefficient between SMA and surrounding fluid due to the reduced values of the bundle compared to the single wire. This reduction aligns with the experimentally observed decrease in thermal energy output for bundles [35]. Additionally, the calculated values correlate with the fluid flow simulation.

Calculation method

The heat exchange coefficient between SMA and fluid is calculated according to the approach of Whitaker [275] for staggered tube bundles, as presented in this section. This empirical estimation can be used in case the length of the element in the fluid channel is much larger than the diameter of the wire, and the bundle consists of more than ten rows in the flow direction.

The heat exchange coefficient (h) is given by Equation 5.30.

$$h = \frac{1}{vf} \cdot \frac{Nu \cdot \kappa_{\mathrm{fld}}}{l_{\mathrm{char}}} \tag{5.30}$$

It contains the thermal conductivity of the fluid (κ_{fld}), the characteristic length (l_{char}) of the SMA bundle, and the Nusselt number (Nu). The wall of the channel does not interact with the bundle because the distance to the SMA wire is much greater than the diameter of the wire. Therefore, only the arrangement of the bundle needs to be considered when calculating the heat exchange coefficient.
The void fraction (vf) describes the influence of the wire arrangement on the flowing fluid, and is calculated using Equation 5.31.

$$vf = \frac{\overbrace{\frac{1}{2} \cdot lh_{\mathrm{lay}} \cdot lw_{\mathrm{lay}}}^{\mathrm{a}} - \overbrace{\frac{1}{2} \cdot \frac{\pi}{4} \cdot {d_{\mathrm{sma}}}^2}^{\mathrm{b}}}{\underbrace{\frac{1}{2} \cdot lh_{\mathrm{lay}} \cdot lw_{\mathrm{lay}}}_{\mathrm{a}}} \tag{5.31}$$

For the calculation of the void volume between the wires in the bundle, the area is segmented into triangle cells: The total volume in one triangle cell is defined by Equation 5.31 (a). The particle volume in one triangle cell is defined by Equation 5.31 (b). The characteristics of the bundle is defined by the diameter of the SMA wire (d_{sma}), the distance between SMA wires in flow direction (lw_{lay}), and the distance between SMA wires tangentially to the flow direction (lh_{lay}), as illustrated in Figure 5.13.
The characteristic length depends on the flow case. To account for the impact of the wires on the flow, the description of characteristic length (l_{char}) known from Equation 5.28, is adjusted to Equation 5.32 with the bundle geometry, and the void fraction (vf).

$$l_{\mathrm{char}} = \frac{3}{2} \cdot \frac{d_{\mathrm{sma}}}{1 - vf} \tag{5.32}$$

The Nusselt number (Nu) provides a description of convective HE between a solid surface and a flowing fluid, and is defined by Equation 5.33 and Equation 5.34 depending on the Reynolds number.

$$Nu\left(Re < 10^2\right) = 2 \cdot Re^{1/3} \cdot Pr^{1/3} \tag{5.33}$$

$$Nu\left(10^2 < Re\right) = \left(0.5 \cdot Re^{1/2} + 0.2 \cdot Re^{2/3}\right) \cdot Pr^{1/3} \tag{5.34}$$

This simplified empirical correlation only depends on the Reynolds number and the Prandtl number, since a temperature-independent dynamic viscosity of the fluid can be assumed due to the small temperature range expected in the EC system.
The Reynolds number characterizes the flow behavior of the setup, and the characteristic length of Equation 5.32 has to be used in Equation 5.26.
In the case of a large void fraction ($vf > 0.65$), the Nusselt number is set to the double value as presented in Equation 5.35.

$$Nu\,(vf > 0.65) = 2 \cdot Nu \tag{5.35}$$

The Prandtl number gives a measure for the ratio of fluid flow and temperature boundary layer thickness. It can be calculated using Equation 5.36 with the specific heat capacity (c_{fld}), the dynamic viscosity (ψ_{fld}), and the thermal conductivity (κ_{fld}) of the fluid.

$$Pr = \frac{c_{\mathrm{fld}} \cdot \psi_{\mathrm{fld}}}{\kappa_{\mathrm{fld}}} \tag{5.36}$$

With these formulas, the heat exchange coefficient can be estimated.

5.2.5 Viscous losses

The thermo-mechanical behavior of the EC HP is influenced not only by the cross-flow and the heat exchange coefficient but also by flow losses due to the channel itself and the SMAs obstructing the flow.
The pressure difference of the fluid in the duct ($\Delta p_{\mathrm{fld,duct}}$) without interaction of the SMA arrangement can be calculated using Equation 5.37 from the *VDI Heat Atlas* [185]. The SMA arrangement in the channel is ignored in the calculation of the pressure difference due to the large void fraction (vf) of the bundle calculated in Equation 5.30.

$$\Delta p_{\mathrm{fld,duct}} = \zeta_{\mathrm{fld,duct}} \cdot \frac{l_{\mathrm{duct}}}{d_{\mathrm{hyd,duct}}} \cdot \frac{{v_{\mathrm{fld,duct}}}^2}{2} \tag{5.37}$$

The length of the duct (l_{duct}), defined between the inlet and outlet, and the corresponding fluid velocity ($v_{\mathrm{fld,duct}}$) are used for this calculation. The resistance coefficient of the fluid ($\zeta_{\mathrm{fld,duct}}$) and the hydraulic diameter ($d_{\mathrm{hyd,duct}}$) specifies in more detail the properties of the duct for fluid flows with non-circular cross-sections.
For any cross-section, the hydraulic diameter ($d_{\mathrm{hyd,duct}}$) can be calculated using Equation 5.38 with the area (A_{duct}) and the circumference (U_{duct}) of the duct.

$$d_{\mathrm{hyd,duct}} = 4 \cdot \frac{A_{\mathrm{duct}}}{U_{\mathrm{duct}}} \tag{5.38}$$

The resistance coefficient of the fluid ($\zeta_{\mathrm{fld,duct}}$) is calculated using Equation 5.39 with the aspect ratio coefficient (ab) from 0.89 to 1.5. This value is obtained from a lookup table using the width-to-height ratio of the duct from 0 to 1.

$$\zeta_{\mathrm{fld,duct}}\left(Re \leq Re_{\mathrm{crit}}\right) = ab \cdot \frac{64}{Re} \tag{5.39}$$

The Reynolds number (Re) can be calculated using Equation 5.26 and replacing the characteristic length (l_{char}) with the hydraulic diameter ($d_{\mathrm{hyd,duct}}$). The critical Reynolds number (Re_{crit}) is chosen to 2320. Beyond this value, the resistance coefficient of the fluid ($\zeta_{\mathrm{fld,duct}}$) can be obtained from the *Moody-Diagram* [278] for hydraulically smooth surfaces.
The power of the viscous losses ($P_{\mathrm{vis,fld,duct}}$) consumed by the fluid in the duct can be calculated using Equation 5.40 with fluid velocity ($v_{\mathrm{fld,duct}}$) and the cross-sectional area (A_{duct}) of the duct.

$$P_{\mathrm{vis,fld,duct}} = \dot{V}_{\mathrm{fld,duct}} \cdot \Delta p_{\mathrm{fld,duct}} = v_{\mathrm{fld,duct}} \cdot A_{\mathrm{duct}} \cdot \Delta p_{\mathrm{fld,duct}} \tag{5.40}$$

The resulting pressure difference of the fluid for the hot and cold duct is presented in Figure 5.15 as a black curve. It is calculated for different flow rates using the channel configuration introduced in section 5.1. Additionally, to the pressure needed for the fluid

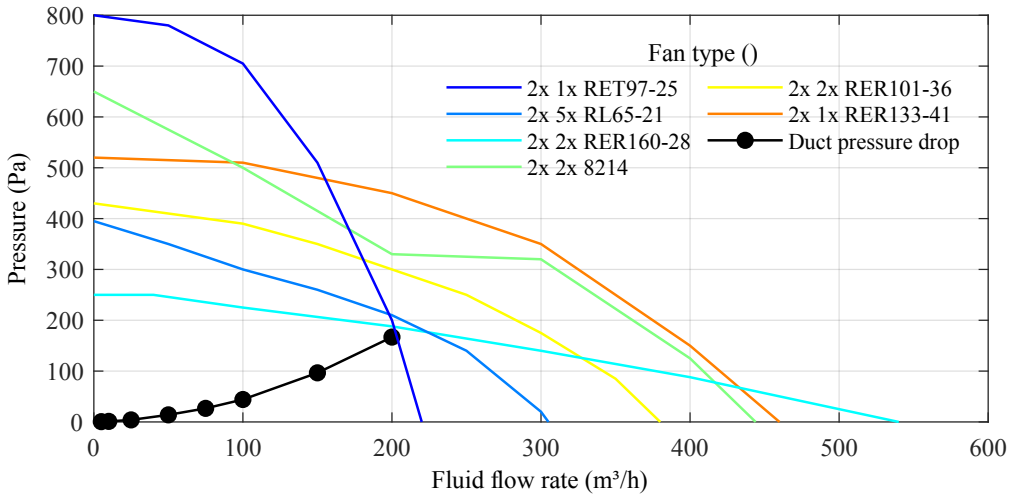

Figure 5.15: Viscous losses: Resulting pressure drop of the fluid in the duct (black), and fan characteristics of different fan types (color) for different flow rates.

flow with a certain flow rate, the fan characteristics of different fan types for various flow rates are presented in color. The fan type name is enlarged by the number of ducts and the quantity per duct. These characteristics, as outlined in the datasheet, demonstrate the dependence of maximum pressure on the flow rate produced by the specific number of fans, which also corresponds to the maximum electrical power consumption. To evaluate

the electrical power consumption of each fan group for a specific flow rate, the intersection point between pressure difference of the fluid in the duct and the fan pressure characteristic is determined, by scaling the maximum curve for each fan type. The square of the scaling factor times the nominal power is the actual electrical power. The resulting electrical power consumption of the fan group for different flow rates is presented in Figure 5.16. The colors for the different fan types in Figure 5.16 correspond to those in Figure 5.15.

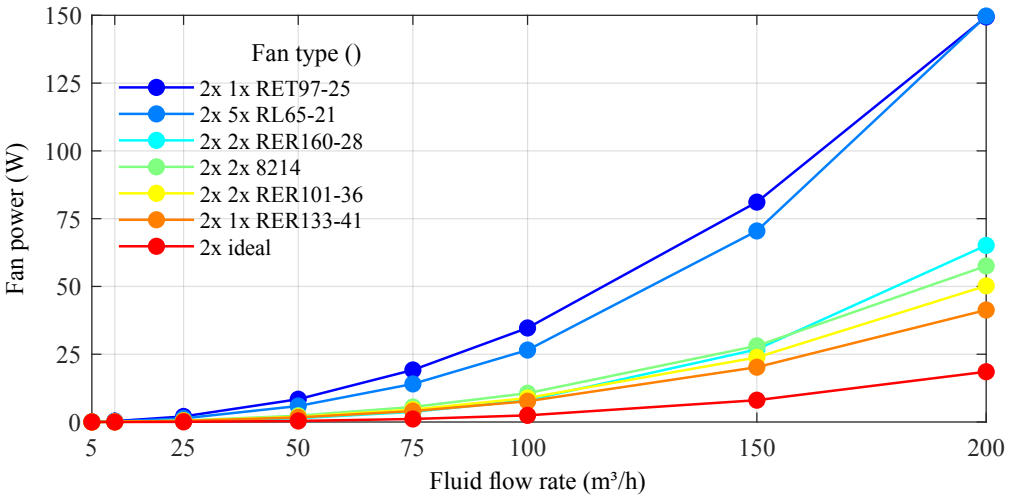

Figure 5.16: Viscous losses: Resulting electrical power consumption of the fans in color for different flow rates.

The curve labeled *ideal* represents a fan with an efficiency of 100 %, thus representing viscous power.

The field of fluid mechanics provides a detailed description of how fluids flow within a channel. For instance, liquids with similar density, average atomic or molecular distance, compressibility, and thermal expansion values may exhibit different viscous behaviors. Under normal conditions, gases have a density approximately 1000 times smaller than that of liquids. However, the same principles of motion can be applied to both gases and liquids as long as the pressures are not excessively high and the speed remains below the speed of sound.

This work focuses on predicting the behavior of an air-based EC HP. Therefore, the viscous losses are discussed in producing a fluid flow using fans without restricting generality.

5.3 Implementation

In order to model the system structure of the EC HP, known from Figure 5.4, the code of the simulation tool should be based on object-oriented and structured programming. The object-oriented approach involves storing data as fields with attributes and properties and writing code as procedures and methods. The aim is to organize the simulation tool

into separate modules, each with a specific and understandable purpose. The interaction between defined modules should minimize computational effort. The structured-based programming allows for more straightforward procedures in some cases, such as when exception handling must be performed.
To create a versatile simulation tool, the modules should be self-contained. This allows for the exchangeability of single modules, as well as simplified calibration and validation of each module. The code in this module should combine imperative and functional programming, allowing for multiple simultaneous parameter studies on a multi-core system.
Due to the numerous adjustable design and operating parameters of the EC HP presented in section 5.1, there is a large number of possible parameter sweeps. It is essential to have a simulation tool that can handle complex design relationships and allows for fast computation. Additionally, it is also essential to develop a control tool that supports systematic study and massively parallel computation of different parameter sets. The ability to quickly and comprehensively scan all system parameters within a specified range requires a data visualization tool (subsection 5.3.4) that manages the clear and comprehensive representation of the results from the parameter studies.
MATLAB is a proprietary multi-paradigm programming language and numeric computing environment. It supports the programming of the module-based structure of the simulation tool while allowing matrix manipulations and algorithm implementation. The ability to interface with programs written in other languages enables the implementation of a control tool. Additionally, the possibility of plotting functions and data, as well as creating user interfaces, enables the implementation and user-friendly use of the data visualization tool.
As introduced before, the SMA material model and the approximation of the fluidics comprise PDEs. In literature, different approaches for solving these PDEs are known. The finite difference (FD) method is the oldest technique, based on applying a spatial local Taylor series expansion to approximate the PDE. It utilizes a topologically square network of lines to construct the discretization of the PDE. When dealing with complex geometries in multiple dimensions, using the FE becomes necessary. However, it is associated with increased implementation and computational effort.
The approximation of the SMA arrangement, in combination with the fluidics discussed in section 5.2, exhibits one-dimensional physical problems. Therefore, with regard to the application scope and the efficient use of computation time, FD are used. This approach also facilitates increasing the order of accuracy. Furthermore, the FD method can also be used for two-dimensional physical problems.
The following presents the calculation procedure and the implementation of the SMA model and kinematics, as well as the fluidics, as specified in section 5.2.
The next step is to take a system of field equations, represented by PDEs, that describe the physics of the EC HP and formulate these equations for each sub-system.

5.3.1 Calculation procedure

A dynamic system is simulated by calculating its states at successive time steps over a specified time span, using information provided by the model. The process of calculating the successive states of a system from its model is known as solving the model. The solver is provided with a function that is called at every time step. This function is known as derivative function (DF). This DF receives the current point in time and the solution of the previous step as inputs. The solution consists of a state vector ($\boldsymbol{Y}$) where all dependent variables of the system are included. The solver obtains the temporal derivatives of all entities of the state vector from the DF. Small enough time steps are taken to ensure that the error is negligible when considering the derivative of the previous time step. The solver performs test steps between the normal step sizes to determine if the temporal derivative changes significantly. Based on this, the solver decides if smaller steps are necessary. At each step, the solver applies a particular algorithm to the results of previous steps using the results of the DF. These algorithms compensate for the error due to the temporal derivative of the previous time step by applying internal mathematical methods such as *Euler* and *Runge-Kutta*, depending on the chosen solver type.
At the first step, the initial condition provides the necessary information needed to start the integration. The solver receives an initial state vector from an external source containing all initial values for each entry. There is a separate function, known as initial state function (ISF), that determines the initial states. Finally, the solver returns a vector of time points, as well as the corresponding solution of the state vector for each step.
The DF contains the calculation procedure for each system variable to specify the physical characteristics of the aimed simulation model. This is also known as ordinary differential equation (ODE) system. An ODE contains one or more derivatives of a dependent variable with respect to a single independent variable, usually time. The order of the ODE is equal to the highest-order derivative of the dependent variables that appear in the equation. In cases where higher orders than the first occur, these derivatives have to be substituted by an additional entry of the state vector so that a system of first-order ODEs is reached.
The ODE can be classified as explicit or implicit. An explicit ODE describes a direct relationship between the dependent variables and their derivatives using a function. In contrast, an implicit ODE describes a relationship between the mathematical function of the dependent variable and its derivatives, where the dependence cannot be easily resolved to the highest order of derivative. In the case that some of the derivatives of the dependent variables are not directly available, the equation is called differential algebraic equation (DAE).

The state vector for the simulation model of the EC system is provided in Equation 5.41 along with its temporal derivative.

$$\boldsymbol{Y} = \begin{pmatrix} \varphi \\ \dot{\varphi} \\ \boldsymbol{\xi} \\ \boldsymbol{T}_{\mathrm{sma}} \\ \boldsymbol{T}_{\mathrm{fld}} \end{pmatrix} = \begin{pmatrix} \varphi \\ \dot{\varphi} \\ \xi_1 \\ \vdots \\ \xi_{N_{\mathrm{bun}}} \\ T_{\mathrm{sma},1} \\ \vdots \\ T_{\mathrm{sma},N_{\mathrm{bun}}} \\ T_{\mathrm{fld},1} \\ \vdots \\ T_{\mathrm{fld},N_{\mathrm{fld}}} \end{pmatrix} \tag{5.41}$$

$$\dot{\boldsymbol{Y}} = \begin{pmatrix} \dot{\varphi} \\ \ddot{\varphi} \\ \dot{\boldsymbol{\xi}} \\ \dot{\boldsymbol{T}}_{\mathrm{sma}} \\ \dot{\boldsymbol{T}}_{\mathrm{fld}} \end{pmatrix} = \begin{pmatrix} \dot{\varphi} \\ \ddot{\varphi} \\ \dot{\xi}_1 \\ \vdots \\ \dot{\xi}_{N_{\mathrm{bun}}} \\ \dot{T}_{\mathrm{sma},1} \\ \vdots \\ \dot{T}_{\mathrm{sma},N_{\mathrm{bun}}} \\ \dot{T}_{\mathrm{fld},1} \\ \vdots \\ \dot{T}_{\mathrm{fld},N_{\mathrm{fld}}} \end{pmatrix} \tag{5.42}$$

It comprises the rotation angle (φ), the angular velocity $(\dot{\varphi})$ the phase fraction $(\xi_{+,j})$, and the temperature $(T_{\mathrm{sma},j})$ of each SMA element $(_j)$ from 1 to N_{bun}. It also includes the temperature $(T_{\mathrm{fld},k})$ for each fluid element $(_k)$ from 1 to N_{fld}.
For simulations with a constant rotation frequency, the first derivative of the rotation angle $(\dot{\varphi})$ is constant, and set to $2\pi f$. In this case, the second derivative of the rotation angle $(\ddot{\varphi})$ is zero.
In the following, the ODE and the further dependencies of the implementation for SMA model, kinematics, and fluidics will be described.

5.3.2 Shape memory alloy model and kinematics

The thermo-mechanical behavior of the SMA described by two coupled ODEs: the phase fraction $(\xi_{+,k})$, introduced in Equation 2.11, and the SMA temperature $(T_{\mathrm{sma},j})$, introduced in Equation 5.2. Both equations can be rearranged to separate the temporal derivative of the dependent variable of interest, leading to explicit ODE.
The coupling of the SMA model and kinematics realizes the constitutive relation, introduced in Equation 5.1. The SMA model, as introduced in section 2.2 and subsection 3.2.4, is implemented in the DF.
The rotational movement of each SMA element, based on the rotation frequency (ω), induces a change of the rotation angle (φ) in every time step. The direction of rotation is determined by the sign of the rotation frequency. A positive rotation frequency causes the SMA elements to move clockwise, while a negative frequency causes them to move counterclockwise.

The load profile requires an update of the strain (ε_j) for each element in every time step. This is performed in a subfunction of the DF that uses the rotation angle (φ) of each solution. The combination of the rotational movement of each SMA element and the fixed finite fluid elements requires the allocation of the temperature of the corresponding fluid ($T_{\mathrm{fld},k}$) to each SMA element in each time step. This is done by a subfunction of the DF that uses the rotation angle (φ) of each solution.
The resulting torque into the EC system, introduced in Equation 5.10, is also calculated using a subfunction of the DF in every time step.
The used SMA geometry and size, as well as the thermo-mechanical setup, allow for the use of one set of entries for each SMA element in the state vector in the initial version of the simulation tool, as introduced in section 5.2. However, this can be easily upgraded to consider more entries per SMA element.

5.3.3 Fluidics

The temperature of the fluid ($T_{\mathrm{fld},k}$) described by one PDE in Equation 5.16, and can be discretized by FD for each fluid element into one coupled ODE per index of fluid element ($_k$). The number of fluid elements in the EC system reaches from 1 to N_{fld}. The material-specific parameters of the fluid, density (ρ_{fld}), specific heat capacity (c_{fld}), and thermal conductivity (κ_{fld}) can be assumed as time and space independent in the scope of this work. The solver calculation procedure in MATLAB discretizes the temporal derivative of the temperature for each element of the fluid ($\frac{\partial}{\partial t}(T_{\mathrm{fld},k})$), as previously introduced.
The spatiotemporal transport equation of the thermal energy in the fluid, introduced in Equation 5.16, includes, in addition to the temporal derivative, two Spatial terms (b and c). In literature, different methods are presented for discretizing and implementing the transport equation, each with its own advantages and drawbacks [274, 228, 207, 178, 101]. The thermal energy transfer to neighboring elements based on the thermal conductivity of the fluid (κ_{fld}) is introduced in Equation 5.16 (b), and the mass transport out of the stationary considered fluid element based on the velocity of the fluid (v_{fld}) is introduced

in Equation 5.16 (c). In Equation 5.43, the discretized transport equation of the fluid is displayed.

$$\begin{pmatrix} \dot{T}_1 \\ \vdots \\ \dot{T}_k \\ \vdots \\ \dot{T}_{N_{\text{fld}}} \end{pmatrix} = \underbrace{\begin{pmatrix} a_{1,1} & & & & & & 0 & \\ & & & \ddots & & & & \\ \dots & 0 & a_{k,k-2} & a_{k,k-1} & a_{k,k} & a_{k,k+1} & 0 & \dots \\ & & & & & \ddots & & \\ 0 & & & & & & & a_{N_{\text{fld}},N_{\text{fld}}} \end{pmatrix}}_{A} \begin{pmatrix} T_1 \\ \vdots \\ T_k \\ \vdots \\ T_{N_{\text{fld}}} \end{pmatrix}$$

$$+ \underbrace{\begin{pmatrix} d_{1,1} & \dots & d_{1,N_{\text{duct}}} \\ \vdots & d_{k,n} & \vdots \\ d_{N_{\text{fld}},1} & \dots & d_{N_{\text{fld}},N_{\text{duct}}} \end{pmatrix}}_{D} \begin{pmatrix} T_{D,1} \\ \vdots \\ T_{D,n} \\ \vdots \\ T_{D,N_{\text{duct}}} \end{pmatrix} + \frac{1}{\rho_{\text{fld}} \cdot c_{\text{fld}} \cdot V_{\Delta x}} \cdot (P_{\text{sma}} + P_{\text{wall}}) \quad (5.43)$$

The spatial derivatives of Equation 5.16 are summarized in the diagonal matrix (A) in Equation 5.43, populated on the principal and secondary diagonals. Table 5.1 presents the entries of the fluid transport diagonal matrix (A) for different discretization schemes. These methods fragment the fluid channel into a uniform grid with a spacing of Δl, as introduced in Figure 5.9 (b).

Typ	$\mathbf{a_{k,k-2}}$	$\mathbf{a_{k,k-1}}$	$\mathbf{a_{k,k}}$	$\mathbf{a_{k,k+1}}$	$\mathbf{a_{k,k+2}}$
S1	0	$\frac{1}{2} \cdot \frac{v_{\text{fld}}}{\Delta x} + \frac{\tilde{\kappa}}{\Delta x^2}$	$-2 \cdot \frac{\tilde{\kappa}}{\Delta x^2}$	$-\frac{1}{2} \cdot \frac{v_{\text{fld}}}{\Delta x} + \frac{\tilde{\kappa}}{\Delta x^2}$	0
U1	0	$\frac{1}{1} \cdot \frac{v_{\text{fld}}}{\Delta x} + \frac{\tilde{\kappa}}{\Delta x^2}$	$-\frac{1}{1} \cdot \frac{v_{\text{fld}}}{\Delta x} - 2 \cdot \frac{\tilde{\kappa}}{\Delta x^2}$	$\frac{\tilde{\kappa}}{\Delta x^2}$	0
U2	$-\frac{1}{2} \cdot \frac{v_{\text{fld}}}{\Delta x}$	$\frac{4}{2} \cdot \frac{v_{\text{fld}}}{\Delta x} + \frac{\tilde{\kappa}}{\Delta x^2}$	$-\frac{3}{2} \cdot \frac{v_{\text{fld}}}{\Delta x} - 2 \cdot \frac{\tilde{\kappa}}{\Delta x^2}$	$\frac{\tilde{\kappa}}{\Delta x^2}$	0
U3	$-\frac{1}{6} \cdot \frac{v_{\text{fld}}}{\Delta x}$	$\frac{6}{6} \cdot \frac{v_{\text{fld}}}{\Delta x} + \frac{\tilde{\kappa}}{\Delta x^2}$	$-\frac{3}{6} \cdot \frac{v_{\text{fld}}}{\Delta x} - 2 \cdot \frac{\tilde{\kappa}}{\Delta x^2}$	$-\frac{2}{6} \cdot \frac{v_{\text{fld}}}{\Delta x} + \frac{\tilde{\kappa}}{\Delta x^2}$	0
Q	$-\frac{1}{8} \cdot \frac{v_{\text{fld}}}{\Delta x}$	$\frac{7}{8} \cdot \frac{v_{\text{fld}}}{\Delta x} + \frac{\tilde{\kappa}}{\Delta x^2}$	$-\frac{3}{8} \cdot \frac{v_{\text{fld}}}{\Delta x} - 2 \cdot \frac{\tilde{\kappa}}{\Delta x^2}$	$-\frac{3}{8} \cdot \frac{v_{\text{fld}}}{\Delta x} + \frac{\tilde{\kappa}}{\Delta x^2}$	0
with $\tilde{\kappa} = \kappa_{\text{fld}} / \rho_{\text{fld}} \cdot c_{\text{fld}}$					

Table 5.1: Entries of fluid transport diagonal matrix (A) for different discretization schemes.

The first row (S1) of Table 5.1 displays the entries for the Central Difference (S) scheme, which has a first-order spatial accuracy. This accuracy is achieved by using a Taylor series expansion and involving derivatives of the second order while neglecting higher-order terms. In this scheme, each derivative is replaced by a different quotient in its classic formulation. It offers a direct approach to the numerical solution of the PDE. The drawbacks of the FD

methods are lower accuracy and reduced flexibility. However, only the directly neighboring elements are needed for the calculation.
The discretization schemes discussed below discretize the channel by considering the flow direction in each duct. Each duct is characterized by the rotation angle of its input ($\varphi_{\mathrm{hi}} = \varphi_{1,\mathrm{i}}, \varphi_{\mathrm{ci}} = \varphi_{2,\mathrm{i}}$) and output$\varphi$ ($\varphi_{\mathrm{ho}} = \varphi_{1,\mathrm{o}}, \varphi_{\mathrm{co}} = \varphi_{2,\mathrm{o}}$). The index of duct ($_n$) specifies the individual ducts up to the maximum number (N_{duct}). In each duct, the fluid velocity (v_{fld}) is assumend as constant.
In rows two to four (U1, U2, U3) of Table 5.1, the entries for the Upwind scheme (U) with order one to three are presented. The U basically mimics the essential physics of advection in the current fluid element, depending on the flow direction. In the case of the first-order spatial accuracy, as shown in row two (U1), the estimation for the current element only considers the state of the fluid in the first previous element.
The third row (U2) shows the entries for U with the second-order spatial accuracy. U2 considers two previous elements and one following element, concerning the direction of the fluid flow. The velocity of the fluid (v_{fld}) is asymmetrically considered with the weight on the previous fluid elements.
The entries for U with third-order spatial accuracy are shown in the fourth row (U3). Compared to U2, U3 does not consider more elements. However, it also takes into account the direction of the fluid flow in the following element. Therefore, the weight of the fluid velocity is more shifted to the first previous element.
The fifth row (Q) displays the entries for the QUICK scheme (Q) [272] with the third-order spatial accuracy, equal to U3. This *Quadratic Upstream Interpolation for Convective Kinematics* scheme involves interpolating the dependent variable's value at each edge of the element using a quadratic polynomial, biased toward the upstream direction. The value obtained from interpolation is used to calculate the convective term in the governing equations for the dependent variable. Q is regarded as the most suitable discretization method for steady or quasi-steady highly convective elliptic flow. The three-point upstream weighted quadratic interpolation results in almost the same weighting of the fluid velocity as U3. Q uses two previous elements and one following element, similar to U2 and U3.
Figure 5.17 presents the unrolled fluid channel and the boundary conditions at the inlets and outlets of the duct. At the inlets of the hot and cold duct, the temperature of the fluid (T_{hi}, T_{ci}) is known. Therefore, a Dirichlet boundary condition (DC) is used to prescribe the fluid temperature at the entry element of each duct to a specific value ($T(\varphi_{\mathrm{hi}},t) = T_{\mathrm{hi}}(t)$, $T(\varphi_{\mathrm{ci}},t) = T_{\mathrm{ci}}(t)$). The DCs are also used for the transition zones between the hot and cold side.
Table 5.2 presents the modified entries for the system matrix (A) and the Dirichlet matrix (D) of Equation 5.43 to prescribe temperature ($T_{D,k}$) for each fluid element ($_k$).

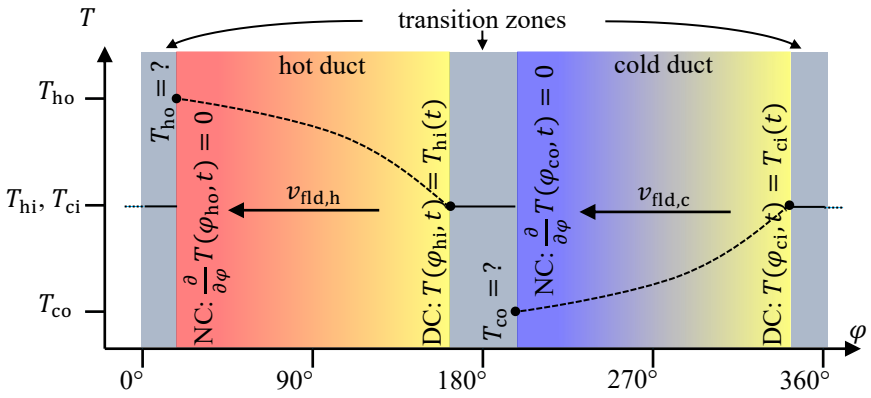

Figure 5.17: Temperature (T) - rotation angle (φ) diagram of the unrolled fluid channel and the boundary conditions at the inlets and outlets of the duct.

Typ	$\mathbf{a_{k,k-2}}$	$\mathbf{a_{k,k-1}}$	$\mathbf{a_{k+1,k-1}}$	$\mathbf{d_{k,n}}$	$\mathbf{d_{k+1,n}}$
S1	n.m.	0	n.m.	$\frac{1}{2}\cdot\frac{v_{fld}}{\Delta x}+\frac{\tilde{\kappa}}{\Delta x^2}$	0
U1	n.m.	0	n.m.	$\frac{1}{1}\cdot\frac{v_{fld}}{\Delta x}+\frac{\tilde{\kappa}}{\Delta x^2}$	0
U2	0	0	0	$\frac{3}{2}\cdot\frac{v_{fld}}{\Delta x}+\frac{\tilde{\kappa}}{\Delta x^2}$	$-\frac{1}{2}\cdot\frac{v_{fld}}{\Delta x}$
U3	0	0	0	$\frac{5}{6}\cdot\frac{v_{fld}}{\Delta x}+\frac{\tilde{\kappa}}{\Delta x^2}$	$-\frac{1}{6}\cdot\frac{v_{fld}}{\Delta x}$
Q	0	0	0	$\frac{6}{8}\cdot\frac{v_{fld}}{\Delta x}+\frac{\tilde{\kappa}}{\Delta x^2}$	$-\frac{1}{8}\cdot\frac{v_{fld}}{\Delta x}$
with $\tilde{\kappa} = \kappa_{fld}/\rho_{fld}\cdot c_{fld}$					

Table 5.2: Modified entries of system matrix A and Dirichlet matrix D for DC at fluid duct inlets.

The entries with *n.m.* in the first and second row of the Table 5.2 do not need to be modified because the initial entries (Table 5.1) were set to zero beforehand by the scheme.
At the outlets of the hot and cold duct, the spatial derivative of the fluid temperature is known as zero. Therefore, a Neumann boundary condition (NC) is used to describe the profile assumption at the exit point of each duct. The NCs are used at the outlets to ensure a vanishing temperature gradient ($\frac{\partial}{\partial\varphi}T(\varphi_{ho},t) = 0$, $\frac{\partial}{\partial\varphi}T(\varphi_{co},t) = 0$). This is caused by the last fluid element of each duct, unaffected by any HE.
The modified entries of system matrix Equation 5.43 (A) for NC at the fluid duct outlet element ($_k$) are summarized in Table 5.3.
The bundle width can be specified in degrees as an input parameter. In the pre-process, the simulation tool calculates the number of individual fluid elements affected by an SMA element. During the calculation, the thermal power of the SMA (P_{sma}), as defined in Equation 5.43, is distributed to the specified number of fluid elements. If the SMA element or a part of it is present in the corresponding fluid element, the fluid element's temperature change is calculated by considering the proportioned HE power, as introduced in Equation 5.16 (d). This term is omitted in fluid elements with no SMA interaction.

Typ	$\mathbf{a_{k,k-1}}$	$\mathbf{a_{k,k+1}}$
S1	$2 \cdot \frac{\tilde{\kappa}}{\Delta x^2}$	0
U1	$\frac{1}{1} \cdot \frac{v_{\mathrm{fld}}}{\Delta x} + 2 \cdot \frac{\tilde{\kappa}}{\Delta x^2}$	0
U2	$\frac{4}{2} \cdot \frac{v_{\mathrm{fld}}}{\Delta x} + 2 \cdot \frac{\tilde{\kappa}}{\Delta x^2}$	0
U3	$\frac{4}{6} \cdot \frac{v_{\mathrm{fld}}}{\Delta x} + 2 \cdot \frac{\tilde{\kappa}}{\Delta x^2}$	0
Q	$\frac{4}{8} \cdot \frac{v_{\mathrm{fld}}}{\Delta x} + 2 \cdot \frac{\tilde{\kappa}}{\Delta x^2}$	0
with $\tilde{\kappa} = \kappa_{\mathrm{fld}} / \rho_{\mathrm{fld}} \cdot c_{\mathrm{fld}}$		

Table 5.3: Modified entries of system matrix (A) for NC at fluid duct outlet.

This decision is made by correlating the angular potition (φ_k) of each fluid element with the rotation angle (φ_j) of each SMA element.
The interaction of fluid element and SMA elements is constantly changing because the fluid elements are stationary while the arrangement of the SMAs rotates. As a result, the coupling between fluid element and SMA arrangement needs to be updated in each time step during computation, even though the spatial discretization of each fluid duct remains fixed.

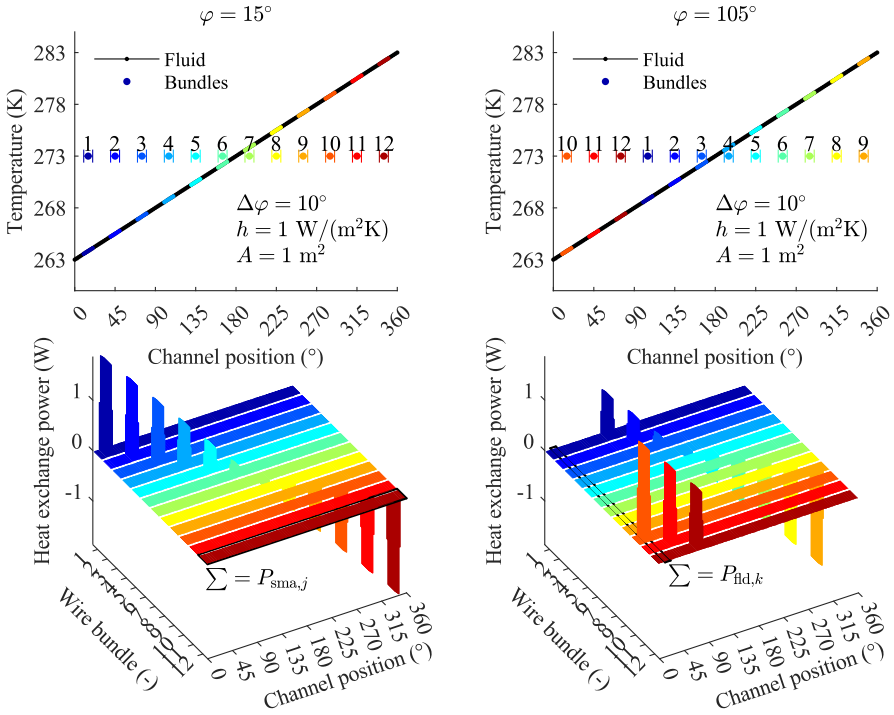

Figure 5.18: Visualisation of HE matrix for different rotation angles.

Figure 5.18 presents the HE matrix for different rotation angles. The SMA element and fluid element numbers are firmly connected to the individual element. The SMA arrangement rotates while the fluid element is stationary, and fluid flows through it at a

specified flow velocity. For illustrative purposes, this setup is shown with a rotation angle of 15° on the left side and 105° on the right side of Figure 5.18.
In the top row, the temperatures of the SMA and the corresponding fluid element are shown via the channel position. In the bottom row, a three-dimensional plot with the HE power is displayed. The HE power is highest when the temperature difference between SMA and fluid element is largest. The total HE power of each SMA element is calculated by adding the rows of the HE matrix, as shown in the black frame at the bottom left. The total HE power of each fluid element is calculated by summing over the columns of the HE matrix, as shown in the black frame at the bottom right.
For the visualization of the HE, a constant SMA temperature of 273 K is chosen. The heat exchange coefficient betweeen the SMA and the fluid ($h_{\mathrm{sma,fld}}$) is chosen to be $1\,\mathrm{W/(m^2{\cdot}K)}$. The area ($A_{\mathrm{sma,surf}}$) of the SMA is choosen as $1\,\mathrm{m}^2$. The HE power through the wall (P_{wall}), as defined in Equation 5.43, is calculated using Equation 5.16 (e) for each fluid element. In the current case, the HE power through the wall (P_{wall}) is chosen to zero.
MATLAB provides excellent capabilities for handling vectors and matrices, which are nearly independent of physical complexity and space dimension [228]. Therefore, the presented discretization can be easily extended by adding additional entries into the matrix A of Equation 5.43. The versatile implementation enables the easy extension of the EC HP with additional fluid ducts by splitting the channel. This can be used for investigating the cross-flow between the hot and cold fluid duct, as presented in Figure 5.11. Additionally, the number of ducts has to be increased by using the concept of internal heat recovery, as presented in Figure 5.12. In this concept, it is also needed to handle the fluid flows of multiple ducts and to interconnect the flows between ducts. These adjustments and their parameters can be easily managed in the parameter set table when defining the angular position of the inlets and outlets of each duct, its fluid flow rate, and the individual inlet temperatures as constant value or depending parameter.
The simulation model will provide a MATLAB file with the input parameters, the results, and the output parameters obtained by post-processing the solver results for each time step.

5.3.4 Visualization tool

The visualization tool uses MATLAB to visualize a single parameter set. In this visualization, the input parameters and the output parameters will be presented based on the results for each time step. MATLAB facilitates the implementation and user-friendly utilization of the data visualization tool by providing the capability to plot functions and data, as well as to create user interfaces.
Figure 5.19 shows an overview of the visualization tool implemented in MATLAB. It is necessary to gain a better understanding of the heating and cooling process in the EC

system, as well as the interaction of the SMA element with the surrounding fluid. On the left side of the tool, an animated cross-section of the EC HP displays the distribution of temperature in color for each SMA element and each fluid element. This view is extended by the inlet and outlet temperature, as well as flow rate of each duct. In the center, specific values for the number of bundles, wires per bundle, and total mass of the SMA in the simulated EC system are shown. Additionally, the presentation includes the rotation direction of the SMA arrangement, the load profile, and the flow direction of the fluid in each duct.

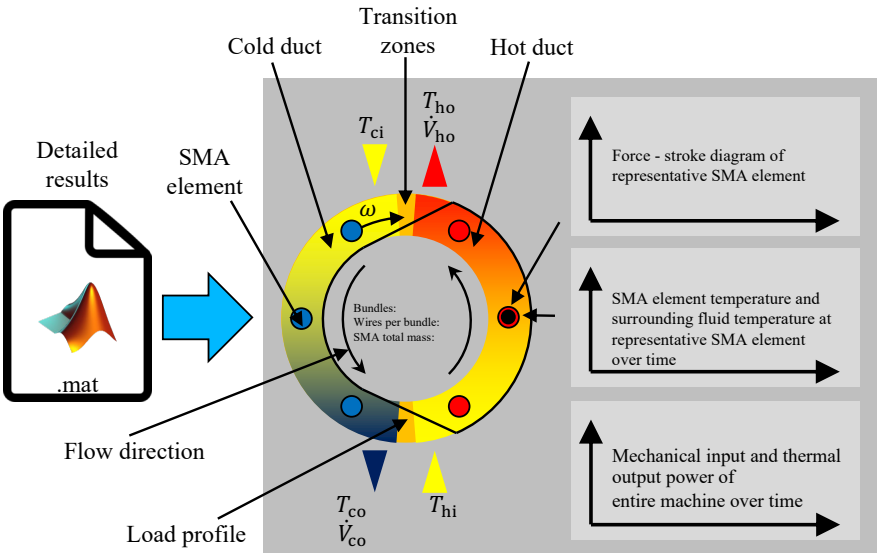

Figure 5.19: Visualization tool of the EC HP simulation tool.

On the right side, the upper diagram presents the force-stroke relationship of the representative SMA element, highlighted with a black dot in the cross-sectional view. The middle diagram shows the temperature of the SMA material in red and the temperature of the corresponding surrounding fluid element in blue over simulation time. The lower diagram depicts the mechanical power in green, as well as the thermal power of the hot and cold duct in red and blue over simulation time.
A slider enables interactive use of the visualization tool, allowing the user to select each time step of the simulation by scrolling. Changing the time step will update the temperature profile in the cross-sectional view and highlight the selected point in time with a circle in the plots.

5.3.5 Parallel computation tool

The time-efficient study of the EC system's wide range of input parameters demands parallel computation of multiple simulations. The current personal computers' multicore architecture, with more than 20 physical cores included in one CPU, enables simulating numerous parameter sets simultaneously. MATLAB allows for the implementation of the

parallel computation tool by interfacing with programs written in other programming languages. Figure 5.20 shows the process of parallel computation in the EC system simulation tool. The parameters for the simulations are listed in an Excel-table. The

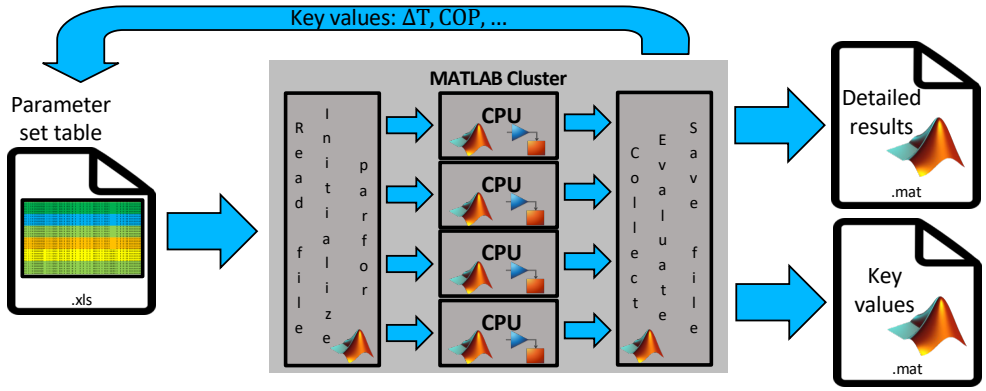

Figure 5.20: Parallel computation tool of the EC HP simulation tool.

parallel computation tool imports the parameter sets and initializes a simulation model for each set, depending on the computer's specific core number. This is done using the MATLAB's *parfor* function. At the completion of each simulation, the results are collected. Meaningful output parameters, also known as key values, are evaluated for each simulation and saved in the dedicated position in the table. Additionally, the key values are saved for each parameter set group as MATLAB file.

The large number of possible simulations per time requires careful consideration of the amount of data. Therefore, the size of the time step (t_{step}) of the solver is chosen to 0.001 s as a trade-off between the amount of data for each simulation and the ability to visualize the results. The simulation duration (t_{end}) is chosen to achieve a steady state operational behavior of the EC HP and reduce the amount of data. Due to the changing rotation frequency and flow velocities over all performed simulations, the simulation duration is adapted automatically by using an error function to detect the stationary operation behavior for the individual simulation.

The error function compares the most recent completed revolution with the previously completed revolution. In this function, both matrices of state vector ($\boldsymbol{Y}$) for all time steps during each revolution are compared using the method of squared distances. This compares values of the same rotation angle concerning a constant rotation frequency of the EC HP. To assume a stationary operational behavior, the sum of all squared distances must be smaller than the limit value defined in the parameter set table.

5.3.6 Parameter comparison tool

The presented simulation tool supports the calculation and presentation of various parameter sets, utilizing sub-tools such as the visualization tool and the parallel computation

tool. To enable the evaluation of different parameter sets, a parameter comparison tool is needed to present the key values of a parameter group in an overview as presented in Figure 5.21. Initially, the interactive tool displays a list of all key values that change in

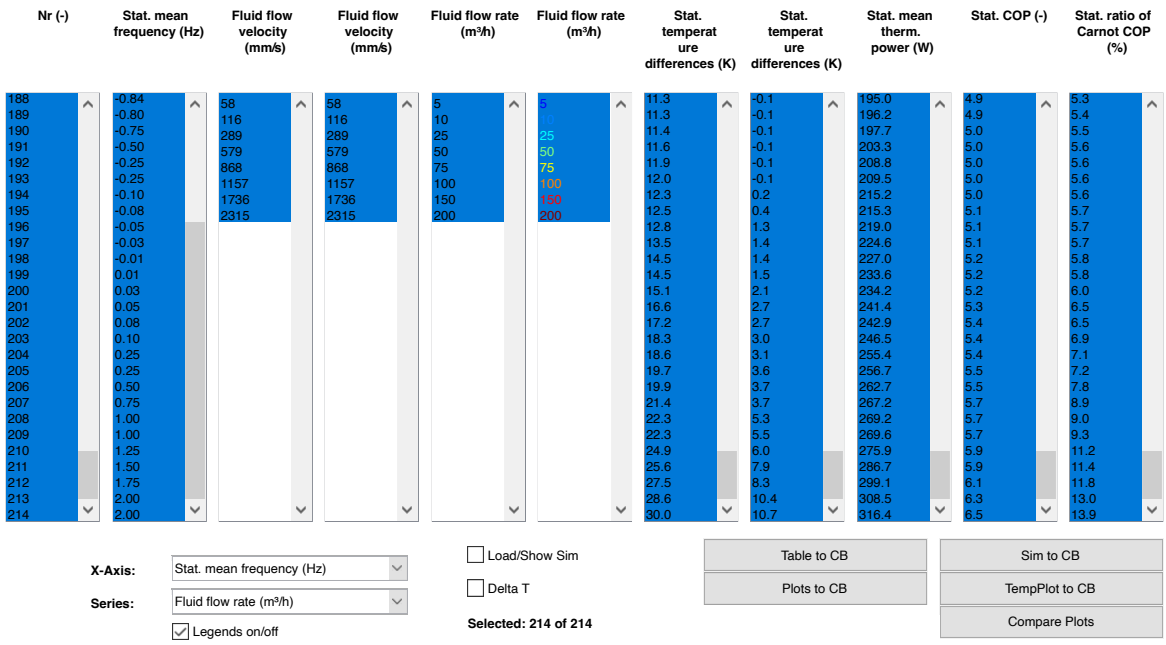

Figure 5.21: *Parameter comparison tool* of the EC HP *simulation tool*.

the parameter group. Then, the user can select which parameter or key value to set on the x-axis. After that, the user can choose which parameter or key value to plot as a color series of curves. Finally, the user can limit the display area for each parameter or key value by selecting or deselecting value areas or individual simulations.

The simulation of a parameter group is always compared with the standard diagrams for temperature at inlets and outlets, as well as the thermal power of all ducts. Additionally, the mechanical power of the EC system and the resulting *COP* will be presented. Additional diagrams can be generated using the *Compare Plots* button to observe details of the chosen series in the EC HP. These diagrams will illustrate the phase fraction-rotation angle, cam stroke-rotation angle, and stress-strain diagram of the SMA, as well as the temperature of the SMA and the corresponding fluid element along the rotation angle.

Furthermore, the visualization tool of the selected simulations can be loaded with a button. Finally, the legends of all diagrams can be switched on or off, and the diagrams can be exported and saved as an svg-file.

The presented simulation tool not only supports the design process of the EC HP by predicting the influence of specific design choices but also enables the evaluation of the best design choice using the parameter comparison tool without developing time-consuming and costly prototypes and conducting measurements in the lab.

In the following, the *simulation tool* with its sub-tools is calibrated and validated. Therefore, different parameter studies will be discussed. These studies follow the calculation procedure introduced in this part. They are organized in the *parameter set table*, simulated with the *simulation tool*, using the *parallel computation tool*, and evaluated using the *parameter comparison tool*, as well as the *visualization tool*.

5.4 Calibration and validation

This section evaluates the parameters for the simulation model and the SMA material, with the methods introduced in chapter 4.
First, the mechanical and thermal parameters were determined for the SMA element, taking into account the specific sample, the performed loading procedure, and the constraints to the ambient. These parameters are summarized with the model-specific parameters for the MAS model in Table 5.5. Finally, the parameter set is validated using different EC cycles with changing mean strain and strain amplitude.
Next, the discretization of the fluid channel is compared by considering the error, time step, number of evaluations, as well as CPU time for different implemented schemes. Afterward, a comparison of various fluid discretizations is conducted. In this examination, the resulting inlet and outlet temperatures at hot and cold ducts, resulting thermal and mechanical power, as well as *COP*, and resulting computation time for solving the EC system model are analyzed for different numbers of fluid elements. The basic fluid parameters, typically found in table books, are summarized in Table 5.4.
At last, the method for solving the ODE system is chosen by evaluating the computation time for solving the EC system model with standard parameters using different ODE solver types. The solver settings are summarized in Table 5.6.

5.4.1 Shape memory alloy model and kinematics

The versatile implementation of the kinematics with the cam track, combined with the SMA element using the MAS model, enables the adaptation of the load profile to the experiment performed using an ordinary tensile test stand. To perform a tensile test, the standard configuration of the EC system model, known from Table 5.7, is adjusted to one SMA element ($N_{\mathrm{bun}} = 1$) which consists of a single wire segment ($N_{\mathrm{wpb}} = 1$). The operating parameters of the performed simulation are set to the standard values of Table 5.8 while using air as HE and HT fluid.
In the following, a parameter study with different loading profiles and thermodynamic boundary conditions will be discussed. This study follows the calculation procedure introduced in section 5.3. It is organized in the *parameter set table*, simulated with the

simulation tool, using the *parallel computation tool*, and evaluated using the *parameter comparison tool*.

Figure 5.22 (a) presents the loading profile of the SMA elements with the stroke along the circumference for the isothermal cycle. These diagrams are generated using the parameter comparison tool, introduced in section 5.3, with the channel position at the x-axis and the disk type as a series in different colors. The disk type classifies the minimum strain ($\varepsilon_{\min}$) and the maximum strain ($\varepsilon_{\max}$) in thousanths with which the simulation is performed. The resulting stroke is determined by utilizing the geometry of the SMA element. This name is accompanied by classifying the thermal boundary conditions using the names of the thermodynamic cycles such as *isothermal*, *adiabatic*, and *EC*. The EC cycle is characterized by almost adiabatic loading and unloading and HE in the zones with fluid ducts. If a change in SMA strain is induced by the load profile while traveling along the ducts, the loading and unloading processes are not performed purely adiabatic.

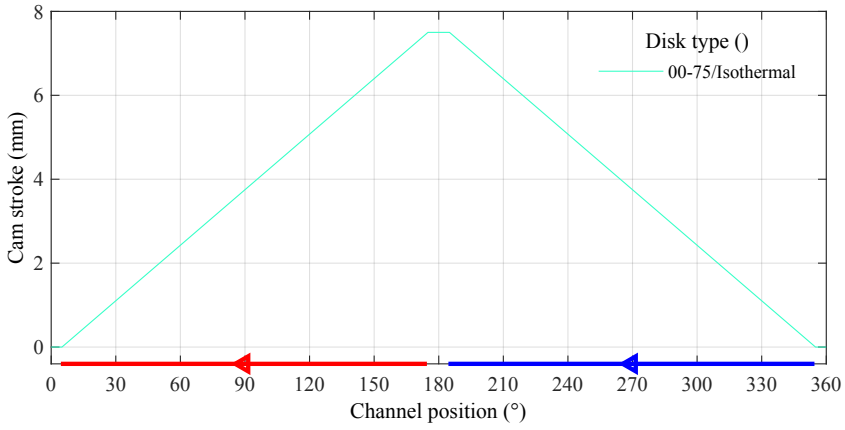

(a)

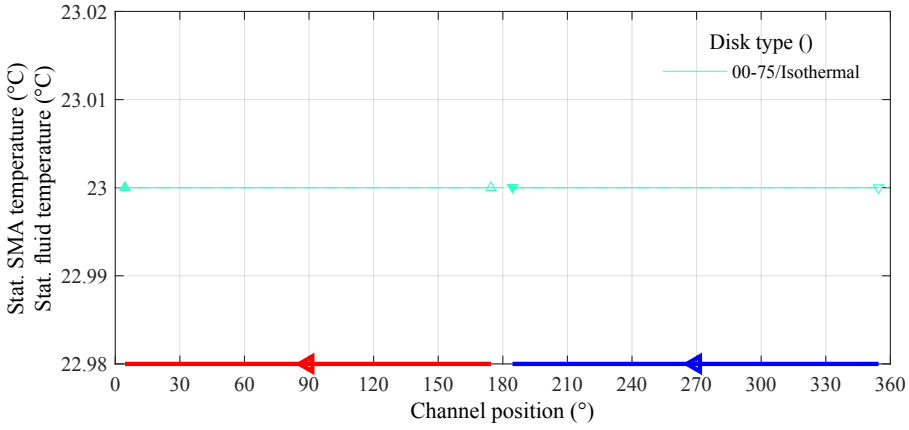

(b)

Figure 5.22: Calibration of the simulation tool's kinematic and SMA model: a) Loading profile along the channel position for an isothermal cycle. b) Temperature profile of the SMA as dashed line and the fluid as solid line along the circumference for the isothermal cycle.

The cam stroke increases continuously from minimum strain ($\varepsilon_{\min} = 0$) strain to the maximum strain ($\varepsilon_{\max} = 0.075$) as the channel position on the cam track changed due to rotation along the rotation angle (φ) from approximately 0° to 180°, accompanied by a constant counter-flow in the hot duct. Afterward, the stroke in the SMA element decreases back to zero during the rotation from approximately 180° to 360°, accompanied by a constant counter-flow in the cold duct. The colored lines with arrows along the x-axis highlight the regions of the ducts and the flow direction.
The fluid ducts are specified by the midpoint, and the length. Fluid duct midpoint can be determined for the hot duct ($(\varphi_{\mathrm{hi}} + \varphi_{\mathrm{ho}})/2$), and the cold duct ($(\varphi_{\mathrm{ci}} + \varphi_{\mathrm{co}})/2$) using the positions of the input and output. The fluid duct length is given for the hot duct ($\varphi_{\mathrm{hi}} - \varphi_{\mathrm{ho}}$), and the cold duct ($\varphi_{\mathrm{ci}} - \varphi_{\mathrm{co}}$) using the input's and output's positions.
Figure 5.22 (b) presents the temperature profile of the SMA element as a dashed line and the fluid as a solid line along the circumference for the isothermal cycle. Each temperature curve of the fluid is framed at the edges by triangles that are upturned at the hot duct and downturned at the cold duct. The triangles at the inlets are empty, and the triangles at the outlets are filled. The straight horizontal line of the temperature indicates isothermal conditions during the loading and unloading of the SMA material with no visible temperature change. The combination of the chosen flow rate in the hot duct ($\dot{V}_{\mathrm{h}}$) and cold duct ($\dot{V}_{\mathrm{c}}$) with the rotational frequency (f) of the SMA arrangement enables a sufficiently hight HE between the SMA element and fluid, as well as HT of the fluid out of the individual duct.
Figure 5.23 (a) presents the load profile with the stroke along the circumference for the EC cycle. In this diagram, different types of disks for the EC cycle with changing mean strain and strain amplitude are shown. The cam stroke increases for each simulation continuously from minimum strain ($\varepsilon_{\min}$) strain to the maximum strain ($\varepsilon_{\max}$) depending on the values mentioned in the disk type. To ensure correlation with the conducted experiments, shown below, the strain input is slightly adjusted by 0.0075 to align with the experimental data range. Therefore, the stroke of the first four simulations does not reach the zero line. The loading and unloading of the SMA element in each simulation is performed within the same sector of the channel position with a rotation angle (φ) from 315° to 45° for loading, and from 135° to 225° for unloading. In these regions, no HE is assumed to fulfill the boundary conditions of an adiabatic EC cycle. The HE between the SMA element and the surrounding fluid is enabled as counter-flow along the channel position in the regions from 50° to 130° for the hot duct, and from 230° to 310° for the cold duct.
Figure 5.23 (b) presents the temperature profile of the SMA element as dashed line and the fluid as solid line along the channel position for different EC cycles. Each temperature curve of the fluid is framed at the edges by triangles that are upturned at the hot duct and downturned at the cold duct. The triangles at the inlets are empty, and the triangles

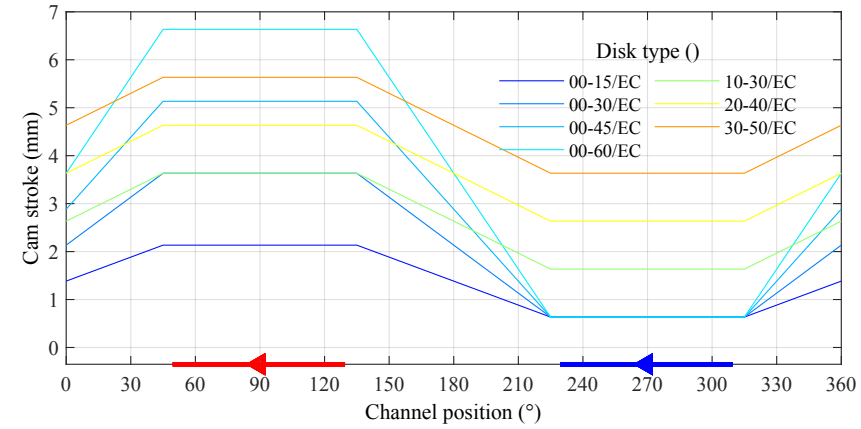

(a)

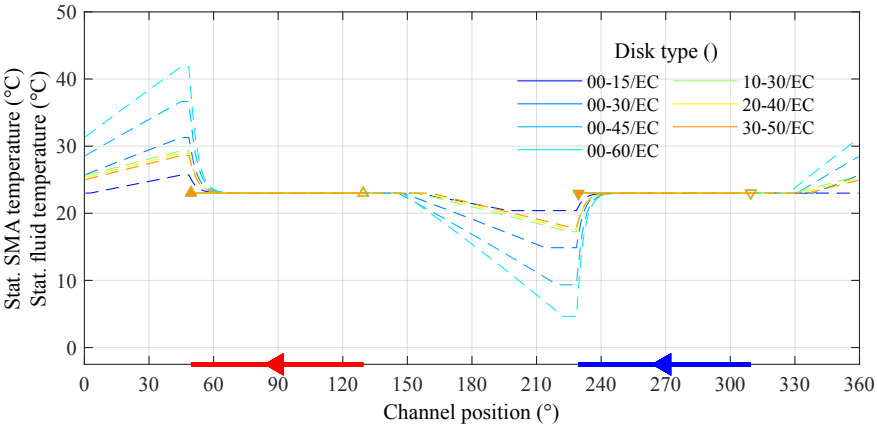

(b)

Figure 5.23: Validation of the simulation tool's kinematic and SMA model: a) Load profile along the circumference for the EC cycle. b) Temperature profile of the SMA as dashed line and the fluid as solid line along the circumference for the EC cycle. Different types of disks are presented.

at the outlets are filled. During loading and unloading, the SMA material undergoes the PT and releases or absorbs specific latent heat without exchanging thermal energy with the environment. Therefore, the temperature of the SMA element changes with strain. During the regions with constant strain, the temperature of the SMA element decreases after loading and increases after unloading due to the enabled HE with the surrounding fluid. The combination of the chosen flow rate in the hot duct ($\dot{V}_\mathrm{h}$) and cold duct ($\dot{V}_\mathrm{c}$) with the rotational frequency (f) of the SMA arrangement enables a sufficiently high HE between the SMA element and fluid, as well as HT of the fluid out of the individual duct, that the initial temperature of the SMA element is reached at the end of each holding phase.

Thermodynamic conditions

Figure 5.24 presents the stress-strain diagram in the upper part, and temperature-strain diagram in the lower part. The isothermal cycle is represented by a solid blue line for

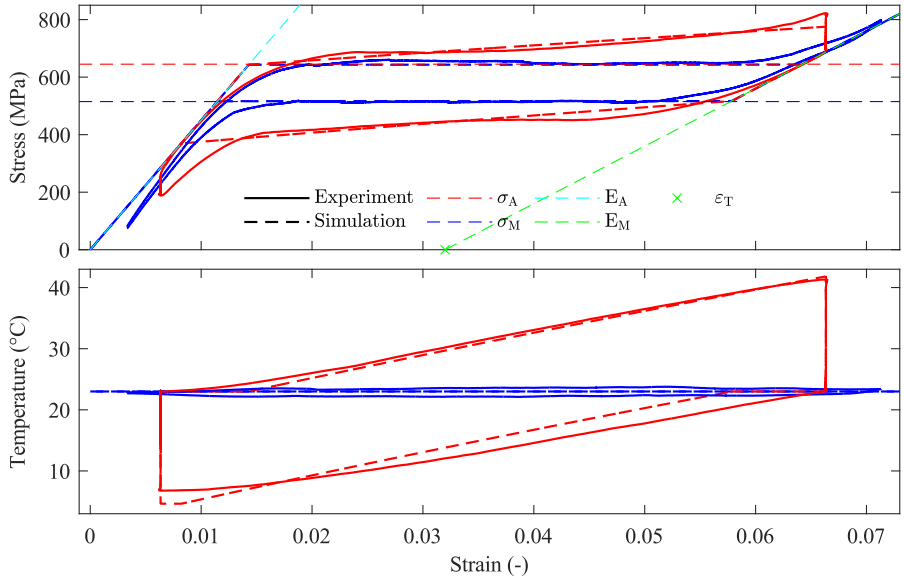

Figure 5.24: Validation of the simulation tool's kinematic and SMA model: Stress-strain diagram (upper), and temperature-strain diagram (lower) of the simulation results as dashed line, and the experimental data as solid line for the isothermal cycle colored in blue and the EC cycle with adiabatic loading and unloading in red.

the experimental data and a dashed blue line for the simulation results, while the EC cycle with nearly adiabatic loading and unloading is represented by a solid red line for the experimental data and a dashed red line for the simulation results.
The stress-strain behavior in the simulation closely matches the experimental data using the material properties evaluated with the methods introduced in chapter 4 and summarized in Table 5.5. The deviation in the areas where the PT starts and ends is correlated with the

polycrystalline material behavior and the single crystalline approximation of the material model.
Despite this variation in the mechanical behavior, the temperature-strain behavior in the simulation of the PT from A to M closely matches the experimental data. The deviation in the simulation during the adiabatic FT is due to the prolonged linear loading in the A state, which results in a delayed temperature increase compared to the experiments. In the experiments, the early PT of some cells in the polycrystalline SMA material generates an earlier temperature change. However, the maximum temperature of the simulation at the end of the FT fits perfectly with the experiment.
This is caused by the trade-off during the calibration process of the specific latent heat. In one case, the value of the specific latent heat is adjusted so that the slope of the temperature-strain behavior in the simulation matches that of the experiment. This approach would lead to a smaller maximum temperature of the SMA and, amongst other things, to a smaller thermal energy output. The alternative is to adjust the value of the specific latent heat so that the maximum temperature of the SMA after the FT matches that of the experiment. This approach results in a larger temperature gradient during the PT, which allows for a more realistic prediction of the HE between the SMA and the surrounding fluid, as well as resulting in a more accurate prediction of the thermal energy output of the EC system. In most cases, the area of the fluid channel where the PT occurs does not contribute to the thermal energy output. Therefore, the influence of the larger temperature gradient in the simulated behavior of the EC HP is negligible. The value of the specific latent heat is due to the mechanical loading significantly smaller than the material value obtained by the DSC, as discussed in subsection 1.2.3.
At the end of the loading, the stress drops due to the post-transformation from A to M. The stress-strain point and the temperature-strain behavior after the post-transformation in the simulation matches perfectly that of the experimental data. The relaxation of the stress and temperature to nearly the same point for the different strain rates shows that the duration of the holding phase is sufficiently long for this sample geometry in combination with the given ambient conditions.
During the initial phase of the PT from M to A, the simulation and experimental data of the stress-strain behavior indicate a small mismatch due to the polycrystalline SMA material analogous to the behavior during FT. The middle part of the transition from M to A in the simulation aligns perfectly with that of the experiment. The deviation is also smaller at the end of the BT. The difference of the mismatch between FT and BT is caused by the varying Young's moduli of A and M.
During the beginning of the BT, the smaller Young's modulus of M leads to a more significant delay in temperature decrease in the temperature-strain behavior compared to the FT.

The temperature development of the transition between M and A is described by the value of the specific latent heat. A closer look at the temperature span during the FT and the BT shows a smaller temperature drop during the BT. This asymmetric temperature development is also known from literature [54].
During FT and BT, internal friction occurs when the phase boundary passes through the crystal lattice [197], releasing frictional heat. Therefore, in relation to the area of mechanical hysteresis [110, 18, 9], a thermal energy input can be assumed during loading and unloading, which leads to a reduced cooling capability of the SMA material.
To reproduce the asymmetry of the temperature development between FT and BT, the additional thermal energy input to the isothermal mechanical hysteresis is implemented as asymmetrical specific latent heat. The specific latent heat during the FT from A to M (H_{A}) can be calculated using Equation 5.44 with the half of the isothermal hysteresis losses (ΔH).

$$H_{\mathrm{A}} = H_{\mathrm{mean}} + \Delta H \tag{5.44}$$

The specific latent heat during the BT from M to A (H_{M}) can be calculated using Equation 5.45 with the half of the isothermal hysteresis losses (ΔH).

$$H_{\mathrm{M}} = H_{\mathrm{mean}} - \Delta H \tag{5.45}$$

With this modification, the temperature drop after the BT of the simulation nearly fits the value of the experimental data in the temperature-strain behavior. The holding phase after unloading leads to the same points in the simulation results and the experimental data for the stress-strain and temperature-strain behavior.

Maximum strain

The values for the mean specific latent heat and the specific latent heat difference are chosen to fit the thermo-mechanical behavior of the FT perfectly. A slight difference in the thermo-mechanical behavior during the BT is expected after the maximum applied strain. A comparison of the EC cycle with different maximum strain values is presented in Figure 5.25. The diagram in the upper part shows the stress-strain relationship between the simulation results (dashed line) and the experimental data (solid line). The mechanical behavior between the simulation and the experiment demonstrates an excellent agreement for all presented cycles. The lower part displays the temperature-strain diagram, with the simulation results as a dashed line and the experimental data as a solid line. This diagram highlights the close match between the simulation results and experimental data of the temperature development, especially for EC cycles with smaller maximum strain.

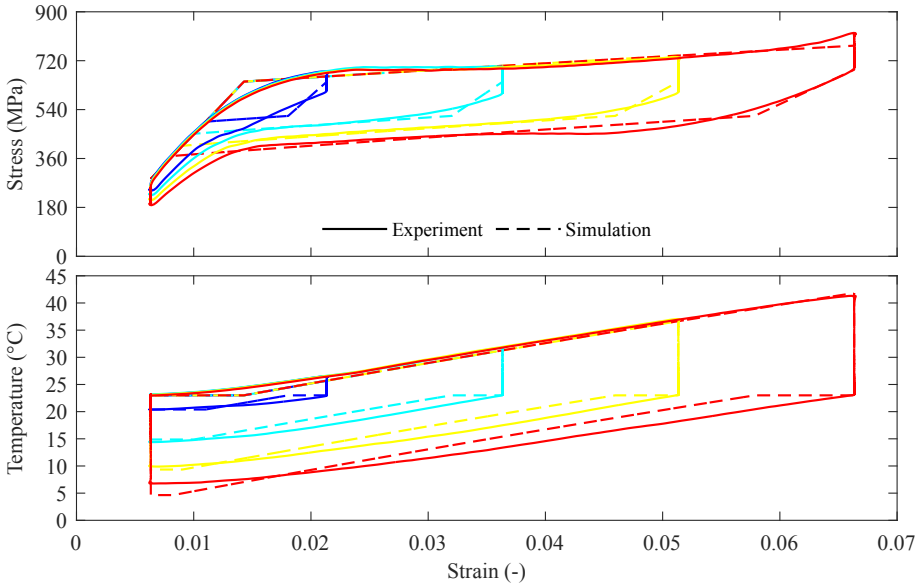

Figure 5.25: Validation of the simulation tool's kinematic and SMA model: Stress-strain diagram (upper), and temperature-strain diagram (lower) of the simulation results as dashed line, and the experimental data as solid line for the EC cycle with different maximum strain values.

Mean strain

Figure 5.26 presents EC cycle with different mean strain values. This diagram presents the thermo-mechanical behavior of internal hysteresis loops introduced in subsection 1.3.1. This is based on the stress-strain diagram in the upper part and temperature-strain diagram in the lower part. The simulation results are shown as a dashed line, and solid lines represent the experimental data. Even if the reproduction of the thermo-mechanical behavior was not focused on internal hysteresis, the physically based model approach offers sufficient accuracy in the prediction of internal EC cycles with different mean strain values. The simulation results for the mechanical and thermal behavior closely match those of the experiments. Additionally, the maximum and minimum temperatures are nearly perfectly reached after loading and unloading.

The simulation accurately predicts the thermo-mechanically coupled material behavior of the SMA observed in experiments. The agreement between the experiment and simulation in the stress-strain diagram and the temperature-strain diagram for all different strain rates, as well as different elastocaloric cycles, shows the good accuracy of the evaluated thermal and mechanical parameters. Therefore, the calibration and validation of the SMA element and kinematics can be considered complete.

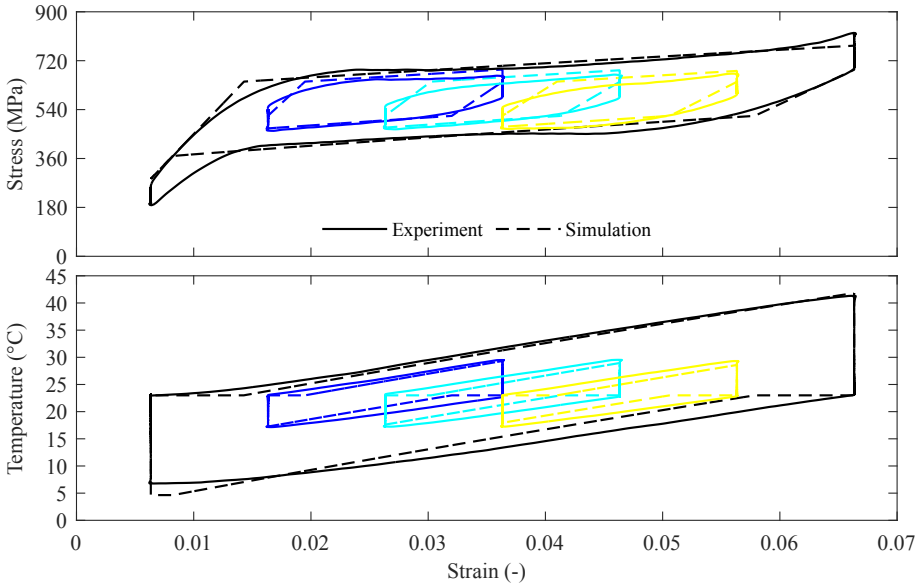

Figure 5.26: Validation of the simulation tool's kinematic and SMA model: Stress-strain diagram (upper), and temperature-strain diagram (lower) of the simulation results as dashed line, and the experimental data as solid line for the EC cycle with different mean strain values.

5.4.2 Fluid channel discretisation scheme

The energy balance of the fluid includes, in addition to the temporal derivative, the spatial derivative with an order of up to two. The temporal derivative of the PDE will be discretized using the solving procedure of MATLAB's ODE solvers. To discretize the fluid channel with respect to space coordinates, the discretization schemes, introduced in Equation 5.43, are implemented and can be used.

In the following, a parameter study with different spatial discretization schemes will be discussed. This study follows the calculation procedure introduced in section 5.3.

Figure 5.27 compares the temperature distribution in the fluid channel without SMA interaction for different discretization approaches. The temperature development along the circumference with a fluid flow velocity of 100 mm/s is presented for different points in time. The temperature increase at the inlet at t=1 s from 273 K to 274 K leads to different reactions of the schemes. Only the U3 and the Q react like the reference result (R) without overshooting. During the fluid flow from inlet to outlet, the transition from the lower temperature to the higher fits most physically meaningful in these two schemes. All schemes are very close when reaching the outlet (t=9 s), but the U3 and Q show no overshooting.

Figure 5.28 compares the thermal energy and computational performance of the fluid channel without SMA interaction for different discretization approaches. The upper diagram shows the thermal energy over simulation time. In this diagram, the thermal energy inserted by the inlet, the thermal energy inside the channel, and the thermal energy

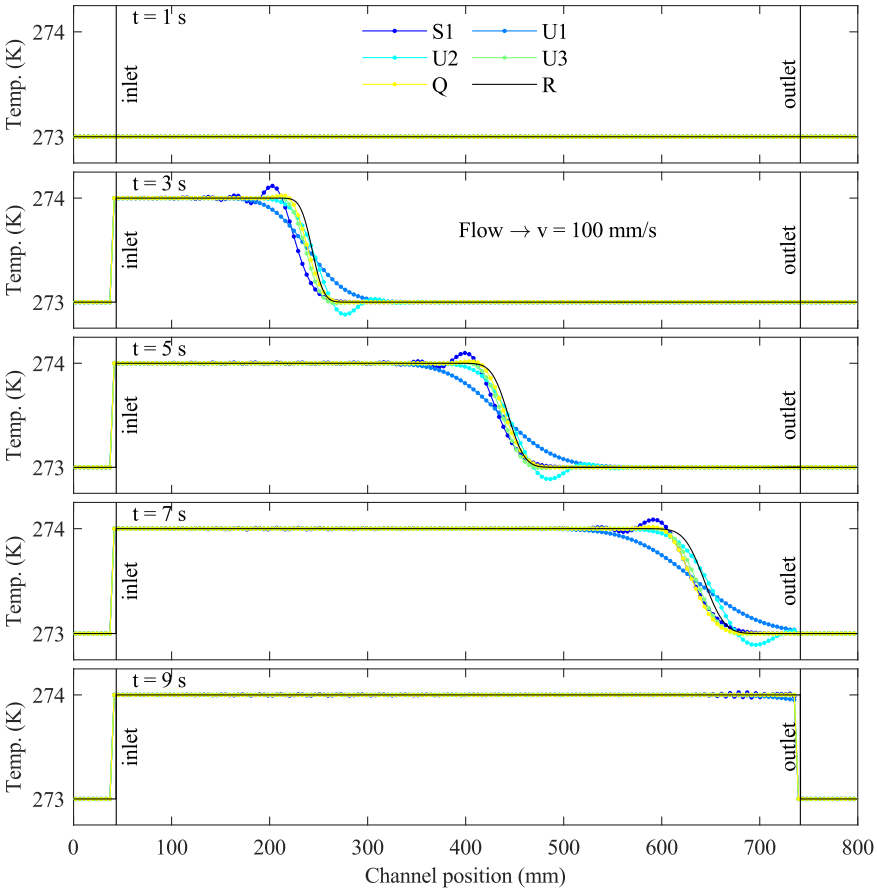

Figure 5.27: Comparision of the temperature distribution in the fluid channel without SMA interaction for different discretization approaches.

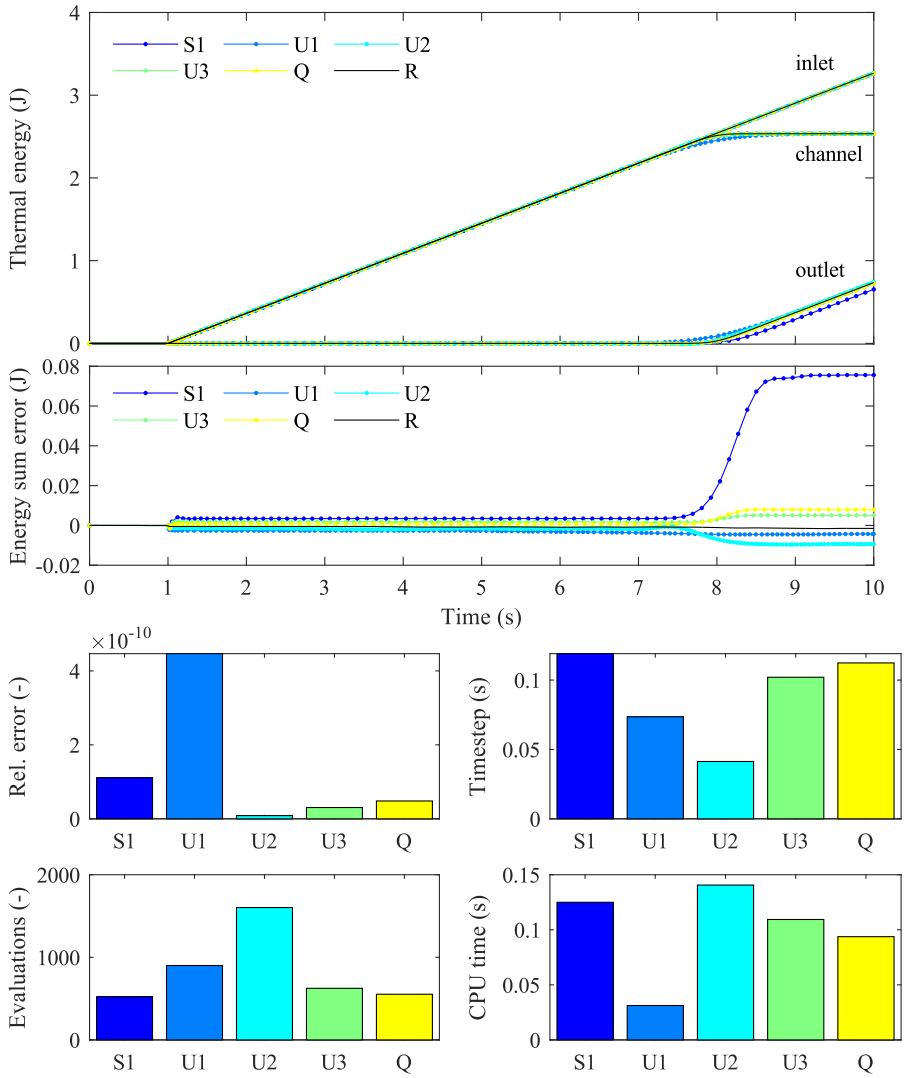

Figure 5.28: Comparision of the thermal energy and computational performance of the fluid channel without SMA interaction for different discretization approaches.

extracted at the outlet are pictured. The thermal energy inserted by the inlet increases over time without changing the slope. The thermal energy in the channel increases over time due to the continuous inflow with higher temperature. At the point in time when the temperature of the fluid in the channel is constant, the thermal energy changes its slope and remains constant after the transition zone of the temperature passes the outlet. Therefore, this curve is reaching a plateau. The thermal energy extracted at the outlet increases with the same slope as the inlet energy when the transition zone reaches the channel's end. In this diagram, all schemes are very close.
The following diagram presents the error of the thermal energy in the channel over simulation time. In this, the U3 and Q show a larger error than the U1 and U2, but with a maximal range of 0.005 J.
The computational performance of different implemented schemes is compared in the lower part of Figure 5.28. This includes the relative error, time step size, number of evaluations, and needed CPU time.
As mentioned earlier, scheme U2 achieves the lowest error. However, it also requires a small time step, a high number of evaluations, and a large CPU time.
The U3 and Q schemes exhibit comparable errors, time step sizes, and numbers of evaluations. During CPU time, the U3 demonstrates better performance.
Figure 5.29 compars the temperature distribution in the fluid channel including SMA interaction for different discretization approaches. The temperature development along the channel with a fluid flow velocity of 100 mm/s and a motion velocity of the SMA of 100 mm/s in cross-flow to the fluid is presented for different points in time. The fluid temperature increase at the inlet at t=1 s from 273 K to 274 K leads to different reactions of the schemes. The initial temperature of the SMA of 274 K lead also to a temperature change of the fluid at the end of the channel. The U3 and Q schemes react similarly to the reference result (R) without overshooting, even at the point where the temperature transition of the inserted fluid merges with the temperature increase of the SMA.
Figure 5.30 compars the thermal energy and computational performance of the fluid channel including SMA interaction for different discretization approaches. The upper diagram shows the thermal energy over simulation time. In this diagram, the thermal energy inserted by the fluid flow from the inlet, the thermal energy extracted by the fluid flow at the outlet, the thermal energy of the fluid inside the channel, and thermal energy of the SMA are combined. The thermal energy by the fluid flow from the inlet increases over time without changing the slope. The thermal energy extracted by the fluid flow at the outlet increases constantly due to the HE with the SMA and changes its slope when the temperature front reaches the outlet.
The thermal energy of the fluid inside the channel increases at the beginning with the highest slope due to the energy input of the inlet and the HE with the SMA. In the middle,

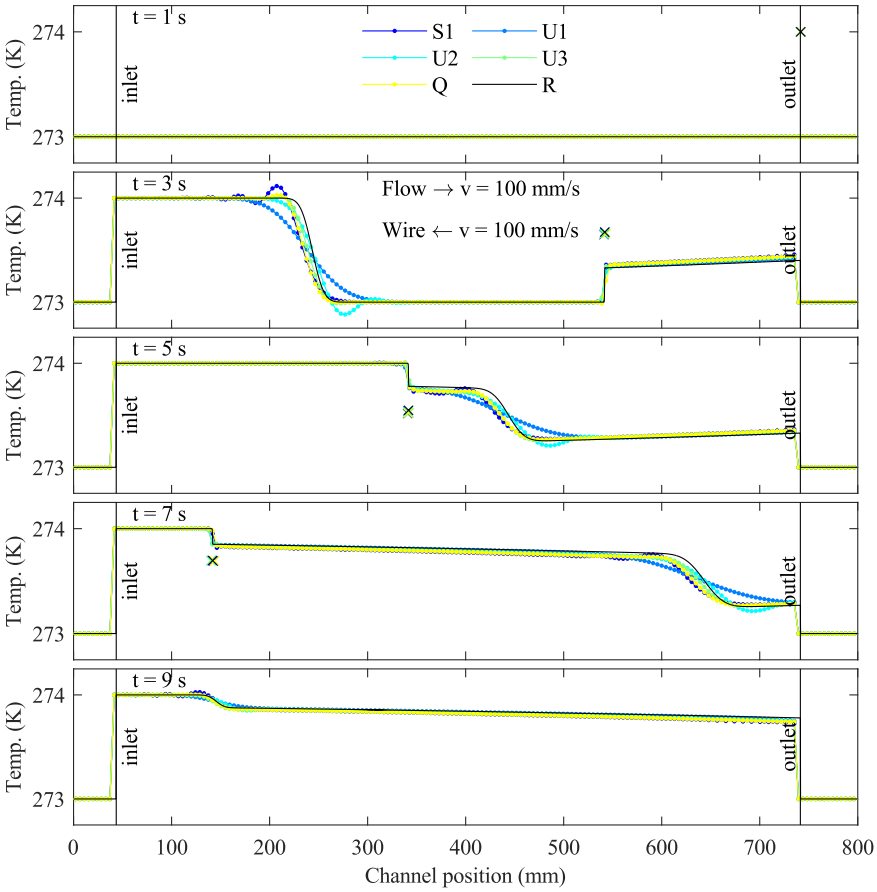

Figure 5.29: Comparision of the temperature distribution in the fluid channel including SMA interaction for different discretization approaches.

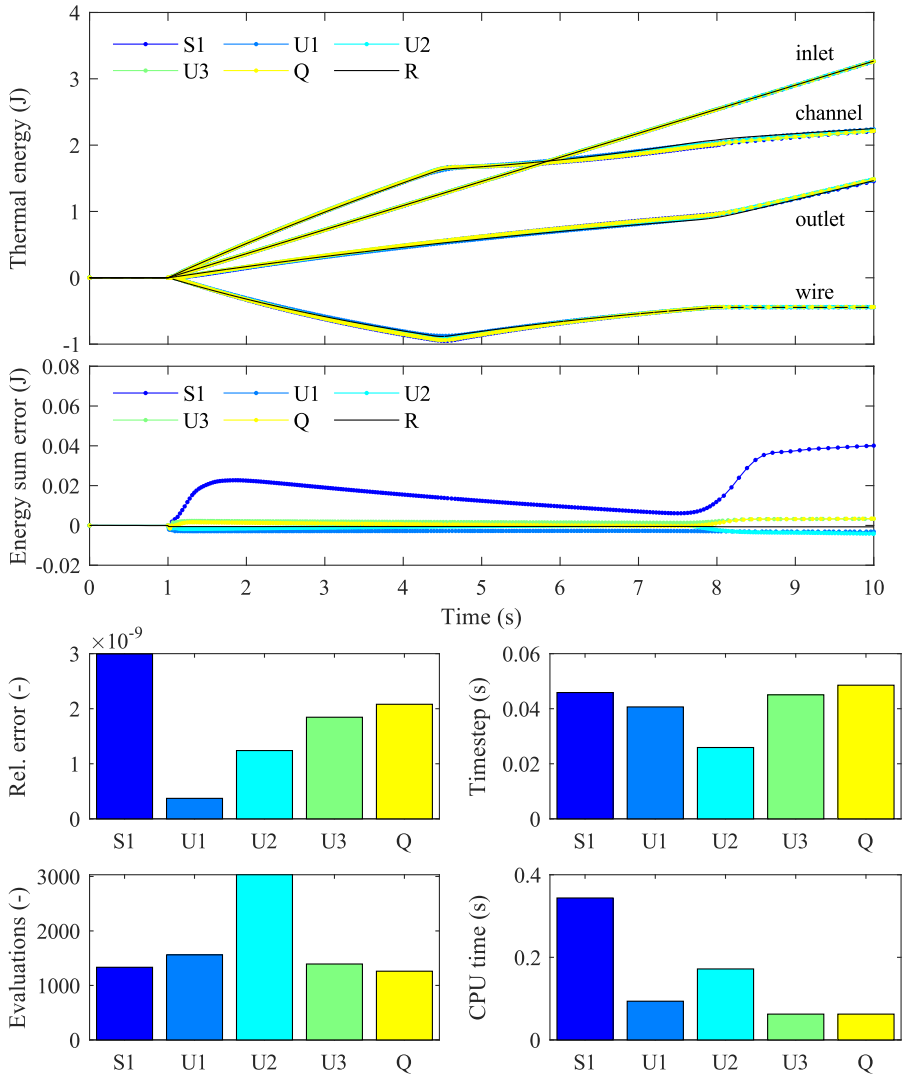

Figure 5.30: Comparision of the thermal energy and computational performance of the fluid channel including SMA interaction for different discretization approaches.

at the point in time where the temperature transition of the inserted fluid merges with the temperature increase of the SMA, the slope decreases. In the end, when the temperature transition of the inserted fluid passes the outlet, the slope of the channel thermal energy decreases again.
The thermal energy of the SMA decreases at the beginning due to the HE with the fluid. At the merging point with the temperature transition of the inserted fluid, the thermal energy of the SMA increases due to the higher temperature of the fluid. In the end, the thermal energy of the SMA is nearly constant due to small temperature difference between fluid and SMA.
In this diagram, all schemes are very close. The next diagram presents the error of the thermal energy in the channel over time, including the energy of the SMA. In this, the U3 and Q show again a larger error than the U1 and U2, but with a maximal range of 0.005 J.
The computational performance of different implemented schemes is compared in the lower part of Figure 5.30. This includes the relative error, time step size, number of evaluations, and consumed CPU time.
In this representation, scheme U1 achieves the lowest error. However, it requires, similar to U2, a large CPU time.
The U3 and Q schemes demonstrate higher errors but are in the acceptable range. However, these schemes demonstrate better performance in time step sizes, numbers of evaluations, and CPU time.
U3 and Q are similar discretization methods with nearly identical coefficients. The Q method can employ a larger time step and requires fewer evaluations when using the *ode113* solver to simulate the behavior of fluid in conjunction with SMA. Therefore, the Q scheme is chosen for the following work as the main discretization scheme. Nevertheless, the other schemes are also implemented in the simulation tool, as introduced in section 5.3, and can be switched easily for each parameter group in the parameter set table.

5.4.3 Number of fluid elements

The spatial discretization of the fluid channel raises the question of the required number of fluid elements. For each element, an entry must be created in the state vector (Equation 5.41) and therefore in the fluid's ODE system (Equation 5.43).
In the following, a parameter study with different numbers of fluid elements in the channel will be discussed. This study follows the calculation procedure introduced in section 5.3. It is organized in the *parameter set table*, simulated with the *simulation tool*, using the *parallel computation tool*, and evaluated using the *parameter comparison tool*, as well as the *visualization tool*.
Figure 5.31 shows an overview of the computation time for solving the EC HP simulation model with standard parameters, introduced in section 5.5, using different numbers of

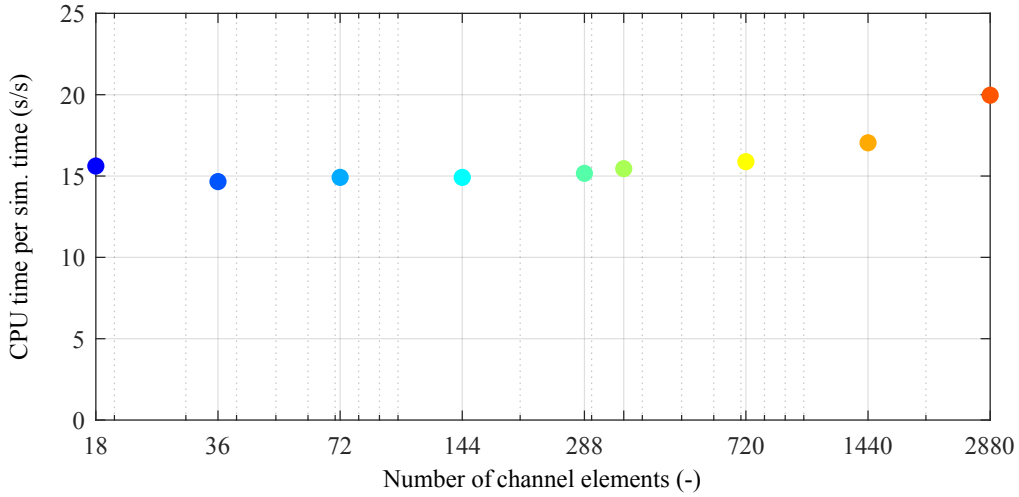

Figure 5.31: Computation time for solving the EC HP simulation model with standard parameters using different numbers of fluid elements in the channel.

fluid elements (N_{fld}) in the channel. In this presentation, the CPU time is given as needed seconds for calculating one second of the simulated EC HP runtime. The calculation procedure and the required updating in each time step require a proportional effort for each additional element, which is visible in the increasing computation time. The calculation time using a very small number of fluid elements is elongated due to the high iteration number.

In order to minimize simulation costs and data management efforts, it's essential to carefully select the number of fluid elements while considering the simulation tool's predictive capabilities with mechanical input and thermal output. To reach the error limit demanded for the solver, the computational effort involved should also be taken into account, along with the simulation time and data storage requirements.

Figure 5.32 shows the still frame of the visualization tool of EC HP, discussed in section 5.3, using standard parameters, from section 5.5 with a fluid element number (N_{fld}) of 18 along the circumference. In this presentation, the spatial discretization steps are clearly visible in the cross-sectional view. Additionally, the curve of the fluid temperature over time shows significant unphysical kinks.

Figure 5.33 shows the still frame of the visualization tool of EC HP, using standard parameters, with a fluid element number (N_{fld}) of 360 along the circumference. In this presentation, no spatial discretization steps are visible in the cross-sectional view. Additionally, the curve of the fluid temperature-time diagram shows only very small kinks.

Figure 5.34 presents the still frame of the EC HP, for a fluid element number (N_{fld}) of 2880 along the circumference. In this presentation, no spatial discretization steps are visible in the cross-sectional view. Additionally, the fluctuations in the curve of the fluid temperature over time are slightly lower than those in the previous discretization approach with 360 elements.

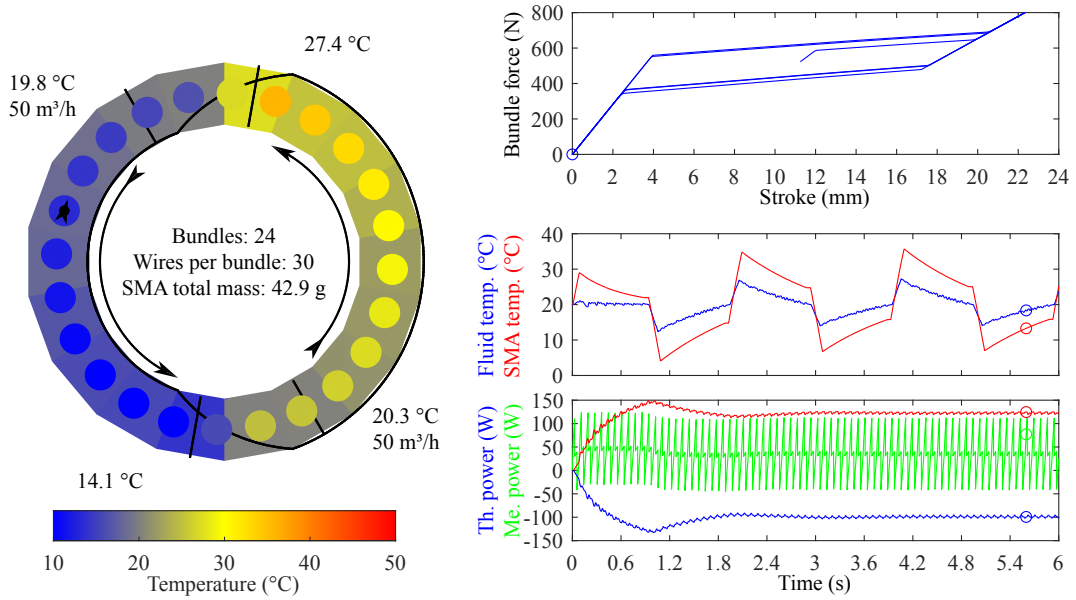

Figure 5.32: Fluid channel discretization: Visualization of EC device with 18 fluid elements in the channel.

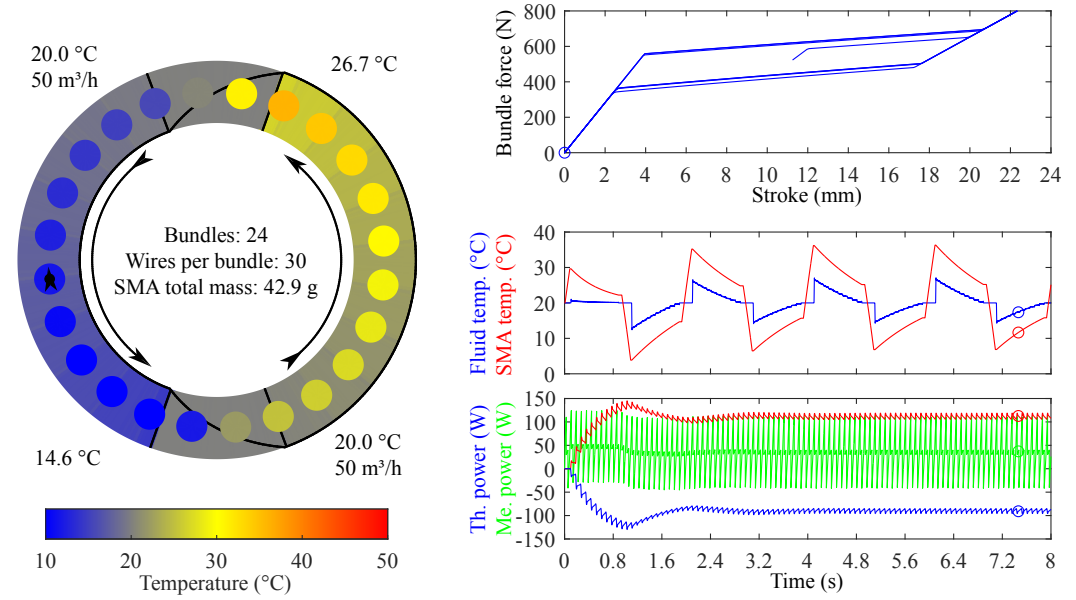

Figure 5.33: Fluid channel discretization: Visualization of EC device with 360 fluid elements in the channel.

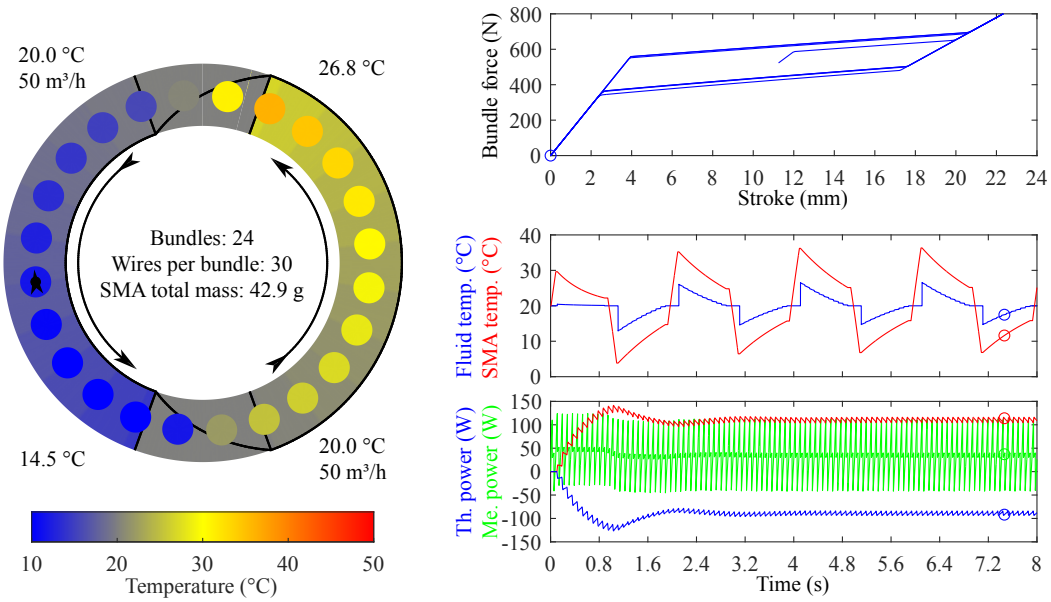

Figure 5.34: Fluid channel discretization: Visualization of EC device with 2880 fluid elements in the channel.

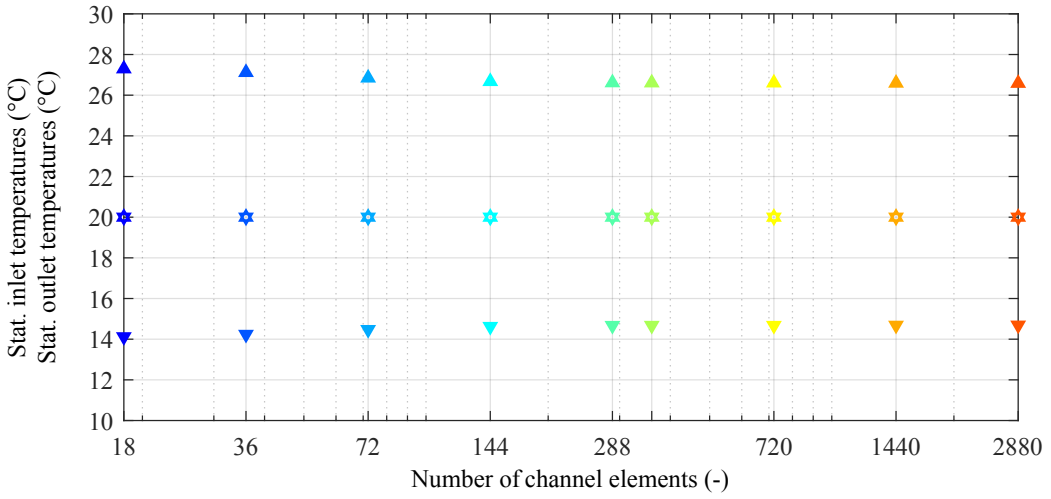

Figure 5.35: Resulting inlet and outlet temperature at hot and cold duct for different numbers of fluid elements in the channel.

The resulting inlet and outlet temperature of the hot and cold duct for different numbers of fluid elements in the channel are shown in Figure 5.35. This presentation is generated using the parameter comparison tool, introduced in section 5.3, with the number of fluid elements in the channel at the x-axis and as series to obtain the different colors. The inlet temperature of the hot duct, indicated with an empty triangle with the tip upwards, and cold duct, indicated with an empty triangle with the tip downwards, is constant at 20 °C. At the outputs, the hot duct temperature, indicated with a filled triangle pointing upwards, and cold duct temperature, indicated with a filled triangle pointing downwards, are consistent for a fluid element number larger than 244.
Figure 5.36 shows the resulting mechanical input and the thermal output as well as *COP* of the EC HP for different numbers of fluid elements in the channel. This presentation is generated using the parameter comparison tool, with the number of fluid elements in the channel at the x-axis and as color series. The thermal output and *COP* of the hot duct are indicated with empty triangles pointing upwards, and cold duct with empty triangles pointing downwards. For a fluid element number of 244 and higher, no significant change in the results is seen. This correlates with the observation in the temperature development introduced before.
Therefore, the number of fluid elements in the channel is chosen to 360 for the following work. Nevertheless, other numbers can be easily selected for each parameter group in the parameter set table.

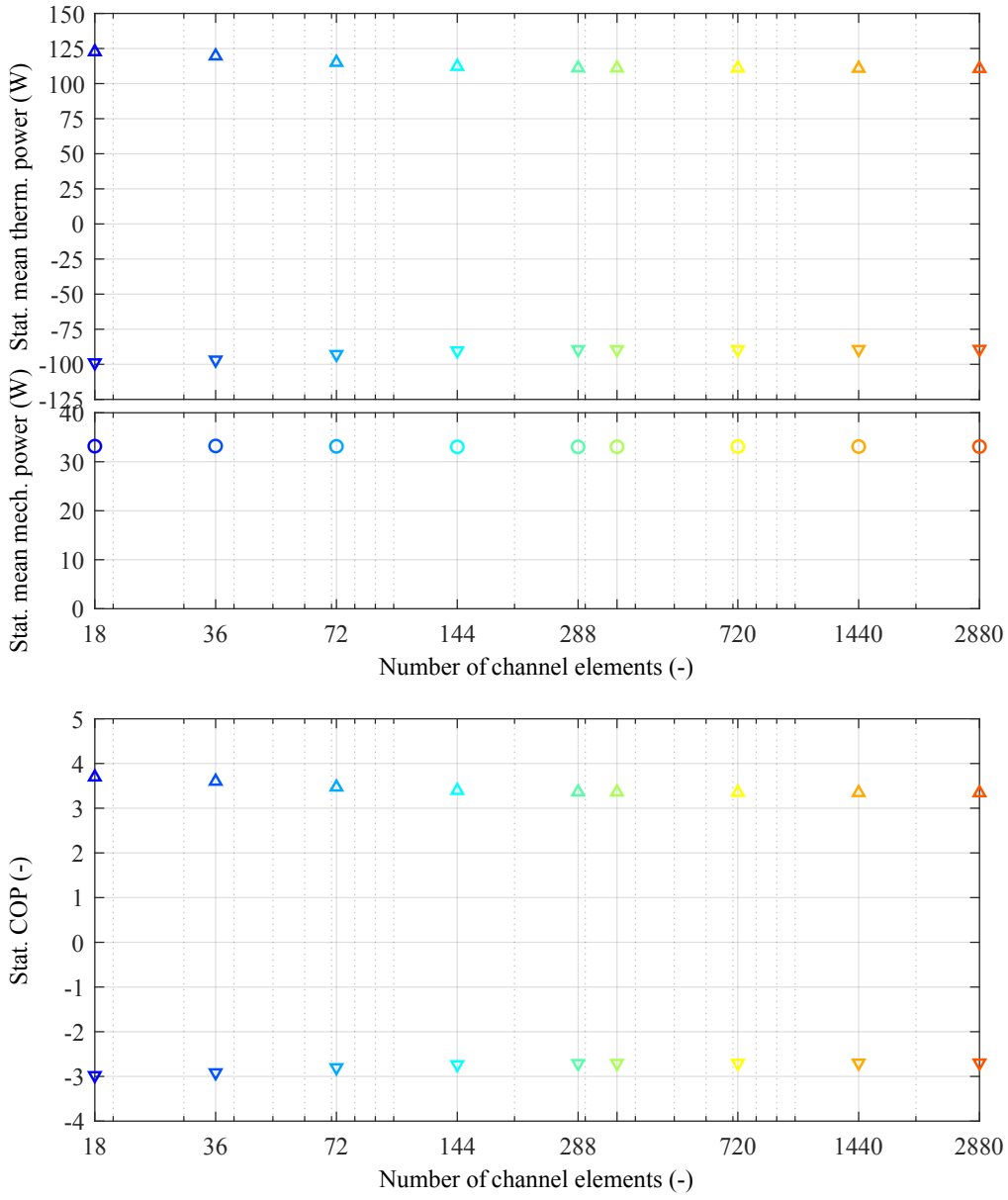

Figure 5.36: Resulting mechanical input and the thermal output and *COP* of the EC HP for different numbers of fluid elements in the channel.

5.4.4 Solver type

Due to each simulation model's specific physical dependency and complexity, different solving methods should be used to improve, among other things, the solution's accuracy and computation speed. Therefore, MATLAB provides a set of solvers, each embodying a particular approach depending on the model's system dynamics, solution stability, and solver robustness [214]. Stability refers to the ability of a system not to be significantly affected by a slight disturbance. The solution stability is crucial in physical problems; small variations in the initial values due to unavoidable errors should not proportionally affect the steady-state solution. This attribute is crucial for calculating the thermo-mechanical behavior of the SMA using strain, and consequently, the phase fraction as the initial value for the various SMA elements in the EC system.
Solver robustness refers to the ability to produce consistent output values for small changes in input parameters; it is also known as immunity to perturbations. This attribute is essential for calculating parameter sweeps with meaningful results to identify trends for changing parameters and predict the influence of various design choices on the EC system. The solvers are classified by evaluating the system properties, such as discrete states only or dependence on ODE and DAE, as well as the step size control, whether fixed-steps or variable-steps.
The presented model, implemented in MATLAB, should enable accurate computation. Computation time is an essential factor in the simulation tool that enables parameter optimization. Figure 5.37 presents the computation time for solving the EC system model with standard parameters using different ODE solvers. The time required to solve the simulation model is divided by the simulated time span of the EC system to provide a comparable unit of computational effort.

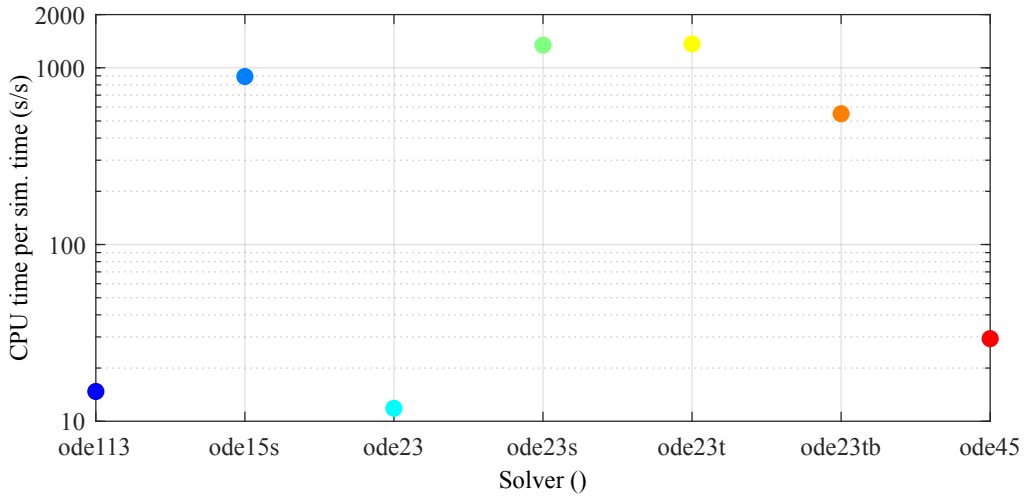

Figure 5.37: ODE solver: Computation time for solving the EC system model with standard parameters using different ODE solvers.

Some ODE systems can be challenging to evaluate, exemplary stiff problems. Stiffness occurs when there is a huge difference in scaling within the problem. For instance, the equation might be considered stiff if an ODE has two solution components that vary on drastically different time scales. These solver types are often specified by an "s" in its name. Identify a problem as stiff; nonstiff solvers are unable to solve the problem accurately or are extremely slow.
Solvers that enable solving an implicit ODE system are specified by an "i" in their name. The number in the solver's name specifies the solving technique.
The realized simulation tool exhibits a computation time of about 10 s/s on a single CPU core of an Intel Core i7 processor. This is marginal and allows multiple parameter studies on a multi-core system simultaneously.
The nonstiff solver *ode23* is the fastest option for solving the implemented model. Usually, the MAS model is known as stiff, but the implementation in combination with the chosen time step enables solving with a nonstiff solver. The *ode113* exhibits a comparable computation time to the *ode23* but enables a higher accuracy due to its variable order of the numerical integration technique. The *ode113* is a variable-step, variable-order solver based on the *Adams-Bashforth-Moulton* method with orders of 1 to 13. Therefore, the nonstiff *ode113* multistep solver is chosen in the following work.

5.5 Parameters of the Simulation Tool

The parameters utilized in this EC HP simulation tool are summarized and organized for better clarity in this section. These parameters are grouped based on their domains, such as properties of the fluid, properties of the SMA material and model-specific values, solver settings, design parameters of the EC HP, which can only be changed during the development process, and operating parameters of the EC HP, which can be changed during operation. Additionally, this section serves as a repository for the scientific parameter studies conducted in this work using the developed EC HP simulation tool. The parameter tables include the section number, where the study of each specific parameter is discussed.

5.5.1 Fluid properties

The properties of the fluid for HE and HT are presented in Table 5.4. The required parameters are limited to common physical properties. Therefore, the values from the literature are sufficient, and no further experiments are required.
The fluids used in this work are dry air under standard conditions and distilled water. The developed simulation tool can handle a wide range of magnitudes for density (ρ_{fld}), specific heat capacity (c_{fld}), thermal conductivity (κ_{fld}), and dynamic viscosity (ψ_{fld}), as

demonstrated by the chosen fluids. The heat exchange coefficient between the fluid and the SMA is calculated internally in the simulation tool using the current flow conditions of the simulated EC HP configuration.
In addition to these fluid properties, the impact of individual fluid parameters of custom fluids on the EC system can be studied by adjusting the corresponding values in the parameter set table.

Name	**Symbol**	**Value for air**	**Value for water**
Fluid density	ρ_{fld}	$1.204\,\mathrm{kg/m^3}$	$1000\,\mathrm{kg/m^3}$
Specific heat capacity	c_{fld}	$1005\,\mathrm{J/(kg \cdot K)}$	$4184\,\mathrm{J/(kg \cdot K)}$
Thermal conductivity	κ_{fld}	$0.0261\,\mathrm{W/(m \cdot K)}$	$0.5562\,\mathrm{W/(m \cdot K)}$
Dynamic viscosity	ψ_{fld}	$18.24 \times 10^{-6}\,\mathrm{Pa\,s}$	$1 \times 10^{-3}\,\mathrm{Pa\,s}$
Study in section		5.6	5.7

Table 5.4: EC system model parameters: Fluid properties.

5.5.2 Shape memory alloy properties

The properties of the used SMA material and the model-specific values are presented in Table 5.5. These parameters are experimentally investigated using the test procedures introduced in chapter 4 and validated in section 5.4 for the specific SMA material used in this work.
This work utilizes the material properties of SE SMA wires made of NiTiCo, manufactured by *Fort Wayne Metals* under the name *NiTi#3*. The aim is to replicate and predict the heating and cooling characteristics of the realized EC HP system described in section 5.1. The EC behavior of this particular SE SMA material is reproduced due to its availability in large quantities with consistent thermo-mechanical properties over a large amount of material, as indicated in literature [10]. Note that this work is not focused on the potential of EC technology itself in terms of heating and cooling capabilities and efficiency. The main focus is to demonstrate the potential and versatility of the developed simulation tool. It involves investigating and identifying the trends and influences of different design and operation parameters of the EC HP using the developed parameter comparison tool.
This aggregation contains the dissipated mechanical work during an isothermal cycle, as well as the ideal material *COP* for heating and cooling. This allows for a comparison between NiTiCo and other materials optimized for EC applications.
To illustrate the potential of the EC, this work not only presents the commercially available SMA material but also conducts a further parameter study using the EC optimized material NiTiCuV, which was introduced in the literature [93].

Further, the aggregation includes the time constant of the phase fraction as the material-specific scaling constant and the characteristic material volume size. Both are material model-specific parameters, introduced with the MAS in section 2.2.
In addition to these SMA properties, the impact of individual SMA parameters of custom SMA materials in the EC system can be studied by adjusting the corresponding values in the parameter set table.

Name	**Symbol**	**NiTi#3**	**NiTiCuV**
SMA density	ρ_{sma}	$6317\,\mathrm{kg/m^3}$	$6317\,\mathrm{kg/m^3}$
Specific heat capacity	c_{sma}	$463\,\mathrm{J/(kg\cdot K)}$	$463\,\mathrm{J/(kg\cdot K)}$
Mean of specific latent heat	H_{mean}	$9.0\,\mathrm{J/g}$	$9.2\,\mathrm{J/g}$
Specific latent heat difference	ΔH	$0.5\,\mathrm{J/g}$	$0.17\,\mathrm{J/g}$
Young's modulus of A	E_{A}	$45\,\mathrm{GPa}$	$35\,\mathrm{GPa}$
Young's modulus of M	E_{M}	$20\,\mathrm{GPa}$	$20\,\mathrm{GPa}$
Transformation strain	ε_{t}	0.032	0.024
Transformation stress from A to M	$\sigma_{\mathrm{A}}(T_{\mathrm{ref},\sigma_{\mathrm{A}}})$	$645\,\mathrm{MPa}$	$372\,\mathrm{MPa}$
Reference temperature of σ_{A}	$T_{\mathrm{ref},\sigma_{\mathrm{A}}}$	$296.15\,\mathrm{K}$	$288.35\,\mathrm{K}$
Temperature dependence of σ_{A}	$\frac{\partial\sigma_{\mathrm{A}}}{\partial T}$	$7\,\mathrm{MPa/K}$	$7\,\mathrm{MPa/K}$
Transformation stress from M to A	$\sigma_{\mathrm{M}}(T_{\mathrm{ref},\sigma_{\mathrm{M}}})$	$515\,\mathrm{MPa}$	$300\,\mathrm{MPa}$
Reference temperature of σ_{M}	$T_{\mathrm{ref},\sigma_{\mathrm{M}}}$	$296.15\,\mathrm{K}$	$288.35\,\mathrm{K}$
Temperature dependence of σ_{M}	$\frac{\partial\sigma_{\mathrm{M}}}{\partial T}$	$8\,\mathrm{MPa/K}$	$7\,\mathrm{MPa/K}$
Characteristic material volume size	V_{char}	$5\times10^{-23}\,\mathrm{m^3}$	$5\times10^{-23}\,\mathrm{m^3}$
Time constant of the phase fraction $0\,\mathrm{Hz} < \lvert f\rvert < 2\,\mathrm{Hz}$ $2\,\mathrm{Hz} < \lvert f\rvert < 10\,\mathrm{Hz}$	τ_ξ	 $0.001\,\mathrm{s}$ $0.0001\,\mathrm{s}$	 $0.001\,\mathrm{s}$ $0.0001\,\mathrm{s}$
Dissipated mechanical work in isothermal cycle	$W_{\mathrm{dis,iso}}$	$0.96\,\mathrm{J/g}$	$0.34\,\mathrm{J/g}$
Adiabatic temperature difference	ΔT_{ad}	$+20.5\,\mathrm{K}$ $-18.4\,\mathrm{K}$	$+20.2\,\mathrm{K}$ $-19.5\,\mathrm{K}$
Ideal material *COP* for heating	$COP_{\mathrm{heat,ideal}}$	9.9	27.6
Ideal material *COP* for cooling	$COP_{\mathrm{cool,ideal}}$	8.9	26.6

Table 5.5: EC system model parameters: SMA model material parameters for *NiTi#3* validated in section 5.4.

5.5.3 Solver settings

The solver settings are presented in Table 5.6. The size of the time step (t_{step}) is chosen as a trade-off between the amount of data for each simulation and the ability to visualize the results. The simulation duration (t_{end}) is chosen to achieve a steady operational behavior of the EC HP and reduce the amount of data. Due to the changing rotation frequency and flow velocities over all performed simulations, the simulation duration is adapted automatically by using an error function to detect the stationary operation behavior for the individual simulation, as described in section 5.3.
The solver type is set to the standard solver *ode113* as described in subsection 5.4.4 with the specified relative and absolute tolerances. The number fluid element is set to the standard value as described in subsection 5.4.3. This is a trade-off between the amount of data for each simulation, accuracy, and computation time.
In addition to these solver settings, one can adjust the individual solver parameters of the EC system by modifying the corresponding values in the parameter set table.

Name	**Symbol**	**Standard value**	**Variation**	**Study in section**
Time step	t_{step}			
$0\,\text{Hz} < \lvert f \rvert < 5\,\text{Hz}$		0.001 s	-	-
$5\,\text{Hz} < \lvert f \rvert < 10\,\text{Hz}$		0.0005 s	-	-
Simulation duration	t_{end}	10 s	8–120 s	-
Solver type	-	ode113	ode113, ode15s, ode23(s/t/tb), ode45	5.4.4
Relativ tolerance	Tol_{rel}	1×10^{-5}	-	-
Absolute tolerance	Tol_{abs}	1×10^{-5}	-	-
Fluid element number discretization	N_{fld}	360	18–2880	5.4.3

Table 5.6: EC system model parameters: Solver settings.

5.5.4 Design parameter

The design parameters of the EC HP, which can only be changed during the development process, are presented in Table 5.7.
The standard values from system diameter to total SMA mass are taken from the realized EC HP system, as described in section 5.1.
The standard cam track is a replica of the realized system. To present the impact on the thermo-mechanical behavior of the EC HP and the versatile implementation of the

simulation tool, various cam tracks are studied in this work using linear equations or mathematical functions, as indicated in Figure 5.6. This feature is particularly useful for analyzing the thermo-mechanical behavior of a heat engine with a defined load stiffness, as discussed in section 5.8.

In addition, the implemented simulation tool is able to study the overall EC HP efficiency by considering the friction losses caused by the motion of the mechanical parts, the thermal losses due to the thermal conductivity of the walls, as shown in Figure 5.10, and the losses related to the efficiency of the fans. The parameters to simulate the rolling friction of the cam rollers and wall's thermal conductivity are limited to the typical values found in the literature. To account for the viscous losses of the flow, the resulting pressure drop in the duct is correlated with different fan types as introduced in Figure 5.15.

To increase the maximum meaningful temperature difference of the inlets while keeping the same EC material, the concept of internal heat recovery is discussed and studied in subsection 5.6.12. The angular position of the different ducts, described in Figure 5.12, is selected in an iterative way to demonstrate the potential of this concept.

The cross-flow concept and the internal heat recovery are utilized to demonstrate the versatile architecture of the implemented simulation tool. The adjustments and their parameters can be easily managed in the parameter set table to handle fluid flows of multiple ducts and the interconnection of the flows between these ducts. The ducts are defined by the rotation angle (φ) of the inlets and outlets for each duct, its fluid flow rate $(\dot{V})$, and the individual inlet temperature (T) as a constant or a depending parameter. In addition to these design parameters, the impact of individual designs of the EC system can be studied by adjusting the corresponding values in the parameter set table.

Name	Symbol	Standard value	Variation	Study in section
System diameter	$d_{\mathrm{cam}}, d_{\mathrm{channel}}$	220 mm	25–440 mm	5.6.1
System length	l_{sma}	300 mm	75–1200 mm	5.6.2
Number of bundles	N_{bun}	24	1–720	5.6.4
Number of wires per bundle	N_{wpb}	30 (15x2)	1–720	5.6.4 5.6.9
SMA wire air diameter water	d_{sma}	200 µm 500 µm	25–1000 µm 100–5000 µm	5.6.8 5.7.2
Total SMA mass	m_{sma}	42.9 g	1.4–85.7 g	5.6.9
Layer distance in bundle	lh_{lay}	3.34 mm	-	-
Wire distance in layer	lw_{lay}	0.7 mm	-	-
Cam stroke max	-	(15) in fig. 5.90	(1-8) in fig. 5.90	5.6.16
Cam stroke range	-	(15) in fig. 5.94	(1-8) in fig. 5.94	5.6.17
Cam geometry	-	(1) in fig. 5.98	(1-8) in fig. 5.98	5.6.18
Fluid channel height	lh_{channel}	8 mm	-	-
Fluid duct midpoint	$(\varphi_{\mathrm{hi}} + \varphi_{\mathrm{ho}})/2$ $(\varphi_{\mathrm{ci}} + \varphi_{\mathrm{co}})/2$	90° 270°	- -	- -
Fluid duct length	$\varphi_{\mathrm{hi}} - \varphi_{\mathrm{ho}}$ $\varphi_{\mathrm{ci}} - \varphi_{\mathrm{co}}$	140° 140°	10–170° 10–170°	5.6.3 5.6.3
Friction in cam rollers	μ_{cam}	0	0–0.01	5.6.13
Wall heat conductivity	κ_{wall}	0 W/(m · K)	0–0.2 W/(m K)	5.6.14
Viscous/Fan losses	P_{fan}	0 W	see fig. 5.16	5.6.15
Heat recovery duct inlet	φ_{hhri} φ_{chri}	160° 340°	- -	- -
Heat recovery duct length	$\varphi_{\mathrm{hhri}} - \varphi_{\mathrm{hhro}}$ $\varphi_{\mathrm{chri}} - \varphi_{\mathrm{chro}}$	0° 0°	0–45° 0–45°	5.6.12 5.6.12
Heat engine rotational inertia	I	0 kg/m^2	0–0.097 kg/m^2	5.8.2
Heat engine load stiffness	k_{load}	0 Nm/Hz	0–1000 Nm/Hz	5.8.2

Table 5.7: EC system model parameters: Design parameters.

5.5.5 Operating parameter

The operating parameters that can be modified during the operation of the EC HP are summarized in Table 5.8. The inlet temperatures of the hot and cold duct, along with the temperature span, as well as the rotation frequency, can be utilized to adjust the operation of the EC HP according to the current environmental conditions. Consequently, the trends when each parameter is altered are studied and discussed in this work.
The flow rates for hot and cold ducts are chosen based on values from the literature for air and water applications. Additionally, the flow rate for the EC HP with heat recovery, as shown in Figure 5.12, demonstrates the capacity of the simulation tool to simulate flow rates over several magnitudes.
Besides these operating parameters, the impact of individual designs with varying operation spans of the EC system can be studied by adjusting the corresponding values in the parameter set table.

Name	**Symbol**	**Standard value**	**Variation**	**Study in section**
Inlet temperatures level	$(T_{\mathrm{hi}} + T_{\mathrm{ci}})/2$	20 °C	0–40 °C	5.6.5
Inlet temperatures span	$T_{\mathrm{hi}} - T_{\mathrm{ci}}$	0 K	0–40 K	5.6.6
Rotation frequency	f			
with air		0.5 Hz	−2 Hz to 2 Hz	5.6.7
with water		5 Hz	−10 Hz to 10 Hz	5.7.1
Flow rate	$\dot{V}_{\mathrm{h}}$, $\dot{V}_{\mathrm{c}}$			
with air		50 $\mathrm{m^3/h}$	5–200 $\mathrm{m^3/h}$	5.6.7
with water		5 L/min	1–20 L/min	5.7.1
Cross-flow rate	$\dot{V}_{\mathrm{hc}}$, $\dot{V}_{\mathrm{ch}}$	0 $\mathrm{m^3/h}$	0–25 $\mathrm{m^3/h}$	5.6.11
Heat recovery flow rate	$\dot{V}_{\mathrm{hhr}}$, $\dot{V}_{\mathrm{chr}}$	0 $\mathrm{m^3/h}$	0–500 $\mathrm{m^3/h}$	5.6.12

Table 5.8: EC system model parameters: Operating parameters

5.6 Parameter studies using air as fluid

In this section, the calibrated and validated simulation tool, along with its sub-tools, is utilized to investigate the thermo-mechanical behavior of the EC HP with air as HE and HT fluid.

To simulate the presented parameter studies, the fluid properties of Table 5.4, the SMA properties of Table 5.5, the solver settings of Table 5.6, as well as the design and operating parameter of Table 5.7 and Table 5.8 are used. The standard values summarized in section 5.5 are used unless otherwise mentioned. The presented parameter studies follow the calculation procedure introduced in section 5.3. They are organized in the *parameter set table*, simulated with the *simulation tool*, using the *parallel computation tool*, and evaluated using the *parameter comparison tool*, as well as the *visualization tool*.
The most of these parameter studies are performed with the commercially available SMA material NiTiCo. To outline the potential of using an optimized EC material, the last studie (subsection 5.6.19) is performed with NiTiCuV.

5.6.1 System diameter

In this part, the design parameter, diameter of the EC HP (d_{channel}), is variated within the range from 25 mm to 440 mm.
Figure 5.38 presents the resulting temperature evolution for the SMA element as dashed line and fluid as solid line along the circumference for the different system diameters. The arrangements of the hot and cold duct are shown in color at the x-axis. The flow

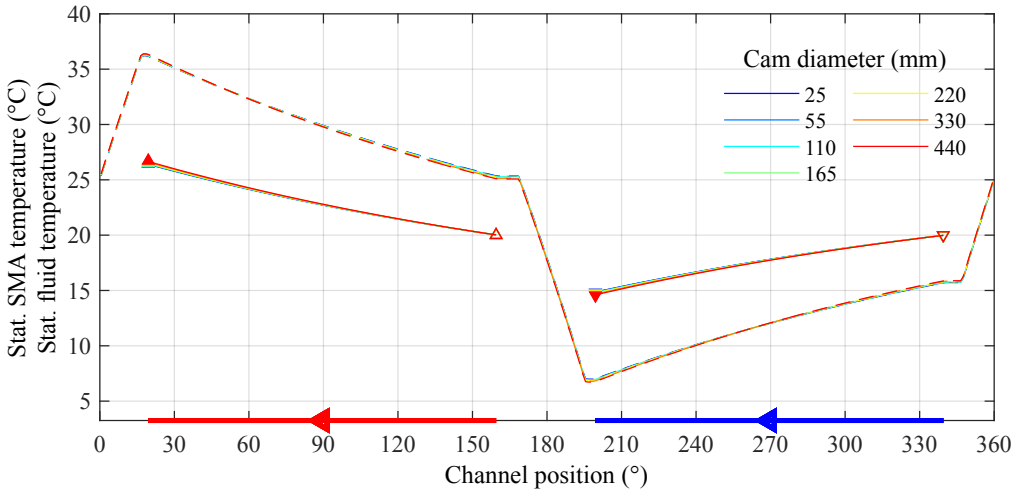

Figure 5.38: System diameter: Resulting SMA element (dashed) and fluid (solid) temperature along the circumference for different system diameters.

direction of the fluid is indicated with an arrow, creating a counter-flow in both ducts due to the clockwise rotation of the SMA arrangement. The temperature of the SMA element increases during loading and decreases during unloading adiabatically due to the suppressed HE in the transition zones. During the motion along the ducts, the SMA elements exchange their thermal energy with the fluid and cool down after loading or heat up after unloading. Therefore, the fluid heats up during traveling along the hot duct and cools down during traveling through the cold duct.

Each temperature curve of the fluid is framed at the edges by triangles that are upturned at the hot duct and downturned at the cold duct. The triangles at the inlets are empty, and the triangles at the outlets are filled.
Due to the same amount of SMA material (m_{sma}) and the loading or unloading characteristic related to the rotation angle (φ), the performed EC cycles leads to nearly the same thermo-mechanical conditions in the SMA element for each system diameter. Therefore, the temperature evolution along the circumference is nearly the same for each system diameter. A closer look shows that the temperature difference of the SMA element, due to the HE in the hot and cold duct, slightly increases with increasing system diameter. The larger system diameter leads to a higher circumferential speed of the SMA (v_{sma}) at the same rotation frequency. This results in an increased heat exchange coefficient (h), following Equation 5.30, at a constant fluid velocity (v_{fld}) due to the rising relative velocity (v_{rel}), following Equation 5.27.
The slightly improved HE at a larger system diameter leads to a larger temperature difference of the SMA in each duct. This allows for starting the PT with a lower temperature for the unloading and with a higher temperature for the loading. As a result, the total temperature range of the SMA element over the whole EC cycle increases. Since the temperature difference caused by the PT remains constant, and the maximum temperature of the SMA after loading increases, while the minimum temperature of the SMA after unloading decreases.
Figure 5.39 shows the thermal and mechanical power, as well as the *COP* of the EC HP over the system diameter. The colors for the system diameter correspond to those of Figure 5.38. The amount of the thermal power at the hot duct, represented by upturned triangles, and at the cold duct, shown as downturned triangles, slightly increases with increasing system diameter due to the larger heat exchange coefficient. Whereas the mechanical power input also slightly increases by the change of the system diameter due to the thermal dependence of the transformation stress as introduced in Equation 2.5 and Equation 2.7. As a result, the *COP* value of the EC HP slightly increases with increasing system diameter.
To summarize, this parameter study indicates that the system diameter varies by more than one and a half orders of magnitude, yet the resulting impact on the thermo-mechanical behavior of the EC HP is less than 5 %. Therefore, the system diameter does not significantly influence the behavior of the EC HP. Thus, it should be kept as small as possible to save design space.

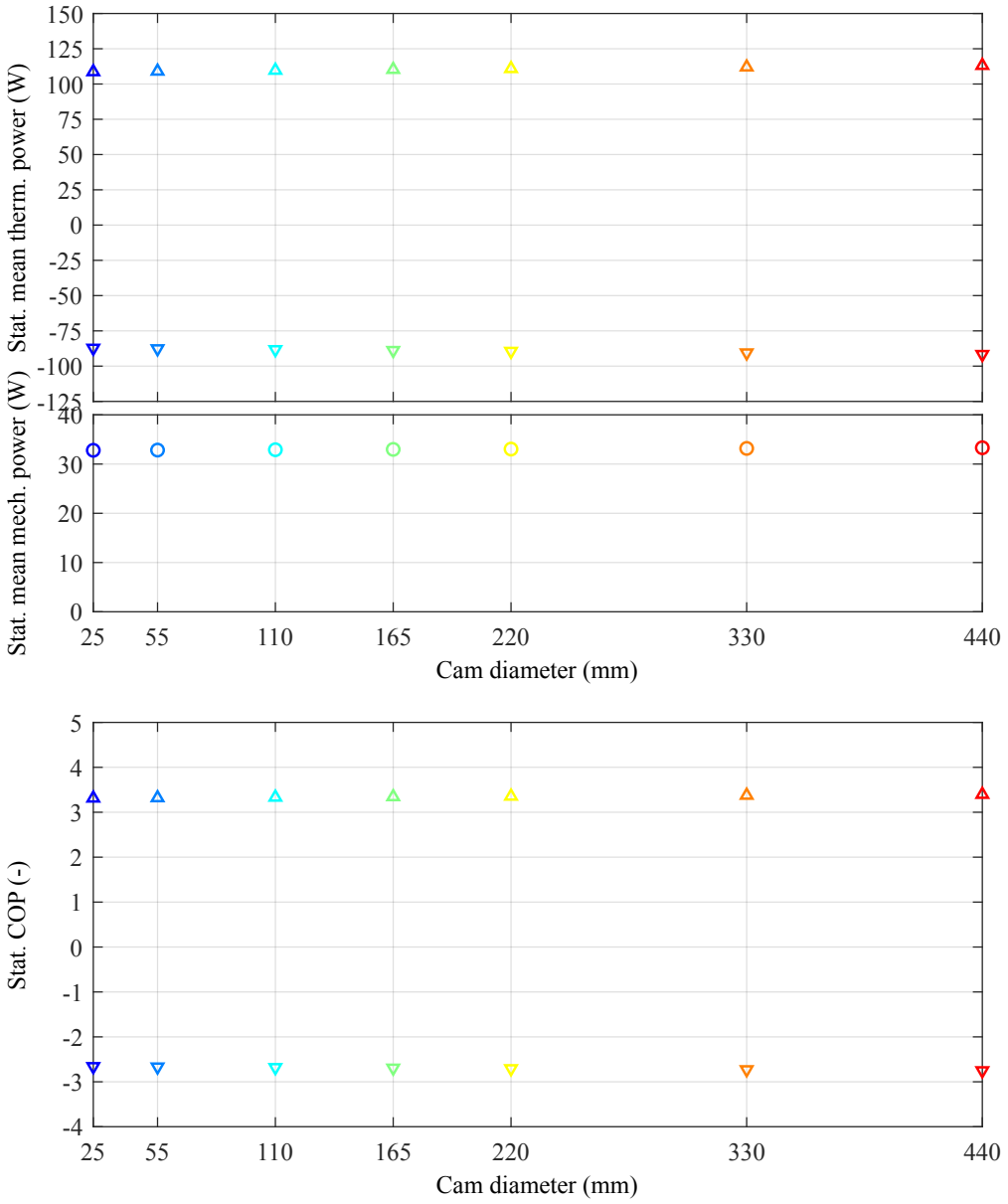

Figure 5.39: System diameter: Resulting thermal and mechanical power and the *COP* of the EC HP for different system diameters.

5.6.2 System length

In this part, the design parameter, length of the EC HP (l_{sma}), is variated within the range from 75 mm to 1200 mm.

Figure 5.40 illustrates the loading profile with its stroke along the circumference for various SMA element lengths in the A state. The arrangements of the hot and cold duct are shown in color at the x-axis. To maintain the thermodynamic conditions of the performed

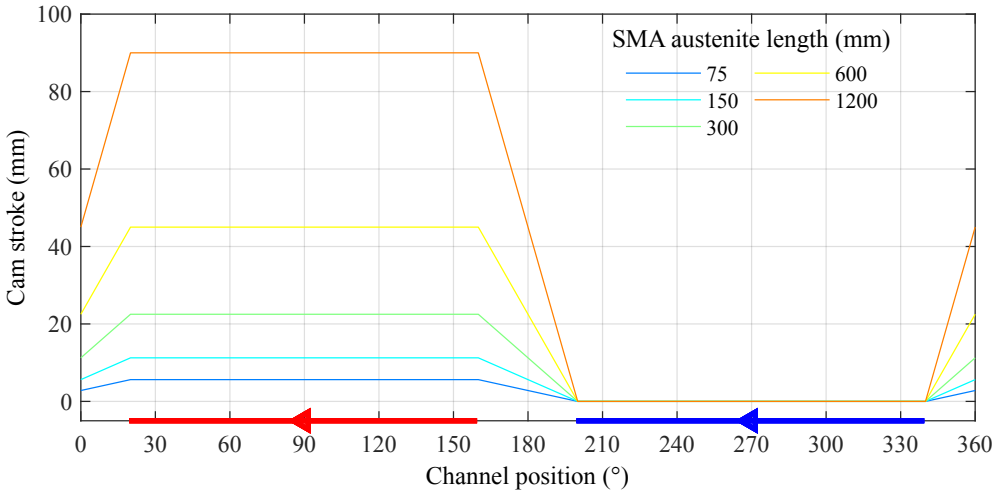

Figure 5.40: System length: Symmetric loading and unloading profiles with different strokes to reach equal maximum strain ($\varepsilon_{\mathrm{max}}$) of 7.5 % for each SMA element length.

EC cycle the maximum strain ($\varepsilon_{\mathrm{max}}$) of 7.5 % is kept constant, thus the maximum stroke is adapted to each SMA length. Therefore, the maximum stroke increases as the system length grows, resulting in a higher slope of the cam track while maintaining strain rate of the SMA element.

Figure 5.41 presents the resulting temperature evolution for the SMA element as dashed line and fluid as solid line along the circumference for the different system lengths. The colors of the system length correspond to those of Figure 5.40. The flow direction of the fluid is indicated with an arrow at the bottom, creating a counter-flow in both ducts due to the clockwise rotation of the SMA arrangement. The temperature of the SMA element increases during loading and decreases during unloading adiabatically due to the suppressed HE in the transition zones (no duct). During the motion along the ducts, the SMA elements exchange their thermal energy with the fluid and cool down after loading or heat up after unloading. Therefore, the fluid heats up while traveling through the hot duct and cools down in the cold duct.

Each temperature curve of the fluid is framed at the edges by triangles that are upturned at the hot duct and downturned at the cold duct. The triangles at the inlets are empty, and the triangles at the outlets are filled.

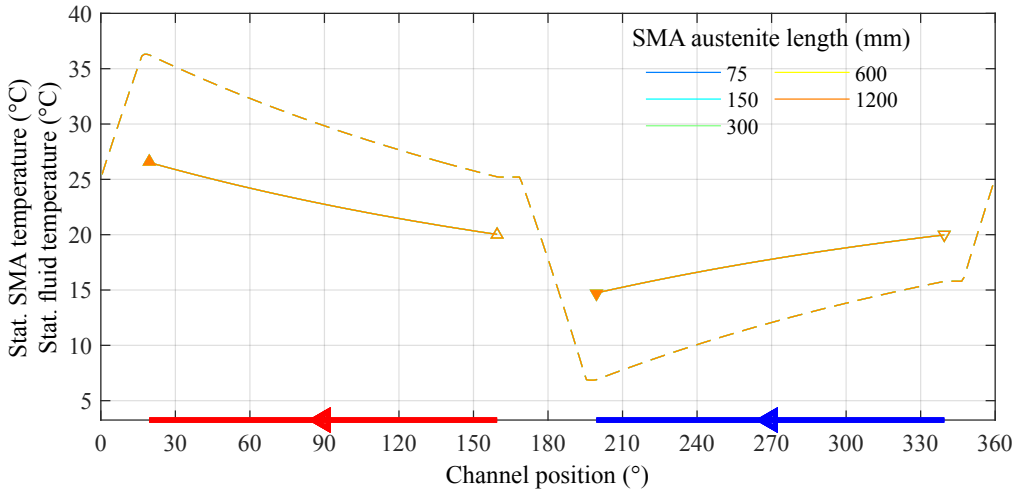

Figure 5.41: System length: Resulting SMA element (dashed) and fluid (solid) temperature along the circumference for different system lengths.

Due to the same ratio between the amount of SMA material (m_{sma}) and width of the fluid duct, as well as the loading or unloading characteristic related to the rotation angle (φ), the performed EC cycles leads to exactly the same thermo-mechanical conditions in the SMA element for each system length. Therefore, the temperature evolution along the circumference is exactly the same for each system length. The increased slope of the loading profile does not influence the temperature difference generated by the PT due to the maintained strain rate in the SMA element.

Figure 5.42 shows the thermal and mechanical power, as well as the *COP* of the EC HP along the system length. The colors of the system length correspond to those of Figure 5.40. The amount of the thermal power at the hot duct, represented by upturned triangles, and at the cold duct, as downturned triangles, increases with increasing system length. This is caused by the enlargement of the SMA mass in the EC HP, thereby the amount of released and absorbed specific latent heat per rotation is increased by larger system lengths. The higher system length also enlarges the fluid flow rate due to the expanded fluid duct. The mechanical power input also increases with system length due to the larger stroke. As a result, the *COP* remains constant over system length variation.

To summarize, this parameter study shows that the system length varies by more than one and a half orders of magnitude, significantly affecting the thermal power output of the EC HP by maintaining the *COP*. The system's length influences are proportional to the amount of SMA material, as well as thermal and mechanical performance.

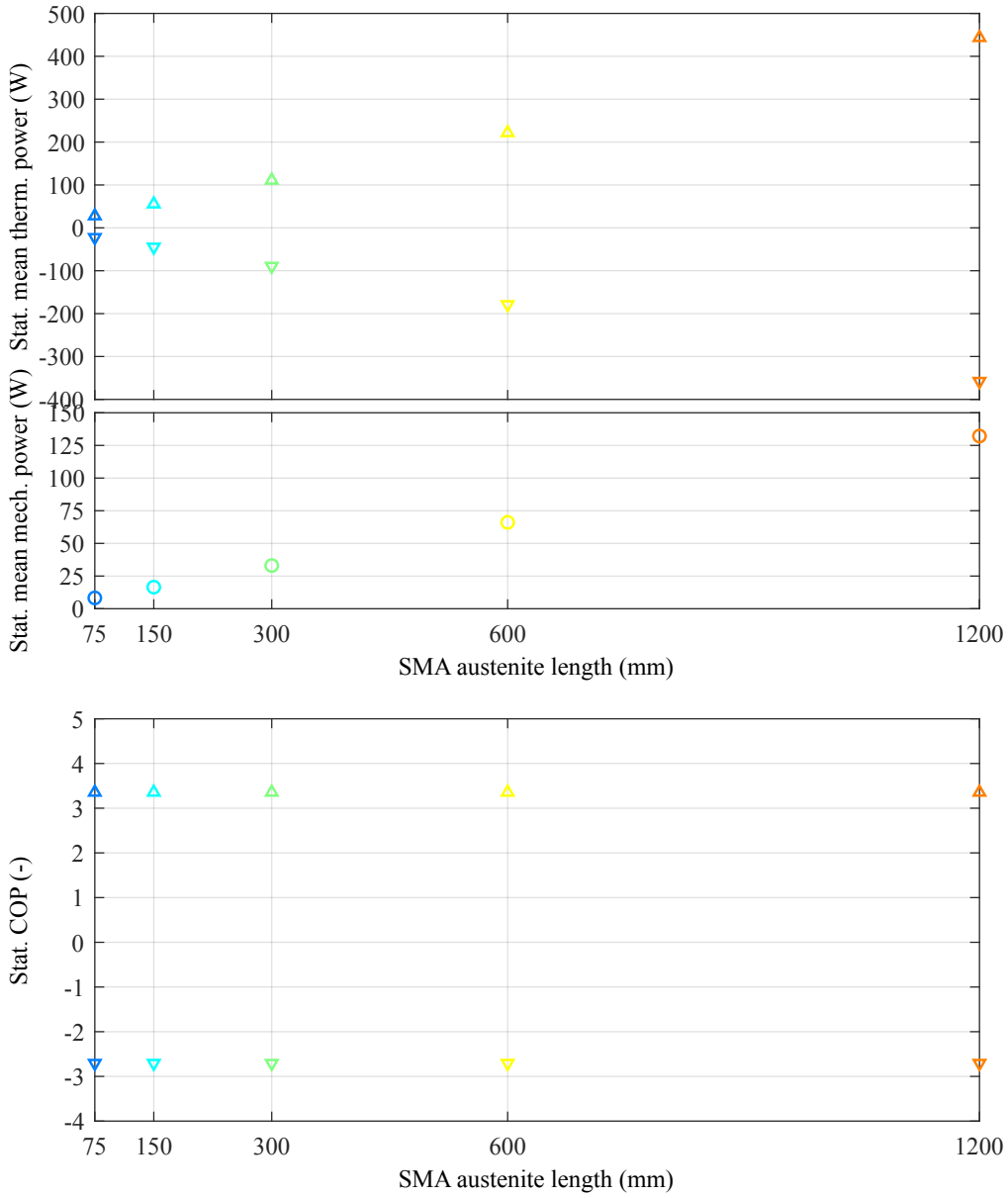

Figure 5.42: System length: Resulting thermal and mechanical power and *COP* for different system lengths.

5.6.3 Angular fluid duct length

In this part, the design parameter, fluid duct's length at the hot and cold duct ($\varphi_{\mathrm{hi}} - \varphi_{\mathrm{ho}}$ and $\varphi_{\mathrm{ci}} - \varphi_{\mathrm{co}}$), is symmetrically variated within the range from 10° to 170° by maintaining the midpoint of the ducts.
Figure 5.43 presents the resulting temperature evolution for the SMA element as dashed line and fluid as solid line along the circumference for the different fluid duct lengths. The arrangements of the hot and cold duct are shown in color at the x-axis as an overlay.

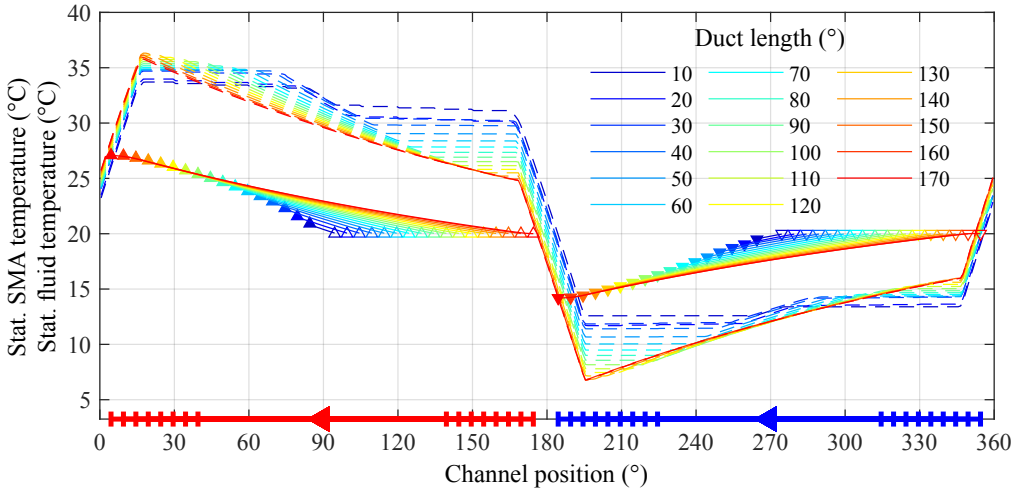

Figure 5.43: Fluid duct length: Resulting SMA element (dashed) and fluid (solid) temperature along the circumference for different fluid duct lengths.

Therefore, only the start and end of the largest ducts are visible. The flow direction of the fluid is indicated by arrows, creating a counter-flow in both ducts due to the clockwise rotation of the SMA arrangement. The temperature of the SMA element increases during loading and decreases during unloading adiabatically due to the suppressed HE in the transition zones. During the motion along the ducts, the SMA elements exchange their thermal energy with the fluid and cool down after loading or heat up after unloading. Therefore, the fluid heats up during traveling along the hot duct and cools down during traveling along the cold duct.
Each temperature curve of the fluid is framed at the edges by triangles that are upturned at the hot duct and downturned at the cold duct. The triangles at the inlets are empty, and the triangles at the outlets are filled.
The temperature difference of the SMA element reached by the HE along the hot and cold duct increases with increasing duct length due to the longer time for HE. This leads to a smaller SMA temperature when the SMA element exits the hot duct and to a larger one at the exit of the cold duct. As a result, the maximum temperature of the SMA after loading increases, while the minimum temperature after unloading decreases, due to the

same temperature change during PT. Finally, the temperature difference of the fluid also increases with increasing duct length due to the longer time for HE.
Figure 5.44 presents the resulting inlet and outlet temperatures of the fluid at hot and cold duct along different fluid duct lengths. The colors of the inlet temperature spans correspond to those of Figure 5.43. The temperature at the hot duct is represented by

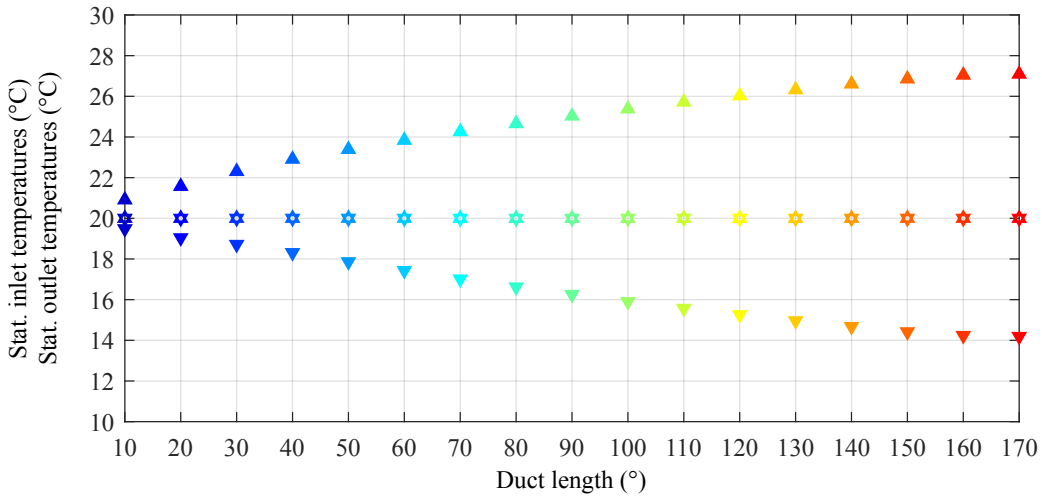

Figure 5.44: Flow rate asymmetry: Resulting inlet and outlet temperature at hot and cold duct along different fluid duct lengths.

upturned triangles and at the cold duct as downturned triangles. The triangles at the inlets are empty, and the triangles at the outlets are filled.
The outlet temperature at the hot and cold duct increases with increasing fluid duct length due to the increasing time for HE, following Equation 5.2 and Equation 5.16. The lower temperature difference at the cold duct is based on asymmetric specific latent heat, which favors heating, as introduced in Equation 5.44 and Equation 5.45.
Figure 5.45 shows the thermal and mechanical power, as well as the *COP* along the fluid duct length. The colors of the fluid duct lengths correspond to those of Figure 5.43. The amount of the thermal power at the hot duct, represented by upturned triangles, and at the cold duct as downturned triangles, significantly increases with increasing length of the fluid ducts due to the longer time for HE, following Equation 5.16. Whereas the mechanical power input also increases with fluid duct length due to the thermal dependence of the transformation stress, as introduced in Equation 2.5 and Equation 2.7. As a result, the *COP* increases with increasing fluid duct length.
In summary, this parameter study shows that the length of the fluid duct varies by more than one and a half orders of magnitude, resulting in a significant impact on the thermo-mechanical behavior of the EC HP. Thereby, the thermal power and *COP* increases by a factor of about four. The longer the length of the fluid duct, the better due to the longer dwell time for HE between SMA element and fluid.

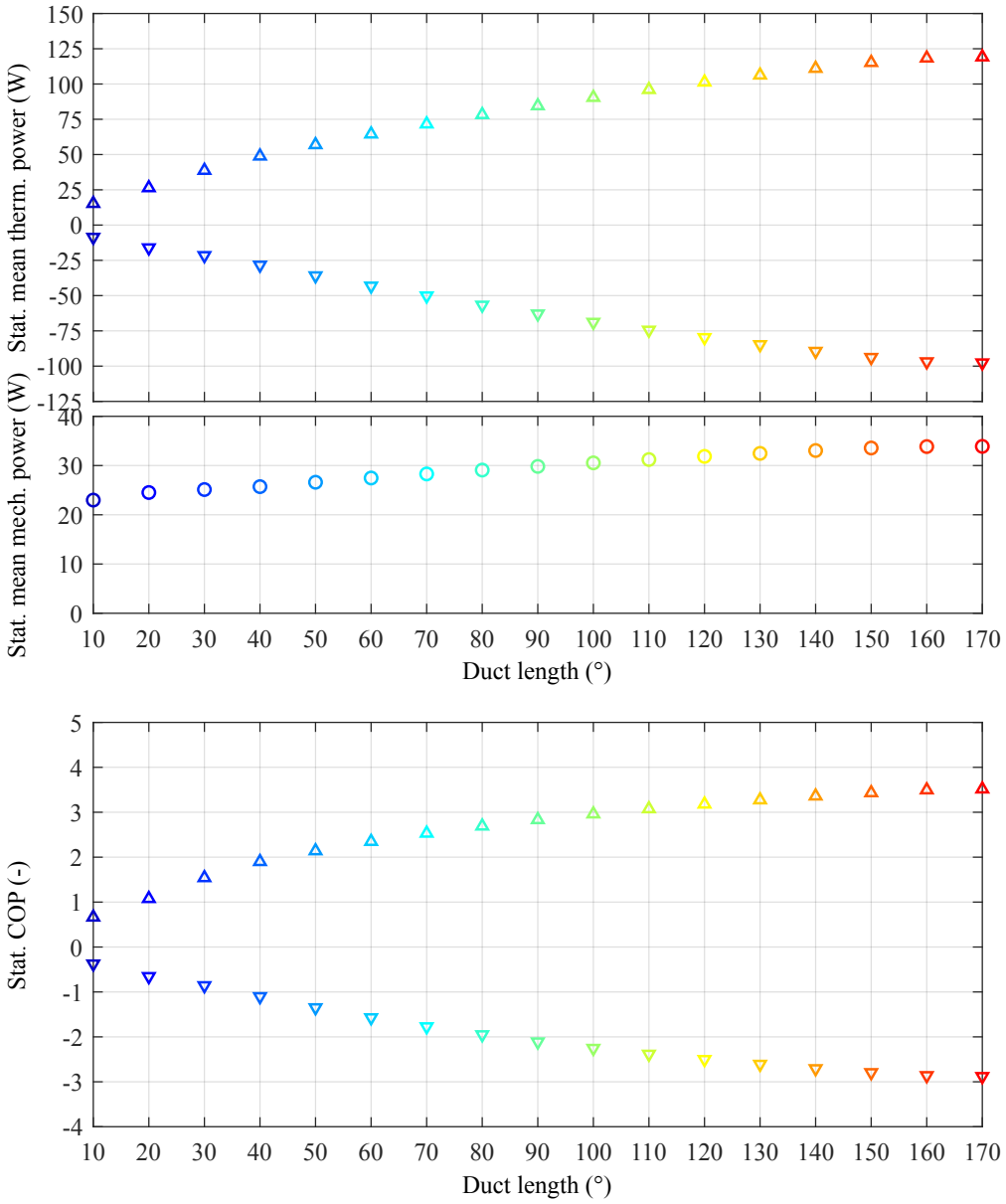

Figure 5.45: Fluid duct length: Resulting thermal and mechanical power and the *COP* of the EC HP for different fluid duct lengths.

5.6.4 Subdivision in SMA elements

In this part, the design parameter number of bundles in the EC HP (N_{bun}) is variated within the range from 1 to 720. To maintain a consistent mass of the SMA material in the system, the number of wires per bundle in the EC HP (N_{wpb}) is adjusted inversely, ranging from 720 to 1.

Figure 5.46 shows a still frame of the EC HP, with a bundle number (N_{bun}) of 1. In this

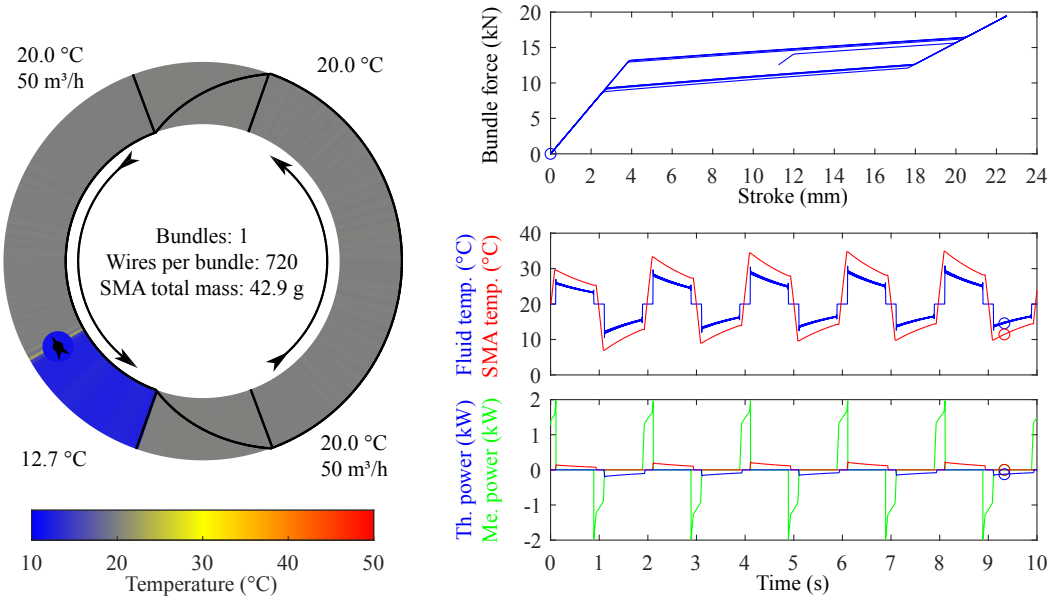

Figure 5.46: Subdivision in SMA elements: Visualization of EC HP cross-section with 1 bundle consisting of 720 SMA wires.

configuration, only either a hot or a cold thermal power output is generated, depending on the location of the single bundle during rotation. Two gaps per rotation occur in the thermal power output when the bundle moves through the transition zones. Additionally, due to the absence of an antagonist bundle during loading or unloading, the mechanical power input also exhibits asymmetric behavior.

Figure 5.47 shows a still frame of the EC HP with two bundles symmetrically arranged around the circumference. In this configuration, a hot and cold thermal power output is generated at the time when the bundles moves through the ducts. A gap still occurs in the thermal power output when the bundles moves through the transition zones. The antagonist bundle enables mechanical energy recovery during the loading or unloading processes. Consequently, the mechanical power is more symmetric compared to only one bundle presented in Figure 5.46. Additionally, the maximum of the mechanical power input is reduced to about a half due to the halved SMA wires number in each bundle.

Figure 5.48 shows a still frame of the EC HP with a bundle number (N_{bun}) of 4. These bundles are symmetrically arranged along the circumference. A hot and cold thermal power output is continuously generated in this configuration. The thermal power output

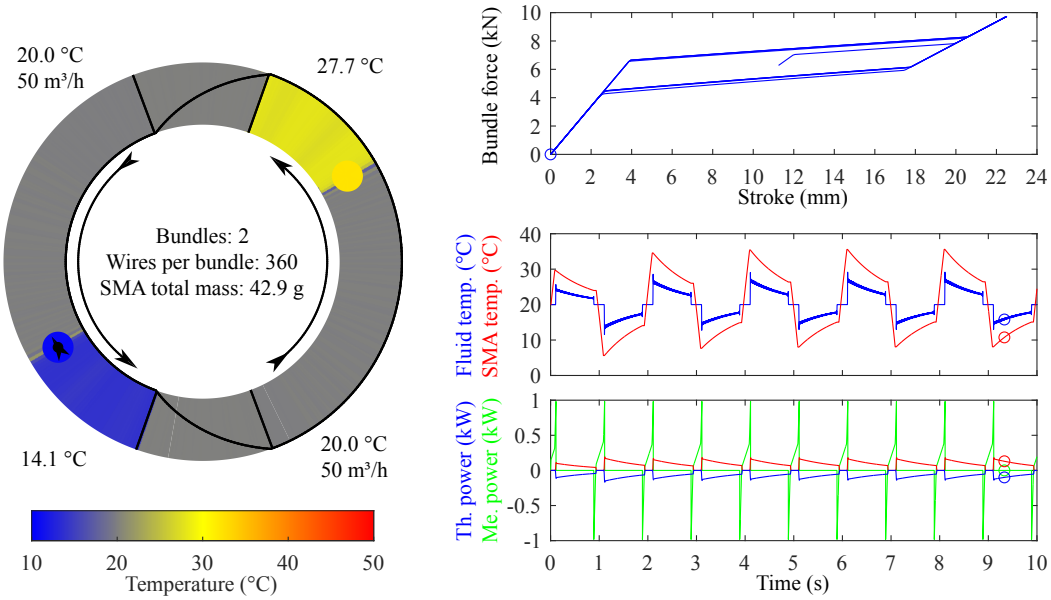

Figure 5.47: Subdivision in SMA elements: Visualization of EC HP cross-section with 2 bundles consisting of 360 SMA wires.

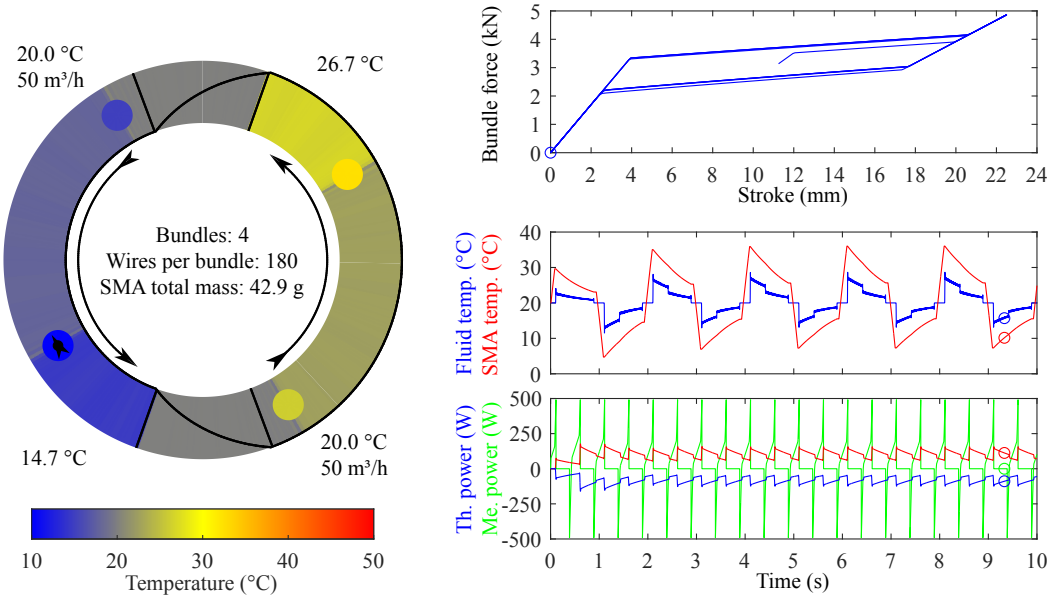

Figure 5.48: Subdivision in SMA elements: Visualization of EC HP cross-section with 4 bundles consisting of 180 SMA wires.

in this SMA arrangement is gapless even when two bundles move through the transition zones since the two other bundles are still traveling through the ducts. Additionally, the maximum of the mechanical power input is reduced to about a quarter due to the quartered SMA wire number in each bundle, compared to the single bundle case.
Figure 5.49 shows a still frame of the EC HP with a bundle number (N_{bun}) of 720, which are symmetrically arranged on the circumference. A hot and cold thermal power output is

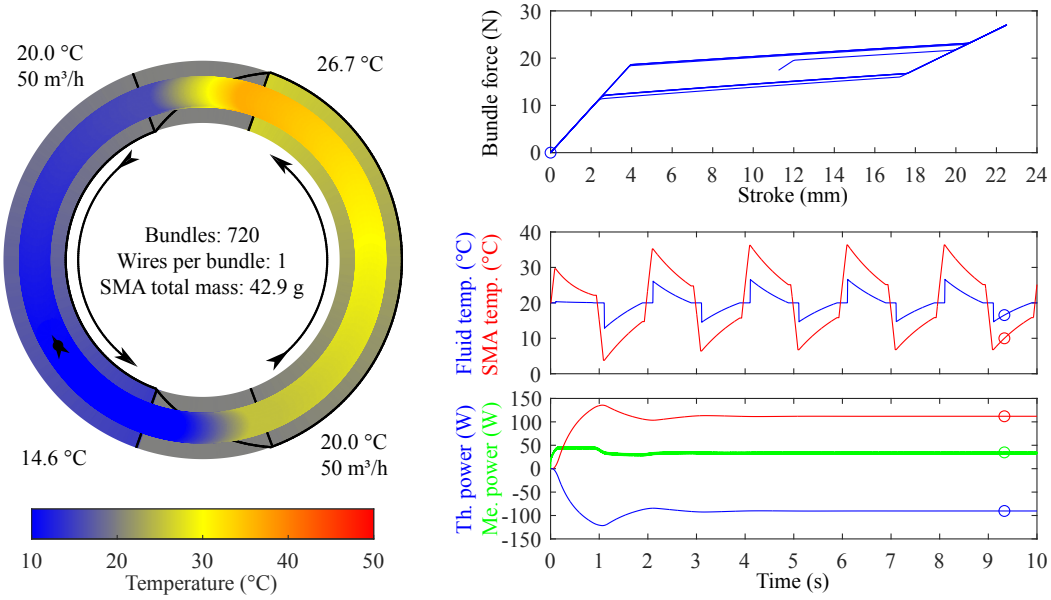

Figure 5.49: Subdivision in SMA elements: Visualization of EC HP cross-section with 720 bundles consisting of 1 SMA wire.

continuously generated in this configuration. The numerous antagonist bundles enable excellent mechanical energy recovery during loading and unloading. The huge number of bundles in the transition zones leads to a very smooth behavior of the mechanical power, compared to four bundles presented in Figure 5.48. Additionally, the maximum of the mechanical power input is drastically reduced since the SMA element contains only one wire.
Figure 5.50 presents the resulting temperature evolution for the SMA element as dashed line and fluid as solid line along the circumference for the different numbers of bundles in the EC HP. The arrangement of the hot and cold duct is shown in color at the x-axis. The flow direction of the fluid is indicated with arrows, creating a counter-flow in both ducts due to the clockwise rotation of the SMA arrangement. The temperature of the SMA element increases during loading and decreases during unloading adiabatically due to the suppressed HE in the transition zones. During the motion along the ducts, the SMA elements exchange their thermal energy with the fluid and cool down after loading or heat up after unloading. Therefore, the fluid heats up while flowing through the hot duct and cools down in the cold duct.

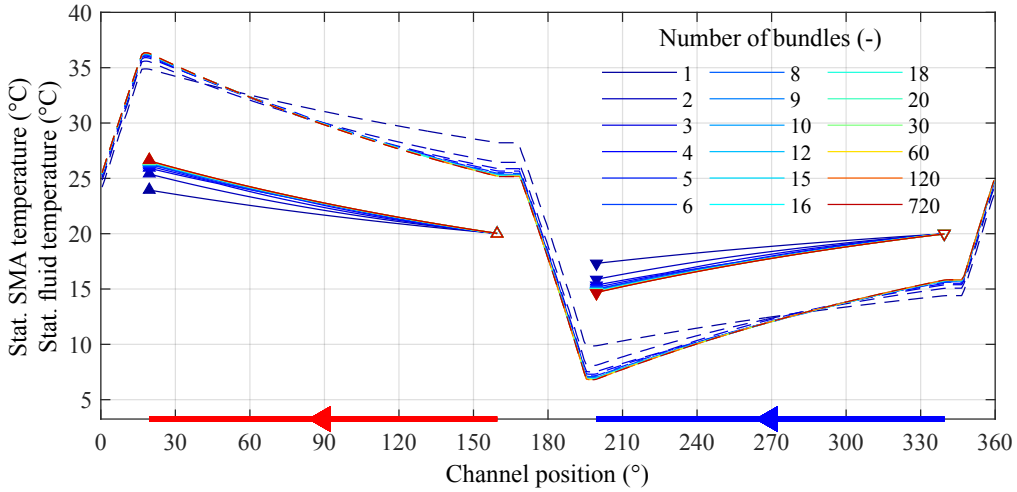

Figure 5.50: Subdivision in SMA elements: Resulting SMA element (dashed) and fluid (solid) temperature along the circumference for different subdivision of SMA elements.

For lower bundle numbers, combined with the large thermal energy provided by an individual SMA element, the HT in the fluid restricts the HE between SMA and fluid. The small number of bundles heats or cools the surrounding fluid and due to the decreasing temperature difference no further HE occurs until new fluid will surround the SMA element, following Equation 5.16.

Suppose the number of bundles in the EC HP increases, then the thermal energy in the SMA arrangement will be more distributed along the circumference. With this, the thermal energy provided by the individual SMA element will decrease, leading to a smaller influence of the insufficient HT in the fluid.

Figure 5.51 shows the resulting average temperature of the fluid during one rotation, represented by upturned triangles at the hot duct and downturned ones at the cold duct, for different subdivisions in SMA elements. The triangles at the inlets are empty, and the triangles at the outlets are filled. The colors correspond to those of Figure 5.50. The outlet average temperature reaches a constant value at a bundle number (N_{bun}) greater than 12.

Figure 5.52 presents in detail the resulting maximal and minimal fluid temperatures of the hot and cold duct outlets during one rotation in stationary operation for different subdivisions in SMA elements. The triangles representing the fluid temperature at the hot duct outlet are empty, and the triangles for the cold duct outlet are filled. The maximal temperature is represented by upturned triangles, and the minimal temperature is shown as downturned triangles. The colors correspond to those of Figure 5.50. The temperature fluctuation at the outlet during one rotation decreases significantly at both ducts with increasing number of bundles. At a bundle number (N_{bun}) greater than 24 the temperature fluctuation dereases below 0.8 K.

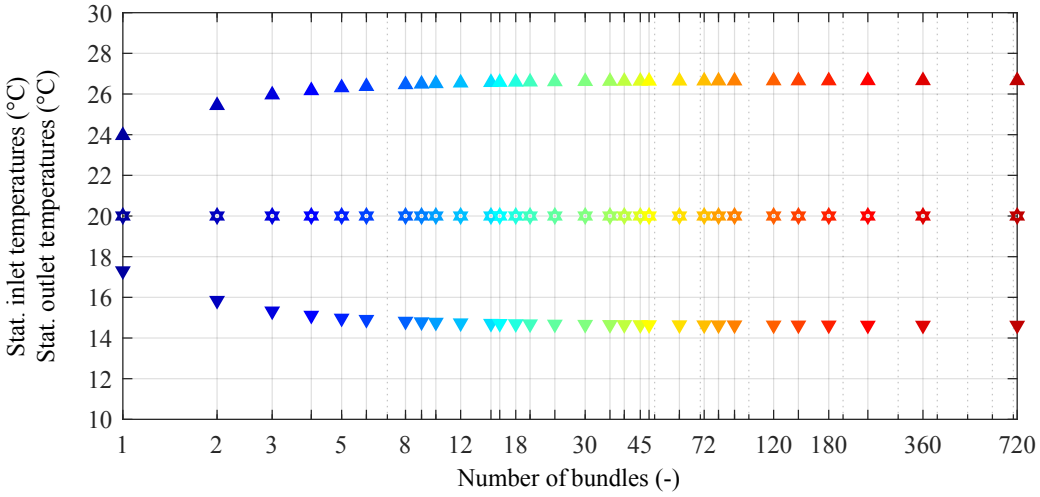

Figure 5.51: Subdivision in SMA elements: Resulting inlet and outlet temperatures of the hot and cold duct for different subdivisions in SMA elements.

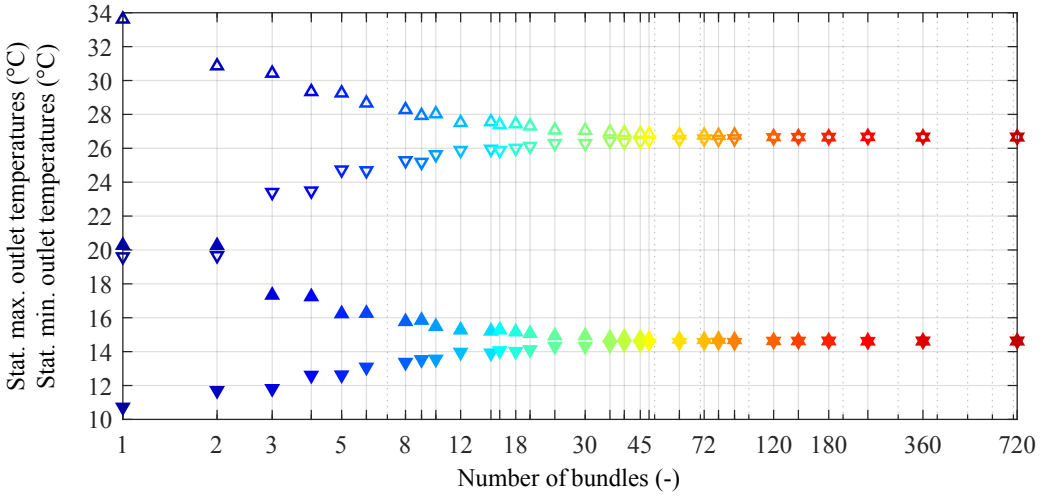

Figure 5.52: Subdivision in SMA elements: Resulting maximal and minimal fluid temperatures of the hot and cold duct outlets in stationary operation for different subdivisions in SMA elements.

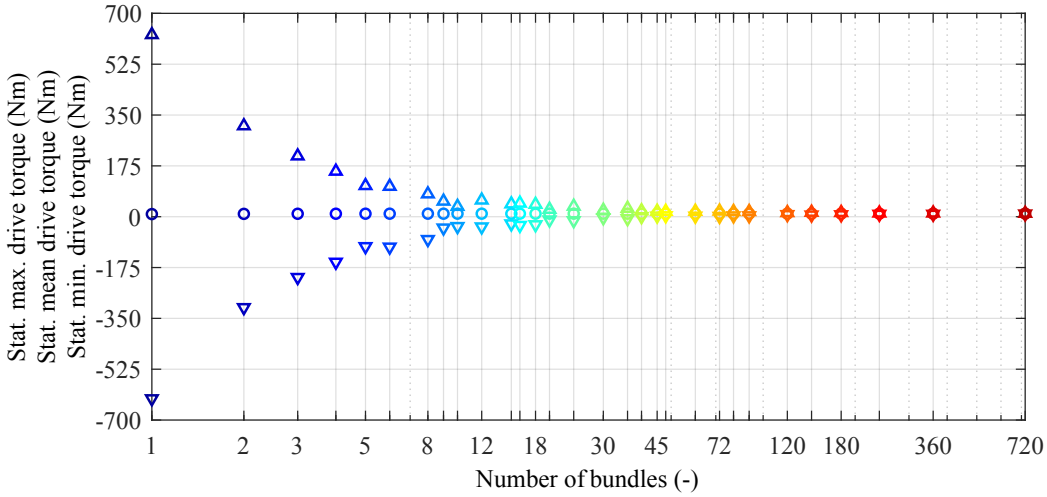

Figure 5.53: Subdivision in SMA elements: Resulting maximal and minimal torque in stationary operation for different subdivisions in SMA elements.

Figure 5.53 presents the resulting maximal and minimal torque during one rotation in stationary operation for different subdivisions in SMA elements. The maximal torque is represented by upturned triangles, the minimal torque by downturned triangles, and the average torque by circles. The colors correspond to those of Figure 5.50. The configuration of the system with an SMA mass of 42.9 g requires a stationary mean torque of 9.5 N m. The torque fluctuation during one rotation decreases significantly with increasing number of bundles. At a bundle number (N_{bun}) greater than 12 the torque fluctuation dereases below 90 N m. Wheras, at a bundle number (N_{bun}) greater than 24 the torque fluctuation dereases below 35 N m.
Figure 5.54 shows the thermal and mechanical power, as well as the *COP* over the number of bundles. The colors of the number of bundles correspond to those of Figure 5.50. Two cases must be distinguished in the following:

- First, the thermo-mechanical behavior of the EC HP for a bundle number (N_{bun}) up to 12 will be discussed. The amount of the thermal power at the hot duct and cold duct significantly increases with increasing number of bundles in the EC HP. This is caused by the improved distribution of the SMA element's thermal energy, and the more uniformly HE between SMA and fluid, following Equation 5.16. As the number of bundles increases, the average mechanical power input also rises, despite the more efficient energy recovery. This increase is attributed to the rising temperature difference and the thermal dependence of the transformation stress, as introduced in Equation 2.5 and Equation 2.7. As a result, the *COP* increases with increasing number of bundles.

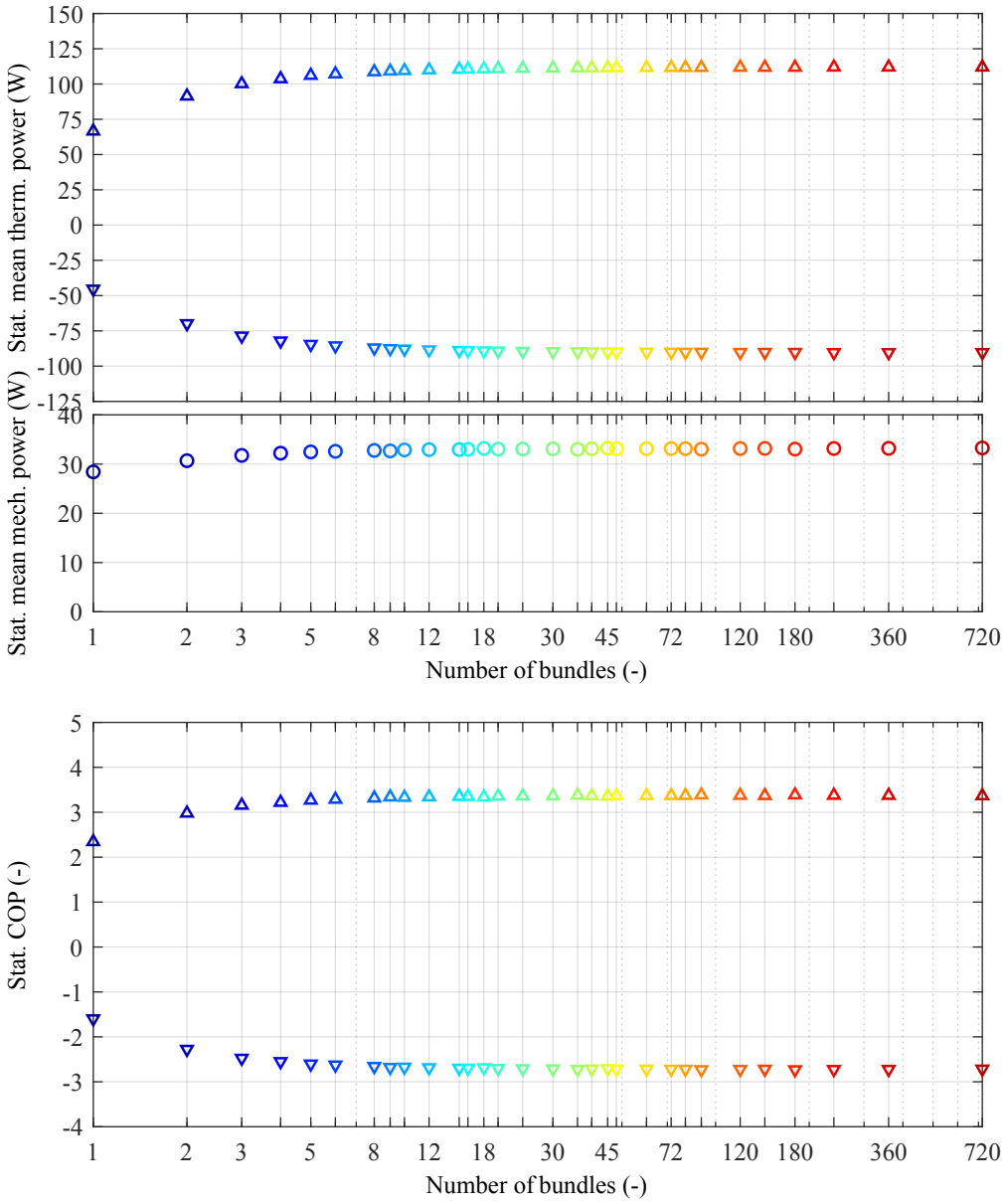

Figure 5.54: Subdivision in SMA elements: Resulting thermal and mechanical power and the *COP* of the EC HP for different subdivisions in SMA elements.

- The thermo-mechanical behavior of the EC HP for a bundle number (N_{bun}) greater than 12 show no influence on the changing bundle number. At this point, the chosen parameters of the HE suit each other to perform a reliable EC cycle.

In summary, this parameter study shows that the number of bundles has a significant impact on the thermo-mechanical behavior of the EC HP, which results in reduced thermal power and *COP* for smaller bundle numbers. The subdivision of the SMA material symmetrically along the circumference reduces the ripple in the mechanical and thermal power as the number of SMA elements increases. The bundle number must be sufficiently high to enable uniform thermal energy distribution around the circumference. No further significant improvements are observed when the number of bundles reaches more than 12.

5.6.5 Inlet temperature level

In this section, the operating parameter inlet temperature level of the EC HP is varied in the range from 0 °C to 40 °C by maintaining a temperature span of 0 K between hot and cold inlet.
Figure 5.55 presents the resulting temperature evolution for the SMA element as dashed line and fluid as solid line along the circumference for the different inlet temperature levels. In this parameter study, the temperature level for the hot and cold duct is simultaneously

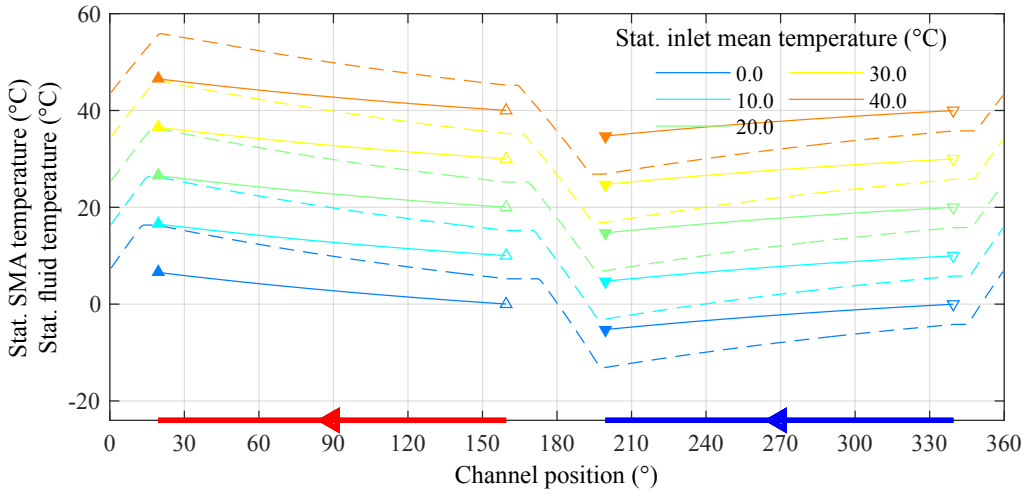

Figure 5.55: Inlet temperature level: Resulting SMA element (dashed) and fluid (solid) temperature along the circumference for different inlet temperature levels.

varied. The arrangements of the hot and cold duct are shown in color at the x-axis. The flow direction of the fluid is indicated with an arrow, creating a counter-flow in both ducts. The temperature of the SMA element increases during loading and decreases during unloading adiabatically due to the suppressed HE in the transition zones. The SMA material undergoes complete PT in the transition zones. During the motion along

the ducts, the SMA elements exchange their thermal energy with the fluid. Thus, the fluid heats up during traveling along the hot duct and cools down in the cold duct. The temperature difference of the SMA element reached during PT, as well as at the HE with the fluid, is independent of the inlet temperature level of the fluid.
Each temperature curve of the fluid is framed at the edges by triangles that are upturned at the hot duct and downturned at the cold duct. The triangles at the inlets are empty, and the triangles at the outlets are filled. The temperature difference of the fluid is also independent of the inlet temperature level of the fluid. This leads to the assumption that the thermo-mechanical conditions are the same for each EC cycle.
Figure 5.56 presents the resulting stress-strain diagram of one SMA element for the different inlet temperature levels. The colors of the different inlet temperature levels correspond to those of Figure 5.55. The hysteresis height decreases with higher temperature levels

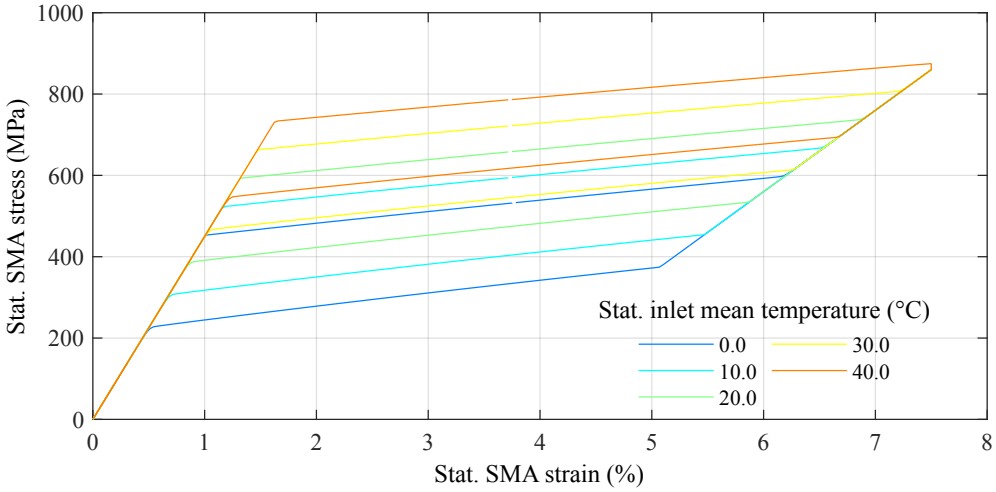

Figure 5.56: Inlet temperature level: Resulting stress-strain diagram of one SMA element for the different inlet temperature levels.

since the transformation stress from M to A rises faster with the temperature than the transformation stress from A to M, as introduced in Equation 2.5 and Equation 2.7. However, the hysteresis width increases with temperature due to the difference in slopes for the A and M branche. This is due to the same temperature difference of the SMA achieved during the PTs and HE with the fluid. This consistency is attributed to the linear temperature dependency of the transformation stress.
Figure 5.57 presents the resulting inlet and outlet temperatures of the fluid at hot and cold duct along the different inlet temperature levels. The colors correspond to those of Figure 5.55. The temperature at the hot duct is represented by upturned triangles and at the cold duct as downturned ones. The triangles at the inlets are empty, and the outlets are filled. The temperature difference remains constant for different inlet temperature levels due to the similar thermo-mechanical conditions during the EC cycles.

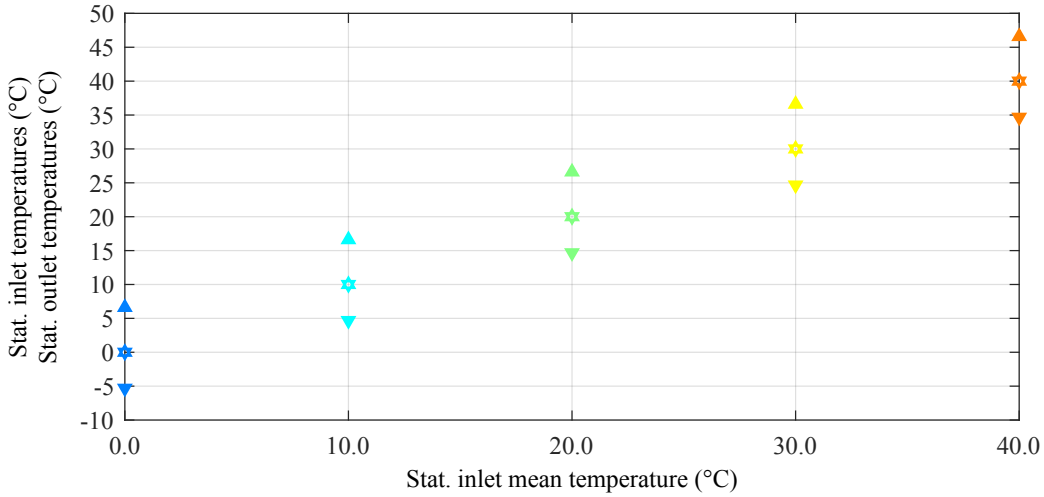

Figure 5.57: Inlet temperature level: Resulting inlet and outlet temperatures at hot and cold duct for different inlet temperature levels.

Figure 5.58 shows the thermal and mechanical power, as well as the *COP* for the different inlet temperature levels. The colors and triangles correspond to those of Figure 5.55. The amount of the thermal power at the hot duct and cold duct remains constant for different inlet temperature levels. This is caused by the same temperature difference between the SMA and the fluid, and the same HE conditions, following Equation 5.16.
The mechanical power input is nearly identical for the different inlet temperature levels since the effects of decreased hysteresis height and increased hysteresis width when increasing the SMA temperature, cancel each other out for this specific material.
The *COP* value remains consistent throughout the parameter study because of the equal thermal and mechanical power for the different inlet temperature levels.
To summarize, this parameter study demonstrates that the variation in the inlet temperature level of the fluid ducts does not affect the mechanical power for *NiTi#3*. The thermal power output is kept constant when the EC cycles are conducted under similar thermo-mechanical conditions. This requirement is met if the stress of SMA during FT does not exceed the material's tensile strength, and the temperature of the SMA during BT does not fall below the austenite finish temperature.

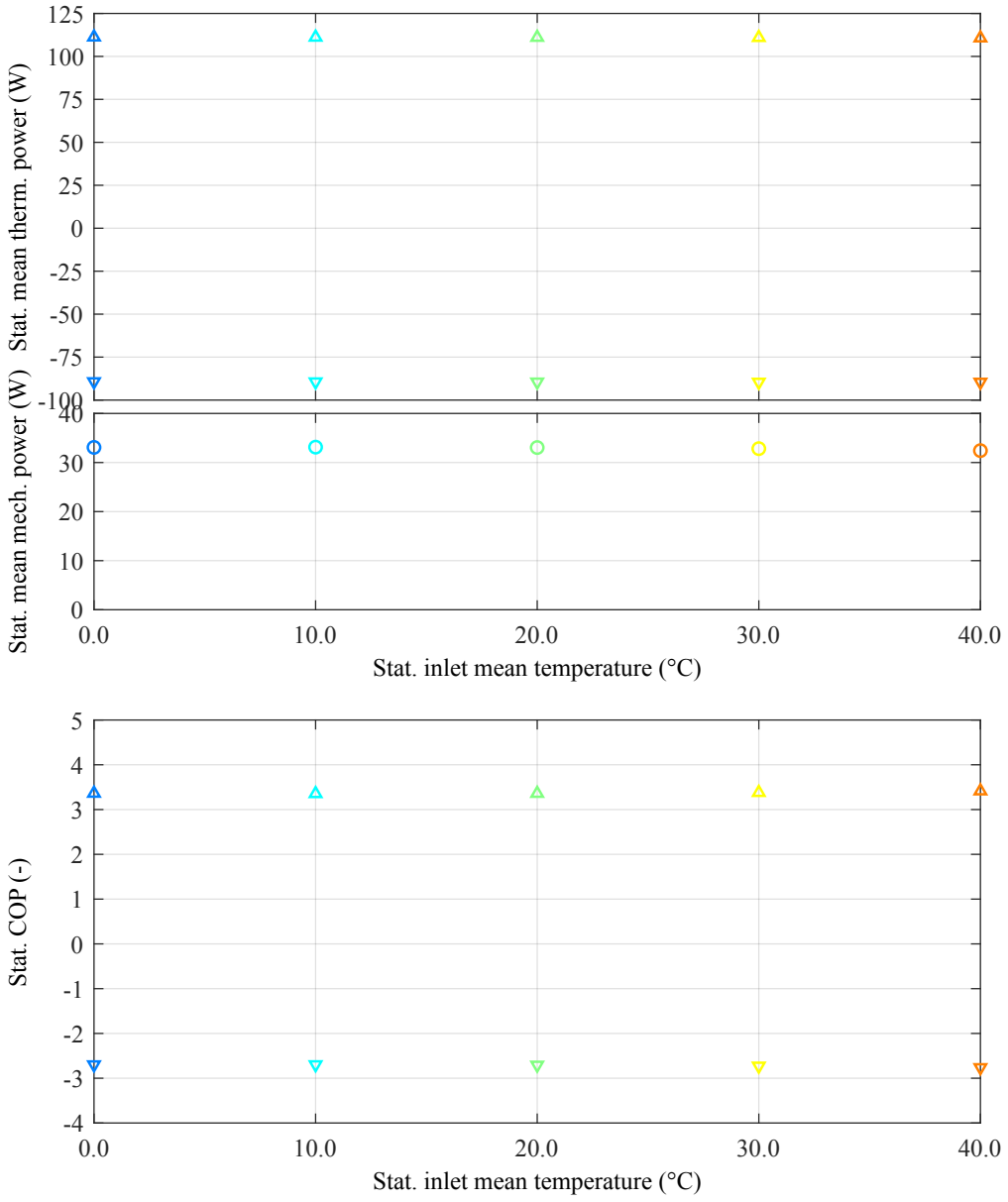

Figure 5.58: Inlet temperature level: Resulting thermal and mechanical power and *COP* for different inlet temperature levels.

5.6.6 Inlet temperature span

In this section, the operating parameter inlet temperature span is varied symmetrically in the range from 0 K to 24 K, while maintaining a mean temperature level of 20 °C for hot and cold inlet.

Figure 5.59 presents the resulting temperature evolution of the SMA element as a dashed line and of the fluid as solid line along the circumference for the different inlet temperature spans. In this parameter study, the temperature span for the hot and cold duct is

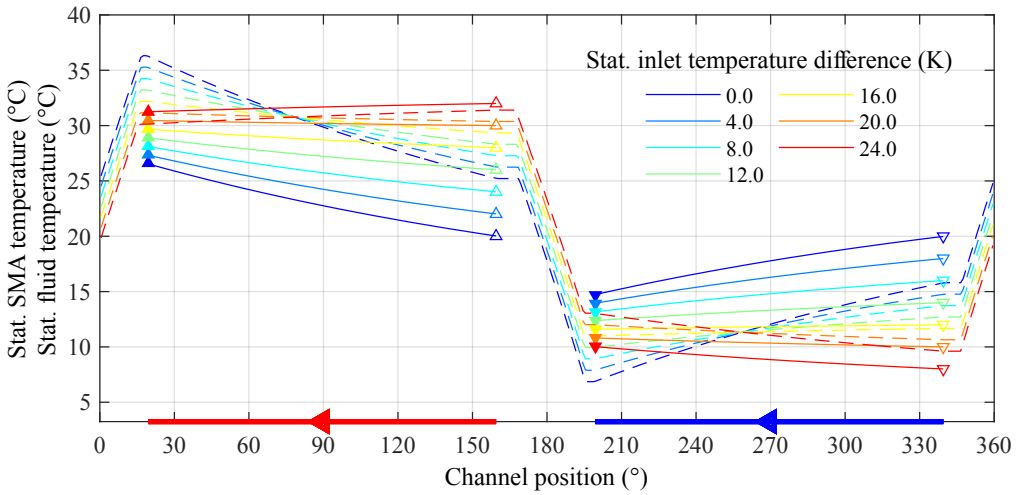

Figure 5.59: Inlet temperature span: Resulting SMA element (dashed) and fluid (solid) temperature along the circumference for different inlet temperature spans.

symmetrically arranged around 20 °C. The arrangement of the hot and cold duct is shown in color at the x-axis. The counter-flow of the fluid is indicated with arrows. The temperature of the SMA element increases during loading and decreases during unloading adiabatically due to the suppressed HE in the transition zones. The SMA material undergoes complete PT in the transition zones. During the motion through the ducts, the SMA elements exchange their thermal energy with the fluid so that the fluid heats up in the hot duct and cools in the cold duct. The temperature difference of the SMA element reached during FT and BT remains constant by the variation of the inlet temperature span of the fluid because this temperature change is defined by the specific latent heat and the specific heat capacity of the SMA. Whereas the temperature difference between the maximum and minimum temperature of the SMA along the EC cycle decreases with increasing inlet temperature span. This is caused by the decreasing temperature difference between the SMA element and the fluid, along with the reduced HE, as described in Equation 5.2.

At the hot duct, the SMA can not exchange sufficiently its thermal energy with the fluid; therefore, the SMA leaves the duct with a high temperature. During the PT from M

to A, the material temperature drops by the prescribed temperature difference but the reached minimum temperature depends on the start temperature; therefore the minimum temperature increases with increasing inlet temperature span of the fluid. At the cold duct, the SMA can not fully exchange its thermal energy with the fluid; therefore, the SMA leaves the duct with a low temperature. During the PT from A to M, the material temperature rises, but the reached maximum temperature depends on the start temperature; thus the maximum temperature decreases with increasing inlet temperature span. The maximum temperature difference of the SMA element along the EC cycle is reached at the minimum inlet temperature span.

Each temperature curve of the fluid is framed at the edges by triangles that are upturned at the hot duct and downturned at the cold duct. The triangles at the inlets are empty, and the ones at the outlets are filled. The temperature difference of the fluid along each duct also decreases by increasing inlet temperature span. This is also caused by the decreasing temperature difference between fluid and SMA and the reduced HE, following Equation 5.16.

Figure 5.60 presents the resulting stress-strain diagram of one SMA element for the different inlet temperature spans. The colors correspond to those of Figure 5.59. The hysteresis

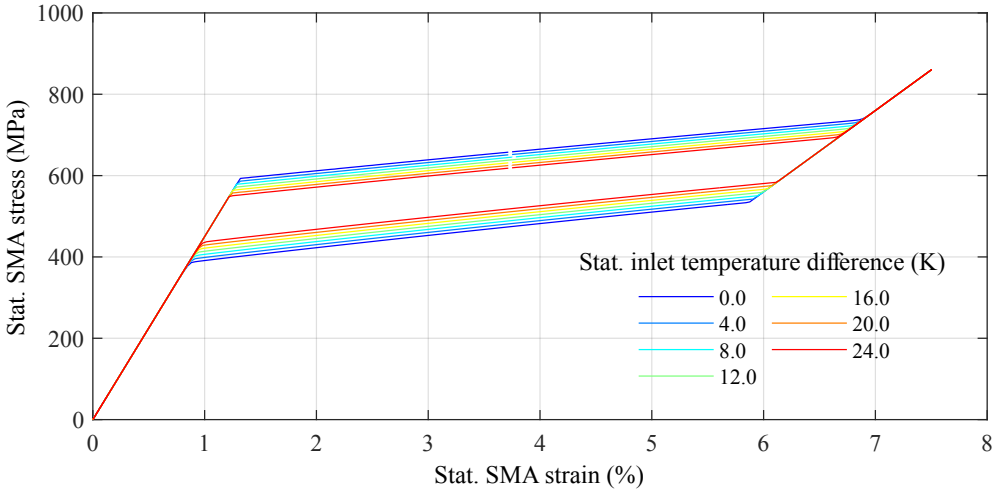

Figure 5.60: Inlet temperature span: Resulting stress-strain diagram of one SMA element for the different inlet temperature spans.

area decreases with increasing inlet temperature span. This is caused by the decreasing temperature difference between the maximum and minimum temperature of the SMA element throughout the EC cycle. This leads to a decreased change in the temperature dependent transformation stress, following Equation 2.5 and Equation 2.7.

Figure 5.61 presents the resulting inlet and outlet temperatures of the fluid at the hot and cold duct for the different inlet temperature spans. The colors correspond to those of Figure 5.59. The hot duct is represented by upturned triangles, and the cold duct by downturned ones. The triangles at the inlets are empty; the outlets are filled. As previously

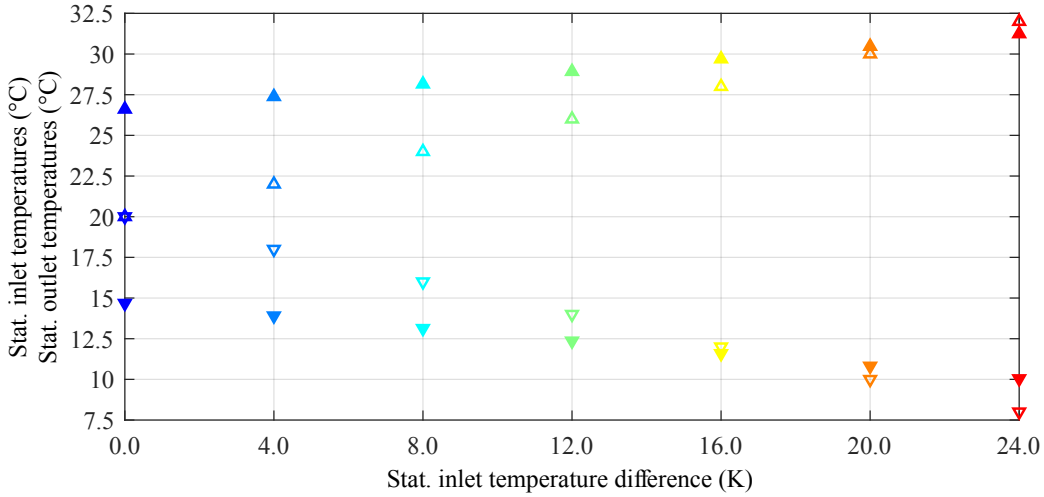

Figure 5.61: Inlet temperature span: Resulting inlet and outlet temperatures at hot and cold duct for different inlet temperature spans.

discussed, the temperature difference decreases with increasing inlet temperature spans. At the point where inlet temperature span exceeds the temperature difference of the SMA reached by the PT, the inlet temperature of the fluid into the hot duct is larger than its outlet. Respectively, the cold duct's inlet temperature is lower than its outlet. Thus, EC HP cools the fluid in the hot duct and heats it in the cold duct.

Figure 5.62 shows the thermal and mechanical power, as well as the *COP* along the inlet temperature spans. The colors correspond to those of Figure 5.59. The amount of the thermal power at the hot duct (upturned triangles), and cold duct (downturned triangles) decreases with increasing inlet temperature span. This is caused by the smaller temperature difference between the SMA and the fluid, and the downgraded HE conditions, following Equation 5.16. If the inlet temperature span is too large, thermal power cools the hot side and heats the cold side.

The mechanical power input also decreases with inlet temperature spans due to the smaller hysteresis area during the performed EC cycles. As a result, the *COP* decreases with increasing inlet temperature spans significantly. If the inlet temperature span is too large, the *COP* value can become negative.

To summarize, this parameter study demonstrates that the variation in the inlet temperature span drastically affects the mechanical and thermal power in- and output of the EC HP. The thermal output power decreases to zero if the temperature difference between both inlets increases up to the adiabatic limit of the SMA material.

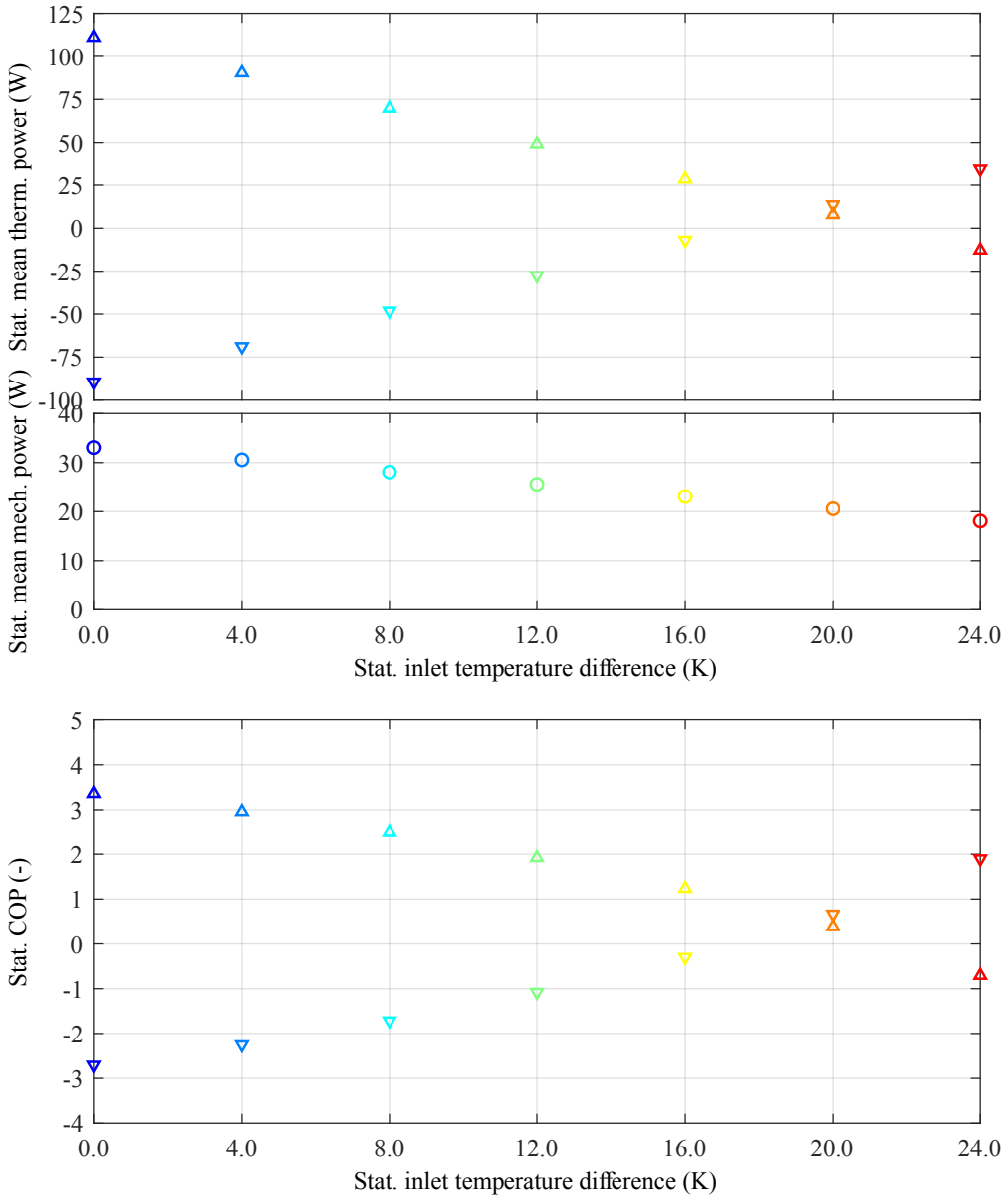

Figure 5.62: Inlet temperature span: Resulting thermal and mechanical power and *COP* for different inlet temperature spans.

5.6.7 Flow rate and frequency with flow direction

In this section, the operating parameter flow rate of the hot and cold duct is varied in the range from 5 m^3/h to 200 m^3/h, along the rotation frequency of the SMA arrangement in the range from -2 Hz to 2 Hz.

Figure 5.63 presents the resulting inlet and outlet temperatures of the fluid at the hot and cold duct along the rotation frequency for different flow rates. The temperature at the hot duct is represented by upturned triangles, and the cold duct is shown as downturned triangles. The triangles at the inlets are empty, and the ones at the outlets are filled. The positive values of the rotation frequency combined with the standard arrangement of

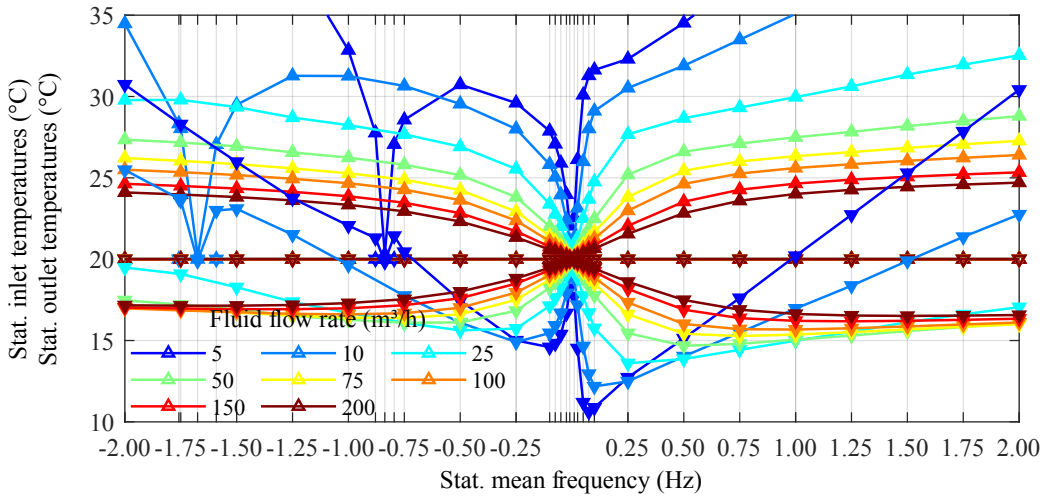

Figure 5.63: Flow rate and frequency: Resulting inlet and outlet temperature at hot and cold duct along the rotation frequency for different flow rates.

the fluid ducts create a counter-flow between the SMAs and the fluid. During negative values of the rotation frequency, the SMA arrangement moves counter-clockwise, and a parallel-flow between SMA and fluid is created for the standard arrangement. Due to the symmetric load profile, a similar EC cycle is generated during loading and unloading for both counter-flow and parallel-flow.

The temperature change of the SMA reached during the PT is defined by the specific latent heat and the specific heat capacity. Therefore, the temperature difference of the SMA element reached during FT and BT remains constant for the variation of the rotation frequency when similar EC cycles are performed. This is fulfilled as long as the PT is performed adiabatically, the stress of SMA during FT does not pass over the tensile strength, and the temperature of the SMA during BT does not fall below the austenite finish temperature.

The thermal energy of the SMA arrangement, which can be exchanged with the fluid, following Equation 5.2 and Equation 5.16, increases with increasing rotation frequency due to growing number of performed EC cycles per time. Therefore, the temperature difference

between inlet and outlet increases with increasing rotation frequency for a specific flow rate. In the case of high enough flow rates, this temperature difference nearly reaches saturation with further increasing rotation frequency. Whereas, if the dwell-time of fluid portion in the duct increases at small flow rates, the temperature difference along each duct increases due to the increasing thermal energy exchanged per fluid volume.
The curve shift of the outlet temperatures towards heating is related to the asymmetric temperature development in the SMA during PT. This is based on the asymmetric specific latent heat, which favors heating, as introduced in Equation 5.44 and Equation 5.45.
At parallel-flow, the falling-in of the outlet temperature is caused by the diminishing relative velocity between SMA element and fluid, as described by Equation 5.27. This reduction in relative velocity leads to a rapid decline in the heat exchange coefficient, ultimately approaching zero, which will be explained in detail below.
The comparison between counter-flow and parallel-flow exhibits a higher temperature difference between the inlet and outlet for the counter-flow. Figure 5.64 presents the resulting temperature evolution for the SMA element as dashed line and fluid as solid line along the circumference for counter-flow and parallel-flow at the standard flow rate. The arrangement of hot and cold duct is shown in color at the x-axis. The flow direction of

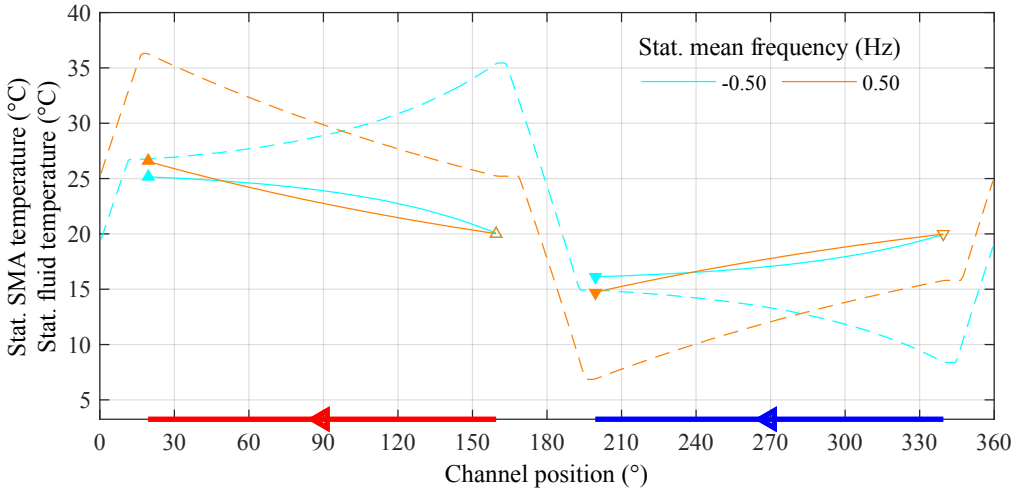

Figure 5.64: Flow rate and frequency: Resulting SMA element (dashed) and fluid (solid) temperature along the circumference for the counter-flow and parallel-flow at a fluid flow rate of 75 m^3/h.

the fluid is indicated with an arrow. For the positive rotation frequency, as indicated in orange, a counter-flow in both ducts is created due to the clockwise rotation of the SMA arrangement. Whereas a parallel-flow in both ducts is created due to the counter-clockwise rotation of the SMA arrangement for the negative rotation frequency indicated in cyan. Each temperature curve of the fluid is framed at the edges by triangles that are upturned at the hot duct and downturned at the cold duct. The triangles at the inlets are empty, and the triangles at the outlets are filled.

The temperature of the SMA element increases during loading and decreases during unloading adiabatically due to the suppressed HE in the transition zones. The SMA material undergoes complete PT in the transition zones. During the motion along the ducts, the SMA elements exchange their thermal energy with the fluid and cool down after loading or heat up after unloading. Therefore, the fluid heats up in the hot duct and cools down in the cold duct.
The temperature difference of the SMA element reached during the FT and the BT remains constant by the variation of the flow condition because this temperature change is defined by the specific latent heat and the specific heat capacity of the SMA. Whereas the temperature difference between the maximum and minimum temperature of the SMA along the EC cycle changes with the flow condition:

- At counter-flow, a SMA element with maximum temperature meets the pre-heated fluid. Therefore, a nearly constant large temperature difference is achieved, leading to a nearly constant HE along the hot duct. This is also realized for the cold duct where a SMA element with minimum temperature meets the pre-chilled fluid. The temperature development of the SMA element and fluid build lines with the same gradients in this diagram at the counter-flow.

- At the parallel-flow, a SMA with maximum temperature meets the fluid of the inlet. In the first part, the temperature difference is larger than the one of the counter-flow, leading to a larger HE in this part of the hot duct. But the SMA rapidly cools down, and the fluid heats up. Therefore, in the second part of the hot duct, the temperature difference is lower than the one of the counter-flow, leading to a lower HE. Furthermore, at the end of the duct, the SMA temperature is too low to significantly heat the fluid. The same effect is observed in the cold duct with the cold SMA and the not pre-chilled fluid. Therefore, the fluid temperature at the outlets does not reach the same values as in counter-flow. The temperature development of the SMA and fluid build lines with opposite gradients in this diagram at the parallel-flow. Due to the insufficient temperature change of the SMA in the ducts, the temperature span of the SMA element along the EC cycle is reduced.

To sum up, a higher temperature difference between inlet and outlet ducts is reached for counter-flow due to the temperature development in the duct, and the increased heat exchange coefficient based on the increased relative velocity for the same rotation frequency and flow rate. Additionally, the temperature difference remains consistent for the counter-flow across all combinations of rotation frequency and flow rate, allowing for improved controllability of the EC HP.
Figure 5.65 shows the thermal and mechanical power, as well as the *COP* over rotation frequency for different flow rates. The colors correspond to those of Figure 5.63. The

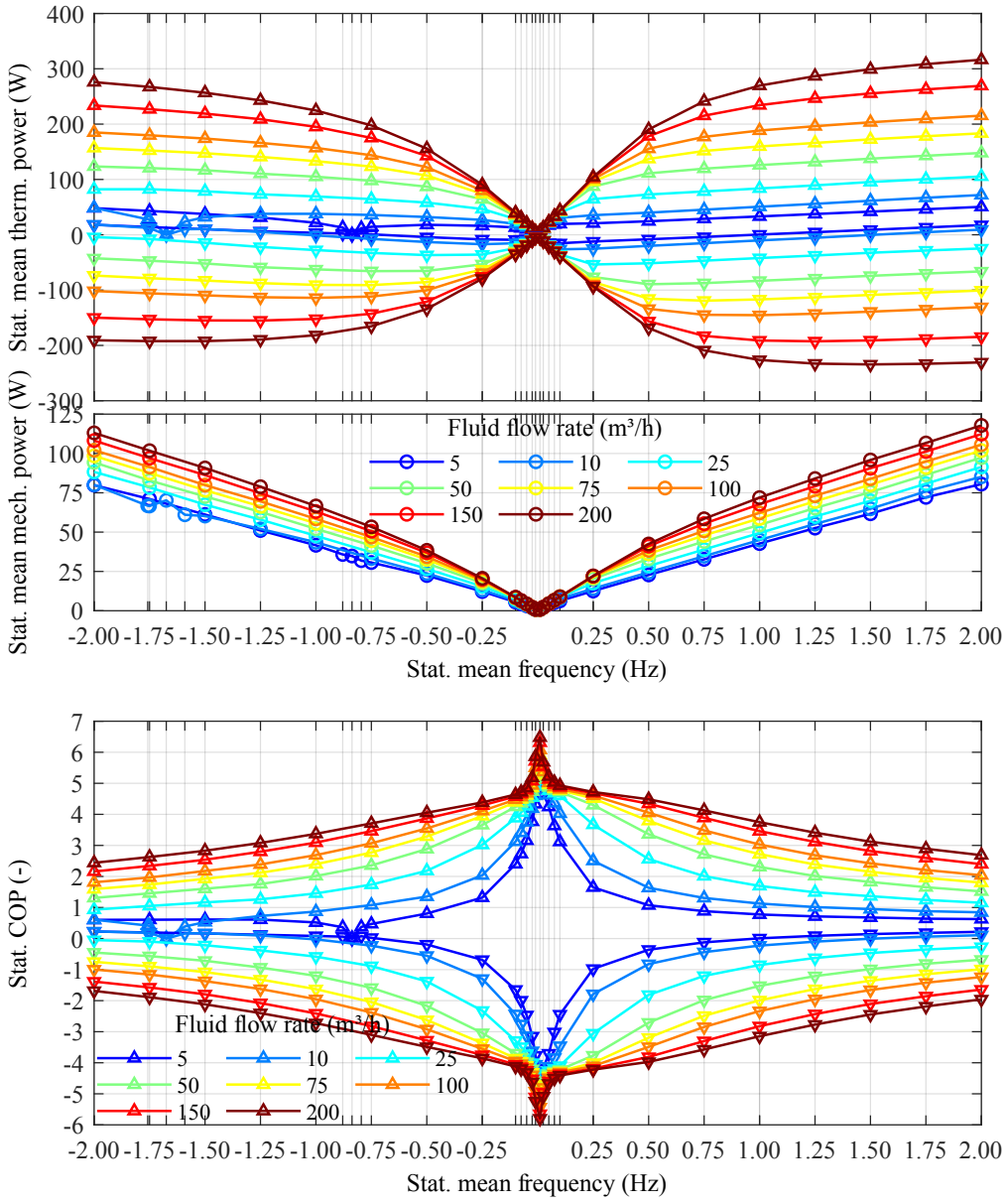

Figure 5.65: Flow rate and frequency: Resulting thermal and mechanical power and *COP* along the rotation frequency for different flow rates.

thermal power output at the hot duct (upturned triangles) and cold duct (downturned triangles) increases with increasing flow rate due to the better HE between SMA and fluid. For a lower rotation frequency, a lower flow rate is sufficient to fully exchange the thermal energy between SMA and fluid. Therefore, thermal power increases with increasing rotation frequency up to a specific point for each flow rate where a kind of saturation starts. At negative rotation frequencies, the misalignment of the curves for small flow rates is caused by the discontinuous and unsteady relative velocity between SMA elements and fluid. Additionally, the thermal power output is larger for the counter-flow for the same combinations of rotation frequency and flow rate.
The mechanical power input increases with increasing rotation frequency due to the growing number of performed EC cycles per time. The increased HE between SMA and fluid for increasing flow rate results in a higher maximum and minimum temperature difference of the SMA element during the EC cycle, leading to an increase in mechanical power input with rising flow rate.
As a result, the *COP* decreases with increasing rotation frequency and increases with increasing flow rate.
To summarize, this parameter study demonstrates that the variation of rotation frequency and flow rate significantly affects the mechanical and thermal power in- and output, as well as the temperature output of the EC HP. In a system of the same size, a higher rotation frequency can transmit more thermal energy. Increasing the rotation frequency results in a higher thermal power output when the fluid flow conditions are adapted to meet the rising demand on HE. If the flow rate remains constant while the rotation frequency increases, the thermal power output will reach a saturation point. With the rotation frequency and flow rate, the thermo-mechanical behavior of a defined EC HP can be controlled. For air as HE and HT fluid and an SMA diameter of 200 µm, the sensible limit is reached at a rotation frequency of 1 Hz. As an additional outcome, in all cases, counter flow between SMA element and fluid offers better performance and efficiency than parallel flow. Parallel-flow does not provide any advantages; therefore, it will be omitted from the following discussion.

5.6.8 SMA diameter and frequency

In this section, the design parameter SMA diameter is variated in the range from 25 µm to 1000 µm along the rotation frequency of the SMA arrangement in the range from 0 Hz to 2 Hz.
Figure 5.66 presents the resulting inlet and outlet temperatures of the fluid at hot and cold duct along the rotation frequency for different SMA diameters. The temperature at the hot duct is represented by upturned triangles and at the cold duct as downturned

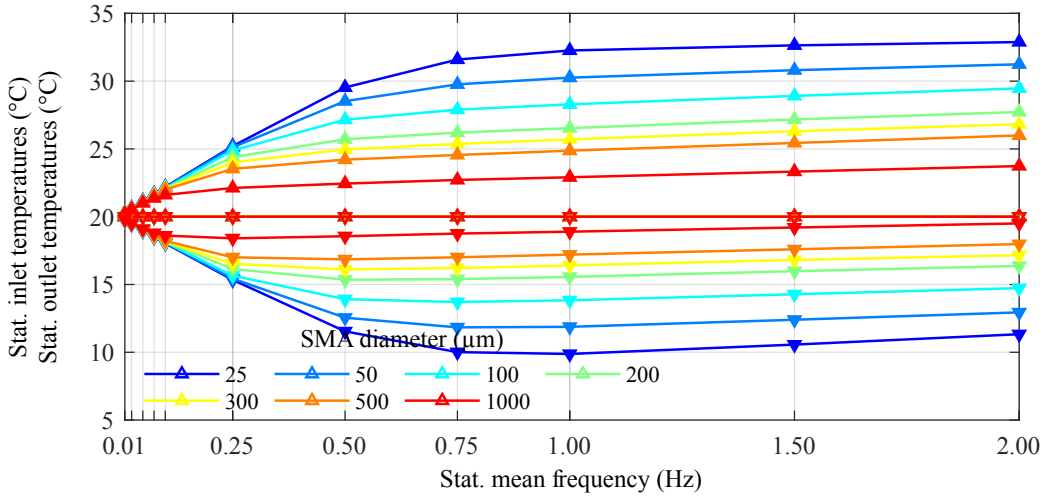

Figure 5.66: SMA diameter and frequency: Resulting inlet and outlet temperature at hot and cold duct along the rotation frequency for different SMA diameters.

triangles. The triangles at the inlets are empty, and the triangles at the outlets are filled. The positive values of the rotation frequency create a counter-flow between SMA and fluid. The thermal energy of the SMA arrangement, which can exchanged with the fluid, following Equation 5.2 and Equation 5.16, increases with increasing rotation frequency due to growing number of performed EC cycles per time. Therefore, the temperature difference between the inlet and outlet of the fluid ducts increases with increasing rotation frequency for a specific SMA diameter. For each SMA diameter, this temperature difference nearly reaches saturation with further increasing rotation frequency. At this point, the HE between SMA and fluid reaches the best value for a specific SMA diameter, rotation frequency and fluid flow rate. An additional increase in rotation frequency does not benefit the temperature difference at the specific SMA diameter.

In addition, the temperature difference between the inlet and outlet of the fluid ducts also increases with decreasing SMA diameters. This is caused by the improved HE, related to the increasing surface area of the SMA arrangement, following Equation 5.2 and Equation 5.16.

Figure 5.67 shows the thermal and mechanical power, as well as the *COP* along the rotation frequency for different SMA diameters. The colors correspond to those of Figure 5.66. The thermal power output at the hot duct is represented by upturned triangles and at the cold duct by downturned triangles. The thermal power of the SMA arrangement increases with increasing rotation frequency due to the growing number of performed EC cycles per time. The rotation frequency, at which the HE process reaches its saturation, decreases with increasing SMA diameter. For a lower rotation frequency, a larger SMA diameter is sufficient to fully exchange the thermal energy between SMA and fluid. Therefore, thermal power at the ducts increases with increasing rotation frequency up to a specific point for each diameter where a kind of saturation starts.

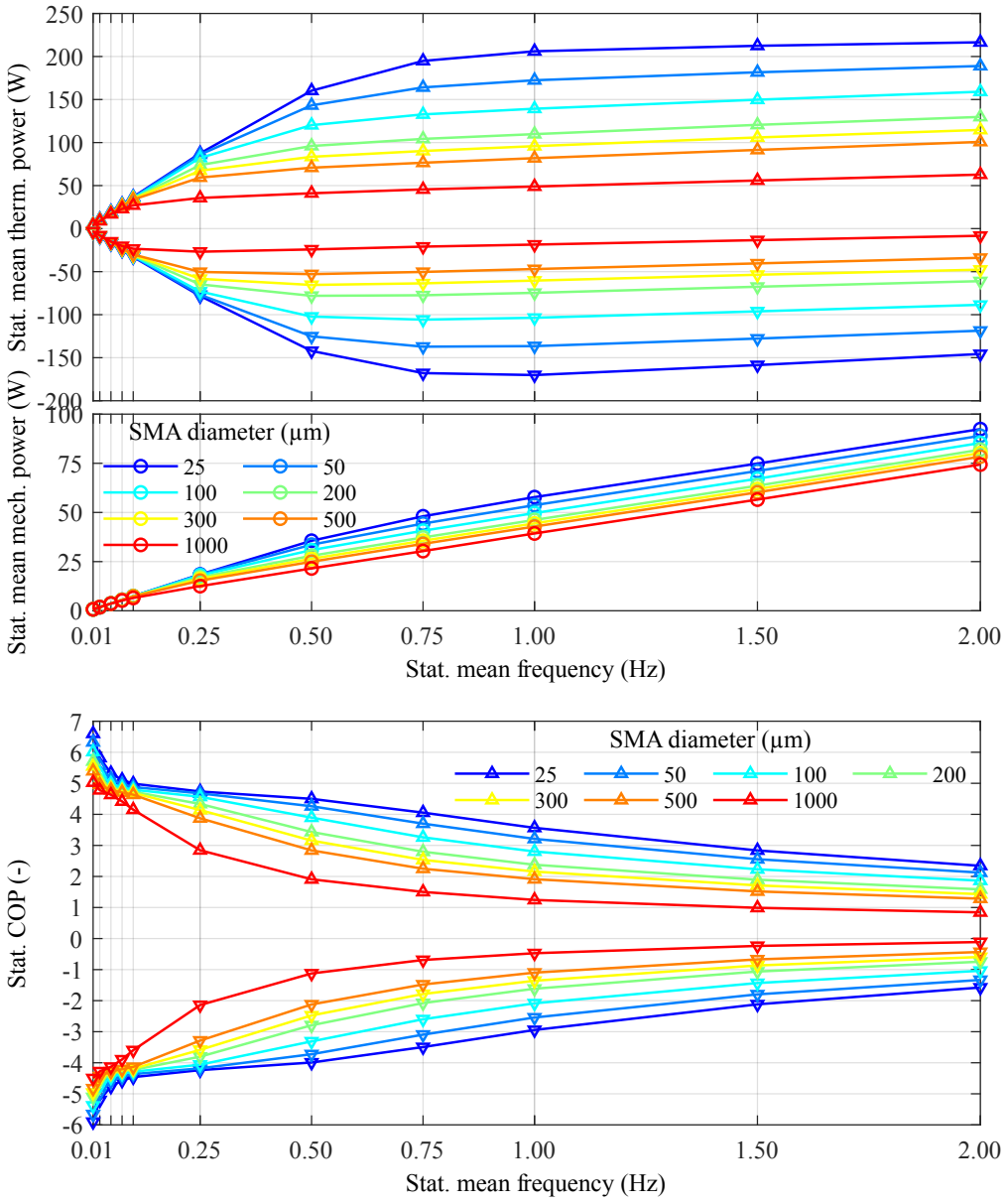

Figure 5.67: SMA diameter and frequency: Resulting thermal and mechanical power and *COP* along the rotation frequency for different SMA diameters.

The mechanical power input increases with increasing rotation frequency due to the growing number of performed EC cycles per time. The increased HE between SMA and fluid for decreasing diameter results in a higher maximum and minimum temperature difference of the SMA element during the EC cycle. Due to the temperature dependent transformation stress, following Equation 2.5 and Equation 2.7, the mechanical power input increases as the diameter falls.
As a result, the *COP* decreases with increasing rotation frequency and increases with decreasing diameter.
To summarize, this parameter study demonstrates that the variation of the rotation frequency and diameter significantly affects the mechanical and thermal power in- and output, as well as the temperature output of the EC HP. Higher rotation frequency can transmit more thermal energy within the same system size. This thermal power can be increased by enlarging the surface area of the defined SMA mass in the EC HP. With the rotation frequency, the thermo-mechanical behavior of a defined EC HP can be controlled. For air as HE and HT fluid the SMA diameter should be in the range from 25 µm to 300 µm.

5.6.9 SMA mass and flow rate

In this section, the design parameter SMA mass in the EC HP is varied in the range from 1.4 g to 71.4 g along the flow rate in the hot and cold duct from 5 m^3/h to 200 m^3/h.
Figure 5.68 presents the resulting inlet and outlet temperatures of the fluid at hot and cold duct over the flow rate for different amounts of SMA material in the EC HP. The amount of SMA material in the EC HP is variated in this parameter study by changing the number of SMA wires per bundle (N_{wpb}). Consequently, the total SMA mass values are decimal numbers.

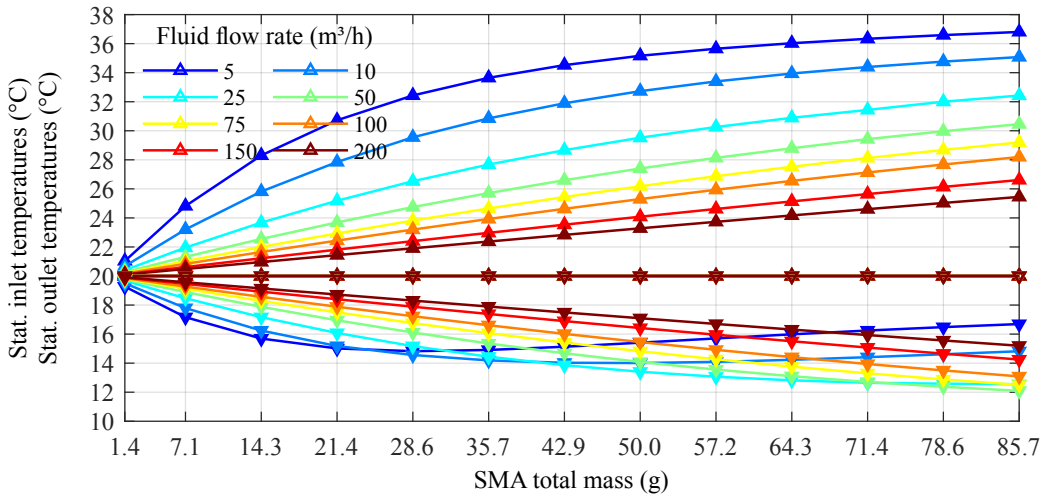

Figure 5.68: SMA mass and flow rate: Resulting inlet and outlet temperature at hot and cold duct along the flow rate for changing SMA mass.

The temperature at the hot duct is represented by upturned triangles, and the cold duct is shown as downturned triangles. The triangles at the inlets are empty, and the ones at the outlets are filled. The standard values of the rotation frequency combined with the standard arrangement of the fluid ducts, as introduced in Table 5.8, create a counter-flow between SMA and fluid.
The thermal energy of the SMA arrangement, which can be exchanged with the fluid, following Equation 5.2 and Equation 5.16, depends on the released or absorbed specific latent heat. Therefore, the temperature difference of the fluid between inlet and outlet for the hot and cold duct decreases with increasing flow rate for a specific amount of SMA material. The asymmetric curve shift towards heating in the cold duct for smaller flow rates and larger SMA masses is related to the asymmetric temperature development in the SMA during PT. This is based on the asymmetric specific latent heat, which favors heating, as introduced in Equation 5.44 and Equation 5.45.
The thermal energy of the SMA arrangement increases with increasing SMA mass. Therefore, the temperature difference between inlet and outlet of the fluid ducts increases with increasing SMA total mass for a specific flow rate.
Figure 5.69 shows thermal and mechanical power, as well as *COP* along the flow rate for different amounts of SMA material. The colors correspond to those of Figure 5.68. The amount of the thermal power output at the hot duct is represented by upturned triangles and at the cold duct as downturned triangles. The thermal power of the SMA arrangement is constant for a specific total SMA mass. The SMA mass, at which the HE process reaches its saturation, decreases with increasing the flow rate. For a lower total SMA mass, a lower flow rate is sufficient to fully exchange the thermal energy between SMA and fluid. Therefore, thermal power at the ducts increases with increasing flow rate up to a specific point for each total SMA mass where a saturation starts. Additionally, the thermal power output increases with increasing SMA mass, following Equation 5.2 and Equation 5.16.
The increased HE between SMA and fluid for increasing flow rate results in a higher maximum and minimum temperature difference of the SMA element during the EC cycle. Due to the temperature dependent transformation stress, following Equation 2.5 and Equation 2.7, the mechanical power input increases with the flow rate. Additionally, the mechanical power input increases with increasing SMA mass due to the growing number of SMA wires per bundle.
As a result, the *COP* increases with increasing flow rate. Additionally, the *COP* decreases with increasing SMA mass for lower flow rates due to the unused mechanical power input related to incomplete HE between SMA and fluid.
To summarize, this parameter study demonstrates that the variation of the flow rate and total SMA mass significantly affects the mechanical and thermal power in- and output, as

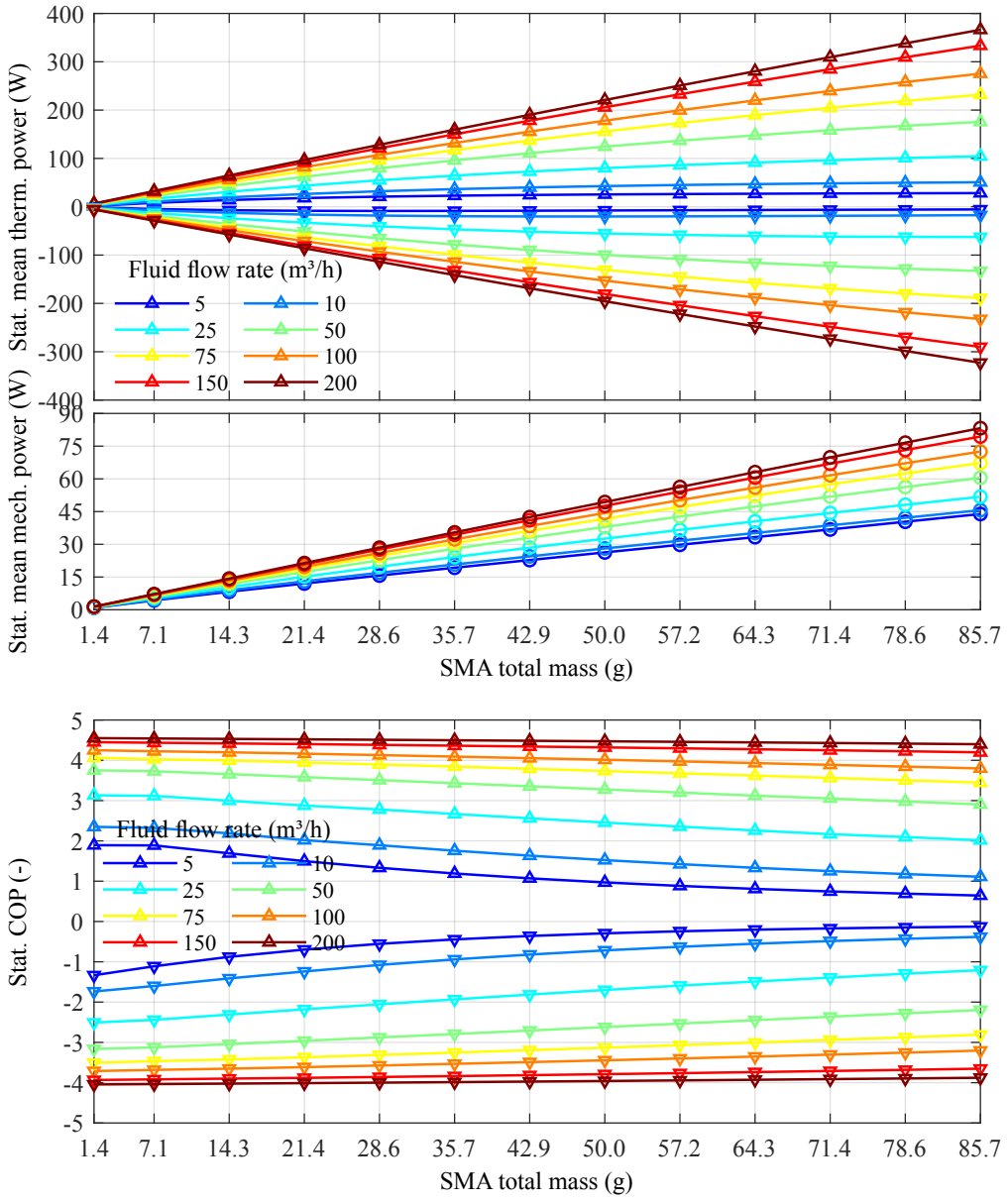

Figure 5.69: SMA mass and flow rate: Resulting thermal and mechanical power and *COP* along the flow rate for changing SMA mass.

well as the temperature output of the EC HP. Increasing the SMA mass results in a higher thermal power output while adapting the fluid flow conditions to meet the rising demand on HE. If the flow rate remains constant while the SMA mass increases, the thermal power output will reach a saturation point. With the flow rate, the thermo-mechanical behavior of a defined EC HP can be controlled.

5.6.10 Flow rate asymmetry

In this section, the operating parameter flow rate is variated only in the cold duct in a range from 5 m^3/h to 200 m^3/h. The flow rate in the hot duct is kept constant at the standard value.

Figure 5.70 presents the resulting temperature evolution for the SMA element as a dashed line and fluid as a solid line along the circumference for different flow rates in the cold duct. The arrangements of the ducts are shown in color at the x-axis. The standard

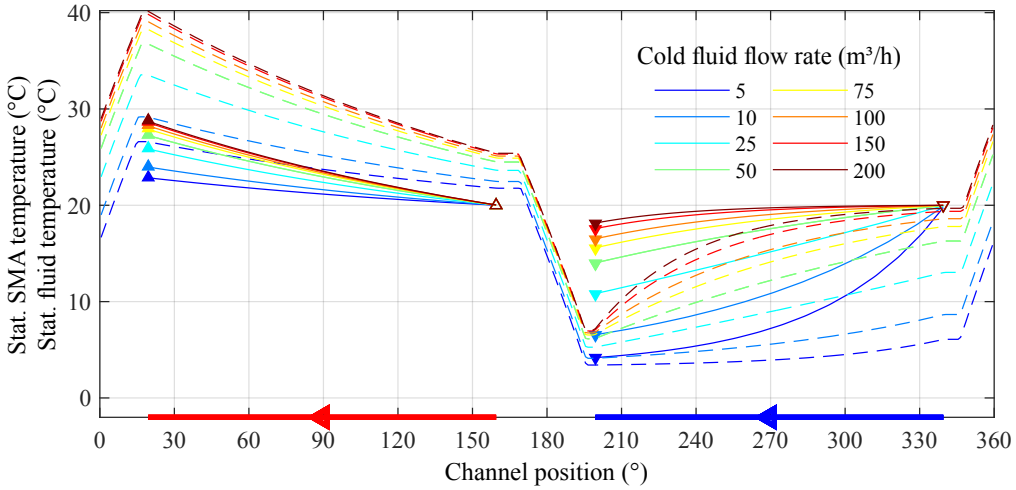

Figure 5.70: Flow rate asymmetry: Resulting SMA element (dashed) and fluid (solid) temperature along the circumference for different flow rates in the cold duct.

values for frequency and flow directions create a counter-flow between SMA and fluid. The temperature of the SMA elements changes adiabatically during the complete PT due to the suppressed HE in the transition zones. During the motion along the ducts, the SMA elements exchange their thermal energy with the fluid. Therefore, the fluid heats up during traveling along the hot duct and cools down in the cold duct.

The variation of the flow rate in only the cold duct by maintaining the standard flow rate of 50 m^3/h in the hot duct leads to an asymmetric fluid flow, resulting in an asymmetric temperature development along the circumference. The temperature difference of the SMA element reached during the FT and the BT remains constant by the variation of the flow rate in the cold duct because this temperature change is defined by the specific latent heat

and the specific heat capacity of the SMA. Whereas the temperature difference between the maximum and minimum temperature of the SMA along the EC cycle increases with increasing flow rate in the cold duct. This is caused by the increasing HE between SMA and fluid, following Equation 5.2, resulting in a higher SMA temperature before the FT starts.

During the PT from A to M, the material temperature rises by the prescribed temperature difference. But the reached maximum temperature depends on the start temperature of the FT, which increases as the flow rate in the cold duct increases. Consequently, the maximum temperature increases also. The maximum temperature difference of the SMA element along the EC cycle is reached at the maximum flow rate in the cold duct.

Each temperature curve of the fluid is framed at the edges by triangles that are upturned at the hot duct and downturned at the cold duct. The triangles at the inlets are empty, and the outlets are filled. The temperature difference of the fluid in the hot duct increases as the flow rate in the cold duct increases due to the increasing SMA temperature. The temperature difference of the fluid in the cold duct decreases as the flow rate in the cold duct increases. This is due to decreasing HE time for each portion of the fluid, following Equation 5.16.

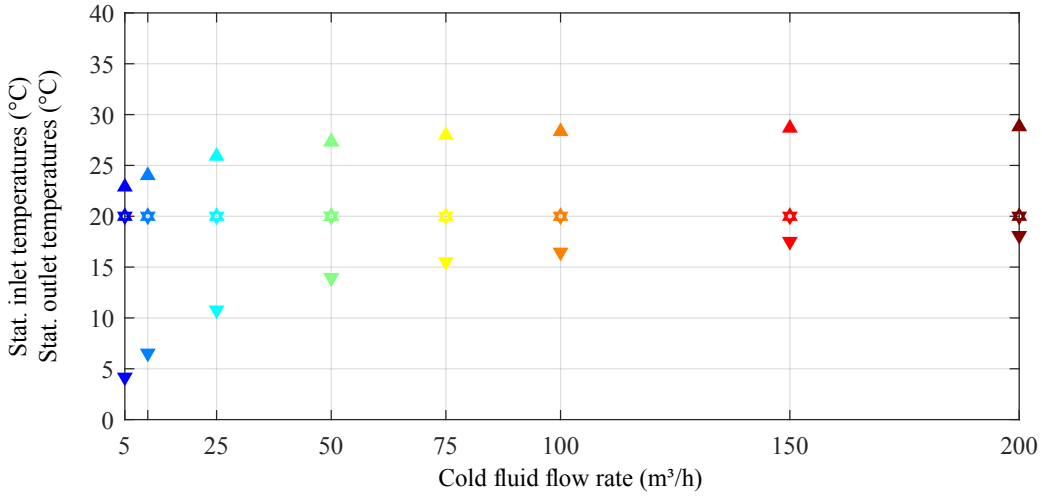

Figure 5.71: Flow rate asymmetry: Resulting inlet and outlet temperature at hot and cold duct along the flow rate of the cold duct.

Figure 5.71 presents the resulting inlet and outlet temperatures at the ducts along the flow rate in the cold duct. The colors correspond to those of Figure 5.70. The temperature at the hot duct is represented by upturned triangles and at the cold duct as downturned triangles. The triangles at the inlets are empty, and the triangles at the outlets are filled. The outlet temperature at the hot duct increases with increasing flow rate in the cold duct. Whereas the temperature difference between the inlet and the outlet of the cold duct decreases with increasing flow rate in the cold duct. Thus, increasing the flow rate of the cold duct can shift the preference of the EC HP from cooling to heating.

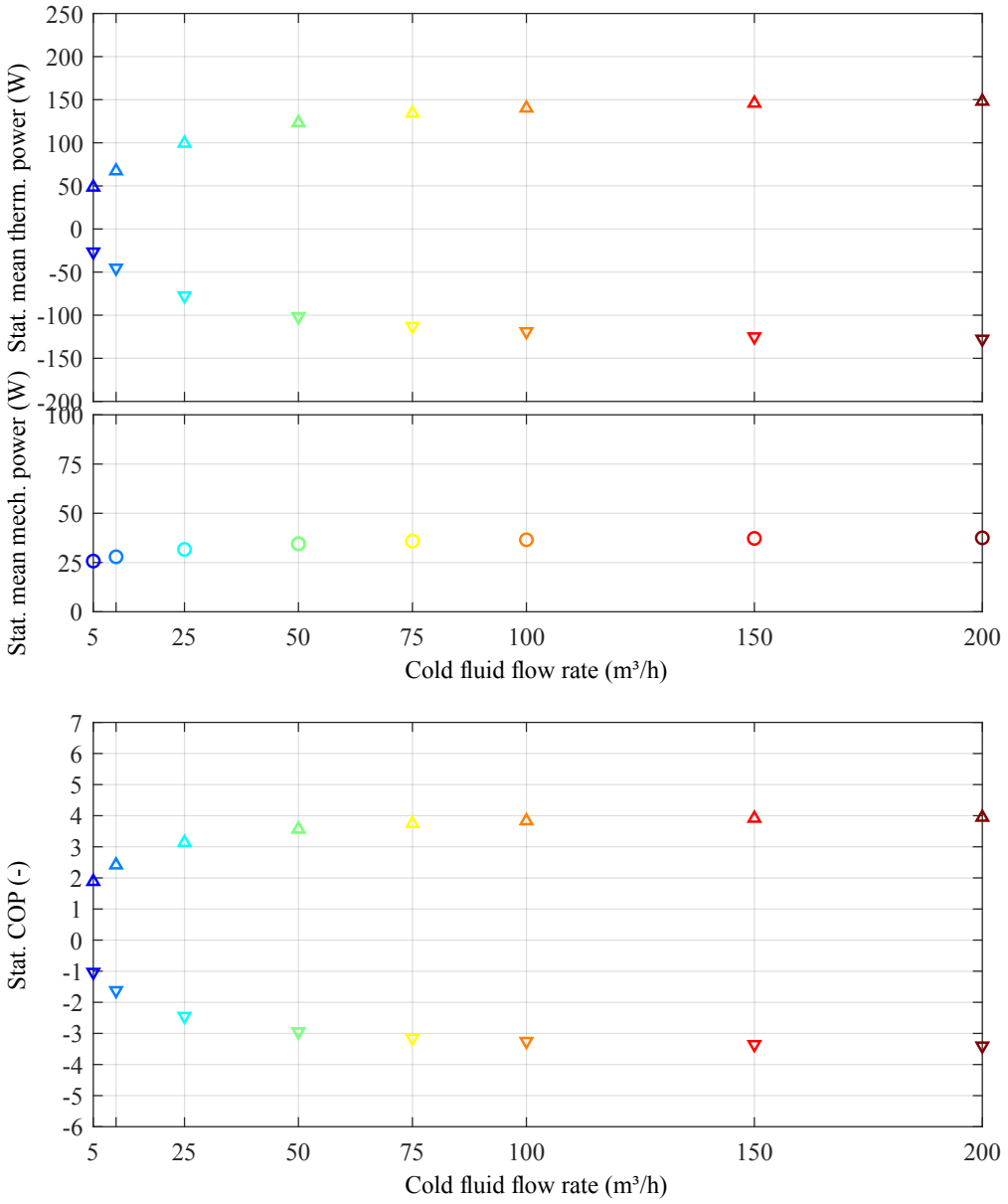

Figure 5.72: Flow rate asymmetry: Resulting thermal and mechanical power and *COP* along the flow rate in the cold duct.

Figure 5.72 shows the thermal and mechanical power, as well as the *COP* along the flow rate in the cold duct. The colors correspond to those of Figure 5.70. The amount of the thermal power output at the hot duct is represented by upturned triangles, and at the cold duct as downturned triangles. The thermal power of the SMA arrangement is constant due to the constant specific latent heat released or absorbed by the SMA for each performed EC cycle. Whereas, the thermal power output at the ducts depends on the SMA temperature and the HE in the ducts, following Equation 5.2 and Equation 5.16. Therefore, the thermal power increases along the flow rate in the cold duct due to the increasing HE and the rising SMA temperature. The increased HE between SMA and fluid for increasing flow rate results in a larger range of maximum and minimum temperature difference of the SMA element during the EC cycle. Due to the temperature dependent transformation stress, following Equation 2.5 and Equation 2.7, the mechanical power input increases with the flow rate. As a result, the *COP* increases with increasing flow rate in the cold duct.
To summarize, this parameter study demonstrates that the asymmetric variation of the flow rate significantly affects the mechanical and thermal power in- and output, as well as the temperature output of the EC HP. Applying different flow rates at the hot and cold duct can be used to produce a higher temperature difference between the inlet and the outlet of the duct with the lower flow rate, but this approach reduces the thermal power output and efficiency. With the flow rate, the thermo-mechanical behavior of a defined EC HP can be controlled. The preference for cooling or heating of the EC HP, in detail, the temperature difference between the outlets, can be adjusted by varying the flow rate of the ducts asymmetrically. The presented thermo-mechanical behavior is likewise assignable to the variation of the flow rate in the hot duct. Therefore, in this work, only one side is presented.

5.6.11 Inlet temperature span with cross-flow

In this part, the design parameter inlet temperature span between the hot and cold inlet is variated symmetrically in the range from 0 K to 15 K, while maintaining the mean temperature level of 20 °C along a symmetric cross-flow in the range from 0 m^3/h to 25 m^3/h. Figure 5.73 shows a still frame of the EC HP with additional ducts in the transition zones, as introduced in Figure 5.11. The duct in the transition zone from the cold to the hot duct enables the HE during the FT of the SMA but also leads to a direct fluid flow from the cold inlet to the hot outlet. Similarly, the duct in the transition zone from the hot to the cold duct enables the HE during the BT of the SMA but also leads to a direct fluid flow from the hot inlet to the cold outlet. These ducts are referred to in the following as cross-flow ducts.

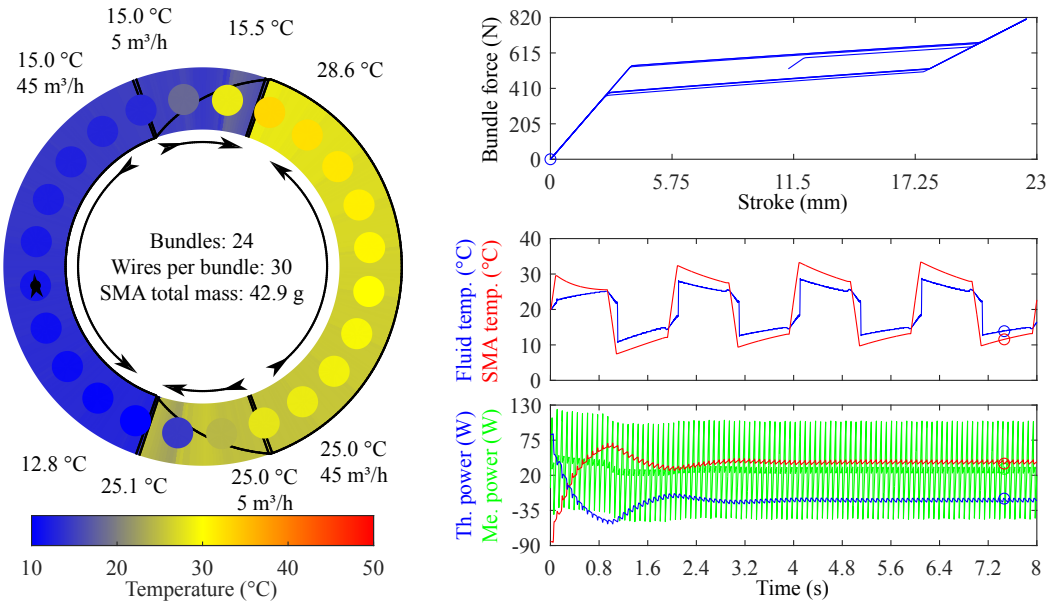

Figure 5.73: Inlet temperature span with cross-flow: Visualization of EC HP cross-section with additional ducts in the transition zones.

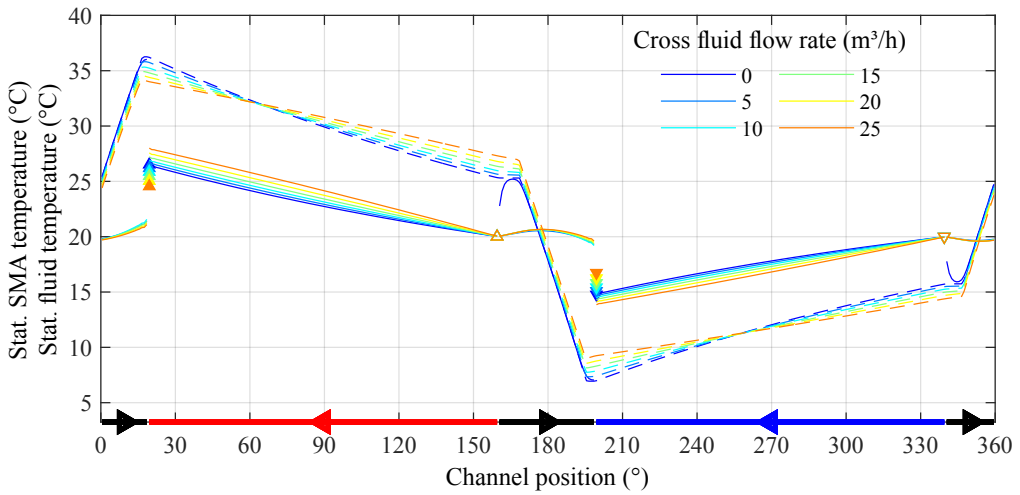

Figure 5.74: Inlet temperature span with cross-flow: Resulting SMA element (dashed) and fluid (solid) temperature along the circumference at an inlet temperature span of 0 K for different cross-flow rates.

Figure 5.74 presents the resulting SMA temperature evolution as dashed line and fluid as solid line along the circumference at an inlet temperature span of 0 K for different cross-flow rates. The arrangement of hot, cold, and cross-flow ducts is shown in color at the x-axis. The flow direction of the fluid is indicated with arrows, creating a counter-flow in the hot and cold duct due to the clockwise rotation of the SMA arrangement. The cross-flow ducts are shown in black at the x-axis and indicate a parallel-flow.
The temperature of the SMA elements changes during PT, not adiabatically, due to the enabled HE in the transition zones. The temperature difference of the SMA elements reached during FT and BT is defined by the specific latent heat and the specific heat capacity of the SMA. In the case of cross-flow, the temperature difference of the SMA elements during PT decreases due to the HE with the fluid, following Equation 5.2. Therefore, the maximum temperature reached at the end of the FT decreases and minimum temperature reached at the end of the BT decreases with increasing cross-flow rate.
During the motion of the SMA element along the hot and cold ducts, the SMA elements exchange their thermal energy with the surrounding fluid. Therefore, the fluid heats up during traveling along the hot duct and cools down during traveling along the cold duct. The temperature difference of the SMA elements, caused by the HE along the hot and cold duct, decreases as the cross-flow rate increases. This occurs because the flow rate in the hot and cold duct reduces in proportion to the cross-flow rate in order to maintain the same flow rate at the outlets of 50 m^3/h as in the standard EC HP. This leads to a higher SMA temperature when the SMA elements exit the hot duct and to a smaller SMA temperature when the SMA element exits the cold duct. As a result, the maximum temperature of the SMA after loading decreases, while the minimum temperature of the SMA after unloading increases, due to the same temperature difference reached by the PT. In addition, the temperature changes are affected by the HE in each transition zone. The asymmetry between the hot and cold side is based on asymmetric specific latent heat, which favors heating, as introduced in Equation 5.44 and Equation 5.45.
Each temperature curve of the fluid is framed at the edges by triangles that are upturned at the hot duct and downturned at the cold duct. The triangles at the inlets are empty, and the triangles at the outlets are filled. The cross-flow leads to modified outlet temperatures, which are calculated using the weighted arithmetic mean at the hot outlet, as introduced in Equation 5.24 and at the cold outlet, as introduced in Equation 5.25. Consequently, the triangles showing the resulting outlet temperatures are neither directly located at the ends of the lines for the hot and cold ducts nor at the ends of the lines for the cross-flow ducts. The temperature difference of the fluid between the inlet and outlet of each duct decreases as the cross-flow rate increases. This resulting temperature difference is influenced by the HE along the hot and cold duct and the mixture with the cross-flow.

Figure 5.75 presents the resulting temperature evolution for the SMA element as dashed line and fluid as solid line along the circumference at a cross-flow rate of 15 m^3/h for different inlet temperature spans. In this parameter study, the temperature span for the

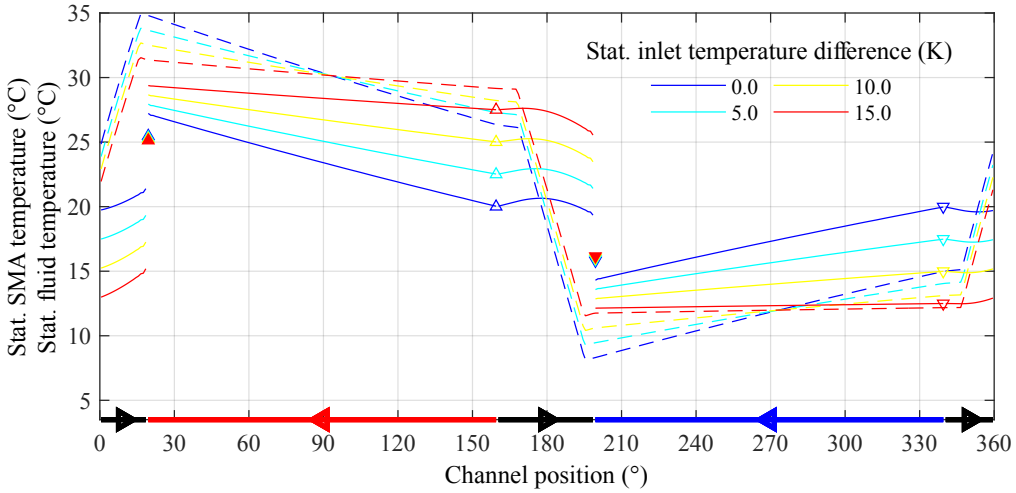

Figure 5.75: Inlet temperature span with cross-flow: Resulting SMA element (dashed) and fluid (solid) temperature along the circumference at a cross-flow rate of 15 m^3/h for different inlet temperature spans.

hot and cold duct is symmetrically arranged around 20 °C. As known from subsection 5.6.6, temperature difference between the maximum and minimum temperature of the SMA along the EC cycle decreases with increasing inlet temperature span of the fluid. This is caused by the decreasing temperature difference between SMA and fluid and the reduced HE, following Equation 5.2. The maximum temperature difference of the SMA element along the EC cycle is reached at the minimum inlet temperature span of the fluid.
The temperature difference of the fluid also decreases by increasing the inlet temperature span of the fluid. This is also caused by the decreasing temperature difference between fluid and SMA and the reduced HE, following Equation 5.16. The cross-flow decreases the outlet temperatures additionally. At the inlet temperature span of 15 K, the hot side is cooled, and the cold side is heated. Nevertheless, the maximum temperature output increases, and the minimum temperature output decreases with increasing inlet temperature span. Figure 5.76 presents the resulting inlet and outlet temperatures at hot and cold duct along the cross-flow rate for different inlet temperature spans. The colors correspond to those of Figure 5.75. The temperature at the hot duct is represented by upturned triangles and at the cold duct as downturned triangles. The triangles at the inlets are empty, and the ones at the outlets are filled.
The temperature difference between the maximum and minimum temperature of the SMAs along the EC cycle decreases with increasing cross-flow rate and increasing inlet temperature span. Therefore, the outlet temperature at the hot duct decreases, and at cold duct increases with increasing cross-flow rate. Additionally, the outlet temperature

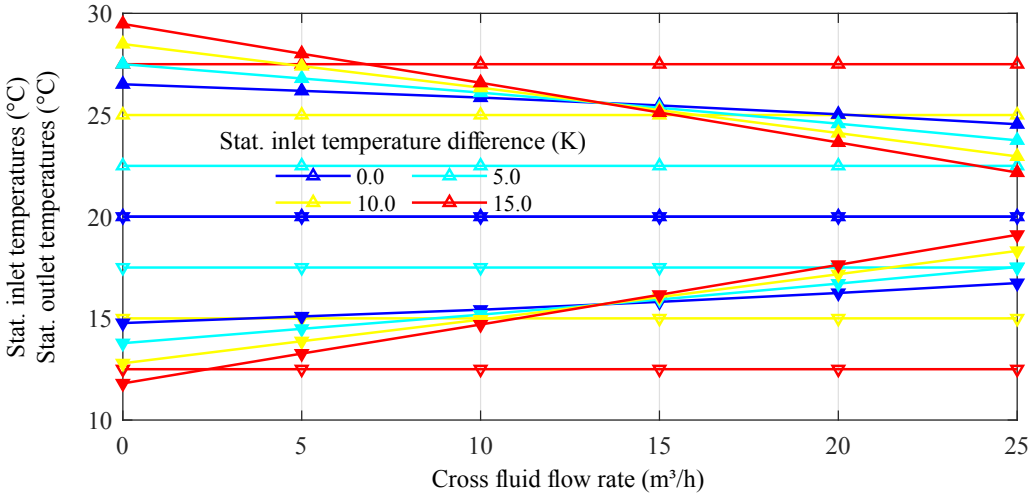

Figure 5.76: Inlet temperature span with cross-flow: Resulting inlet and outlet temperature at hot and cold duct along the cross-flow rate for different inlet temperature spans.

at the hot duct increases and at cold duct decreases with increasing inlet temperature span for cross-flow rates lower than 15 m^3/h. Beyond this point, the outlet temperature of the hot duct decreases, and of cold duct increases with increasing inlet temperature span. The point where the hot side of the EC HP is cooled and the cold side is heated moves to smaller cross-flow rates with increasing inlet temperature spans.

Figure 5.77 shows the thermal and mechanical power, as well as the *COP* along the cross-flow rate for different inlet temperature spans. The colors correspond to those of Figure 5.75. The amount of the thermal power at the hot duct (upturned triangles) and cold duct (downturned triangles) significantly decreases with increasing cross-flow rate and increasing inlet temperature span. The mechanical power input also decreases with increasing cross-flow rate and increasing inlet temperature span due to the thermal dependence of the transformation stress, as introduced in Equation 2.5 and Equation 2.7. As a result, the *COP* value of the EC HP decreases with increasing cross-flow rate and increasing inlet temperature span. At the point where the hot side is cooled, and the cold side is heated, the *COP* values are negative for the hot side and positive for the cold side, leading to a negative efficiency of the EC HP.

In summary, this parameter study shows that the cross-flow rate and inlet temperature span drastically influences the thermo-mechanical behavior of the EC HP. With increasing cross-flow rate, the thermal power and *COP* decreases significantly and leads to uneconomical operating conditions of the EC HP. Each combination of cross-flow rate and inlet temperature span shows a point where the hot side of the EC HP is cooled and the cold side is heated. Therefore, the valuable operation span of the EC HP by applying an inlet temperature span with a cross-flow rate is restricted.

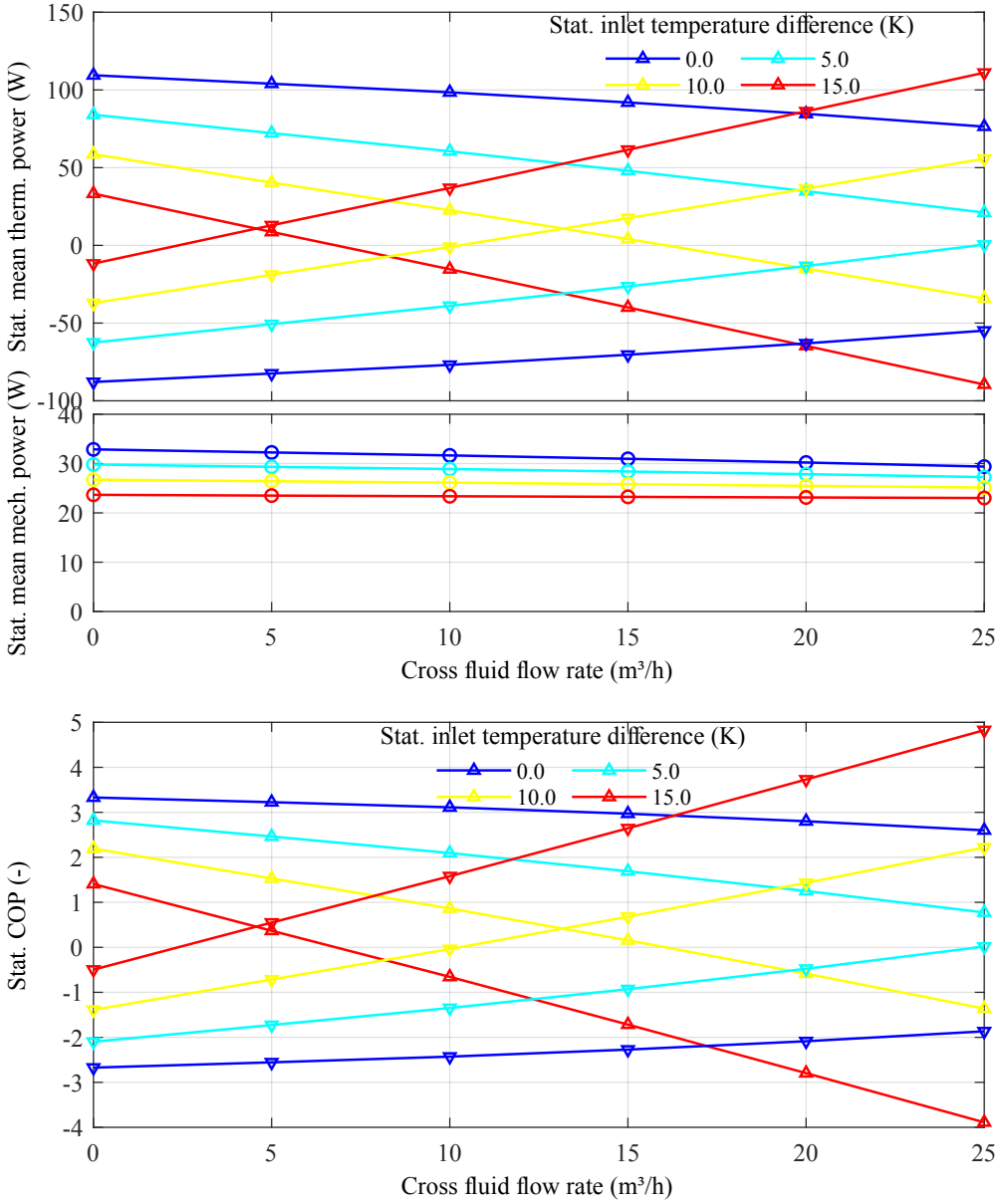

Figure 5.77: Inlet temperature span with cross-flow: Resulting thermal and mechanical power and the *COP* of the EC HP for along the cross-flow rate for different inlet temperature spans.

5.6.12 Inlet temperature span with internal heat recovery

In this part, the design parameter temperature span between hot and cold inlet is variated symmetrically in the range from 0 K to 40 K. The mean temperature level is maintained at 20 °C. Additionally, a heat recovery zone is incorporated into the hot and cold duct of the EC HP system.

Figure 5.78 shows a still frame of the EC HP with ducts for internal heat recovery. These additional ducts are located between the transition zones and the inlets of the main ducts, as introduced in Figure 5.12. In the recovery duct at the 11 o'clock position, the cool

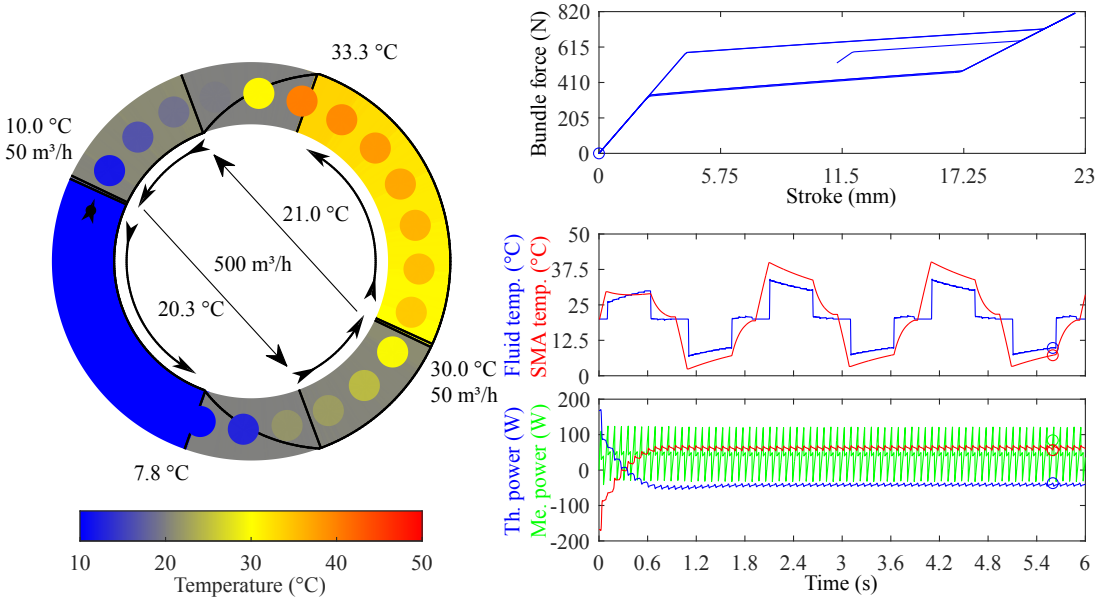

Figure 5.78: Internal heat recovery: Visualization of EC HP cross-section with additional ducts for internal heat recovery.

SMAs leaving the cold duct are pre-heated by a fluid at an intermediate temperature level in a counter-flow manner. In the recovery duct at the 5 o'clock position, the warm SMAs leaving the hot duct are pre-chilled by the same fluid. The two recovery ducts are interconnected to each other to transfer the excessive thermal energy of the SMAs after leaving the hot duct to the SMAs with insufficient thermal energy before FT.

Figure 5.79 presents the resulting temperature evolution of the SMA elements as dashed line and fluid as solid line along the circumference for the different duct arrangements. The arrangements of the ducts are shown in color at the x-axis as an overlay. The black color indicates heat recovery zones, whereas red and blue represent the hot and cold duct. The flow direction of the fluid is indicated with arrows, creating a counter-flow in all ducts due to the clockwise rotation of the SMA arrangement. As a result, the SMAs are warmer before FT and colder before BT, allowing larger temperature difference between hot and cold duct with the same limited adiabatic temperature change during PT.

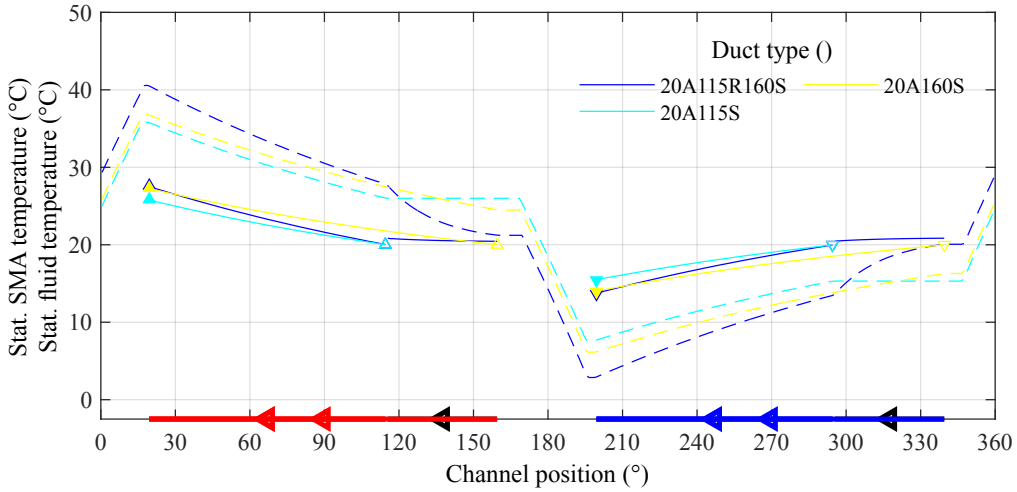

(a)

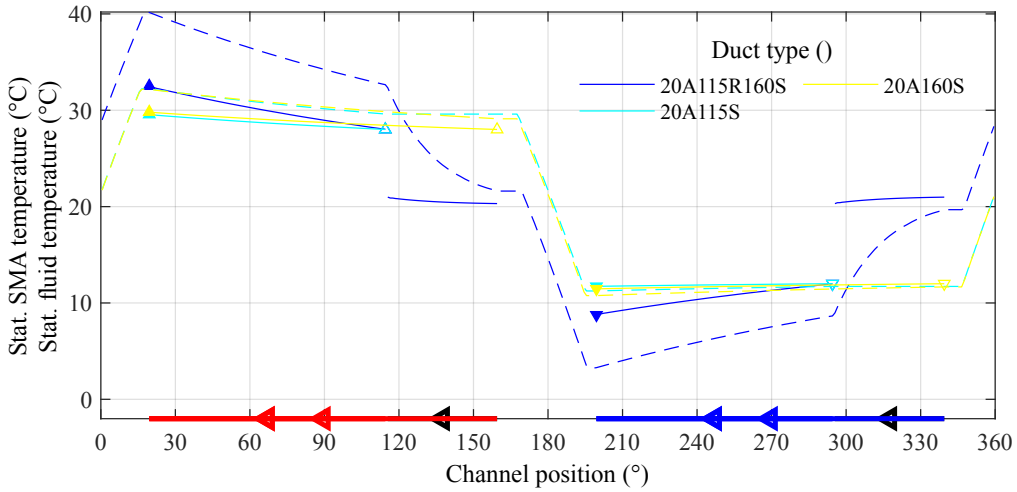

(b)

Figure 5.79: Internal heat recovery and inlet temperature span: Resulting SMA element (dashed) and fluid (solid) temperature along the circumference for different duct arrangements at an inlet temperature span of 0 K (a) and at an inlet temperature span of 16 K (b).

In the upper part of Figure 5.79, the temperature along the circumference for different duct arrangements at an inlet temperature span of 0 K is presented. The standard duct with the type name *20A160S* exhibits a HE area ranging from 20° to 160°, that is symmetrically duplicated at the rotation angle of 180° around the circumference using air as HE and HT fluid. The SMA material undergoes complete and adiabatic PT due to the suppressed HE in the transition zones. During the motion along the ducts, the SMA elements exchange their thermal energy with the fluid. Therefore, the fluid heats up in the hot duct and cools down in the cold duct.
Each temperature curve of the fluid is framed at the edges by triangles that are upturned at the hot duct and downturned at the cold duct. The triangles at the inlets are empty, and the triangles at the outlets are filled.
The duct type with the name *20A115S* exhibits shortened main ducts ranging from 20° to 115°, that are symmetrically arranged. The temperature difference of the SMA element reached during FT and BT remains constant because this temperature change is defined by the material's specific latent heat and specific heat capacity. Whereas the temperature difference between the maximum and minimum temperature of the SMA during the EC cycle decreases. The temperature development between *20A115S* and *20A160S* follows the behavior for a smaller duct length described in subsection 5.6.3. The corresponding shorter duration of the HE results in a higher temperature of the SMA as it exits the hot duct and a lower temperature as it exits the cold duct, following Equation 5.2. Therefore, temperature difference between the inlets and the outlets of the fluid also decreases slightly. This is also caused by the decreasing temperature difference between fluid and SMA and the reduced HE, following Equation 5.16.
The gained space can be used for heat recovery ducts. The duct type with the name *20A115R160S* has main ducts which ranges from 20° to 115°, symmetrically, and exhibits, in addition an internal heat recovery zone, introduced in Figure 5.78, which ranges symmetrically from 115° to 160°. The heat recovery decreases the temperature of the SMA after it exits the hot duct. At the same time, the heat recovery increases the temperature of the SMA after it exits the cold duct. This leads to a significant increase of the temperature difference between the maximum and minimum temperature of the SMA along the EC cycle, resulting in an increased fluid temperature difference across each duct.
In the lower part of Figure 5.79 temperature along the circumference for different duct arrangements at an inlet temperature span of 16 K is presented. The temperature span for the hot and cold duct is symmetrically arranged around 20 °C.
The duct *20A160S* and *20A115S* can not exchange the thermal energy with the fluid sufficiently due to the large inlet temperature span, as introduced in subsection 5.6.6. Therefore, the temperature difference between the inlets and the outlets of the fluid is significantly reduced compared to Figure 5.79 (a).

The heat recovery in *20A115R160S* enables the return of the SMA temperature to nearly 20 °C after passing the main and subsequent heat recovery duct. Therefore, the temperature difference between inlets and outlets at an inlet temperature span of 16 K (b) reaches an almost equal level to that of an inlet temperature span of 0 K (b).
Figure 5.80 presents the resulting inlet and outlet temperatures of the fluid of the main ducts along the different inlet temperature spans. The colors correspond to those of

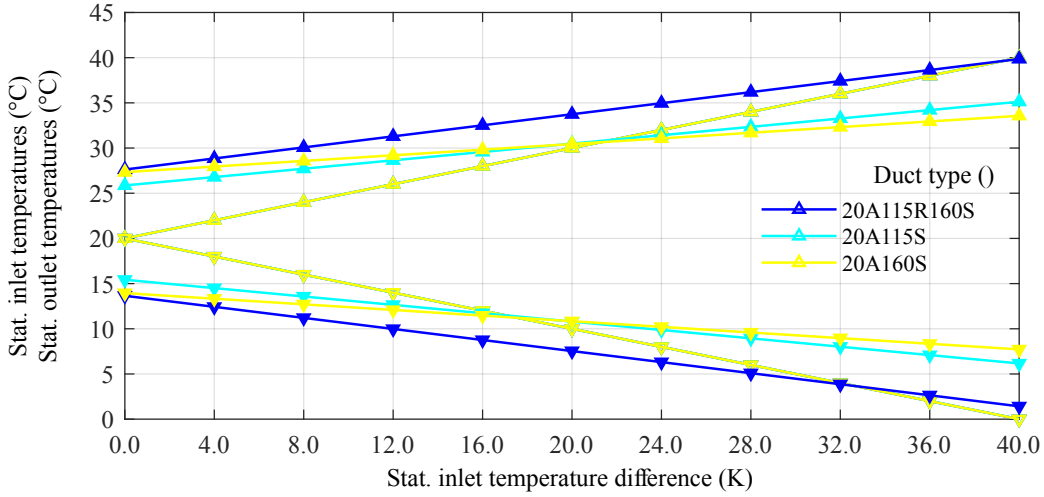

Figure 5.80: Internal heat recovery and inlet temperature span: Resulting inlet and outlet temperatures at hot and cold duct along the inlet temperature spans for different duct types.

Figure 5.79. The temperature at the hot duct is represented by upturned triangles and at the cold duct as downturned triangles. The triangles at the inlets are empty, and the triangles at the outlets are filled.
As previously discussed, the temperature difference between the inlet and outlet temperature of each duct decreases with increasing inlet temperature spans. At the point where the inlet temperature span exceeds the temperature difference of the SMA reached by the PT, no meaningfully HE is possible anymore. In this case, the SMA arrangement cools the fluid in the hot duct and heats it in the cold duct. This is the case for the duct types *20A160S* and *20A115S* without heat recovery at an inlet temperature span of approximately 16 K. The duct arrangement *20A115R160S* with internal heat recovery exhibits a useful inlet temperature span of approximately 32 K.
Figure 5.81 shows the thermal and mechanical power, as well as the *COP* along different inlet temperature spans. The colors correspond to those of Figure 5.79. The amount of the thermal power at the hot duct (upturned triangles) and cold duct (downturned triangles) decreases with increasing inlet temperature spans. This is caused by the smaller temperature difference between SMA and fluid, and the downgraded HE conditions, following Equation 5.16. If the inlet temperature span is too large, the hot side is cooled, and the cold side is heated. However, the internal heat recovery exhibits larger values

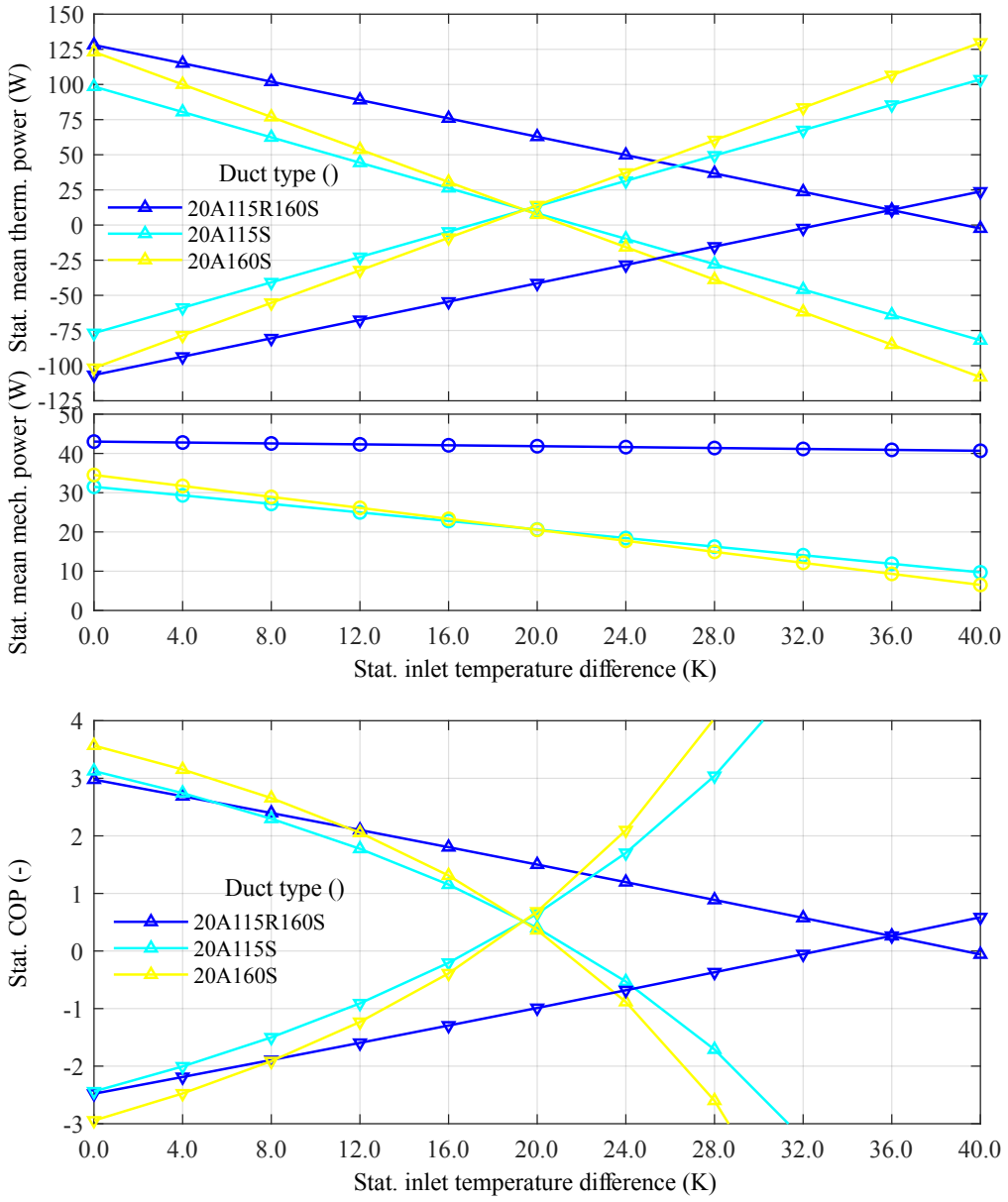

Figure 5.81: Internal heat recovery and inlet temperature span: Resulting thermal and mechanical power and *COP* along different inlet temperature spans for different duct types.

of the thermal power due to the larger temperature difference between SMA and fluid resulting in an improved HE. In this case, the EC HP can be utilized with an extended inlet temperature span of up to approximately 32 K.
The mechanical power input also decreases with increasing inlet temperature spans due to a reduction in hysteresis area within the performed EC cycles. This is caused by the decreasing temperature difference between the maximum and minimum temperature of the SMA element throughout the EC cycle, affecting the dependent transformation stress, following Equation 2.5 and Equation 2.7.
As a result, the *COP* decreases with increasing inlet temperature spans. For too large temperature spans, the *COP* value can become negative. However, the internal heat recovery improves the *COP* significantly.
To summarize, this parameter study demonstrates that the internal heat recovery improves the thermo-mechanical dependency of the EC HP. The possible inlet temperature range between both fluid ducts can be significantly enlarged from the adiabatic material limit of approximately 16 K, following subsection 5.6.6, up to twice that limit, around 32 K, by applying internal heat recovery concepts. With this concept, the unwanted consequences of the cross-flow mixture in combination with the inlet temperature span, following subsection 5.6.11, can be significantly reduced.

5.6.13 Mechanical friction and frequency

In this section, the influence of the design parameter mechanical friction of the cam rollers, is investigated by varying the friction coefficient (μ_{cam}) in the range from 0 to 0.01, along the rotation frequency of the SMA arrangement in the range from 0 Hz to 2 Hz. This range represents the cam roller bearing's performance under various conditions:

- ideal scenarios with no friction (μ=0)
- involving air bearings (μ=0.0001)
- low-friction ball bearings with metal-to-metal surfaces (μ=0.001)
- ball bearings interacting with polymer surfaces (μ=0.01)

Figure 5.82 presents the resulting inlet and outlet temperatures of the ducts along the rotation frequency for different friction coefficients. The temperature at the hot duct is represented by upturned triangles and the cold duct by downturned triangles. The triangles at the inlets are empty and filled for the outlets. The positive values of the rotation frequency combined with the standard arrangement of ducts create a counter-flow between SMA and fluid.
The exchangeable thermal energy of the SMA arrangement increases with increasing rotation frequency due to the growing number of performed EC cycles per time. Therefore,

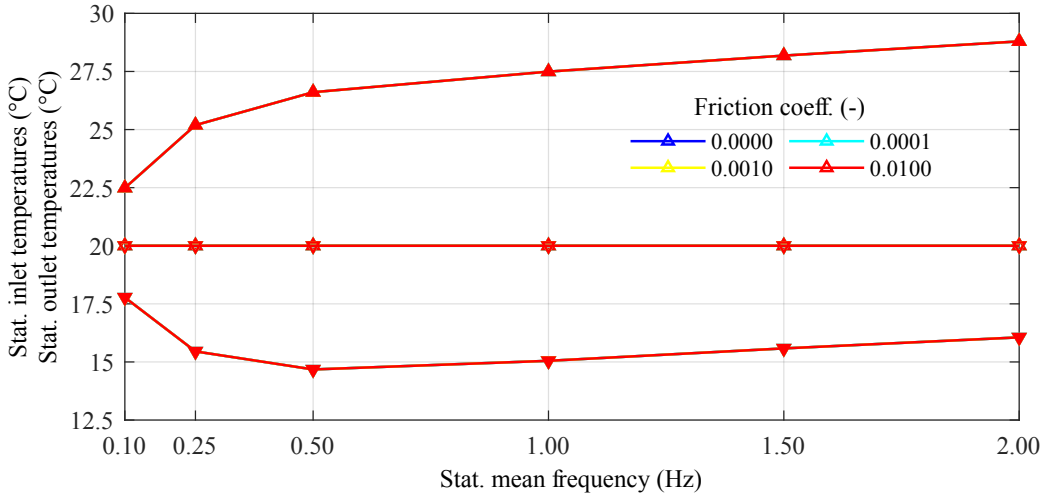

Figure 5.82: Mechanical friction and frequency: Resulting inlet and outlet temperature at hot and cold duct along the rotation frequency for different friction coefficients.

the temperature difference between inlet and outlet increases with increasing rotation frequency for the standard SMA diameter, following subsection 5.6.8. With further increasing rotation frequency, the slope of the temperature difference changes towards saturation. At this rotation frequency, the HE between SMA and fluid reaches the best value for a specific SMA diameter, and fluid flow rate. An additional increase in rotation frequency does not significantly benefit the temperature difference.

The friction coefficient of the cam rollers does not influence the temperature evolution in the EC HP. Therefore, the resulting temperatures are equal for the different friction coefficients.

Figure 5.83 presents the resulting drive torque at a rotation frequency of 0.5 Hz during one rotation for the diffrent friction coefficients. The colors correspond to those of Figure 5.82. The torque evolution enables the identification of each SMA bundle traveling along the circumference and passing the loading and unloading ramp of the load profile. The asymmetric shift towards positive values is caused by the dissipated mechanical work of the SMA material in each bundle, following Equation 1.4. The averaged torque increases with increasing friction coefficient due to the higher force during loading and the smaller returned force during unloading, following Equation 5.10 and Equation 5.14.

Figure 5.65 shows the thermal and mechanical power, as well as the *COP* along the rotation frequency for different friction coefficients. The colors of the friction coefficients correspond to those of Figure 5.82. The amount of the thermal power output at the hot duct is represented by upturned triangles, and at the cold duct is shown as downturned triangles. The thermal power of the SMA arrangement increases with rotation frequency due to a growing number of performed EC cycles per time. The thermal power at the ducts increases with increasing rotation frequency up to a specific point where a kind of

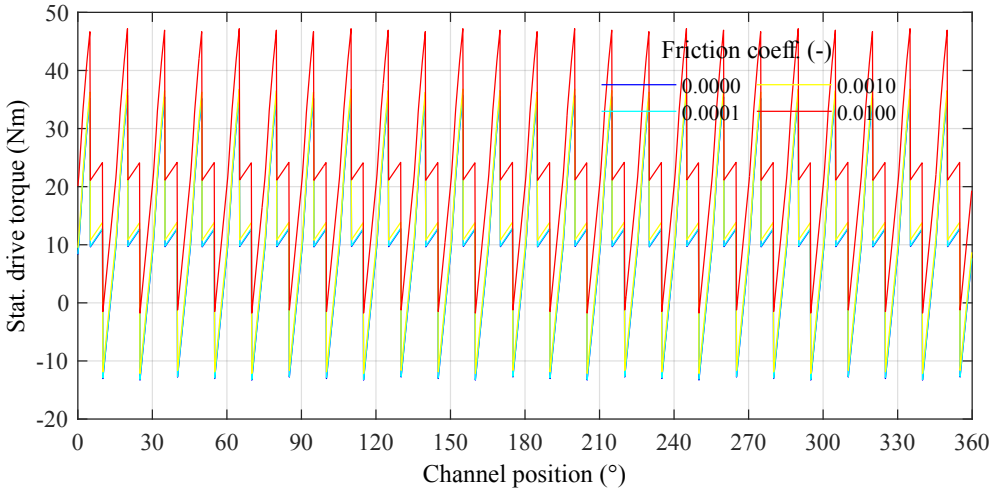

Figure 5.83: Mechanical friction and frequency: Resulting drive torque over one rotation at a rotation frequency of 0.5 Hz for diffrent friction coefficients.

saturation starts. At this rotation frequency, the HE between SMA and fluid reaches the optimal value for a specific SMA diameter, and fluid flow rate.

The mechanical power input increases with increasing rotation frequency due to the growing number of performed EC cycles per time. The increased required torque elevates the mechanical power for a certain rotation frequency as the friction coefficient rises.

As a result, the *COP* decreases with increasing rotation frequency and also decreases with increasing friction coefficient.

To summarize, this parameter study demonstrates that the variation of the rotation frequency and friction coefficient significantly affects the mechanical power input of the EC HP. When using low friction ball bearings with metal-to-metal surfaces with a friction coefficient of 0.001 or lower, the mechanical friction of cam rollers only marginal influence the system efficiency. Using bearings with higher friction significantly reduces the *COP* as the rotational frequency rises.

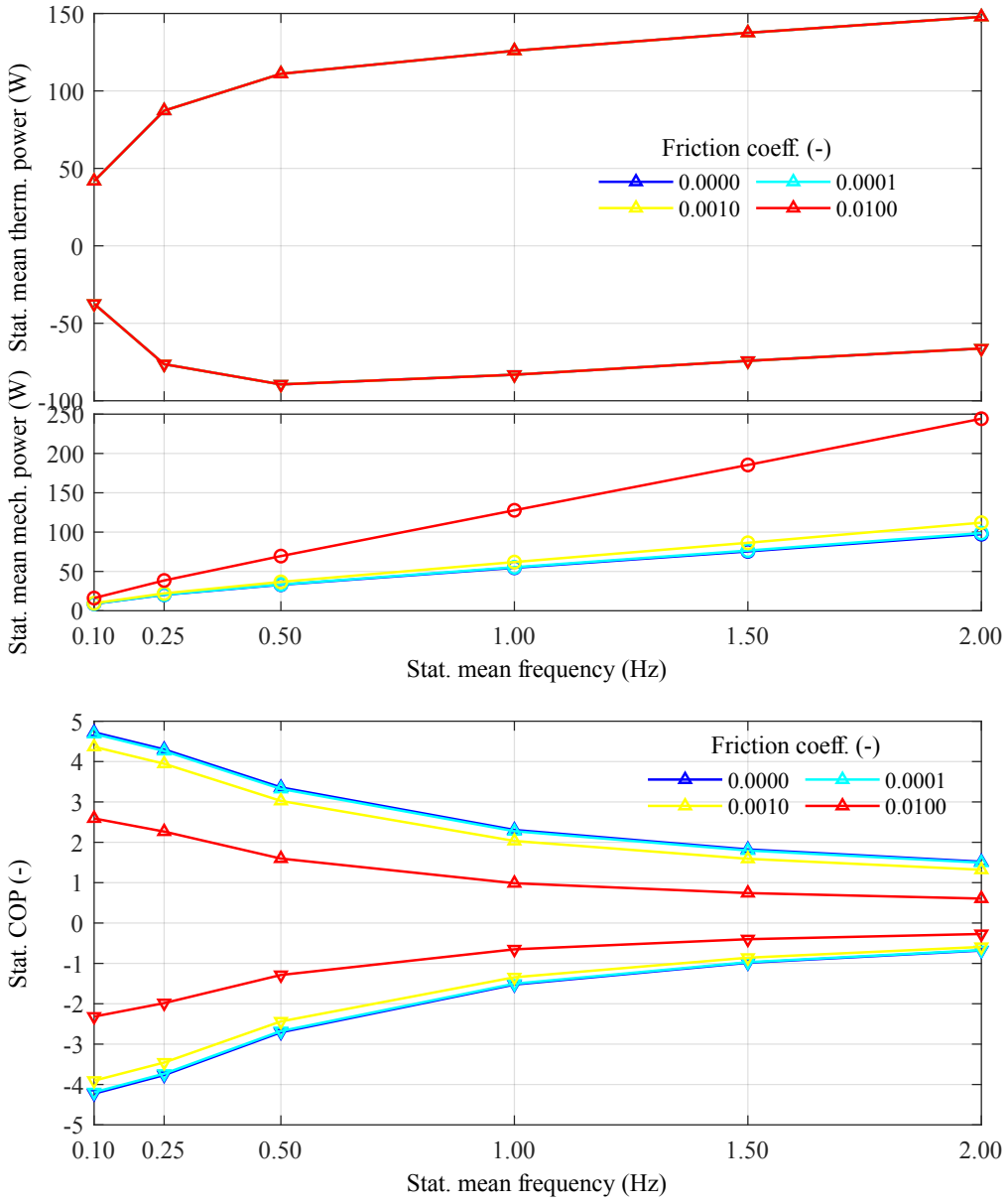

Figure 5.84: Mechanical friction and frequency: Resulting thermal and mechanical power and *COP* along the rotation frequency for different friction coefficients.

5.6.14 Thermal wall losses and frequency

In this section, the influence of the design parameter thermal losses through the wall, is investigated by varying the thermal conductivity of the wall (κ_{wall}) in the range from 0 W/(m K) to 0.2 W/(m K), along the rotation frequency of the SMA arrangement in the range from 0 Hz to 2 Hz. The ambient temperature of the EC HP is set to 20 °C. This range represents the thermal performance of the duct walls under various conditions:

- ideal scenarios with no thermal losses through the walls (κ_{wall}=0)
- vacuum insulation panels (κ_{wall}=0.005)
- expanded polystyrene (κ_{wall}=0.04)
- uninsulated acrylic glass (κ_{wall}=0.2)

Figure 5.85 presents the resulting temperature evolution for the SMA element as dashed line and fluid as solid line along the circumference at a rotation frequency of 1.0 Hz for diffrent thermal conductivities. In this parameter study, the thermal conductivity of the

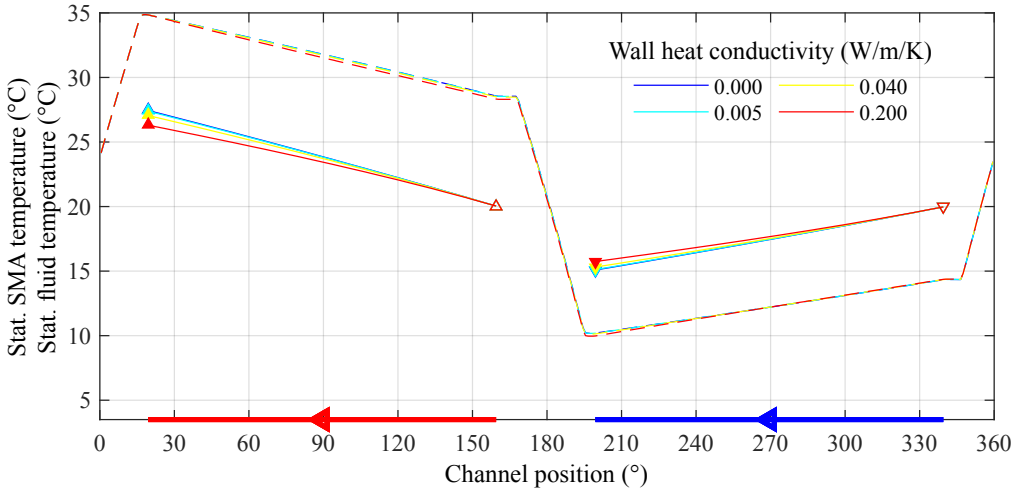

Figure 5.85: Thermal wall losses and frequency: Resulting SMA element (dashed) and fluid (solid) temperature along the circumference at a rotation frequency of 1.0 Hz for diffrent thermal conductivities.

walls from both ducts is symmetrically variated, following Figure 5.10. The arrangement of the ducts is shown in color at the x-axis. The flow direction of the fluid is indicated with an arrow, creating a counter-flow in both ducts. The temperature of the SMA element increases during the full PT adiabatically due to the suppressed HE in the transition zones. During the motion along the ducts, the SMA elements exchange their thermal energy with the fluid. Therefore, the fluid heats up in the hot duct and cools down in the cold duct. Each temperature curve of the fluid is framed at the edges by triangles that are upturned at the hot duct and downturned at the cold duct. The triangles at the inlets are empty and filled at the outlets.

The temperature difference of the SMA element reached during the FT and the BT remains constant in this study since this temperature change is defined by the SMA' material properties.

The HE between fluid, wall, and environment tries to equalize the fluid temperature to the ambient temperature following Equation 5.16. Therefore, the temperature difference between SMA and fluid increases sightly, following Equation 5.2. Finally, the temperature difference between the maximum and minimum temperature of the SMA along the EC cycle slightly increases with increasing thermal conductivity of the wall.

Figure 5.86 presents the resulting inlet and outlet temperatures of both ducts along the rotation frequency for different thermal conductivities. The colors correspond to those of Figure 5.85. The temperature at the hot duct is represented by upturned triangles, and

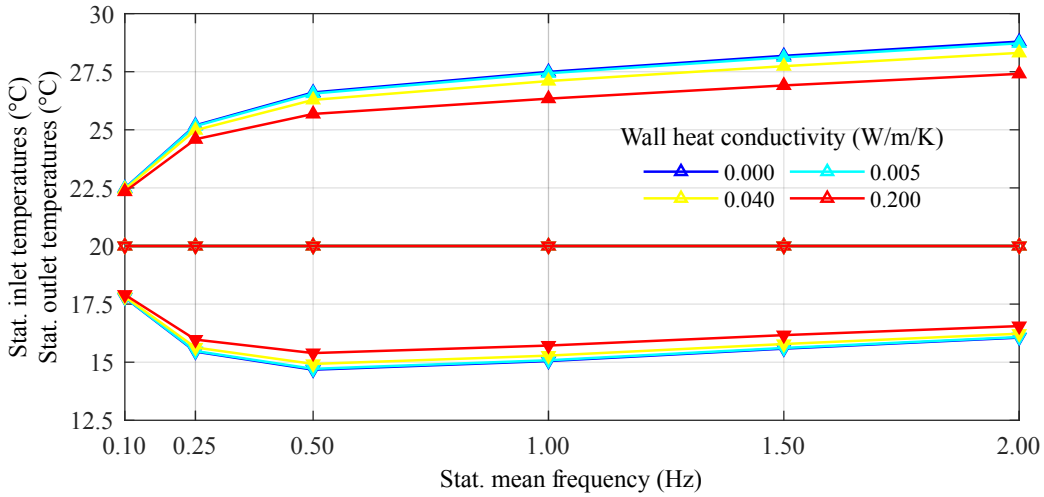

Figure 5.86: Thermal wall losses and frequency: Resulting inlet and outlet temperature at hot and cold duct along the rotation frequency for different thermal conductivities.

the cold duct is shown as downturned triangles. The triangles at the inlets are empty, and the triangles at the outlets are filled.

Similar to subsection 5.6.8, the temperature difference between the inlet and the outlet of the fluid ducts increases with increasing rotation frequency for the standard SMA diameter. With further increasing rotation frequency, the temperature difference nearly reaches saturation.

The increasing thermal conductivity of the wall reduces the resulting inlet and outlet temperature difference at hot and cold duct.

Figure 5.87 shows the thermal and mechanical power, as well as the *COP* along the rotation frequency for different thermal conductivities. The colors correspond to those of Figure 5.85. Upturned triangles represent the thermal power output at the hot duct and downturned triangles at the cold duct. The thermal power at the ducts exhibits the same behavior as the outlet temperature since the flow rate is kept constant.

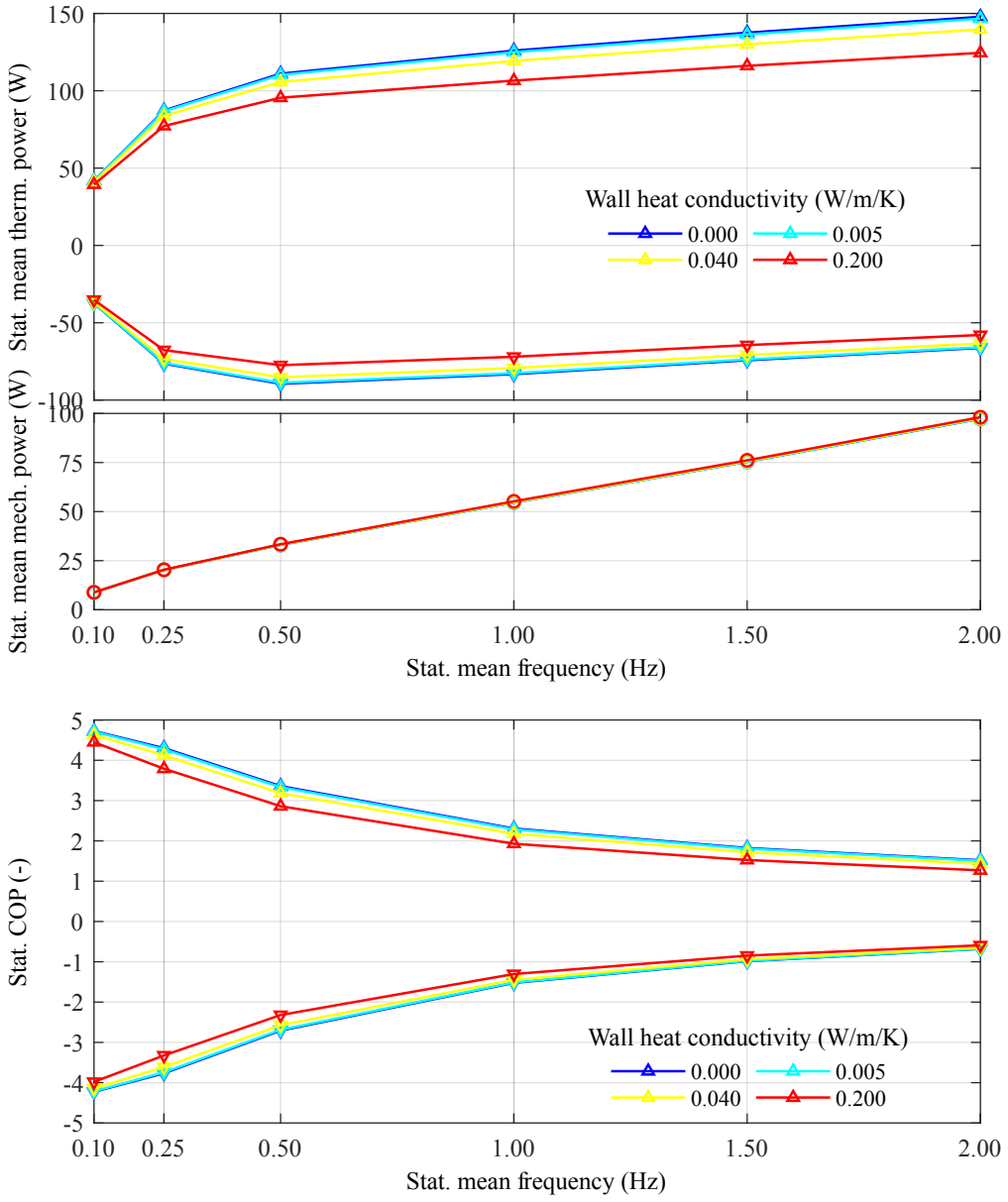

Figure 5.87: Thermal wall losses and frequency: Resulting thermal and mechanical power and *COP* along the rotation frequency for different thermal conductivities.

Therefore, the thermal power output at the hot and cold duct decreases with increasing thermal conductivity of the wall.
The mechanical power input increases with increasing rotation frequency due to the growing number of performed EC cycles per time. The slightly increased temperature difference of the SMA along the EC cycle leads to a slight increase in the mechanical power as the thermal conductivity of the wall rises.
As a result, the *COP* decreases with increasing rotation frequency and also decreases with increasing thermal conductivity of the wall.
To summarize, this parameter study demonstrates that the variation of the rotation frequency and thermal conductivity of the wall marginal affects the mechanical and thermal power in- and output, as well as the temperature output of the EC HP. Higher wall losses reduce the thermal power output and efficiency of the EC HP slightly. Even when using uninsulated acrylic glass, it only has a marginal influence on system *COP*.

5.6.15 Viscous losses and flow rate

In this section, the design parameter viscous losses is studied by using different fan types and flow rates from 5 m^3/h to 200 m^3/h for both ducts.
The characteristics and electrical power consumption of the different fan types are introduced in Figure 5.15 and Figure 5.16. Figure 5.88 presents the resulting inlet and outlet temperatures of the fluid at hot (upturned triangles) and cold duct (downturned triangles) along the flow rate for different fan types. The colors of the different fan types are consistent for all figures in this section and correspond to those of Figure 5.15 and Figure 5.16.

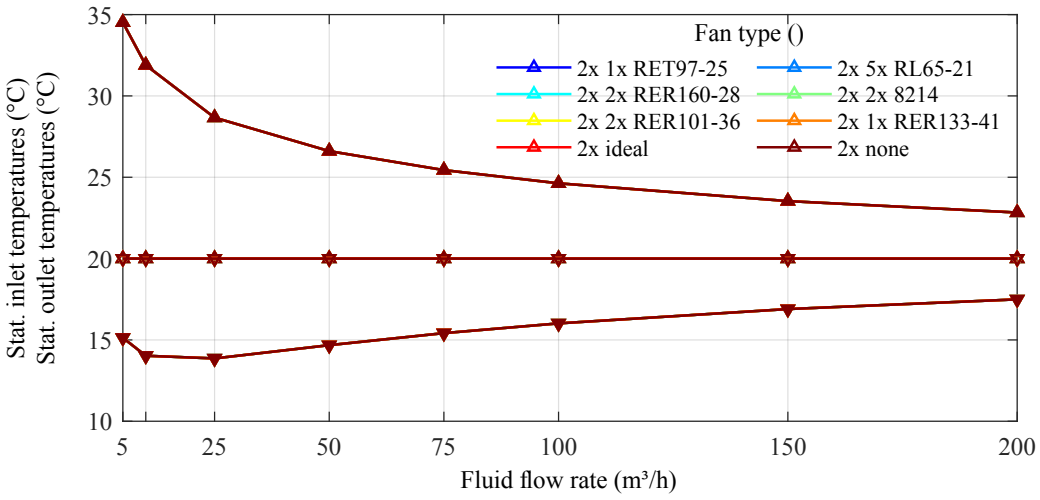

Figure 5.88: Viscous losses and flow rate: Resulting inlet and outlet temperature at hot and cold duct along the flow rate for different fan types.

The triangles at the inlets are empty and filled at the outlets. The standard values for rotation frequency and fluid duct arrangement create a counter-flow condition.
The thermal energy of the SMA arrangement, which can be exchanged with the fluid, following Equation 5.2 and Equation 5.16, depends on the released or absorbed specific latent heat. Therefore, the fluid temperature difference across each duct decreases with increasing flow rate for a specific amount of SMA material. The asymmetric curve shift towards heating of the cold outlet for smaller flow rates is related to the asymmetric temperature development in the SMA during PT. This is based on asymmetric specific latent heat, which favors heating, as introduced in Equation 5.44 and Equation 5.45.
The viscous losses influence neither the thermo-mechanical properties of the EC cycle nor the temperature of the fluid. Therefore, the fluid temperatures for the different fan types are equal.
Figure 5.89 shows the thermal and input power, as well as the *COP* along the flow rate for different fan types used in the EC HP. The colors correspond to those of Figure 5.88, Figure 5.15 and Figure 5.16. The thermal power for hot duct (upturned triangles) and cold duct (downturned triangles) is independent of the viscous losses and remains constant. The thermal power at the ducts increases with increasing flow rate up to a specific point where a kind of saturation starts. At this rotation frequency and flow rate, the HE between SMA and fluid reaches the optimal value for the selected SMA diameter. An additional increase in flow rate can not transport more thermal energy at this rotation frequency.
Whereas the mean input power increases with increasing flow rate due to the growing electrical power consumption of the fans, following Figure 5.16.
As a result, the *COP* of the EC HP system decreases with increasing flow rate and decreasing efficiency of the different fan types.
To summarize, this parameter study demonstrates that the variation of the flow rate and fan types significantly affects the total power input of the EC HP and its efficiency. With increasing flow rate, the flow resistance in the duct increases and reduces significantly the efficiency of the system, following subsection 5.6.15. Therefore, flow rates larger than $75\,\mathrm{m^3/s}$ while using air as HE and HT fluid should be avoided. Fans with higher electrical power consumption reduce the *COP* of the EC HP significantly in addition to the viscous losses.

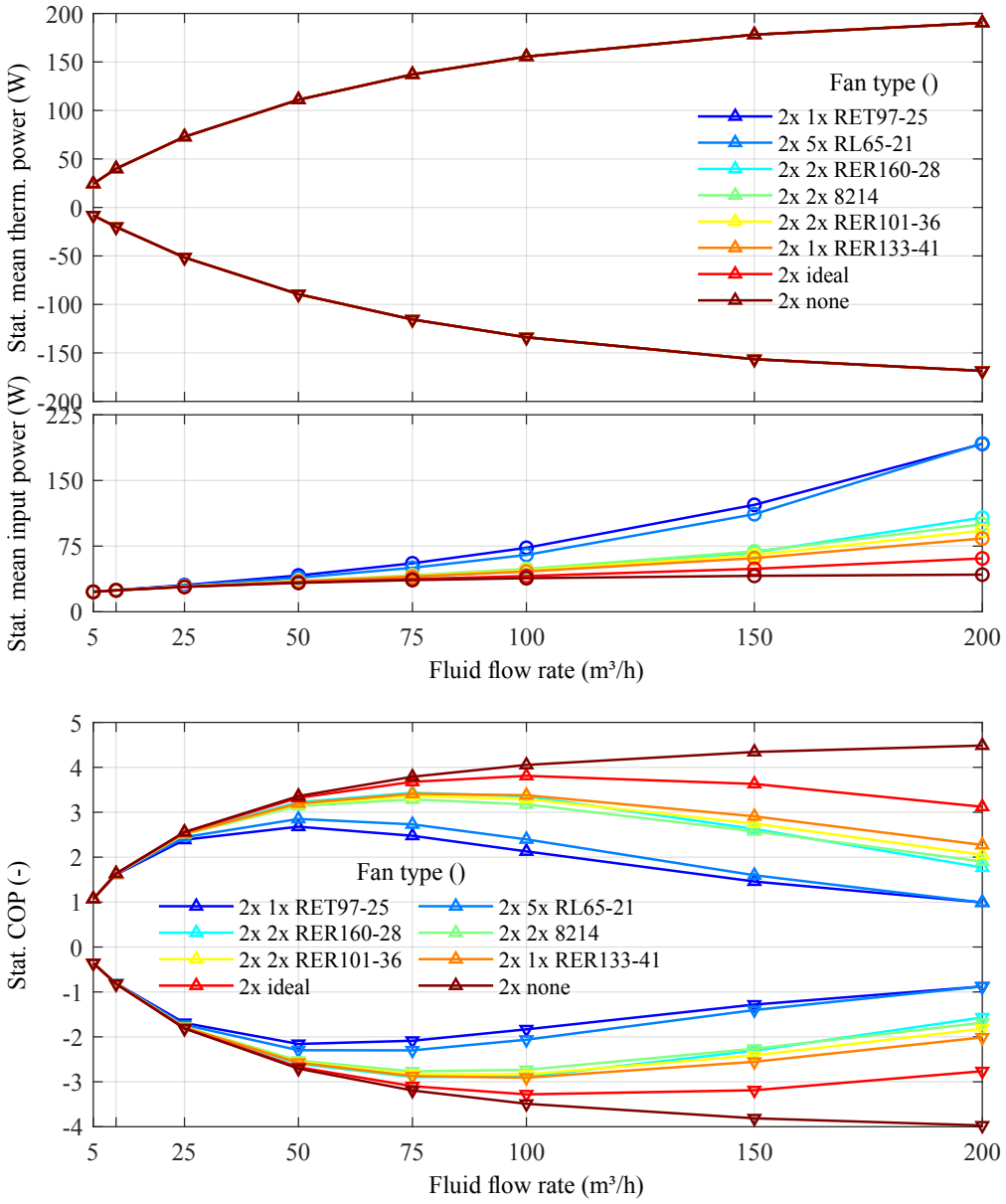

Figure 5.89: Viscous losses and flow rate: Resulting thermal and mechanical power and *COP* along the flow rate for different fan types.

5.6.16 Maximum strain

In this section, the design parameter maximum cam stroke and therefore the maximum strain of the SMA elements, is varied from 0.5 to 7.5 % in 0.5 % steps.
Figure 5.90 illustrates the 15 loading profiles and the corresponding M+ phase fraction in the SMA elements along the channel position. The arrangements of the hot and cold duct are shown in color at the x-axis. The colors used for the simulation number are consistent for all diagrams in this section. The load profile is symmetrically adjusted for loading and

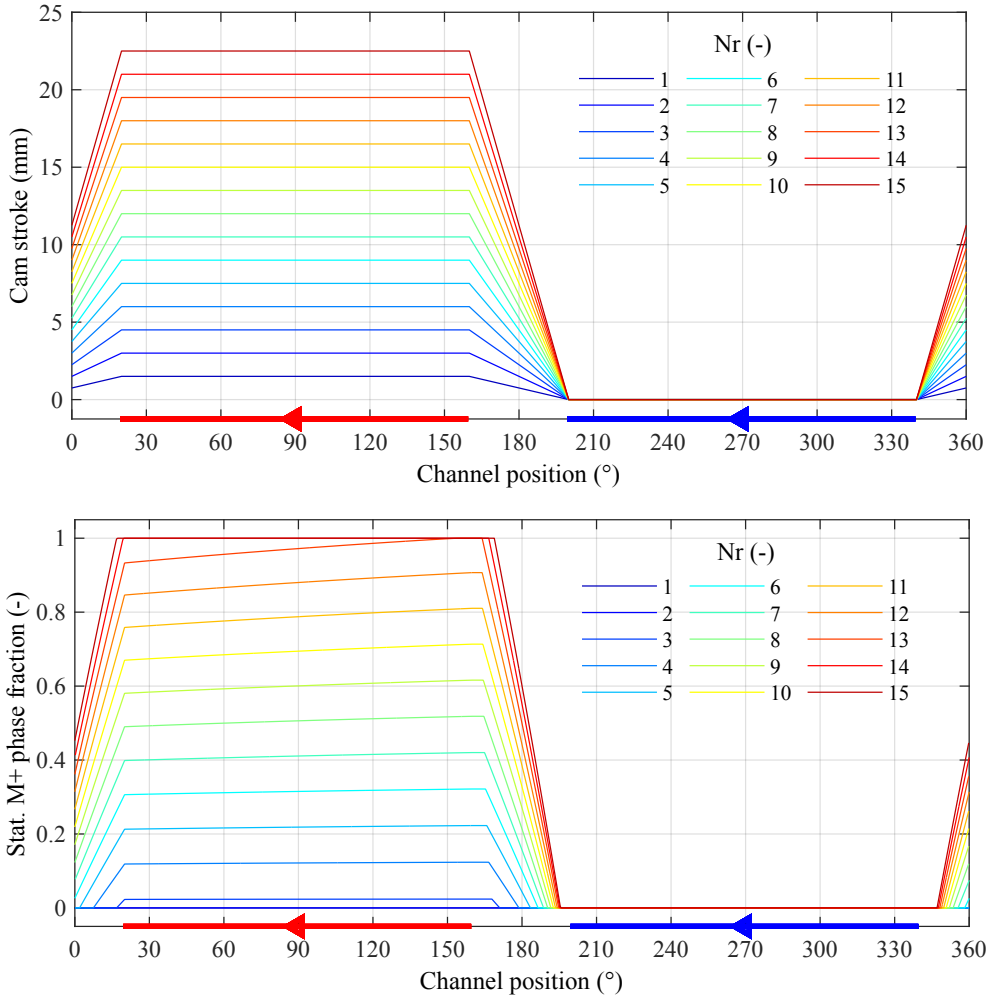

Figure 5.90: Maximum cam stroke: Symmetric loading and unloading profile with different maximum stroke and resulting M+ phase fraction in the SMA elements along the circumference.

unloading by modifying the slope for each simulation, ensuring that the strain change of the SMA element begins with entering the transition zone and ends with exiting it. The resulting different strain rates do not influence the thermo-mechanic boundaries of the EC cycle during loading and unloading due to the adiabatic condition in the transition zone. After loading the SMA material exhibits in simulation number 3 to 13 a post-PT, indicated by the increasing M+ phase fraction of the SMA during the holding phase.

Figure 5.91 presents the resulting temperature evolution for the SMA element as dashed line and fluid as solid line along the circumference for the 15 different maximal cam strokes. The arrangement of the hot and cold duct is shown in color at the x-axis. The

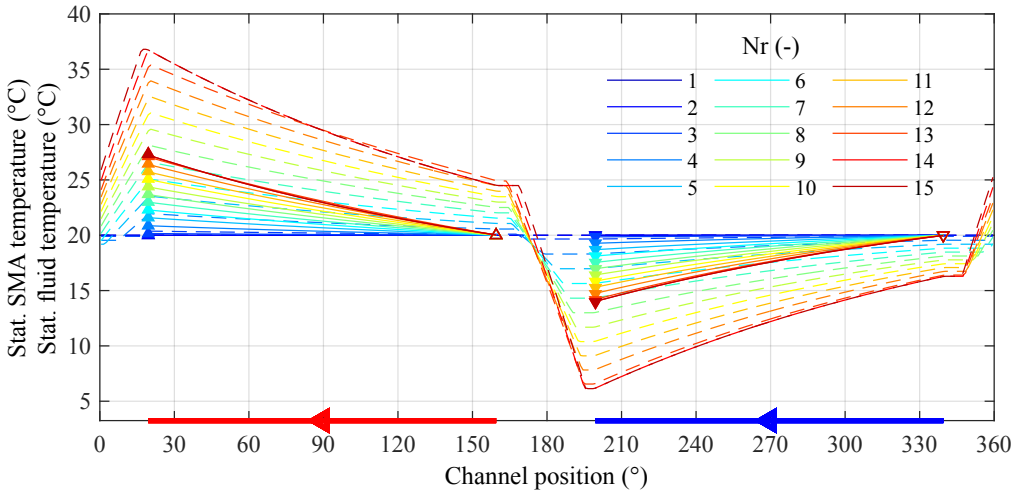

Figure 5.91: Maximum cam stroke: Resulting SMA element (dashed) and fluid (solid) temperature along the circumference for different maximum cam strokes.

flow direction of the fluid is indicated with an arrow, creating a counter-flow in both ducts. Each temperature curve of the fluid is framed at the edges by triangles that are upturned at the hot duct and downturned at the cold duct. The temperature of the SMA element increases during loading and decreases during unloading adiabatically due to the suppressed HE in the transition zones.

In the simulations with number 14 and 15, the SMA material undergoes complete PT in the transition zones, resulting in a purely adiabatic EC cycle, as introduced in Figure 1.2 and Figure 1.3. During the motion along the ducts, the SMA elements exchange their thermal energy with the fluid and cool down after loading or heat up after unloading. Therefore, the fluid heats up in the hot duct and cools down in the cold duct.

From simulation number 3 and 13, the SMA material performs a part of its PT in the ducts, due to the post-PT, resulting in a hybrid EC cycle, as introduced in Figure 1.5. The post-PT explains the shallower temperature decay of the SMAs compared to the simulation with the fully transformed material. Therefore, in simulation number 15, the temperature change of the SMA caused by the PT with the suppressed HE is larger than the others.

The largest temperature change of the SMA element during PT and HE is achieved in the simulations with full PT. The maximum temperature difference of the fluid correlates with the applied strain change. The triangles at the inlets are empty, and the triangles at the outlets are filled.

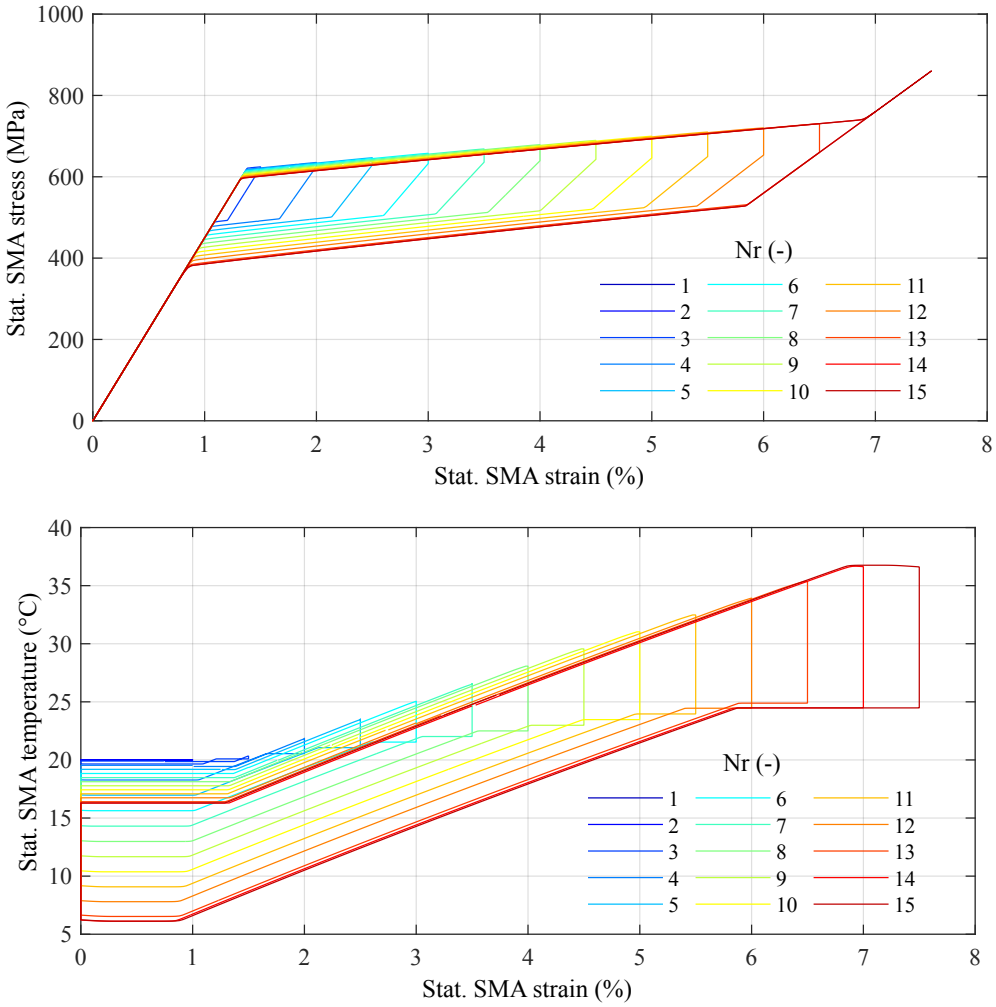

Figure 5.92: Maximum cam stroke: Resulting stress-strain diagram and temperature-strain diagram of one SMA element for the different maximum cam strokes.

Figure 5.92 presents the resulting stress-strain diagram and the temperature-strain diagram of a SMA element for the different maximum strains. As expected, the hysteresis height increases with increasing maximum strain due to the corresponding increase in temperature difference of the SMA element during PT. In addition to the temperature difference between maximum and minimum SMA temperature, the start temperature of the FT decreases and the start temperature of the BT increases, due to the incomplete HE between SMA and fluid. Therefore, the position of the upper plateau decreases and the hysteresis height increases with increasing maximum strain due to the temperature dependent transformation stress as introduced in Equation 2.5 and Equation 2.7.

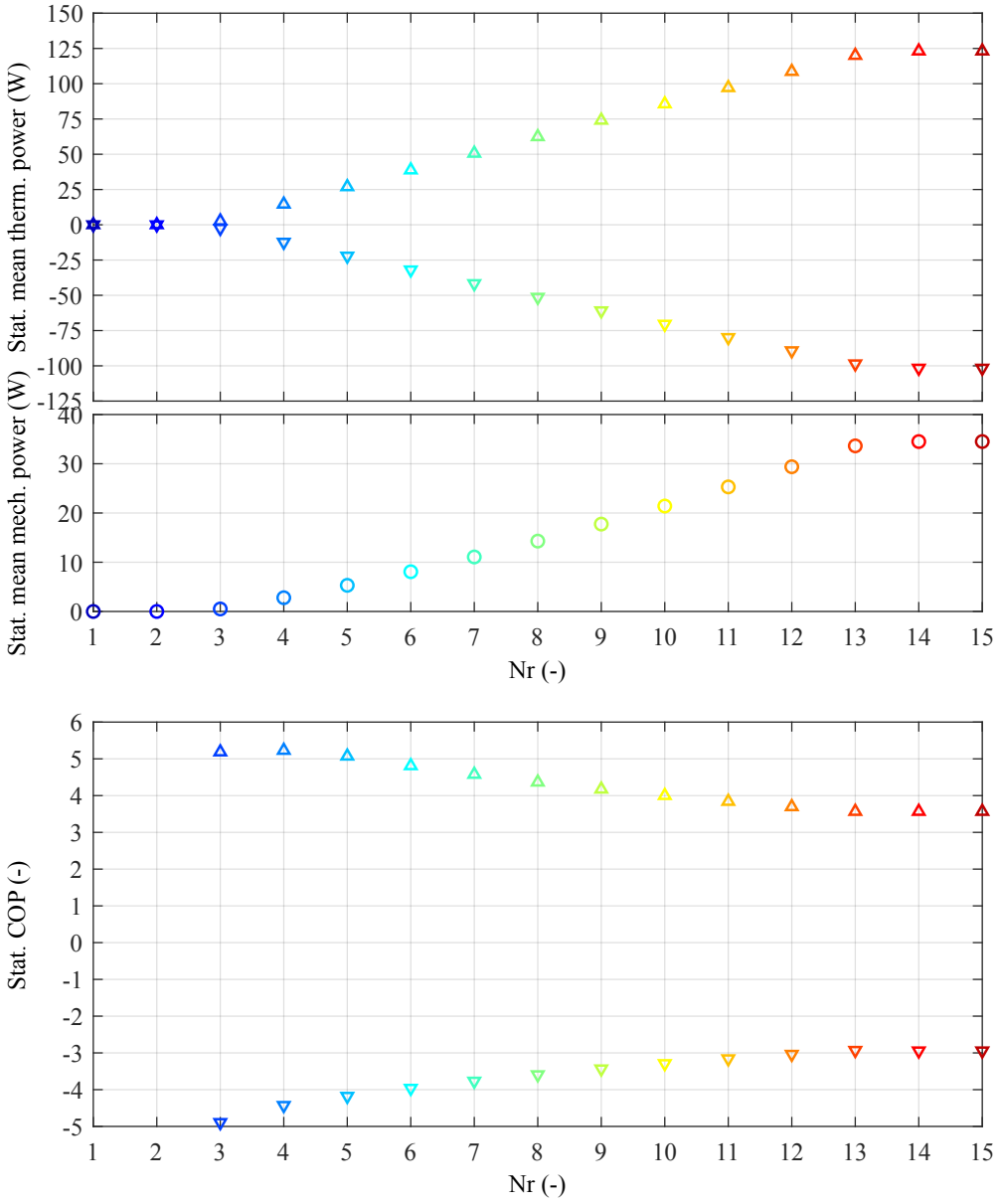

Figure 5.93: Maximum cam stroke: Resulting thermal and mechanical power and *COP* for different maximum cam strokes.

Figure 5.93 shows the thermal and mechanical power, as well as the *COP* along the simulation number of the parameter study. The colors correspond to those of Figure 5.90. The amount of the thermal power at the hot duct (upturned triangles) and cold duct (downturned triangles) increases with increasing maximum strain change. This is caused by the increasing release and absorption of specific latent heat and increasing temperature difference between SMA and fluid with increasing maximum strain change, following Equation 5.2 and Equation 5.16. The mechanical power input also increases with increasing hysteresis area. The *COP* slightly decreases with rising maximum strain since the mechanical power increases faster than the thermal power.
To summarize, this parameter study shows that the variation of the strain change by adapting its maximum value significantly affects the mechanical and thermal power in- and output of the EC HP. The thermal power depends on the amount of transformed SMA material activated by the applied strain change.

5.6.17 Strain range

In this section, the design parameter cam stroke range, and thereby the SMA's strain range, is varied from 0.5 to 7.5 % while maintaining its mean value at 3.75 %, in steps of 0.5 %.
Figure 5.94 illustrates the loading profile in relation to the stroke and the corresponding M+ phase fraction in the SMA elements along the channel position for the 15 different simulations. The arrangement of the hot and cold duct is shown in color at the x-axis. The colors used for the simulation numbers are consistent in all diagrams of this section. The load profile is symmetrically adjusted for loading and unloading by modifying the slope for each simulation, ensuring that the strain change of the SMA element begins with entering the transition zone and ends with exiting it. The resulting different strain rates do not influence the EC cycle during loading and unloading due to the adiabatic condition in the transition zone.
After loading, the SMA material exhibits in the simulation numbers 2 to 12 a post-PT, indicated by the changing phase fraction of the SMA during the holding phases.
Figure 5.95 presents the resulting temperature evolution for the SMA element as dashed line and fluid as solid line along the circumference for the different cam strokes. The arrangement ducts is shown at the x-axis indicating counter-flow. The temperature of the SMA element increases during loading and decreases during unloading adiabatically due to the suppressed HE in the transition zones. The SMA's in simulation number 1 exhibit almost no PT and thus no temperature change, as the applied strain change is so small that only elastic deformation takes place.
In the simulation number 13 to 15, the SMA material undergoes complete PT in the transition zones, resulting in a purely adiabatic EC cycle, as introduced in Figure 1.2 and

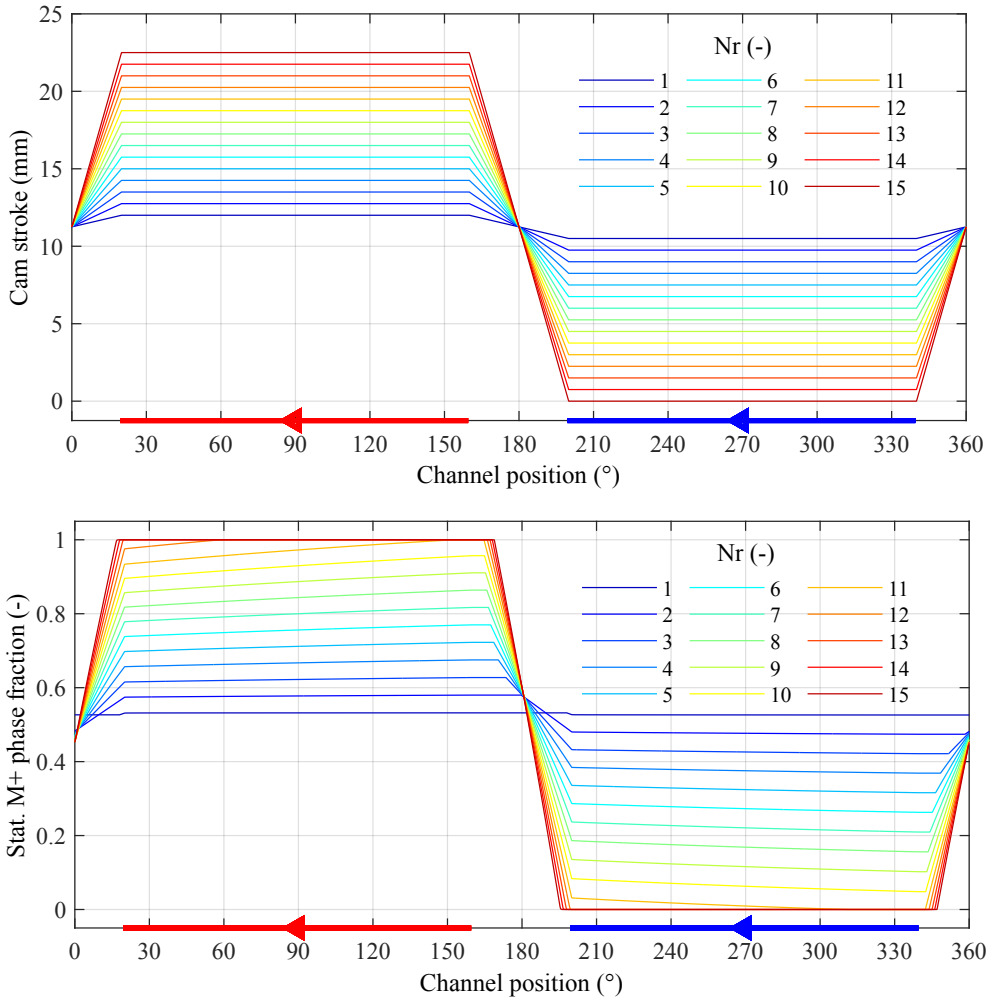

Figure 5.94: Minimum and maximum cam stroke: Symmetric loading and unloading profile with different minimum and maximum cam stroke and resulting M+ phase fraction in the SMA elements along the circumference.

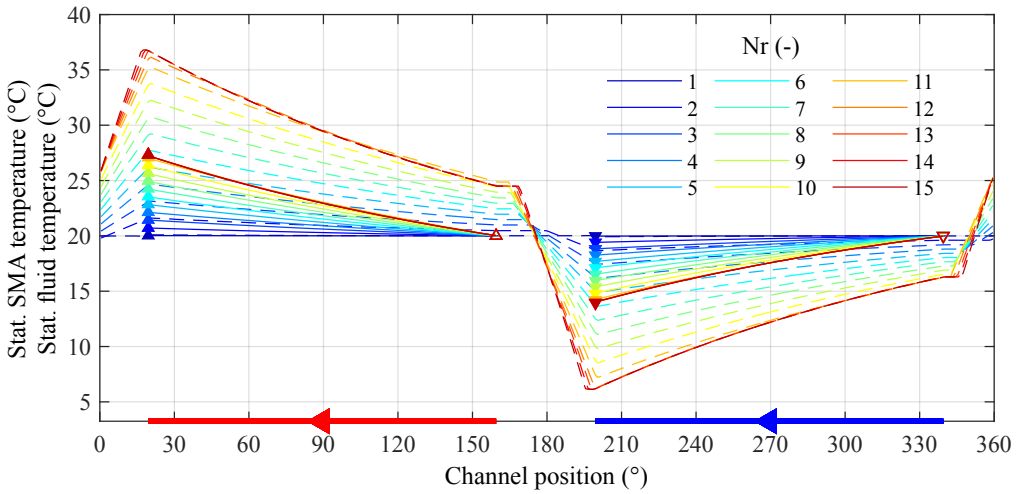

Figure 5.95: Minimum and maximum cam stroke: Resulting SMA element (dashed) and fluid (solid) temperature along the circumference for different Minimum and maximum cam strokes.

Figure 1.3. During the motion along the ducts, the SMA elements exchange their thermal energy with the fluid. Therefore, the fluid heats up in the hot duct and cools down in the cold duct.
From simulation number 2 to 12, the SMA material performs a part of its PT in the ducts, due to the post-PT, resulting in a hybrid EC cycle, as introduced in Figure 1.5. During the motion along the ducts, the SMA elements exchange its thermal energy with the fluid while the ongoing PT releases or absorbs of thermal energy. This explains, amongst other things, the shallower temperature decay of the SMAs compared to the simulation with full PT in the transition zone. Therefore, in simulation number 13 to 15, the temperature change of the SMA caused by HE is larger than the others.
Each temperature curve of the fluid is framed at the edges by triangles that are upturned at the hot duct and downturned at the cold duct. The triangles at the inlets are empty, and the triangles at the outlets are filled. The temperature difference of the fluid between in- and outlets correlates with the strain change prescribed by the parameter study.
Figure 5.96 presents the resulting stress-strain diagram and the temperature-strain diagram of a SMA element for the different strain amplitudes. As expected, the hysteresis height increases with increasing strain change and the corresponding increasing temperature difference of the SMA element during the PT. In addition to the difference between the maximum and minimum SMA temperature, the start temperature of the FT decreases and the start temperature of the BT increases, due to the incomplete HE between SMA and fluid.
Figure 5.97 shows the thermal and mechanical power, as well as the *COP* along the simulation number of the parameter study. The amount of the thermal power at the hot duct (upturned triangles) and cold duct (downturned triangles) increases with increasing strain change. This is caused by the increasing release and absorption of specific latent heat during the EC cycle and increasing HE between SMA and fluid with increasing strain change, following Equation 5.2 and Equation 5.16.
The mechanical power input also increases with increasing strain change due to the increasing SMA's temperature difference and the thermal dependence of the transformation stress as introduced in Equation 2.5 and Equation 2.7.
The *COP* slightly decreases throughout the parameter study due to the steeper increase in mechanical than the thermal power.
To summarize, this parameter study shows that the variation of the strain amplitude significantly affects the mechanical and thermal power in- and output of the EC HP. The comparison between partly loading the SMA material with internal hysteresis loops in the stress-strain diagram indicates that the thermal power output depends on the amount of transformed SMA material similar to subsection 5.6.16.

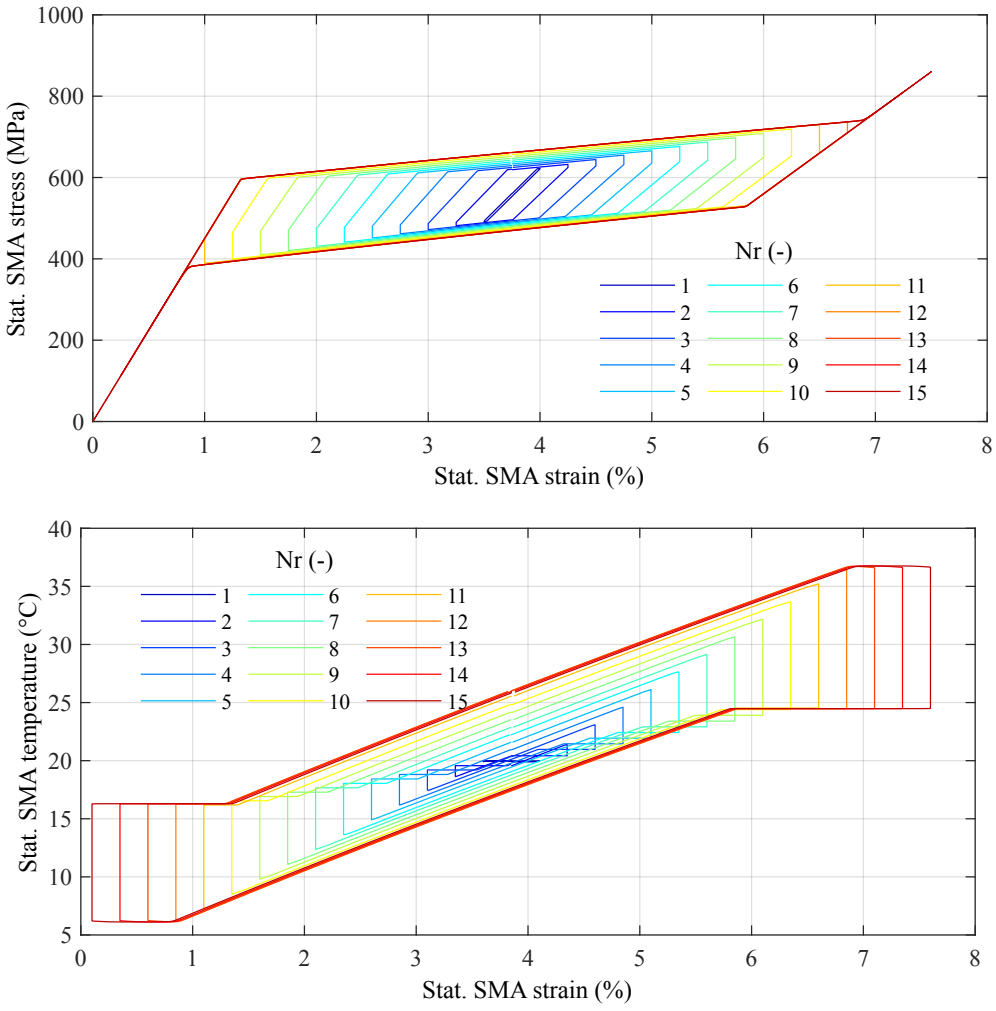

Figure 5.96: Minimum and maximum cam stroke: Resulting stress-strain diagram and temperature-strain diagram of one SMA element for the different minimum and maximum cam strokes with a mean strain of 4 %.

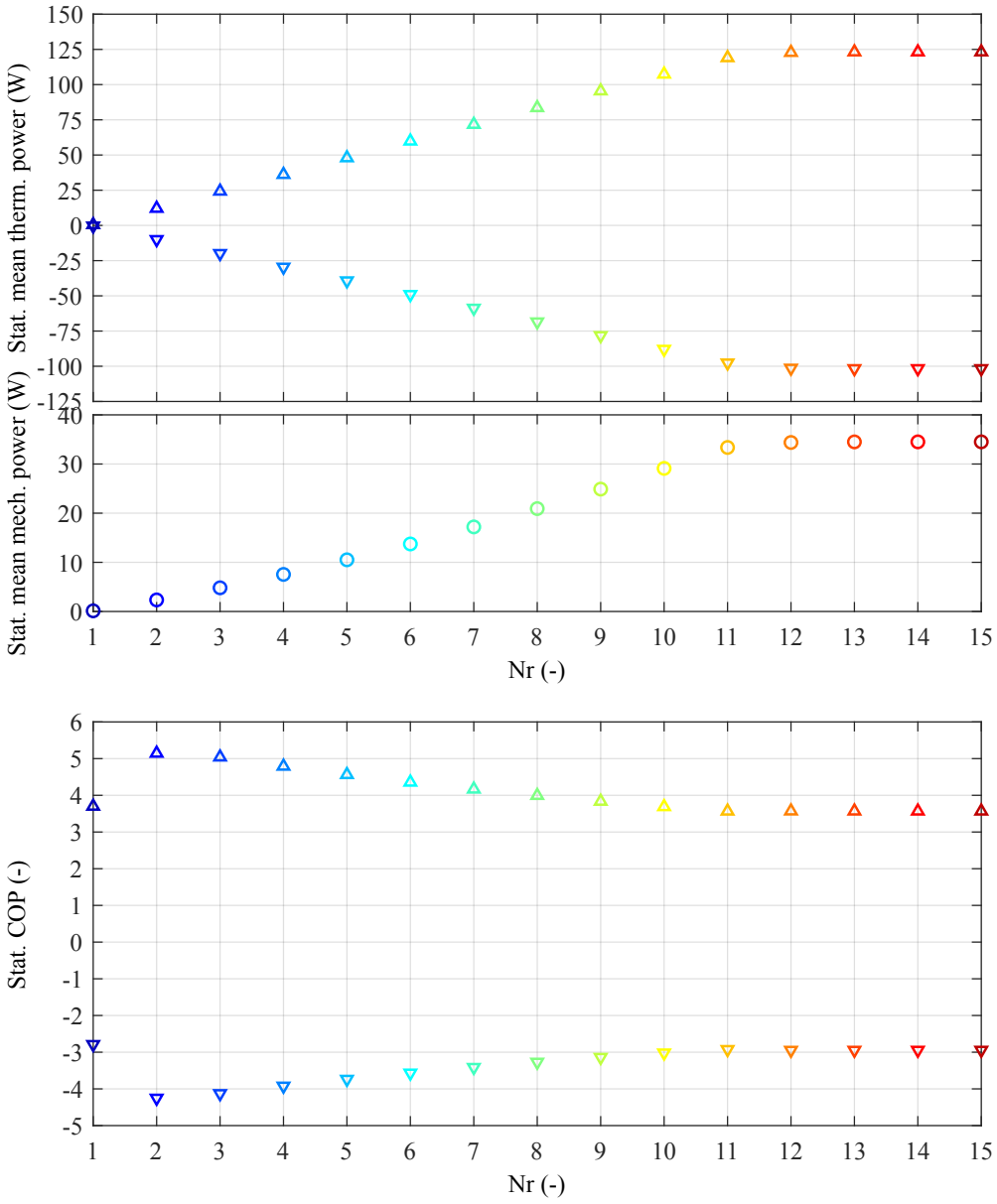

Figure 5.97: Minimum and maximum cam stroke: Resulting thermal and mechanical power and *COP* for different minimum and maximum cam strokes with a mean strain of 4 %.

5.6.18 Cam track geometry

In this section, the design parameter cam track geometry, as shown in Figure 5.6, is varied in eight simulations.
Figure 5.98 illustrates the loading profile and the corresponding M+ phase fraction in the SMA elements along the channel position for the different simulations. The arrangement of the hot and cold duct is shown in color at the x-axis. The colors used for the simulation number are consistent in all diagrams of this section. The loading and unloading profile is

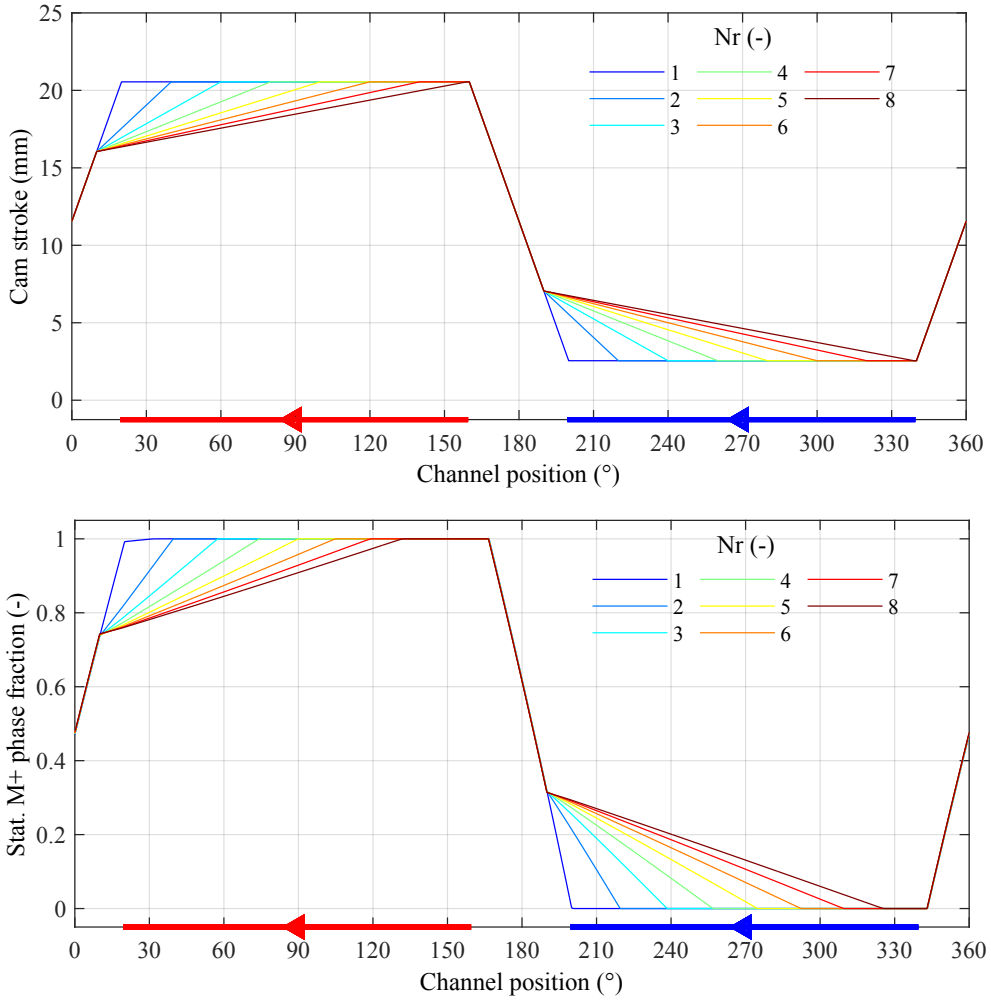

Figure 5.98: Cam track geometry: Symmetric loading and unloading profile with different slopes and resulting M+ phase fraction in the SMA elements along the circumference.

symmetrically altered by adjusting the slope, beginning at the same point in the transition zone for each simulation. This adjustment results in a variation of the endpoint along each semicircle for both loading and unloading. A full FT during loading and a full BT during unloading is reached approximately at the midpoint of the corresponding duct for the shallowest load profile.

Figure 5.99 presents the resulting temperature evolution for the SMA element as dashed line and fluid as solid line along the circumference for the different simulations. The

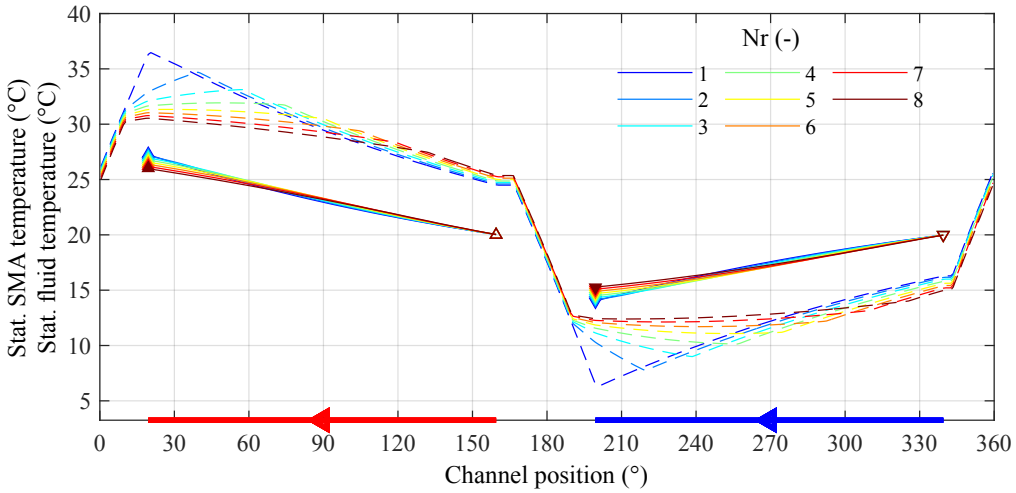

Figure 5.99: Cam track geometry: Resulting SMA element (dashed) and fluid (solid) temperature along the circumference for different loading profiles.

arrangement of the duct is shown at the x-axis. The flow direction of the fluid creates a counter-flow in both ducts. Each temperature curve of the fluid is framed at the edges by triangles that are upturned at the hot duct and downturned at the cold duct. The triangles at the inlets are empty, and the triangles at the outlets are filled. The temperature of the SMA element increases during loading and decreases during unloading in the transition zones adiabatically due to the suppressed HE.

In the simulation number 1, the SMA material undergoes complete PT in the transition zones, resulting in a purely adiabatic EC cycle, as introduced in Figure 1.2 and Figure 1.3. During the motion along the ducts, the SMA elements exchange their thermal energy with the fluid and cool down after loading or heat up after unloading. Therefore, the fluid heats up during traveling along the hot duct and cools down during traveling along the cold duct.

From simulation number 2 to 8, the SMA material performs a part of its PT in the ducts, resulting in an hybrid EC cycle, as introduced in Figure 1.5. During the motion along the ducts, the SMA elements exchange their thermal energy with the fluid while the ongoing PT releases or absorpts specific latent heat. Therefore, in the first part of the ducts after PT, the SMA still heats up after loading and still cools down after unloading. After reaching the state of full PT, the SMA temperature follows the pure exponential decay. The fluid heats up during traveling along the hot duct and cools down in the cold duct.

The largest temperature difference of the SMA element is achieved during the purely adiabatic EC cycle. The temperature difference of the fluid is very similar for all simulations. However, the maximum temperature difference of the fluid is also reached during this purely adiabatic EC cycle. Whereas, in the hybrid EC cycles, the SMA temperature

difference during PT, and HE, decreases with shallower load profiles. This trend correlates with the decreasing temperature difference of the fluid, with longer load profiles. Therefore, the minimum temperature difference of the fluid is also reached during EC cycle with the largest portion of PT during HE in the ducts.
Figure 5.100 presents the resulting stress-strain diagram of a SMA element for the different EC cycles. As expected, the hysteresis area decreases shallower load profiles due to the

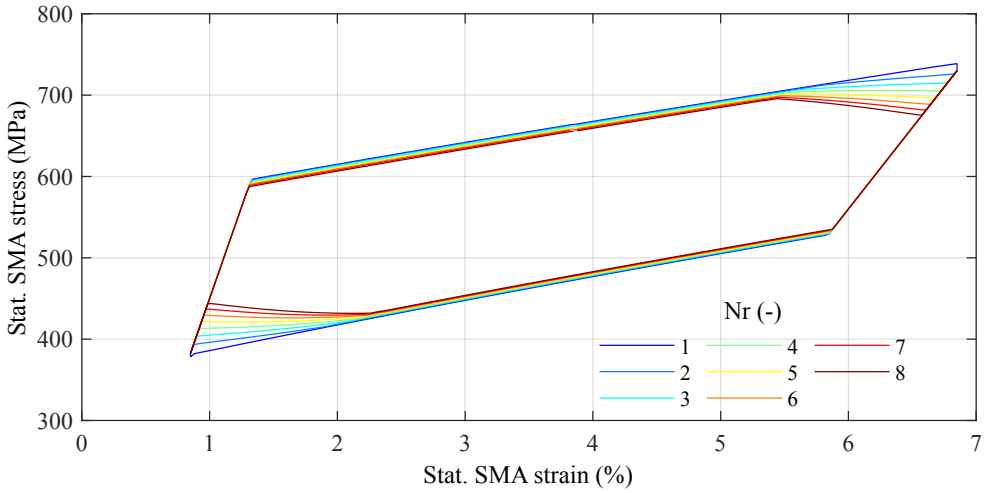

Figure 5.100: Cam track geometry: Resulting stress-strain diagram of one SMA element for the different EC cycles.

corresponding decreasing temperature difference of the SMA element.
Figure 5.101 shows the thermal and mechanical power, as well as the *COP* along the simulation number of the parameter study. The amount of the thermal power at the hot duct (upturned triangles) and cold duct (downturned triangles) slightly decreases with longer load profiles. This is caused by the decreasing temperature difference between SMA and fluid and resulting reduced HE, following Equation 5.16. The change in the HE is also indicated by the crossing of the lines for the different simulation numbers.
The mechanical power input slightly decreases with increasing PT portion in the ducts due to the smaller hysteresis area in the stress-strain behavior, seen in Figure 5.100.
The *COP* of the EC HP remains consistent throughout the parameter study because of the equal reduction in thermal and mechanical power.
To summarize, this parameter study shows that the variation of the EC cycle affects the mechanical and thermal power in- and output of the EC HP. An adiabatic-isothermal combined EC cycle can reduce the requiered mechanical power.

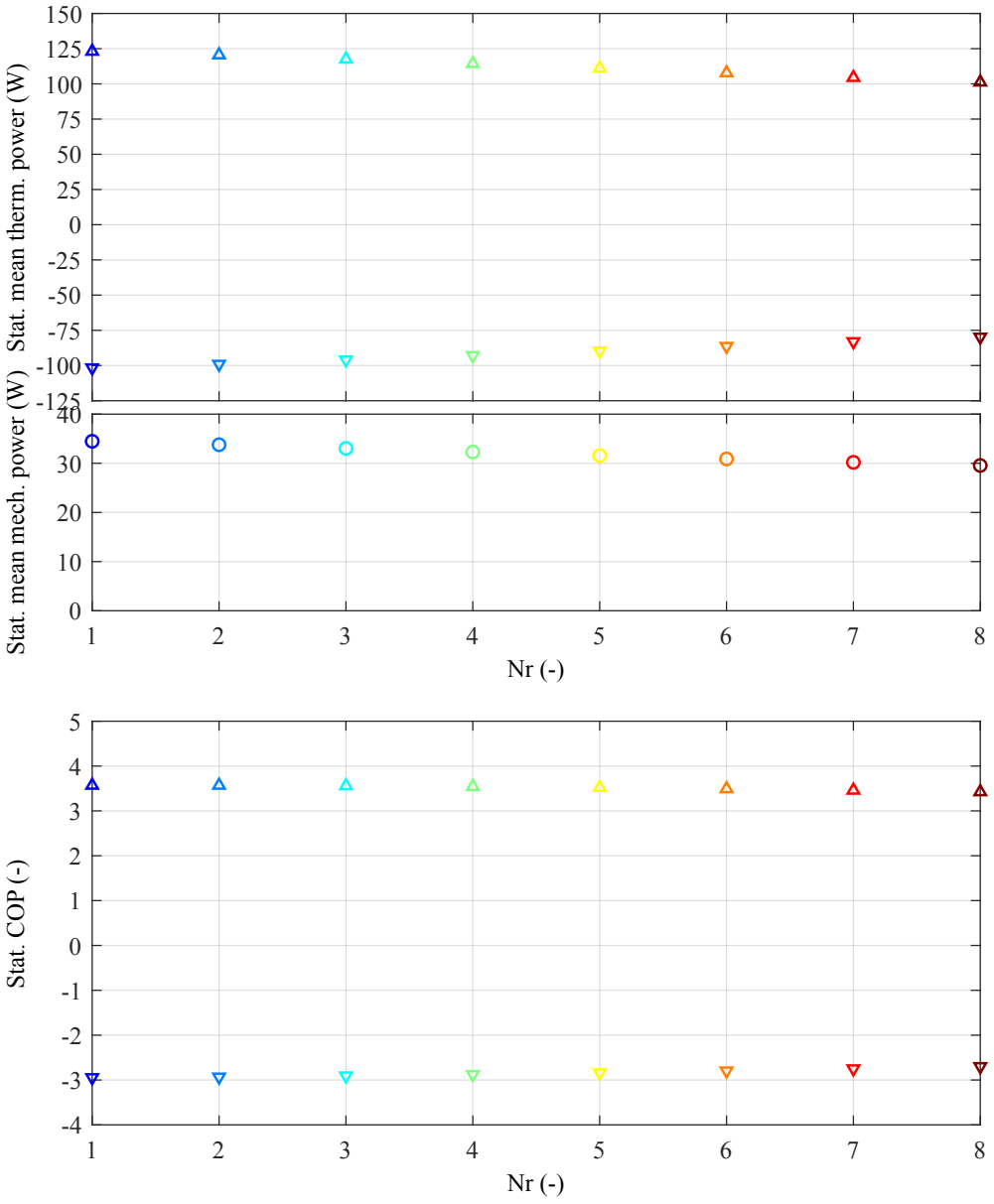

Figure 5.101: Cam track geometry: Resulting thermal and mechanical power and *COP* for different loading proflies.

5.6.19 EC-optimized material

In this section, a parameter study using the optimized EC material NiTiCuV [93], with its properties in Table 5.5 is performed. The operating parameter flow rate of the ducts is varied in the range from $5\,m^3/h$ to $200\,m^3/h$. Additionally, the rotation frequency of the SMA arrangement is adjusted in the range from $-2\,Hz$ to $2\,Hz$.

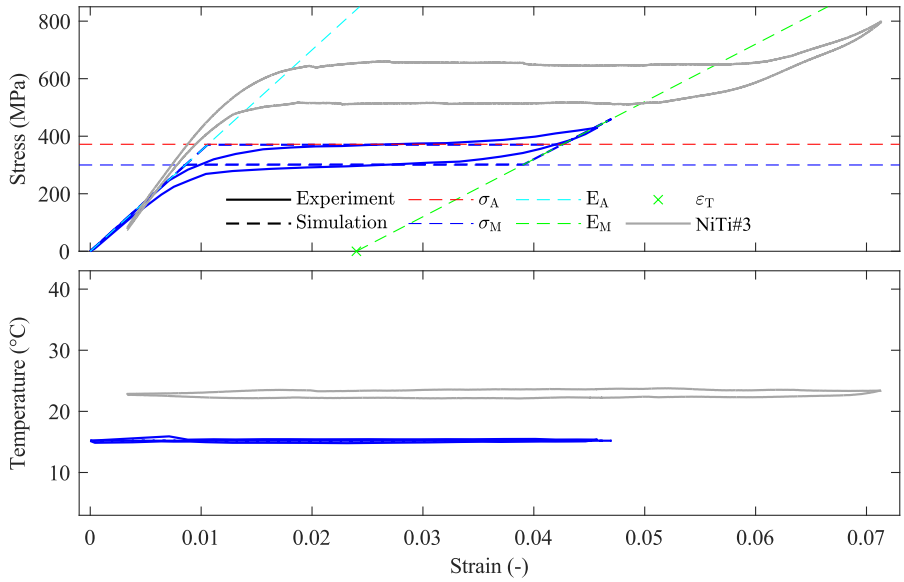

Figure 5.102: EC-optimized material: Stress-strain diagram (upper) and temperature-strain diagram (lower) of the simulation results as dashed line, and the experimental data as solid line for the isothermal cycle, NiTiCuV colored in blue, NiTiCo colored in gray.

Figure 5.102 compares the thermo-mechanical properties of the isothermal cycle between NiTiCo, colored in gray, and NiTiCuV, colored in blue, while using two diagrams: stress-strain diagram (upper) and temperature-strain diagram (lower). The results of the calibrated material model are represented as dashed lines, while the experimental data are shown as solid lines. The stress-strain relationship shows that the mean stress is lower, as well as the hysteresis width and height is smaller for the NiTiCuV. The temperature-strain shows that the almost isothermal PT occurs at a lower temperature for the NiTiCuV.
The following diagrams of this subsection are presented for NiTiCuV, comparable diagrams for NiTiCo are presented in subsection 5.6.7.
Figure 5.103 presents the resulting inlet and outlet temperatures at the hot and cold duct along the rotation frequency for different flow rates. The temperature at the hot duct is represented by upturned triangles, and the cold duct is shown as downturned triangles. The triangles at the inlets are empty, and the triangles at the outlets are filled. The positive values of the rotation frequency combined with the standard arrangement of the fluid ducts create a counter-flow between SMA and fluid. At negative values of the rotation frequency, the SMA arrangement moves counter-clockwise, resulting in a parallel-flow

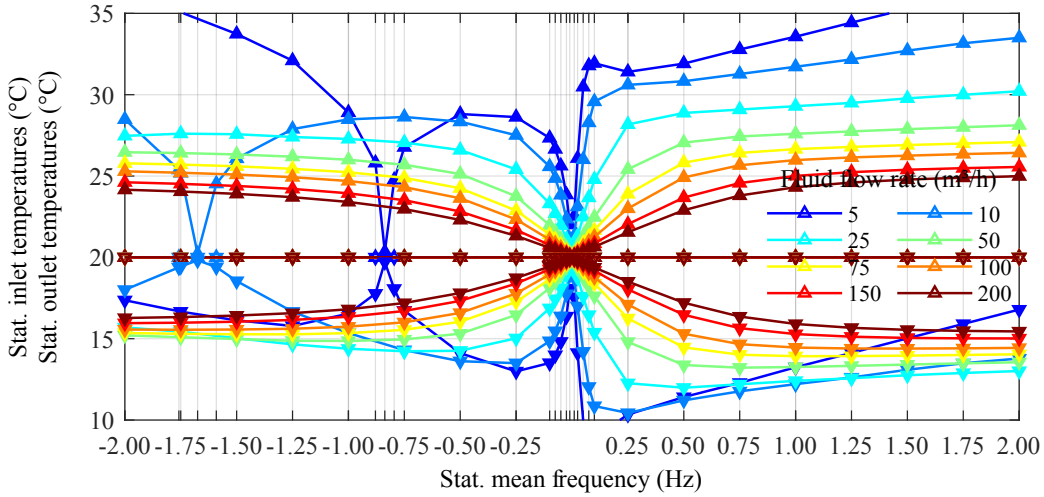

Figure 5.103: EC-optimized material: Resulting inlet and outlet temperature at hot and cold duct along the rotation frequency for different flow rates.

between SMA and fluid. Due to the symmetric load profile, a similar EC cycle is generated during loading and unloading for both the counter-flow and parallel-flow.

The temperature change of the SMA reached during the PT is defined by its specific latent heat and specific heat capacity. Therefore, the temperature difference of the SMA element reached during FT and BT remains constant by the variation of the rotation frequency when similar EC cycles are performed. This is fulfilled since the PT is performed adiabatically, and the stress during FT does not pass over the tensile strength, as well as the temperature of the SMA during BT does not fall below the austenite finish temperature. The thermal energy of the SMA arrangement, which can be exchanged with the fluid, following Equation 5.2 and Equation 5.16, increases with increasing rotation frequency due to growing number of performed EC cycles per time. Therefore, the temperature difference between inlet and outlet of the fluid ducts increases with increasing rotation frequency for a specific fluid flow rate. In the case of high enough flow rates, this temperature difference nearly reaches saturation with further increasing rotation frequency. Whereas, if the dwell-time of a fluid portion in the duct increases, with small flow rates, the temperature difference of the fluid increases due to the increasing HE with the fluid.

The curve shift towards heating of the outlet temperatures is related to the asymmetric temperature development in the SMA during PT. This is based on the asymmetric specific latent heat, which favors heating, as introduced in Equation 5.44 and Equation 5.45. The falling-in of the outlet temperature at parallel-flow is caused by the diminishing relative velocity between SMA and fluid, following Equation 5.27, resulting in a rapidly decreasing heat exchange coefficient down to zero.

The comparison between the counter-flow and the parallel-flow exhibits a higher temperature difference between inlet and outlet for the counter-flow, as discussed in detail in Figure 5.64. A higher temperature difference between the inlet and the outlet of the fluid

ducts is reached for counter-flow due to the temperature development in the duct, and the increased heat exchange coefficient based on the increased relative velocity for the same rotation frequency and flow rate. Additionally, the temperature difference remains consistent for the counter-flow across all combinations of rotation frequency and flow rate, allowing for improved controllability of the EC HP.

Figure 5.104 shows the thermal and mechanical power, as well as the *COP* along the rotation frequency for different flow rates. The colors of the flow rates correspond to those of Figure 5.103. The amount of the thermal power output at the hot duct (upturned triangles) and cold duct (downturned triangles) increases with increasing flow rate due to the better HE between SMA and fluid. For a lower rotation frequency, a lower flow rate is sufficient to exchange the complete thermal energy provided by the SMAs. Therefore, thermal power at the ducts increases with increasing rotation frequency up to a specific point for each flow rate where a kind of saturation starts. At the negative rotation frequency, the misalignment of the curves for small flow rates is caused by the unsteady relative velocity between SMA and fluid.

Additionally, the thermal power output is larger at counter-flow for the same combination of rotation frequency and flow rate compared to the parallel-flow. The mechanical power input increases with increasing rotation frequency due to the growing number of performed EC cycles per time. The increased HE between SMA and fluid for increasing flow rate results in a higher maximum and minimum temperature difference of the SMA element during the EC cycle, leading to an increase in mechanical power input with rising flow rate. As a result, the *COP* decreases with increasing rotation frequency and increases with increasing flow rate.

To summarize, this parameter study demonstrates that the variation of the rotation frequency and flow rate significantly affects the mechanical and thermal power in- and output, as well as the temperature output of the EC HP. The comparison between Figure 5.65 and Figure 5.104 demonstrates that the same EC HP, utilizing an optimized EC material such as NiTiCuV, can reduce the mechanical power requirement by over 50 % while maintaining its thermal power output. As a result, the efficiency can be more than doubled, significantly increasing the *COP* from 6.5 to 13.

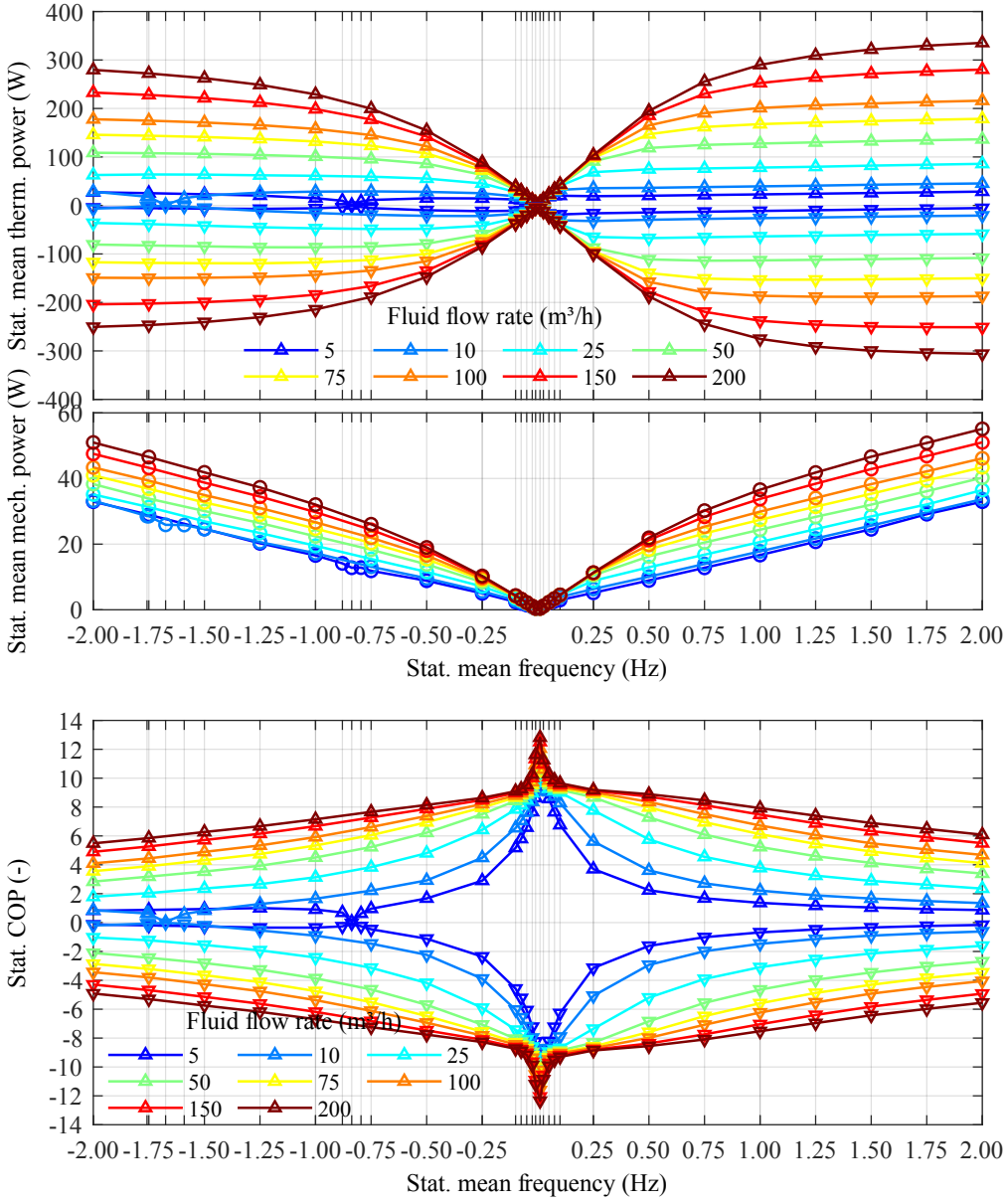

Figure 5.104: EC-optimized material: Resulting thermal and mechanical power and *COP* along the rotation frequency for different flow rates.

5.7 Parameter studies using water as fluid

In this section, the calibrated and validated simulation tool, along with its sub-tools, is utilized to investigate the thermo-mechanical behavior of the EC HP with water as HE and HT fluid.

As known from the foregoing section, use the fluid properties of Table 5.4, the SMA properties of Table 5.5, the solver settings of Table 5.6, as well as the design and operating parameters of Table 5.7 and Table 5.8. The standard parameter from section 5.5 are used unless otherwise mentioned.

Different parameter studies following the calculation procedure introduced in section 5.3 will be discussed. They are organized in the *parameter set table*, simulated with the *simulation tool*, using the *parallel computation tool*, and evaluated using the *parameter comparison tool*, as well as the *visualization tool*.

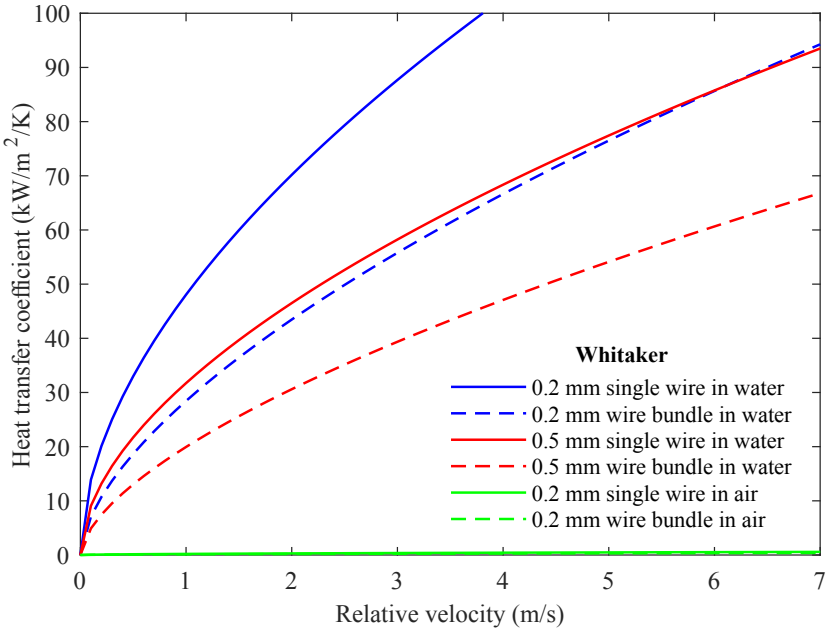

Figure 5.105: Comparison of different approaches for calculating the heat exchange coefficient between SMA and fluid.

Figure 5.105 compares the heat exchange coefficient of air and water as HT medium for different relative velocities. This relationship is based on the calculation method by *Whitaker*, as outlined in Equation 5.30 and Equation 5.26. The values of the heat exchange coefficient increase as the relative velocity between the SMA arrangement and the fluid increases, with a degressive dependency. Using a single wire or a bundle in the SMA arrangement, water exhibits a significant advantage compared to air. The relationship between heat exchange coefficient and relative velocity for air is presented at an appropriate scale in Figure 5.14. The heat exchange coefficient in cross-flow for single wires is larger for both SMA diameters than for SMA bundles with the same SMA diameter.

In the following subsections, the potential for water as HE and HT fluid is discussed in various parameter studies.

5.7.1 Flow rate and frequency with flow direction

In this section, the operating parameter flow rate of the hot and cold duct is varied in the range from 1 L/min to 20 L/min. Additionally, the rotation frequency of the SMA arrangement in the EC HP is adjusted in the range from −10 Hz to 10 Hz. The material used is the commercially available NiTiCo, with the material parameter in Table 5.5.
The following diagrams of this subsection are presented for water as HE and HT fluid, comparable diagrams for air are presented in subsection 5.6.7.
Figure 5.106 presents the resulting inlet and outlet temperatures at the hot and cold duct along rotation frequency for different flow rates. The temperature at the hot duct is represented by upturned triangles and at the cold duct as downturned triangles. The triangles at the inlets are empty, and the triangles at the outlets are filled. The positive

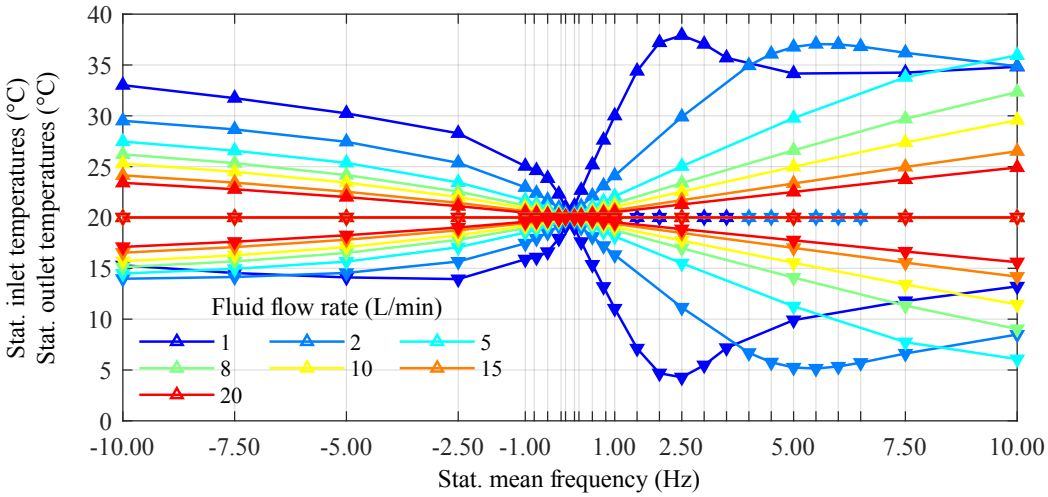

Figure 5.106: Flow rate and frequency using water: Resulting inlet and outlet temperature at hot and cold duct along the rotation frequency for different flow rates.

values of the rotation frequency combined with the standard arrangement of the fluid ducts create a counter-flow between the SMA and the fluid. At the negative values of the rotation frequencies, the SMA arrangement moves counter-clockwise, creating a parallel-flow between SMA and fluid. Due to the symmetric load profile, a similar EC cycle is generated for counter-flow and parallel-flow.
The temperature change of the SMA reached during the PT is defined by the specific latent heat and specific heat capacity. Therefore, temperature difference of the SMA element reached during FT and BT remains constant by the variation of the rotation frequency when similar EC cycles are performed. This is fulfilled as the PT is performed

adiabatically, the stress of SMA during FT does not pass over the tensile strength, and the temperature of the SMA during BT does not fall below the austenite finish temperature. The thermal energy of the SMA arrangement, which can be exchanged with the fluid, following Equation 5.2 and Equation 5.16, increases with increasing rotation frequency due to growing number of performed EC cycles per time. Therefore, the temperature difference between inlet and outlet increases with increasing rotation frequency for a specific fluid flow rate. In the case of low flow rates, this temperature difference nearly reaches saturation with further increasing rotation frequency. Whereas, if the dwell-time of the fluid portion in the duct increases, at small flow rates, the temperature of the fluid increases due to the increasing HE with the fluid.

The curve shift towards heating of the outlet temperatures is related to the asymmetric temperature development in the SMA during PT, based on asymmetric specific latent heat, as introduced in Equation 5.44 and Equation 5.45. Due to the large relative velocity between SMA and fluid, no falling-in of the outlet temperature at parallel-flow is observed in comparison to Figure 5.63.

In the case of the two lowest flow rates, the outlet temperatures decreases with increasing rotation frequency at a certain point. At this point, the small fluid flow can not extract the thermal energy out of the ducts. Therefore, the temperature difference of the SMA while traveling along the ducts decreases. Following, the SMA starts the FT at a low temperature and the BT at a high temperature, resulting in a lower output temperature of the hot duct and a higher output temperature of the cold duct, visible in Figure 5.107. This diagram presents the resulting temperature evolution for the SMA element as a dashed line and fluid as a solid line along the circumference for counter-flow and a fluid flow rate of 1 L/min. The arrangements of the hot and cold duct are shown in color at the x-axis. The flow direction of the fluid is indicated with an arrow. For the positive rotation frequency, a counter-flow in both ducts is created due to the clockwise rotation of the SMA arrangement. Each temperature curve of the fluid is framed at the edges by triangles that are upturned at the hot duct and downturned at the cold duct. The triangles at the inlets are empty, and the triangles at the outlets are filled.

The temperature of the SMA element increases during loading and decreases during unloading adiabatically due to the suppressed HE in the transition zones. The SMA material undergoes complete PT in the transition zones. During the motion along the ducts, the SMA elements exchange their thermal energy with the fluid and cool down after loading or heat up after unloading. Therefore, the fluid heats up during traveling along the hot duct and cools down during traveling along the cold duct.

The temperature difference of the SMA element reached during FT and BT remains constant by the variation of the flow condition because this temperature change is defined by the specific latent heat and the specific heat capacity of the SMA. Whereas the

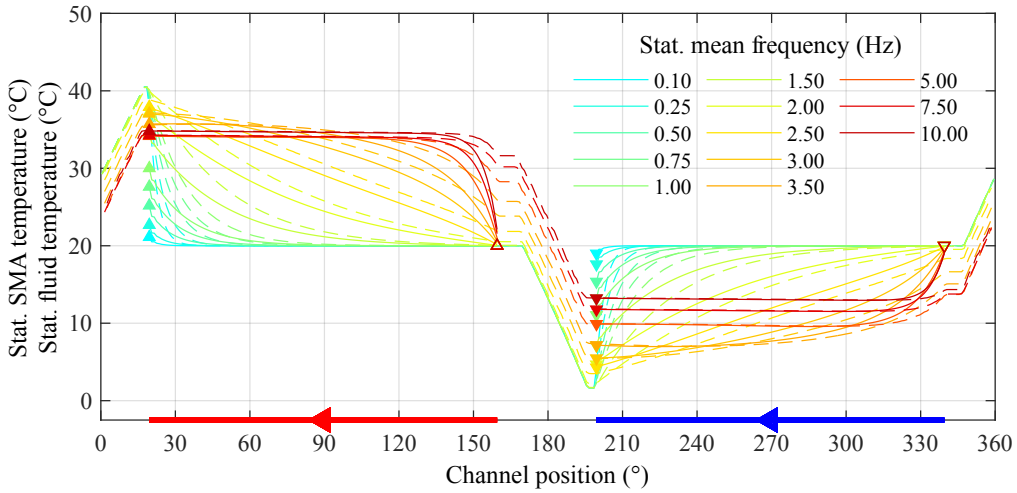

Figure 5.107: Flow rate and frequency: Resulting SMA element (dashed) and fluid (solid) temperature along the circumference for the counter-flow at a fluid flow rate of 1 L/min.

temperature difference between the maximum and minimum temperature of the SMA along the EC cycle changes with the flow condition. This is the case of rotation frequencies lower than 2 Hz. In these simulations, the temperature evolution of the SMA and fluid build lines with the same gradient.

With further increasing rotation frequency, the amount of the fluid per time is not sufficient to extract the thermal energy from the SMA arrangement. Therefore, the SMA temperature does not reach the inlet temperature before the PT starts, leading to a reduced maximum after FT and minimum after BT. Due to the insufficient temperature change of the SMA in the ducts, the temperature span of the SMA element along the EC cycle is reduced.

Figure 5.106 presents also the comparison between counter-flow and parallel-flow. A higher temperature difference between inlet and outlet is reached at counter-flow due to the advantageous temperature development in the duct, and the increased heat exchange coefficient based on the increased relative velocity for the same rotation frequency and flow rate.

Figure 5.108 shows the thermal and mechanical power, as well as the *COP* along the rotation frequency for different flow rates. The colors correspond to those of Figure 5.106. The amount of the thermal power output at the hot duct (upturned triangles) and cold duct (downturned triangles) increases with increasing flow rate due to the better HE between SMA and fluid. For a lower rotation frequency, a lower flow rate is sufficient to exchange the complete thermal energy between SMA and fluid. Therefore, thermal power at the ducts increases with increasing rotation frequency up to a specific point for each flow rate where a kind of saturation starts. Additionally, the thermal power output is larger for counter-flow at the same combination of rotation frequency and flow rate compared to parallel-flow.

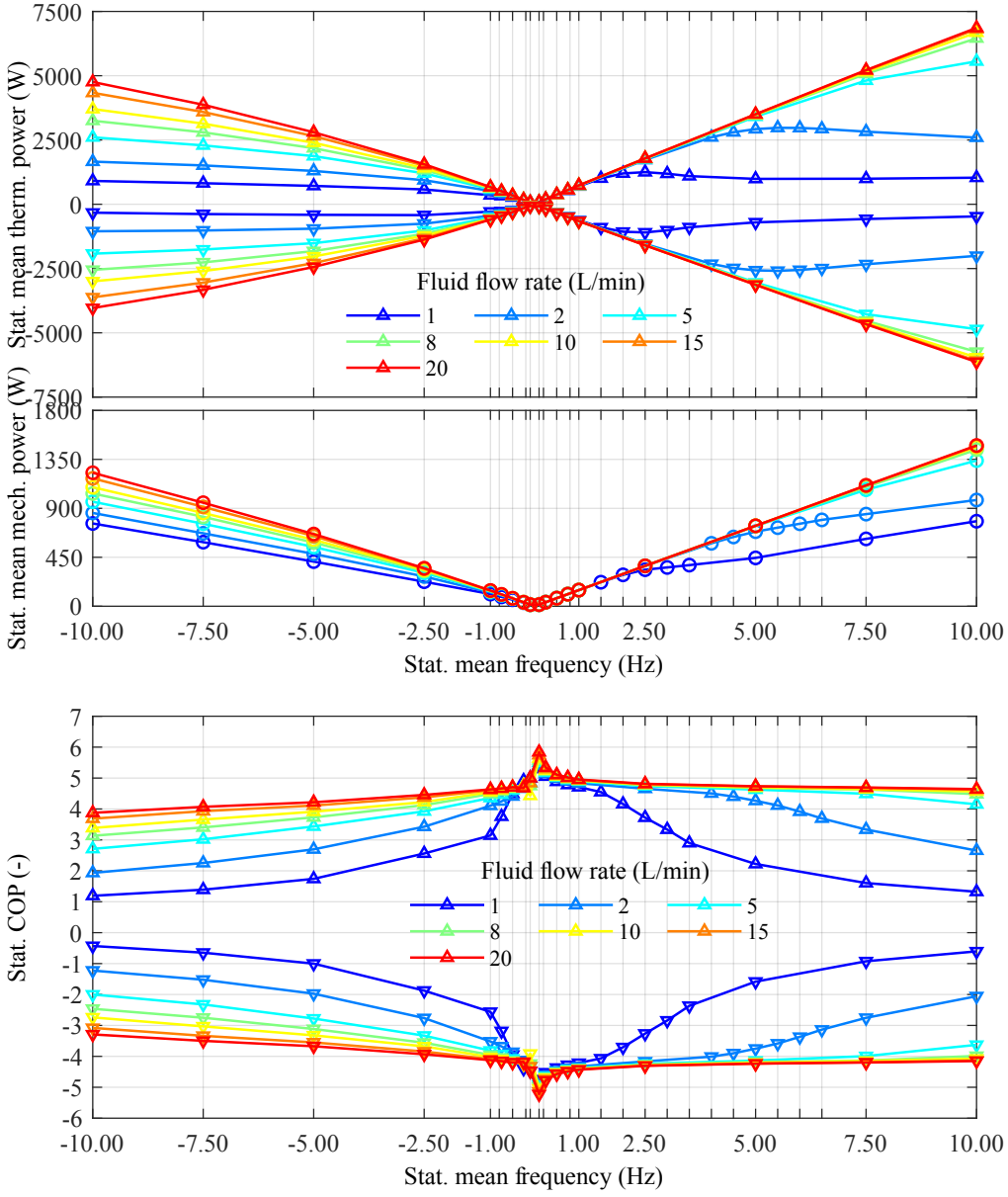

Figure 5.108: Flow rate and frequency using water: Resulting thermal and mechanical power and *COP* along the rotation frequency for different flow rates.

The mechanical power input increases with increasing rotation frequency due to the growing number of performed EC cycles per time. The increased HE between SMA and fluid for increasing flow rate results in a higher maximum and minimum temperature difference of the SMA element during the EC cycle, leading to an increase in mechanical power input. As a result, the *COP* decreases with increasing rotation frequency and increases with increasing flow rate.
To summarize, this parameter study demonstrates that the variation of the rotation frequency and flow rate significantly affects the mechanical and thermal power in- and output, as well as the temperature output of the EC HP. The comparison between Figure 5.65 and Figure 5.108 demonstrates that the same EC HP using water can provide a thermal power that is approximately 25 times higher than the system using air. This is due to the improved heat exchange coefficient, which leads to a faster HE and allows for higher rotation frequencies. Using water and an SMA diameter of 500 µm, the sensible limit for the rotation frequency is reached at 10 Hz due to the approximately 100 times larger heat exchange coefficient compared to air, following Figure 5.14 and Figure 5.105.

5.7.2 SMA diameter and frequency

In this section, the design parameter SMA diameter is variated in the range from 100 µm to 5000 µm along the rotation frequency of the SMA arrangement in the range from 0.1 Hz to 10 Hz.
The following diagrams of this subsection are presented for water as HE and HT fluid. The comparable diagrams for air are presented in subsection 5.6.8.
Figure 5.109 presents the resulting inlet and outlet temperatures of the fluid at hot and cold duct along the rotation frequency for different SMA diameters. The temperature at the hot duct is represented by upturned triangles, and the cold duct is shown as downturned triangles. The triangles at the inlets are empty, and the ones at the outlets are filled. The positive values of the rotation frequency create a counter-flow between SMA and fluid.
The thermal energy of the SMA arrangement, which can be exchanged with the fluid, following Equation 5.2 and Equation 5.16, increases with increasing rotation frequency due to growing number of performed EC cycles per time. Therefore, the temperature difference between the inlet and outlet of the ducts increases with increasing rotation frequency for a specific SMA diameter. For the larger SMA diameters, this temperature difference nearly reaches saturation with further increasing rotation frequency. At this point, the HE between SMA and fluid reaches the best value for a specific SMA diameter, rotation frequency and fluid flow rate. An additional increase in rotation frequency does not benefit the temperature difference at the specific SMA diameter.

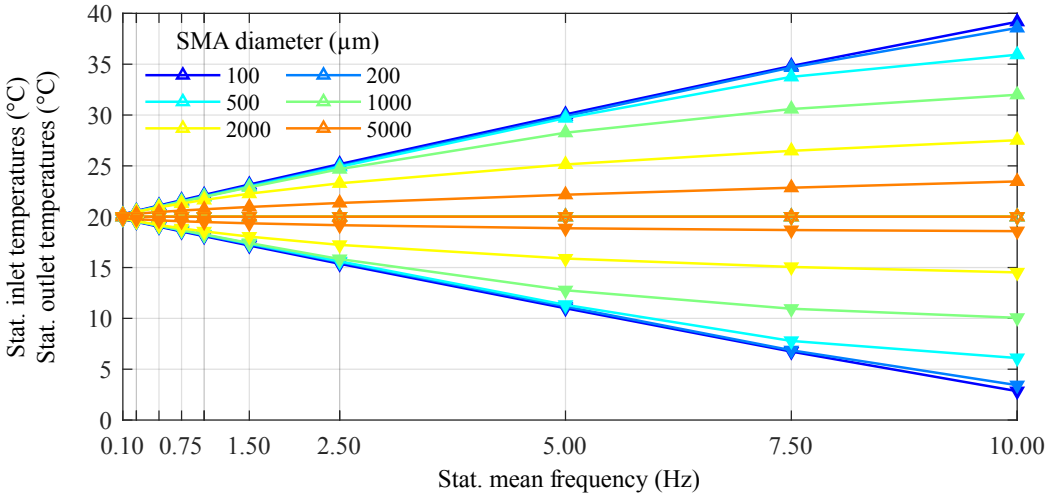

Figure 5.109: SMA diameter and frequency using water: Resulting inlet and outlet temperature at hot and cold duct along the rotation frequency for different SMA diameters.

In addition, the temperature difference between inlet andoutlet of the ducts also increases with decreasing SMA diameters. This is caused by the improved HE, related to the increasing surface area of the SMA arrangement, following Equation 5.2 and Equation 5.16. Figure 5.110 shows the thermal and mechanical power, as well as the *COP* along the rotation frequency for different flow rates. The colors correspond to those of Figure 5.109. The amount of the thermal power output at the hot duct is represented by upturned triangles and as downturned triangles for the cold duct. The thermal power of the SMA arrangement increases with increasing rotation frequency due to a growing number of performed EC cycles per time. For a lower SMA diameter, a larger rotation frequency can be applied to fully exchange the thermal energy between SMA and fluid. The thermal power at the ducts increases with increasing rotation frequency up to a specific point for each diameter where a kind of saturation starts.

The mechanical power input increases with increasing rotation frequency due to the growing number of performed EC cycles per time. The increased HE between SMA and fluid for decreasing diameter results in a higher temperature difference of the SMA element during the EC cycle. Due to the temperature dependent transformation stress, following Equation 2.5 and Equation 2.7, the mechanical power input increases as the diameter falls. As a result, the *COP* decreases with increasing rotation frequency and increases with decreasing diameter.

To summarize, this parameter study demonstrates that the variation of the rotation frequency and diameter significantly affects the mechanical and thermal power in- and output, as well as the temperature output of the EC HP.

The comparison between Figure 5.67 and Figure 5.110 demonstrates that the same EC HP using water can efficiently use SMA wires with a diameter that is approximately 10 times

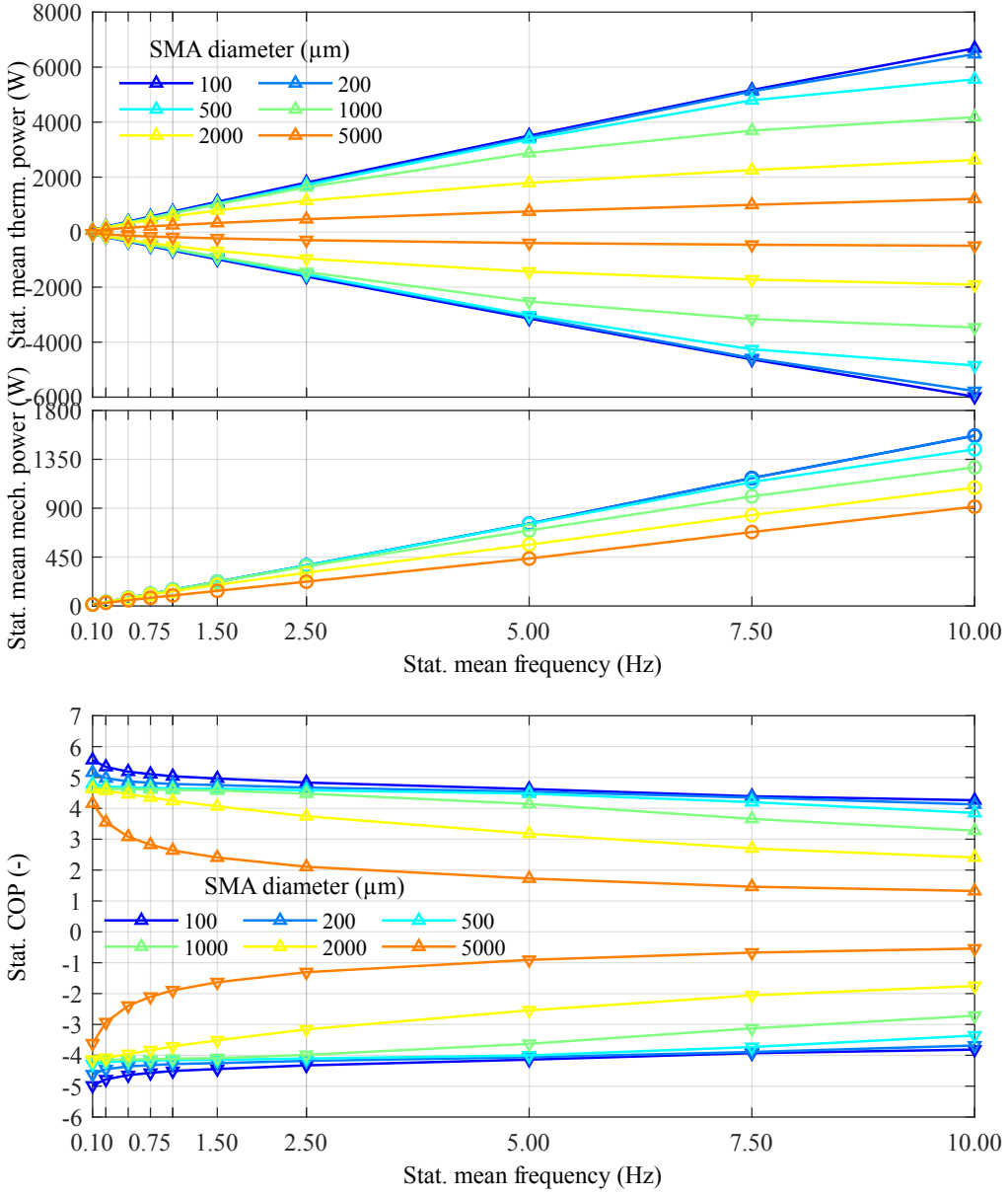

Figure 5.110: SMA diameter and frequency using water: Resulting thermal and mechanical power and *COP* along the rotation frequency for different SMA diameters.

higher than the system using air. This is due to the improved heat exchange coefficient, which leads to a faster HE. For water as HE and HT fluid the SMA diameter should be in the range from 200 µm to 1000 µm. This practical range is up to four times higher than that of air, following subsection 5.6.8.

5.8 Parameter studies as heat engine

Heat engines are the fundamental technology from which the EC HP is developed, based on the thermodynamic behavior of SMAs as actuators, as introduced in section 1.1. In a heat engine, the reverse EC effect is used to generate mechanical work from thermal energy.
In contrast to the prescribed homogeneous motion behavior of the EC HP, the motion and thus the rotation frequency of the heat engine is not constant. It strongly depends on the temperature of the fluid in the ducts, the HE between SMA and fluid, as well as on the mechanical load. Therefore, the first derivative of the rotation angle ($\dot{\varphi}$) is variable, and the second derivative of the rotation angle ($\ddot{\varphi}$) is unequal to zero.
In section 5.3 the state vector is introduced in Equation 5.41. To simulate the thermo-mechanical behavior of a heat engine, the second derivative of the rotation angle ($\ddot{\varphi}$) is set by Equation 5.46.

$$\ddot{\varphi} = \frac{(M_{\mathrm{load}} - M_{\mathrm{sma}})}{I} \tag{5.46}$$

This calculation involves the sum of the torques that either accelerate or decelerate the rotational part of the heat engine and its rotational inertia (I). The extracted torque (M_{load}) describes the characteristics of the mechanical load, for example an electrical generator. For a load with a linear characteristic, it can be calculated using Equation 5.47.

$$M_{\mathrm{load}} = k_{\mathrm{load}} \cdot \left(f_{\mathrm{load}} - \frac{\dot{\varphi}}{2\pi} \right) \tag{5.47}$$

The nominal rotation frequency (f_{load}) of the load is the frequency, where the load generates no torque. In this work, the nominal frequency is set to zero. The load stiffness (k_{load}) descrips the change of the load torque when the load is forced to a rotation frequency unequal its mechanical frequency. In the case of the EC HP, a positive load torque is required to move the SMA arrangement along the load profile. In the case of the heat engine, the motion is induced by a negative SMA torque (M_{sma}), calculated using Equation 5.6, generated from different transformation stress of the SMAs at different temperatures. The produced mechanical power is consumed by the negative torque of the mechanical load.

In the following section, the simulated setup of the heat engine is introduced and completed with parameter studies.

5.8.1 Mechanical setup

Figure 5.111 shows a still frame of the heat engine with a hot and cold duct and no HE in the transition zones. The simulated cam track geometry consists of a loading ramp in the

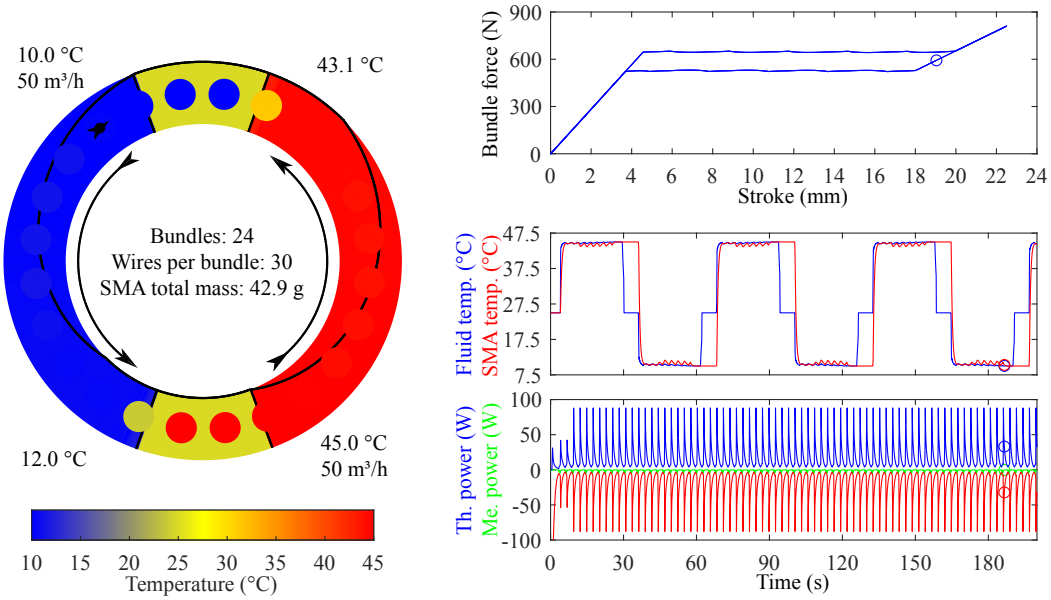

Figure 5.111: Heat engine: Visualization of heat engine, a cross-section with symmetric loading and unloading profiles along the circumference.

cold duct and an unloading ramp in the hot duct.

Figure 5.112 illustrates the loading profile as stroke of the SMA elements along the channel position, based on Figure 5.6 (b). The arrangement of the hot and cold duct is shown in color at the x-axis. The flow direction of the fluid is indicated with an arrow, creating a counter-flow in both ducts for clockwise rotation of the SMA arrangement. The load profile is symmetrically adjusted for complete loading and unloading in the ducts while providing an area for preheating and precooling.

The upper part of Figure 5.113 presents the resulting temperature evolution for the SMA element as dashed line and fluid as solid line along the circumference. Whereas the lower part of Figure 5.113 illustrates the corresponding M+ phase fraction in the SMA elements along the channel position. The hot and cold duct are shown in color at the x-axis and indicate the flow direction of the fluid by an arrow. The temperature curve of the fluid is framed at the edges by triangles that are upturned at the hot duct and downturned at the cold duct. The triangles at the inlets are empty, and the triangles at the outlets are filled. The SMA elements in the hot duct are heated by the fluid, following Equation 5.2. After reaching the austenite start temperature, the SMA material starts the PT from M

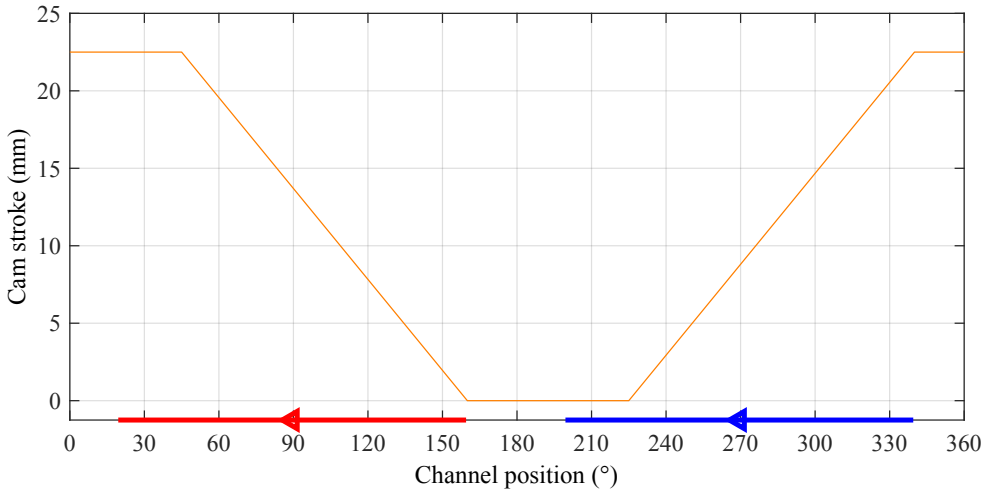

Figure 5.112: Heat engine: Symmetric loading and unloading profile along the circumference.

to A. This induces an increase in tensile force in the elements, which leads, in combination with the slope of the load profile, to a tangential force, as introduced in Equation 5.14, resulting in a torque, following Equation 5.6. This torque induces a clockwise rotation of the SMA arrangement, as indicated by the black arrow in the SMA arrangement on the left side of Figure 5.111. To enable an efficient HE between SMA and fluid with a minimum needed fluid temperature for the hot side, the fluid is guided counter-clockwise, resulting in a counter-flow. The end of the unloading slope and the completion of the PT from M to A match with the inlet of the hot duct.

The SMA elements are cooled as they enter the cold duct, following Equation 5.2. The loading slope in the cold duct leads to a PT from A to M. To enable an efficient HE between SMA and fluid, with the highest possible fluid temperature for the cold side, the fluid is guided counter-clockwise, resulting in a counter-flow. The end of the loading slope and the completion of the PT from A to M match with the inlet of the cold duct.

During the motion of the SMA elements along the ducts, the SMA elements exchange their thermal energy with the fluid while the ongoing PT releases or absorbs the specific latent heat. The temperature of the SMA element stays constant in the transition zones due to the suppressed HE.

The following presents an exemplary parameter study of the heat engine using the simulation tool.

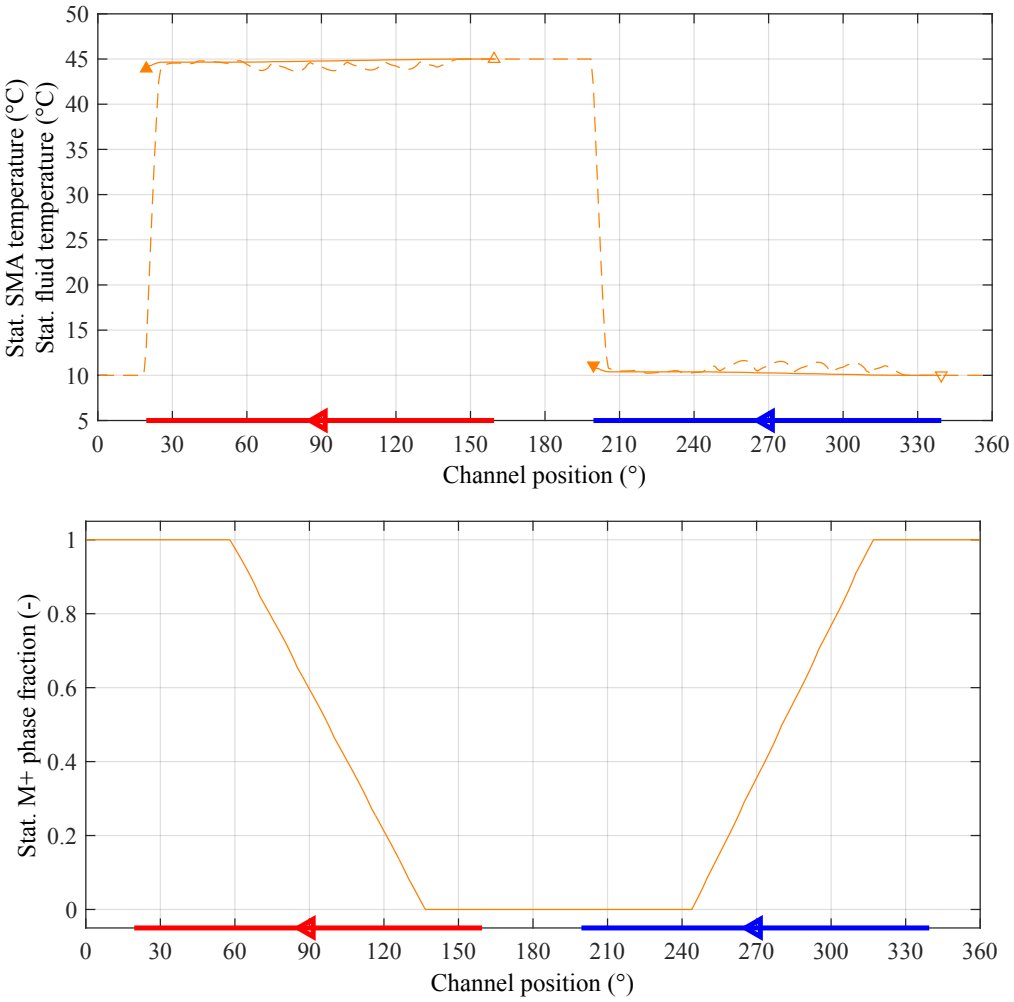

Figure 5.113: Heat engine: Resulting SMA element (dashed) and fluid (solid) temperature (a), and resulting M+ phase fraction in the SMA elements (b) along the circumference at an inlet temperature span of 35 K.

5.8.2 Inlet temperature span and mechanical load

In this section, the operating parameter inlet temperature span is varied in the range from 0 K to 70 K, while maintaining a cold inlet temperature of 10 °C. The maximum temperature is chosen not to exceed the permissible tensile stress in the SMA material. Figure 5.114 shows the resulting rotation frequency in the upper part, and the generated torque in the lower part, along the inlet temperature spans for different load stiffnesses. When the inlet temperature difference between hot and cold duct exceeds 30 K, the heat

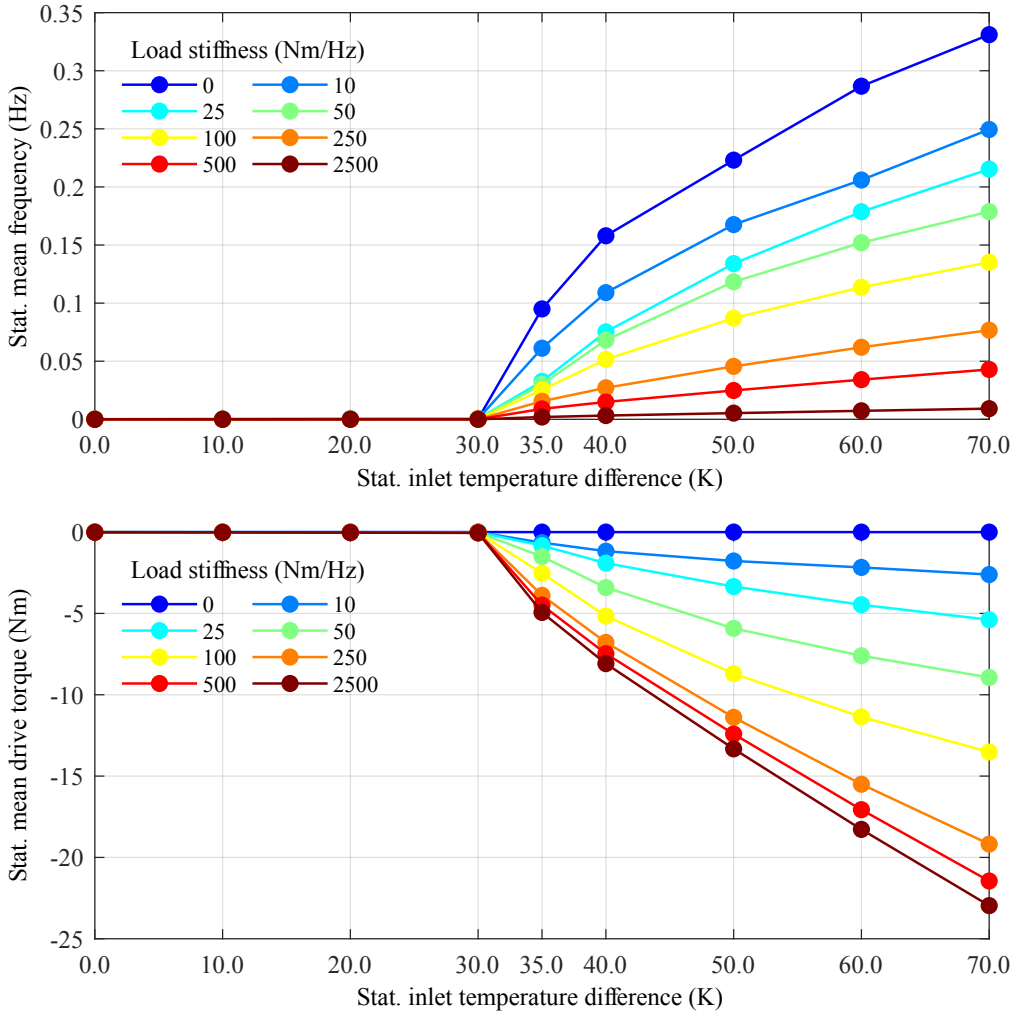

Figure 5.114: Inlet temperature span and mechanical load: Resulting rotation frequency and torque of the load along the inlet temperature spans for different values of load stiffness.

engine begins to rotate. The reached rotation frequency increases, with decreasing load stiffness due to the lower load torque, following Equation 5.47. The rotation frequency increases with increasing inlet temperature spans for a specific load stiffness due to the reduced time required for the SMA material to reach the austenite start temperature after

entering the hot duct. Due to the higher temperature difference between fluid and SMA, the HE is speeds up, the time for PT decreases, and a higher rotation frequency is reached. With increasing load stiffness, the SMA element has to provide more torque for rotation. Therefore, the temperature, at which the SMA material starts the PT, increases with increasing load stiffness, following Equation 5.2. The increasing time span between two torque events results in a decreasing rotation frequency of the heat engine for increasing load stiffness. Following Equation 5.46 and Equation 5.6, the torque generated by the heat engine, introduced in Figure 5.114, increases with increasing temperature span at a specific load stiffness due to the increasing rotation frequency.

Figure 5.115 presents the resulting inlet and outlet temperatures of the ducts for the different inlet temperature spans. The colors correspond to those of Figure 5.114. The temperature at the hot duct is represented by upturned triangles and the cold duct as downturned triangles. The triangles at the inlets are empty, and the triangles at the outlets are filled. The outlet temperature difference increases with increasing inlet temperature

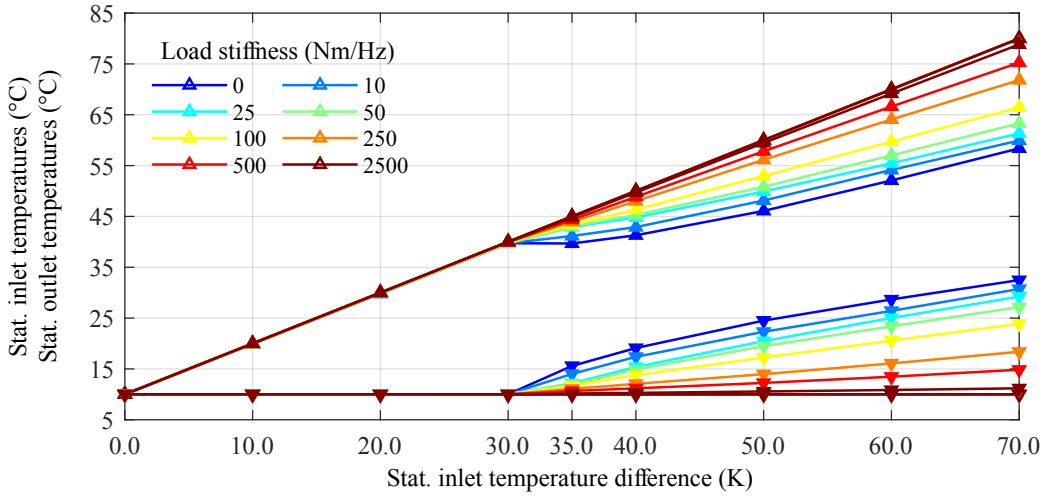

Figure 5.115: Inlet temperature span and mechanical load: Resulting inlet and outlet temperatures at hot and cold duct along the inlet temperature spans for different values of load stiffness.

spans at a specific load stiffness, due to the nearly constant thermal energy required for PT of the SMA elements, following Equation 5.2.

With larger load stiffness, the heat engine rotates more slowly. As a result, the number of PT per time decreases. This reduction leads to a lower HE between SMA and fluid, which, in turn, causes a smaller temperature difference between inlet and outlet of a duct. Figure 5.116 shows the thermal and mechanical power, as well as the efficiency of the heat engine along the inlet temperature spans. The colors correspond to those of Figure 5.114. The amount of the thermal power absorbed by the SMA elements at the hot duct, represented by upturned triangles, and released at the cold duct, shown as downturned triangles, increases with increasing inlet temperature spans at a specific load stiffness.

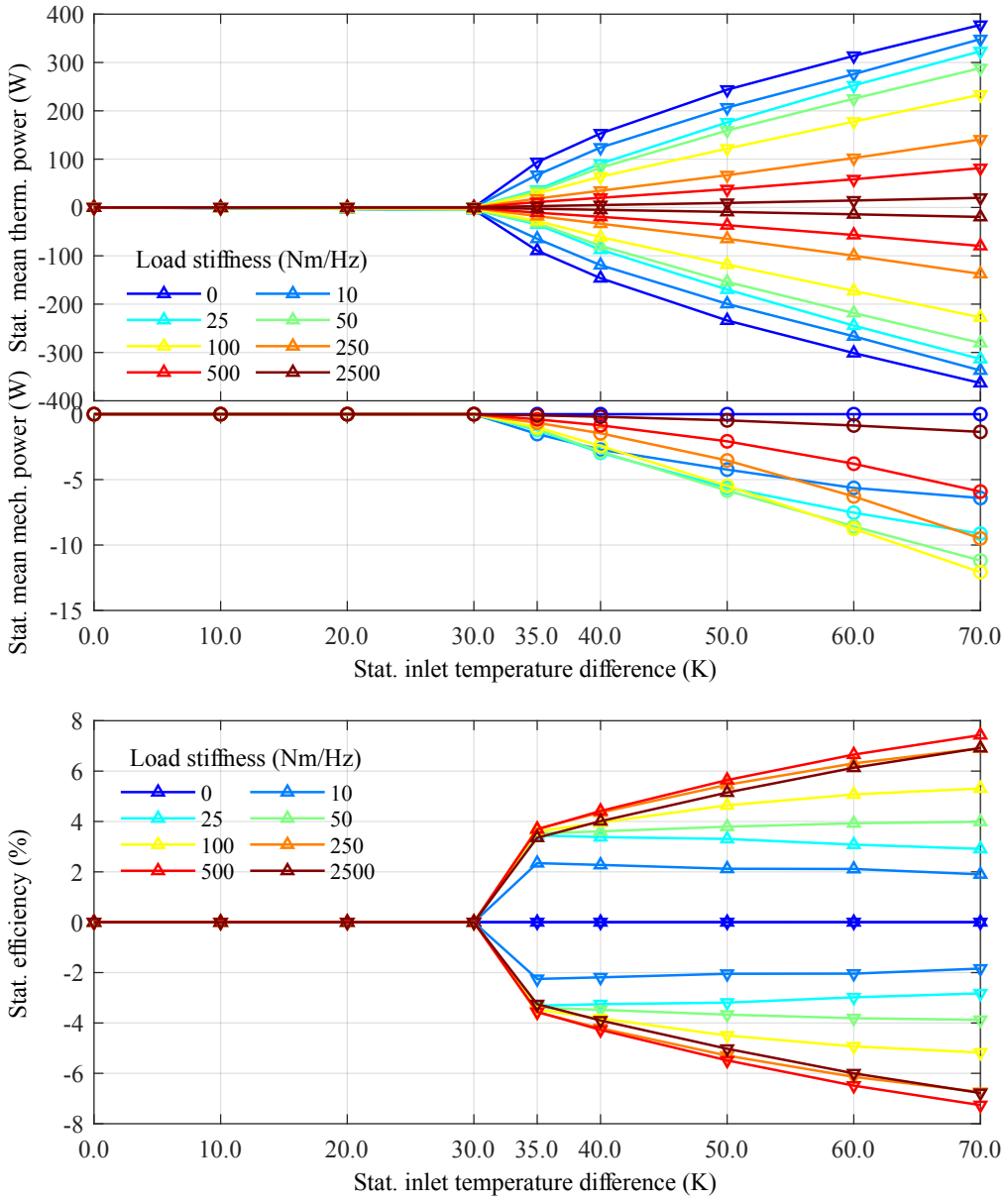

Figure 5.116: Inlet temperature span and mechanical load: Resulting thermal and mechanical power and efficiency along the inlet temperature spans for different values of load stiffness.

This is caused by the larger numbers of PTs, following Equation 5.2. If the load stiffness increases, the value of the thermal power decreases due to the decreasing rotation frequency, following Equation 5.47.
The mechanical power output also increases with increasing inlet temperature spans at a specific load stiffness due to the increasing rotation frequency and the higher generated torque. At a specific inlet temperature span, the value of the mechanical power reaches a maximum dependent on the load stiffness. With lower values of the load stiffness, the value of the mechanical power decreases due to low consumed torque. For larger values of the load stiffness, the value of the mechanical power decreases also, since the reached rotation frequency is low. The highest mechanical output power is reached at a load stiffness between 50 N m/Hz and 100 N m/Hz for all inlet temperature spans.
The efficiency describes the relation between the outputed mechanical power and the absorbed thermal power of the heat engine. This value increases for high load stiffnesses, and decreases for low load stiffnesses with increasing inlet temperature spans. In this parameter study, the best efficiency for all inlet temperature spans is reached at a load stiffness of 500 N m/Hz.

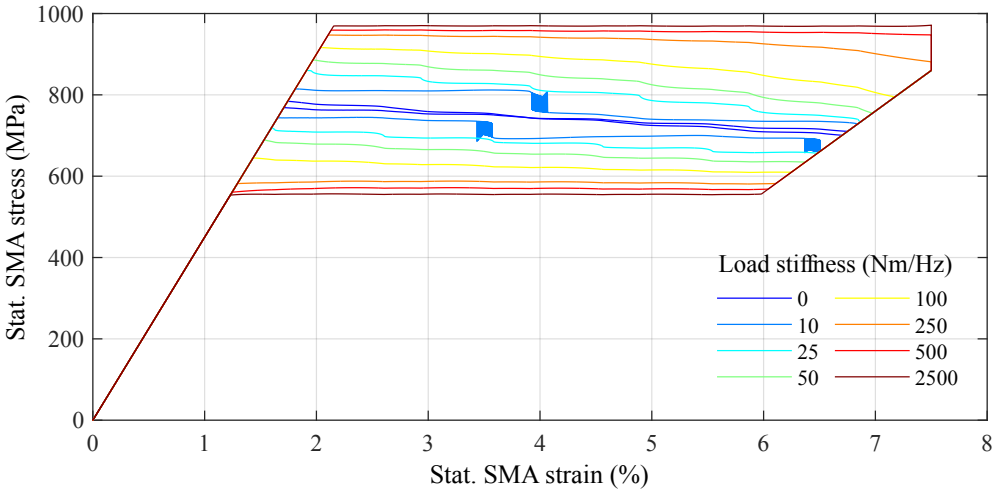

Figure 5.117: Inlet temperature span and mechanical load: Resulting stress-strain diagram of one SMA element for the different values of load stiffness at an inlet temperature span of 70 K.

Figure 5.117 presents the resulting stress-strain diagram of one SMA element for the different load stiffnesses at an inlet temperature span of 70 K. The colors correspond to those of Figure 5.114. With larger values of the load stiffness, the hysteresis height of the stress - strain behavior gets larger, since the generated torque, and thus the required difference in transformation stress between FT and BT increases. Therefore, the mechanical power output increases.
To summarize, this parameter study demonstrates that the variation in the inlet temperature span significantly affects the thermal and mechanical power in- and output of the

heat engine. The generated mechanical power and efficiency exhibit a strong dependency from the load stiffness. The maximum efficiency and maximum performance do not occur at the same operating point, but optimization can be achieved through adjusting the operational parameters. The parameter study of the low-temperature heat engine using *NiTi#3* enables an energy conversion from thermal energy to mechanical energy at a temperature difference of 35 K or higher. The efficiency of the heat engine achieved in this parameter study reaches up to 7 %, which aligns with typical values for SMAs in actuation systems.

Conclusion and outlook

This chapter summarizes the most important insights of this work in the conclusion and focuses on the future implications and potential applications of this work in the outlook.

Conclusion

In this work, a fully coupled thermo-mechanical system-level simulation tool based on a physics-motivated SMA model is developed, implemented in the numerical computing environment MATLAB [74], and validated. This compact simulation tool is qualified for massively parallel computation of different parameter sets on modern multi-core computers, which allows fast and comprehensive parameter scans using the parameter comparison and visualization tools [62, 40]. The material model of the system simulation tool is calibrated to a commercially available SE SMA material, which is available in large quantities for predicting the thermo-mechanical behavior of the realized EC HP. The validation of the SE SMA wires made from NiTiCo, manufactured by *Fort Wayne Metals* under the name *NiTi#3* is presented in detail in section 5.4. In addition, the model is calibrated to a novel EC optimized material to highlight its advantages in the EC applications. The validation and the results of the EC optimized material made from NiTiCuV [93] are presented in subsection 5.6.19.
To demonstrate the versatility of the simulation tool, different parameter studies, characterizing a multi-element EC HP system, using air (section 5.6), and water (section 5.7) as HE and HT fluid are discussed in terms of thermo-mechanical behavior, performance, and efficiency. The following key aspects are identified:

- The system's diameter at which the SMA elements are arranged has no impact; thus, it should be kept as small as possible to save design space, following subsection 5.6.1.
- The system's length influence is proportional to the amount of SMA material. Consequently, mechanical and thermal performance scales linearly with the length, following subsection 5.6.2.
- The thermal power scales proportionally to the SMA mass, as long as the fluid flow rate is adapted to the required HE, following subsection 5.6.9.
- The angular length of the fluid duct influences the performance and efficiency. The longer the duct, the higher the transferred thermal energy due to the longer dwell time for HE, following subsection 5.6.3.

- The subdivision of the SMA material uniformly along the circumference reduces the ripple in mechanical and thermal power as the number of SMA elements increases, following subsection 5.6.4. No further significant improvement is observed above 12 bundles.
- The inlet temperature level of the fluid ducts does not affect the mechanical and thermal performance for similar thermo-mechanical conditions during the performed EC cycles, following subsection 5.6.5.
- The inlet temperature span of the fluid ducts strongly influences the thermo-mechanical performance and efficiency. The thermal output power decreases to zero if the temperature difference between both inlets reaches the adiabatic limit of the SMA material, following subsection 5.6.6. To expand the potential inlet temperature range, heat recovery methods can be utilized, allowing the range to be increased to twice the adiabatic material limit, following subsection 5.6.12.
- Counter-flow between the SMA element and fluid consistently offers better performance and efficiency than parallel-flow, following subsection 5.6.7.
- Higher rotation frequency can transfer more thermal energy within the same system size if the fluid flow rate is adapted to the required HE, following subsection 5.6.7. For air as HE and HT fluid at an SMA diameter of 200 µm, the sensible limit is reached at a rotation frequency of 1 Hz. Whereas, for water and an SMA diameter of 500 µm, the sensible limit is reached at a rotation frequency of 10 Hz, following subsection 5.7.1. These increases in SMA diameter and rotation frequency are possible due to the approximately 100 times larger heat exchange coefficient of water compared to air, following Figure 5.14 and Figure 5.105.
- In general, thinner SMA diameters ensure better performance and efficiency of the system due to the better surface-to-volume ratio. For air as HE and HT fluid the SMA diameter should be in the range from 25 µm to 300 µm, following subsection 5.6.8. Whereas, for water the SMA diameter should be in the range from 200 µm to 1000 µm, following subsection 5.7.2.
- Asymmetry in flow rate between hot and cold duct can be used to produce a higher temperature difference between inlet and outlet of the duct with the lower flow rate, but this approach reduces the thermal performance and efficiency, following subsection 5.6.10.
- During the investigation of system losses, it was observed that even a slight crossflow in the transition zones between hot and cold ducts leads to a significant reduction in performance, especially as the inlet temperature difference between both ducts

increases, following subsection 5.6.11. Therefore, crossflow should be avoided to enable high thermal performance and efficiency.

- The mechanical friction of cam rollers has a marginal influence on the system efficiency when using low friction ball bearings with metal-to-metal surfaces and a friction coefficient of 0.001 or lower, following subsection 5.6.13. Using bearings with higher friction significantly reduces system efficiency as the rotation frequency increases.

- The thermal losses through the duct walls only have a marginal influence on the system efficiency, even when using an uninsulated acrylic glass, following subsection 5.6.14.

- With increasing flow rate, the flow resistance in the duct increases and reduces significantly the efficiency of the system, following subsection 5.6.15. Therefore, flow rates larger than 75 m^3/h should be avoided while using air as fluid. Because viscous and electrical losses significantly affect the system efficiency, fans with high efficiency should be chosen.

- The thermal power depends on the amount of transformed SMA material, following subsection 5.6.16 and subsection 5.6.17. An adiabatic-isothermal combined EC cycle can reduce the requiered mechanical power, following subsection 5.6.18.

- The use of EC optimized SMA material can reduce the mechanical power requirement by more than half, while maintaining the thermal power output. As a result, the efficiency can be more than doubled, significantly increasing the *COP* from 6.5 to 13, following subsection 5.6.7 and subsection 5.6.19.

Finally, the developed simulation tool is used to simulate a heat engine (section 5.8), demonstrating its full capabilities. The parameter study of the low-temperature heat engine using the *NiTi#3* enables an energy conversion from thermal energy to mechanical energy at a temperature difference of 35 K or higher, following subsection 5.8.2. The generated mechanical power and the efficiency exhibit a strong dependency from the load stiffness. The efficiency of the heat engine achieved in the performed parameter study reaches values up to 7 %, which aligns with typical values for SMAs in actuation systems. Preliminary work was necessary to enable the efficient implementation and real-material-

based validation of the simulation tool, saving time and cost in calculations. The physics-based localized model based on the MAS model [80] is presented in chapter 3. The 1D model enables the prediction of heterogenic nucleation behavior in materials with nearly perfect CLS and is developed and implemented in the FE software package COMSOL.

This part of the work accurately predicts the PT of thin-film SMAs over two magnitudes of strain rates and, therefore, supports the understanding of the PT behavior. These results enable the economic and scientific selection of the SMA model's complexity in the simulation tool and call for an extended test bench.
The work on the developed scientific test setup is presented in chapter 4 [74, 11]. It enables the thermo-mechanical investigation of macroscopic material samples like SMA wires, including the effects of local strain and temperature distribution along the SMA element. Therefore, it allows for the complete characterization of the thermo-mechanical material parameters in a single experiment under similar load conditions as the realized EC HP system will provide. These experimental results are used to support the implementation and validation of the system-level simulation tool, for example, to choose the suited modeling approaches for the kinematics, SMA model, and fluidics. Thermo-mechanical investigations of the SE SMA wires made from NiTiCo, manufactured by *Fort Wayne Metals* under the name *NiTi#3* show that the local PT behavior changes from an inhomogeneous to a homogeneous within the first 100 loading cycles. This enables, due to the homogeneous HE along the SMA element in the EC HP the implementation of the simplified MAS in the system simulation tool.
The presented work focuses on utilizing the material properties of the commercially available SMA material, *NiTi#3*. The objective is to replicate and predict the heating and cooling characteristics of the engineered EC HP system introduced in section 5.1 using the developed simulation tool. This specific SE SMA material is selected due to its availability in large quantities and its consistent thermo-mechanical properties, as indicated in the literature [10]. It is important to note that this work does not focus on evaluating the potential of the EC technology itself regarding its heating and cooling capabilities or efficiency. This is caused by the currently fast development of new SMA material compositions with enhanced EC properties. Therefore, the primary goal is to showcase the potential and versatility of the developed simulation tool. This involves investigating and identifying trends, as well as influences of different design and operational parameters of the EC HP using the developed parameter comparison tool.

Outlook

In addition to the parameter studies, the presented simulation tool can be used to examine the EC HP system according to the status of a national standard for heat pumps and air conditioning units [15]. For this purpose, specific thermal loads for the hot and cold duct are entered in the parameter set table as constant, formula, or time-dependend values. These parameter studies can be simulated directly using the parallel computation tool and evaluated using the parameter comparison tool as well as the visualization tool.

The parameters studies of subsection 5.6.12 present that the possible inlet temperature span between hot and cold duct can be significantly enlarged by using heat recovery concepts in the EC HP. A further approach for increasing the application range while maintaining the system specification is to cascade or parallelize numerous EC HPs. The simulation tool's object-oriented and modular implementation allows for the easy implementation and interconnection of the combined devices in the favored modality. Multiple combinations of mechanical arrangements, combined with multiple SMA material combinations, can be simulated directly with the presented simulation tool to find key values and optimized combinations.

In the parameter studies presented in this work, the SMA element is implemented with a single transformation stress leading to a single crystalline material behavior. However, implementation enables the combination of different SMA geometries, sizes, and quantities, as well as the adaption of the thermo-mechanical material behavior for each SMA element. Therefore, parameter studies with the polycrystalline material behavior can be easily performed due to the modular structure of the simulation tool.

Regarding the application of the EC HP while using air as HE and HT fluid, humidity is one of the most important operating parameters in the field of *Heating, Ventilation and Air Conditioning* (HVAC). Due to the strong temperature dependency of the humidity, the water trapped in the air condenses in the cold duct at the surface of the SMA elements. This effect significantly changes the thermal characteristics of EC HP, and with this, the system performance and efficiency. The modularity of the simulation tool enables easy implementation of the absolute humidity as an additional transport variable in the fluid model and the expansion of the SMA energy balance regarding the specific latent heat of water condensation and vaporization, as well as the additional mass balance of the condensate [3].

Besides the listed suggestions for future work, the modularity of the simulation tool supports any further ideas.

Acknowledgement

At this point, I would like to thank Prof. Dr.-Ing. Stefan Seelecke, Prof. Dr. rer. nat. Andreas Schütze, and Prof. Dr.-Ing. Stefan Diebels, for offering me the opportunity to work as a scientific assistant in this novel, disruptive, and innovative research area and accompanying me throughout the path to this dissertation.
Additionally, I would also like to thank my work colleagues at the Saarland University and the Intelligent Material Systems Lab for the successful collaboration and great time together, Susanne-Marie Kirsch and Nicolas Michaelis should be mentioned in particular. After years of working together in the priority program *Ferroic Cooling*, I am looking forward to further cooperation, starting with the *EXIST Transfer of Research*. Finally, I would like to thank my family and friends, who have always supported me.
Furthermore, I would also gratefully acknowledge the support of the German Research Foundation through Priority Program SPP 1599 [67] *Caloric effects in ferroic materials: New concepts for cooling* in the projects SCHU2217/2-1, and SE704/2-1, for the fundamental research and especially for the second funding period SCHU2217/3-2, and SE704/2-2.

List of Figures

List of Tables

Nomenclature

Abbreviations

Short	Description
1D	one dimensional
2D	two dimensional
3D	tree dimensional
A	austenite
Au	Gold
BDF	Backward Differentiation Formula
BT	backward transformation
CFD	computational fluid dynamics
CLS	crystal lattice structure
CMOS	complementary metal-oxide-semiconductor
Co	Cobalt
COMSOL	COMSOL Multiphysics
CPU	Central Processing Unit
cRIO	National Instuments cRIO
csv	character-separated values
Cu	Copper
DAE	differential algebraic equation
DC	Dirichlet boundary condition
DF	derivative function
DIC	digital image correlation
DSC	differential scanning calorimetry
EC	elastocaloric
Excel	Microsoft Excel
FD	finite difference
FE	finite element
FT	forward transformation
hdf	hierarchical data format
HE	heat exchange
HP	heat pump
HT	heat transport
InSb	Indium-Antimonide

IR	infrared
ISF	initial state function
LV	National Instuments LabVIEW
M	martensite
M+	tensile martensite
M-	compression martensite
MAS	Müller-Achenbach-Seelecke
MATLAB	MathWorks MATLAB
NC	Neumann boundary condition
Ni	Nickel
NiTi	Nickel-Titanium
ODE	ordinary differential equation
PC	personal computer
Pd	Palladium
PDE	partial differential equation
PF	phase front
PT	phase transformation
Q	QUICK
R	reference result
S	Central Difference
S1	Central Difference with second spatial order
SE	superelastic
Simulink	MathWorks MATLAB Simulink
SM	shape memory
SMA	shape memory alloy
svg	scalable vector graphics
Ti	Titanium
TTL	transistor–transistor logic
U	Upwind
U1	Upwind with first spatial order
U2	Upwind with second spatial order
U3	Upwind with third spatial order
V	Vanadium
VI	virtual instrument
VIS	visible
x-axis	axis of abscissa
y-axis	axis of ordinate

Symbols

Greek

Greek	Description
α	angle
β_A	phase fraction dependence of σ_A
β_M	phase fraction dependence of σ_M
δ	transition probability
ε	strain
ε_A	corresponding strain from A to M
ε_M	corresponding strain from M to A
ε_t	transformation strain
$\dot{\varepsilon}$	strain rate
ζ	resistance coefficient
η	phase fraction diffusion coefficient
κ	thermal conductivity
κ_A	thermal conductivity for A
κ_M	thermal conductivity for M
μ	friction coefficient
ν	Poisson's ratio
ξ	phase fraction
$\boldsymbol{\xi}$	phase fraction vector
π	Archimedes' constant, ≈ 3.14159
ρ	density
σ	stress
σ_A	transformation stress from A to M
σ_M	transformation stress from M to A
σ_A or σ_M	transformation stress
$\Delta\sigma$	hysteresis height
$\dot{\sigma}$	stress rate
τ	time constant
φ	rotation angle
ψ	dynamic viscosity
ω	rotation frequency

Roman

Roman	Description
A	area
ab	aspect ratio coefficient
COP	coefficient of performance

c	specific heat capacity
cf	cross flow coefficient
DFC	general diffusion coefficient
d	diameter
E	Young's modulus
e	Euler's constant, ≈ 2.71828
exp	natural exponential function, $\exp(x) = \mathrm{e}^x$
F	force
f	frequency
G	Gibbs free enthalpy
ΔG	Gibbs free energy difference
H	specific latent heat
H_A	specific latent heat from A to M
H_M	specific latent heat from M to A
ΔH	specific latent heat difference
HFE	Helmholz free energy
h	heat exchange coefficient
I	rotational inertia
i	index
j	applied energy
k	load stiffness
$\mathrm{k_B}$	Boltzmann constant, $\approx 1.380\,649 \times 10^{-23}\,\mathrm{J/K}$
l	length
ld	depth
lh	height
lw	width
Δl	grid step
M	torque
m	mass
N	number
Nu	Nusselt number
P	power
Pr	Prandtl number
p	pressure
Δp	pressure difference
$pc1$	parabola coefficient one
$pc2$	parabola coefficient two

$pc3$	parabola coefficient tree
Q	thermal energy
$\dot{Q}$	thermal power
q	specific thermal energy
$\dot{q}$	specific thermal power
R	resistance
Re	Reynolds number
r	radius
S	entropy
ST	energy source or sink
s	specific entropy
T	temperature
ΔT	temperature difference
$\boldsymbol{T}$	temperature vector
$\tilde{T}$	normalized temperature
$\dot{T}$	temperature rate
Tol	tolerance
t	time
t'	alternate time
U	circumference
u	specific internal energy
V	volume
$\dot{V}$	flow rate
v	velocity
$\mathbf{v}$	velocity field
vf	void fraction
W	mechanical work
w	specific mechanical work
x	position
Δx	displacement
$\boldsymbol{Y}$	state vector
$\dot{\boldsymbol{Y}}$	state rate vector

Sub- and Superscripts

Subscripts	Description
$_-$	compression martensite
$_+$	tensile martensite
$_0$	initial
$_A$	austenite
$_{ab}$	absorbed
$_{abs}$	absolute
$_{ad}$	adiabatic
$_{AF}$	austenite finish
$_{air}$	air
$_{amb}$	ambient
$_{ap}$	applied
$_{AS}$	austenite start
$_{bun}$	bundle
$_c$	cold
$_{cam}$	cam track
$_{ch}$	cold to hot
$_{channel}$	channel
$_{char}$	characteristic
$_{chr}$	cold heat recovery
$_{chri}$	cold heat recovery input
$_{chro}$	cold heat recovery output
$_{ci}$	cold input
$_{co}$	cold output
$_{cool}$	cooling
$_{crit}$	critical
$_{dis}$	dissipated
$_{DSC}$	determined by DSC
$_{duct}$	duct
$_{elast}$	elastic
$_{elec}$	electrical
$_{end}$	end
$_{ex}$	extremum
$_f$	finish
$_{fan}$	fan
$_{fld}$	fluid

fri	friction
h	hot
hc	hot to cold
heat	heating
hhr	hot heat recovery
hhri	hot heat recovery input
hhro	hot heat recovery output
hi	hot input
ho	hot output
hyd	hydraulic
i	index
i	input
ideal	ideal
inner	inner
iso	isothermal
j	index of SMA element
k	index of fluid element
lay	layer
load	load
M	martensite
max	maximum
me	mechanical
mean	mean
MF	martensite finish
min	minimum
MS	martensite start
N	normal
n	index of duct
o	output
outer	outer
rc	recovered
re	released
ref	reference
rel	relative
s	start
sim	determined by simulation
sma	shape memory alloy

step	step
surf	surface
t	transformation
tan	tangential
th	thermal
tot	total
vis	viscous
wall	wall
water	water
wpb	wires per bundle
x	horizontal direction
y	vertical direction
α	source phase fraction
β	target phase fraction
ξ	phase fraction

Bibliography

[1] Rawan Barakat, Susanne-Marie Kirsch, et al. “Bidirectional rotational antagonistic shape memory alloy actuators for high-frequency artificial muscles”. In: *Scientific Reports* 15.1 (2025), p. 9108. DOI: 10.1038/s41598-025-93209-9.

[2] Guoan Zhou, Lingyun Zhang, et al. “Achieving kilowatt-scale elastocaloric cooling by a multi-cell architecture”. In: *Nature* 639.8053 (Mar. 2025), pp. 87–92. DOI: 10.1038/s41586-024-08549-9.

[3] David Zimmermann, Franziska Louia, et al. “Modeling Moist Air Effects and Shape Memory Alloys in Elastocaloric Devices”. In: *Energy Materials* 12 (2025). DOI: 10.3389/fmats.2025.1559800.

[4] Luca Cirillo, Adriana Greco, and Claudia Masselli. “The energy performances of an elastocaloric device for air conditioning through numerical investigation”. In: *Applied Thermal Engineering* 236 (2024). DOI: 10.1016/j.applthermaleng.2023.121517.

[5] Stefano Dall’Olio, Žiga Ahčin, et al. “Development of a Tube-Based Elastocaloric Regenerator Loaded in Compression: A Review”. In: *Shape Memory and Superelasticity* 10.2 (2024), pp. 99–118. DOI: 10.1007/s40830-024-00483-z.

[6] Jingyuan Xu, Florian Bruederlin, et al. “SMA Film-Based Elastocaloric Cooling Devices”. In: *Shape Memory and Superelasticity* 10.2 (2024), pp. 119–133. DOI: 10.1007/s40830-024-00484-y.

[7] Guoan Zhou, Zexi Li, et al. “A multi-material cascade elastocaloric cooling device for large temperature lift”. In: *Nature Energy* 9.7 (2024), pp. 862–870. DOI: 10.1038/s41560-024-01537-3.

[8] Žiga Ahčin and Jaka Tušek. “Parametric analysis of fatigue-resistant elastocaloric regenerators: Tensile vs. compressive loading”. In: *Applied Thermal Engineering* 231 (2023). DOI: 10.1016/j.applthermaleng.2023.120996.

[9] Siyuan Cheng. “Comprehensive characterization of the adiabatic temperature change and (convection) heat transfer coefficient of a NiTi tube elastocaloric refrigerant”. In: *Advances* 13.6 (June 2023). DOI: 10.1063/5.0147729.

[10] Susanne-Marie Kirsch, Felix Welsch, et al. “Systematic Thermo-Mechanical Validation of Numerous Tensile-Loaded NiTi Wire Bundles Used for Elastocaloric Heating and Cooling”. In: *SMASIS - Conference on Smart Materials, Adaptive Structures and Intelligent Systems*. ASME, 2023. DOI: 10.1115/SMASIS2023-110889.

[11] Felix Welsch, Susanne-Marie Kirsch, et al. “Investigation of the thermal heat exchange between NiTi-wire bundles and airflow for different wire arrangements.” In: *SMASIS - Conference on Smart Materials, Adaptive Structures and Intelligent Systems*. ASME, 2023. DOI: 10.1115/SMASIS2023-111395.

[12] Žiga Ahčin, Stefano Dall’Olio, et al. “High-performance cooling and heat pumping based on fatigue-resistant elastocaloric effect in compression”. In: *Joule* 6.10 (2022), pp. 2338–2357. DOI: 10.1016/j.joule.2022.08.011.

[13] Žiga Ahčin, Parham Kabirifar, et al. “Numerical Modeling of Shell-and-Tube-like Elastocaloric Regenerator”. In: *Energies* 15.23 (2022). DOI: 10.3390/en15239253.

[14] Nora Bachmann, Daniel Schwarz, et al. “Modeling of an Elastocaloric Cooling System for Determining Efficiency”. In: *Energies* 15.14 (2022). DOI: 10.3390/en15145089.

[15] BSi. *Air conditioners, liquid chilling packages and heat pumps, with electrically driven compressors for space heating and cooling - Testing and rating at part load conditions and calculation of seasonal performance*. 2022. URL: https://standardsdevelopment.bsigroup.com/projects/2020-00933.

[16] Bergita Ganse, Marcel Orth, et al. “Concepts and clinical aspects of active implants for the treatment of bone fractures”. In: *Acta Biomaterialia* 146 (2022). DOI: 10.1016/j.actbio.2022.05.001.

[17] Sergej Grednev, Stefan Bronder, et al. “Applicability of correlated digital image correlation and infrared thermography for measuring mesomechanical deformation in foams and auxetics”. In: *GAMM-Mitteilungen* 45.3-4 (2022). DOI: 10.1002/gamm.202200014.

[18] Parham Kabirifar, Jonas Trojer, et al. “From the elastocaloric effect towards an efficient thermodynamic cycle”. In: *Journal of Physics: Energy* 4.4 (2022), p. 044009. DOI: 10.1088/2515-7655/ac92a5.

[19] Žiga Ahčin, Jierong Liang, et al. “Thermo-hydraulic evaluation of oscillating-flow shell-and-tube-like regenerators for (elasto)caloric cooling”. In: *Applied Thermal Engineering* 190 (2021). DOI: 10.1016/j.applthermaleng.2021.116842.

[20] Nora Bachmann, Andreas Fitger, et al. “Long-term stable compressive elastocaloric cooling system with latent heat transfer”. In: *Communications Physics* 4.1 (2021). DOI: 10.1038/s42005-021-00697-y.

[21] Wesley Ballew. “Mesoscopic Free Energy Model for Shape Memory Alloys Under Complex Loading”. PhD Thesis. Universität des Saarlandes, 2021. DOI: 10.22028/D291-34522.

[22] Philip Kosky, Robert Balmer, et al. “Mechanical Engineering”. In: *Exploring Engineering*. Elsevier, 2021, pp. 317–340. DOI: 10.1016/B978-0-12-815073-3.00014-4.

[23] Qiang Li, Junye Shi, et al. “Concept design and numerical evaluation of a highly efficient rotary electrocaloric refrigeration device”. In: *Applied Thermal Engineering* 190.February (May 2021), p. 116806. DOI: 10.1016/j.applthermaleng.2021.116806.

[24] M. Masche, L. Ianniciello, et al. “Impact of hysteresis on caloric cooling performance”. In: *International Journal of Refrigeration* 121 (2021), pp. 302–312. DOI: 10.1016/j.ijrefrig.2020.10.012.

[25] Aleksander Sendrowicz, Aleksander Omholt Myhre, et al. “Challenges and Accomplishments in Mechanical Testing Instrumented by In Situ Techniques: Infrared Thermography, Digital Image Correlation, and Acoustic Emission”. In: *Applied Sciences* 11.15 (2021). DOI: 10.3390/app11156718.

[26] Girolamo Costanza and Maria Elisa Tata. “Shape Memory Alloys for Aerospace, Recent Developments, and New Applications: A Short Review”. In: *Materials* 13.8 (2020). DOI: 10.3390/ma13081856.

[27] Dynalloy. *Nitinol*. 2020. URL: https://www.dynalloy.com/nitinol.php (visited on 07/08/2020).

[28] Erneuerbaren Energien. *Wärmepumpen mit Prüf-/Effizienznachweis*. 2020. URL: https://www.bafa.de/SharedDocs/Downloads/DE/Energie/ee%7B%5C_%7Dwaermepumpen%7B%5C_%7Danlagenliste%7B%5C_%7Dbis%7B%5C_%7D2020.html (visited on 01/31/2021).

[29] Metals Fort Wayne. *Nitinol*. 2020. URL: https://www.fwmetals.com/materials/nitinol/ (visited on 07/08/2020).

[30] Xiaojun Gu, Yinfeng Cao, et al. “Shape optimization of SMA structures with respect to fatigue”. In: *Materials & Design* 189 (2020). DOI: 10.1016/j.matdes.2019.108456.

[31] Y. Heredia-Aricapa, J. M. Belman-Flores, et al. “Overview of low GWP mixtures for the replacement of HFC refrigerants: R134a, R404A and R410A”. In: *International Journal of Refrigeration* 111 (Mar. 2020), pp. 113–123. DOI: 10.1016/j.ijrefrig.2019.11.012.

[32] *Improving Convergence of Transient Models*. 2020. URL: https://www.comsol.de/support/knowledgebase/1262 (visited on 07/08/2020).

[33] Andrej Kitanovski. “Energy Applications of Magnetocaloric Materials”. In: *Advanced Energy Materials* 10.10 (2020). DOI: 10.1002/aenm.201903741.

[34] Manfred Kohl. *Shape memory effect*. 2020. URL: https://www.imt.kit.edu/889.php (visited on 07/08/2020).

[35] Nicolas Michaelis, Susanne-Marie Kirsch, et al. "Investigation of Elastocaloric Air Cooling potential based on Superelastic SMA wire bundles". In: *SMASIS - Conference on Smart Materials, Adaptive Structures and Intelligent Systems*. ASME, 2020. DOI: 10.1115/SMASIS2020-2404.

[36] Safaa Najah Saud Al-Humairi. "Cu-Based Shape Memory Alloys: Modified Structures and Their Related Properties". In: *Recent Advancements in the Metallurgical Engineering and Electrodeposition*. IntechOpen, 2020. DOI: 10.5772/intechopen.86193.

[37] Luka Porenta, Parham Kabirifar, et al. "Thin-walled Ni-Ti tubes under compression: ideal candidates for efficient and fatigue-resistant elastocaloric cooling". In: *Applied Materials Today* 20 (2020). DOI: 10.1016/j.apmt.2020.100712.

[38] Mario S. Reis. "Magnetocaloric and barocaloric effects of metal complexes for solid state cooling: Review, trends and perspectives". In: *Coordination Chemistry Reviews* 417 (Aug. 2020), p. 213357. DOI: 10.1016/j.ccr.2020.213357.

[39] SAES Getters. *Nitinol*. 2020. URL: https://www.saesgetters.com/products-functions/products/shape-memory-alloys-nitinol (visited on 07/08/2020).

[40] Felix Welsch, Susanne-Marie Kirsch, et al. "System simulation of an elastocaloric heating and cooling device based on SMA". In: *SMASIS - Conference on Smart Materials, Adaptive Structures and Intelligent Systems*. ASME, 2020. DOI: 10.1115/SMASIS20-2262.

[41] Junyu Chen, Kuo Zhang, et al. "Ultra-high fatigue life of NiTi cylinders for compression-based elastocaloric cooling". In: *Applied Physics Letters* 115.9 (2019). DOI: 10.1063/1.5115793.

[42] Kurt Engelbrecht. "Future prospects for elastocaloric devices". In: *Journal of Physics: Energy* 1.2 (2019), p. 021001. DOI: 10.1088/2515-7655/ab1573.

[43] Cheng Fang, Yue Zheng, et al. "Superelastic NiTi SMA cables: Thermal-mechanical behavior, hysteretic modelling and seismic application". In: *Engineering Structures* 183.August 2018 (Mar. 2019), pp. 533–549. DOI: 10.1016/j.engstruct.2019.01.049.

[44] Adriana Greco, C. Aprea, et al. "A review of the state of the art of solid-state caloric cooling processes at room-temperature before 2019". In: *International Journal of Refrigeration* 106 (2019), pp. 66–88. DOI: 10.1016/j.ijrefrig.2019.06.034.

[45] A. B. M. Rezaul Islam and Ernur Karadoğan. "Sensitivity and Uncertainty Analysis of One-Dimensional Tanaka and Liang-Rogers Shape Memory Alloy Constitutive Models". In: *Materials* 12.10 (2019). DOI: 10.3390/ma12101687.

[46] Anne Jung, K. Al Majthoub, et al. "Correlative digital image correlation and infrared thermography measurements for the investigation of the mesoscopic deformation behaviour of foams". In: *Journal of the Mechanics and Physics of Solids* 130 (2019), pp. 165–180. DOI: 10.1016/j.jmps.2019.06.009.

[47] Parham Kabirifar, Andrej Žerovnik, et al. "Elastocaloric Cooling: State-of-the-art and Future Challenges in Designing Regenerative Elastocaloric Devices". In: *Journal of Mechanical Engineering* 65.11-12 (Nov. 2019), pp. 615–630. DOI: 10.5545/sv-jme.2019.6369.

[48] Susanne-Marie Kirsch, Felix Welsch, and Stefan Seelecke. "Solid-state-based energy converter, heating/cooling apparatus comprising such an energy converter, and methode for operating a heatin/cooling apparatus". CN114144626; DE102019113696; EP3973181; US12006920; US2022228575; WO2020234235. 2019.

[49] Susanne-Marie Kirsch, Felix Welsch, et al. "Continuous operating elastocaloric cooling device: First experimental results". In: *SMST - International Conference on Shape Memory and Superelastic Technologies*. ASM International, 2019. URL: https://asm.confex.com/asm/smst19/webprogram/Paper47348.html.

[50] Susanne-Marie Kirsch, Felix Welsch, et al. "Continuous operating elastocaloric heating and cooling device: Air flow investigation and experimental parameter study". In: *SMASIS - Conference on Smart Materials, Adaptive Structures and Intelligent Systems*. ASME, 2019. DOI: 10.1115/SMASIS2019-5633.

[51] Prashant Kumar, Ravi Anant Kishore, et al. "Shape memory alloy engine for high efficiency low-temperature gradient thermal to electrical conversion". In: *Applied Energy* 251 (2019). DOI: 10.1016/j.apenergy.2019.05.080.

[52] J. N. Lemke and A. Coda. "DSC and microstructure analysis of high temperature Ni-Ti-Hf, low hysteresis Ni-Ti-Cu and conventional super-elastic and shape memory Ni-Ti alloy ingots and wires". In: *Materials Today Communications* 21 (2019). DOI: 10.1016/j.mtcomm.2019.100666.

[53] Nicolas Michaelis, Andreas Schütze, et al. "Experimental determination of elastocaloric latent heat". In: *SMST - International Conference on Shape Memory and Superelastic Technologies*. ASM International, 2019, pp. 212–213. ISBN: 9781-5108-9272-9.

[54] Nicolas Michaelis, Andreas Schütze, et al. “Novel Experimental Approach to Determine Elastocaloric Latent Heat”. In: *Shape Memory and Superelasticity* 5.4 (2019), pp. 352–361. DOI: 10.1007/s40830-019-00249-y.

[55] Nicolas Michaelis, Felix Welsch, et al. “Experimental parameter identification for elastocaloric air cooling”. In: *International Journal of Refrigeration* 100 (2019), pp. 167–174. DOI: 10.1016/j.ijrefrig.2019.01.006.

[56] Nicolas Michaelis, Felix Welsch, et al. “Resistance monitoring of shape memory material stabilization during elastocaloric training”. In: *Smart Materials and Structures* 28.10 (2019). DOI: 10.1088/1361-665X/ab3d62.

[57] Gianluca Rizzello, Michele A. Mandolino, et al. “An accurate dynamic model for polycrystalline shape memory alloy wire actuators and sensors”. In: *Smart Materials and Structures* 28.2 (2019). DOI: 10.1088/1361-665X/aae3b8.

[58] Ryan Snodgrass and David Erickson. “A multistage elastocaloric refrigerator and heat pump with 28 K temperature span”. In: *Scientific Reports* 9.1 (2019). DOI: 10.1038/s41598-019-54411-8.

[59] Joachim Strittmatter, Paul Gümpel, and Marc Hiefer. “Intelligent materials in modern production – Current trends for thermal shape memory alloys”. In: *Procedia Manufacturing* 30 (2019), pp. 347–356. DOI: 10.1016/j.promfg.2019.02.049.

[60] Jaka Tušek and Nini Pryds. “Cooling with a Squeeze”. In: *Physics* 12.June (2019), p. 72. DOI: 10.1103/Physics.12.72.

[61] Run Wang, Shaoli Fang, et al. “Torsional refrigeration by twisted, coiled, and supercoiled fibers”. In: *Science* 366.6462 (2019), pp. 216–221. DOI: 10.1126/science.aax6182.

[62] Felix Welsch, Susanne-Marie Kirsch, et al. “Continuous Operating Elastocaloric Heating and Cooling Device: Model-Based Parameter Study With Airflow Losses”. In: *SMASIS - Conference on Smart Materials, Adaptive Structures and Intelligent Systems*. ASME, 2019. DOI: 10.1115/SMASIS2019-5636.

[63] L. Xu, T. Baxevanis, and Dimitris C. Lagoudas. “A three-dimensional constitutive model for the martensitic transformation in polycrystalline shape memory alloys under large deformation”. In: *Smart Materials and Structures* 28.7 (2019). DOI: 10.1088/1361-665X/ab1acb. arXiv: 1903.02187.

[64] Daniel B. Biggs, Christopher B. Churchill, and John A. Shaw. “Heat Transfer of Springs in Oblique Crossflows”. In: *Journal of Heat and Mass Transfer* 140.4 (2018). DOI: 10.1115/1.4038338.

[65] Florian Bruederlin, Lars Bumke, et al. “Elastocaloric Cooling on the Miniature Scale: A Review on Materials and Device Engineering”. In: *Energy Technology* 6.8 (2018), pp. 1588–1604. DOI: 10.1002/ente.201800137.

[66] Piyas Chowdhury. “Frontiers of Theoretical Research on Shape Memory Alloys: A General Overview”. In: *Shape Memory and Superelasticity* 4.1 (2018), pp. 26–40. DOI: 10.1007/s40830-018-0161-4.

[67] Sebastian Fähler. *Caloric Effects in Ferroic Materials: New Concepts for Cooling*. 2018. URL: https://www.ferroiccooling.de (visited on 07/23/2020).

[68] Sebastian Fähler. “Front Cover”. In: *Energy Technology* 6.8 (2018). DOI: 10.1002/ente.201880801.

[69] Jan Frenzel, Gunther Eggeler, et al. “High-performance elastocaloric materials for the engineering of bulk- and micro-cooling devices”. In: *MRS Bulletin* 43.4 (2018), pp. 280–284. DOI: 10.1557/mrs.2018.67.

[70] Tino Gottschall, Adrià Gràcia-Condal, et al. “A multicaloric cooling cycle that exploits thermal hysteresis”. In: *Nature Materials* 17.10 (2018), pp. 929–934. DOI: 10.1038/s41563-018-0166-6.

[71] Hanlin Gu, Lars Bumke, et al. “Phase engineering and supercompatibility of shape memory alloys”. In: *Materials Today* 21.3 (2018), pp. 265–277. DOI: 10.1016/j.mattod.2017.10.002.

[72] William Imamura, Lucas S. Paixão, et al. “I-Caloric Effects: A proposal for normalization”. In: *Thermag - International Converence on Caloric cooling*. IIR, 2018, pp. 179–184. DOI: 10.18462/iir.thermag.2018.0029.

[73] Susanne-Marie Kirsch, Felix Welsch, et al. “Continuously Operating Elastocaloric Cooling Device based on Shape Memory Alloys: Development and Realization”. In: *Thermag - International Conference on Caloric Cooling*. IIR, 2018. DOI: 10.18462/iir.thermag.2018.0039.

[74] Susanne-Marie Kirsch, Felix Welsch, et al. “NiTi-Based Elastocaloric Cooling on the Macroscale: From Basic Concepts to Realization”. In: *Energy Technology* 6.8 (2018), pp. 1567–1587. DOI: 10.1002/ente.201800152.

[75] Nicolas Michaelis, Felix Welsch, et al. “Investigation of single wire elastocaloric air cooling potential”. In: *Thermag - International Conference on Caloric Cooling*. IIR, 2018. DOI: 10.18462/iir.thermag.2018.0027.

[76] Suxin Qian, Lifen Yuan, et al. “Accurate prediction of work and coefficient of performance of elastocaloric materials with phase transformation kinetics”. In: *Science and Technology for the Built Environment* 24.6 (2018), pp. 673–684. DOI: 10.1080/23744731.2018.1457411.

[77] H. Sehitoglu, Y. Wu, and E. Ertekin. “Elastocaloric effects in the extreme”. In: *Scripta Materialia* 148 (2018), pp. 122–126. DOI: 10.1016/j.scriptamat.2017.05.017.

[78] Darin J. Sharar, Joshua Radice, et al. “First Demonstration of a Bending-Mode Elastocaloric Cooling ‘Loop’”. In: *IEEE - Intersociety Conference on Thermal and Thermomechanical Phenomena in Electronic Systems (ITherm)*. IEEE, 2018, pp. 218–226. DOI: 10.1109/ITHERM.2018.8419513.

[79] Jaka Tušek, Andrej Žerovnik, et al. “Elastocaloric effect vs fatigue life: Exploring the durability limits of Ni-Ti plates under pre-strain conditions for elastocaloric cooling”. In: *Acta Materialia* 150 (2018), pp. 295–307. DOI: 10.1016/j.actamat.2018.03.032.

[80] Felix Welsch, Johannes Ullrich, et al. “Numerical simulation and experimental investigation of the elastocaloric cooling effect in sputter-deposited TiNiCuCo thin films”. In: *Continuum Mechanics and Thermodynamics* 30.1 (2018), pp. 53–68. DOI: 10.1007/s00161-017-0582-x.

[81] Florian Bruederlin, Hinnerk Ossmer, et al. “SMA foil-based elastocaloric cooling: from material behavior to device engineering”. In: *Journal of Physics D: Applied Physics* 50.42 (2017). DOI: 10.1088/1361-6463/aa87a2.

[82] T. W. Duerig, Alan R. Pelton, and K. Bhattacharya. “The Measurement and Interpretation of Transformation Temperatures in Nitinol”. In: *Shape Memory and Superelasticity* 3.4 (2017), pp. 485–498. DOI: 10.1007/s40830-017-0133-0.

[83] Kurt Engelbrecht, Jaka Tušek, et al. “A regenerative elastocaloric device: experimental results”. In: *Journal of Physics D: Applied Physics* 50.42 (2017). DOI: 10.1088/1361-6463/aa8656.

[84] Andreas Heintz. *Thermodynamik*. Springer, 2017. DOI: 10.1007/978-3-662-49922-1.

[85] Guillaume Helbert, Luc Saint-Sulpice, et al. “A uniaxial constitutive model for superelastic NiTi SMA including R-phase and martensite transformations and thermal effects”. In: *Smart Materials and Structures* 26.2 (2017), p. 025007. DOI: 10.1088/1361-665X/aa5141.

[86] Mark O. McLinden, J. Steven Brown, et al. “Limited options for low-global-warming-potential refrigerants”. In: *Nature Communications* 8.1 (2017), p. 14476. DOI: 10.1038/ncomms14476.

[87] Suxin Qian, Lifen Yuan, et al. “Numerical modeling of an active elastocaloric regenerator refrigerator with phase transformation kinetics and the matching principle for materials selection”. In: *Energy* 141 (2017), pp. 744–756. DOI: 10.1016/j.energy.2017.09.116.

[88] Suxin Qian, Lifen Yuan, et al. “The mechanism of ΔT variation in coupled heat transfer and phase transformation for elastocaloric materials and its application in materials characterization”. In: *Applied Physics Letters* 111.22 (2017). DOI: 10.1063/1.5001971.

[89] Marvin Schmidt. “Elastokalorisches Kühlen mit Ni-Ti-basierten Formgedächtnislegierungen: Thermodynamische Analyse, experimentelle Untersuchungen, Prozessoptimierung”. PHD. Saarland University, 2017. ISBN: 9783-8440-5225-1.

[90] Johanna Waimann, Philipp Junker, and Klaus Hackl. “Modeling the Cyclic Behavior of Shape Memory Alloys”. In: *Shape Memory and Superelasticity* 3.2 (2017), pp. 124–138. DOI: 10.1007/s40830-017-0105-4.

[91] Jun Wang, Ziad Moumni, and Weihong Zhang. “A thermomechanically coupled finite-strain constitutive model for cyclic pseudoelasticity of polycrystalline shape memory alloys”. In: *International Journal of Plasticity* 97 (2017), pp. 194–221. DOI: 10.1016/j.ijplas.2017.06.003.

[92] Frank Wendler, Hinnerk Ossmer, et al. “Mesoscale simulation of elastocaloric cooling in SMA films”. In: *Acta Materialia* 136 (2017), pp. 105–117. DOI: 10.1016/j.actamat.2017.06.044.

[93] André Wieczorek, Jan Frenzel, et al. “Optimizing Ni–Ti-based shape memory alloys for ferroic cooling”. In: *Functional Materials Letters* 10.1 (2017). DOI: 10.1142/S179360471740001X.

[94] Y. Wu, E. Ertekin, and H. Sehitoglu. “Elastocaloric cooling capacity of shape memory alloys – Role of deformation temperatures, mechanical cycling, stress hysteresis and inhomogeneity of transformation”. In: *Acta Materialia* 135 (2017), pp. 158–176. DOI: 10.1016/j.actamat.2017.06.012.

[95] Kenneth Kanayo Alaneme and Eloho Anita Okotete. “Reconciling viability and cost-effective shape memory alloy options – A review of copper and iron based shape memory metallic systems”. In: *Engineering Science and Technology, an International Journal* 19.3 (2016), pp. 1582–1592. DOI: 10.1016/j.jestch.2016.05.010.

[96] Christoph Chluba, Wenwei Ge, et al. “Effect of crystallographic compatibility and grain size on the functional fatigue of sputtered TiNiCuCo thin films”. In: *Philosophical Transactions of the Royal Society A: Mathematical, Physical and Engineering Sciences* 374.2074 (2016), p. 20150311. DOI: 10.1098/rsta.2015.0311.

[97] Cheikh Cisse, Wael Zaki, and Tarak Ben Zineb. “A review of constitutive models and modeling techniques for shape memory alloys”. In: *International Journal of Plasticity* 76 (2016), pp. 244–284. DOI: 10.1016/j.ijplas.2015.08.006.

[98] Kurt Engelbrecht, Jaka Tušek, et al. “Effects of surface finish and mechanical training on Ni-Ti sheets for elastocaloric cooling”. In: *APL Materials* 4.6 (2016). DOI: 10.1063/1.4955131.

[99] Heinz Herwig, Christian Kautz, and Andreas Moschallski. *Technische Thermodynamik*. Springer, 2016. DOI: 10.1007/978-3-658-11888-4.

[100] Susanne-Marie Kirsch, Felix Welsch, and Stefan Seelecke. “Energiewandler mit thermoelastischer Anordnung sowie Heiz-/Kühlsystem”. DE102016118776; EP3306082. 2016.

[101] F. Moukalled, L. Mangani, and M. Darwish. *The Finite Volume Method in Computational Fluid Dynamics*. Vol. 113. Fluid Mechanics and Its Applications. Springer, 2016, E1–E1. DOI: 10.1007/978-3-319-16874-6.

[102] Hinnerk Ossmer, Christoph Chluba, et al. “TiNi-based films for elastocaloric microcooling— Fatigue life and device performance”. In: *APL Materials* 4.6 (2016). DOI: 10.1063/1.4948271.

[103] Hinnerk Ossmer, Frank Wendler, et al. “Energy-efficient miniature-scale heat pumping based on shape memory alloys”. In: *Smart Materials and Structures* 25.8 (2016). DOI: 10.1088/0964-1726/25/8/085037.

[104] Suxin Qian, Yunlong Geng, et al. “A review of elastocaloric cooling: Materials, cycles and system integrations”. In: *International Journal of Refrigeration* 64 (2016), pp. 1–19. DOI: 10.1016/j.ijrefrig.2015.12.001.

[105] Suxin Qian, Yunlong Geng, et al. “Design of a hydraulically driven compressive elastocaloric cooling system”. In: *Science and Technology for the Built Environment* 22.5 (2016), pp. 500–506. DOI: 10.1080/23744731.2016.1171630.

[106] Marvin Schmidt, Susanne-Marie Kirsch, et al. “Elastocaloric cooling: From fundamental thermodynamics to solid state air conditioning”. In: *Science and Technology for the Built Environment* 22.5 (2016), pp. 475–488. DOI: 10.1080/23744731.2016.1186423.

[107] Marvin Schmidt, Andreas Schütze, and Stefan Seelecke. "Elastocaloric cooling processes: The influence of material strain and strain rate on efficiency and temperature span". In: *APL Materials* 4.6 (2016). DOI: 10.1063/1.4953433.

[108] Marvin Schmidt, Johannes Ullrich, et al. "Experimental Methods for Investigation of Shape Memory Based Elastocaloric Cooling Processes and Model Validation". In: *Journal of Visualized Experiments* 111 (2016). DOI: 10.3791/53626.

[109] Jaka Tušek, Kurt Engelbrecht, et al. "A regenerative elastocaloric heat pump". In: *Nature Energy* 1.10 (2016), p. 16134. DOI: 10.1038/nenergy.2016.134.

[110] Jaka Tušek, Kurt Engelbrecht, et al. "Understanding the Thermodynamic Properties of the Elastocaloric Effect Through Experimentation and Modelling". In: *Shape Memory and Superelasticity* 2.4 (2016), pp. 317–329. DOI: 10.1007/s40830-016-0094-8.

[111] VHK and ARMINES. *Preparatory study: Commission Regulation (EC) No. 643/2009 with regard to ecodesign requirements for household refrigeration appliances and Commission Delegated Regulation (EU) No. 1060/2010 with regard to energy labelling of household refrigeration*. Tech. rep. 2016. URL: https://ecodesign-fridges.eu/sites/ecodesign-fridges.eu/files/Household%20Refrigeration%20Review%20FINAL%20REPORT%2020160304.pdf.

[112] Deqing Xue, Ruihao Yuan, et al. "Design of High Temperature Ti-Pd-Cr Shape Memory Alloys with Small Thermal Hysteresis". In: *Scientific Reports* 6.1 (2016). DOI: 10.1038/srep28244.

[113] Christoph Chluba, Wenwei Ge, et al. "Ultralow-fatigue shape memory alloy films". In: *Science* 348.6238 (2015), pp. 1004–1007. DOI: 10.1126/science.1261164.

[114] S. Crossley, Neil D. Mathur, and Xavier Moya. "New developments in caloric materials for cooling applications". In: *Advances* 5.6 (2015), p. 067153. DOI: 10.1063/1.4922871.

[115] Jan Frenzel, André Wieczorek, et al. "On the effect of alloy composition on martensite start temperatures and latent heats in Ni–Ti-based shape memory alloys". In: *Acta Materialia* 90 (2015), pp. 213–231. DOI: 10.1016/j.actamat.2015.02.029.

[116] Stefanie Jaeger, Burkhard Maaß, et al. "On the widths of the hysteresis of mechanically and thermally induced martensitic transformations in Ni–Ti-based shape memory alloys". In: *International Journal of Materials Research* 106.10 (2015), pp. 1029–1039. DOI: 10.3139/146.111284.

[117] Philipp Junker, Stefanie Jaeger, et al. “Variational prediction of the mechanical behavior of shape memory alloys based on thermal experiments”. In: *Journal of the Mechanics and Physics of Solids* 80 (2015), pp. 86–102. DOI: 10.1016/j.jmps.2015.04.015.

[118] Andrej Kitanovski, Uroš Plaznik, et al. “Present and future caloric refrigeration and heat-pump technologies”. In: *International Journal of Refrigeration* 57 (2015), pp. 288–298. DOI: 10.1016/j.ijrefrig.2015.06.008.

[119] Leonardo Lecce and Antonio Concilio. *Shape Memory Alloy ENGINEERING for Aerospace, Structural and Biomedical Applications Editors-in-Chief*. Elsevier, 2015. ISBN: 9780-08-099920-3.

[120] Paulo Silva Lobo, João Almeida, and Lúis Guerreiro. “Shape Memory Alloys Behaviour: A Review”. In: *Procedia Engineering* 114 (2015), pp. 776–783. DOI: 10.1016/j.proeng.2015.08.025.

[121] Xavier Moya, Emmanuel Defay, et al. “Too cool to work”. In: *Nature Physics* 11.3 (2015), pp. 202–205. DOI: 10.1038/nphys3271.

[122] Hinnerk Ossmer, Christoph Chluba, et al. “Local Evolution of the Elastocaloric Effect in TiNi-Based Films”. In: *Shape Memory and Superelasticity* 1.2 (2015), pp. 142–152. DOI: 10.1007/s40830-015-0014-3.

[123] Hinnerk Ossmer, Shuichi Miyazaki, and Manfred Kohl. “Elastocaloric heat pumping using a shape memory alloy foil device”. In: *Transducers - International Conference on Solid-State Sensors, Actuators and Microsystems (TRANSDUCERS)*. IEEE, 2015, pp. 726–729. DOI: 10.1109/TRANSDUCERS.2015.7181026.

[124] Suxin Qian, Abdullah Alabdulkarem, et al. “Performance enhancement of a compressive thermoelastic cooling system using multi-objective optimization and novel designs”. In: *International Journal of Refrigeration* 57 (2015), pp. 62–76. DOI: 10.1016/j.ijrefrig.2015.04.012.

[125] Suxin Qian, Jiazhen Ling, et al. “Thermodynamics cycle analysis and numerical modeling of thermoelastic cooling systems”. In: *International Journal of Refrigeration* 56 (2015), pp. 65–80. DOI: 10.1016/j.ijrefrig.2015.04.001.

[126] Scott W. Robertson, Maximilien Launey, et al. “A statistical approach to understand the role of inclusions on the fatigue resistance of superelastic Nitinol wire and tubing”. In: *Journal of the Mechanical Behavior of Biomedical Materials* 51 (2015), pp. 119–131. DOI: 10.1016/j.jmbbm.2015.07.003.

[127] Marvin Schmidt, Andreas Schütze, and Stefan Seelecke. "Scientific test setup for investigation of shape memory alloy based elastocaloric cooling processes". In: *International Journal of Refrigeration* 54 (2015), pp. 88–97. DOI: 10.1016/j.ijrefrig.2015.03.001.

[128] Marvin Schmidt, Johannes Ullrich, et al. "Thermal Stabilization of NiTiCuV Shape Memory Alloys: Observations During Elastocaloric Training". In: *Shape Memory and Superelasticity* 1.2 (2015), pp. 132–141. DOI: 10.1007/s40830-015-0021-4.

[129] H. Jesse Smith. *Adoption of the Paris Agreement*. Tech. rep. 2015. DOI: 10.1126/science.364.6435.39-f.

[130] Ichiro Takeuchi and Karl Sandeman. "Solid-state cooling with caloric materials". In: *Physics Today* 68.12 (2015), pp. 48–54. DOI: 10.1063/PT.3.3022.

[131] Jaka Tušek, Kurt Engelbrecht, et al. "The Elastocaloric Effect: A Way to Cool Efficiently". In: *Advanced Energy Materials* 5.13 (2015). DOI: 10.1002/aenm.201500361.

[132] Diana Ürge-Vorsatz, Luisa F. Cabeza, et al. "Heating and cooling energy trends and drivers in buildings". In: *Renewable and Sustainable Energy Reviews* 41 (Jan. 2015), pp. 85–98. DOI: 10.1016/j.rser.2014.08.039.

[133] Andrzej Ziółkowski. *Pseudoelasticity of Shape Memory Alloys*. Elsevier, 2015. DOI: 10.1016/B978-0-12-801697-8.09989-0.

[134] Johannes Ziske, Fabian Ehle, et al. "A Simple Phenomenological Model for Magnetic Shape Memory Actuators". In: *IEEE - Transactions on Magnetics* 51.1 (2015), pp. 1–8. DOI: 10.1109/TMAG.2014.2338833.

[135] S. Barbarino, E. I Saavedra Flores, et al. "A review on shape memory alloys with applications to morphing aircraft". In: *Smart Materials and Structures* 23.6 (2014). DOI: 10.1088/0964-1726/23/6/063001.

[136] O. Benafan, J. Brown, et al. "Shape memory alloy actuator design: CASMART collaborative best practices and case studies". In: *International Journal of Mechanics and Materials in Design* 10.1 (2014), pp. 1–42. DOI: 10.1007/s10999-013-9227-9.

[137] Dorian Depriester, Anne Maynadier, et al. "Thermomechanical modelling of a NiTi SMA sample submitted to displacement-controlled tensile test". In: *International Journal of Solids and Structures* 51.10 (2014), pp. 1901–1922. DOI: 10.1016/j.ijsolstr.2014.01.027.

[138] European Parliament. *Regulation (EU) No 517/2014 of the European Parliament and of the Council of 16 April 2014 on fluorinated greenhouse gases and repealing Regulation (EC) No 842/2006*. 2014.

[139] William Goetzler, Richard Shandross, et al. *Energy Savings Potential and RD&D Opportunities for Non-Vapor-Compression HVAC Technologies*. Tech. rep. U.S. Department of Energy, 2014. DOI: 10.2172/1220817.

[140] Intergovernmental Panel on Climate Change. *Climate Change 2014: Mitigation of Climate Change*. Cambridge University Press, 2014. DOI: 10.1017/CBO9781107415416.

[141] A. Kitanovski, Uroš Plaznik, et al. "New thermodynamic cycles for magnetic refrigeration". In: *International Journal of Refrigeration* 37.1 (2014), pp. 28–35. DOI: 10.1016/j.ijrefrig.2013.05.014.

[142] Maximilien Launey, Scott W. Robertson, et al. "Influence of microstructural purity on the bending fatigue behavior of VAR-melted superelastic Nitinol". In: *Journal of the Mechanical Behavior of Biomedical Materials* 34 (2014), pp. 181–186. DOI: 10.1016/j.jmbbm.2014.02.008.

[143] Jaronie Mohd Jani, Martin Leary, et al. "A review of shape memory alloy research, applications and opportunities". In: *Materials & Design* 56 (2014), pp. 1078–1113. DOI: 10.1016/j.matdes.2013.11.084.

[144] Xavier Moya, S Kar-Narayan, and Neil D. Mathur. "Caloric materials near ferroic phase transitions". In: *Nature Materials* 13.5 (2014), pp. 439–450. DOI: 10.1038/nmat3951.

[145] Hinnerk Ossmer, Franziska Lambrecht, et al. "Evolution of temperature profiles in TiNi films for elastocaloric cooling". In: *Acta Materialia* 81 (Dec. 2014), pp. 9–20. DOI: 10.1016/j.actamat.2014.08.006.

[146] M. Ožbolt, Andrej Kitanovski, et al. "Electrocaloric refrigeration: Thermodynamics, state of the art and future perspectives". In: *International Journal of Refrigeration* 40 (2014), pp. 174–188. DOI: 10.1016/j.ijrefrig.2013.11.007.

[147] M. Ožbolt, Andrej Kitanovski, et al. "Electrocaloric vs. magnetocaloric energy conversion". In: *International Journal of Refrigeration* 37.1 (2014), pp. 16–27. DOI: 10.1016/j.ijrefrig.2013.07.001.

[148] Benjamin Reedlunn, Christopher B. Churchill, et al. "Tension, compression, and bending of superelastic shape memory alloy tubes". In: *Journal of the Mechanics and Physics of Solids* 63.1 (2014), pp. 506–537. DOI: 10.1016/j.jmps.2012.12.012.

[149] Marvin Schmidt, Andreas Schütze, and Stefan Seelecke. "Experimental Investigation on the Efficiency of a Control Dependent NiTi-Based Cooling Process". In: *SMASIS - Conference on Smart Materials, Adaptive Structures and Intelligent Systems*. ASME, 2014. DOI: 10.1115/SMASIS2014-7561.

[150] Henning Struchtrup. *Thermodynamics and Energy Conversion*. Springer, 2014. DOI: 10.1007/978-3-662-43715-5.

[151] Etsuko Sugawara and Hiroshi Nikaido. "Properties of AdeABC and AdeIJK Efflux Systems of Acinetobacter baumannii Compared with Those of the AcrAB-TolC System of Escherichia coli". In: *Antimicrobial Agents and Chemotherapy* 58.12 (2014), pp. 7250–7257. DOI: 10.1128/AAC.03728-14.

[152] Johannes Ullrich, Marvin Schmidt, et al. "Experimental Investigation and Numerical Simulation of the Mechanical and Thermal Behavior of a Superelastic Shape Memory Alloy Beam During Bending". In: *SMASIS - Conference on Smart Materials, Adaptive Structures and Intelligent Systems*. ASME, 2014. DOI: 10.1115/SMASIS2014-7619.

[153] K. C. Atli, B. E. Franco, et al. "Influence of crystallographic compatibility on residual strain of TiNi based shape memory alloys during thermo-mechanical cycling". In: *Materials Science and Engineering: A* 574 (2013), pp. 9–16. DOI: 10.1016/j.msea.2013.02.035.

[154] S. Bagavathiappan, B. B. Lahiri, et al. "Infrared thermography for condition monitoring – A review". In: *Infrared Physics & Technology* 60 (2013), pp. 35–55. DOI: 10.1016/j.infrared.2013.03.006.

[155] Hartmut Janocha. *Unkonventionelle Aktoren - Eine Einführung*. Oldenbourg Verlag, 2013. ISBN: 9783-486-71886-7.

[156] Christian Mennerich, Frank Wendler, et al. "Rearrangement of martensitic variants in Ni2MnGa studied with the phase-field method". In: *The European Physical Journal B* 86.4 (2013). DOI: 10.1140/epjb/e2013-30941-6.

[157] A. R. Pelton, J. Fino-Decker, et al. "Rotary-bending fatigue characteristics of medical-grade Nitinol wire". In: *Journal of the Mechanical Behavior of Biomedical Materials* 27 (2013), pp. 19–32. DOI: 10.1016/j.jmbbm.2013.06.003.

[158] Mustafa Rahim, Jan Frenzel, et al. "Bending rotation HCF testing of pseudoelastic Ni-Ti shape memory alloys". In: *Materialwissenschaft und Werkstofftechnik* 44.7 (2013), pp. 633–640. DOI: 10.1002/mawe.201300118.

[159] Mustafa Rahim, Jan Frenzel, et al. "Impurity levels and fatigue lives of pseudoelastic NiTi shape memory alloys". In: *Acta Materialia* 61.10 (June 2013), pp. 3667–3686. DOI: 10.1016/j.actamat.2013.02.054.

[160] Benjamin Reedlunn, S. Daly, et al. "Tips and Tricks for Characterizing Shape Memory Wire: Part 5 Full-Field Strain Measurement by Digital Image Correlation". In: *Experimental Techniques* 37.3 (2013), pp. 62–78. DOI: 10.1111/j.1747-1567.2011.00717.x.

[161] Benjamin Reedlunn, Samantha Daly, and John A. Shaw. “Superelastic shape memory alloy cables: Part I – Isothermal tension experiments”. In: *International Journal of Solids and Structures* 50.20-21 (2013), pp. 3009–3026. DOI: 10.1016/j.ijsolstr.2013.03.013.

[162] Marvin Schmidt, Andreas Schütze, and Stefan Seelecke. “Cooling Efficiencies of a NiTi-Based Cooling Process”. In: *SMASIS - Conference on Smart Materials, Adaptive Structures and Intelligent Systems*. ASME, 2013. DOI: 10.1115/SMASIS2013-3249.

[163] Jaka Tušek, Andrej Kitanovski, and Alojz Poredoš. “Geometrical optimization of packed-bed and parallel-plate active magnetic regenerators”. In: *International Journal of Refrigeration* 36.5 (2013), pp. 1456–1464. DOI: 10.1016/j.ijrefrig.2013.04.001.

[164] Christoph Bechtold, Christoph Chluba, et al. “High cyclic stability of the elastocaloric effect in sputtered TiNiCu shape memory films”. In: *Applied Physics Letters* 101.9 (2012). DOI: 10.1063/1.4748307.

[165] Jun Cui, Yiming Wu, et al. “Demonstration of high efficiency elastocaloric cooling with large ΔT using NiTi wires”. In: *Applied Physics Letters* 101.7 (2012). DOI: 10.1063/1.4746257.

[166] DUH. *Environmentally friendly cooling*. Tech. rep. 2012. URL: http://www.autoklimaanlage.info/fileadmin/user%7B%5C_%7Dupload/pdfs/ProKlima%7B%5C_%7DLaymansReport%7B%5C_%7DGB%7B%5C_%7D280414.pdf.

[167] Sebastian Fähler, Ulrich K. Rößler, et al. “Caloric Effects in Ferroic Materials: New Concepts for Cooling”. In: *Advanced Engineering Materials* 14.1-2 (2012), pp. 10–19. DOI: 10.1002/adem.201100178.

[168] Stephen J. Furst, John H. Crews, and Stefan Seelecke. “Numerical and experimental analysis of inhomogeneities in SMA wires induced by thermal boundary conditions”. In: *Continuum Mechanics and Thermodynamics* 24.4-6 (2012), pp. 485–504. DOI: 10.1007/s00161-012-0238-9.

[169] Stephen J. Furst and Stefan Seelecke. “Modeling and experimental characterization of the stress, strain, and resistance of shape memory alloy actuator wires with controlled power input”. In: *Journal of Intelligent Material Systems and Structures* 23.11 (2012), pp. 1233–1247. DOI: 10.1177/1045389X12445036.

[170] D. Grandi, M. Maraldi, and L. Molari. “A macroscale phase-field model for shape memory alloys with non-isothermal effects: Influence of strain rate and environmental conditions on the mechanical response”. In: *Acta Materialia* 60 (2012), pp. 179–191. DOI: 10.1016/j.actamat.2011.09.040. arXiv: 1107.5998.

[171] Sxot W. Robertson, Alan R. Pelton, and R O Ritchie. "Mechanical fatigue and fracture of Nitinol". In: *International Materials Reviews* 57.1 (2012), pp. 1–37. DOI: 10.1179/1743280411Y.0000000009.

[172] April Saylor. *ARPA-E Summit Technology Showcase - Thermoelastical cooling.* 2012. URL: https://www.energy.gov/articles/2012-arpa-e-summit-technology-showcase%20https://www.energy.gov/sites/prod/files/styles/borealis%7B%5C_%7Dphoto%7B%5C_%7Dgallery%7B%5C_%7Dlarge%7B%5C_%7Drespondlarge/public/fileY8GIAe?itok=a7PAB7J%7B%5C_%7D (visited on 02/22/2018).

[173] H. Sayyaadi, M. R. Zakerzadeh, and H. Salehi. "A comparative analysis of some one-dimensional shape memory alloy constitutive models based on experimental tests". In: *Scientia Iranica* 19.2 (2012), pp. 249–257. DOI: 10.1016/j.scient.2012.01.005.

[174] Yves Chemisky, Arnaud Duval, et al. "Constitutive model for shape memory alloys including phase transformation, martensitic reorientation and twins accommodation". In: *Mechanics of Materials* 43.7 (2011), pp. 361–376. DOI: 10.1016/j.mechmat.2011.04.003.

[175] A. Duval, M. Haboussi, and T. Ben Zineb. "Modelling of localization and propagation of phase transformation in superelastic SMA by a gradient nonlocal approach". In: *International Journal of Solids and Structures* 48.13 (2011), pp. 1879–1893. DOI: 10.1016/j.ijsolstr.2011.02.019.

[176] Jan Frenzel, Juri A. Burow, et al. "Improvement of NiTi Shape Memory Actuator Performance Through Ultra-Fine Grained and Nanocrystalline Microstructures". In: *Advanced Engineering Materials* 13.4 (2011), pp. 256–268. DOI: 10.1002/adem.201000285.

[177] J. F. Scott. "Electrocaloric Materials". In: *Annual Review of Materials Research* 41.1 (Aug. 2011), pp. 229–240. DOI: 10.1146/annurev-matsci-062910-100341.

[178] Jaka Tušek, Andrej Kitanovski, et al. "Dynamic operation of an active magnetic regenerator (AMR): Numerical optimization of a packed-bed AMR". In: *International Journal of Refrigeration* 34.6 (2011), pp. 1507–1517. DOI: 10.1016/j.ijrefrig.2011.04.007.

[179] C. B. Churchill, John A. Shaw, and M. A. Iadicola. "Tips and Tricks for Characterizing Shape Memory Alloy Wire: Part 4-Thermo-Mechanical Coupling". In: *Experimental Techniques* 34.2 (2010), pp. 63–80. DOI: 10.1111/j.1747-1567.2010.00619.x.

[180] Samantha H. Daly. “Digital Image Correlation in Experimental Mechanics for Aerospace Materials and Structures”. In: *Encyclopedia of Aerospace Engineering*. Wiley, 2010, pp. 1–12. DOI: 10.1002/9780470686652.eae542.

[181] Jan Frenzel, E. P. George, et al. “Influence of Ni on martensitic phase transformations in NiTi shape memory alloys”. In: *Acta Materialia* 58.9 (May 2010), pp. 3444–3458. DOI: 10.1016/j.actamat.2010.02.019.

[182] Gunther Hohne, Wolfgang F. Hemminger, et al. *Differential Scanning Calorimetry: An Introduction for Practitioners*. Vol. 53. 9. Springer, 2010, pp. 1689–1699. ISBN: 9783-540-59012-5.

[183] W. M. Huang, Z. Ding, et al. “Shape memory materials”. In: *Materials Today* 13.7-8 (2010), pp. 54–61. DOI: 10.1016/S1369-7021(10)70128-0.

[184] Valery I. Levitas, Dong-Wook Lee, and Dean L. Preston. “Interface propagation and microstructure evolution in phase field models of stress-induced martensitic phase transformations”. In: *International Journal of Plasticity* 26.3 (2010), pp. 395–422. DOI: 10.1016/j.ijplas.2009.08.003.

[185] U. Muschelknautz. *VDI Heat Atlas*. Springer, 2010. DOI: 10.1007/978-3-540-77877-6.

[186] John A. Shaw, Christopher B. Churchill, et al. “Shape Memory Alloys”. In: *Encyclopedia of Aerospace Engineering*. Wiley, 2010, pp. 1–16. DOI: 10.1002/9780470686652.eae232.

[187] StanisŁaw Stupkiewicz and Henryk Petryk. “A bi-crystal aggregate model of pseudoelastic behaviour of shape-memory alloy polycrystals”. In: *International Journal of Mechanical Sciences* 52.2 (2010), pp. 219–228. DOI: 10.1016/j.ijmecsci.2009.09.012.

[188] M. L. Young, M. F.-X. Wagner, et al. “Phase volume fractions and strain measurements in an ultrafine-grained NiTi shape-memory alloy during tensile loading”. In: *Acta Materialia* 58.7 (2010), pp. 2344–2354. DOI: 10.1016/j.actamat.2009.12.021.

[189] Robert Zarnetta, Ryota Takahashi, et al. “Identification of Quaternary Shape Memory Alloys with Near-Zero Thermal Hysteresis and Unprecedented Functional Stability”. In: *Advanced Functional Materials* 20.12 (June 2010), pp. 1917–1923. DOI: 10.1002/adfm.200902336.

[190] Hans Dieter Baehr and Karl Stephan. *Wärme- und Stoffübertragung*. Springer Berlin Heidelberg, 2009. DOI: 10.1007/978-3-540-87689-2.

[191] C. B. Churchill, John A. Shaw, and M. A. Iadicola. "Tips and Tricks for Characterizing Shape Memory Alloy Wire: Part 2-Fundamental Isothermal Responses". In: *Experimental Techniques* 33.1 (2009), pp. 51–62. DOI: 10.1111/j.1747-1567.2008.00460.x.

[192] C. B. Churchill, John A. Shaw, and M. A. Iadicola. "Tips and Tricks for Characterizing Shape Memory Alloy Wire: Part 3-Localization and Propagation Phenomena". In: *Experimental Techniques* 33.5 (2009), pp. 70–78. DOI: 10.1111/j.1747-1567.2009.00558.x.

[193] Veronica Evangelista, Sonia Marfia, and Elio Sacco. "Phenomenological 3D and 1D consistent models for shape-memory alloy materials". In: *Computational Mechanics* 44.3 (2009), pp. 405–421. DOI: 10.1007/s00466-009-0381-8.

[194] Christian Grossmann, Jan Frenzel, et al. "Elementary Transformation and Deformation Processes and the Cyclic Stability of NiTi and NiTiCu Shape Memory Spring Actuators". In: *Metallurgical and Materials Transactions A* 40.11 (2009), pp. 2530–2544. DOI: 10.1007/s11661-009-9958-2.

[195] Lluís Mañosa, Antoni Planes, et al. "The Use of Shape-Memory Alloys for Mechanical Refrigeration". In: *Functional Materials Letters* 02.02 (2009), pp. 73–78. DOI: 10.1142/S1793604709000594.

[196] Frank Richter, Oliver Kastner, and Gunther Eggeler. "Implementation of the Müller-Achenbach-Seelecke Model for Shape Memory Alloys in ABAQUS". In: *Journal of Materials Engineering and Performance* 18.5-6 (2009), pp. 626–630. DOI: 10.1007/s11665-009-9483-x.

[197] Florian Schiedeck. "Entwicklung eines Modells für Formgedächtnisaktoren im geregelten dynamischen Betrieb". Master of Science. Gottfried Wilhelm Leibniz Universität Hannover, 2009. ISBN: 9783-941416-23-9.

[198] S. A. Tassou, G. De-Lille, and Y. T. Ge. "Food transport refrigeration – Approaches to reduce energy consumption and environmental impacts of road transport". In: *Applied Thermal Engineering* 29.8-9 (2009), pp. 1467–1477. DOI: 10.1016/j.applthermaleng.2008.06.027.

[199] S. Yang and Stefan Seelecke. "FE analysis of SMA-based bio-inspired bone–joint system". In: *Smart Materials and Structures* 18.10 (2009). DOI: 10.1088/0964-1726/18/10/104020.

[200] Zhiyong Zhang, Richard D. James, and Stefan Müller. "Energy barriers and hysteresis in martensitic phase transformations". In: *Acta Materialia* 57.15 (2009), pp. 4332–4352. DOI: 10.1016/j.actamat.2009.05.034.

[201] Eric Zimmerman, Vlad Muntean, et al. “Novel Pre-Crash-Actuator-System based on SMA for Enhancing Side Impact Safety”. In: *Advanced Microsystems for Automotive Applications*. Springer Berlin Heidelberg, 2009, pp. 49–64. DOI: 10.1007/978-3-642-00745-3_4.

[202] Erell Bonnot, Ricardo Romero, et al. “Elastocaloric Effect Associated with the Martensitic Transition in Shape-Memory Alloys”. In: *Physical Review Letters* 100.12 (2008), p. 125901. DOI: 10.1103/PhysRevLett.100.125901.

[203] Bijan Azadi Borujeni, Daan M. Maijer, and Nimal Rajapakse. “Finite element simulation of strain rate effects on localized unstable pseudoelastic response of shape memory alloys”. In: *Journal of Mechanics of Materials and Structures* 3.10 (2008), pp. 1811–1829. DOI: 10.2140/jomms.2008.3.1811.

[204] Olaf Heintze and Stefan Seelecke. “A coupled thermomechanical model for shape memory alloys—From single crystal to polycrystal”. In: *Materials Science and Engineering: A* 481-482 (2008), pp. 389–394. DOI: 10.1016/j.msea.2007.08.028.

[205] Dimitris C. Lagoudas. *Shape Memory Alloys*. Springer, 2008. DOI: 10.1007/978-0-387-47685-8.

[206] A. Pelton, V. Schroeder, et al. “Fatigue and durability of Nitinol stents”. In: *Journal of the Mechanical Behavior of Biomedical Materials* 1.2 (2008), pp. 153–164. DOI: 10.1016/j.jmbbm.2007.08.001.

[207] Fatemeh Shakeri and Mehdi Dehghan. “The method of lines for solution of the one-dimensional wave equation subject to an integral conservation condition”. In: *Computers & Mathematics with Applications* 56.9 (2008), pp. 2175–2188. DOI: 10.1016/j.camwa.2008.03.055.

[208] John A. Shaw, C. B. Churchill, and M. A. Iadicola. “Tips and Tricks for Characterizing Shape Memory Alloy Wire: Part 1-Differential Scanning Calorimetry and Basic Phenomena”. In: *Experimental Techniques* 32.5 (2008), pp. 55–62. DOI: 10.1111/j.1747-1567.2008.00410.x.

[209] Eric Williams and Mohammad H. Elahinia. “An Automotive SMA Mirror Actuator: Modeling, Design, and Experimental Evaluation”. In: *Journal of Intelligent Material Systems and Structures* 19.12 (2008), pp. 1425–1434. DOI: 10.1177/1045389X07087328.

[210] B. Azadi, R. K. N. D. Rajapakse, and D. M. Maijer. “Multi-dimensional constitutive modeling of SMA during unstable pseudoelastic behavior”. In: *International Journal of Solids and Structures* 44.20 (2007), pp. 6473–6490. DOI: 10.1016/j.ijsolstr.2007.02.039.

[211] Brian L. Ball, Ralph C. Smith, et al. "A Stress-dependent Hysteresis Model for Ferroelectric Materials". In: *Journal of Intelligent Material Systems and Structures* 18.1 (2007), pp. 69–88. DOI: 10.1177/1045389X07070937.

[212] D. J. Hartl and Dimitris C. Lagoudas. "Aerospace applications of shape memory alloys". In: *Proceedings of the Institution of Mechanical Engineers, Part G: Journal of Aerospace Engineering* 221.4 (2007), pp. 535–552. DOI: 10.1243/09544100JAERO211.

[213] Mark A. Iadicola and John A. Shaw. "An experimental method to measure initiation events during unstable stress-induced martensitic transformation in a shape memory alloy wire". In: *Smart Materials and Structures* 16.1 (2007), pp. 155–169. DOI: 10.1088/0964-1726/16/1/S16.

[214] William H. Press, Saul A. Teukolsky, et al. *Numerical recipes - The art of Scientific Computing*. Third Edit. Cambridge University Press, 2007. ISBN: 9780-511-33555-6.

[215] Bi-Chiau Chang, John A. Shaw, and Mark A. Iadicola. "Thermodynamics of Shape Memory Alloy Wire: Modeling, Experiments, and Application". In: *Continuum Mechanics and Thermodynamics* 18.1-2 (2006), pp. 83–118. DOI: 10.1007/s00161-006-0022-9.

[216] Jun Cui, Yong S. Chu, et al. "Combinatorial search of thermoelastic shape-memory alloys with extremely small hysteresis width". In: *Nature Materials* 5.4 (2006), pp. 286–290. DOI: 10.1038/nmat1593.

[217] Akihiko Kumagai, Tien-I. Liu, and Paul Hozian. "Control of Shape Memory Alloy Actuators with a Neuro-fuzzy Feedforward Model Element". In: *Journal of Intelligent Manufacturing* 17.1 (Feb. 2006), pp. 45–56. DOI: 10.1007/s10845-005-5512-2.

[218] B. Peultier, T. Ben Zineb, and E. Patoor. "Macroscopic constitutive law of shape memory alloy thermomechanical behaviour. Application to structure computation by FEM". In: *Mechanics of Materials* 38.5-6 (2006), pp. 510–524. DOI: 10.1016/j.mechmat.2005.05.026.

[219] E. A. Pieczyska, S. P. Gadaj, et al. "Phase-Transformation Fronts Evolution for Stress- and Strain-Controlled Tension Tests in TiNi Shape Memory Alloy". In: *Experimental Mechanics* 46.4 (2006), pp. 531–542. DOI: 10.1007/s11340-006-8351-y.

[220] Ralph C. Smith, Stefan Seelecke, et al. "A unified framework for modeling hysteresis in ferroic materials". In: *Journal of the Mechanics and Physics of Solids* 54.1 (2006), pp. 46–85. DOI: 10.1016/j.jmps.2005.08.006.

[221] K. Otsuka and X. Ren. “Physical metallurgy of Ti–Ni-based shape memory alloys”. In: *Progress in Materials Science* 50.5 (2005), pp. 511–678. DOI: 10.1016/j.pmatsci.2004.10.001.

[222] P. Sittner, Y. Liu, and V. Novak. “On the origin of Lüders-like deformation of NiTi shape memory alloys”. In: *Journal of the Mechanics and Physics of Solids* 53.8 (2005), pp. 1719–1746. DOI: 10.1016/j.jmps.2005.03.005.

[223] Mohammed Es-Souni, Martha Es-Souni, and Helge Fischer-Brandies. “Assessing the biocompatibility of NiTi shape memory alloys used for medical applications”. In: *Analytical and Bioanalytical Chemistry* 381.3 (Feb. 2005), pp. 557–567. DOI: 10.1007/s00216-004-2888-3.

[224] L. Catherine Brinson. “Stress-induced transformation behavior of a polycrystalline NiTi shape memory alloy: micro and macromechanical investigations via in situ optical microscopy”. In: *Journal of the Mechanics and Physics of Solids* 52.7 (2004), pp. 1549–1571. DOI: 10.1016/j.jmps.2004.01.001.

[225] Gunther Eggeler, E. Hornbogen, et al. “Structural and functional fatigue of NiTi shape memory alloys”. In: *Materials Science and Engineering: A* 378.1-2 (2004), pp. 24–33. DOI: 10.1016/j.msea.2003.10.327.

[226] Olaf Heintze. “A Computationally Efficient Free Energy Model for Shape Memory Alloys - Experiments and Theory”. PHD Thesis. North carolina state University, 2004.

[227] Mark A. Iadicola and John A. Shaw. “Rate and thermal sensitivities of unstable transformation behavior in a shape memory alloy”. In: *International Journal of Plasticity* 20.4-5 (2004), pp. 577–605. DOI: 10.1016/S0749-6419(03)00040-8.

[228] H. S. Lee, C. J. Matthews, et al. “A MATLAB method of lines template for transport equations”. In: *Environmental Modelling & Software* 19.6 (2004), pp. 603–614. DOI: 10.1016/j.envsoft.2003.08.017.

[229] Carosena Meola, Giovanni M. Carlomagno, and Luca Giorleo. “The use of infrared thermography for materials characterization”. In: *Journal of Materials Processing Technology* 155-156.1-3 (2004), pp. 1132–1137. DOI: 10.1016/j.jmatprotec.2004.04.268.

[230] Nb B Morgan, J Painter, and A Moffat. “Mean strain effects and microstructural observations during in vitro fatigue testing of NiTi”. In: *SMST- International Conference on Shape Memory and Superelastic Technologies*. Vol. 79. 1. 2004, pp. 303–310.

[231] J Quarini and A Prince. "Solid state refrigeration: Cooling and refrigeration using crystalline phase changes in metal alloys". In: *Proceedings of the Institution of Mechanical Engineers, Part C: Journal of Mechanical Engineering Science* 218.10 (2004), pp. 1175–1179. DOI: 10.1243/0954406042369062.

[232] W. W. Schmahl, J. Khalil-Allafi, et al. "Investigation of the phase evolution in a super-elastic NiTi shape memory alloy (50.7at.%Ni) under extensional load with synchrotron radiation". In: *Materials Science and Engineering: A* 378.1-2 (2004), pp. 81–85. DOI: 10.1016/j.msea.2003.11.081.

[233] Stefan Seelecke and Ingo Müller. "Shape memory alloy actuators in smart structures: Modeling and simulation". In: *Applied Mechanics Reviews* 57.1 (2004), pp. 23–46. DOI: 10.1115/1.1584064.

[234] T. Duerig, Dieter Stoeckel, and D. Johnson. "SMA: smart materials for medical applications". In: *SPIE - European Workshop on Smart Structures in Engineering and Technology*. Ed. by Brian Culshaw. Vol. 4763. SPIE, 2003, pp. 7–15. DOI: 10.1117/12.508666.

[235] Tobias Hesse, Mehrdaad Ghorashi, and Daniel J. Inman. "Comparison of the experimental behavior of a shape memory alloy in compression and tension". In: *American Society of Mechanical Engineers, Aerospace Division (Publication) AD* 68 (2003), pp. 471–478. DOI: 10.1115/IMECE2003-43786.

[236] F. Khelfaoui and G. Guénin. "Influence of the recovery and recrystallization processes on the martensitic transformation of cold worked equiatomic Ti–Ni alloy". In: *Materials Science and Engineering: A* 355.1-2 (2003), pp. 292–298. DOI: 10.1016/S0921-5093(03)00068-6.

[237] M. P. Annaorazov, S. A. Nikitin, et al. "Heat pump cycles based on the AF–F transition in Fe–Rh alloys induced by tensile stress". In: *International Journal of Refrigeration* 25.8 (2002), pp. 1034–1042. DOI: 10.1016/S0140-7007(02)00028-2.

[238] A. Bekker. "Impact induced propagation of phase transformation in a shape memory alloy rod". In: *International Journal of Plasticity* 18.11 (2002), pp. 1447–1479. DOI: 10.1016/S0749-6419(02)00025-6.

[239] Mark A. Iadicola and John A. Shaw. "The Effect of Uniaxial Cyclic Deformation on the Evolution of Phase Transformation Fronts in Pseudoelastic NiTi Wire". In: *Journal of Intelligent Material Systems and Structures* 13.March (2002), pp. 143–155. URL: https://api.semanticscholar.org/CorpusID:8804663.

[240] Andreas Lendlein and Steffen Kelch. "Shape-Memory Polymers". In: *Angewandte Chemie International Edition* 41.12 (2002), p. 2034. DOI: 10.1002/1521-3773(20020617)41:12<2034::AID-ANIE2034>3.0.CO;2-M.

[241] Ean H. Schiller. “Heat Engine Driven by Shape Memory Alloys : Prototyping and Design”. Master of Science. Virginia Polytechnic Institute and State University, 2002. URL: https://vtechworks.lib.vt.edu/bitstream/handle/10919/35185/ETD.pdf?sequence=3.

[242] Stefan Seelecke. “Modeling the dynamic behavior of shape memory alloys”. In: *International Journal of Non-Linear Mechanics* 37.8 (2002), pp. 1363–1374. DOI: 10.1016/S0020-7462(02)00030-6.

[243] John A. Shaw. “A thermomechanical model for a 1-D shape memory alloy wire with propagating instabilities”. In: *International Journal of Solids and Structures* 39.5 (2002), pp. 1275–1305. DOI: 10.1016/S0020-7683(01)00242-6.

[244] David A. Miller and Dimitris C. Lagoudas. “Influence of cold work and heat treatment on the shape memory effect and plastic strain development of NiTi”. In: *Materials Science and Engineering: A* 308.1-2 (2001), pp. 161–175. DOI: 10.1016/S0921-5093(00)01982-1.

[245] Ingo Müller and Stefan Seelecke. “Thermodynamic aspects of shape memory alloys”. In: *Mathematical and Computer Modelling* 34.12-13 (2001), pp. 1307–1355. DOI: 10.1016/S0895-7177(01)00134-0.

[246] M. G. Faulkner, J. J. Amalraj, and A. Bhattacharyya. “Experimental determination of thermal and electrical properties of Ni-Ti shape memory wires”. In: *Smart Materials and Structures* 9.5 (2000), pp. 632–639. DOI: 10.1088/0964-1726/9/5/307.

[247] John A. Shaw. “Simulations of localized thermo-mechanical behavior in a NiTi shape memory alloy”. In: *International Journal of Plasticity* 16.5 (2000), pp. 541–562. DOI: 10.1016/S0749-6419(99)00075-3.

[248] K. Gall, H. Sehitoglu, et al. “Tension–compression asymmetry of the stress–strain response in aged single crystal and polycrystalline NiTi”. In: *Acta Materialia* 47.4 (1999), pp. 1203–1217. DOI: 10.1016/S1359-6454(98)00432-7.

[249] S. Miyazaki, K Mizukoshi, et al. “Fatigue life of Ti–50 at.% Ni and Ti–40Ni–10Cu (at.%) shape memory alloy wires”. In: *Materials Science and Engineering: A* 273-275 (1999), pp. 658–663. DOI: 10.1016/S0921-5093(99)00344-5.

[250] W. Tang, B. Sundman, et al. “New modelling of the B2 phase and its associated martensitic transformation in the Ti–Ni system”. In: *Acta Materialia* 47.12 (Sept. 1999), pp. 3457–3468. DOI: 10.1016/S1359-6454(99)00193-7.

[251] Z. K. Lu and G. J. Weng. “A self-consistent model for the stress-strain behavior of shape-memory alloy polycrystals”. In: *Acta Materialia* 46.15 (1998), pp. 5423–5433. DOI: 10.1016/S1359-6454(98)00203-1.

[252] Hisaaki Tobushi, Yoshirou Shimeno, et al. “Influence of strain rate on superelastic properties of TiNi shape memory alloy”. In: *Mechanics of Materials* 30.2 (1998), pp. 141–150. DOI: 10.1016/S0167-6636(98)00041-6.

[253] Ferdinando Auricchio and Robert L. Taylor. “Shape-memory alloys: modelling and numerical simulations of the finite-strain superelastic behavior”. In: *Computer Methods in Applied Mechanics and Engineering* 143.1-2 (Apr. 1997), pp. 175–194. DOI: 10.1016/S0045-7825(96)01147-4.

[254] George B. Kauffman and Isaac Mayo. “The Story of Nitinol: The Serendipitous Discovery of the Memory Metal and Its Applications”. In: *The Chemical Educator* 2.2 (1997). DOI: 10.1007/s00897970111a.

[255] John A. Shaw and S Kyriakides. “On the nucleation and propagation of phase transformation fronts in a NiTi alloy”. In: *Acta Materialia* 45.2 (1997), pp. 683–700. DOI: 10.1016/S1359-6454(96)00189-9.

[256] J. G. Boyd and D. C. Lagoudas. “A thermodynamical constitutive model for shape memory materials. Part I. The monolithic shape memory alloy”. In: *International Journal of Plasticity* 12.6 (1996), pp. 805–842. DOI: 10.1016/S0749-6419(96)00030-7.

[257] Stefan Seelecke. “Equilibrium thermodynamics of pseudoelasticity and quasiplasticity”. In: *Continuum Mechanics and Thermodynamics* 8.5 (1996), pp. 309–322. DOI: 10.1007/s001610050046.

[258] Edwin G. Corr. “Societal Transformation for Peace in El Salvador”. In: *The ANNALS of the American Academy of Political and Social Science* 541.1 (1995), pp. 144–156. DOI: 10.1177/0002716295541001010.

[259] John A. Shaw. “Thermomechanical aspects of NiTi”. In: *Journal of the Mechanics and Physics of Solids* 43.8 (1995), pp. 1243–1281. DOI: 10.1016/0022-5096(95)00024-D.

[260] Dieter Stoeckel. “The Shape Memory Effect - Phenomenon, Alloys, and Applications”. In: *Shape Memory Alloys for Power Systems EPRI*. 1995, pp. 1–13. URL: https://www.nitinol.com/wp-content/uploads/2012/01/038.pdf.

[261] L. Catherine Brinson. “One-Dimensional Constitutive Behavior of Shape Memory Alloys: Thermomechanical Derivation with Non-Constant Material Functions and Redefined Martensite Internal Variable”. In: *Journal of Intelligent Material Systems and Structures* 4.2 (1993), pp. 229–242. DOI: 10.1177/1045389X9300400213.

[262] L. Catherine Brinson and R. Lammering. “Finite element analysis of the behavior of shape memory alloys and their applications”. In: *International Journal of Solids and Structures* 30.23 (1993), pp. 3261–3280. DOI: 10.1016/0020-7683(93)90113-L.

[263] S. Fu, Y. Huo, and I. Müller. “Thermodynamics of pseudoelasticity - an analytical approach”. In: *Acta Mechanica* 99 (1993). DOI: 10.1007/BF01177231.

[264] T. I. Liu, E. J. Ko, and J. Lee. “Intelligent control of dynamic systems”. In: *Journal of the Franklin Institute* 330.3 (1993), pp. 491–503. DOI: 10.1016/0016-0032(93)90095-C.

[265] P. G. McCormick, Yinong Liu, and S. Miyazaki. “Intrinsic thermal-mechanical behaviour associated with the stress-induced martensitic transformation in NiTi”. In: *Materials Science and Engineering: A* 167.1-2 (1993), pp. 51–56. DOI: 10.1016/0921-5093(93)90336-D.

[266] C. M. Wayman. “Shape Memory Alloys”. In: *MRS Bulletin* 18.4 (1993), pp. 49–56. DOI: 10.1557/S0883769400037350.

[267] Manfred Achenbach. “A model for an alloy with shape memory”. In: *International Journal of Plasticity* 5.4 (1989), pp. 371–395. DOI: 10.1016/0749-6419(89)90023-5.

[268] S. Miyazaki and K. Otsuka. “Mechanical behaviour associated with the premartensitic rhombohedral-phase transition in a Ti50 Ni47 Fe3 alloy”. In: *Philosophical Magazine A* 50.3 (1985), pp. 393–408. DOI: 10.1080/01418618408244235.

[269] K. Mukherjee, S. Sircar, and Narendra B. Dahotre. “Thermal effects associated with stress-induced martensitic transformation in a TiNi alloy”. In: *Materials Science and Engineering* 74.1 (1985), pp. 75–84. DOI: 10.1016/0025-5416(85)90111-9.

[270] R. Salzbrenner. “Shape memory heat engines”. In: *Journal of Materials Science* 19.6 (1984), pp. 1827–1835. DOI: 10.1007/BF00550253.

[271] L. C. Brown. “The Thermal Effect in Pseudoelastic Single Crystals of β-CuZnSn”. In: *Metallurgical Transactions A* 12.8 (1981), pp. 1491–1494. DOI: 10.1007/BF02643695.

[272] B. P. Leonard. “A stable and accurate convective modelling procedure based on quadratic upstream interpolation”. In: *Computer Methods in Applied Mechanics and Engineering* 19.1 (1979), pp. 59–98. DOI: 10.1016/0045-7825(79)90034-3.

[273] S. W. Churchill and M. Bernstein. “A Correlating Equation for Forced Convection From Gases and Liquids to a Circular Cylinder in Crossflow”. In: *Journal of Heat and Mass Transfer* 99.2 (1977), pp. 300–306. DOI: 10.1115/1.3450685.

[274] Richard E. Ewing. “Numerical Solution of Sobolev Partial Differential Equations”. In: *Journal on Numerical Analysis* 12.3 (1975), pp. 345–363. DOI: 10.1137/0712028.

[275] Stephen Whitaker. "Forced convection heat transfer correlations for flow in pipes, past flat plates, single cylinders, single spheres, and for flow in packed beds and tube bundles". In: *AIChE Journal* 18.2 (1972), pp. 361–371. DOI: 10.1002/aic.690180219.

[276] W. J. Buehler, J. V. Gilfrich, and R. C. Wiley. "Effect of Low-Temperature Phase Changes on the Mechanical Properties of Alloys near Composition TiNi". In: *Journal of Applied Physics* 34.5 (1963), pp. 1475–1477. DOI: 10.1063/1.1729603.

[277] L. C. Chang and T. A. Read. "Plastic Deformation and Diffusionless Phase Changes in Metals — the Gold-Cadmium Beta Phase". In: *JOM* 3.1 (1951), pp. 47–52. DOI: 10.1007/BF03398954.

[278] Lewis F. Moody. "Friction Factors for Pipe Flow". In: *Journal of Fluids Engineering* 66.8 (1944), pp. 671–678. DOI: 10.1115/1.4018140.

[279] J. P. Joule. "V. On some thermo-dynamic properties of solids". In: *Philosophical Transactions* 149 (1859), pp. 91–131. DOI: 10.1098/rstl.1859.0005.

[280] Holme. "VII. A description of a property of caoutchouc, or indian rubber; with some reflections on the cause of the elasticity of this substance. In a letter to Dr. Holme". In: *The Philosophical Magazine* 24.93 (1806), pp. 39–43. DOI: 10.1080/14786440608563329.

Zusammenfassung

Deutsch

Diese Arbeit entwickelt ein Multiphysik-Simulationspaket für mehrelementige, elastokalorische Wärmepumpen (ekWP), basierend auf dem thermo-mechanisch gekoppelte Verhalten von Formgedächnislegierungen (FGL).
Zum Verständnis der Phasentransformation in FGL, wird ein physikbasiertes, ortsaufgelöstes Modell auf der Grundlage von Müller-Achenbach-Seelecke entwickelt und anhand von Dünnfilmexperimenten validiert.
Der entwickelte Materialprüfstand erlaubt die Kalibrierung anwendungsbezogener Materialmodelle durch Messung der ortsaufgelösten Dehnungs- und Temperaturverteilung im Probekörper. Dadurch wird die vollständige Charakterisierung der thermo-mechanischen Materialparameter in einem einzigen Prüfstand unter ähnlichen Bedingungen wie in realen ekWP möglich.
Das Systemmodell für ekWP wird entsprechend der Kinematik und Fluidik des realen Systems in MATLAB implementiert. Um den Einfluss unterschiedlicher Parameter systematisch zu untersuchen und auszuwerten, wird das Berechnungsmodell in eine Steuerungs- und Datenvisualisierungsumgebung eingebettet.
Mit dem entwickelten Simulationspaket wird das Systemverhalten der ekWP unter verschiedenen Lastprofile, Systemabmessungen, Rotationsfrequenzen, Durchflussraten, Dehnungen und Systemverluste für verschiedene FGL und Wärmeträger simuliert, verglichen und interpretiert. Abschließend wird die Vielseitigkeit des Simulationspakets durch die Verwendung des Systems als Niedertemperatur-Wärmekraftmaschine demonstriert.

Englisch

This work develops a multi-physics simulation tool for multi-element elastocaloric (EC) heat pumps (HPs), based on the thermo-mechanical coupled behavior of shape memory alloys (SMAs).
To understand the phase transformation behavior of SMAs, a physics-based localized model adapted from the Müller-Achenbach-Seelecke is developed and validated using thin-film experiments.
The developed material test bench enables the calibration of application-related material models by measuring the specimen's local strain and temperature distribution. Therefore, it enables the complete characterization of the thermo-mechanical material parameters in a single test bench under similar conditions as in real EC HPs.
The EC HP system simulation model is implemented in MATLAB according to the kinematics and fluidics of a real system. To systematically investigate and evaluate the influence of different parameters, the calculation model is embedded in a control and data visualization environment.
Using the developed simulation tool, the EC HP system behavior is simulated, compared, and interpreted under various load profiles, system dimensions, rotation frequencies, flow rates, strains, and system losses for different SMA materials and heat exchange fluids. Finally, the versatility of the simulation tool is demonstrated by performing a parameter study using the system as a low-temperature heat engine.

Publikationen

Patente

[P1] Susanne-Marie Kirsch, Felix Welsch, et al. “Linearstellgeber mit variabler Einstellung einer Steifigkeit”. DE102023136664. 2023.

[P2] Susanne-Marie Kirsch, Felix Welsch, and Stefan Seelecke. “Verfahren zum Herstellen eines Drahtbündel-Aktorelements aus thermoelastischen Aktordrahtabschnitten sowie Drahtbündel-Aktorelement”. DE102021127368. 2021.

[P3] Susanne-Marie Kirsch, Felix Welsch, and Stefan Seelecke. “Energiewandler mit einer thermoelastischen Wandleranordnung sowie Verfahren zur Herstellung einer thermoelastischen Wandleranordnung für einen Energiewandler”. DE102020110694; EP4139572; WO2021213933. 2020.

[P4] Susanne-Marie Kirsch, Felix Welsch, and Stefan Seelecke. “Solid-state-based energy converter, heating/cooling apparatus comprising such an energy converter, and methode for operating a heatin/cooling apparatus”. CN114144626; DE102019113696; EP3973181; US12006920; US2022228575; WO2020234235. 2019.

[P5] Susanne-Marie Kirsch, Felix Welsch, and Stefan Seelecke. “Energiewandler mit thermoelastischer Anordnung sowie Heiz-/Kühlsystem”. DE102016118776; EP3306082. 2016.

Journal paper

[J1] Rawan Barakat, Susanne-Marie Kirsch, et al. “Bidirectional rotational antagonistic shape memory alloy actuators for high-frequency artificial muscles”. In: *Scientific Reports* 15.1 (2025), p. 9108. DOI: 10.1038/s41598-025-93209-9.

[J2] David Zimmermann, Franziska Louia, et al. “Modeling Moist Air Effects and Shape Memory Alloys in Elastocaloric Devices”. In: *Energy Materials* 12 (2025). DOI: 10.3389/fmats.2025.1559800.

[J3] Bergita Ganse, Marcel Orth, et al. “Concepts and clinical aspects of active implants for the treatment of bone fractures”. In: *Acta Biomaterialia* 146 (2022). DOI: 10.1016/j.actbio.2022.05.001.

[J4] Sergej Grednev, Stefan Bronder, et al. “Applicability of correlated digital image correlation and infrared thermography for measuring mesomechanical deformation in foams and auxetics”. In: *GAMM-Mitteilungen* 45.3-4 (2022). DOI: 10.1002/gamm.202200014.

[J5] Bettina Fasolt, Felix Welsch, et al. “Effect of actuation parameters and environment on the breakdown voltage of silicone dielectric elastomer films”. In: *Smart Materials and Structures* 28.9 (2019). DOI: 10.1088/1361-665X/ab2f34.

[J6] Anne Jung, K. Al Majthoub, et al. “Correlative digital image correlation and infrared thermography measurements for the investigation of the mesoscopic deformation behaviour of foams”. In: *Journal of the Mechanics and Physics of Solids* 130 (2019), pp. 165–180. DOI: 10.1016/j.jmps.2019.06.009.

[J7] Nicolas Michaelis, Andreas Schütze, et al. “Novel Experimental Approach to Determine Elastocaloric Latent Heat”. In: *Shape Memory and Superelasticity* 5.4 (2019), pp. 352–361. DOI: 10.1007/s40830-019-00249-y.

[J8] Nicolas Michaelis, Felix Welsch, et al. “Experimental parameter identification for elastocaloric air cooling”. In: *International Journal of Refrigeration* 100 (2019), pp. 167–174. DOI: 10.1016/j.ijrefrig.2019.01.006.

[J9] Nicolas Michaelis, Felix Welsch, et al. “Resistance monitoring of shape memory material stabilization during elastocaloric training”. In: *Smart Materials and Structures* 28.10 (2019). DOI: 10.1088/1361-665X/ab3d62.

[J10] Susanne-Marie Kirsch, Felix Welsch, et al. “NiTi-Based Elastocaloric Cooling on the Macroscale: From Basic Concepts to Realization”. In: *Energy Technology* 6.8 (2018), pp. 1567–1587. DOI: 10.1002/ente.201800152.

[J11] Felix Welsch, Johannes Ullrich, et al. “Numerical simulation and experimental investigation of the elastocaloric cooling effect in sputter-deposited TiNiCuCo thin films”. In: *Continuum Mechanics and Thermodynamics* 30.1 (2018), pp. 53–68. DOI: 10.1007/s00161-017-0582-x.

Conference paper

[C1] Rawan Barakat, Susanne-Marie Kirsch, et al. “High-Frequently SMA actuation based on Micro-Wire bundling”. In: *SMST - International Conference on Shape Memory and Superelastic Technologies*. ASM International, 2024. URL: https://asm.confex.com/asm/smst24/webprogram/Paper59928.html.

[C2] Susanne-Marie Kirsch, Felix Welsch, et al. “SMA Micro-Wire Bundle With High Cyclic Actuation Frequency”. In: *SMASIS - Conference on Smart Materials, Adaptive Structures and Intelligent Systems*. ASME, 2023. DOI: 10.1115/SMASIS2023-110997.

[C3] Susanne-Marie Kirsch, Felix Welsch, et al. “Systematic Thermo-Mechanical Validation of Numerous Tensile-Loaded NiTi Wire Bundles Used for Elastocaloric Heating and Cooling”. In: *SMASIS - Conference on Smart Materials, Adaptive Structures and Intelligent Systems*. ASME, 2023. DOI: 10.1115/SMASIS2023-110889.

[C4] Felix Welsch, Susanne-Marie Kirsch, et al. “Active Implant System Based on SMA Actuators for Improved Bone Fracture Healing”. In: *SMASIS - Conference on Smart Materials, Adaptive Structures and Intelligent Systems*. ASME, 2023. DOI: 10.1115/SMASIS2023-110858.

[C5] Felix Welsch, Susanne-Marie Kirsch, et al. “Investigation of the thermal heat exchange between NiTi-wire bundles and airflow for different wire arrangements.” In: *SMASIS - Conference on Smart Materials, Adaptive Structures and Intelligent Systems*. ASME, 2023. DOI: 10.1115/SMASIS2023-111395.

[C6] Christian Grossmann, Burkhard Maass, et al. “Mechanical properties and latent heats of low hysteresis NiTi shape memory alloy components for elastocaloric cooling applications”. In: *SMST - International Conference on Shape Memory and Superelastic Technologies*. ASM International, 2022. URL: https://asm.confex.com/asm/smst22/webprogram/Paper54932.html.

[C7] Lukas Längler, Susanne-Marie Kirsch, et al. “Development and Comparison of Design Concepts for Elastocaloric Cooling and Heating Devices”. In: *SMST - International Conference on Shape Memory and Superelastic Technologies*. ASM International, 2022. URL: https://asm.confex.com/asm/smst22/webprogram/Paper54893.html.

[C8] Nicolas Michaelis, Felix Welsch, et al. “Impedance based Fatigue Monitoring of Shape Memory Alloys in Elastocaloric Applications”. In: *SMST - International Conference on Shape Memory and Superelastic Technologies*. ASM International, 2022. URL: https://asm.confex.com/asm/smst22/webprogram/Paper54918.html.

[C9] Claudia Daut, Susanne-Marie Kirsch, et al. “Optimization and experimental validation of a vacuum suction cup operated by shape memory actuators”. In: *SMASIS - Conference on Smart Materials, Adaptive Structures and Intelligent Systems*. ASME, 2021. DOI: 10.1115/SMASIS2021-67934.

[C10] Michele A. Mandolino, Felix Welsch, et al. “Hybrid dynamical model for elastocaloric heating and cooling device based on shape memory alloy wires”. In: *ACTUATOR - International Conference and Exhibition on New Actuators and Drive Systems*. VDE, 2021. ISBN: 9783-8007-5454-0.

[C11] Lukas Zimmer, Felix Welsch, et al. “Development of an sma based end-effector prototype for material handling in manufacturing processes”. In: *ACTUATOR - International Conference and Exhibition on New Actuators and Drive Systems*. VDE, 2021. ISBN: 9783-8007-5454-0.

[C12] Susanne-Marie Kirsch, Felix Welsch, et al. “SMA Antagonistic-Micro-Wire Bundle - First Measurement Results”. In: *SMASIS - Conference on Smart Materials, Adaptive Structures and Intelligent Systems*. ASME, 2020. DOI: 10.1115/SMASIS2020-2261.

[C13] Susanne-Marie Kirsch, Felix Welsch, et al. “SMA Antagonistic-Micro-Wire Bundle - First measurement Results - Presentation”. In: *SMASIS - Conference on Smart Materials, Adaptive Structures and Intelligent Systems*. ASME, 2020.

[C14] Nicolas Michaelis, Susanne-Marie Kirsch, et al. “Investigation of Elastocaloric Air Cooling potential based on Superelastic SMA wire bundles”. In: *SMASIS - Conference on Smart Materials, Adaptive Structures and Intelligent Systems*. ASME, 2020. DOI: 10.1115/SMASIS2020-2404.

[C15] Felix Welsch, Susanne-Marie Kirsch, et al. “System simulation of an elastocaloric heating and cooling device based on SMA”. In: *SMASIS - Conference on Smart Materials, Adaptive Structures and Intelligent Systems*. ASME, 2020. DOI: 10.1115/SMASIS20-2262.

[C16] Felix Welsch, Susanne-Marie Kirsch, et al. “System simulation of an elastocaloric heating and cooling device based on SMA - Presentation”. In: *SMASIS - Conference on Smart Materials, Adaptive Structures and Intelligent Systems*. ASME, 2020.

[C17] Lukas Zimmer, Felix Welsch, et al. “Adaptive material handling system based on shape memory alloy actuators”. In: *SMASIS - Conference on Smart Materials, Adaptive Structures and Intelligent Systems*. ASME, 2020. DOI: 10.1115/SMASIS2020-2280.

[C18] Susanne-Marie Kirsch, Felix Welsch, and Iryna Work. *Episode 21 - Susanne-Marie Kirsch talks about a new tech to replace existing vapor-compression refrigeration systems - Podcast*. 2019. URL: https://www.instagram.com/p/Bx0tLg0lzxT/.

[C19] Susanne-Marie Kirsch, Felix Welsch, et al. “Continuous operating elastocaloric cooling device: First experimental results”. In: *SMST - International Conference on Shape Memory and Superelastic Technologies*. ASM International, 2019. URL: https://asm.confex.com/asm/smst19/webprogram/Paper47348.html.

[C20] Susanne-Marie Kirsch, Felix Welsch, et al. “Continuous operating elastocaloric cooling device: First experimental results - Presentation”. In: *SMST- International Conference on Shape Memory and Superelastic Technologies*. ASM International, 2019.

[C21] Susanne-Marie Kirsch, Felix Welsch, et al. “Continuous operating elastocaloric heating and cooling device: Air flow investigation and experimental parameter study”. In: *SMASIS - Conference on Smart Materials, Adaptive Structures and Intelligent Systems*. ASME, 2019. DOI: 10.1115/SMASIS2019-5633.

[C22] Susanne-Marie Kirsch, Felix Welsch, et al. “Continuous Operating Elastocaloric Heating and Cooling Device: Air Flow Investigation and Experimental Parameter Study - Presentation”. In: *SMASIS - Conference on Smart Materials, Adaptive Structures and Intelligent Systems*. ASME, 2019.

[C23] Susanne-Marie Kirsch, Felix Welsch, et al. “Elastocaloric Cooling From Basic Concepts to Realization - Invited Talk”. In: *Deutsche Kälte- und Klimatagung*. Deutscher Kälte- u. Klimatechnik Verband, 2019. ISBN: 9783-932715-52-5.

[C24] Nicolas Michaelis, Andreas Schütze, et al. “Experimental determination of elastocaloric latent heat”. In: *SMST - International Conference on Shape Memory and Superelastic Technologies*. ASM International, 2019, pp. 212–213. ISBN: 9781-5108-9272-9.

[C25] Felix Welsch, Susanne-Marie Kirsch, et al. “A fully-coupled simulation tool for elastocaloric air-cooling devices”. In: *IUTAM Symposium: Phase Transformations in Shape Memory Materials: Modeling and Applications*. 2019. URL: https://sites.utexas.edu/cmssm/files/2021/07/SMA-IUTAM-2019-Program.pdf.

[C26] Felix Welsch, Susanne-Marie Kirsch, et al. “A fully-coupled simulation tool for elastocaloric air-cooling devices - Presentation”. In: *IUTAM Symposium: Phase Transformations in Shape Memory Materials: Modeling and Applications*. Austin, Texas, USA: The University of Texas at Austin, 2019, pp. 51–54. URL: https://sites.utexas.edu/cmssm/files/2021/07/SMA-IUTAM-2019-Program.pdf.

[C27] Felix Welsch, Susanne-Marie Kirsch, et al. “Continuous operating elastocaloric cooling device: First modeling results - Presentation”. In: *SMST - International Conference on Shape Memory and Superelastic Technologies*. ASM International, 2019.

[C28] Felix Welsch, Susanne-Marie Kirsch, et al. “Continuous operating elastocaloric cooling device: First modelling results”. In: *SMST - International Conference on Shape Memory and Superelastic Technologies*. ASM International, 2019. URL: https://asm.confex.com/asm/smst19/webprogram/Paper47996.html.

[C29] Felix Welsch, Susanne-Marie Kirsch, et al. “Continuous Operating Elastocaloric Heating and Cooling Device: Model-Based Parameter Study With Airflow Losses”. In: *SMASIS - Conference on Smart Materials, Adaptive Structures and Intelligent Systems*. ASME, 2019. DOI: 10.1115/SMASIS2019-5636.

[C30] Felix Welsch, Susanne-Marie Kirsch, et al. “Continuous Operating Elastocaloric Heating and Cooling Device: Model-Based Parameter Study With Airflow Losses - Presentation”. In: *SMASIS - Conference on Smart Materials, Adaptive Structures and Intelligent Systems*. ASME, 2019. URL: https://asmedigitalcollection.asme.org/SMASIS/proceedings/SMASIS2019/59131/Louisville,%20Kentucky,%20USA/1071369.

[C31] Felix Welsch, Susanne-Marie Kirsch, et al. “Elastocalorics – SMA-Based Cooling Technology for the Future - Invited Talk”. In: *VDI-Expertenforum: Smart Materials – aus der Forschung in die industrielle Anwendung*. VDI, 2019.

[C32] Rouven Britz, Felix Welsch, et al. “SMA Wire Bundles - Mechanical and Electrical Concepts”. In: *ACTUATOR - International Conference and Exhibition on New Actuators and Drive Systems*. VDE, 2018. ISBN: 9783-8007-4675-0.

[C33] Rouven Britz, Felix Welsch, et al. “SMA Wire Bundles - Mechanical and Electrical Concepts - Poster”. In: *ACTUATOR - International Conference and Exhibition on New Actuators and Drive Systems*. VDE, 2018.

[C34] Susanne-Marie Kirsch, Felix Welsch, et al. “Bistable SMA Vacuum Suction Cup”. In: *ACTUATOR - International Conference and Exhibition on New Actuators and Drive Systems*. VDE, 2018. ISBN: 9783-8007-4675-0.

[C35] Susanne-Marie Kirsch, Felix Welsch, et al. “Bistable SMA Vacuum Suction Cup: Development and Realization - Presentation”. In: *ACTUATOR - International Conference and Exhibition on New Actuators and Drive Systems*. VDE, 2018.

[C36] Susanne-Marie Kirsch, Felix Welsch, et al. “Continuously Operating Elastocaloric Cooling Device based on Shape Memory Alloys: Development and Realization”. In: *Thermag - International Conference on Caloric Cooling*. IIR, 2018. DOI: 10.18462/iir.thermag.2018.0039.

[C37] Susanne-Marie Kirsch, Felix Welsch, et al. “Continuously Operating Elastocaloric Cooling Device based on Shape Memory Alloys: Development and Realization - Poster”. In: *Thermag - International Conference on Caloric Cooling*. IIR, 2018. DOI: 10.18462/iir.thermag.2018.0039.

[C38] Susanne-Marie Kirsch, Felix Welsch, et al. “Elastocalorics - Ultra-efficient cooling systems - Invited Talk”. In: *VDI Workshop: Funktionale Materialien für mechatronische Systeme*. VDI, 2018.

[C39] Nicolas Michaelis, Felix Welsch, et al. “Investigation of single wire elastocaloric air cooling potential”. In: *Thermag - International Conference on Caloric Cooling*. IIR, 2018. DOI: 10.18462/iir.thermag.2018.0027.

[C40] Nicolas Michaelis, Felix Welsch, et al. “Investigation of single wire elastocaloric air cooling potential - Poster”. In: *Thermag - International Conference on Caloric Cooling*. IIR, 2018. DOI: 10.18462/iir.thermag.2018.0027.

[C41] Stefan Seelecke, Felix Welsch, and Bettina Fasolt. “Dielectric breakdown test setup for dielectric elastomers: design and validation”. In: *SPIE - Electroactive Polymer Actuators and Devices (EAPAD)*. Ed. by Yoseph Bar-Cohen. 105941A. SPIE, Mar. 2018. DOI: 10.1117/12.2296995.

[C42] Felix Welsch, Susanne-Marie Kirsch, et al. “Continuously Operating Elastocaloric Cooling Device based on Shape Memory Alloys: Modeling”. In: *Thermag - International Conference on Caloric Cooling*. IIR, 2018. DOI: 10.18462/iir.thermag.2018.0040.

[C43] Felix Welsch, Susanne-Marie Kirsch, et al. “Continuously Operating Elastocaloric Cooling Device based on Shape Memory Alloys: Modeling - Poster”. In: *Thermag - International Conference on Caloric Cooling*. IIR, 2018. DOI: 10.18462/iir.thermag.2018.0040.

[C44] Felix Welsch, Susanne-Marie Kirsch, et al. “Elastocaloric cooling: System design, simulation, and realization”. In: *SMASIS - Conference on Smart Materials, Adaptive Structures and Intelligent Systems*. ASME, 2018. DOI: 10.1115/SMASIS2018-7982.

[C45] Felix Welsch, Susanne-Marie Kirsch, et al. “Vacuum Gripper System based on Bistable SMA Actuation”. In: *SMASIS - Conference on Smart Materials, Adaptive Structures and Intelligent Systems*. Vol. 1. ASME, 2018, SMASIS2018–7980. DOI: 10.1115/smasis2018-7980.

[C46] Felix Welsch, Susanne-Marie Kirsch, et al. “Vacuum Gripper System Based on Bistable SMA Actuation - Poster”. In: *SMASIS - Conference on Smart Materials, Adaptive Structures and Intelligent Systems*. ASME, 2018. DOI: 10.1115/smasis2018-7980.

[C47] Susanne-Marie Kirsch, Marvin Schmidt, et al. “Development of a shape memory based air conditioning system”. In: *Scientific Colloquium*. Vol. 59. 3.1.03. Technische Universität Ilmenau, 2017. URL: https://www.db-thueringen.de/receive/dbt%7B%5C_%7Dmods%7B%5C_%7D00033169%20urn:nbn:de:gbv:ilm1-2017iwk-046:4.

Elektronische Version der Dissertation

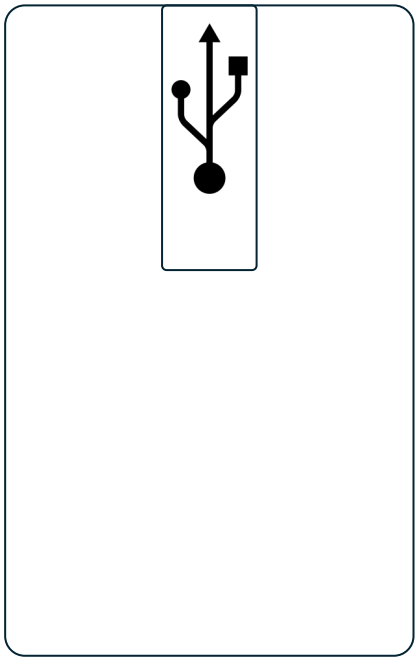

Dokument erzeugt am: 22.04.2025, 16:58:53 MESZ

Eidesstattliche Versicherung

Hiermit versichere ich an Eides statt, dass ich die vorliegende Arbeit selbstständig und ohne Benutzung anderer als der angegebenen Hilfsmittel angefertigt habe. Die aus anderen Quellen oder indirekt übernommenen Daten und Konzepte sind unter Angabe der Quelle gekennzeichnet.

Die Arbeit wurde bisher weder im In- noch im Ausland in gleicher oder ähnlicher Form in einem Verfahren zur Erlangung eines akademischen Grades vorgelegt.

Ich erkläre darüber hinaus mit meiner Unterschrift, dass ich

- keine im Merkblatt "Hinweise zur Vermeidung von Plagiaten" der Naturwissenschaftlich-Technischen Fakultät beschriebenen Form des Plagiats begangen habe,
- alle Methoden, Daten und Arbeitsabläufe wahrheitsgetreu dokumentiert habe und
- keine Daten manipuliert habe.

Ich versichere, dass die eingereichte gedruckte Version der Dissertation mit der elektronischen Fassung bei Abgabe übereinstimmt.

Zusätzlich bin ich mit einer Überprüfung der Arbeit mittels einer Plagiatssoftware, sowie der damit verbundenen Speicherung in einer Datenbank externer Dienste einverstanden.

Saarbrücken, den 22.04.2025	
Ort, Datum	M.Sc. Felix Ulrich Welsch